BEILSTEIN JOURNAL OF NANOTECHNOLOGY

Materials for sustainable energy production, storage, and conversion

Edited by Maximilian Fichtner

Imprint

Beilstein Journal of Nanotechnology
www.bjnano.org
ISSN 2190-4286
Email: journals-support@beilstein-institut.de

The *Beilstein Journal of Nanotechnology* is published by the Beilstein-Institut zur Förderung der Chemischen Wissenschaften.

Beilstein-Institut zur Förderung der Chemischen Wissenschaften
Trakehner Straße 7–9
60487 Frankfurt am Main
Germany
www.beilstein-institut.de

BEILSTEIN JOURNAL OF NANOTECHNOLOGY

Materials for sustainable energy production, storage, and conversion

Maximilian Fichtner

Editorial

Open Access

Address:
Helmholtz Institut Ulm (HIU), Helmholtzstraße 11, 89081 Ulm, Germany

Email:
Maximilian Fichtner - maximilian.fichtner@kit.edu

Beilstein J. Nanotechnol. **2015,** *6,* 1601–1602.
doi:10.3762/bjnano.6.163

Received: 24 June 2015
Accepted: 17 July 2015
Published: 23 July 2015

The article is part of the Thematic Series "Materials for sustainable energy production, storage, and conversion".

Editor-in-Chief: T. Schimmel

A steadily growing human population and the growing global economy have led to increasing energy consumption and the realization that fossil fuels are a finite resource on earth. Moreover, due to the rising global temperature, there is a need to reduce CO_2 emissions to mitigate or prevent further global warming. Both needs have fueled international efforts to convert the current energy supply strategy into an economy which must eventually be based on renewable energy sources such as solar, wind, biomass, geothermal, and water power. Hence, these factors have driven the intensified and ever-growing interest in the fields of energy harvesting and storage seen during the past two decades.

The harvesting of light is still a challenge, and solutions are needed to achieve both high efficiency and low cost electricity generation. While wind and sun are among the most powerful options for electricity generation in general, their intermittent nature makes large storage capacity necessary. Storage is also needed to balance electricity grids and to avoid overcapacity.

A particular challenge is the storage of electrical energy for stationary, mobile, and portable applications. Here, solutions are needed that are based either on chemical compounds, such as hydrogen or hydrocarbons, or on safe, low cost and powerful batteries, which have a long cycle and calendar life and a high energy density. At the same time, any long term option for energy storage must be based on sustainable materials involving abundant elements in the Earth's crust. For the reconversion of hydrogen or organic liquids (energy carriers), efficient fuel cells are needed as converters, preferably those based on non-noble metals with a long lifetime and a low kinetic barrier for conversion. For electrochemical storage, batteries based on new ionic shuttles such as sodium or magnesium are being explored. Moreover, oxygen from air could serve as an active cathode material, which does not need to be intrinsically integrated in the cell.

In addition to the harvesting and storage of electrical energy, the storage of heat is another essential element in the future

energy landscape. Thus, the heating of homes and the efficiency of industrial processes will greatly benefit from the availability of cost efficient, heat storage devices.

This Thematic Series collects selected contributions from the last Materials for Energy Conference (ENMAT 2013) in Karlsruhe, Germany, which addressed important research topics in the abovementioned fields. The articles summarize the state-of-the art in the field, give perspectives, and present recent results from the respective working groups.

In the field of energy harvesting and photovoltaics, Benedikt Iffland and Christian Jooss [1] report on current–voltage characteristics of manganite–titanite perovskite junctions. State-of-the art and recent progress in energy conversion from chemical carriers are discussed in two contributions covering materials issues in two different types of fuel cells: Gregorii L. Soloveichik reports on challenges and perspectives in the field of liquid fuel cells [2]. Materials issues in polymer electrolyte membrane fuel cells operating at moderately elevated temperatures (HT-PEMFC) below 200 °C are discussed by Roswitha Zeis [3].

The field of electrochemical energy storage is particularly challenging. Current Li-ion batteries are not only expensive and have a relatively short lifetime, they are also considered to not have enough energy content to meet the demands of future applications. Efficient systems based on powerful and sustainable materials beyond lithium are needed in order to provide long term solutions. In this respect, three contributions were selected from Rana Mohtadi, Luc Aymard, and Philip Adelhelm [4-6], presenting the progress on novel systems involving Mg batteries, conversion electrodes based on hydrides, and Na and Li air batteries, respectively. In the fields of fuel cells and batteries, multiscale theoretical modeling is considered to be essential to both understand the structures and energetics of energy materials as well as their function when integrated into a battery electrode. Not only can a better understanding of the transport processes and chemical reactions at the microscale be gathered, but also the development of strategies for optimizing the electrode. Such a multiscale modeling approach is presented with examples in the contribution by Arnulf Latz and Jochen Zausch [7]. Last but not least, Nicole Pfleger, Antje Wörner and colleagues [8] discuss the current state-of-the art and future options for thermal storage using nitrate salts.

I would like to thank all authors and the referees for their effort and excellent contributions. Special thanks go to the team at the Beilstein Journal of Nanotechnology for their continuous support in the handling of this series. The open access policy of the Beilstein-Institut was a strong motivation for both the editor and the authors of this series to contribute, as colleagues from all over the world are able to freely access the contributions in this journal. Finally, I would like to thank the DECHEMA for their strong and highly professional support in realizing the ENMAT conference.

Maximilian Fichtner

Ulm, June 2015

References

1. Ifland, B.; Peretzki, P.; Kressdorf, B.; Saring, P.; Kelling, A.; Seibt, M.; Jooss, C. *Beilstein J. Nanotechnol.* **2015,** *6,* 1467–1484. doi:10.3762/bjnano.6.152
2. Soloveichik, G. I. *Beilstein J. Nanotechnol.* **2014,** *5,* 1399–1418. doi:10.3762/bjnano.5.153
3. Zeis, R. *Beilstein J. Nanotechnol.* **2015,** *6,* 68–83. doi:10.3762/bjnano.6.8
4. Mohtadi, R.; Mizuno, F. *Beilstein J. Nanotechnol.* **2014,** *5,* 1291–1311. doi:10.3762/bjnano.5.143
5. Aymard, L.; Oumellal, Y.; Bonnet, J.-P. *Beilstein J. Nanotechnol.* **2015,** in press.
6. Adelhelm, P.; Hartmann, P.; Bender, C. L.; Busche, M.; Eufinger, C.; Janek, J. *Beilstein J. Nanotechnol.* **2015,** *6,* 1016–1055. doi:10.3762/bjnano.6.105
7. Latz, A.; Zausch, J. *Beilstein J. Nanotechnol.* **2015,** *6,* 987–1007. doi:10.3762/bjnano.6.102
8. Pfleger, N.; Bauer, T.; Martin, C.; Eck, M.; Wörner, A. *Beilstein J. Nanotechnol.* **2015,** *6,* 1487–1497. doi:10.3762/bjnano.6.154

License and Terms

BEILSTEIN JOURNAL OF NANOTECHNOLOGY

Magnesium batteries: Current state of the art, issues and future perspectives

Rana Mohtadi* and Fuminori Mizuno

Review

Open Access

Address:
Materials Research Department, Toyota Research Institute of North America, Ann Arbor MI 48105 (USA), Fax: (+1)734-995-2549

Email:
Rana Mohtadi* - rana.mohtadi@tema.toyota.com

* Corresponding author

Keywords:
cathode; electrolyte; magnesium anode; magnesium battery; magnesium metal

Beilstein J. Nanotechnol. **2014,** *5,* 1291–1311.
doi:10.3762/bjnano.5.143

Received: 18 March 2014
Accepted: 14 July 2014
Published: 18 August 2014

This article is part of the Thematic Series "Materials for sustainable energy production, storage, and conversion".

Guest Editor: M. Fichtner

Abstract

"...each metal has a certain power, which is different from metal to metal, of setting the electric fluid in motion..." Count Alessandro Volta. Inspired by the first rechargeable magnesium battery prototype at the dawn of the 21st century, several research groups have embarked on a quest to realize its full potential. Despite the technical accomplishments made thus far, challenges, on the material level, hamper the realization of a practical rechargeable magnesium battery. These are marked by the absence of practical cathodes, appropriate electrolytes and extremely sluggish reaction kinetics. Over the past few years, an increased interest in this technology has resulted in new promising materials and innovative approaches aiming to overcome the existing hurdles. Nonetheless, the current challenges call for further dedicated research efforts encompassing fundamental understanding of the core components and how they interact with each other to offering new innovative solutions. In this review, we seek to highlight the most recent developments made and offer our perspectives on how to overcome some of the remaining challenges.

Introduction

Fueled by an ever increasing demand for electrical energy to power the numerous aspects of modern human life, energy storage systems or batteries occupy a central role in driving the electrification of our societies [1]. The basic principles of a battery are rather old; its invention by Allessandro Volta dates back to the eighteenth century [2] (archeological findings in the 20th century even suggest that the first battery was developed in Mesopotamia dating back to 2000 BC, to what is referred to as the "Baghdad battery" [3]). Since its invention, and most particularly in the twentieth century, advancements in energy storage technologies continued to evolve over time resulting in a myriad of distinct batteries and energy storage chemistries [1]. Out of the several known battery technologies, secondary or rechargeable batteries, such as nickel metal hydride and

lithium-ion, which allow for reversibly storing and harnessing power on demand while providing high power and energy conversion efficiencies, have played an invaluable role in driving the evolution of new technologies. Nowadays, their usage as an integral part in several modern applications on a variable size scale is apparent, encompassing miniature and portable devices; such as in cell phones, laptops, medium scale; such as in hybrid (HV), plug-in hybrid (PHEV) and electric vehicles (EV) up to large scale stationary and grid applications [1,4]. As one of the scalable battery systems, lithium-ion batteries have been at the forefront in attracting great interests since the great discovery and ingenious use of Li-ion intercalation compounds as negative electrodes [1]. Although the capacities (measure of electrons number obtained from the active material) offered by most common lithium-ion intercalation compounds are lower than those provided by the Li metal (i.e., 372 mAh g^{-1}, 837 mAh cm^{-3} for LiC_6 vs 3862 mAh g^{-1}, 2061 mAh cm^{-3} for Li metal), their specific energy densities were proven to be more competitive than that of other rechargeable batteries, such as nickel (Ni)–metal hydride, Ni-cadmium (Cd), and lead (Pb)–acid (about 2.5 times). They also provide higher specific power and have had long durability [1]. The fascinating advancements in Li-ion batteries have resulted in a state of the art battery which uses graphitized carbon as the anode, a transition metal oxide as the cathode, coupled such that 240 Wh kg^{-1}, 640 Wh L^{-1} are provided for thousands of cycles [1]. The wide spread use of Li-ion battery, has been and remains a testament for the numerous breakthroughs and technical advancements made thus far.

One of the main challenges that current rechargeable battery technologies face is their inability to maintain energy and power densities sufficient to meet those demanded by their applications. In fact, the gap between the energy storage needs and what state of the art systems are capable of providing is increasing. This ever increasing gap has been a persistent force that drove many of the innovations made over the last 40 years [1]. For example, lithium batteries using lithium metal anodes have attracted attention as a candidate to fill up the aforementioned gap. However, this system suffers from the intrinsic property of lithium to form needle-like lithium crystals, known as dendrites, when it is plated. These grow with subsequent plating/stripping cycles, resulting in an internal short circuit and fire hazards [5,6]. While effective countermeasures are still being discussed [6], the birth of the first commercial Li-ion battery in the early 1990s was catalyzed by the need to overcome these challenges. This resulted in a decline in further technical progresses and commercialization of what was referred to as the "ultimate lithium metal anode". If we wish to move forward towards achieving an ultimate energy density goal, technologies beyond Li-ion batteries would be needed. Fortunately, in recent years, such desire has led to an increased interest in other chemistries that employ metals poised to provide higher energy densities without compromising the safety of the battery. For example metals such as magnesium and aluminum were proposed [1,7]. Magnesium metal has been attracting an increased attention as it possesses higher volumetric capacities than lithium metal, i.e., 3832 mAh cm^{-3} vs 2061 mAh cm^{-3} for lithium. It may also provide an opportunity for battery cost reductions due to its natural abundance in the earth crust (5th most abundant element) [7,8]. More importantly, despite the fact that magnesium metal is not competitive with lithium metal on both specific capacity (2205 mAh g^{-1} vs 3862 mAh g^{-1} for lithium) and redox potential levels (−2.3 V compared to −3.0 V for Li vs NHE), the electrochemical processes related to its reversible plating/stripping have demonstrated the absence of dentrites formation which has thus far alleviated safety concerns related to employing it as a negative electrode in batteries [9]. However, several technical challenges that hamper the commercialization of rechargeable magnesium batteries are currently present. In fact, the absence of practical electrolytes and cathodes has confined demonstrations of rechargeable magnesium batteries to research laboratories. That is, low gravimetric energy densities in the order of few hundreds watt hour per kilogram and a limited shown durability coupled with very sluggish kinetics make magnesium batteries currently far from being practical. Fortunately, critical technical advancements geared towards overcoming the existing hurdles are made continuosly [7,9]. These, along with past and future dedicated research efforts, would play a vital role in enabling the maturity and readiness of rechargeable magnesium battery technologies. Herein, a technical review of rechargeable magnesium batteries is provided with focus on the most recent scientific advancements. We provide a brief summary of past breakthroughs as they were comprehensively reviewed elsewhere [7-10]. Keeping in-line with high academic quality, non-peer reviewed articles, patents and conference abstracts are not included. As the battery is a complex system employing several components, the review will individually address progresses related to the major components which are the anode, the electrolyte and the cathode. For each of these components, the existing hurdles are individually outlined and our suggestions for future research needs are provided.

Review

1 Magnesium battery anodes

Since demonstrating the first rechargeable magnesium battery, magnesium metal has been viewed as an attractive battery anode due to the desirable traits outlined in the Introduction. Nonetheless, the undesirable reactivity of this metal coupled with a relatively highly reducing electrochemical environment remains a source of several challenges as explained in subsec-

tion 1.1 Aiming at overcoming these, magnesium ion insertion anodes have been recently proposed and demonstrated. These are explained in subsection 1.2.

1.1 The magnesium metal anode

When discussing the magnesium metal, the nature of its interaction with the electrolyte represents an important and complex topic. That is, interfaces formed on the metal resulting from metal–electrolyte interaction have a direct impact on electrochemical properties related to the dissolution and plating of the metal, i.e., discharge and charge of the battery. Therefore a discussion of the magnesium metal anode is primarily that of its interactions with the electrolytes. In fact, it is well established [7,9-11] that the formation of a surface layer as a result of metal–electrolyte chemical/electrochemical interaction is detrimental for reversible magnesium deposition, as it blocks the diffusion of the magnesium ions thereby preventing reversible electrochemical dissolution and plating from taking place (for illustration see Figure 1). While the nature of this "blocking" layer has not been fully established, its formation was explained by the instability of the electrolytes in proximity of the magnesium metal [11], namely electrolyte decomposition occurred. The passivating nature of this layer is astonishingly in stark contrast to what is observed when analogous electrolytes are in contact with lithium metal as the layer formed, referred to as SEI or solid electrolyte interface, allows for lithium ion diffusion and was proven critical in preventing further decomposition of the electrolyte in the highly reducing environment during lithium plating [5,6].

The challenge resulting from the electrolyte decomposition at the interface of the magnesium metal has plagued the development of electrolytes for rechargeable magnesium batteries. For example, simple ionic magnesium salts such as perchlorates and tetrafluroborates were deemed unsuitable as they formed a blocking layer on the magnesium metal [9-12]. Polar aprotic solvents such carbonates and nitriles also formed a blocking layer on the magnesium metal [9-11]. This exacerbated the challenge of electrolytes development as it limited the choices of electrolytes to a handful of organo-magnesium reagents–solvents combinations which were found to suffer from several disadvantages as described in section 2. Therefore, the discovery of new electrolytes that are compatible with rechargeable magnesium batteries and carry the promise of overcoming the existing hurdles represents an important milestone in the magnesium battery R&D. Section 2 provides a review of a variety of new promising electrolytes which we have categorized based on their type and physical state.

An important property related to the electrochemical plating of magnesium is the morphology of the magnesium deposits. Although reports related to this topic are scarce [9], they show

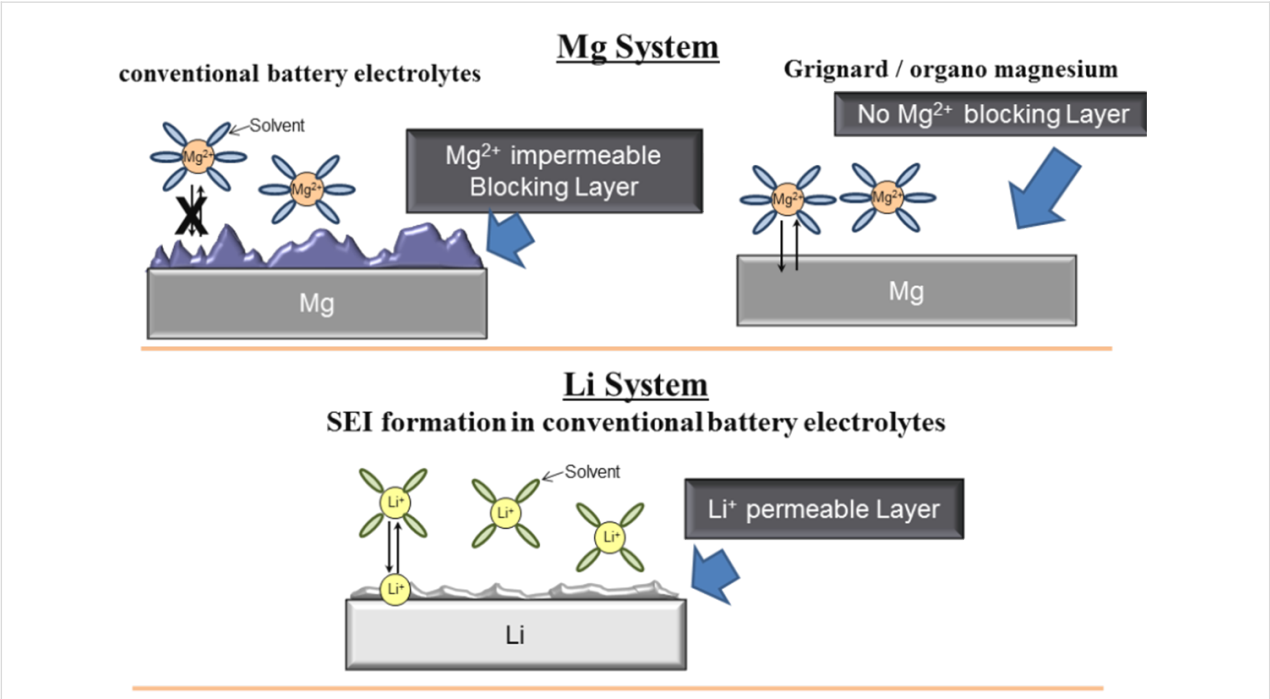

Figure 1: Schematic depicting a simplified image of metal–electrolyte interfaces for magnesium and lithium metals. The magnesium metal case; unlike the lithium, experiences a blocking layer formation when exposed to conventional electrolytes, i.e., ionic salts and polar solvents. No Mg passivation (bare Mg) occurs in ethereal organo-magnesium electrolytes.

the absence of dendritic formations following magnesium plating from organohalo-aluminate electrolytes. A recent systematic study examined the morphology of the magnesium deposits from a magnesium organohalo-aluminate complex function of deposition current densities. Although no dendritic morphologies were observed as in Figure 2, the preferred orientation of the deposits was found to depend on the current densities. For example, the deposits obtained at low current densities exhibited the (001) preferred orientation while the (100) was favored at high current densities [13]. This suggested that crystals growth of deposited magnesium is determined by the thermodynamic stability and the diffusion rates of Mg ions.

1.2 Magnesium ion insertion anodes

In order to overcome limitations of the electrolytes induced by their reactivity with the magnesium metal, insertion type anodes were proposed as one potential solution. As described below, magnesium insertion anodes did offer the opportunity of using electrolytes made from magnesium ionic salts in polar aprotic solvents. However, they are currently faced with challenges caused by extremely sluggish magnesium insertion/extraction kinetics and electrode pulverization due to volume change.

The use of insertion anodes was reported by Arthur et al. [14] who sought to demonstrate the possibility of electrochemical reversible insertion/extraction of magnesium ion into Bi, Sb, $Bi_{0.88}Sb_{0.12}$ and $Bi_{0.55}Sb_{0.45}$ alloys at potentials less than 0.4 V vs Mg using an organohalo-aluminate/tetrahydrofuran electrolyte. While the highest initial specific capacity at 1 C rate was reported for the $Bi_{0.88}Sb_{0.12}$ (298 mAh g^{-1}), it dropped to 215 mAh g^{-1} after 100 cycles. The smallest capacity fade with cycling was observed for the Bi anode (pulverization due to volume expansion during magnesium insertion was observed). They also provided a proof of concept for the possibility of magnesium ions insertion/extraction into Bi from magnesium bis(trifluoromethansulfonyl)imide, $Mg(TFSI)_2$, in acetonitrile solvent, which are known to form a blocking layer on the magnesium metal. Reaction mechanisms of magnesium ion insertion/extraction into these anodes are currently under investigation as the interfaces likely formed on the anode surface are non- or just partially blocking.

Motivated by improving the capacity and lowering the insertion/extraction voltages of the magnesium ion, Singh el. al. [15] utilized Sn to demonstrate reversible and comparable anode performances in both organohalo-aluminate/tetrahydrofuran and

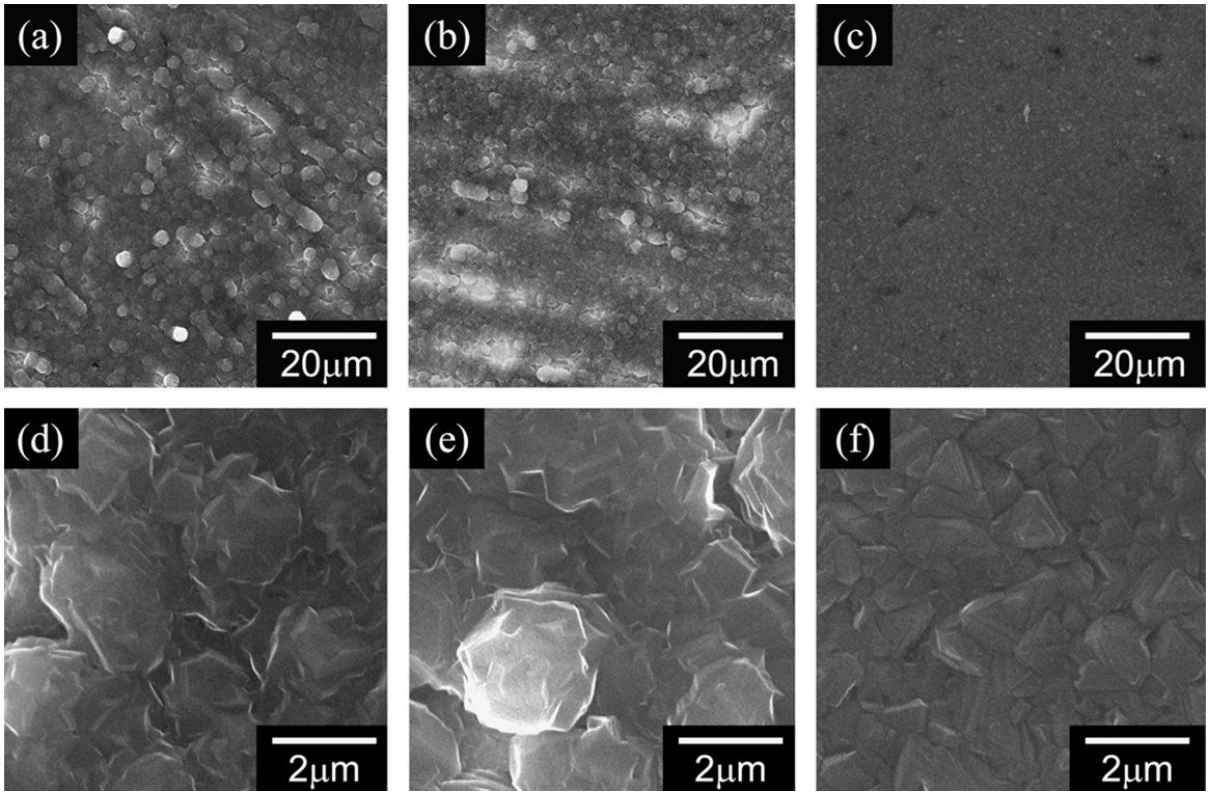

Figure 2: SEM images of the electrodeposited magnesium (a) 500×, 0.5 mA cm^{-2}, (b) 500×, 1.0 mA cm^{-2}, (c) 500×, 2.0 mA cm^{-2}, (d) 5000×, 0.5 mA cm^{-2}, (e) 5000×, 1.0 mA cm^{-2}, and (f) 5000×, 2.0 mA cm^{-2}. Reprinted with permission from [13]. Copyright 2011 Elsevier.

$Mg(TFSI)_2$/acetonitrile electrolytes (Figure 3a). The first insertion cycle showed a magnesiation capacity close to the theoretical value (903 mAh g^{-1} vs 384 mAh g^{-1} for Bi, ran at 0.005 C), a low working potential (0.15 V vs Mg) and lower hysteresis than that afforded by the Bi (50 mV vs 90 mV). Pulverization due to substantial volume expansion during magnesium insertion was also observed. A major challenge with these anodes is the low capacities obtained even at relatively low cycling rates. For example, the capacity when magnesium was inserted at 0.05 C rate into Bi and Sn was maintained at 70% and 20% of the theoretical values, respectively (Figure 3b).

Enhancement of magnesium ion solid state diffusion during the insertion/extraction process is expected to increase the reaction kinetics and improve the capacity retention. Shao et al. [16] recently reported a Bi anode with improved rate capabilities and capacity retention using Bi nanotubes (Figure 3c). The idea was to reciprocate the improved diffusion rates observed for Li ion insertion into nanostructured anodes; i.e., Si and Sn [17,18]. The Bi nanotubes particularly displayed improved rate capabilities, for example, when cycled at a 5 C rate, about 60% of the theoretical capacity was obtained (note that capacity retention was only shown for few cycles). Operation at 0.05 C resulted in a minimal capacity fade of 7.7% after 200 cycles. This was despite the fact that these nanotubes did not retain their structure and converted into what was described as interconnected nanoparticles upon the 1st magnesiation (Figure 3d). Interestingly, in a control experiment, the capacity retention of the nanotubes was found to be higher than that of Bi nanoparticles (fade of 16.2% after 200 cycles). Further studies examining the evolution and nature of structural and morphological transformations during magnesium ion insertion/extraction cycles would be desired.

1.3 Perspectives on future developments of magnesium battery anodes

When it comes to discussing the magnesium metal, the topic is mainly about the nature of the interfaces formed. Under-

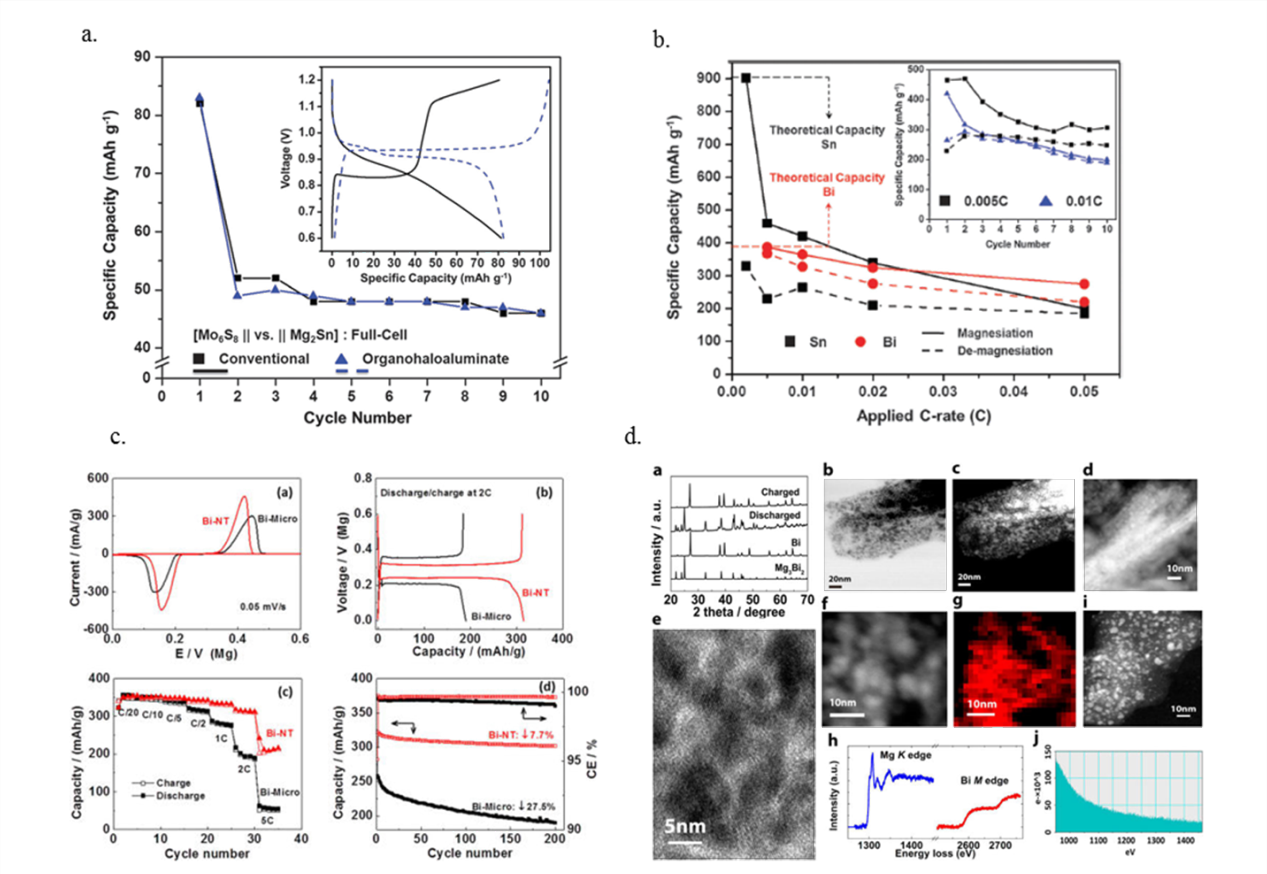

Figure 3: For Sn anode: a) The first 10 cycles for a Mg_2Sn (anode), Mo_6S_8 (cathode) in conventional and organohalo-aluminate electrolytes, inset – 1st cycle voltage profiles; b) insertion/extraction capacities for Sn/Mg and Bi/Mg (half-cells) in an organohaloaluminate electrolyte at various C-rates. Inset – 10 cycles of a Sn/Mg half-cell at 0.005 C and 0.01 C. Figures 3a and 3b are reproduced with permission from [15]. Copyright 2013 The Royal Society of Chemistry. For Bi nanotubes anode: c) Performance comparison between Bi micro and nanotube (half cell); d) Morphology and structure evolution of Bi nanotubes during Mg insertion /extraction. Figure 3c and 3d are reprinted with permission from [16]. Copyright 2013 American Chemical Society.

standing these interfacial layers, as new electrolytes are proposed, goes into the heart of enabling practical rechargeable magnesium batteries. That is, the future knowledge gained may result in discovering or even designing appropriate SEIs. This is important, as one should not forget the role the SEIs play in minimizing the decomposition of the electrolytes in Li based batteries, thereby having a direct impact on the durability of these batteries. Also, it is essential that the morphologies of the deposited magnesium, function of the electrolyte, current density and prolonged cycling continue to be examined especially as new electrolytes are emerging.

Since the great success of Li-ion batteries resulted from replacing lithium metal with the graphite anode, a similar fate may await magnesium batteries that use Mg-ion insertion anodes. What is unique about magnesium-ion insertion anodes is the possibility to reversibly insert/extract magnesium ions in conventional ionic magnesium salts, such as $Mg(TFSI)_2$, dissolved in a variety of organic solvents. While the reason for this behavior has yet to be determined, one plausible explanation could be related to the thermodynamic potential of magnesium ion insertion into the host matrices. It may be possible that it occurs at higher electrochemical potentials than that of magnesium plating. Although the discovery and optimization of new materials are certainly required, several properties would need to be carefully examined in order for these anodes to become practical. First of all, it would be crucial that potential applications are considered as anodes are being developed given the very low gravimetric and volumetric capacities compared to magnesium metal. Also, the capacities of these anodes should be taken into account in the value proposition of the overall system. The second relates to the sluggish kinetics induced by the slow diffusion of magnesium ions. Indeed, the Li-ion battery literature is rich with innovative strategies proven effective in increasing the rate capabilities, some of which might be adoptable to magnesium insertion type anodes. The third point relates to examining the presence and nature of possible insertion anode–electrolyte interfaces which may form electrochemically/chemically. Not only these impact the rate of magnesium ions insertion/extraction, but also provide valuable insight into potential interfaces that may enable facile magnesium ion diffusion, that up to this point, remain unknown.

2 Magnesium battery electrolytes: State of the art and design guiding principles

The earliest report on a magnesium battery electrolyte that enables reversible electrochemical dissolution/plating of magnesium dates back to the 1990s. Gregory et al. [12] proposed several electrolytes for a rechargeable magnesium battery initially guided by earlier reports on successfully plating magnesium metal from the electrolysis of Grignard reagents. These included Grignard, aminomagnesium chlorides and organoborate reagents in ethereal solvents. They screened electrolytes based on the possibility of reversibly electrodepositing/stripping magnesium metal and intercalating magnesium ions into host compounds which served as cathodes. The results were used to guide the selection of the most promising electrolytes subsequently used in demonstrating the first rechargeable magnesium battery. Key findings included: 1) Ionic salts such as $Mg(BF_4)_2$ and $Mg(ClO_4)_2$ enabled reversible magnesium insertion into host materials, however formed passivating film on the magnesium metal. This observation led them to correlate the ionicity of the salt, measured by the partial charge of the magnesium ion, to its compatibility with the magnesium metal, i.e., salts with higher charge on the magnesium ion show low or no compatibility with magnesium. 2) Alkyl Grignard reagents had undesirable chemical reactivity towards the cathodes and were deemed inappropriate for battery demonstrations. 3) Some of the organoborates (magnesium dibutyldiphenyl $Mg(BPh_2Bu_2)_2$ and tributylphenyl $Mg(BPhBu_3)_2$) supported reversible magnesium stripping/plating and Mg ions insertion into cathodes. These were also chemically inert towards the cathodes and had a high solubility in tetrahydrofuran (THF) solvent (>0.4 molar). Other organoborates were excluded from further studies due to their reactivity with the cathode ($Mg(BBu_4)_2$) or low solubility ($Mg(BPh_3Bu)_2 \approx 0.1$ M, $Mg(BPh_4)_2 < 0.01$ M).

$Mg(BPh_2Bu_2)_2$ was used in the first demonstration of a rechargeable magnesium battery. Unfortunately the battery was operated at less than 2 V due to the low stability of $Mg(BPh_2Bu_2)_2$ against electrochemical oxidation. Substitution of the boron with aluminum or the hydrogen in the aromatic rings with fluoride (as was demonstrated recently [8]) was proposed to help enhance its oxidative stability. Note that a recent report by Muldoon et al. [19] confirmed the low solubility of $Mg(BPh_4)_2$, $Mg(BPh_3Bu)_2$ and found that $Mg(BPh_3Bu)_2$ had similar oxidative stability and magnesium metal compatibility as $Mg(BPh_2Bu_2)_2$.

In the early 2000, Aurbach et al. reported a breakthrough which constituted preparing an electrolyte with higher oxidative stability (2.5 V vs Mg) than the organoborates (1.9 V vs Mg for $Mg(BPh_2Bu_2)_2$) by combining a Grignard reagent with aluminum-based Lewis acids such as $AlCl_{3-n}R_n$; where R was an alkyl [20]. Their concept was to strengthen the Mg–C bond in the Grignard reagent, through increasing its ionic character, by adding an electron withdrawing Lewis acid. The optimized compositions of the organohalo-aluminate electrolytes enabled highly reversible magnesium deposition/stripping (100% coulombic efficiency) and insertion into host cathodes with faster insertion kinetics than the organoborates [21,22]. Their approach of using a Lewis base/Lewis acid combination to

prepare magnesium battery electrolytes provided a foundation that was used to prepare other organohalo-aluminate electrolytes with high stability against electrochemical oxidation. Subsequent extensive studies by the same group reported other electrolytes based on combining Grignard reagents with other Lewis acids, such as those boron based. The electrochemical performances for the ones based on aluminum Lewis acids outperformed those boron based [22]. Later reports by Aurbach et al. demonstrated another organohalo-aluminate electrolyte that, while possessing the optimized electrochemical performance of those reported previously, had an impressive stability against oxidation exceeding 3.0 V vs Mg. The idea was to remove the source of β-H elimination, believed to be causing the lower oxidative stability in previous electrolytes, by exchanging the Grignard alkyl ligand with a phenyl group [23]. More recently, other organohalo-aluminate electrolytes with high oxidative stability were reported by other groups. Examples included adding $AlCl_3$ to less nucleophilic amidomagnesium chloride (hexamethyldisilazide) [24]; previously known to allow for reversible magnesium deposition/stripping [25]. Kim et al. [24] found that the crystalized product outperformed the in situ produced electrolyte (oxidative stability of up to 3.2 V vs Mg and higher magnesium deposition/stripping current densities). Another approach used a phenylmagnesium chloride combination with a boron-based Lewis acid in tetrahydrofuran such as tris(pentafluorophenyl)borane [8] or (tri(3,5-dimethylphenyl borane) [26] to form stable electrolytes up to 3.7 V and 3.5 V, respectively. Unfortunately, all these electrolytes, while demonstrated with impressive electrochemical stability windows, reversible magnesium dissolution/deposition properties, and high bulk conductivity (i.e., 2 mS cm^{-1}), share several critical draw backs which are: 1) The presence of chloride; which is an integral part in the make of these salts/complexes. This was found to cause severe corrosion of non-noble metals that becomes apparent at potentials exceeding 2 V vs Mg [7,8,26]. This is problematic as it prohibits using materials such as steel or aluminum as current collectors when using these electrolytes. 2) Tetrahydrofuran is the preferred solvent which is undesirable due to its high volatility and tendency to form peroxides. Aurbach et al. [22] demonstrated optimized compositions obtained from mixing the electrolytes they developed with less volatile ethers such as tetraglymes. However, tetrahydrofuran was still part of the best performing electrolytes; albeit in lesser amounts. 3) Although no systematic studies addressing the extent of the electrolytes' air sensitivity exist, it is likely that they would degrade following exposure to air.

Motivated by overcoming the above problems, research efforts recently started shifting from typical organohalo-aluminates/organoborate-based electrolytes, and the discovery of new systems belonging to a variety of different reagents became of interest. In the next subsections, we review and present these new electrolytes based on their type and physical state. Table 1 summarizes the properties of representative electrolytes classified based on their types. Only those that enable highly reversible magnesium deposition and stripping (i.e., >80% coulombic efficiency) are shown.

2.1 Liquid electrolytes

Given the reactivity of magnesium metal towards most solvents such as carbonates, sulfoxides and nitriles, ethers have been the solvents of choice. New liquid electrolytes are reviewed below with emphasis on those that are tetrahydrofuran-free. We also summarize recent information reported on the nature of the electroactive species in typical organohalo-aluminates and in some of the new electrolytes.

2.1.1 Inorganic ionic salts: Until very recently, it has been generally accepted that simple ionic salts such as $Mg(TFSI)_2$ and $Mg(ClO_4)_2$ are incompatible with magnesium metal (see the Introduction section). Motivated by solving the corrosion problem caused by chloride ions and eliminating tetrahydrofuran as a solvent/cosolvent, Mohtadi et al. [27] proposed a magnesium borohydride based electrolyte for the magnesium battery. The premise of their concept was that the BH_4^- ion, being a relatively strong reducing agent, could withstand the reducing environment of the magnesium anode. Their results demonstrated the first inorganic, halide free, and relatively ionic salt that could reversibly deposit and strip magnesium using magnesium borohydride. Indeed, the work confirmed that ionic salts could be made compatible with the magnesium metal if the anion in the salt has sufficient reductive stability (note that this was also the first time to show Mg plating possibility in a BH_4^--containing system, as an old report on Mg plating using electrolysis (on Cu cathode and Al anode) of a $MgBr_2$, $LiBH_4$ mixture in diethylether/tetrahydrofuran showed lots of boron impurities, likely generated from the electrolysis side reaction. No information supporting $Mg(BH_4)_2$ formation were given [38]).

Mohtadi et al. [27] also developed a magnesium borohydride–lithium borohydride electrolyte in dimethoxyethane (DME) solvent with a reversible magnesium deposition/stripping at high coulombic efficiency (94%), high current densities (25 mA cm^{-2} stripping peak current) and low deposition overpotentials (−0.3 V) as shown in Figure 4. The stability against electrochemical oxidation was 1.7, 2.2 and 2.3 V (vs Mg) on platinum, stainless steel and glassy carbon electrodes, respectively. As the borohydride electrolytes are not corrosive, these stability trends are opposite of those observed for other magnesium electrolytes. The higher stability of the borohydride

Table 1: Summary of Mg battery electrolytes based on their types. Properties of representative examples, including reported stability against oxidation E_{ox}, are provided.

electrolyte type	composition	E_{ox} on Pt vs Mg^{2+}/Mg	solvent	remarks	ref.
		Liquid State			
organo/ organo-halo					
organo borates	$Mg(BPh_2Bu_2)_2$	1.9	THF		[12,19]
	2:1 PhMgCl: Me_3B	3.5	THF	E_{ox} = 2.2 V on SS	[26]
	$(Mg_2(\mu\text{-}Cl)_3{\cdot}6THF)[B(C_6F_5)_3Ph]$ Ph = phenyl, Bu = butyl, Me = methyl	3.7	THF	E_{ox} = 2.2 V on SS	[8]
Grignard halo-aluminate	$Mg(AlCl_{3-n}R_nR')_2$ R, R' = alkyl or aryl	2.2	THF/glymes	optimum in THF	[20-22]
	2:1 RMgCl:$AlCl_3$ R = phenyl	3.2	THF/glymes	E_{ox} = 2.2 V on SS	[23]
inorganic ionic salts non-halide based					
borohydrides	1:X $Mg(BH_4)_2$:$LiBH_4$, X = 0–6	1.7	monoglyme/ diglyme	non-corrosive E_{ox} = 2.2 on SS	[27,28]
non-Grignard halo-aluminates					
phenolates & aloxides	2:1 ROMgCl:$AlCl_3$			less air sensitive	
	R = phenyl alkyl	2.6	THF		[29]
	R = phenyl fluoroalkyl	2.9	THF		[30]
	6:1 ROMgCl:$AlCl_3$ R = Me_3SiO	2.5	THF		[31]
amido based	3:1 (HMDS)MgCl:$AlCl_3$	3.2	THF	E_{ox} = 2.2 V on SS	[24]
	1:2 $Mg(HMDS)_2$:$AlCl_3$ HMDS = hexamethyldisilazide	3.5	diglyme	E_{ox} = 2.6 V on SS low nucleophilicity	[32]
inorganic halide based	2:1 $MgCl_2$:$AlCl_3$	3.1, 3.4	monoglyme		[33,34]
	2:1 $MgCl_2$:$AlCl_{4-n}R_n$ R = alkyl,aryl	2.9	THF	E_{ox} = 1.8 V on SS low nucleophilicity	[34]
icosahedral boron cluster					
carboranyl Mg salt	1-(1,7-$C_2B_{10}H_{11}$) MgCl	3.3	THF	least corrosive E_{ox} > 3.0 V on SS, Al	[35]
		Solid State			
gel polymer	$Mg(AlCl_2EtBu)_2$	2.5	tetraglyme/ PVDF	3.7 mS cm^{-1} at 25 °C	[36]
inorganic salts	$Mg(BH_4)(NH_2)$	>3.0	none	10^{-3} mS cm^{-1} 150 °C coulombic efficiency <50%	[37]

on a non-noble metal suggests catalytic effects of platinum on BH_4^- decomposition. Until this point, the borohydride electrolytes remain the only ionic and halide free salts that are highly compatible with magnesium metal.

2.1.2 Non-Grignard-based haloaluminate reagents: In order to increase the stability of the electrolytes in air, avoiding the use of Grignard reagents is needed (i.e., RMgCl or R_2Mg Lewis base). Wang et al. [29] used phenolates to prepare new electrolytes (ROMgCl) with improved air stability, i.e., due to the stronger bond in Mg–O compared to Mg–C. Three phenolate electrolytes exhibiting good Mg reversibility were prepared, however the conductivity and electrochemical oxidative stability were dependent on the alkyl group. The highest

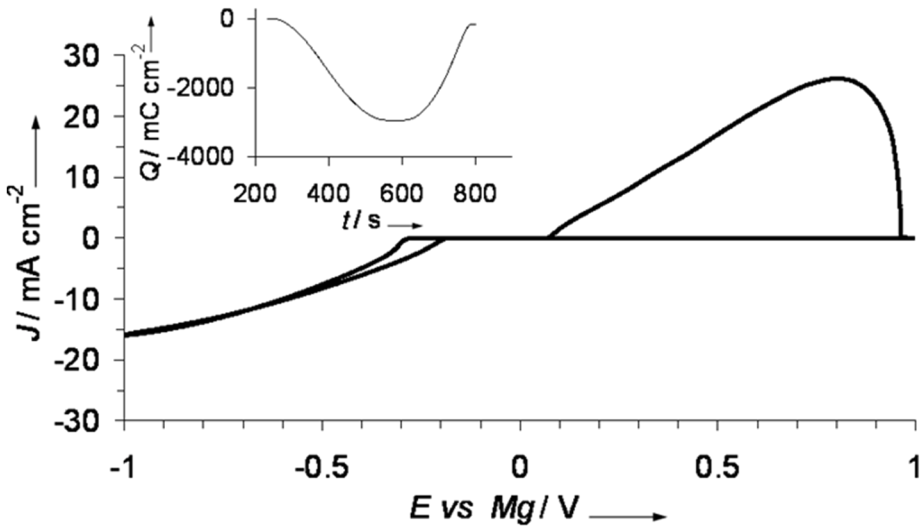

Figure 4: Cyclic voltammogram for $LiBH_4$ (0.6 M)/$Mg(BH_4)_2$ (0.18 M) in DME, (inset shows deposition/stripping charge balance). Reprinted from [27] with permission. Copyright © 2012, Wiley-VCH Verlag GmbH & Co. KGaA, Weinheim.

conductivity and oxidative stability measured on a platinum electrode were observed for a 0.5 M 2:1 2-*tert*-butyl-4-methylphenolate magnesium chloride:$AlCl_3$ in tetrahydrofuran at 2.56 mS cm^{-1} and 2.6 V vs Mg, respectively. Reversible magnesium deposition/stripping, albeit with an increased overpotential, was observed for the same electrolyte following exposure to air for three hours. A new systematic study by Nelson et al. [30] examined the oxidative stability of phenolates as a function of the substituents on the phenyl ring. Several electrolytes were prepared with electron withdrawing (pentafluoro, trifluoromethyl) or donating (methoxy) substituents. Oxidative stability, measured on a platinum electrode, of up to 2.9 V vs Mg was obtained for a 2:1 4-(trifluoromethyl)-phenolate magnesium:$AlCl_3$ in tetrahydrofuran. This electrolyte supported reversible magnesium deposition/stripping and had a high conductivity (2.44 mS cm^{-1}). However, some degradation in the electrochemical performance was observed following exposure to air for six hours (i.e., lower current densities and higher overpotentials). Unfortunately, this suggested the instability of the phenolates upon prolonged exposure to air. Electrolytes prepared by the replacement of the phenolates with alkoxides were reported by Liao et al. [31], who prepared three new butoxy and siloxy based electrolytes. Their interest was to access the vast numbers of ligands offered by the alkoxides such that electrolytes with improved oxidative stability could be prepared. In the absence of $AlCl_3$ Lewis acid, the alkoxides had higher solubility in tetrahydrofuran than the phenolates and supported reversible Mg deposition/stripping. However, the addition of $AlCl_3$ was necessary to improve their oxidative stability (one sixth an equivalent $AlCl_3$ was added to mitigate its negative impact on the solubility of the alkoxides). For example, the addition of $AlCl_3$ increased the oxidative stability of Me_3SiO–MgCl from 1.95 to 2.5 V vs Mg (on a platinum electrode). Both phenolate- and alkoxide-based electrolytes supported reversible magnesium ion insertion in the Chevrel phase Mo_6S_8 cathode [29-31].

As mentioned in the introduction, Kim et al. [24] reported a less nucleophilic 3:1 (hexamethyldisilazide)MgCl:$AlCl_3$ electrolyte where the crystallized product had an oxidative stability of 3.2 V vs Mg on a platinum electrode (note that crystallization was necessary to achieve this performance). More recently, Zhao-Krager et. al [32], also motivated by the lower nucleophilicity of sterically hindered amides, used magnesium bisamides to prepare two electrolytes by reacting magnesium bis(diisopropyl)amide (iPr_2N) and magnesium bis(hexamethyldisilazide) (HMDS) with two equivalents of $AlCl_3$. As shown in Figure 5, the HMDS based electrolyte (both as prepared and crystallized) exhibited the best electrochemical performance and had a higher oxidative stability (3.3 V vs Mg) than the iPr_2N based. Interestingly, the structure of the crystallized material obtained from the $Mg(HMDS)_2$:$2AlCl_3$ was the same as that reported by Kim et al. [24] for the (HMDS)MgCl:$AlCl_3$. Another recent progress on using non-Grignard halo-aluminate electrolytes was reported by Doe et al. [33], who showed the possibility of magnesium deposition/stripping at high coulombic efficiencies simply from $MgCl_2$, $AlCl_3$ mixture in tetrahydrofuran. Similar results were concurrently reported by Liu et al., who also showed the mixture to have a very low nucleophilicity [34]. Unfortunately, the $MgCl_2$ electrolytes were found to be very corrosive; i.e., stability on stainless steel was as low as 1.8 V vs Mg [34]. What is notable about the

$Mg(HMDS)_2$:$AlCl_3$ and $MgCl_2$:$AlCl_3$ systems is that the in situ products exhibited wide electrochemical windows and high electrochemical performances thereby eliminating the necessity of additional crystallization steps.

2.1.3 New design strategies for forming high stability electrolytes: As was described before, the high electrochemical oxidative stability of magnesium electrolytes has been primarily enabled by the formation of strong Al–C, Al–N or B–C bonds (formed by the addition of appropriate Lewis acids). A very recent study by Carter et al. [35] targeted to increase the oxidative stability of the $Mg(BH_4)_2$ electrolytes by strengthening the B–H bond through forming 3-dimensional B–B bonds as in icosahedral boron clusters (*closo*-boranes). As such, the group exploited the high oxidative and thermal stability of *closo*-boranes to prepare electrolytes with wide electrochemical stability window. The results demonstrated a novel carboranyl magnesium chloride electrolyte (1-(1,7-$C_2B_{10}H_{11}$) MgCl) that is compatible with magnesium metal, possesses high oxidative stability (3.3 V vs Mg), and to date, exhibits the lowest tendency to corrode non-noble metals observed from a chloride bearing electrolyte (Figure 6). What was also notable is that the stable anion consisted of a magnesium Mg–C center as shown in Figure 6 below, indicating unique effects of the carborane scaffold. The cation was found to be the $Mg_2Cl_3^+$ observed before for other systems (see section 2.1.5). This was the first

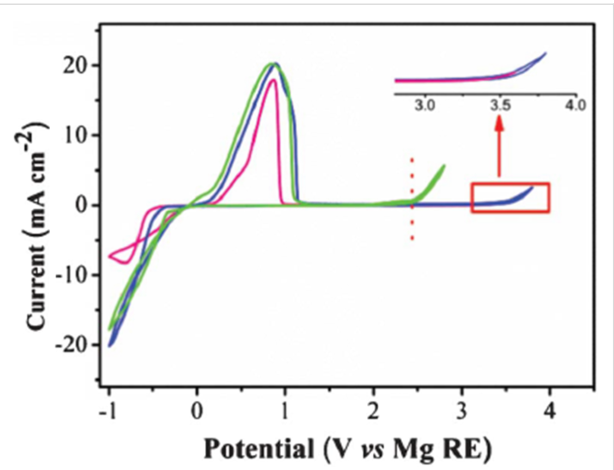

Figure 5: Cyclic voltammograms of the Mg deposition/dissolution in 0.25 M THF solution containing as-prepared $(HMDS)_2Mg–2AlCl_3$ (blue) and redissolved crystals $[Mg_2(\mu\text{-}Cl)_3.6THF][HMDSAlCl_3]\cdot THF$ (pink). The as-prepared $[(iPr_2N)_2Mg–2AlCl_3]$ is also shown (green). Reproduced with permission from [32]. Copyright 2013 The Royal Society of Chemistry.

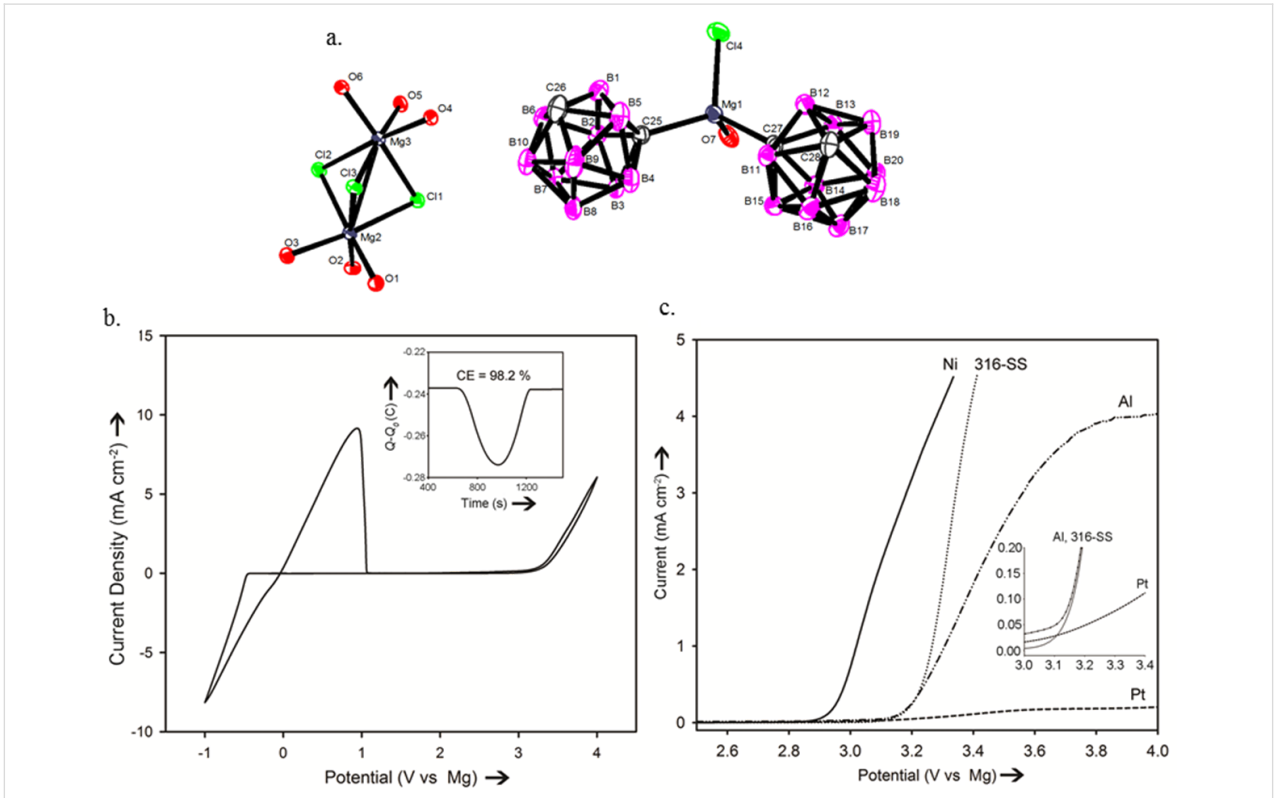

Figure 6: a) X-ray crystal structure of 1-(1,7-$C_2B_{10}H_{11}$) MgCl. Hydrogen atoms and THF carbon atoms are omitted for clarity. b) Cyclic voltammogram in THF solution (inset: charge balance of Mg deposition/stripping). c) Linear sweep voltammograms of $Mg(C_2B_{10}H_{11})Cl$/THF on Pt, Stainless steel (316-SS), Ni and Al electrodes (inset: expanded view of the oxidation onset). Reprinted with permission from [35]. Copyright 2012 Wiley-VCH Verlag GmbH & Co. KGaA, Weinheim.

time to show that electrolytes with a wide electrochemical window could be prepared beyond known approaches that use Lewis base, Lewis acid systems. This work opens new horizons for designing highly stable magnesium battery electrolytes.

2.1.4 Tetrahydrofuran-free electrolytes: Given the volatile nature of tetrahydrofuran (143 mm Hg at 20 °C, and 66 °C boiling temperature), it would be vital to discover electrolytes that are tetrahydrofuran-free. Aurbach et al. [22] demonstrated that they could utilize their organohalo-aluminate electrolytes in solvent mixtures of tetrahydrofuran and longer chain ethers such as tetragylmes without inducing losses in their electrochemical performances. However, it would be hard to fully eliminate the presence of tetrahydrofuran as the organohalo-aluminates based on Grignard reagents tended to have a favorable performance in this solvent. Therefore, an important step in the development of the electrolytes would be demonstrating optimum performances in a tetrahydrofuran-free system. This may be enabled using electrolytes beyond those that use a Grignard Lewis base/Lewis acid reaction. In fact, highly reversible performance from a magnesium borohydride, lithium borohydride electrolyte, developed by Mohtadi et al. [27], was found in dimethoxyethane (monoglyme) solution. Actually, the magnesium borohydride had far superior electrochemical performance in monoglyme than that observed in tetrahydrofuran. Very recently, highly reversible performance (100% coulombic efficiency) for a similar borohydride electrolyte was demonstrated in diglyme solvent [28]. High cycling magnesium deposition/stripping efficiencies approaching 100% were reported for 0.35 M $(HMDS)_2Mg–2AlCl_3$ in diglyme solution where high oxidative stability above 3.5 V vs Mg was obtained. Interestingly, the electrolyte stability measured on a stainless steel electrode was 0.4 V higher than that of a similar system in tetrahydrofuran (2.2 V vs Mg) [8]. At this time, all the electrolytes use ethereal solvents which are more or less volatile. An attractive choice for eliminating the safety hazards of ethers would be using ionic liquids due to their very low volatility. Reversible magnesium deposition/ dissolution from phenyl magnesium bromide [39] and alkylmagnesium bromide [40] was shown in ionic liquid solvents. The caveat was that tetrahydrofuran was used as a cosolvent and as discussed earlier, a shift from Grignard reagents is hence necessary to allow for more flexibility in the solvent selection. Nuli et al. [41] reported reversible magnesium plating using conventional salts such magnesium triflate ($Mg(CF_3SO_3)_2$) in imidazolium-based ionic liquids. However, magnesium metal passivation was reported to take place [39,42].

2.1.5 On the electroactive species: In the case of typical organohalo-aluminate electrolytes, formed following the reaction between a Grignard reagent and $AlCl_3$, it has been generally accepted that the magnesium charge carriers in the bulk are magnesium-chloride bonded ions existing as monomeric ($MgCl^+$) and/or dimeric ($Mg_2Cl_3^+$) species [43]. Kim et al. showed that $Mg_2Cl_3^+$ is one of the electroactive species present in 3:1 (HMDS)MgCl:$AlCl_3$ [24]. Studies on organoborates (crystallized out of their synthesis solution) suggested similar electroactive species as those in the organohalo-aluminates, i.e., MgR^+ and $Mg(BR_4)^+$, R = alkyl or aryl [44]. Given that the organohalo-aluminate electrolytes are by far the most established, detailed studies exist which were concerned with identifying the nature of magnesium species, in both the bulk and at the interface of magnesium metal–electrolyte. As the organohalo-aluminates were reviewed extensively [10], the discussion here is focused on the most recent studies concerning these. The discovery of new types of magnesium ion electroactive species, which enable reversible magnesium plating, is important for advancing the research and development of magnesium battery electrolytes. Below, we shed light on the nature of the different species suggested for the new electrolytes per the available information.

a. Grignard organohalo-aluminate systems: The nature of the electroactive species present at equilibrium in the bulk solution and at the magnesium metal–electrolyte interface during magnesium plating were studied previously [43,44]. For the $Mg(AlCl_{4-n}R_n)_2$ electrolyte, the presence of the adsorbed intermediate $MgCl^+·5THF$ at the metal surface during the deposition of magnesium was suggested. More recently, the presence of an intermediate during magnesium deposition from a 1:2 molar RMgCl:R_2AlCl/THF; R = C_2H_5, was observed by Arthur [45] and Benmayza et al. [46] using the magnesium K-edge in an in operando soft X-ray spectroscopy. Their results, combined with the transport properties of the magnesium species, also suggested the interfacial electroactive species to be $MgCl^+·5THF$. The dimeric $Mg_2Cl_3^+$ species present in the bulk, was discounted from being electrochemically active at the interface during magnesium deposition. Another important result was related to the measured low transport numbers of the magnesium ions. For example, the diffusion coefficient of the magnesium ionic species (i.e., $Mg_2Cl_3^+$) was very low (2.26×10^{-7} cm^2 s^{-1} in 0.2 M solution which is 10 times lower than that observed in 1 M $LiPF_6$-based electrolyte). Interestingly, the transference number t^+, which determines the rate at which reversible magnesium deposition/stripping takes place, ranged between 0.018–0.19 at 0.40–0.15 M, respectively. This astonishing reduction in t^+ values with increasing the electrolyte concentration was attributed to lowered mobility of the dimeric magnesium ions and an increased number of counter and non-magnesium ions at high Lewis acid concentrations. This study helped to provide a better understanding of the electrochemical and transport properties in this complex system.

b. Non-Grignard-based electrolyte systems: Indeed, the magnesium borohydride electrolytes offered new electroactive species beyond known monomeric, dimeric Mg–Cl and RMg^+ species, present in the organohalo-aluminate and probably in the organoborate electrolytes. Guided by spectroscopic analyses of the borohydride electrolytes, Mohtadi et al. [27] proposed the magnesium electroactive species to be a magnesium ion bridge bonded to a one BH_4^-, although the presence of magnesium ions that are solely coordinated to the solvent molecule was not discounted. The electrochemical performance was suggested to be governed by the extent of salt dissociation. The substantial improvements in the electrochemical performance as the dendicity of the solvent was increased, and following the addition of $LiBH_4$, used as a source of a Lewis acid cation, further supported this hypothesis.

In the case of the amidomagnesium (HMDS) based electrolyte [32], the dimeric $Mg_2Cl_3^+$ electroactive species was similar to that found in other Grignard- and non-Grignard-based haloaluminate systems [24,26]. A similar species was reported for the carboranyl MgCl electrolyte [35]. Note that $Mg_2Cl_3^+$ was also present in the crystallized products from $MgCl_2$ mixtures with aluminum based Lewis acids [34].

The electroactive species was investigated for the alkoxide 6:1 *n*-butyl-OMgCl:$AlCl_3$/THF electrolyte, however the crystallized product yielded an inactive species [31]. In the phenolate electrolytes, the crystallized product from the trifluoromethyl phenolate:$AlCl_3$ solution contained the $Mg_2Cl_3^+$ cation [30].

Based on the current progresses, we could summarize that two distinct species that enable reversible magnesium deposition/stripping are known: 1) The $Mg_2Cl_3^+$ and/or $MgCl^+$ in organo/non-organo haloaluminates, organoborates, and in the carboranyl electrolyte and 2) the $MgBH_4^+$ in the borohydride electrolytes. For any of the electrolytes reported thus far, there is no evidence that support Mg^{2+} presence.

As described above, for future material design of magnesium battery electrolytes, it is of significant importance to discern the electroactive species in both the bulk and at the interface between the anode and electrolyte. This is expected to be more beneficial than solely relying on optimizing the compositions/ratios of the reagents.

2.2 Solid magnesium electrolytes

As explained above, the solvents known to support optimum reversible Mg deposition/stripping are volatile as they are ether-based. To overcome this challenge, one strategy would be trapping the solvent, used to solvate the magnesium ions, within a polymeric matrix. The electrolyte formed in this case is referred to as a gel electrolyte. This concept was previously applied to Li-ion battery electrolytes [5] and was adopted later for rechargeable Mg batteries [10]. Nonetheless, demonstrating a viable gel electrolyte for rechargeable magnesium batteries is not trivial as it requires using magnesium reagents/salts that enable reversible magnesium deposition/stripping, while being chemically inert towards the polymeric matrix selected. The electrolyte would also need to have an acceptable conductivity of the magnesium ions at room temperature. Another strategy, which is far more challenging, is to create a solvent free solid state medium that enables magnesium ion conduction, under practical conditions, through magnesium ion diffusion, i.e., solid state magnesium salts. While few reports exist on the formation of gel electrolytes for magnesium batteries, reports on magnesium ion conduction in the solid state media are scarce. In fact, until recently, magnesium ion conduction at values in the order of 10^{-3} mS cm^{-1} occurred only at temperatures exceeding 500 °C. A review of the developments related to both strategies, with focus on those that demonstrated viable electrolytes is presented below.

2.2.1 Organic solid/semi solid electrolytes: The immobilization of magnesium electrolyte in polymeric matrices such as poly(vinylene difluoride) PVDF and poly(ethylene oxide) PEO, was reported by Chusid et al. [36]. The group impregnated magnesium organohalo-aluminate salts, such as $Mg(AlCl_2EtBu)_2$ dissolved in tetrahydrofuran and tetraglyme, in both PEO and PVDF matrices. These complex solutions were found to be inert towards the polymers used and reversible magnesium deposition/stripping from these gel electrolytes was shown. The best electrochemical performance reported was for the $Mg(AlCl_2EtBu)_2$/tetraglyme/PVDF gel as high specific conductivity (3.7 mS cm^{-1} at 25 °C) was measured. This study not only showed the possibility to prepare gel electrolytes that are compatible with magnesium metal but also allowed for reversible Mg intercalation into the Chevrel phase Mo_6S_8 cathode. Other gel polymer electrolytes were reported [47-49]. Examples include those incorporating dispersed inorganic oxides such as nano fumed silica. The oxides were added to improve the mechanical and electrochemical properties (1 mS cm^{-1} reported at room temperature) [49]. Unfortunately, all these gel electrolytes used magnesium salts known to be incompatible with the magnesium metal. A very recent study proposed using coordinatively unsaturated metal-organic frameworks (MOFs) as nano media to immobilize magnesium phenolate and/or $Mg(TFSI)_2$/triglyme electrolytes (phenolates were found to be more soluble in triglyme than in tetrahydrofuran) [50]. As the phenolates were strongly interacting with the MOF's crystallites, addition of $Mg(TFSI)_2$ (i.e., weakly coordinating anion) was necessary to achieve a good conductivity (0.25 vs 0.0006 mS cm^{-1} in just phenolates/MOF). No results

addressing the compatibility with magnesium metal or oxidative stability were provided. It may be possible that this system is incompatible with the magnesium metal due to the passivating nature of $Mg(TFSI)_2$.

2.2.2 Inorganic solid state magnesium ion conductor: Until very recently, the observation of magnesium ion conduction in inorganic salts occurred only at temperatures exceeding 500 °C [51,52]. Recently, Matsuo et al. [53] studied the possibility of magnesium ion conduction in the high temperature phase of magnesium borohydride using first-principles molecular dynamics simulations FPMD [53,54]. The magnesium ions, present in the center of a tetrahedral cage surrounded by the BH_4^- anions, were found to have limited mobility. This was attributed to the strong coulombic interactions with BH_4^- resulting from the small cage size. They proposed that increasing the cage size, by partial substitution of BH_4^- with the larger AlH_4^-, may enable magnesium ion migration, however, this was not experimentally demonstrated. Another study of borohydride-based solid state electrolytes was reported by Higashi et al. [37]. Guided by their first-principles calculations based on density functional theory (DFT), they experimentally investigated the conduction of magnesium ions in both $Mg(BH_4)_2$ and $Mg(BH_4)(NH_2)$. The selection of these compounds was motivated by the ionic bonding nature of the magnesium ions, judged from the calculated Bader charge on the magnesium, and presence of cavities large enough to enable magnesium ion conduction through the hopping mechanism. They measured a conductivity of about 10^{-3} mS cm^{-1} at 150 °C for $Mg(BH_4)(NH_2)$, which is three orders of magnitude higher than that of $Mg(BH_4)_2$, presumably due to the shorter distance between the two nearest Mg atoms (3.59 Å in $Mg(BH_4)(NH_2)$ vs 4.32 Å in $Mg(BH_4)_2$). In addition, reversible magnesium deposition/stripping was demonstrated for the $Mg(BH_4)(NH_2)$ electrolyte as shown in Figure 7. Interestingly, the oxidative stability of the $Mg(BH_4)(NH_2)$ salt was found to be in excess of 3 V vs Mg at 150 °C, which is higher than that reported for liquid $Mg(BH_4)_2$–ether systems at room temperature [27]. The high ionic conductivity in $Mg(BH_4)(NH_2)$, albeit at 150 °C, reversible Mg deposition/stripping and high voltage stability provide opportunities for developing practical Mg solid state electrolytes based on novel borohydride salts.

2.3 Perspectives on future developments of magnesium battery electrolytes

Unlike in the the case of rechargeable lithium and sodium batteries, the development of electrolytes for rechargeable magnesium batteries has been faced with a distinct and an unavoidable challenge. This is thanks to the formation of a passivation layer upon magnesium metal exposure to numerous salts/solvents. Generally speaking, the battery system imposes several stringent requirements on the electrolytes as they represent the bridge linking the anode with the cathode. Not only they are required to highly perform in the proximity of two electrochemical environments operating at two opposite extremes, but also provide acceptable bulk transport properties

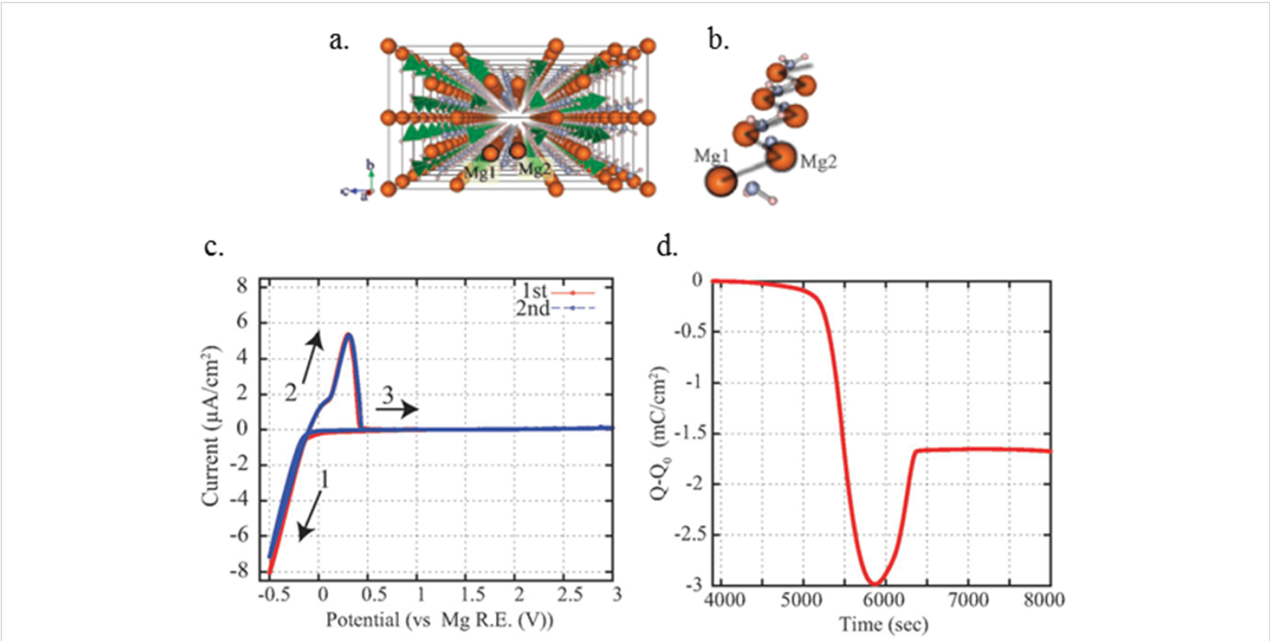

Figure 7: a) Crystal structure of $Mg(BH_4)(NH_2)$. Atomic sizes are depicted by sphere radii. b) Mg zigzag structure from the crystal structure a). c) Cyclic voltammograms of $Mg/Mg(BH_4)(NH_2)/Pt$ and, d) deposition/stripping charge balance (first cycle). Reproduced with permission from [37]. Copyright 2012 The Royal Society of Chemistry.

that allow them to respond swiftly to the power demands of the system. Additionally, it is essential that the electrolytes have acceptable safety properties which include high thermal stability, low volatility, low flammability, low toxicity, and low reactivity with ambient air. Therefore, developing electrolytes possessing the aforementioned traits, no doubt, represents a key challenge. Since the first rechargeable magnesium battery was demonstrated in the early nineties, the R&D efforts have primarily focused on the creation of electrolytes that are highly compatible with the magnesium metal, followed by applying innovative strategies to improve other electrochemical properties. A main focus was increasing their stability against electrochemical oxidation, so that a competitive, high voltage battery system could be ultimately enabled. Over the past two decades, the technical advancements made on magnesium battery electrolytes resulted in state of the art systems that primarily consist of organohalo-aluminate complexes possessing electrochemical properties that rival those observed in lithium ion batteries. These are represented by a highly reversible performance, high bulk conductivity, and wide electrochemical windows. However, despite these scientific feats, these electrolytes had several drawbacks which include their corrosive properties, nucleophilicity (for those Grignard based), air sensitivity and the use of volatile solvents.

Over the past two years, motivated by the desire to overcome the challenges with the known electrolytes, several new electrolytes that are compatible with the magnesium metal have been proposed. It is interesting to see that in previous and most recent electrolytes, the familiar monomeric and dimeric Mg–Cl active species were found. One important challenge with these same species is the slow transport properties. Another is the presence of chloride ions making them prime suspects in the corrosion issue. Hence, we believe that the discovery/design of new electroactive species is needed. Recent development in this direction is manifested in the borohydride electrolytes, where opportunities for increasing the oxidative stability are being explored and were demonstrated using *closo*-borane anions. Another common property among magnesium electrolytes is their air sensitivity. New approaches offered lowered sensitivity to air using alkoxides and phenolates. It would be interesting to determine their long term durability and see future designs that build on these systems, which are hopefully non-corrosive. In order to overcome the challenges with the liquid systems, solid electrolytes could be an ideal choice. The discovery of magnesium compatability and conduction in magnesium amide borohydride inspires confidence in this direction.

Indeed, the portfolio of magnesium battery electrolytes has widened and we hope that the current research will fuel the next wave of innovations. This could be driven by further understanding of the properties of the electrolytes and their behavior in a battery system. Topics we suggest include: 1) Discerning the electroactive species and their interactions with both the magnesium metal and the cathode material. This may prove powerful in paving the path for designing modified electrolytes; 2) Determining important electrochemical transport properties in both the bulk and at the interface with the magnesium metal; 3) Understanding the extent of the air stability, thermal stability and long term durability of the electrolyte; 4) Understanding the effects of a battery environment on the electrochemical stability window. For example, examining the oxidative stability on the cathode material rather than solely using metals/glassy carbon electrodes; 5) Lastly, developing corrosion resistant substrates, such as pretreated surfaces, as this may be helpful in overcoming the corrosion issue. However, we think that this effort may be worthwhile when electrolytes become demonstrated with very competitive performances.

Would future electrolytes help magnesium metal one day become the “ultimate battery anode”? There is no clear answer at this time. However, the numerous breakthroughs and scientific advancements made so far make one hopeful that at least it may have come one step closer.

3 Rechargeable Mg battery cathode

Much effort has been devoted to development of Mg batteries and their cathodes over the past 70 years. Some cathode materials have been practically investigated for a reserve-type Mg battery system, which were typically used together with Mg and Mg–Al–Zn (AZ) alloy as anode, and electrolytes based on either sea water or magnesium perchlorate ($Mg(ClO_4)_2$) solutions. The reserve battery requires high energy density, high power output, long lifetime and superior low temperature performance. Therefore, typical examples of cathodes for such Mg batteries, which have been summarized in the battery handbook so far were AgCl, CuCl, $PdCl_2$, Cu_2I_2, CuSCN, MnO_2 and air [1]. These batteries could be operated as primary batteries which fulfilled the aforementioned requirements, however they could not be operated as secondary batteries enabling us to recharge them. One of the reasons considered for the non-rechargeability was the water passivation of the anode surface. As the metal was exposed to water, a blocking layer such as $Mg(OH)_2$ was formed accompanied with hydrogen gas generation. To recharge the battery, applying large overpotential was necessary due to the formation of highly resistive blocking layer, and finally the interface between anode and electrolyte, which determines the battery performances, could not be fully recovered. Due to the major hurdles with the anode, the challenges of Mg battery cathode may have been masked. Actually, a proper understanding of the cathode reaction and a further

enhancement of the cathode performance are vital to realize the rechargeable system. Nowadays, the studies on rechargeable Mg battery cathodes have gained more momentum in order to improve the primary battery characteristics such as voltage, capacity, cycle life and so on. Currently, traditional cathode materials which are briefly summarized below have been intensively reconsidered recently, while other candidates, which are not described in this review, have been addressed. For example, $Mg_{0.5}Ti_2(PO_4)_3$ [55], Mg_xMnSiO_4 [56-58], WSe [59], sulfur [24,60] and oxygen [61-63]. In order to discover the next generation Mg battery cathode, the most important challenges are overcoming the negative impact arising from divalent Mg^{2+} ions and also maintaining higher mobility of Mg^{2+} ions in the diffusion pathway. So far, despite the research efforts to overcome these challenges, the very slow diffusion of Mg^{2+} ions and the structural instability remain as key hurdles in the development of working high voltage cathodes. Here, we strongly focus on the recent progresses of representative cathode materials for rechargeable Mg batteries.

3.1 Cobalt-based cathode materials

Since the 1990s, a variety of non-aqueous electrolytes have been adopted to evaluate and improve the rechargeability of the battery. It was believed that the non-aqueous electrolytes consisting of either magnesium perchlorate in acetonitrile solvent or magnesium organoborate in tetrahydrofuran solvent were capable of overcoming the issue resulting from water-containing systems. Gregory et al. surveyed some candidates among many cathode materials by chemical intercalation experiments using typical electrochemical methods [12]. Based on XPS analyses it was reported that ZrS_2 as a host material was able to receive Mg. Also, they proposed that RuO_2 and Co_3O_4 were hopeful candidates expected to capture Mg ions. These materials were also studied by Sutto et al. to demonstrate the redox capability in a different non-aqueous electrolyte system [64,65]. According to their discussion, Co_3O_4 did not allow for a sufficient magnesium insertion because of i) strong interactions between Mg^{2+} cations and oxygen atoms in the host lattice and ii) a drastic change of host structure and particle size after magnesiation. The initial capacity of 74 mAh g^{-1} was observed at around 1.5–2.0 V against Mg and a capacity retention of 60% after 30 cycles was reported. As such, the magnesiated Co_3O_4 did not show the high capacity obtained in the Li system. Recently, Ichitsubo et al. studied disordered $MgCo_2O_4$ (precisely, $(Mg_{1-x}Co_x)(Mg_{1-y}Co_y)O_4$) which is a semiconductor with high electrical conductivity [66]. Compared with spinel-phase Co_3O_4, the disordered spinel, $MgCo_2O_4$ increased the open circuit voltage (OCV) by about 2.0 V at the initial stage just after a constant voltage charge as shown in Figure 8. One reason for this increase could be resulting from an enhanced Mg^{2+} ion diffusion compared to the ordered structure. The disordered spinel $Mg_{0.67}Ni_{1.33}O_2$ also showed high OCV based on the same principle [66]. Unfortunately, the high initial voltage (over 3.0 V vs Mg) observed for these spinel materials

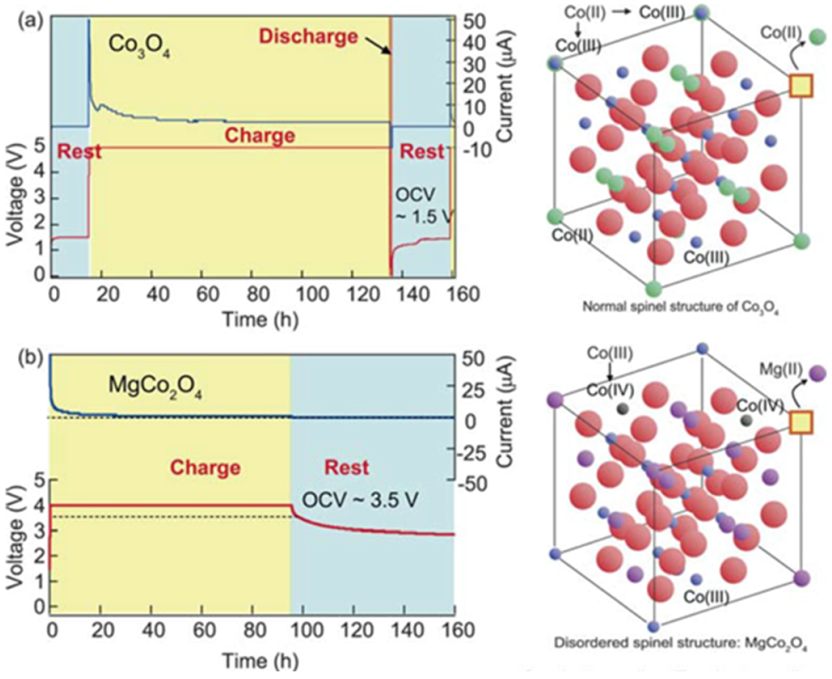

Figure 8: The OCV values of the test cells after constant voltage charge: positive electrode, (a) ordered Co_3O_4 and (b) disordered $MgCo_2O_4$; negative electrode, Mg; electrolyte, $Mg(ClO_4)_2$ in acetonitrile. Reproduced with permission from [66]. Copyright 2011 The Royal Society of Chemistry.

could not be maintained during the rest time following charging as a continuous voltage decay was observed. This meant that these cathode materials possessed high polarization due to slow diffusion of Mg^{2+} in the host lattice. Thus, even for these materials it was not possible to discharge the battery at a higher voltage over 3.0 V vs Mg. Although these cathodes did not enable stable high voltage performance, the introduction of the disordered structure into the Mg battery cathode is indeed a good idea to neutralize the local charge density occurring between inserted Mg^{2+} ions and the host lattice, and to furthermore accelerate intrinsic Mg^{2+} ion diffusion.

3.2 Vanadium-based cathodes

Other well-researched materials for Mg battery cathodes are V_2O_5 and a series of vanadate oxides [67-72]. Novak et al. proposed a water-containing V_2O_5 cathode system in an organic electrolyte such as $Mg(ClO_4)_2$ in propylene carbonate [68,69]. It was expected that V_2O_5 was capable of accommodating 2 mol of Mg^{2+} ions, which is equivalent to the V^{5+}/V^{3+} redox reaction. However, according to their report, the electrochemical insertion of Mg^{2+} ion into V_2O_5 was dependent on the amount of water in the electrolyte. Additionally, the maximum content of Mg^{2+} ions was observed to be less than 0.6 mol. This is because chemically bounded water was present in the channel of the V_2O_5 host which prevented further magnesiation. Although the observed capacity was much lower than the expected value, hydration of Mg^{2+} ions is expected to mitigate difficulty of their electrochemical insertion into the host lattice as explained in a previous review [69]. Imamura et al. followed this approach and used V_2O_5 xerogel and its carbon composite, where the V_2O_5 xerogel with 50 nm in thickness was coated on the carbon support [70,71] (Figure 9a). It was reported that in the wide operation range, the xerogel enabled achieving high content of magnesiation of up to $x = 1.84$ in $Mg_xV_2O_5$, resulting in a high capacity of about 600 mAh g^{-1} in the potential range from −1.0 to +0.3 V vs Ag/Ag^+. On the other hand, Amatucci et al. demonstrated the electrochemical performance of V_2O_5 in the non-aqueous media with negligible amount of water [72] (Figure 9b). Nano-sized V_2O_5, which had a particle size distribution of 20–50 nm, brought about a higher discharge capacity and a narrower hysteresis with a higher working voltage than micron-sized V_2O_5. In both Imamura's and Amatucci's approaches, using a thin layer and nanoparticles allowed for a short diffusion length of Mg^{2+} ions, thereby improving the Mg battery performance. Although the possibility of H_2O associated intercalation for V_2O_5 has only been suggested, these approaches could be eventually one of the important ways that help accelerate Mg^{2+} ion diffusion in the lattice.

3.3 Molybdenum-based cathodes

A big success in developing a cathode for Mg batteries was presented in 2000 by Aurbach et al. They discovered an excellent material, the Chevrel phase (CP) Mo_6S_8, as a rechargeable Mg battery cathode [20]. The CP cathode was proven to have a very stable performance with less than 15% capacity fade over 2000 cycles at 100% depth of discharge. Note that practical rates of 0.1–1.0 mA/cm^2 and wide temperature ranges from −20 to +80 °C were used. As described in previous articles [7,20,73], these promising properties are enabled by the following features of the CP cathode; 1) electroneutrality derived from delocalized Mo_6 metallic cluster, 2) plenty of sites per cluster where Mg^{2+} ions can be accommodated for solid-

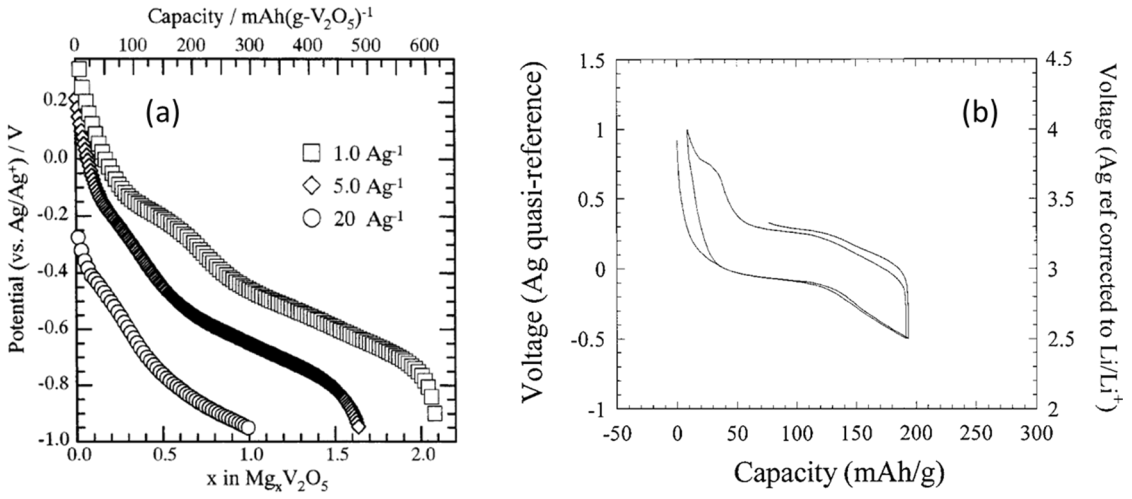

Figure 9: (a) Discharge curves of V_2O_5/carbon composites in the $Mg(ClO_4)_2$/acetonitrile electrolyte solution at various current densities. Reproduced with permission from [70]. Copyright 2003 ECS–The Electrochemical Society. (b) Charge–discharge curves of nanocrystalline V_2O_5 in the $Mg(ClO_4)_2$/propylene carbonate electrolyte solution. Reproduced with permission from [72]. Copyright 2001 ECS–The Electrochemical Society.

state diffusion, 3) high electronic conductivity. One of the drawbacks of the CP cathode is that the kinetics of Mg^{2+} ion diffusion was strongly dependent on the composition and operating temperature [23]. During initial magnesiation, 20–25% of Mg^{2+} ions were trapped in the CP lattice and were not extracted unless the temperature was elevated. Moreover, when the CP cathode was tested at a low temperature around 15 °C, the capacity of about 80 mAh g^{-1} observed at 1/10 C rate, decreased to about 40 mAh g^{-1} at 1 C rate. An effective countermeasure to promote fast kinetics of the CP cathode was the partial substitution of Mo_6S_8 by Se. It was observed that the Se-substituted CP cathode showed an excellent accessibility of Mg^{2+} ions, resulting in a higher capacity at higher rate and at lower temperature. Unfortunately, the CP cathode families showed relatively low working voltages at around 1.2 V vs Mg and relatively low capacities of around 110 mAh g^{-1}. To make the magnesium battery more practical, a Mg cathode with high energy density is strongly desired. Recently, it was reported that graphene-like MoS_2 also worked as a Mg battery cathode [74-76] (Figure 10a). Chen et al. found that this material exhibited an operating voltage of 1.8 V and a reversible capacity of about 170 mAh g^{-1} by combining with Mg nanoparticles as an anode. Additionally, in a similar way, TiS_2 has been considered as a common cathode material even in Mg batteries [77] (Figure 10b). The operating voltage of TiS_2 was not high enough compared with Mo_6S_8, and it suffered from limited rate and temperature performances. However, a higher capacity of about 180 mAh g^{-1} vs Mg was obtained by the state of art nanotechnology. Therefore, transition metal sulfides as prototypical intercalation host materials may bring in a new breakthrough for Mg battery cathodes.

3.4 Manganese-based cathodes

Finally, the remaining attractive materials as Mg battery cathode was MnO_2 and its polymorph [78-82]. MnO_2 is widely regarded as a common cathode material in primary batteries including either Zn or Mg anodes, in lithium-ion secondary batteries and furthermore in metal–air batteries. The unique MnO_2 polymorphs have been used as Mg battery cathodes coupled with either a magnesium organohaloaluminate electrolyte solution or magnesium perchlorate non-aqueous electrolyte solution. In 2011, Zhang et al. presented the redox capability of α-MnO_2 during magnesiation and demagnesiation [81] (Figure 11a). α-MnO_2 with 2×2 tunnel structure showed a high initial capacity of about 240 mAh g^{-1} and could be repeatedly discharged and recharged. Unfortunately, this cathode had severe capacity fading due to a drastic structural deformation from the tetragonal phase to the orthorhombic phase during magnesiation. While this is known to occur in all manganese-based cathodes for lithium-ion batteries, such structural instability during magnesiation is thought to be a key trigger that severely deteriorates α-MnO_2 in non-aqueous Mg batteries. Very recently, Ling et al. proposed an alternative manganese material for a Mg battery cathode, which was called a post-spinel compound, $MgMn_2O_4$ with 2×2×1×1 structure [82] (Figure 11b). Theoretical calculations predicted that the above-described structural stability was significantly improved by controlling the tunnel size and shape for Mg^{2+} ion diffusion. As a result, the post-spinel compound facilitated Mg insertion/extraction reaction more than α-MnO_2 with bigger tunnel size, and then had a relatively high operation voltage. In addition, the cooperative hopping of Mg^{2+} ions in the tunnel 2×2×1×1 was estimated to aid faster diffusion, resulting in a low diffusion

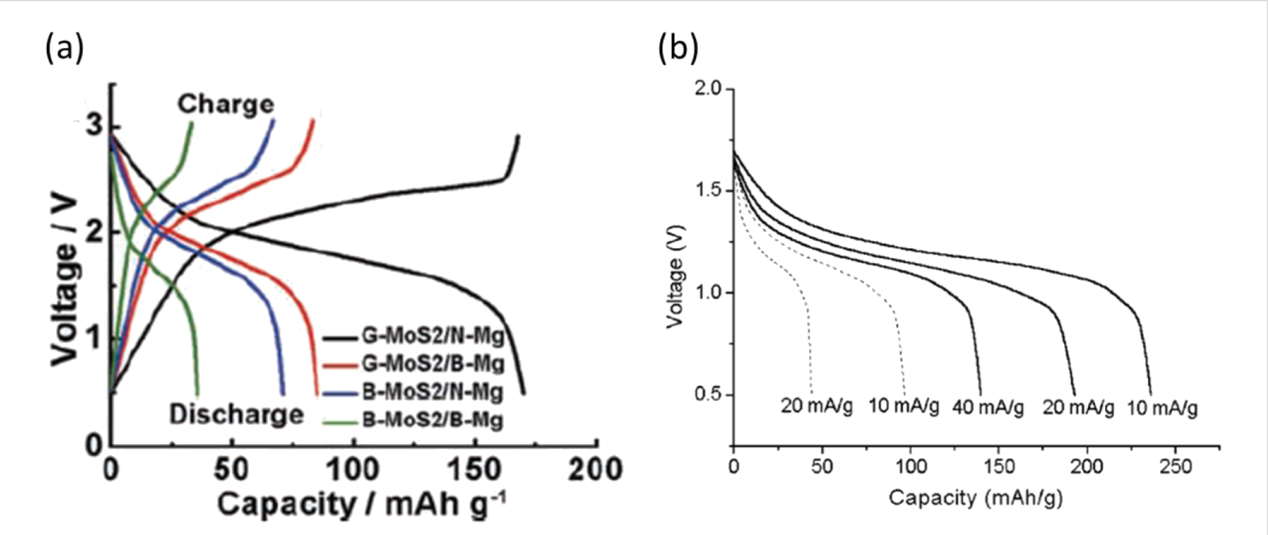

Figure 10: (a) Charge–discharge curves of graphene-like MoS_2 in the $Mg(AlCl_3Bu)_2$/tetrahydrofuran electrolyte solution. Reprinted with permission from [74]. Copyright 2011 Wiley-VCH Verlag GmbH & Co. KGaA, Weinheim. (b) Discharge curves of TiS_2 nanotubes in the $Mg(ClO_4)_2$/acetonitrile electrolyte solution at various current densities. Reproduced with permission from [77]. Copyright 2004 The Royal Society of Chemistry.

barrier (≈400 meV) that is comparable with that for $LiMn_2O_4$, a typical lithium-ion battery cathode. Thus, the structural modification for Mg^{2+} ion diffusion is also one of the approaches which could be used to achieve fast kinetics in the cathode and minimize the interactions of strongly bounded Mg^{2+} ions with host tunnels.

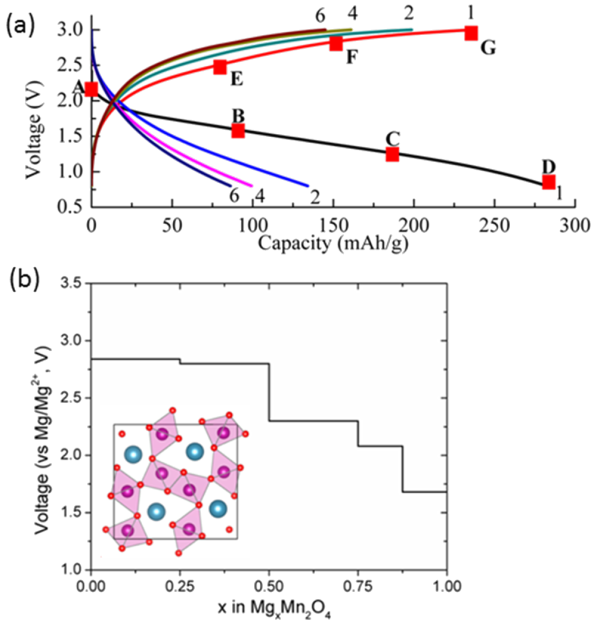

Figure 11: (a) Charge–discharge curves of α-MnO_2 in organohaloaluminate/tetrahydrofuran electrolyte solution. Reprinted with permission from [81]. Copyright 2012 Elsevier. (b) Predicted voltage for electrochemical insertion of Mg into the post spinel, $MgMn_2O_4$ which was drawn in the inset. Adopted with permission from [82]. Copyright 2013 American Chemical Society.

3.5 Perspectives on rechargeable cathodes

In order to establish the non-aqueous Mg battery as a system, it is noteworthy that the cathode strongly governs the battery performance. High energy density of the cathode is an indispensable requirement for Mg batteries to become a reality. To realize this, two approaches can be generally followed; one is having a high voltage operation, while the other is having a high capacity operation. In the latter, despite the fact that either sulfur or oxygen cathodes have to be truly demonstrated for Mg battery, they may offer potential high capacity future cathodes. However, it is expected that these cathodes would have challenges similar to those encountered in the Li battery system. An important point would be whether the typical issues present in the Li–air and Li–sulfur systems could be solved using the Mg system. Herein, we focus on the cathode materials for high voltage operation. Generally, oxide-based materials should be suitable to meet such a request, since oxide-based materials are theoretically able to show higher redox potential as demonstrated in lithium-ion batteries. However, in terms of the Mg^{2+} ion mobility, oxide materials currently have the issue of sluggish diffusion. This resulted in an overall battery performance that was not so promising compared to that using the sulfide materials.

To the best of our knowledge, there have been a couple of key solutions to overcome this undesirable situation. First is to discover an appropriate host structure with faster kinetics as was already discussed above. From the viewpoint of the guest ion size relative to the host structure, Mg^{2+} as a guest ion does not have an issue because the ionic radius of Mg^{2+} (0.74 Å) is close to that of Li^+ (0.68 Å). However, when considering the interaction between the guest ion and the host structure, the divalent nature of Mg^{2+} ions notably suppresses fast diffusion observed in the monovalent Li^+ system, because of the: 1) tightly bounded attraction between Mg^{2+} and the host and 2) strong repulsion between Mg^{2+} ions. As a result, sluggish diffusion of Mg^{2+} ions causes poor magnesiation and non-dynamic situation which means that mobile ions are stuck either in the diffusion pathway or on the surface. Structural designs that promote Mg^{2+} ion diffusion is thought to be the best way to discover promising Mg battery cathodes operating at high voltage.

Another key challenge is how to control the charge transfer resistance observed at the cathode/electrolyte interface, which should become more apparent after the sluggish diffusion issue is fully overcome. In fact, the charge transfer resistance has been carefully studied in lithium-ion batteries and was found to have a significant role that determines the battery performance. A surface film formed on a cathode active material should allow for transporting Mg^{2+} ions, but sometimes it may act as a blocking layer, thus hampering the charge transport. Even though the solvated Mg^{2+} ions can go through the surface film, a desolvation process needs to take place before the ions could migrate inside a host structure. Probably, Mg^{2+} ions would have a stronger solvation than Li^+ ions, therefore the charge transfer resistance is expected to be considerably higher. In a practical setup, this is an important factor necessary to promote further magnesiation. As it has been the case for state of art technologies such as those in lithium-ion batteries, Mg battery electrolytes will also need to be optimized for such high voltage operation of the cathode. The cathode/electrolyte interface will have to be considered so as we do not lose the superior electrochemical properties especially those for the high voltage cathodes.

Finally, for high voltage battery operation, close attention needs to be paid to the corrosion of the current collectors. In any environment having an electrolyte salt (e.g., magnesium perchlorate and magnesium organoborate) dissolved in an organic solvent,

the corrosion of current collectors must be suppressed in order to properly monitor the cathode properties in a battery setup. In particular, high voltage systems need to be understood in a suitable electrolyte environment with wide electrochemical window. Further progresses in Mg battery cathodes are needed and should go hand-in-hand with the developments of non-corrosive and electrochemically stable electrolytes.

Conclusion

Indeed, current state of the art rechargeable magnesium battery technologies are far from reaching its promised potential, where several hurdles, particularly resulting from the absence of appropriate electrolytes and high capacity/voltage robust cathodes remain. Nonetheless, we are hopeful that an improved understanding of the chemistry/physics of these batteries and future innovative ideas may after all allow for battery engineering and system optimization per application needs. This may enable commercialization of these batteries, sooner or later.

Acknowledgements

R.M. and F.M. would like to thank Dr. Koji Suto for his insightful suggestions. Funding for meeting the costs of this article was provided by Toyota Motor Engineering and Manufacturing North America TEMA.

References

1. Linden, D.; Reddy, T. B. *Handbook of Batteries,* 4th ed.; McGraw-Hill: New York, 2011.
2. Encyclopædia Britannica: Conte Alessandro Volta. http://www.britannica.com/EBchecked/topic/632433/Conte-Alessandro-Volta (accessed Feb 1, 2014).
3. Haughton, B. The Baghdad battery. *Hidden History: Lost Civilizations, Secret Knowledge, and Ancient Mysteries;* Career Press: New Jersey, 2007; pp 129–132.
4. Dunn, B.; Kamath, H.; Tarascon, J.-M. *Science* **2011,** *334,* 928. doi:10.1126/science.1212741
5. Xu, K. *Chem. Rev.* **2004,** *104,* 4303. doi:10.1021/cr030203g
6. Kim, H.; Jeong, G.; Kim, Y.-U.; Kim, J.-H.; Park, C.-M.; Sohn, H.-J. *Chem. Soc. Rev.* **2013,** *42,* 9011. doi:10.1039/c3cs60177c
7. Yoo, H.-D.; Shterenberg, I.; Gofer, Y.; Gershinsky, G.; Pour, N.; Aurbach, D. *Energy Environ. Sci.* **2013,** *6,* 2265. doi:10.1039/C3EE40871J
8. Muldoon, J.; Bucur, C. B.; Oliver, A. G.; Sugimoto, T.; Matsui, M.; Kim, H. S.; Allred, G. D.; Zajicek, J.; Kotani, Y. *Energy Environ. Sci.* **2012,** *5,* 5941. doi:10.1039/C2EE03029B
9. Aurbach, D.; Weissman, I.; Gofer, Y.; Levi, E. *Chem. Rec.* **2003,** *3,* 61. doi:10.1002/tcr.10051
10. Gofer, Y.; Pour, N.; Aurbach, D. Electrolytic solutions for rechargeable magnesium batteries. *Lithium Batteries: Advanced Technologies and Applications;* Wiley:-VCH: Weinheim, Germany, 2013; pp 328–345.
11. Lu, Z.; Schechter, A.; Moshkovich, M.; Aurbach, D. *J. Electroanal. Chem.* **1999,** *466,* 203. doi:10.1016/S0022-0728(99)00146-1
12. Gregory, T. D.; Hoffman, R. J.; Winterton, R. C. *J. Electrochem. Soc.* **1990,** *137,* 775. doi:10.1149/1.2086553
13. Matsui, M. *J. Power Sources* **2011,** *196,* 7048. doi:10.1016/j.jpowsour.2010.11.141
14. Arthur, T. S.; Singh, N.; Matsui, M. *Electrochem. Commun.* **2012,** *16,* 103. doi:10.1016/j.elecom.2011.12.010
15. Singh, N.; Arthur, T. S.; Ling, C.; Matsui, M.; Mizuno, F. *Chem. Commun.* **2013,** *49,* 149. doi:10.1039/c2cc34673g
16. Shao, Y.; Gu, M.; Li, X.; Nie, Z.; Zuo, P.; Li, G.; Liu, T.; Xiao, J.; Cheng, Y.; Wang, C.; Zhang, J.-G.; Liu, J. *Nano Lett.* **2014,** *14,* 255. doi:10.1021/nl403874y
17. Park, M. H.; Kim, M. G.; Joo, J.; Kim, K.; Kim, J.; Ahn, S.; Cui, Y.; Cho, J. *Nano Lett.* **2009,** *9,* 3844–3847. doi:10.1021/nl902058c
18. Magasinski, A.; Dixon, P.; Hertzberg, B.; Kvit, A.; Ayala, J.; Yushin, G. *Nat. Mater.* **2010,** *9,* 353–358. doi:10.1038/nmat2725
19. Muldoon, J.; Bucur, C. B.; Oliver, A. G.; Zajicek, J.; Allred, G. D.; Boggess, W. C. *Energy Environ. Sci.* **2013,** *6,* 482. doi:10.1039/C2EE23686A
20. Aurbach, D.; Lu, Z.; Schechter, A.; Gofer, Y.; Gizbar, H.; Turgeman, R.; Cohen, Y.; Moshkovich, M.; Levi, E. *Nature* **2000,** *407,* 724. doi:10.1038/35037553
21. Aurbach, D.; Gofer, Y.; Lu, Z.; Schechter, A.; Chusid, O.; Gizbar, H.; Cohen, Y.; Ashkenazi, V.; Moshkovich, M.; Turgeman, R.; Levi, E. *J. Power Sources* **2001,** *97–98,* 28. doi:10.1016/S0378-7753(01)00585-7
22. Aurbach, D.; Gizbar, H.; Schechter, A.; Chusid, O.; Gottlieb, H. E.; Gofer, Y.; Goldberg, I. *J. Electrochem. Soc.* **2002,** *149,* A115. doi:10.1149/1.1429925
23. Aurbach, D.; Suresh, G. S.; Levi, E.; Mitelman, A.; Mizrahi, O.; Chusid, O.; Brunelli, M. *Adv. Mater.* **2007,** *19,* 4260. doi:10.1002/adma.200701495
24. Kim, H. S.; Arthur, T. S.; Allred, G. D.; Zajicek, J.; Newman, J. G.; Rodnyansky, A. E.; Oliver, A. G.; Boggess, W. C.; Muldoon, J. *Nat. Commun.* **2011,** *2,* 427. doi:10.1038/ncomms1435
25. Liebenow, C.; Yang, Z.; Lobitz, P. *Electrochem. Commun.* **2000,** *2,* 641. doi:10.1016/S1388-2481(00)00094-1
26. Guo, Y. S.; Zhang, F.; Yang, J.; Wang, F. F.; NuLi, Y. N.; Hirano, S. I. *Energy Environ. Sci.* **2012,** *5,* 9100. doi:10.1039/c2ee22509c
27. Mohtadi, R.; Matsui, M.; Arthur, T. S.; Hwang, S. J. *Angew. Chem., Int. Ed.* **2012,** *51,* 9780. doi:10.1002/anie.201204913 *J. Angew. Chem.* **2012**, *124*, 9918.
28. Shao, Y. Y.; Liu, T. B.; Li, G. S.; Gu, M.; Nie, Z. M.; Engelhard, M. H.; Xiao, J.; Lv, D. P.; Wang, C. M.; Zhang, J. G.; Liu, J. *Sci. Rep.* **2013,** *3,* 3130. doi:10.1038/srep03130
29. Wang, F. F.; Guo, Y. S.; Yang, J.; Nuli, Y.; Hirano, S. *Chem. Commun.* **2012,** *48,* 10763. doi:10.1039/c2cc35857c
30. Nelson, E. G.; Kampf, J. W.; Bartlett, B. M. *Chem. Commun.* **2013,** *50,* 5193. doi:10.1039/c3cc47277a
31. Liao, C.; Guo, B.; Jiang, D.; Custelcean, R.; Mahurin, S. M.; Sun, X.-G.; Dai, S. *J. Mater. Chem. A* **2014,** *2,* 581. doi:10.1039/c3ta13691d
32. Zhao-Karger, Z.; Zhao, X.; Fuhr, O.; Fichtner, M. *RSC Adv.* **2013,** *3,* 16330. doi:10.1039/c3ra43206h
33. Doe, R. E.; Han, R.; Hwang, J.; Gmitter, A. J.; Shterenberg, I.; Yoo, H. D.; Pour, N.; Aurbach, D. *Chem. Commun.* **2014,** *50,* 243. doi:10.1039/c3cc47896c
34. Liu, T.; Shao, Y.; Li, G.; Gu, M.; Hu, J.; Xu, S.; Nie, Z.; Chen, X.; Wang, C.; Liu, J. *J. Mater. Chem. A* **2014,** *2,* 3430. doi:10.1039/c3ta14825d

35. Carter, T. J.; Mohtadi, R.; Arthur, T. S.; Mizuno, F.; Zhang, R.; Shirai, S.; Kampf, J. W. *Angew. Chem., Int. Ed.* **2014,** *53,* 3173. doi:10.1002/anie.201310317
36. Chusid, O.; Gofer, Y.; Gizbar, H.; Vestfrid, Y.; Levi, E.; Aurbach, D.; Riech, I. *Adv. Mater.* **2003,** *15,* 627. doi:10.1002/adma.200304415
37. Higashi, S.; Miwa, K.; Aoki, M.; Takechi, K. *Chem. Commun.* **2013,** *50,* 1320. doi:10.1039/c3cc47097k
38. Connor, J. H.; Reid, W. E., Jr.; Wood, G. B. *J. Electrochem. Soc.* **1957,** *104,* 38. doi:10.1149/1.2428492
39. Cheek, G. T.; O'Grady, W. E.; El Abedin, S. Z.; Moustafa, E. M.; Endres, F. *J. Electrochem. Soc.* **2008,** *155,* D91. doi:10.1149/1.2804763
40. Yoshimoto, N.; Matsumoto, M.; Egashia, M.; Morita, M. *J. Power Sources* **2010,** *195,* 2096. doi:10.1016/j.jpowsour.2009.10.073
41. NuLi, Y.; Yang, J.; Wu, R. *Electrochem. Commun.* **2005,** *7,* 1105. doi:10.1016/j.elecom.2005.07.013
42. Amir, N.; Vestfrid, Y.; Chusid, O.; Gofer, Y.; Aurbach, D. *J. Power Sources* **2007,** *174,* 1234. doi:10.1016/j.jpowsour.2007.06.206
43. Viestfrid, Yu.; Levi, M. D.; Gofer, Y.; Aurbach, D. *J. Electroanal. Chem.* **2005,** *576,* 183. doi:10.1016/j.jelechem.2004.09.034
44. Aurbach, D.; Turgeman, R.; Chusid, O.; Gofer, Y. *Electrochem. Commun.* **2001,** *3,* 252. doi:10.1016/S1388-2481(01)00148-5
45. Arthur, T. S.; Glans, P.-A.; Matsui, M.; Zhang, R.; Ma, B.; Guo, J. *Electrochem. Commun.* **2012,** *24,* 43. doi:10.1016/j.elecom.2012.08.018
46. Benmayza, A.; Ramanathan, M.; Arthur, T. S.; Matsui, M.; Mizuno, F.; Guo, J.; Glans, P.-A.; Prakash, J. *J. Phys. Chem. C* **2013,** *117,* 26881. doi:10.1021/jp4077068
47. Kumar, G. G.; Munichandraiah, N. *Electrochim. Acta* **1999,** *44,* 2663. doi:10.1016/S0013-4686(98)00388-0
48. Morita, M.; Yoshimoto, N.; Yakushiji, S.; Ishikawa, M. *Electrochem. Solid-State Lett.* **2001,** *4,* A177. doi:10.1149/1.1403195
49. Pandey, G. P.; Agrawal, R. C.; Hashmi, S. A. *J. Solid State Electrochem.* **2011,** *15,* 2253. doi:10.1007/s10008-010-1240-4
50. Aubrey, M. L.; Ameloot, R.; Wiers, B. M.; Long, J. R. *Energy Environ. Sci.* **2014,** *7,* 667. doi:10.1039/C3EE43143F
51. Ikeda, S.; Takahashi, M.; Ishikawa, J.; Ito, K. *Solid State Ionics* **1987,** *23,* 125. doi:10.1016/0167-2738(87)90091-9
52. Kawamura, J.; Morota, K.; Kuwata, N.; Nakamura, Y.; Maekawa, H.; Hattori, T.; Imanaka, N.; Okazaki, Y.; Adachi, G.-y. *Solid State Commun.* **2001,** *120,* 295. doi:10.1016/S0038-1098(01)00386-6
53. Matsuo, M.; Oguchi, H.; Sato, T.; Takamura, H.; Tsuchida, E.; Ikeshoji, T.; Orimo, S. *J. Alloys Compd.* **2013,** *580,* S98. doi:10.1016/j.jallcom.2013.01.058
54. Unemoto, A.; Matsuo, M.; Orimo, S.-I. *Adv. Funct. Mater.* **2014,** *24,* 2267. doi:10.1002/adfm.201303147
55. Makino, K.; Katayama, Y.; Miura, T.; Kishi, T. *J. Power Sources* **2001,** *97–98,* 512. doi:10.1016/S0378-7753(01)00694-2
56. NuLi, Y.; Yang, J.; Wang, J.; Li, Y. *J. Phys. Chem. C* **2009,** *113,* 12594. doi:10.1021/jp903188b
57. NuLi, Y.; Yang, J.; Li, Y.; Wang, J. *Chem. Commun.* **2010,** *46,* 3794. doi:10.1039/C002456B
58. Ling, C.; Banerjee, D.; Song, W.; Zhang, M.; Matsui, M. *J. Mater. Chem.* **2012,** *22,* 13517. doi:10.1039/c2jm31122d
59. Liu, B.; Luo, T.; Mu, G.; Wang, X.; Chen, D.; Shen, G. *ACS Nano* **2013,** *7,* 8051–8058. doi:10.1021/nn4032454
60. NuLi, Y.; Guo, Z.; Liu, H.; Yang, J. *Electrochem. Commun.* **2007,** *9,* 1913. doi:10.1016/j.elecom.2007.05.009
61. Li, W.; Li, C.; Zhou, C.; Ma, H.; Chen, J. *Angew. Chem., Int. Ed.* **2006,** *45,* 6009. doi:10.1002/anie.200600099
62. Khoo, T.; Somers, A.; Torriero, A. A. J.; MacFarlane, D. R.; Howlett, P. C.; Forsyth, M. *Electrochim. Acta* **2013,** *87,* 701. doi:10.1016/j.electacta.2012.09.072
63. Shiga, T.; Hase, Y.; Kato, Y.; Inoue, M.; Takechi, K. *Chem. Commun.* **2013,** *49,* 9152. doi:10.1039/c3cc43477j
64. Sutto, T. E.; Duncan, T. T. *Electrochim. Acta* **2012,** *79,* 170. doi:10.1016/j.electacta.2012.06.099
65. Sutto, T. E.; Duncan, T. T. *Electrochim. Acta* **2012,** *80,* 413. doi:10.1016/j.electacta.2012.07.050
66. Ichitsubo, T.; Adachi, T.; Yagi, S.; Doi, T. *J. Mater. Chem.* **2011,** *21,* 11764. doi:10.1039/c1jm11793a
67. Bruce, P. G.; Krok, F.; Nowinski, J.; Gibson, V. C.; Tavakkoli, K. *J. Mater. Chem.* **1991,** *1,* 705. doi:10.1039/jm9910100705
68. Novák, P.; Desilvestro, J. *J. Electrochem. Soc.* **1993,** *140,* 140. doi:10.1149/1.2056075
69. Novák, P.; Imhof, R.; Haas, O. *Electrochim. Acta* **1999,** *45,* 351. doi:10.1016/S0013-4686(99)00216-9
70. Imamura, D.; Miyayama, M.; Hibino, M.; Kudo, T. *J. Electrochem. Soc.* **2003,** *150,* A753. doi:10.1149/1.1571531
71. Imamura, D.; Miyayama, M. *Solid State Ionics* **2003,** *161,* 173. doi:10.1016/S0167-2738(03)00267-4
72. Amatucci, G. G.; Badway, F.; Singhal, A.; Beaudoin, B.; Skandan, G.; Bowmer, T.; Plitz, I.; Pereira, N.; Chapman, T.; Jawaorski, R. *J. Electrochem. Soc.* **2001,** *148,* A940. doi:10.1149/1.1383777
73. Levi, E.; Gofer, Y.; Aurbach, D. *Chem. Mater.* **2010,** *22,* 860. doi:10.1021/cm9016497
74. Liang, Y.; Feng, R.; Yang, S.; Ma, H.; Liang, J.; Chen, J. *Adv. Mater.* **2011,** *23,* 640. doi:10.1002/adma.201003560
75. Yang, S.; Li, D.; Zhang, T.; Tao, Z.; Chen, J. *J. Phys. Chem. C* **2012,** *116,* 1307–1312. doi:10.1021/jp2097026
76. Liu, Y.; Jiao, L.; Wu, Q.; Du, J.; Zhao, Y.; Si, Y.; Wang, Y.; Yuan, H. *J. Mater. Chem. A* **2013,** *1,* 5822. doi:10.1039/c3ta10786h
77. Tao, Z.-L.; Xu, L.-N.; Gou, X.-L.; Chen, J.; Yuan, H.-T. *Chem. Commun.* **2004,** 2080. doi:10.1039/b403855j
78. Kumagai, N.; Komaba, S.; Sakai, H.; Kumagai, N. *J. Power Sources* **2001,** *97–98,* 515. doi:10.1016/S0378-7753(01)00726-1
79. Rasul, S.; Suzuki, S.; Yamaguchi, S.; Miyayama, M. *Solid State Ionics* **2012,** *225,* 542. doi:10.1016/j.ssi.2012.01.019
80. Rasul, S.; Suzuki, S.; Yamaguchi, S.; Miyayama, M. *Electrochim. Acta* **2012,** *82,* 243. doi:10.1016/j.electacta.2012.03.095
81. Zhang, R.; Yu, X.; Nam, K.-W.; Ling, C.; Arthur, T. S.; Song, W.; Knapp, A. M.; Ehrlich, S. N.; Yang, X.-Q.; Matsui, M. *Electrochem. Commun.* **2012,** *23,* 110. doi:10.1016/j.elecom.2012.07.021
82. Ling, C.; Mizuno, F. *Chem. Mater.* **2013,** *25,* 3062. doi:10.1021/cm401250c

BEILSTEIN JOURNAL OF NANOTECHNOLOGY

Liquid fuel cells

Grigorii L. Soloveichik

Review

Open Access

Address:
General Electric Global Research, Niskayuna, NY 12309, USA

Email:
Grigorii L. Soloveichik - soloveichik@ge.com

Keywords:
anion exchange membranes; direct alcohol fuel cells; direct borohydride fuel cells; electrocatalysts; liquid fuel cells; organic fuel; proton exchange membranes

Beilstein J. Nanotechnol. **2014,** *5,* 1399–1418.
doi:10.3762/bjnano.5.153

Received: 27 March 2014
Accepted: 04 August 2014
Published: 29 August 2014

This article is part of the Thematic Series "Materials for sustainable energy production, storage, and conversion".

Guest Editor: M. Fichtner

Abstract

The advantages of liquid fuel cells (LFCs) over conventional hydrogen–oxygen fuel cells include a higher theoretical energy density and efficiency, a more convenient handling of the streams, and enhanced safety. This review focuses on the use of different types of organic fuels as an anode material for LFCs. An overview of the current state of the art and recent trends in the development of LFC and the challenges of their practical implementation are presented.

Introduction

Fuel cells are considered to be one of the key elements of the "hydrogen economy", in which hydrogen generated from renewable energy sources would be widely used as a clean energy carrier [1]. They do not produce greenhouse gases and other pollutants during their operation, and they have a higher efficiency entitlement (no Carnot cycle limitation) and lower maintenance (no moving parts) than internal combustion engines [2]. The total reaction of hydrogen oxidation in a fuel cell is described by Equation 1 and the cell has an open circuit potential (OCP) of 1.23 V under ambient conditions.

$$H_2 + 1/2\ O_2 \leftrightarrow H_2O \quad (1)$$

There are three major types of hydrogen/air fuel cells differing in the types of ions (protons, hydroxyl, and oxygen anions) transported through the membrane (Figure 1). In all cases the structure of the fuel cell is similar and consists of a cathode and an anode with a current collector (bipolar plate), a gas diffusion layer, and a catalyst layer. The electrodes are separated by an ion-conducting insulating membrane (Figure 1). Bipolar or field plates separating the individual cells in the stack should have a high corrosion resistance, good electronic and thermal conductivity, and be designed to evenly distribute reactants and products. It is worth noting that the bipolar plates have an impact on the cost structure comparable with the impact of catalytic electrodes [3].

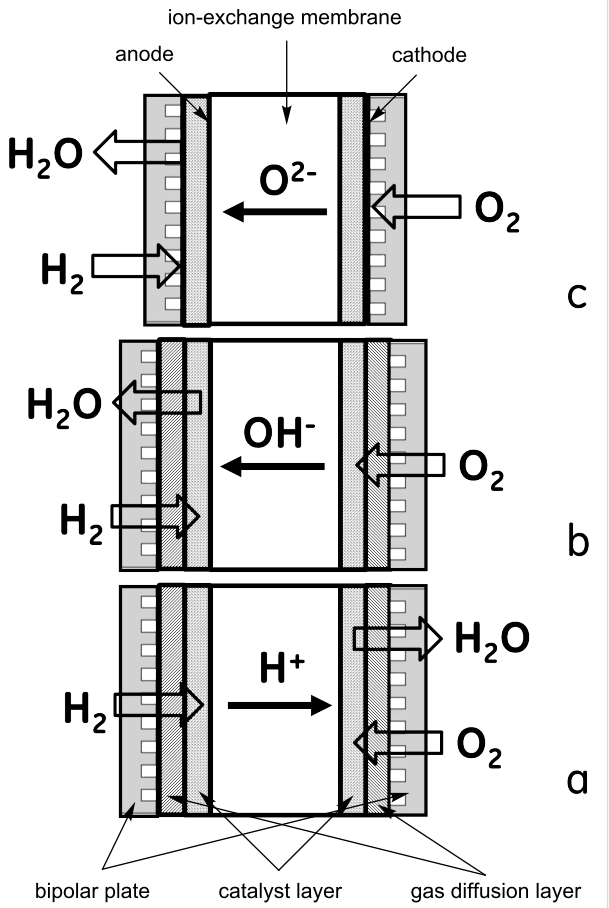

Figure 1: The electrochemistry and major components of liquid fuel cells with proton (a), alkaline (b) and solid oxide (c) ion-exchange membranes.

In a solid oxide fuel cell (SOFC) the electrolyte conducting the negative oxygen ions (Figure 1c) is usually a rare-earth metal oxide doped zirconia, e.g., yttria stabilized zirconia (YSZ) or ceria that operates at high temperature (700–1000 °C). Liquid fuels may be used directly in SOFCs without reforming. For example, toluene, *n*-decane, and synthetic diesel fuel were fed to a SOFC at 700 °C to generate a power density of about 100 mW/cm^2 [4]. Recently, a much higher power density (about 600 mW/cm^2 at 750 °C) has been demonstrated by using a multi-functional anode and iso-octane as fuel [5]. The main issue is the formation of carbon deposits on the anode, which is thermodynamically favorable under the reaction conditions [6]. At these temperatures organic fuels exist as vapors and therefore direct organic fuel SOFCs will not be discussed in this paper.

The most widely used fuel cells are based on proton exchange membranes (PEM), through which protons are transported (Figure 1a). The chemistry of anode and cathode reactions in the PEM hydrogen–oxygen regenerative fuel cell (RFC) is described by Equation 2 and Equation 3, respectively. Commonly used PEMs are generally based on sulfonated fluoropolymers such as Nafion® 117 [7] that are stable and conductive up to 85–90 °C. Composite membranes based on both fluorinated and non-fluorinated materials, e.g., polysulfone polymers and inorganic proton conductors are used to achieve higher operating temperatures and a lower humidity [8]. Solid inorganic proton conductors (e.g., sintered zirconium phosphate) allow for increasing the working temperature up to 150–250 °C [9]. Only platinum group metal (PGM) electrocatalysts are stable enough in the low-pH environment of PEMs. Platinum is the best electrocatalyst for both hydrogen oxidation reaction (HOR) and oxygen reduction reaction (ORR), but it is very expensive. To reduce the Pt loading and therefore the cost for the electrocatalyst, Pt-containing alloys and structured nanoparticles, e.g., "core–shell" materials with less expensive metals are being investigated.

$$\mathrm{H_2 \leftrightarrow 2H^+ + 2e^-} \quad \left(E^0 = 0\ \mathrm{V}\right) \tag{2}$$

$$\mathrm{1/2\,O_2 + 2H^+ + 2e^- \leftrightarrow H_2O} \quad \left(E^0 = +1.23\ \mathrm{V}\right) \tag{3}$$

Alkaline fuel cells are based on the transport of hydroxide ions through an anion-exchange membrane (AEM); the anode and cathode reactions are shown in Equation 4 and Equation 5, respectively (Figure 2b). They have the advantage of a lower redox potential for ORR in basic media (Equation 5). First such cells were developed at GE and used composite electrodes (a Pt black mixed with Teflon) and an AEM impregnated with 30% KOH [10]. An advantage of AEM fuel cells is that it is possible to use non-PGM electrocatalysts while classic PGM-oxide catalysts are less corrosion stable [11]. In general, AEMs have a lower conductivity and oxidative stability than PEMs [12]. The lower conductivity may be compensated for by the larger number of cationic sites, resulting in a high OH^- conductivity and power density. For example, an alkaline fuel cell utilizing a poly(vinylbenzyl(trimethylammonium hydroxide)) ion-exchange membrane showed a conductivity of 0.043 S/cm and current density of 0.72 A/cm^2 at 0.6 V. Unfortunately, it was stable only up to 70 °C [13]. The sensitivity of AEMs towards nucleophilic attack in the working pH ranges and their reactivity with CO_2 from air, which requires a scrubber or a closed system, limits their application.

$$\mathrm{H_2 + 2OH^- \leftrightarrow 2H_2O + 2e^-} \quad \left(E^0 = -0.83\ \mathrm{V}\right) \tag{4}$$

$$\mathrm{1/2\,O_2 + H_2O + 2e^- \leftrightarrow 2OH^-} \quad \left(E^0 = +0.40\ \mathrm{V}\right) \tag{5}$$

In general, in fuel cell systems oxygen is supplied by pumping air through the cathode, and hydrogen is stored on-site. Several types of hydrogen storage are currently considered: compressed gas, liquid hydrogen, metal hydrides (thermal release) or chemical hydrides (hydrolysis) [14].

The transportation and use of hydrogen as a fuel is limited by its physical properties (as the lightest element it has extremely low volumetric energy density) and safety issues (flammability and the formation of explosive mixtures with air). Hydrogen transportation is very expensive, therefore only few hydrogen fueling stations have been built so far, mostly in Europe (about 30) and the US (about 15). Though more fueling stations are planned, implementation of the hydrogen infrastructure will require an enormous capital investment. Compressed gas hydrogen (CGH_2) storage in pressurized tanks (350 or 700 bar for mobile and 120 bar for stationary applications) is currently considered as the only practical option. It is the simplest method, which does not require expensive infrastructure and controls, but the system energy density is low, and there are safety hazards associated with high pressure and extreme flammability of hydrogen gas. Hydrogen can be stored in liquid form (LH_2) in cryogenic tanks. This method has a higher energy density than CGH_2. However, hydrogen liquefaction requires substantial energy (up to 30% of the lower heating value) and there are boil-off losses [15]. Hydrogen can be reversibly stored in metallic hydrides, e.g., intermetallic phases AB_5 and AB_3 [16], or complex hydrides, e.g., metal borohydrides $M(BH_4)_n$ [17]. However, good hydrogen release kinetics and reversibility are inversely correlated with the storage capacity. Dehydrogenation of metal hydrides requires substantial thermal energy, which is technically challenging due to their low thermal conductivity.

The dehydrogenation of methylcyclohexane to toluene for both transportation and seasonal hydrogen storage was proposed 20 years ago [18]. Later the less volatile decalin/naphtalene couple with 7.3 wt % hydrogen content and a density of 64.8 kg-H_2/m^3 was also suggested [19]. In these systems, dehydrogenation can be done at ambient pressure, the heat transfer is not challenging, and the generated hydrogen is CO-free. A feasibility study of these systems showed the production cost of hydrogen to be $5.33/kg with the ratio energy generated/energy consumed of about 4 [20]. However, the hydrogen release from these compounds requires expensive PGM catalysts and high temperature (280 °C) resulting in large catalytic dehydrogenation reactor space and high cost requirements. The use of extended π-systems containing nitrogen atoms, such as *N*-alkylcarbazoles [21], enables a reduction in the heat and temperature of dehydrogenation (up to 200 °C), but the hydrogen content is lower. If all the heat is generated by the electrochemical oxidation of hydrogen, the overall system efficiency would be reduced from 55% to 44% which is still higher than the efficiency of internal combustion engines [22]. Alcohols constitute another class of liquid organic hydrogen carriers (LOHCs). Their hydrogen content is lower, but they can be dehydrogenated to aldehydes or ketones at much lower temperatures (80–90 °C) although side reactions, such as dehydration, are possible [23]. The rate of H_2 generation from LOHCs is high enough to satisfy the demands of mobile applications, and the stability of the dehydrogenation catalyst exceeds several hundred hours [24]. The selectivity of dehydrogenation/hydrogenation reactions, a very important factor for energy storage, was reported to be over 99% for different classes of LOHCs and a promising cycling behavior was demonstrated [23,24]. The use of LOHCs, such as cycloalkanes, for hydrogen storage allows for the use of the existing liquid fuel infrastructure with relatively small modifications. However, in spite of the progress made in the last years, current technology is not yet close to meeting the revised targets of the United States Department of Energy (DOE) [25].

Review

Fuels for liquid fuel cells

Liquid-feed fuel cells can use different types of liquid fuels. Organic compounds that are liquids at ambient conditions can be used both neat and in the form of a solution. However, they are more often used in solution because of their flammability, toxicity and, most importantly, high crossover rates. Solid organic and inorganic compounds, e.g., $NaBH_4$, can be used as a solution. Water is a natural solvent for organic and inorganic fuels, because it is produced at the cathode side, and it is the ion conducting medium in the majority of ion exchange membranes. Some of the proposed organic fuels are produced from renewable biomass, e.g., ethanol by fermentation of sugars, glycerol by transesterification of fats and oil triglycerides (biodiesel process), and furfural by hydrolysis of lignocellulose and agricultural byproducts (corncobs, wheat bran, etc.), which makes them especially attractive. In addition to individual compounds, mixtures can be used to improve electrode kinetics. Hydrazine, for example, was mixed with formic acid and methanol for that purpose [26].

In early works on liquid fuel cells several attempts to use hydrocarbons such as diesel and jet fuel were made. However, electrooxidation of hydrocarbons in low- and intermediate-temperature fuel cells turned out to be very difficult, and later the research focus was shifted to the oxidation of methanol in direct methanol fuel cells (DMFCs). Methanol has a higher energy density than liquid hydrogen and high theoretical fuel cell efficiency (Table 1). It was proposed as the basis for the “methanol economy” [27] as an alternative to the “hydrogen economy”

based on hydrogen gas [1]. Alcohols with higher molecular weights, which contain C–C bonds, have an even higher energy density (Table 1) but their electrooxidation in fuel cells is not complete due to difficulty of activation of the C–C bonds and yields multiple intermediate products along with CO_2 [28-30]. Polyoxomethylenedimethyl ethers ($CH_3O(CH_2O)_nCH_3$ (n = 1–8)) have been proposed as a fuel alternative to higher alcohols [31]. They have low vapor pressure and negligible toxicity, and undergo fast hydrolysis in the presence of acidic catalysts to release a mixture of methanol and formaldehyde that is oxidized several times faster than pure MeOH [31].

In addition to alcohols, other organic compounds such as aldehydes (e.g., furfural) and acids (e.g., formic acid) may be used as liquid fuels for fuel cells. They have a high energy density (Table 1) and solubility in water. Aqueous solutions of sugars (glucose, sucrose, and lactose) were used in implantable bio micro fuel cells [32] but their energy density is too small to be used in large scale applications. Aqueous solutions of some inorganic compounds containing significant amount of hydrogen such as ammonia, hydrazine, alkali metal borohydrides MBH_4 (M = Na, K) are also used as fuels. Theoretically, boron-nitrogen heterocycles proposed for hydrogen storage [33,34] can be used for this purpose.

In most cases the electrooxidation of fuels in fuel cells results in the formation of thermodynamically very stable and kinetically inert products. For instance, the electrooxidation of primary alcohols and formic acid generates CO_2, and the oxidation of hydrazine releases N_2. Such products cannot be directly converted back to starting fuels in a reverse reaction, and their regeneration requires an off-board multi-step process that is usually very energy demanding. For example, sodium borate can be regenerated to $NaBH_4$ via ballmilling with MgH_2 [35]. Another approach, which is a focus of the "Energy Frontier Research Center for Electrocatalysis, Transport Phenomena, and Materials for Innovative Energy Storage", is to use partial electrooxidation of LOHC fuels to extract hydrogen (as protons and electrons) and form a stable dehydrogenated molecule, e.g., an aromatic or carbonyl compound (Equation 6) [36,37]. The overall reaction in the cell is described by Equation 7. The energy density of these systems is lower than those based on the full oxidation, but potentially they can be used for energy storage via electrochemical hydrogenation of the spent fuel

Table 1: Theoretical energy density and fuel cell efficiency for liquid fuels for fuel cells.

fuel	anode products	number of electrons	E^0, V	energy density, Wh/L		η, %
				neat	solution	
liquid H_2	H_2O*	2	1.23	2350	—	83.0
H_2 gas (70 MPa)	H_2O*	2	1.23	1300	—	83.0
formic acid	$CO_2 + H_2O$	2	1.45	2103	1190 (10 M)	105.6
formate	$CO_2 + H_2O$	2	1.45	—	145 (1 M)	105.6
methanol	$CO_2 + H_2O$	8	1.17	5897	305 (2 M)	96.7
ethanol	$CO_2 + H_2O$	12	1.14	6307	915 (3 M)	97.0
ethanol	C_2H_4O	2	0.95	872	109 (3 M)	89.1
ethylene glycol	$C_2H_2O_2$	4	0.87	1652	168 (1 M)	103.7
ethylene glycol	$(COOH)_2$	8	1.09	4180	546 (2 M)	89.8
ethylene glycol	$CO_2 + H_2O$	10	0.87	5800	168 (1 M)	86.0
2-propanol	C_2H_5CHO	2	1.02	695	105 (2 M)	98.1
2-propanol	$(CH_3)_2CO$	2	1.07	750	114 (2 M)	98.2
glycerol	$CO_2 + H_2O$	14	1.21	5965	—	95.1
1,4-butanediol	$C_4H_6O_2$	4	1.13	1361	—	89.9
2,4-pentanediol	$C_5H_8O_2$	4	1.27	1105	—	111.8
furfural	$CO_2 + H_2O$	10	1.16	3915	—	76.3
cyclohexane	C_6H_6	6	1.06	1578	—	94.1
decalin	$C_{10}H_8$	10	1.09	1893	—	93.1
dodecahydro-*N*-ethylcarbazole	$C_{14}H_{13}N$	12	1.18	1715	—	n/a
ammonia	N_2	3	1.17	—	1704 (35 wt %)	88.7
ammonia borane	NH_4BO_2	6	1.62	—	655 (2 M)	83.7
hydrazine hydrate	N_2	4	1.56	4269	873 (4 M)	100.2
sodium borohydride	$NaBO_2$	8	1.64	—	2940 (30 wt %)	93.4

(Equation 6 reverse). This approach is much simpler because it does not require an additional dehydrogenation catalyst nor a heat exchanger, and it has a higher energy density compared to hydrogen-on-demand designs that include the thermal decomposition of LOHCs in a catalytic reactor [38]. The spent (dehydrogenated) LOHC fuels can be re-hydrogenated either on-board (electrochemically) or off-board (electrochemically or chemically at a central plant). In the latter case, the fuel cells can be recharged by using the existing infrastructure for the delivery of liquid fuels.

$$LH_n \leftrightarrow L + nH^+ + ne^- \quad (6)$$

$$LH_n + n/4\ O_2 \leftrightarrow L + n/2\ H_2O \quad (7)$$

The theoretical open circuit potential (OCP) of electrochemical cells based on the reaction in Equation 7 is in the range of 1.06–1.11 V if the dehydrogenation product is an aromatic or carbonyl compound but only about 0.9 V if the product is an olefin [39]. For practical fuels, this results in theoretical energy densities of 1600–2200 Wh/L, which are comparable with that of liquid hydrogen (2540 Wh/L). In addition, the theoretical efficiency of organic fuel cells is higher than that of hydrogen (93–95% vs 83%) [39]. The partial electrochemical oxidation of fuels can also be used to produce valuable chemical products, e.g., acetaldehyde from ethanol or fine chemicals from glycerol, along with energy generation ("the chemical co-generation process") [40,41].

Direct hydrocarbon fuel cells

Saturated hydrocarbons are attractive fuels for LFCs due to their extremely high energy density (9–10 kWh/L for full oxidation), abundance, low costs and the existing infrastructure. Early works on direct organic fuel cells were aimed at the use of liquid hydrocarbons (octane, decane, and, eventually, diesel fuel) as a fuel in phosphoric acid fuel cells. Linear hydrocarbons produced a higher current density on a Pt/PTFE anode in 95 wt % phosphoric acid at 175 °C while the addition of aromatic or branched hydrocarbons increased the anode overpotential [42]. On the other side, the presence of allyl hydrogen atoms in additives reduced the overpotential. A cell with a porous Pt/PTFE anode and cathode catalysts running on decane showed a maximum power density of 21 mW/cm^2 (O_2 cathode) and 17 mW/cm^2 (air cathode) [43]. The addition of iso-alkanes to the fuel decreased the cell performance to about a third. Electrooxidation of hydrocarbon fuels in the presence of phosphoric acid requires a very high Pt loading (50 mg Pt/cm^2), which makes this approach unfeasible. Lower hydrocarbons, e.g., propane [44,45] and cyclohexane [46,47] were used as fuels for PEM fuel cells but in the vapor form.

Direct alcohol fuel cells

Both monohydric and polyhydric alcohols have been proposed and used as fuel for LFCs in aqueous solution. The most extensively studied DMFC technology based on the reaction in Equation 8 has been reviewed in multiple papers [48-56], and will be discussed here only for comparison properties.

$$CH_3OH + 2O_2 \rightarrow CO_2 + 2H_2O \quad (8)$$

Thermodynamic analysis of fuel cells based on C_1–C_5 alcohols showed that these cells have OCVs that are only 10–100 mV lower than hydrogen fuel cells but exhibit a higher theoretical efficiency [57,58]. By combination of parameters such as efficiency, OCV and specific energy, only MeOH and EtOH can compete with hydrogen as a fuel at temperatures below 75 °C while in the intermediate temperature range (up to 300 °C) C_1–C_3 alcohols are preferred [58].

Direct ethanol fuel cells

Ethanol is a renewable, inexpensive feedstock and as a fuel has a very high energy density and theoretical cell efficiency if fully oxidized to CO_2 and water (Table 1). Therefore, ethanol based LFCs are considered for mobile applications [59]. However, breaking the C–C bond is extremely difficult and the CO_2 yield is usually low [57]. This has been explained by the higher energy barrier of the key step of CO formation due to the presence of surface O and OH species [60]. In acidic media two reactions (Equation 9 and Equation 10) are dominant. The formation of acetaldehyde occurs at lower potentials (<0.6 V vs RHE) while acetic acid is produced under consumption of a water molecule at higher potentials (>0.8 V vs RHE) [61]. The product of another two-electron oxidation reaction, ethane-1,1-diol, is formed in substantial quantities when Pt/C is used as a catalyst and is also present as a minor product in the presence of bimetallic catalysts [62]. The selective oxidation of EtOH to ethylacetate, without the formation of CO_2, takes place in sulfuric acid solution at a reduced SO_2-treated porous Pt black anode [63].

$$C_2H_5OH \rightarrow CH_3CHO + 2H^+ + 2e^- \quad \left(E^0 = +0.28\ V\right) \quad (9)$$

$$C_2H_5OH + H_2O \rightarrow CH_3COOH + 4H^+ + 4e^- \quad \left(E^0 = +0.06\ V\right) \quad (10)$$

The kinetics of ethanol electrooxidation on Pt-based anodes in acidic media is much slower than that of hydrogen and results in high fuel cell overpotentials (usually 0.3–0.6V) [64]. This is

partially compensated by lower ethanol crossover through acidic membranes and lesser cathode poisoning [65]. PtRu and PtSn catalysts were much more active than pure Pt [57]. Double-layered anode catalysts consisting of 45 wt % Pt_3Sn/C and PtRu black electrocatalysts showed an improvement of about 40% in power density (up to 96 mW/cm^2) and a higher yield of acetic acid [66]. The addition of Ni to binary Pd–Sn alloys increases the electrocatalytic activity [67]. Intermetallic phases of Pt with In, Sn, Pb, Bi, and As were studied as electrocatalysts for the oxidation of ethanol [68]. In contrast to its inactivity towards MeOH oxidation, the PtBi phase was electrocatalytically active in EtOH oxidation while the $PtBi_2$ phase and other PtM_x phases with a ratio Pt:M (M = Sn) different from 1 were inactive [68].

Low overpotentials for the oxidation of EtOH were achieved with $Pt_n(SnO_2)$/C (n = 1, 3, 9) electrocatalysts. A fuel cell using 2 M EtOH, a Nafion® 117 membrane and a Pt/C cathode catalyst reached a peak power density of 127 mW/cm^2 for n = 3 at 100 °C [69]. Acetaldehyde and acetic acid were the major products, and the yield of CO_2 was below 7%. Acetic acid is not electroactive under the fuel cell conditions while acetaldehyde can be used as a fuel although it generates half the power [69]. Addition of acetaldehyde to ethanol impairs the performance of the fuel cell.

Apart from the development of more active catalysts that are less sensitive to CO poisoning, another approach is to increase the operation temperature. To this end, a composite silica/Nafion® membrane was used at 145 °C to reach a maximum power density 110 mW/cm^2 with 1 M EtOH feed [70]. Under these conditions CO_2 becomes the major product along with a smaller amount of acetaldehyde. Contrary, a vapor-fed fuel cell with H_3PO_4-doped polybenzimidazole (PBI) membrane and similar catalysts produced mostly acetaldehyde at a higher temperature (170 °C) [71,72].

Higher primary alcohols starting from 1-propanol exhibit even slower kinetics in acidic media and, therefore, are not considered as promising fuels [71,73].

The operation of alkaline ethanol LFC has potential benefits compared with PEM LFC including faster kinetics of both ethanol oxidation and oxygen reduction in basic media and lower fuel crossover due to a reversed electro-osmotic effect of anion movement in the membrane. The major product of EtOH electrooxidation in alkaline solution is acetate (Equation 11)

$$C_2H_5OH + 5OH^- \rightarrow CH_3COO^- + 4H_2O + 4e^- \quad \left(E^0 = -0.743\ \text{V}\right) \tag{11}$$

The product distribution of electrochemical ethanol oxidation in basic media depends on the catalyst. A Pt catalyst generates acetate that converts to ethylacetate at higher EtOH concentrations along with some CO_2. Acetate is formed at a Pd catalyst with very high faradaic efficiency while ethylacetate is the only product at a Ag catalyst [74]. The addition of a base (NaOH or KOH) in the concentration of at least 1 M to ethanol solutions is necessary to provide good conductivity. It was found that for 2 M fuel and 3 M KOH the current density was similar for methanol or ethanol but the ethanol cell exhibited a slightly higher voltage [75]. A cell with a non-platinum HYPERMEC^{TM} (Acta) anode and cathode catalyst and Tokuyama® AEM using 3 M EtOH and 5 M KOH showed an OCV of about 900 mV and a peak power density of 60 mW/cm^2 [76]. Replacing the cathode catalyst with Pd_3Au/CNT increased the power density to 185 mW/cm^2 [77].

A thermally stable PBI membrane doped with 2 M KOH was used as AEM in a direct ethanol LFC to expand the operational temperature range [78]. The cell, equipped with a 45% PtRu anode catalyst and a 40% MnO_2/C cathode catalyst, achieved a maximum power density of 30 mW/cm^2 using a 2 M EtOH/2 M KOH fuel mixture, but the cell performance quickly degraded (more than 50% after 200 h) [78].

A cell with hydrogen peroxide as the oxidant and a non-platinum anode showed 44% increase in power density (160 mW/cm^2 at 80 °C) compared to a similar cell with an air cathode [79]. In an innovative cell design proposed by T. Zhao at el. [80], anode (ethanol in a basic media) and cathode (H_2O_2 in an acidic media) are separated by a cation exchange membrane. The cell, equipped with 15 μm Nafion® N211 PEM and PtNi/C electrocatalysts, reached a peak power density of 360 mW/cm^2 at 60 °C, which is a substantial increase compared to the state-of-the-art direct ethanol fuel cells. A high theoretical OCP (2.52 V) is rendered by both the oxidation of ethanol to acetate and the neutralization reaction that gives sodium sulfate as a by-product (Equation 12). Though the highest cell voltage was measured for a fuel concentraion of 5 M , the cell optimal performance was reached for 3 M EtOH and 5 M NaOH [80].

$$CH_3H_2OH + 5NaOH + 2H_2O_2 + 2H_2SO_4 \rightarrow CH_3COONa + 2Na_2SO_4 + 8H_2O \tag{12}$$

Direct isopropanol fuel cells

Isopropanol (IPA) is relatively inexpensive, has a low toxicity and is miscible with water. Electrooxidation of IPA on different catalysts in both acidic [81,82] (Equation 13) and alkaline [83-87] (Equation 14) media has been studied. In both reactions acetone is the single oxidation product but at high potentials the formation of CO_2 was detected [88]. At low current densities,

the formation of H_2 as a result of IPA dehydrogenation on a Pt catalyst was reported [89]. In acidic solutions only Pt and PtRu are used as electrocatalysts [81,82], while in alkaline solutions the catalyst selection is wider. At high pH values Pt is not the most active electrocatalyst, and Pd is at least at par or even superior [83,84]. Although Au is less active than Pd and Pt in a pure form [83], its addition to Pd in the ratio of 1 to 4 increases the catalyst activity and stability for IPA oxidation [85]. Ni metal supported on carbon catalyzed the IPA electrooxidation [28], which was attributed to the formation of surface β-NiOOH species [87].

$$CH_3CHOHCH_3 \rightarrow CH_3COCH_3 + 2H^+ + 2e^- \quad \left(E^0 = +0.13\ \text{V}\right) \quad (13)$$

$$CH_3CHOHCH_3 + 2OH^- \rightarrow CH_3COCH_3 + 2H_2O + 2e^- \quad \left(E^0 = -0.67\ \text{V}\right) \quad (14)$$

A fuel cell with a Ni/C anode catalyst and a Nafion® 117 PEM showed a higher OCV for 2 M IPA in water than for MeOH but the current density was low (about 1 mA/cm^2) and the cell voltage dropped with time [28]. It is noteworthy, that at 80 °C the Ni/C catalyst was more active than the Pt/C catalyst, but exhibited a worse fuel cell performance, presumably due to the catalyst poisoning [28]. The use of PtRu anode catalysts, a Pt cathode catalyst and a Nafion® 112 PEM resulted in a higher peak power density (80 mW/cm^2) and relatively low crossover current (approximately 30% of that for MeOH) [90]. It was found that the cell performance was best with 1 M IPA at 60 °C [90]. A similar cell equipped with a sulfonated poly(ether ether ketone) (SPEEK) membrane using neat IPA as a fuel delivered 97 mW/cm^2 at 60 °C but a stable performance was observed only for low current densities (10 mA/cm^2) [91]. The crossover of neat IPA through the SPEEK PEM was about the same as for the 1 M solution due to lower swelling [91]. A similar LFC operating on 2 M IPA at 90 °C exhibited a high OCV (0.86 V) and achieved a peak power density of 128 mW/cm^2 [89]. The cell voltage was ca. 200 mV higher, and the electrical efficiency (59%) was 27% higher than that of the cell operating on methanol. However, the cell performance sharply dropped when the current density exceeded 200 mA/cm^2, which is attributed to catalyst poisoning by acetone or products of deep oxidation of IPA [89].

The use of neat IPA with liquid 5 M KOH electrolyte and commercial Pt/C catalyst provided a peak power of 22 mW/cm^2 [92], which was higher than for a cell with a PtRu catalyst and a PVA/TiO_2 membrane using 2 M IPA/2 M KOH fuel (16 mW/cm^2) [93]. A mixture of methanol and 2-propanol that has a low electrooxidation onset and higher oxidation current densities than single alcohols was proposed as a fuel [94].

1-Methoxy-2-propanol was used as a fuel in a PEM fuel cell showing a high OCV (0.71 V) but the cell performance degraded faster than with IPA [95].

Direct ethylene glycol fuel cells

The theoretical energy density of ethylene glycol (EG) is comparable to those of methanol and glycerol (Table 1), However, the complete electrooxidation of EG to CO_2 and H_2O, a ten-electron process, has not been achieved [96]. The electrochemical oxidation of EG on Pt yields a mixture of products: glycolic acid and CO_2 in acidic media, and glycolate, oxalate and carbonate in alkaline media [97]. Glycol aldehyde and oxalic acid were also detected in $HClO_4$ solution [98]. The catalyst is poisoned by intermediates that have been identified as CO-like species [99]. The electrochemical oxidation of EG on Pt–Sn catalysts is a four-electron process, which corresponds to the formation of glycolic acid, a major product determined by chromatography (GCMS) [100].

An acidic EG fuel cell using a 100 μm nanoporous proton-conducting membrane and a Pt–Ru anode catalyst demonstrated a peak power density of 300 mW/cm^2 for the anolyte containing 2 M EG and 3 M H_2SO_4, which was higher than a cell with a Nafion® 115 membrane [101]. Replacing the sulfuric acid with triflic acid decreased the anodic overpotential and increased the maximum power density to 320 mW/cm^2 at a lower acid concentration (1.7 M) [102]. In a 10-cell stack with the same membrane fed with 0.5 M EG in 1.7 M triflic acid solution, the power density was 120 mW/cm^2 and two major by-products (glycolic and oxalic acids) were identified [103]. Discharging without EG feeding consumed the by-products almost completely; this shows the possibility of a complete EG oxidation to CO_2 [103].

A basic EG fuel cell with a 28 μm Tokuyama AEM was tested with a PdNi/C anode catalyst and a non-Pt cathode catalyst at different concentrations of EG (0.5–3 M) [104]. It was found that 1 M EG was the optimal EG concentration. The maximum power density reached with 7 M KOH was 67 mW/cm^2 at 60 °C [104]. The use of an alkali-doped polybenzimidazole membrane resulted in the increase of the maximum power density for the same fuel composition to 80 mW/cm^2 (at 60 °C) and 112 mW/cm^2 (at 90 °C), which was 2–3 times higher than for the same cells fueled with MeOH and EtOH [105]. An interesting concept of an EG fuel cell using a $LaSr_3Fe_3O_{10}$ ceramic disk as a membrane and ORR catalyst was demonstrated in a cell with 10 wt % EG, 10% KOH and FeCoNi/C

anode catalyst to give oxalic acid as a major product (Equation 15) and a power density of 27 mW/cm^2 [106].

$$HOCH_2CH_2OH + 8OH^- \rightarrow (COOH)_2 + 6H_2O + 8e^- \quad (E^0 = -0.69\ V) \quad (15)$$

Direct glycerol fuel cells

Glycerol as a nontoxic fuel for fuel cells was proposed in 1964 [107]. Glycerol is the major product in biodiesel production by transesterification of plant oils and animal fats. Although it is used as a raw material in the chemical industry and animal feed, its market is saturated thus limiting the expansion of biodiesel [108]. Having a high energy density (Table 1), glycerol is a promising fuel. However, as in the case of other C_2 and higher alcohols, the total oxidation has not been demonstrated.

The electrooxidation of glycerol in acidic media on a Pt/C electrode gives a mixture of products with glyceraldehyde as the major one. The addition of bismuth as a saturated solution redirects the reaction towards 100% selective formation of dihydroxyacetone [109]. The bulk electrolysis of glycerol in 0.1 M NaOH on Ni/C and NiCo/C anodes gives formate, glycolate and glycerate as major products [110]. The electrooxidation of glycerol on the Au/C anode in alkaline LFC yields predominantly salts of tartronic, glyceric, mesoxalic and oxalic acids with a faradaic efficiency of 53–58% [111]. The electrooxidation of glycerol on an optimized Ru–Ni catalyst was 3–4 times faster than the oxidation of ethanol [112].

A direct glycerol fuel cell fed with glycerol (1 M) in KOH (4 M) using a polybenzimidazole (PBI) membrane impregnated with KOH and PtRu/C and Pt_3Sn/C anode catalysts showed a peak power density of 18 mW/cm^2 at 60 °C, which decreased as the temperature increased to 90 °C [113]. Pd-based electrocatalysts showed a much higher activity than Pt-based ones, e.g., PtRu, which is widely used in DMFCs [114]. An active alkaline fuel cell running on 5% glycerol and using Pd catalyst supported on multi-wall carbon nanotubes generated 80 mW/cm^2 peak power at 80 °C. The product mixture included formate and carbonate [114].

The use of crude glycerol from the biodiesel process in an AEM fuel cell has been reported [115]. The use of dealloyed PtCo nanoparticles on a carbon nanotube support surface in such a cell allowed for a peak power density of 268.5 mW/cm^2 at 80 °C with the anode catalyst loading of 0.5 mg Pt/cm^2 [116].

Fuel cells with other oxygenated fuels

Abundant and energy dense sugars are natural fuels for bio (microbial or enzymatic) fuel cells using whole cells or isolated redox enzymes to catalyze the oxidation [117]. These cells demonstrate very low power densities and will not be discussed in this paper. PGM catalysts exhibit low catalytic activity in electrooxidadion of carbohydrates. The oxidation of glucose in 1 M KOH in alkaline liquid fuel cells with a PtRu electrocatalyst generates gluconic acid (two-electron process) and 1.4 mW/cm^2 peak power [118]. The use of a Pt/C anode with a cobalt phthalocyanine cathode in an alkaline cell with a Tokuyama membrane provided a maximum power density of 2.3 mW/cm^2 in 0.5 M glucose/0.5 M KOH solution [119]. Increasing the KOH concentration to 7 M, in combination with a PdNi anode and a non-platinum HYPERMEC^{TM} cathode (Acta), resulted in a substantial increase in power density to 38 mW/cm^2 at 60 °C [120]. Sorbitol and xylose were also used as fuels but demonstrated slightly slower kinetics [121,122]. The performance of the fuel cells with carbohydrate fuels significantly decreased with time, which was partially attributed to sorbitol and glucose crossover-poisoning the Pt/C cathode [121].

L-Ascorbic acid (AA, also known as vitamin C) has been proposed as a fuel for liquid-fed fuel cells because it is benign, renewable, inexpensive, and highly soluble in water (330 g/L) [123]. PGM catalysts are not necessary for the anodic oxidation of AA, e.g., a polyaniline-based anode produced 4.3 mW/cm^2 at 70 °C with liquid fuel of 1 M AA in 0.5 M H_2SO_4 [124]. The use of treated carbon black (Vulcan X72) produced a four-fold increase of the peak power density [125]. Dehydroascorbic acid was the only electrooxidation product detected [125], which sets the theoretical energy density of 110 Wh/L at the maximum concentration in water. The acidic nature of AA as a fuel reduces its crossover through acidic membranes. Unfortunately, the low power of such fuel cells makes them useful only to long-term portable or implantable applications.

Direct formic acid fuel cells

Formic acid has a high OCP (Table 1), and the fact that it is liquid at room temperature and non-toxic in diluted solutions makes it an attractive fuel candidate [126]. The crossover flux of formic acid through PFSA membranes is less than that of MeOH [127], which allows for the use of much higher concentrations (10×). It results in higher energy densities compared to DMFC in spite of the higher theoretical energy density of methanol (Table 1). Electrooxidation of formic acid is described by Equation 16. A parallel undesirable reaction pathway leads to the formation of adsorbed CO species, which are then oxidized to the final product, CO_2 [128]. All known anode electrocatalysts contain Pt or Pd, though the pure metals cannot be used due to surface poisoning with CO. It was shown that addition of Ru (up to 50 mol %) decreases the quasi-steady-state level of adsorbed CO [128]. Replacement of ruthenium with

gold in the bimetallic catalyst increases catalytic activity that results in higher cell voltage [129]. A series of intermetallic phases of Pt with In, Sn, Pb, Bi, and As was identified as promising electrocatalysts for oxidation of formic acid with $PtBi_2$ being the most active [68]. The use of a Pt_4Mo alloy increases the reaction rate by more than one order of magnitude compared to pure Pt supposedly due to the formation of hydrous molybdenum oxide that reduces the surface poisoning by adsorbed CO [130].

$$\mathrm{HCOOH} \rightarrow \mathrm{CO_2} + 2\mathrm{H^+} + 2\mathrm{e^-} \quad \left(E^0 = -0.22\ \mathrm{V}\right) \quad (16)$$

Palladium-based electrocatalysts deliver higher power densities compared to platinum-based ones. Fuel cells with a Pd black anode catalyst and 3 M HCOOH reached a peak power density of 375 mW/cm^2 at 50 °C [131]. The power density is independent of the formic acid concentration up to 10 M, which allows for high energy densities (Table 1). Unfortunately, limited life-testing data indicates that the catalyst deactivates within several hours, and the rate of deactivation increases with the acid concentration. However, the loss of activity is reversible, and it can be restored by pulsing the potential [131]. In contrast to Pt, the addition of a second component (Ru, Au) decreases the catalyst performance of Pd black [132]. The use of a Pd/C catalyst results in lower power densities (145–170 mW/cm^2 depending on the loading), but a more stable performance [133]. The alloying of Pd with Sb [134] and Bi [135] in carbon-supported catalysts increased the power density, which reached 260 mW/cm^2 for Pd–Bi/C catalyst with 5 M HCOOH. A similar effect was achieved by deposition of bismuth on the Pt nanoparticles by irreversible adatom adsorption [136]. It was claimed that the addition of Ni to Pd/C improves the catalyst performance and stability [137]. Different type of supports have been tried to replace traditional carbon support, e.g., Vulcan XC-72. The addition of more corrosion-resistant ZrC to XC-72 carbon (1:1) provided a narrower particle size distribution and a better dispersion on the surface and resulted in a higher activity during formic acid oxidation [138]. Nanocomposite-based on Pd/MnO_2/nanolamella-graphene sheets showed an activity that was about six times higher than that of a traditional Pd/C catalyst [139]. Although the peak power density for supported Pd-based catalysts is lower than for Pd black, the palladium utilization and specific power density (mW per mass unit) are much higher.

The flux of formic acid across Nafion® membranes increases with concentration. It is only about half of that of MeOH, but the resulting crossover current is much lower (by about a factor of 6) due to the smaller number of participating electrons (8 vs 2, compare Equation 8 and Equation 16) [140]. Due to their high power density, low crossover and an the insufficient stability of the electrocatalysts, the development of direct formic acid fuel cells currently targets small scale portable applications including microcells [126].

The electrooxidation of the formate anion in alkaline media (Equation 17) combined with ORR reaction (Equation 5) is used in a formate alkaline fuel cell [141]. A fuel cell equipped with an AEM demonstrated a high OCV (0.93 V) and a high peak power density (125 mW/cm^2 for a 1:1 mixture of KCOOH and KOH at 60 °C). It was shown that the formate oxidation reaction does not depend on the pH value in a range between pH 9 and 14, so formate fuel can be used without added hydroxide [142]. However, the power density increases with the KOH concentration and drops substantially without the base. A concentration of 1 M KOH seems to be optimal [141]. This limits the energy density of this system (Table 1). The increase of the working temperature to 120 °C and of the KCOOH concentration to 6 M in a similar cell with a Ag cathode catalyst resulted in higher power density (160 mW/cm^2) [143]. Alkaline media is favorable for faster electrooxidation kinetics of the formate anion, and formate salts are non-hazardous and easy to transport. However, the reaction (Equation 17) generates alkaline metal carbonates as a waste, which decreases the attractiveness of this approach.

$$\mathrm{COOH^-} + 3\mathrm{OH^-} \rightarrow \mathrm{CO_3^{2-}} + 2\mathrm{H_2O} + 2\mathrm{e^-} \quad \left(E^0 = -1.05\ \mathrm{V}\right) \quad (17)$$

The mixture of formic acid and formate was proposed as a fuel for a direct fuel cell [144]. In the presence of formate the oxidation potential of formic acid was shifted in the negative direction and the oxidation current increased. In this case only formic acid was oxidized.

Inorganic fuel cells

Direct ammonia fuel cells

The nitrogen hydrides, ammonia and hydrazine, are attractive fuels for direct fuel cells because potentially they can be cleanly oxidized to water and nitrogen [145,146]. Ammonia cannot be used directly in acidic PEM fuel cells due to a sharp drop in membrane conductivity (ammonium salt formation) and catalysts poisoning [147]. In an early work, a fuel cell using aqueous potassium hydroxide and PTFE-bonded Pt black supported on graphite electrodes, combined with an air cathode, demonstrated power densities of 50 mW/cm^2 at 0.5 V at 120 °C [148]. A fuel cell with a Cr-decorated Ni anode, a MnO_2/C cathode, and an Amberlite–based membrane using 35% ammonia solution showed a peak power density of about 9 mW/cm^2 at room temperature, which was nevertheless higher than that for hydrogen fuel under the same conditions [149].

The main challenge of direct ammonia fuel cells is the development of robust anode electrocatalysts. It was found that PtRu/C is much more active than individual metals but still achieves only current densities below 30 mA/cm^2 [150]. Accumulation of adsorbed nitrogen species on the catalyst surface causes catalyst degradation. Another drawback of these cells is the ammonia flux through the anion exchange membrane [150].

Direct hydrazine fuel cells

The concept of a direct hydrazine fuel cell was developed in the 1960s [151,152]. Hydrazine can be electrochemically oxidized as the hydrazonium cation $N_2H_5^+$ in acidic and neutral (due to hydrolysis) media (Equation 18) or as a neutral molecule in basic solutions (Equation 19). The overall cell reaction generates only nitrogen and water, with a standard OCP of 1.56 V.

$$N_2H_5^+ \rightarrow N_2 + 5H^+ + 5e^- \quad \left(E^0 = -0.33\ \text{V}\right) \qquad (18)$$

$$N_2H_4 + 4OH^- \rightarrow N_2 + 4H_2O + 4e^- \quad \left(E^0 = -1.16\ \text{V}\right) \qquad (19)$$

Theoretically hydrazine fuel has a very high energy density (Table 1) but the need to use diluted solutions limits the energy density, e.g., to 340 Wh/L for 10 wt % hydrazine hydrate solutions used in a PEM fuel cell [153]. A cell with 60 wt % Pt on carbon catalyst and Nafion® 117 membrane showed a high OCV (about twice as high as with MeOH) but the higher internal resistance limited the power density to about 100 mW/cm^2 [153]. It was found that the catalytic decomposition of hydrazine on Pt generates both hydrogen and ammonia (via two different pathways), which reduces the OCV. In addition, a substantial flux of hydrazine and ammonia through the PEM, causing degradation of the cathode, was observed [153]. These issues shifted the research focus exclusively to alkaline hydrazine fuel cells in the subsequent years [154].

The search for hydrazine oxidation electrocatalysts is complicated because of the competing reactions leading to a decomposition of hydrazine, which are catalyzed by the same catalysts [155]. Platinum in alkaline media is less active than Ag, Ni and Co, and this opens a pathway to PGM-free fuel cells [156]. The activity of Ag and Pd nanoparticles on carbon was comparable [157]. Nickel-0based electrocatalysts are the most active for hydrazine oxidation. An alloy with the composition $Ni_{0.6}Co_{0.4}$ was about 6 times more active than the pure Ni catalyst [155]. The design space of binary Ni–M (with M = Mn, Fe, Zn, La) and ternary Ni–Mn–Fe and Ni–Zn–La compositions was explored by using the combinatorial approach. The compositions $Ni_{0.87}Zn_{0.13}$ and $Ni_{0.9}La_{0.1}$ prepared by spray pyrolysis were the most active showing power densities of 486 and 459 mW/cm^2, respectively [158]. The enhanced electrocatalytic performance of the latter may be explained by the formation of a $LaNi_5$ coating on the surface [159]. More than 2000 h of continuous operation at 70% efficiency were demonstrated with a cell with a nanotextured Cu–Ni anode, although with a low current density (14 mA/cm^2) [160].

The use of hydrogen peroxide as an oxidant (Equation 20) in a direct hydrazine fuel cell fuel cell delivers a high OCP (2.13 V), which can be even higher when the anode is basic and the cathode is acidic. Thus, a cell, with Ni–Pt/C anode and Au/C cathode catalysts, 10 wt % hydrazine/15 wt % NaOH anolyte and 20 wt % hydrogen peroxide/5 wt % H_2SO_4 catholyte, had a high OCV (1.75) V and showed a very high peak power density (1.02 W/cm^2 at 80 °C) [161]. A higher temperature improves the performance of the cathode but has little effect on the anode [161]. An electrocatalyst consisting of dealloyed nanoporous gold leaves demonstrated activities toward both hydrazine oxidation and hydrogen peroxide reduction that were about 22 times higher than a commercial Pt/C electrocatalyst at the same loading [162].

$$H_2O_2 + 2H^+ + 2e^- \rightarrow 2H_2O \quad \left(E^0 = 1.76\ \text{V}\right) \qquad (20)$$

In an attempt to increase the conductivity and stability of the AEM, a composite membrane of a hydroxyl conducting quaternary ammonium polymer confined in a pre-treated PTFE matrix was prepared through in situ polymerization. It had a conductivity of 0.049 S/cm at room temperature, which resulted in a peak power density of 110 mW/cm^2 [163].

The main drawback of direct hydrazine fuel cells is the high toxicity of N_2H_4 and its derivatives [164]. Less toxic hydrazine derivatives such as carbohydrazide $(N_2H_3)_2CO$ have been proposed to solve this issue [165]. Carbohydrazide has 71% of the capacity of hydrazine, it is miscible with water, and it can be electrochemically oxidized in the presence of inexpensive cobalt porphyrines [165].

Direct borohydride fuel cells

The high OCP and energy density of direct fuel cells with anodes that contain borohydride (tetrahydroborate, BH_4^-) salts make them attractive for portable applications and stimulated recent research in this area [166,167]. Only borohydrides of alkali metals (except Li) are stable towards hydrolysis at high pH values. Electrooxidation of the borohydride anion in alkaline media is an eight-electron reaction (Equation 21). When coupled with ORR (Equation 5, net reaction in Equation 22), the theoretical cell OCP is very high, about 400 mV higher than the OCP of a fuel cell with a hydrogen anode (Table 1).

However, the observed OCV of the direct borohydride fuel cell is much lower, presumably because it is a mixed potential of the reaction in Equation 22 and the thermodynamically favorable reaction in Equation 4, in which hydrogen is generated by the competing hydrolysis of borohydride (Equation 23) [166]. If hydrogen is oxidized fast, e.g., by using active porous electrodes, the total number of transferred electrons is still eight as was shown by rotating disk electrode experiments on an Au electrode [168].

$$BH_4^- + 8OH^- \rightarrow BO_2^- + 6H_2O + 8e^- \left(E^0 = -1.24\ \text{V}\right) \quad (21)$$

$$NaBH_4 + 2O_2 \rightarrow NaBO_2 + 2H_2O \quad (22)$$

$$BH_4^- + H_2O \rightarrow BH_3OH^- + 1/2\,H_2 \quad (23)$$

The electrooxidation of borohydride anions is a multi-step electron transfer process with competing parallel chemical reactions, and its mechanism is not fully understood [169]. The number of electrons removed from the BH_4^- ion depends on the anode electrocatalyst, the concentration of sodium borohydride and the ratio $[OH^-]$:$[BH_4^-]$. For a ratio of about 4.4, the reaction is described by Equation 21, while for lower ratios the reaction in Equation 23 takes place predominantly, which leads to a decrease in the number of electrons [170]. It was shown that on a Pt/C catalyst the borohydride anion is oxidized by an eight-electron reaction at concentrations below 1.5 M, and by a six-electron reaction under H_2 evolution at concentrations above 2 M at a more negative electrode potential (−1.38 V) [171]. The electrode potential increases even further (E^0 = −1.65 V) for a four-electron reaction but this increase does not compensate for the loss of capacity [172] Non-PGM cathode catalysts for direct borohydride fuel cells based on Ni, Co and Mn oxides show activities comparable or sometimes higher than conventional Pt/C, with $LaNiO_3$ being the most active [173].

Charge neutrality during electrooxidation of BH_4^- ions (Equation 21) can be achieved in two ways: (1) by the movement of cations (Na^+) across a cation exchange membrane (CEM) (Figure 2b,c), or (2) by the movement of anions (OH^-) across an anion exchange membrane (AEM) (Figure 2a). Therefore two basic designs using CEM and AEM are known in the literature [166,167]. AEM-based designs offer simpler processes where borohydride, borate and alkali metal ions are confined in the anode compartment, stabilizing the pH of the anolyte. However, AEMs are not stable in concentrated alkali especially at elevated temperatures [12,13]. Another issue of direct borohydride fuel cells with AEMs is crossover of BH_4^- ions to the cathode, which substantially reduces the cell efficiency and poisons the cathode catalyst.

A fuel cell with a Laves phase AB_2 Zr–Ni based alloy and Pd/C as the anode catalyst, a Nafion® NRE-211 membrane and Pt/C as the cathode catalyst delivered a power density of 290 mW/cm^2 at 60 °C [172]. The $NaBH_4$ utilization was only 51% but increased with lower temperatures. Combining a borohydride electrolyte with a mixed anode (Zn + $LaNi_{4.7}Al_{0.3}$) and a MnO_2 cathode catalyst allowed for an increased cell capacity (up to 1800 mA/g for the anode) and an increased peak power compared to a Zn/air cell [174].

Replacing the ion exchange membranes with a fiber separator made of inexpensive polymer materials (polypropylene or polyamide) and allowing the free movement of all ions resulted in substantial increase in the power density compared to Nafion® CEMs. A cell with non-PGM catalysts ($LaNiO_3$ in the cathode and Co(II) oxide in the anode) delivered a peak power of 663 mW/cm^2 at 65 °C [173].

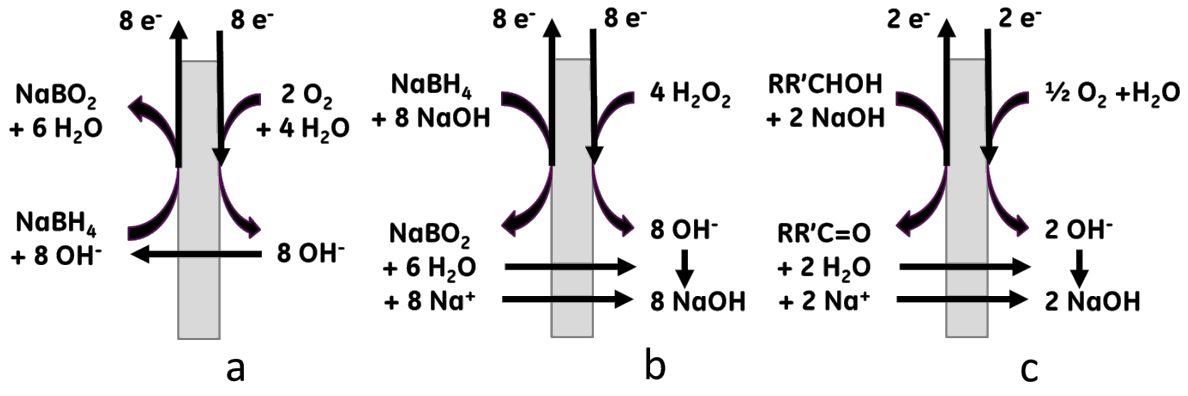

Figure 2: The electrochemistry of a borohydride liquid fuel cell with hydroxyl (a) and cation (b) exchange membranes and an alcohol fuel cell with cation exchange membrane (c).

Another promising modification of the direct borohydride fuel cell is an all-liquid cell with hydrogen peroxide cathode. The standard electrode potential of the H_2O_2 cathode is 530 mV higher than that of the oxygen cathode, with a similar dependence on the pH value. A cell based on the reactions in Equation 21 and Equation 24 has a high OCP (2.14 V) and a high theoretical energy density (2580 Wh/kg), as well as a simpler heat management compared to fuel cells with gas electrodes. The charge is balanced by the transport of Na^+ ions across a CEM.

$$H_2O_2 \rightarrow 2OH^- + 2e^- \quad \left(E^0 = 0.95\ V\right) \tag{24}$$

The all-liquid direct borohydride cell with a mischmetal $MmNi_{3.55}Al_{0.3}Mn_{0.4}Co_{0.75}$ anode and a 60 wt % Pt/C cathode catalyst showed a peak power density of 350 mW/cm^2 at 70 °C when fed with 10 wt % $NaBH_4$ in 20 wt % NaOH to the anode and 15 wt % H_2O_2 (pH 0) to the cathode [175]. The cell voltage at maximum power was 1.2 V and decreased with increasing catholyte pH value. Therefore, to obtain a steady cell performance it is necessary to maintain a high pH in the anolyte and a low pH in the catholyte, thus consuming also a base and an acid (Equation 25) [175]. The cell performance was optimized with 8 wt % $NaBH_4$ in the anolyte and with 2 M H_2O_2 in 1.5 M H_2SO_4 in the catholyte [176]. A similar composition of fuel (10 wt % $NaBH_4$ in 20 wt % NaOH, 15 wt % H_2O_2 in 1 M sulfuric acid) produced 410 mW/cm^2 at 80 °C [177].

$$NaBH_4 + 8NaOH + 4H_2O_2 + 4H_2SO_4 \rightarrow NaBO_2 + 14H_2O + 4Na_2SO_4 \tag{25}$$

The sputtering of metals on a carbon cloth provides well-dispersed nanoscale particles with high catalytic activity resulting in a peak power density of 680 mW/cm^2 at 60 °C, with Pd and Au as anode and cathode catalysts, respectively [178].

Direct ammonia borane fuel cells

Ammonia borane NH_3BH_3 (AB) has 19.6% hydrogen, is easily soluble in water and reasonably stable towards the hydrolysis in the absence of catalysts, which makes it a promising fuel for liquid-fed fuel cells [179]. AB is electrochemically oxidized in alkaline media to environmentally benign products (Equation 26). An AB fuel cell has OCV 1.616 V and theoretical specific energy 2113 Wh/kg at the maximum concentration. In practice, solutions containing a base have a lower specific energy, of about 30% of the theoretical value (Table 1). In principle, ammonia, one of the products of the reaction in Equation 26, can be oxidized in alkaline media [146] thus increasing the cell capacity. However, the large potential difference (450 mV) and slow kinetics make this difficult.

$$NH_3BH_3 + 6OH^- \rightarrow BO_2^- + NH_4^+ + 4H_2O + 6e^- \tag{26}$$

Similarly to sodium borohydride, the hydrolysis of AB decreases the cell voltage and coulombic efficiency [179]. A fuel cell using 46.6 wt % Pt on Vulcan XC-72 reached a maximum power density of 185 mW/cm^2 [180]. Gold electrocatalysts having low activity towards hydrolysis turned out to be more efficient catalysts than platinum. Thiourea, a known hydrogen evolution inhibitor, was also used as an additive to increase the coulombic efficiency [181]. Nanoporous gold electrodes prepared by extracting Ag from an AgAu alloy catalyze the oxidation of AB at a potential more negative by 280 mV, and current densities 5 times higher than those obtained with a pure Au disk electrode [182]. It was found that smooth Cu metal is as good an electrocatalyst as Pt nanoparticles for the oxidation of AB [183]. Nanostructured Cu with petal-like structures possessed a much higher electrocatalytic activity and when used as an anode in a fuel cell with a commercial air cathode provided a power density of about 1 W/cm^2 with an OCV of 1.26 V at room temperature [183].

The recent development of inexpensive Cu electrocatalysts is a substantial progress towards the use of AB as a fuel in practical fuel cells. However, there are a number of issues to be solved including low efficiency due to hydrolysis, fuel and products crossover, product crystallization in MEA and the high cost of AB. Although a one-pot method for the conversion of the thermal decomposition products of AB back to AB by a treatment with hydrazine was recently developed [184], the regeneration of AB from borate will remain a complex multi-step process including the formation of $NaBH_4$. Therefore, there are serious doubts that AB fuel cells would be more practical than the more simple borohydride fuel cells, which have a higher energy density [185].

Regenerative organic fuel cells

The direct use of organic hydrides in LFCs as virtual hydrogen carriers that generate stable organic molecules, protons and electrons upon reversible electrooxidation (Equation 6 direct and reverse) could provide an attractive alternative to hydrogen gas or metal hydride storage coupled with conventional hydrogen-air fuel cells [36,37]. The overall reaction is described by Equation 7.

This ‘virtual hydrogen’ scheme proposed by the Energy Frontier Research Center for Electrocatalysis, Transport Phenomena, and Materials, which was funded by DOE and is led by General Electrics (GE) avoids the release of hydrogen gas thus

by-passing issues associated with hydrogen storage, transportation and safety. Compared to a hydrogen-on-demand design that includes thermal decomposition of organic hydrides in a catalytic reactor [38], this approach is much simpler, does not require additional dehydrogenation catalysts, heat exchangers and has higher energy density [36,37].

This concept of regenerative fuel cells (RFC) was demonstrated for vaporized organic fuels such as cyclohexane/benzene (OCV = 920 mV) [186] and isopropanol/acetone (OCV of the cell = 790 mV) [46] couples by using a Pt/C electrocatalyst. The power density was low (15 and 78 mW/cm^2, respectively) but may be improved by Pt alloying, e.g., with Ni [47]. An attempt to use a neat liquid fuel (*N*-ethyldodecahydrocarbazole, dodecahydrofluorene) while using a PtRu catalyst resulted in a high OCV but very low current density [187]. Therefore, the development of effective and selective electrocatalysts for liquid organic fuels and compatible PEMs remains a major challenge.

A concept of a thermally regenerative fuel cell has been proposed by Ando et al. [188,189]. In this approach power is generated by electrochemical hydrogenation of acetone to IPA at the positive electrode and the dehydrogenation of IPA at the negative electrode by using low-grade heat. In another version, hydrogen that is generated through the thermal catalytic decomposition of IPA (Equation 27) serves as a proton source in the reactions in Equation 2 and Equation 13 (reverse) [188]. The OCV of cells based on the reaction in Equation 27 with Nafion® 117 PEM was close to theoretical but the voltage sharply decreased with the current density showing a peak power density of only about 650 μW/cm^2 [188]. When IPA was used as hydrogen source, the cell power was very low (less than 20 mW). The cell efficiency peaked at IPA concentrations of 50–70%. The hydrogenation of acetone at the cathode was the rate-determining reaction. Replacing the PtRu/C electrocatalyst with PdRu/C or PdFe/C [190] or addition of sulfuric acid to the catholyte [191] increased the cell OCV by a factor of 2 to 4. The electrochemical hydrogenation of acetone dissolved in water and cyclohexane in a polymer electrolyte reactor showed that hydrogen evolution was a competing reaction with a similar reaction rate [192]. In a cell with a PtRu catalyst and a Nafion® 117 PEM, a maximum rate and current efficiency was achieved at an acetone concentration of about 3.5 M [193]. Increasing the cell temperature increases the reaction rate and current efficiency (up to about 60%) [193].

$$CH_3CHOHCH_3 \leftrightarrow CH_3COCH_3 + H_2 \qquad (27)$$

These reactions were successfully implemented in a vapor-fed IPA-based fuel cell with an air cathode [46,194], and they could be used potentially in a RLFC.

Current trends and outlook

Fuel cell design

There are three major types of low temperature LFCs based on the type of ion exchange membrane: proton exchange (PEM), cation (alkali metal) exchange (CEM) and anion (hydroxyl) exchange (AEM). Recently, novel concepts of two layered (acidic–basic) [80] and three layered (basic–acidic–basic) [195] membranes have been proposed. PEM LFCs dominated in the literature but recently AEM LFCs got more attention [196]. In alkaline media the alcohol fuel oxidation rate is higher, and the overpotential for the ORR is lower [197]. In addition, OH^- ions and fuel molecules move in the opposite direction in an AEM, therefore potentially reducing the fuel crossover rate. However, these advantages are offset by the low conductivity of AEMs (at least an order of magnitude lower than that of PEMs) and by their lower stability [198]. Direct comparison of LFCs running on MeOH, EtOH and iPrOH in alkaline (0.5 M KOH) and acidic (0.1 M $HClO_4$) solutions with Fumapem® FAA-2 (FumaTech) and Nafion® 115 (DuPont) membranes, respectively, while using the same PtRu catalyst showed that despite their higher current densities in alkaline solutions, the peak power density of the acidic cells was more than one order of magnitude higher than that of alkaline cells [199]. In a membrane-less fuel cell based on laminar flow, which is considered for small-scale portable applications, the OCV and current density was indeed higher in alkaline media (but still low compared with the AEM cell design) [200]. Noteworthy, for ethanol LFCs with an air cathode the highest power density was reached with an AEM [77]. Unfortunately, the conductivity of AEMs cannot be increased by operating at higher temperatures because of the low chemical stability of these membranes towards bases. Another disadvantage of alkaline LFC, especially targeting the full oxidation like DMFC, is the formation of alkali metal carbonates and bicarbonates that crystallize in the electrolyte-filled pores thus blocking the ion transport. However, only AEMs could be used with nitrogen and boron hydride fuels. DMFC with a sodium conducting CEM (Nafion®) have been proposed, but they showed very low power densities (9 mW/cm^2) [201]. Recently, a cell using 2 M EtOH in 2 M KOH with a KOH-modified Nafion® 112 membrane and a PtRu anode catalyst showed a peak power density comparable with ethanol-powered LFCs with Nafion® PEM [69], PBI/KOH [78] and Tokuyama [77] AEMs. Even better performance was demonstrated for a LFC running on 3 M EtOH in 5 M NaOH with a NaOH-modified Nafion® 112 CEM, a PdNi/C anode catalyst and a FeCo HYPERMEC^{TM} cathode catalyst [202]. Compared to the analogous cell with a Tokuyama A201 AEM it showed a higher power density (135 vs 115 mW/cm^2) and a stable discharge behavior at 90 °C [202]. This finding opens a possibility to run alkaline LFCs at higher temperatures. The formation of a base at the cathode of

CEM LFCs is an issue that needs to be solved (for example by recycling the base to the anode).

Although oxygen is easily obtained from the atmosphere and there is no need for oxidant storage, sluggish kinetics of the ORR prompted search for a fuel cell cathode with better kinetics. Hydrogen peroxide cathodes allowed for the highest power densities for LFCs (vide supra). A bromine cathode has a much smaller overpotential compared to O_2 and is used in hydrogen–bromine fuel cells [203]. Another liquid cathode comprising a water soluble oxidant, e.g., iron [204] or vanadium [205] complexes and a catalyst such as a polyoxometalate was proposed by ACAL Energy. The reduced catholyte is reoxidized in a separated regeneration unit by air oxygen, which serves as the ultimate oxidant.

Electrocatalysts

The anodic oxidation of fuels in LFCs remains the main challenge. Known anode electrocatalysts for LFCs are either too expensive or have low activity, and chemical and thermal stability, or are not selective enough. Pt is the most active electrocatalyst known for oxidation of organic fuels, but it is poisoned by reaction products. To overcome these shortcomings, several approaches are currently investigated, including decreasing the high loading of PGM metals (e.g., by increasing the dispersity or by the use of core–shell structures) or replacing platinum with less expensive PGMs (Pd) or base metals (in alkaline LFCs), while adjusting the electronic structure by adding adatoms, alloying, and using active or constraining supports.

In PEM LFCs the alloying of platinum with other metals, such as Sn, Ru, Ni, Co, etc. leads to more stable catalysts for alcohol oxidation with Pt–Sn alloys being the most active [206]. In alkaline media, an unsupported $PdIn_3$ catalyst synthesized by the sacrificial support method had an increased surface area (40 m^2/g) and demonstrated a very high activity in the oxidation of ethylene glycol and glycerol [207].

The anode catalyst support may play an important role. Pd nanoparticles supported on a Ni–Zn phase on carbon showed an excellent electrocatalytic activity in the oxidation of ethylene glycol and glycerol with peak current densites of 3300 and 2150 A/g Pd, respectively [208]. A Pd catalyst supported by multi-wall carbon nanotubes (MWCNT) showed superior performance compared to that on the conventional Vulcan XC-72 support, which was attributed to both a higher dispersion of Pd nanoparticles and to intrinsic properties of the support [114]. Nitrogen doping of porous carbon nanospheres increases the activity of Pt nanoparticles towards methanol electrooxidation [209]. Polystyrene spheres (diameter 700 nm) were used as a support for AuNi catalysts to form a three-dimensional core–shell structure with improved fuel diffusion into the catalyst layer, which showed a high activity in glycerol electrooxidation in alkaline medium [210]. A study of the electrooxidation of glycerol and EG on Au and Pt nanoparticles supported on different carbon surfaces suggested that oxygenated species formed on their surface serve as additional oxygen suppliers for the oxidation of intermediates adsorbed on the metal particles [211].

Oxidation of fuels on cathode catalysts and the resulting adsorption of intermediate products on the surface due to the crossover effect reduce their activity in the ORR by a factor of 3 to 7; this emphasizes the importance of the development of stable ORR electrocatalysts. It was found that some elements (Ru, Co, and Mo in acid media and Ag, Au in alkaline media) in binary and ternary compositions improve the resistance of the catalysts to poisoning [196].

Fuel development

Inorganic fuels such as hydrazine and sodium borohydrides are fully consumable as the intermediate products are oxidized more easily than the fuel. The only fully consumable organic fuel is methanol, and its disadvantages (high crossover rate leading to the use of diluted solutions, catalyst poisoning by reaction intermediates, toxicity, etc.) are well documented [48-55]. Among MeOH, EtOH and iPrOH fuels, the latter demonstrated the highest current and power densities on a PtRu electrocatalyst in both alkaline and acidic LFCs [199] with the exception of fuel cells with a PBI/PA membrane [71]. Contrary to alkaline LFCs, in acidic LFCs replacing methanol with C_2-alcohols leads to a sharp decline of the power density [212]. The power densities in LFCs running on 1 M alcohol solutions with a PtRu anode catalyst follow a similar order: isopropanol > methanol > ethanol > *n*-propanol > *n*-butanol [73]. The electrooxidation rate of different alcohols on a Pd electrode decreased in the row *n*-propanol > isopropanol > ethanol > ethylene glycol > glycerol > methanol, while on a Pt electrode a different order was observed: isopropanol > ethanol > glycerol > ethylene glycol > *n*-propanol > methanol [213]. In LFCs with a Pd/MWCNT anode catalyst glycerol (5 wt %) delivered higher power density that was higher than that of 10 wt % EtOH but lower than that of 10 wt % MeOH [114].

For fuels containing C–C bonds, a complete electrochemical oxidation to CO_2 and H_2O seems to be unachievable at practical current densities, at least at the operational temperatures of conventional PEM fuel cells and with the known electrocatalysts. Another approach is a partial electrochemical oxidation of the fuel to compounds that are stable under the working conditions of the cell. For example, ethanol in alkaline media

can be selectively converted to acetic acid, which is isolable as alkali metal acetate [114], isopropanol to acetone [88], and cyclohexane to benzene [186]. Clearly, a partial oxidation yields a lesser system energy density compared to complete oxidation. Nevertheless, in many cases the energy density is still much higher than that of conventional batteries. The use of polyhydric alcohols such as diols may substantially increase the energy density compared with monohydric alcohols [214]. Thermodynamic analysis and DFT computation show that the most energy-dense fuels for RLFCs are acyclic compounds and nitrogen-containing saturated heterocycles, especially those with five-membered rings [39]. Electrochemical oxidation of the former is very difficult and was only done in the vapor phase. The latter can be electrochemically oxidized by using inexpensive Ni catalysts [215]. However, they are incompatible with highly acidic PEMs, and the electrochemical oxidation of these compounds in alkaline media leads to the formation of oxygenated species [216]. Polyhydric alcohols having a lower energy density but being compatible with both PEMs and AEMs seem to be a reasonable compromise.

The electrochemical hydrogenation of carbonyl compounds and organic acids on Pt, Pd and Raney Ni electrocatalysts is well known [217] and it can be potentially used in RLFCs. The main challenge is the low selectivity due to the competing hydrogen evolution reaction. If the electrochemical hydrogenation was too slow or uneconomical (e.g., poor efficiency), the dehydrogenated or oxidized fuel could be regenerated ex situ through the well-known catalytic hydrogenation with molecular hydrogen in the gaseous or liquid phase. These hydrogenation processes are well developed for the hydrogenation of aromatic compounds to the related cyclic aliphatic compounds, acetic acid to ethanol, diketones to diols, etc. In this scheme the spent fuel would be collected at refueling stations, sent to a centralized plant for regeneration, and shipped back to the refueling stations in its hydrogenated form by using the existing infrastructure.

Conclusion

The development of cost-competitive LFCs would eliminate a major hurdle in the broad implementation of hydrogen fuel cells: the high cost of transportation and the absence of an infrastructure for hydrogen delivery. In the case of an implementation of LFCs, the existing liquid fuel infrastructure could be used. So far, the most developed organically fueled LFCs, DMFCs, have only reached power densities lower (by large factors) than those achievable by hydrogen fuel cells, even when using much higher Pt loadings [48-56]. Only LFCs using expensive ($NaBH_4$) or toxic (N_2H_4) fuels exhibit power densities comparable with hydrogen powered fuel cells. Therefore, the development of highly active and robust electrocatalysts is critical.

RLFCs based on electrochemical dehydrogenation/hydrogenation have a lower energy density compared with cells based on the complete oxidation of fuels, but they are very attractive for energy storage applications. A variety of organic fuels with tunable properties can be used, but the development of catalysts capable to selectively catalyze electrochemical dehydrogenation and hydrogenation reactions, as well as compatible ion-exchange membranes, is necessary. Fuels forming aromatic structures or carbonyl bonds through the extraction of hydrogen from the C–H or the O–H bonds, respectively, may provide much higher energy densities. Currently, oxygenated fuels seem to be the best compromise between energy density, easiness of electrooxidation and compatibility with existing acidic membranes. It is also possible that basic nitrogen-containing heterocyclic compounds that have good thermodynamics and high energy densities could be used with basic membranes.

Research efforts should be focused on development of inexpensive, selective and active electrocatalysts and minimizing the fuel crossover in ion-conducting membranes. Increasing of the LFC working temperature above 150 °C may ease the requirements for the electrocatalyst by increasing the fuel electrooxidation rate, while reducing electrocatalyst poisoning by intermediate products. For that purpose the development of new ion-conducting membranes that have a high conductivity at a low relative humidity is necessary.

Acknowledgements

This material is based upon work supported as part of the Center for Electrocatalysis, Transport Phenomena, and Materials (CETM) for Innovative Energy Storage, an Energy Frontier Research Center funded by the U.S. Department of Energy, Office of Science, Office of Basic Energy Sciences under Award Number DE-SC0001055. The author thanks Drs. G. Zappi and T. Miebach for useful discussion and help in the preparation of the manuscript.

References

1. Bockris, J. O. M. *Int. J. Hydrogen Energy* **2013,** *38,* 2579–2588. doi:10.1016/j.ijhydene.2012.12.026
2. Srinivasan, S. *Fuel Cells: From Fundamentals to Applications;* Springer, 2006.
3. Tsuchiya, H.; Kobayashi, O. *Int. J. Hydrogen Energy* **2004,** *29,* 985–990. doi:10.1016/j.ijhydene.2003.10.011
4. Kim, H.; Park, S.; Vohs, J. M.; Gorte, R. J. *J. Electrochem. Soc.* **2001,** *148,* A693–A695. doi:10.1149/1.1374216
5. Liu, M.; Choi, Y.; Yang, L.; Blinn, K.; Qin, W.; Liu, P.; Liu, M. *Nano Energy* **2012,** *1,* 448–455. doi:10.1016/j.nanoen.2012.02.006

6. Cimenti, M.; Hill, J. M. *Energies (Basel, Switz.)* **2009,** *2,* 377–410. doi:10.3390/en20200377
7. Swette, L. L.; LaConti, A. B.; McCatty, S. A. *J. Power Sources* **1994,** *47,* 343–351. doi:10.1016/0378-7753(94)87013-6
8. Peighambardoust, S. J.; Rowshanzamir, S.; Amjadi, M. *Int. J. Hydrogen Energy* **2010,** *35,* 9349–9384. doi:10.1016/j.ijhydene.2010.05.017
9. Berger, C.; Strier, M. P. Solid Inorganic Electrolyte Regenerative Fuel Cell System. In *Regenerative EMF Cells, Vol. 64;* Crouthamel, C. E.; Recht, H. L., Eds.; American Chemical Society: Washington, DC, USA, 1967; pp 17–29. doi:10.1021/ba-1967-0064.ch003
10. Bone, J. S.; Gilman, S.; Niedrach, L. W.; Read, M. D. Ion-exchange regenerative fuel cells. 15th Annual Power Source Conference, Ft. Monmouth, NJ; 1961; pp 47–49.
11. Swette, L.; Giner, J. *J. Power Sources* **1988,** *22,* 399–408. doi:10.1016/0378-7753(88)80033-8
12. Merle, G.; Wessling, M.; Nijmeijer, K. *J. Membr. Sci.* **2011,** *377,* 1–35. doi:10.1016/j.memsci.2011.04.043
13. Scott, K.; Mamlouk, M.; Espiritu, R.; Wu, X. *ECS Trans.* **2013,** *58,* 1903–1906. doi:10.1149/05801.1903ecst
14. Jena, P. *J. Phys. Chem. Lett.* **2011,** *2,* 206–211. doi:10.1021/jz1015372
15. Sherif, S. A.; Zeytinoglu, N.; Veziroğlu, T. N. *Int. J. Hydrogen Energy* **1997,** *22,* 683–688. doi:10.1016/S0360-3199(96)00201-7
16. Sakintuna, B.; Lamari-Darkrim, F.; Hirscher, M. *Int. J. Hydrogen Energy* **2007,** *32,* 1121–1140. doi:10.1016/j.ijhydene.2006.11.022
17. Soloveichik, G. L. *Mater. Matters* **2007,** *2,* 11–14.
18. Taube, M.; Rippin, D. W. T.; Cresswell, D. L.; Knecht, W. *Int. J. Hydrogen Energy* **1983,** *8,* 213–225. doi:10.1016/0360-3199(83)90067-8
19. Hodoshima, S.; Arai, H.; Takaiwa, S.; Saito, Y. *Int. J. Hydrogen Energy* **2003,** *28,* 1255–1262. doi:10.1016/S0360-3199(02)00250-1
20. Pradhan, A. U.; Shukla, A.; Pande, J. V.; Karmarkar, S.; Biniwale, R. B. *Int. J. Hydrogen Energy* **2011,** *36,* 680–688. doi:10.1016/j.ijhydene.2010.09.054
21. Pez, G. P.; Scott, A. R.; Cooper, A. C.; Cheng, H. Hydrogen storage by reversible hydrogenation of pi-conjugated substrates. US000007101530B2, Sept 5, 2006.
22. Teichmann, D.; Arlt, W.; Wasserscheid, P.; Freymann, R. *Energy Environ. Sci.* **2011,** *4,* 2767–2773. doi:10.1039/c1ee01454d
23. Angelici, R. J. *ACS Catal.* **2011,** *1,* 772–776. doi:10.1021/cs200176c
24. Shukla, A.; Karmakar, S.; Biniwale, R. B. *Int. J. Hydrogen Energy* **2012,** *37,* 3719–3726. doi:10.1016/j.ijhydene.2011.04.107
25. Satyapal, S.; Petrovic, J.; Read, C.; Thomas, G.; Ordaz, G. *Catal. Today* **2007,** *120,* 246–256. doi:10.1016/j.cattod.2006.09.022
26. Aldous, L.; Compton, R. G. *ChemPhysChem* **2011,** *12,* 1280–1287. doi:10.1002/cphc.201100092
27. Olah, G. A. *Angew. Chem., Int. Ed.* **2005,** *44,* 2636–2639. doi:10.1002/anie.200462121
28. Kobayashi, T.; Otomo, J.; Wen, C.-j.; Takahashi, H. *J. Power Sources* **2003,** *124,* 34–39. doi:10.1016/S0378-7753(03)00622-0
29. Antolini, E.; Gonzalez, E. R. *J. Power Sources* **2010,** *195,* 3431–3450. doi:10.1016/j.jpowsour.2009.11.145
30. Braunchweig, B.; Hibbitts, D.; Neurock, M.; Wieckowski, A. *Catal. Today* **2013,** *202,* 197–209. doi:10.1016/j.cattod.2012.08.013
31. Baranton, S.; Uchida, H.; Tryk, D. A.; Dubois, J. L.; Watanabe, M. *Electrochim. Acta* **2013,** *108,* 350–355. doi:10.1016/j.electacta.2013.06.138
32. Chen, Y.; Prasad, K. P.; Wang, X.; Pang, H.; Yan, R.; Than, A.; Chan-Park, M. B.; Chen, P. *Phys. Chem. Chem. Phys.* **2013,** *15,* 9170–9176. doi:10.1039/c3cp51410b
33. Campbell, P. G.; Zakharov, L. N.; Grant, D. J.; Dixon, D. A.; Liu, S.-Y. *J. Am. Chem. Soc.* **2010,** *132,* 3289–3291. doi:10.1021/ja9106622
34. Luo, W.; Campbell, P. G.; Zakharov, L. N.; Liu, S.-Y. *J. Am. Chem. Soc.* **2011,** *133,* 19326–19329. doi:10.1021/ja208834v
35. Hsueh, C.-L.; Liu, C.-H.; Chen, B.-H.; Chen, C.-Y.; Kuo, Y.-C.; Hwang, K.-J.; Ku, J.-R. *Int. J. Hydrogen Energy* **2009,** *34,* 1717–1725. doi:10.1016/j.ijhydene.2008.12.036
36. Soloveichik, G. L.; Lemmon, J. P.; Zhao, J.-C. Method and apparatus for electrochemical energy conversion. US020080248339A1, Oct 9, 2008.
37. Crabtree, R. H. *Energy Environ. Sci.* **2008,** *1,* 134–138. doi:10.1039/B805644G
38. Pez, G. P.; Scott, A. R.; Cooper, A. C.; Cheng, H. Hydrogen storage by reversible hydrogenation of pi-conjugated substrates. US000007429372B2, Sept 30, 2008.
39. Araujo, C. M.; Simone, D. L.; Konezny, S. J.; Shim, A.; Crabtree, R. H.; Soloveichik, G. L.; Batista, V. S. *Energy Environ. Sci.* **2012,** *5,* 9534–9542. doi:10.1039/c2ee22749e
40. Alcaide, F.; Cabot, P.-L.; Brillas, E. *J. Power Sources* **2006,** *153,* 47–60. doi:10.1016/j.jpowsour.2005.11.041
41. Simões, M.; Baranton, S.; Coutanceau, C. *ChemSusChem* **2012,** *5,* 2106–2124. doi:10.1002/cssc.201200335
42. Luksha, E.; Weissman, E. Y. *J. Electrochem. Soc.* **1969,** *116,* 118–122. doi:10.1149/1.2411722
43. Okrent, E. H.; Heath, C. E. A Liquid Hydrocarbon Fuel Cell Battery. In *Fuel Cell Systems-II, Vol. 90;* Gould, R. F., Ed.; American Chemical Society: Washington, DC, USA, 1969; pp 328–340. doi:10.1021/ba-1969-0090.ch024
44. Cairns, E. J.; McInerney, E. J. *J. Electrochem. Soc.* **1967,** *114,* 980–985. doi:10.1149/1.2424197
45. Savadogo, O.; Rodriguez Varela, F. J. *J. New Mater. Electrochem. Syst.* **2001,** *4,* 93–97.
46. Kariya, N.; Fukuoka, A.; Ichikawa, M. *Phys. Chem. Chem. Phys.* **2006,** *8,* 1724–1730. doi:10.1039/b518369c
47. Kim, H. J.; Choi, S. M.; Nam, S. H.; Seo, M. H.; Kim, W. B. *Catal. Today* **2009,** *146,* 9–14. doi:10.1016/j.cattod.2008.11.012
48. Dillon, R.; Srinivasan, S.; Aricò, A. S.; Antonucci, V. *J. Power Sources* **2004,** *127,* 112–126. doi:10.1016/j.jpowsour.2003.09.032
49. Wasmus, S.; Küver, A. *J. Electroanal. Chem.* **1999,** *461,* 14–31. doi:10.1016/S0022-0728(98)00197-1
50. Heinzel, A.; Barragán, V. M. *J. Power Sources* **1999,** *84,* 70–74. doi:10.1016/S0378-7753(99)00302-X
51. Liu, H.; Song, C.; Zhang, L.; Zhang, J.; Wang, H.; Wilkinson, D. P. *J. Power Sources* **2006,** *155,* 95–110. doi:10.1016/j.jpowsour.2006.01.030
52. García, B. L.; Weidner, J. W. Review of Direct Methanol Fuel Cells. In *Modern Aspects of Electrochemistry, Vol. 40;* White, R.; Vayenas, C. G.; Gamboa-Aldeco, M., Eds.; Springer: New York, 2007; pp 229–284.
53. Ahmed, M.; Dincer, I. *Int. J. Energy Res.* **2011,** *35,* 1213–1228. doi:10.1002/er.1889
54. Zhao, X.; Yin, M.; Ma, L.; Liang, L.; Liu, C.; Liao, J.; Lu, T.; Xing, W. *Energy Environ. Sci.* **2011,** *4,* 2736–2753. doi:10.1039/c1ee01307f
55. Li, X.; Faghri, A. *J. Power Sources* **2013,** *226,* 223–240. doi:10.1016/j.jpowsour.2012.10.061
56. Bahrami, H.; Faghri, A. *J. Power Sources* **2013,** *230,* 303–320. doi:10.1016/j.jpowsour.2012.12.009

57. Lamy, C.; Belgsir, E. M.; Léger, J. M. *J. Appl. Electrochem.* **2001,** *31,* 799–809. doi:10.1023/A:1017587310150
58. Nacef, M.; Affoune, A. M. *Int. J. Hydrogen Energy* **2011,** *36,* 4208–4219. doi:10.1016/j.ijhydene.2010.06.075
59. Kamarudin, M. Z. F.; Kamarudin, S. K.; Masdar, M. S.; Daud, W. R. W. *Int. J. Hydrogen Energy* **2013,** *38,* 9438–9453. doi:10.1016/j.ijhydene.2012.07.059
60. Kavanagh, R.; Cao, X.-M.; Lin, W.-F.; Hardacre, C.; Hu, P. *Angew. Chem., Int. Ed.* **2012,** *51,* 1572–1575. doi:10.1002/anie.201104990
61. Hitmi, H.; Belgsir, E. M.; Léger, J. M.; Lamy, C.; Lezna, R. O. *Electrochim. Acta* **1994,** *39,* 407–415. doi:10.1016/0013-4686(94)80080-4
62. Kim, I.; Han, O. H.; Chae, S. A.; Paik, Y.; Kwon, S.-H.; Lee, K.-S.; Sung, Y.-E.; Kim, H. *Angew. Chem., Int. Ed.* **2011,** *50,* 2270–2274. doi:10.1002/anie.201005745
63. Langer, S. H.; Card, J. C. *J. Mol. Catal.* **1987,** *42,* 331–336. doi:10.1016/0304-5102(87)85007-1
64. Song, S.; Tsiakaras, P. *Appl. Catal., B* **2006,** *63,* 187–193. doi:10.1016/j.apcatb.2005.09.018
65. Song, S.; Zhou, W.; Liang, Z.; Cai, R.; Sun, G.; Xin, Q.; Stergiopoulos, V.; Tsiakaras, P. *Appl. Catal., B: Environ.* **2005,** *55,* 65–72. doi:10.1016/j.apcatb.2004.05.017
66. Wang, Q.; Sun, G. Q.; Cao, L.; Jiang, L. H.; Wang, G. X.; Wang, S. L.; Yang, S. H.; Xin, Q. *J. Power Sources* **2008,** *177,* 142–147. doi:10.1016/j.jpowsour.2007.11.040
67. Spinacé, E. V.; Linardi, M.; Neto, A. O. *Electrochem. Commun.* **2005,** *7,* 365–369. doi:10.1016/j.elecom.2005.02.006
68. Casado-Rivera, E.; Volpe, D. J.; Alden, L.; Lind, C.; Downie, C.; Vázquez-Alvarez, T.; Angelo, A. C. D.; DiSalvo, F. J.; Abruña, H. D. *J. Am. Chem. Soc.* **2004,** *126,* 4043–4049. doi:10.1021/ja038497a
69. Antoniassi, R. M.; Oliveira Neto, A.; Linardi, M.; Spinacé, E. V. *Int. J. Hydrogen Energy* **2013,** *38,* 12069–12077. doi:10.1016/j.ijhydene.2013.06.139
70. Aricò, A. S.; Cretì, P.; Antonucci, P. L.; Antonucci, V. *Electrochem. Solid-State Lett.* **1998,** *1,* 66–68. doi:10.1149/1.1390638
71. Wang, J.; Wasmus, S.; Savinell, R. F. *J. Electrochem. Soc.* **1995,** *142,* 4218–4224. doi:10.1149/1.2048487
72. Linares, J. J.; Rocha, T. A.; Zignani, S.; Paganin, V. A.; Gonzalez, E. R. *Int. J. Hydrogen Energy* **2013,** *38,* 620–630. doi:10.1016/j.ijhydene.2012.06.113
73. Arunkumar, J.; Kalyani, P.; Saravanan, R. *Int. J. Electrochem. Sci.* **2008,** *3,* 961–969.
74. Bayer, D.; Cremers, C.; Baltruschat, H.; Tübke, J. *ECS Trans.* **2011,** *41,* 1669–1680. doi:10.1149/1.3635698
75. Gaurava, D.; Verma, A.; Sharma, D. K.; Basu, S. *Fuel Cells* **2010,** *10,* 591–596. doi:10.1002/fuce.200900039
76. Li, Y. S.; Zhao, T. S.; Liang, Z. X. *J. Power Sources* **2009,** *187,* 387–392. doi:10.1016/j.jpowsour.2008.10.132
77. Xu, J. B.; Zhao, T. S.; Li, Y. S.; Yang, W. W. *Int. J. Hydrogen Energy* **2010,** *35,* 9693–9700. doi:10.1016/j.ijhydene.2010.06.074
78. Hou, H.; Sun, G.; He, R.; Wu, Z.; Sun, B. *J. Power Sources* **2008,** *182,* 95–99. doi:10.1016/j.jpowsour.2008.04.010
79. An, L.; Zhao, T. S.; Zeng, L.; Yan, X. H. *Int. J. Hydrogen Energy* **2014,** *39,* 2320–2324. doi:10.1016/j.ijhydene.2013.11.072
80. An, L.; Zhao, T. S. *Int. J. Hydrogen Energy* **2011,** *36,* 9994–9999. doi:10.1016/j.ijhydene.2011.04.150
81. Sun, S.-G.; Yang, D.-F.; Tian, Z.-W. *J. Electroanal. Chem. Interfacial Electrochem.* **1990,** *289,* 177–187. doi:10.1016/0022-0728(90)87215-6
82. Reis, R. G. C. S.; Martins, C.; Camara, G. A. *Electrocatalysis* **2010,** *1,* 116–121. doi:10.1007/s12678-010-0018-x
83. Ye, J.; Liu, J.; Xu, C.; Jiang, S. P.; Tong, Y. *Electrochem. Commun.* **2007,** *9,* 2760–2763. doi:10.1016/j.elecom.2007.09.016
84. Liu, J.; Ye, J.; Xu, C.; Jiang, S. P.; Tong, Y. *J. Power Sources* **2008,** *177,* 67–70. doi:10.1016/j.jpowsour.2007.11.015
85. Xu, C.; Tian, Z.; Chen, Z.; Jiang, S. P. *Electrochem. Commun.* **2008,** *10,* 246–249. doi:10.1016/j.elecom.2007.11.036
86. Markiewicz, M. E. P.; Bergens, S. H. *J. Power Sources* **2008,** *185,* 222–225. doi:10.1016/j.jpowsour.2008.06.023
87. van Drunen, J.; Napporn, T. W.; Kokoh, B.; Jerkiewicz, G. *J. Electroanal. Chem.* **2014,** *716,* 120–128. doi:10.1016/j.jelechem.2013.08.003
88. Sun, S.-G.; Lin, Y. *Electrochim. Acta* **1996,** *41,* 693–700. doi:10.1016/0013-4686(95)00358-4
89. Cao, D.; Bergens, S. H. *J. Power Sources* **2003,** *124,* 12–17. doi:10.1016/S0378-7753(03)00613-X
90. Qi, Z.; Kaufman, A. *J. Power Sources* **2002,** *112,* 121–129. doi:10.1016/S0378-7753(02)00357-9
91. Qi, Z.; Kaufman, A. *J. Power Sources* **2003,** *118,* 54–60. doi:10.1016/S0378-7753(03)00061-2
92. Markiewicz, M. E. P.; Bergens, S. H. *J. Power Sources* **2010,** *195,* 7196–7201. doi:10.1016/j.jpowsour.2010.05.017
93. Yang, C.-C.; Chiu, S.-J.; Lee, K.-T.; Chien, W.-C.; Lin, C.-T.; Huang, C.-A. *J. Power Sources* **2008,** *184,* 44–51. doi:10.1016/j.jpowsour.2008.06.011
94. Gojković, S. L.; Tripković, A. V.; Stevanović, R. M. *J. Serb. Chem. Soc.* **2007,** *72,* 1419–1425. doi:10.2298/JSC0712419G
95. Qi, Z.; Kaufman, A. *J. Power Sources* **2002,** *110,* 65–72. doi:10.1016/S0378-7753(02)00237-9
96. Serov, A.; Kwak, C. *Appl. Catal., B: Environ.* **2010,** *97,* 1–12. doi:10.1016/j.apcatb.2010.04.011
97. Christensen, P. A.; Hamnett, A. *J. Electroanal. Chem. Interfacial Electrochem.* **1989,** *260,* 347–359. doi:10.1016/0022-0728(89)87149-9
98. Dailey, A.; Shin, J.; Korzeniewski, C. *Electrochim. Acta* **1998,** *44,* 1147–1152. doi:10.1016/S0013-4686(98)00217-5
99. Orts, J. M.; Fernandez-Vega, A.; Feliu, J. M.; Aldaz, A.; Clavilier, J. *J. Electroanal. Chem. Interfacial Electrochem.* **1990,** *290,* 119–133. doi:10.1016/0022-0728(90)87424-I
100. González, M. J.; Hable, C. T.; Wrighton, M. S. *J. Phys. Chem. B* **1998,** *102,* 9881–9890. doi:10.1021/jp982792d
101. Peled, E.; Livshits, V.; Duvdevani, T. *J. Power Sources* **2002,** *106,* 245–248. doi:10.1016/S0378-7753(01)01028-X
102. Livshits, V.; Peled, E. *J. Power Sources* **2006,** *161,* 1187–1191. doi:10.1016/j.jpowsour.2006.04.141
103. Livshits, V.; Philosoph, M.; Peled, E. *J. Power Sources* **2008,** *178,* 687–691. doi:10.1016/j.jpowsour.2007.07.054
104. An, L.; Zhao, T. S.; Shen, S. Y.; Wu, Q. X.; Chen, R. *Int. J. Hydrogen Energy* **2010,** *35,* 4329–4335. doi:10.1016/j.ijhydene.2010.02.009
105. An, L.; Zeng, L.; Zhao, T. S. *Int. J. Hydrogen Energy* **2013,** *38,* 10602–10606. doi:10.1016/j.ijhydene.2013.06.042
106. Takeguchi, T.; Arikawa, H.; Yamauchi, M.; Abe, R. *ECS Trans.* **2011,** *41,* 1755–1759. doi:10.1149/1.3635707
107. Grimes, P. G.; Seibold, J. G. Nontoxic liquid fuel cell. US000003163560A, Dec 29, 1964.
108. Yang, F.; Hanna, M.; Sun, R. *Biotechnol. Biofuels* **2012,** *5,* 13. doi:10.1186/1754-6834-5-13

109. Kwon, Y.; Birdja, Y.; Spanos, I.; Rodriguez, P.; Koper, M. T. M. *ACS Catal.* **2012,** *2,* 759–764. doi:10.1021/cs200599g
110. Oliveira, V. L.; Morais, C.; Servat, K.; Napporn, T. W.; Tremiliosi-Filho, G.; Kokoh, K. B. *J. Electroanal. Chem.* **2013,** *703,* 56–62. doi:10.1016/j.jelechem.2013.05.021
111. Zhang, Z.; Xin, L.; Li, W. *Int. J. Hydrogen Energy* **2012,** *37,* 9393–9401. doi:10.1016/j.ijhydene.2012.03.019
112. Tsivadze, A. Yu.; Tarasevich, M. R.; Bogdanovskaya, V. A.; Ehrenburg, M. R. *Dokl. Chem.* **2008,** *419,* 54–56. doi:10.1134/S0012500808030038
113. Nascimento, A. P.; Linares, J. J. *J. Braz. Chem. Soc.* **2014,** *25,* 509–516. doi:10.5935/0103-5053.20140018
114. Bambagioni, V.; Bianchini, C.; Marchionni, A.; Filippi, J.; Vizza, F.; Teddy, J.; Serp, P.; Zhiani, M. *J. Power Sources* **2009,** *190,* 241–251. doi:10.1016/j.jpowsour.2009.01.044
115. Ragsdale, S. R.; Ashfield, C. B. *ECS Trans.* **2008,** *16,* 1847–1854. doi:10.1149/1.2982025
116. Qi, J.; Xin, L.; Zhang, Z.; Sun, K.; He, H.; Wang, F.; Chadderdon, D.; Qiu, Y.; Liang, C.; Li, W. *Green Chem.* **2013,** *15,* 1133–1137. doi:10.1039/c3gc36955b
117. Zhang, Y.-H. P. *Int. J. Hydrogen Energy* **2010,** *35,* 10334–10342. doi:10.1016/j.ijhydene.2010.07.132
118. Basu, D.; Basu, S. *Electrochim. Acta* **2010,** *55,* 5775–5779. doi:10.1016/j.electacta.2010.05.016
119. Elouarzaki, K.; Haddad, R.; Holzinger, M.; Le Goff, A.; Thery, J.; Cosnier, S. *J. Power Sources* **2014,** *255,* 24–28. doi:10.1016/j.jpowsour.2013.12.109
120. An, L.; Zhao, T. S.; Shen, S. Y.; Wu, Q. X.; Chen, R. *J. Power Sources* **2011,** *196,* 186–190. doi:10.1016/j.jpowsour.2010.05.069
121. Oyarce, A.; Gonzalez, C.; Lima, R. B.; Lindström, R. W.; Lagergren, C.; Lindbergh, G. *Electrochim. Acta* **2014,** *116,* 379–387. doi:10.1016/j.electacta.2013.11.070
122. McGinley, J.; McHale, F. N.; Hughes, P.; Reid, C. N.; McHale, A. P. *Biotechnol. Lett.* **2004,** *26,* 1771–1776. doi:10.1007/s10529-004-4606-9
123. Fujiwara, N.; Yasuda, K.; Ioroi, T.; Siroma, Z.; Miyazaki, Y.; Kobayashi, T. *Electrochem. Solid-State Lett.* **2003,** *6,* A257–A259. doi:10.1149/1.1621287
124. Mondal, S. K.; Raman, R. K.; Shukla, A. K.; Munichandraiah, N. *J. Power Sources* **2005,** *145,* 16–20. doi:10.1016/j.jpowsour.2005.01.001
125. Fujiwara, N.; Yamazaki, S.-i.; Siroma, Z.; Ioroi, T.; Yasuda, K. *J. Power Sources* **2007,** *167,* 32–38. doi:10.1016/j.jpowsour.2007.02.023
126. Yu, X.; Pickup, P. G. *J. Power Sources* **2008,** *182,* 124–132. doi:10.1016/j.jpowsour.2008.03.075
127. Rhee, Y.-W.; Ha, S. Y.; Masel, R. I. *J. Power Sources* **2003,** *117,* 35–38. doi:10.1016/S0378-7753(03)00352-5
128. Marković, N. M.; Gasteiger, H. A.; Ross, P. N., Jr.; Jiang, X.; Villegas, I.; Weaver, M. J. *Electrochim. Acta* **1995,** *40,* 91–98. doi:10.1016/0013-4686(94)00241-R
129. Choi, J.-H.; Jeong, K.-J.; Dong, Y.; Han, J.; Lim, T.-H.; Lee, J.-S.; Sung, Y.-E. *J. Power Sources* **2006,** *163,* 71–75. doi:10.1016/j.jpowsour.2006.02.072
130. Gojković, S. L.; Tripković, A. V.; Stevanović, R. M.; Krstajić, N. V. *Langmuir* **2007,** *23,* 12760–12764. doi:10.1021/la702344s
131. Zhu, Y.; Khan, Z.; Masel, R. I. *J. Power Sources* **2005,** *139,* 15–20. doi:10.1016/j.jpowsour.2004.06.054
132. Ha, S.; Larsen, R.; Zhu, Y.; Masel, R. I. *Fuel Cells* **2004,** *4,* 337–343. doi:10.1002/fuce.200400052
133. Ha, S.; Larsen, R.; Masel, R. I. *J. Power Sources* **2005,** *144,* 28–34. doi:10.1016/j.jpowsour.2004.12.031
134. Haan, J. L.; Stafford, K. M.; Morgan, R. D.; Masel, R. I. *Electrochim. Acta* **2010,** *55,* 2477–2481. doi:10.1016/j.electacta.2009.12.004
135. Larsen, R.; Ha, S.; Zakzeski, J.; Masel, R. I. *J. Power Sources* **2006,** *157,* 78–84. doi:10.1016/j.jpowsour.2005.07.066
136. Sáez, A.; Expósito, E.; Solla-Gullón, J.; Montiel, V.; Aldaz, A. *Electrochim. Acta* **2012,** *63,* 105–111. doi:10.1016/j.electacta.2011.12.076
137. Shen, L.; Li, H.; Lu, L.; Luo, Y.; Tang, Y.; Chen, Y.; Lu, T. *Electrochim. Acta* **2013,** *89,* 497–502. doi:10.1016/j.electacta.2012.10.077
138. Qu, W. L.; Wang, Z. B.; Sui, X. L.; Gu, D. M.; Yin, G. P. *Fuel Cells* **2013,** *13,* 149–157. doi:10.1002/fuce.201200204
139. Huang, H.; Wang, X. *Phys. Chem. Chem. Phys.* **2013,** *15,* 10367–10375. doi:10.1039/c3cp51569a
140. Jeong, K.-J.; Miesse, C. M.; Choi, J.-H.; Lee, J.; Han, J.; Yoon, S. P.; Nam, S. W.; Lim, T.-H.; Lee, T. G. *J. Power Sources* **2007,** *168,* 119–125. doi:10.1016/j.jpowsour.2007.02.062
141. Bartrom, A. M.; Haan, J. L. *J. Power Sources* **2012,** *214,* 68–74. doi:10.1016/j.jpowsour.2012.04.032
142. Nguyen, T. Q.; Bartrom, A. M.; Tran, K.; Haan, J. L. *Fuel Cells* **2013,** *13,* 922–926. doi:10.1002/fuce.201200224
143. Jiang, J.; Wieckowski, A. *Electrochem. Commun.* **2012,** *18,* 41–43. doi:10.1016/j.elecom.2012.02.017
144. Gao, Y.-Y.; Tan, C.-H.; Li, Y.-P.; Guo, J.; Zhang, S.-Y. *Int. J. Hydrogen Energy* **2012,** *37,* 3433–3437. doi:10.1016/j.ijhydene.2011.11.077
145. Cairns, E. J.; Simons, E. L.; Tevebaugh, A. D. *Nature* **1968,** *217,* 780–781. doi:10.1038/217780a0
146. Rees, N. V.; Compton, R. G. *Energy Environ. Sci.* **2011,** *4,* 1255–1260. doi:10.1039/C0EE00809E
147. Cheddie, D. Ammonia as a Hydrogen Source for Fuel Cells: A Review. In *Hydrogen Energy - Challenges and Perspectives;* Minic, D., Ed.; InTech, 2012. doi:10.5772/47759
148. Simons, E. L.; Cairns, E. J.; Surd, D. J. *J. Electrochem. Soc.* **1969,** *116,* 556–561. doi:10.1149/1.2411961
149. Lan, R.; Tao, S. *Electrochem. Solid-State Lett.* **2010,** *13,* B83–B86. doi:10.1149/1.3428469
150. Suzuki, S.; Muroyama, H.; Matsui, T.; Eguchi, K. *J. Power Sources* **2012,** *208,* 257–262. doi:10.1016/j.jpowsour.2012.02.043
151. Karp, S.; Meites, L. *J. Am. Chem. Soc.* **1962,** *84,* 906–912. doi:10.1021/ja00865a006
152. Evans, G. E.; Kordesch, K. V. *Science* **1967,** *158,* 1148–1152. doi:10.1126/science.158.3805.1148
153. Yamada, K.; Asazawa, K.; Yasuda, K.; Ioroi, T.; Tanaka, H.; Miyazaki, Y.; Kobayashi, T. *J. Power Sources* **2003,** *115,* 236–242. doi:10.1016/S0378-7753(03)00008-9
154. Serov, A.; Kwak, C. *Appl. Catal., B: Environ.* **2010,** *98,* 1–9. doi:10.1016/j.apcatb.2010.05.005
155. Sanabria-Chinchilla, J.; Asazawa, K.; Sakamoto, T.; Yamada, K.; Tanaka, H.; Strasser, P. *J. Am. Chem. Soc.* **2011,** *133,* 5425–5431. doi:10.1021/ja111160r
156. Asazawa, K.; Yamada, K.; Tanaka, H.; Oka, A.; Taniguchi, M.; Kobayashi, T. *Angew. Chem., Int. Ed.* **2007,** *46,* 8024–8027. doi:10.1002/anie.200701334

157. Gao, G.; Guo, D.; Wang, C.; Li, H. *Electrochem. Commun.* **2007,** *9,* 1582–1586. doi:10.1016/j.elecom.2007.02.026
158. Sakamoto, T.; Asazawa, K.; Sanabria-Chinchilla, J.; Martinez, U.; Halevi, B.; Atanassov, P.; Strasser, P.; Tanaka, H. *J. Power Sources* **2014,** *247,* 605–611. doi:10.1016/j.jpowsour.2013.08.107
159. Sakamoto, T.; Asazawa, K.; Martinez, U.; Halevi, B.; Suzuki, T.; Arai, S.; Matsumura, D.; Nishihata, Y.; Atanassov, P.; Tanaka, H. *J. Power Sources* **2013,** *234,* 252–259. doi:10.1016/j.jpowsour.2013.01.181
160. Filanovsky, B.; Granot, E.; Presman, I.; Kuras, I.; Patolsky, F. *J. Power Sources* **2014,** *246,* 423–429. doi:10.1016/j.jpowsour.2013.07.084
161. Lao, S. J.; Qin, H. Y.; Ye, L. Q.; Liu, B. H.; Li, Z. P. *J. Power Sources* **2010,** *195,* 4135–4138. doi:10.1016/j.jpowsour.2010.01.059
162. Yan, X.; Meng, F.; Xie, Y.; Liu, J.; Ding, Y. *Sci. Rep.* **2012,** *2,* 941. doi:10.1038/srep00941
163. Zhang, F.; Zhang, H.; Ren, J.; Qu, C. *J. Mater. Chem.* **2010,** *20,* 8139–8146. doi:10.1039/c0jm01311k
164. Demirci, U. B. *J. Power Sources* **2007,** *169,* 239–246. doi:10.1016/j.jpowsour.2007.03.050
165. Yamazaki, S.-i.; Ioroi, T.; Tanimoto, K.; Yasuda, K.; Asazawa, K.; Yamaguchi, S.; Tanaka, H. *J. Power Sources* **2012,** *204,* 79–84. doi:10.1016/j.jpowsour.2011.12.056
166. de Leon, C. P.; Walsh, F. C.; Pletcher, D.; Browning, D. J.; Lakeman, J. B. *J. Power Sources* **2006,** *155,* 172–181. doi:10.1016/j.jpowsour.2006.01.011
167. Ma, J.; Choudhury, N. A.; Sahai, Y. *Renewable Sustainable Energy Rev.* **2010,** *14,* 183–199. doi:10.1016/j.rser.2009.08.002
168. Cheng, H.; Scott, K. *Electrochim. Acta* **2006,** *51,* 3429–3433. doi:10.1016/j.electacta.2005.09.038
169. Escaño, M. C. S.; Gyenge, E.; Arevalo, R. L.; Kasai, H. *J. Phys. Chem. C* **2011,** *115,* 19883–19889. doi:10.1021/jp207768e
170. Gyenge, E. *Electrochim. Acta* **2004,** *49,* 965–978. doi:10.1016/j.electacta.2003.10.008
171. Liu, B. H.; Li, Z. P.; Suda, S. *Electrochim. Acta* **2004,** *49,* 3097–3105. doi:10.1016/j.electacta.2004.02.023
172. Li, Z. P.; Liu, B. H.; Arai, K.; Suda, S. *J. Alloys Compd.* **2005,** *404–406,* 648–652. doi:10.1016/j.jallcom.2005.01.130
173. Yang, X.; Liu, Y.; Li, S.; Wei, X.; Wang, L.; Chen, Y. *Sci. Rep.* **2012,** *2,* 567. doi:10.1038/srep00567
174. Hong, J.; Fang, B.; Wang, C.; Currie, K. *J. Power Sources* **2006,** *161,* 753–760. doi:10.1016/j.jpowsour.2006.05.018
175. Raman, R. K.; Choudhury, N. A.; Shukla, A. K. *Electrochem. Solid-State Lett.* **2004,** *7,* A488–A491. doi:10.1149/1.1817855
176. Khadke, P. S.; Sethuraman, P.; Kandasamy, P.; Parthasarathi, S.; Shukla, A. K. *Energies (Basel, Switz.)* **2009,** *2,* 190–201. doi:10.3390/en20200190
177. Towne, S.; Carella, M.; Mustain, W. E.; Viswanathan, V.; Rieke, P.; Pasaogullari, U.; Singh, P. *ECS Trans.* **2009,** *25,* 1951–1957. doi:10.1149/1.3210751
178. Gu, L.; Luo, N.; Miley, G. H. *J. Power Sources* **2007,** *173,* 77–85. doi:10.1016/j.jpowsour.2007.05.005
179. Zhang, X.-B.; Han, S.; Yan, J.-M.; Chandra, M.; Shioyama, H.; Yasuda, K.; Kuriyama, N.; Kobayashi, T.; Xu, Q. *J. Power Sources* **2007,** *168,* 167–171. doi:10.1016/j.jpowsour.2007.03.009
180. Zhang, X.-B.; Yan, J.-M.; Han, S.; Shioyama, H.; Yasuda, K.; Kuriyama, N.; Xu, Q. *J. Power Sources* **2008,** *182,* 515–519. doi:10.1016/j.jpowsour.2008.04.032
181. Zhang, X.-B.; Han, S.; Yan, J.-M.; Shioyama, H.; Kuriyama, N.; Kobayashi, T.; Xu, Q. *Int. J. Hydrogen Energy* **2009,** *34,* 174–179. doi:10.1016/j.ijhydene.2008.09.083
182. Nagle, L. C.; Rohan, J. F. *J. Electrochem. Soc.* **2011,** *158,* B772–B778. doi:10.1149/1.3583637
183. Filanovsky, B.; Granot, E.; Dirawi, R.; Presman, I.; Kuras, I.; Patolsky, F. *Nano Lett.* **2011,** *11,* 1727–1732. doi:10.1021/nl200282z
184. Sutton, A. D.; Burrell, A. K.; Dixon, D. A.; Garner, E. B., III; Gordon, J. C.; Nakagawa, T.; Ott, K. C.; Robinson, J. P.; Vasiliu, M. *Science* **2011,** *331,* 1426–1429. doi:10.1126/science.1199003
185. Demirci, U. B.; Miele, P. *Energy Environ. Sci.* **2009,** *2,* 627–637. doi:10.1039/B900595A
186. Kariya, N.; Fukuoka, A.; Ichikawa, M. *Chem. Commun.* **2003,** 690–691. doi:10.1039/b211685e
187. Ferrell, J. R., III; Sachdeva, S.; Strobel, T. A.; Gopalakrishan, G.; Koh, C. A.; Pez, G.; Cooper, A. C.; Herring, A. M. *J. Electrochem. Soc.* **2012,** *159,* B371–B377. doi:10.1149/2.029204jes
188. Ando, Y.; Tanaka, T.; Doi, T.; Takashima, T. *Energy Convers. Manage.* **2001,** *42,* 1807–1816. doi:10.1016/S0196-8904(01)00042-5
189. Ando, Y. *J. Jpn. Inst. Energy* **2004,** *83,* 965–969.
190. Ando, Y.; Sasaki, T.; Yatabe, Y.; Saito, Y.; Tanaka, T. *Bull. Chem. Soc. Jpn.* **2005,** *78,* 1026–1031. doi:10.1246/bcsj.78.1026
191. Ando, Y.; Aoyama, Y.; Sasaki, T.; Saito, Y.; Hatori, H.; Tanaka, T. *Bull. Chem. Soc. Jpn.* **2004,** *77,* 1855–1859. doi:10.1246/bcsj.77.1855
192. Benziger, J.; Nehlsen, J. *Ind. Eng. Chem. Res.* **2010,** *49,* 11052–11060. doi:10.1021/ie100631a
193. Green, S. K.; Tompsett, G. A.; Kim, H. J.; Kim, W. B.; Huber, G. W. *ChemSusChem* **2012,** *5,* 2410–2420. doi:10.1002/cssc.201200416
194. Kariya, N.; Fukuoka, A.; Ichikawa, M. *Suiso Enerugi Shisutemu* **2005,** *30,* 91–94.
195. Ünlü, M.; Zhou, J.; Kohl, P. A. *Angew. Chem., Int. Ed.* **2010,** *49,* 1299–1301. doi:10.1002/anie.200906021
196. Brouzgou, A.; Podias, A.; Tsiakaras, P. *J. Appl. Electrochem.* **2013,** *43,* 119–136. doi:10.1007/s10800-012-0513-2
197. Spendelow, J. S.; Wieckowski, A. *Phys. Chem. Chem. Phys.* **2007,** *9,* 2654–2675. doi:10.1039/b703315j
198. Wang, Y.-J.; Qiao, J.; Baker, R.; Zhang, J. *Chem. Soc. Rev.* **2013,** *42,* 5768–5787. doi:10.1039/c3cs60053j
199. Santasalo-Aarnio, A.; Tuomi, S.; Jalkanen, K.; Kontturi, K.; Kallio, T. *Electrochim. Acta* **2013,** *87,* 730–738. doi:10.1016/j.electacta.2012.09.100
200. Jayashree, R. S.; Egas, D.; Spendelow, J. S.; Natarajan, D.; Markoski, L. J.; Kenis, P. J. A. *Electrochem. Solid-State Lett.* **2006,** *9,* A252–A256. doi:10.1149/1.2185836
201. Yu, E. H.; Scott, K.; Reeve, R. W. *J. Appl. Electrochem.* **2006,** *36,* 25–32. doi:10.1007/s10800-005-9017-7
202. An, L.; Zhao, T. S. *Energy Environ. Sci.* **2011,** *4,* 2213–2217. doi:10.1039/C1EE00002K
203. Livshits, V.; Ulus, A.; Peled, E. *Electrochem. Commun.* **2006,** *8,* 1358–1362. doi:10.1016/j.elecom.2006.06.021
204. Knuckey, K.; Creeth, A. Fuel cells. US020100112393A1, May 6, 2010.
205. Knuckey, K.; Kangati, B.; Downs, C.; Potter, A. Regenerative fuel cell with catholyte comprising a polyoxometalate and a vanadium (iv) - compound. WO002012085542A1, June 28, 2012.
206. Antolini, E. *J. Power Sources* **2007,** *170,* 1–12. doi:10.1016/j.jpowsour.2007.04.009
207. Serov, A.; Martinez, U.; Atanassov, P. *Electrochem. Commun.* **2013,** *34,* 185–188. doi:10.1016/j.elecom.2013.06.003

208. Marchionni, A.; Bevilacqua, M.; Bianchini, C.; Chen, Y.-X.; Filippi, J.; Fornasiero, P.; Lavacchi, A.; Miller, H.; Wang, L.; Vizza, F. *ChemSusChem* **2013,** *6,* 518–528. doi:10.1002/cssc.201200866
209. Su, F.; Tian, Z.; Poh, C. K.; Wang, Z.; Lim, S. H.; Liu, Z.; Lin, J. *Chem. Mater.* **2009,** *22,* 832–839. doi:10.1021/cm901542w
210. Song, J.-H.; Yu, J.-Y.; Zhang, M.-Z.; Liang, Y.-J.; Xu, C.-W. *Int. J. Electrochem. Sci.* **2012,** *7,* 4362–4368.
211. Gomes, J. F.; Gasparotto, L. H. S.; Tremiliosi-Filho, G. *Phys. Chem. Chem. Phys.* **2013,** *15,* 10339–10349. doi:10.1039/c3cp50280e
212. Varcoe, J. R.; Slade, R. C. T.; Yee, E. L. H.; Poynton, S. D.; Driscoll, D. J. *J. Power Sources* **2007,** *173,* 194–199. doi:10.1016/j.jpowsour.2007.04.068
213. Xie, S.-W.; Chen, S.; Liu, Z.-Q.; Xu, C.-W. *Int. J. Electrochem. Sci.* **2011,** *6,* 882–888.
214. Soloveichik, G. System and method for electrochemical energy conversion and storage. US000008338055B2, Dec 25, 2012.
215. Luca, O. R.; Huang, D. L.; Takase, M. K.; Crabtree, R. H. *New J. Chem.* **2013,** *37,* 3402–3405. doi:10.1039/c3nj00276d
216. Hammerich, O.; Lund, H. *Organic Electrochemistry,* 4th ed.; Taylor & Francis, 2000.
217. Popp, F. D.; Schultz, H. P. *Chem. Rev.* **1962,** *62,* 19–40. doi:10.1021/cr60215a002

License and Terms

BEILSTEIN JOURNAL OF NANOTECHNOLOGY

Materials and characterization techniques for high-temperature polymer electrolyte membrane fuel cells

Roswitha Zeis

Review

Open Access

Address:
Karlsruhe Institute of Technology, Helmholtz Institute Ulm, D-89081, Ulm, Germany

Email:
Roswitha Zeis - roswitha.zeis@kit.edu

Keywords:
binder; catalysts; characterization techniques; high-temperature polymer electrolyte membrane fuel cell (HT-PEMFC); membrane electrode assembly (MEA); phosphoric acid-doped polybenzimidazole (PBI)

Beilstein J. Nanotechnol. **2015,** *6,* 68–83.
doi:10.3762/bjnano.6.8

Received: 18 July 2014
Accepted: 04 December 2014
Published: 07 January 2015

This article is part of the Thematic Series "Materials for sustainable energy production, storage, and conversion".

Guest Editor: M. Fichtner

Abstract

The performance of high-temperature polymer electrolyte membrane fuel cells (HT-PEMFC) is critically dependent on the selection of materials and optimization of individual components. A conventional high-temperature membrane electrode assembly (HT-MEA) primarily consists of a polybenzimidazole (PBI)-type membrane containing phosphoric acid and two gas diffusion electrodes (GDE), the anode and the cathode, attached to the two surfaces of the membrane. This review article provides a survey on the materials implemented in state-of-the-art HT-MEAs. These materials must meet extremely demanding requirements because of the severe operating conditions of HT-PEMFCs. They need to be electrochemically and thermally stable in highly acidic environment. The polymer membranes should exhibit high proton conductivity in low-hydration and even anhydrous states. Of special concern for phosphoric-acid-doped PBI-type membranes is the acid loss and management during operation. The slow oxygen reduction reaction in HT-PEMFCs remains a challenge. Phosphoric acid tends to adsorb onto the surface of the platinum catalyst and therefore hampers the reaction kinetics. Additionally, the binder material plays a key role in regulating the hydrophobicity and hydrophilicity of the catalyst layer. Subsequently, the binder controls the electrode–membrane interface that establishes the triple phase boundary between proton conductive electrolyte, electron conductive catalyst, and reactant gases. Moreover, the elevated operating temperatures promote carbon corrosion and therefore degrade the integrity of the catalyst support. These are only some examples how materials properties affect the stability and performance of HT-PEMFCs. For this reason, materials characterization techniques for HT-PEMFCs, either in situ or ex situ, are highly beneficial. Significant progress has recently been made in this field, which enables us to gain a better understanding of underlying processes occurring during fuel cell operation. Various novel tools for characterizing and diagnosing HT-PEMFCs and key components are presented in this review, including FTIR and Raman spectroscopy, confocal Raman microscopy, synchrotron X-ray imaging, X-ray microtomography, and atomic force microscopy.

Introduction

Fuel cells are among the enabling technologies toward a safe, reliable, and sustainable energy solution. Yet, the lack of clean hydrogen sources and a sizable hydrogen infrastructure limits the fuel-cell applications today. Due to their elevated operating temperatures, between 150 and 180 °C, HT-PEMFCs can tolerate fuel contaminants such as carbon monoxide (CO) and hydrogen sulfide (H_2S) without significant loss of performance [1-5]. These are typical byproducts of the steam reforming process, which produces hydrogen from hydrocarbon fuels such as methanol or natural gas. So it is an appealing concept to couple a HT-PEMFC stack directly with a fuel processor [6,7]. These so-called auxiliary power units (APU) use the fossil fuel resources more efficiently and help to reduce the emission of CO_2. This might also be a good strategy for the wide deployment of fuel cells before the hydrogen infrastructure is established. The efficiency of the fuel cell system can be further increased by reusing the exhaust heat produced during electrical power generation.

The water management in low-temperature polymer electrolyte membrane fuel cells (LT-PEMFCs) operating between 60 and 100 ºC is highly complex. A lot of research effort has been devoted to this subject [8-10]. The most commonly used membrane material for this type of fuel cell is perfluorinated sulfonic acid (PFSA) polymer, which functions only in a highly hydrated state. On the other hand, water droplets which are building up underneath the gas diffusion layer (GDL) and the flow channels can partially block the gas supply of the cell. Therefore balancing the water content is a delicate task for LT-PEMFCs. In comparison, HT-PEMFCs are far more forgiving regarding the water management. Acid-based PBI-type membranes exhibit a high proton conductivity even in an anhydrous state. Therefore, additional humidification of the gas feeds is not needed. Operating above the water boiling temperature leads to further simplifications as there is only a single phase, the water vapor, present in the catalyst layer. This means that the transport of water in the membrane, electrodes and diffusion layer is easier. Consequently, the structure of the gas diffusion electrode and the design of the flow field plate have only minor effects on the cell performance [11-13] and can be greatly simplified.

The reaction kinetics should also benefit from higher operating temperatures. The exchange current density (j_0) increases exponentially with temperature. However, the specific adsorption of the phosphoric acid electrolyte is known to hamper the oxygen reduction reaction activity on the cathode side. Moreover, the low solubility and diffusivity of oxygen in concentrated phosphoric acid has a negative effect on the ORR [14,15]. These problems are specific to phosphoric acid and not intrinsic to HT-PEMFCs. Alternative electrolytes such as ionic liquids or solid acids might solve the problem and accelerate the oxygen reduction reaction kinetics.

The benefits of operating the fuel cell at elevated temperatures include improved catalyst activity, higher tolerance to impurities such as carbon monoxide in the hydrogen fuel, and much simplified thermal and water management of the system. Hence, there are good reasons to develop fuel cell systems that can operate above 120 °C. At this moment, however, no commercial HT-PEMFCs have been developed to meet the reliability and cost requirements. Both academic and industrial research laboratories are working intensively to get HT-PEMFC technology ready for the market. Great progress has been made over the recent years in the field of HT-PEMFCs, which has been documented in many review articles [4,13,16-20]. The focuses of these investigations were mainly proton-conducting membranes and other materials of the HT-MEA. The techniques available for characterizing these materials were not discussed. Appropriate diagnostic tools are needed to understand the fundamental principles of fuel cell operation at elevated temperatures. Very recently, many advances have been made in this field. This came relatively late because material testing at high temperatures is generally very challenging and the presence of corrosive liquids such as phosphoric acid complicates it even further. Many standard test methods and procedures for LT-PEMFCs cannot be simply adopted for HT-PEMFCs. Adequate tools and tests must be developed to characterize HT-PEMs and their components accurately.

The first part of this review gives a brief summary of materials currently used in HT-PEMFCs. We then present an overview of advanced analytical tools, including novel imaging and spectroscopic techniques, which had been used to characterize HT-PEMFC materials either in situ or ex situ. We focus mainly on fuel cells based on phosphoric-acid-doped PBI membranes as these are the closest to commercialization. But many characterization techniques discussed here are applicable to other types of HT-PEMFCs as well.

Review

Materials for HT-PEMFCs

Phosphoric-acid-doped polybenzimidazole-type membranes

Nafion® (DuPont), the most prominent member of the PFSA membrane group, exhibits an extremly high proton conductivity of up to 0.1 $S \cdot cm^{-1}$ under fully hydrated conditions. This can be explained by the molecular structure of Nafion shown in Figure 1. The polytetrafluoroethylene (Teflon®)-like molecular backbone gives Nafion its mechanical and chemical stability,

while the sulfonic acid functional groups ($–SO_3^-H^+$) provides charge sites for proton transport. Nafion polymer chains aggregate and create voids and channels with walls covered by sulfonic acid functional groups. In the presence of water, protons (H^+) detach from the sulfonic acid groups and combine with water molecules to form hydronium complexes (H_3O^+). To function properly, Nafion needs to be 100% humidified. At temperatures above 100 °C and under ambient pressure, water will evaporate instantly from the membrane. Under such conditions the Nafion membrane is a complete insulator.

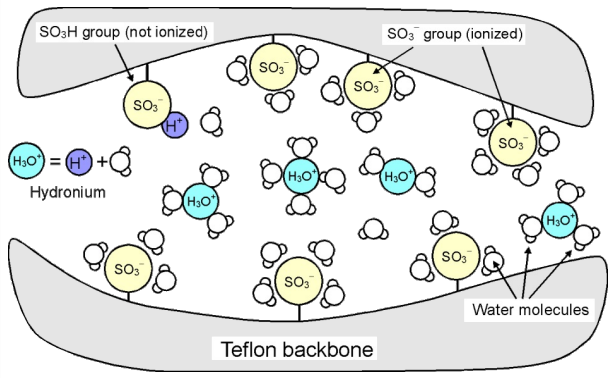

Figure 1: Illustration of the proton-conduction mechanisms of Nafion. Nafion polymer chains self-align into a micro channel structure. The sulfonic acid functional groups along the channel wall enable hydronium conduction.

To avoid this problem in HT-PEMFCs, water is replaced with a less volatile liquid such as phosphoric acid (H_3PO_4). Phosphoric acid is thermally stable at temperatures even above 100 °C. The proton conductivity mechanism is proton hopping between $H_4PO_4^+$ ions, H_3PO_4 molecules, and $H_2PO_4^-$ ions (Figure 2). In 1995, Savinell and co-worker [21,22] proposed to use PBI impregnated with phosphoric acid as a potential electrolyte for HT-PEMs, which is still one of the most promising concepts so far. PBI (poly[2,2'-(*m*-phenylene)-5,5'-bibenzimidazole]) itself is an aromatic heterocyclic polymer. The aromatic backbone provides excellent thermal stability with a glass transition temperature of 430 °C, good chemical resistance, and high mechanical strength. To achieve adequate proton conductivity for fuel cell operation (more than 0.05 $S \cdot cm^{-1}$), however, PBI needs to be doped with acid because its intrinsic conductivity is very low (about 10^{-12} $S \cdot cm^{-1}$) [17]. During the doping process the membrane takes up a large amount of phosphoric acid. The proton conductivity of the fully doped PBI membrane at 200 °C (0.07 $S \cdot cm^{-1}$) [23] is almost as high as that of fully hydrated perfluorinated membranes and far less dependent on the relative humidity, thus allowing its use in HT-PEMFCs without humidifying the gas reactants.

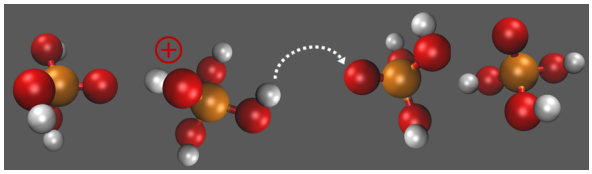

Figure 2: Illustration of the proton conducting mechanisms in phosphoric acid (Grotthuss mechanism). 'Excess' proton or protonic defect diffuses through the hydrogen bond network of phosphoric acid.

A HT-PEMFC based on phosphoric-acid-doped polybenzimidazole membranes shares many common features with the classical phosphoric acid fuel cell (PAFC), which also utilizes phosphoric acid as the electrolyte. Unlike the electrolyte system used in a PAFC, silicon carbide (SiC) soaked in acid, the acid-doped PBI membrane is essentially solid and is therefore easier to handle. It is also more tolerant towards pressure differences between cathode and anode and the leaching of phosphoric acid from the PBI polymer during fuel cell operation is less of a concern.

Besides PBI, there exist a great number of synthetically modified PBI polymers, which can be used as a possible host matrix material for phosphoric acid. Their properties and synthesis are described in many articles and reviews [4,17,19]. Poly(2,5-bibenzimidazole) (AB–PBI) is an important member of this class of materials. It is similar to PBI but does not have the connecting phenyl ring. The chemical structures of PBI and AB-PBI are presented in Figure 3. When fully doped, both polymer membranes show similar fuel cell performances. AB-PBI is the only commercially available membrane material for HT-PEMFCs. Membrane sheets (fumapem® AM) can be ordered from FuMA-Tech GmbH, Germany. This certainly adds to its popularity and explains why its properties have been so intensively studied [12,24].

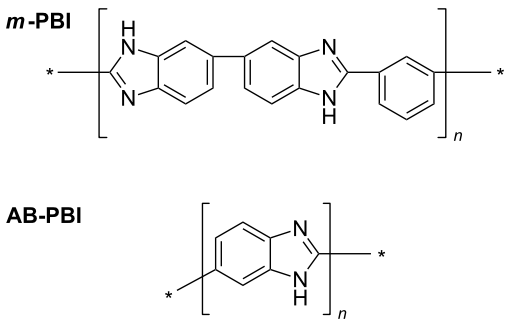

Figure 3: Chemical structures of *m*-PBI (poly[2,2-(*m*-phenylene)-5,5-bibenzimidazole]) and AB-PBI (poly(2,5-benzimidazole)). *m*-PBI and AB-PBI are the two most prominent members of the PBI family. These are aromatic heterocylic polymers containing benzimidazole units.

Doping strategies for PBI-type membranes: The polymer matrix needs to incorporate a large volume of phosphoric acid to achieve sufficient proton conductivity. The acid doping of the membrane can be performed in various ways. One method is simply immersing the PBI-type membrane sheet into hot phosphoric acid [25]. The immersion time in the acid and the acid bath temperature defines the doping level of the membrane (Figure 4). For instance AB-PBI membranes (FuMA-Tech), doped at 120 °C, can absorb phosphoric acid up to 2.5 times their own weight, which corresponds to a chemical formula AB-PBI·$5H_3PO_4$. Notably, the acid up-take during the first few minutes in the acid is particularly large. This causes the membrane to swell considerably. The thickness doubles during the doping process, from 50 µm of the pristine material to approximately 100 µm when it is fully doped [26]. The interaction between acid and polymer host can be explained by the chemical nature of the PBI-type membranes. The polymer bears basic N-sites, which react with strong or medium-strong acids. The basic N-sites of the PBI-type polymer act as proton acceptors like in a standard acid–base reaction, and in this process ion pairs are created.

The enormous acid up-take affects the mechanical integrity of the membrane. Specifically, non-cross-linked polymers tend to dissolve in the hot phosphoric acid. For these materials another method is needed to incorporate the acid into the membrane. Wannek and co-workers [24,27] came up with a different procedure. During MEA assembly, the dry membrane sheet is attached to gas diffusion electrodes loaded with the appropriate amount of acid. The actual membrane doping process occurs then during fuel cell operation as the acid diffuses from the gas diffusion electrodes into the membrane.

Highly doped PBI membranes can also be manufactured by polymerizing the monomers directly in polyphosphoric acid. The polyphosphoric acid is then hydrolyzed to phosphoric acid, which causes a sol–gel transition of the polymer–electrolyte system creating thereby a membrane film [17]. With this method, mechanically stable membranes with acid contents of more than 95 wt % or up to 70 phosphoric acid molecules per PBI repeat unit can be manufactured [28]. It is an elegant approach to have acid doping and membrane formation in one single step.

Proton conductivity: As soon as phosphoric acid gets in contact with the membrane material it starts to neutralize the basic sites of the polymer matrix. The PBI polymer chain has two basic nitrogen atoms per repeating unit (Figure 3) with a maximal capacity to trap two phosphoric acid molecules. Additional acid absorbed during the doping process accumulates in the free volume of the polymer chain network. It is mainly this so-call "free acid" that contributes to the proton conductivity of the membrane. The proton transport occurs through the Grotthus mechanism. Phosphoric acid has an amphoteric nature and could act as either a proton donor (acidic) or a proton acceptor (base). It forms a dynamic hydrogen bond network; in which protons can readily transfer though the formation and cleavage of covalent bonds. Figure 5 illustrates this dynamic hydrogen bond network between PBI and phosphoric acid.

As shown in Figure 6 the conductivity of highly doped PBI is nearly as high as that of Nafion. Since the transfer of protons occurs by "hopping" though the hydrogen bond network, the conductivity of the acid-doped PBI is governed by an activation mechanism that obeys the Arrhenius law [29]. In

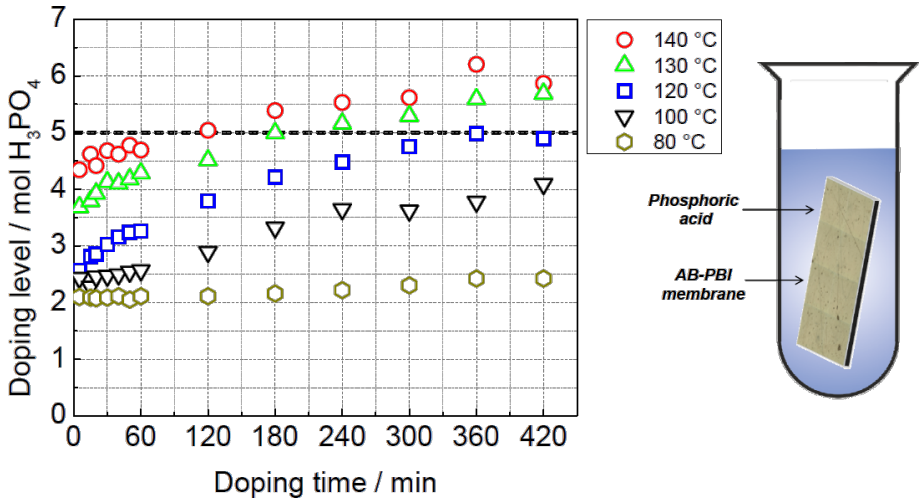

Figure 4: Doping process of an AB-PBI membrane in hot phosphoric acid at various temperatures. The weight increase of AB-PBI membranes correlates with the phosphoric acid solution temperature and immersion time (left). Schematic drawing of an AB-PBI membrane immersed in hot acid (right). Reprinted with permission from [34]. Copyright 2014 Elsevier.

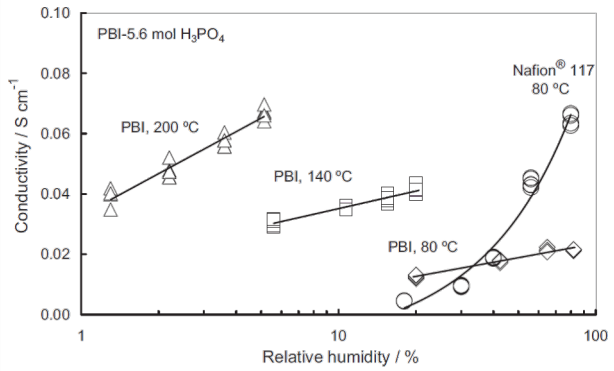

Figure 5: Conductivity of acid-doped PBI and Nafion as a function of humidity at various temperatures. Reproduced with permission from [23]. Copyright 2004 Wiley-VCH.

contrast, the proton conductivity of Nafion is attributed to the vehicle mechanism, which has a weaker temperature dependence. Moreover, the conductivity of acid-doped PBI is less dependent on the relative humidity, although there is a noticeable effect.

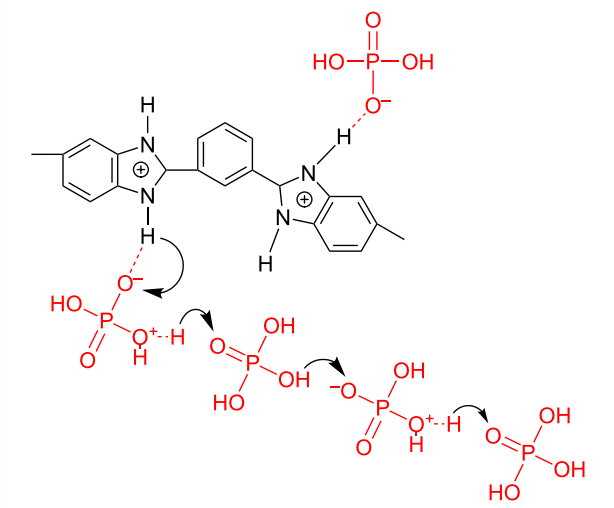

Figure 6: Interaction between PBI polymer host and phosphoric acid. Chemical structures of the proton transfer path along phosphoric acid molecules.

The impact of the doping level on the conductivity has been investigated quite extensively [29-33]. At an acid-doping level lower than two acid molecules per repeating unit, proton transfer most likely happens only between protonated and non-protonated N-sites on neighboring polymer chains, resulting in very low conductivity values. The reported conductivity is approximately 10^{-7} S·cm^{-1} for dry PBI at 30 °C [29]. Increasing the temperature or the humidity level improves the conductivity only marginally. At high acid-doping levels between four and six acid molecules per repeating unit, the conductivity mechanism is similar to that of a concentrated phosphoric acid solution described in the previous section. The measured conductivity is approximately 0.07 S·cm^{-1} at 200 °C [32,33].

The conductivity depends not only on the doping level (the amount of acid) but also on the acid distribution within the membrane. For instance, AB-PBI (fumapem® AM) should remain in the hot acid bath for several hours to ensure that the acid percolates throughout the polymer network and interact with nearly every basic N-site of the polymer host. A membrane doped this way not only exhibits a higher conductivity but also retains the acid better during fuel cell operation [34]. The doping time required to achieve a uniform acid distribution depends on the properties of the polymer defined by the production process, for example, crystallinity, degree of crosslinking, and solvent residues. But this has not been investigated thoroughly.

The conductivity of PBI-type membranes is also affected by the dehydration reaction of phosphoric acid. At temperatures above 140 °C, the conductivity of phosphoric acid decreases under anhydrous conditions due to the formation of pyrophosphoric acid ($H_4P_2O_7$), which is produced by condensing two phosphoric acid molecules and extracting a water molecule:

$$2H_3PO_4 \rightarrow H_4P_2O_7 + H_2O\,(g)\,.$$

As a consequence, at 160 °C the cell resistance of PBI-type HT-PEMFC under open circuit conditions is significantly higher than with an electrical load, which helps to produce water through the fuel cell reaction. The product water rehydrates the membrane in the MEA and shifts the equilibrium between phosphoric acid and pyrophosphoric acid towards the better conducting phosphoric acid [35].

Gas diffusion electrodes

Conventional PEM electrodes are usually prepared by spreading a catalyst layer, a suspension of carbon-supported platinum catalyst, solvent, and binder onto a GDL, followed by a drying step. There exist a wide range of catalyst layer deposition techniques, for instance, spraying [12], decal transfer [36], painting [37], rolling [38], sputter deposition [39], and doctor blade coating [27]. Some of these methods are adapted for the fabrication of GDEs for HT-PEMFCs. In particular, spraying [12] and doctor blade coating [27] are the most common techniques used in research.

The deposition method can affect the morphology, specifically the macro structure, of the GDE significantly. For instance, the catalyst layer fabricated by doctor blade technique shows a complete network of shrinkage cracks, which go all the way

though the catalyst layer. The clots are completely disconnected from each other. The situation is different for sprayed GDEs, where only small hairline cracks on the electrode surface were observed. Despite their different appearances, the sprayed and coated electrodes exhibit similar cell performances.

The absence of liquid water in the system is one of the most important differences compared with LT-PEMFCs. The distribution of the polymer binder in the electrodes and the macro structure of the electrode in general have strong effects on the performance of the LT-PEMFC cell because they are critical for water management. The fact that sprayed and coated HT-PEMFC electrodes lead to more reproducible MEA performance than typical handmade LT-PEMFC electrodes indicates the robustness of the HT-PEMFC against structural variations due to electrode preparation [12]. Still the fabrication technique might have an effect on the long-term stability of the cell. The large shrinkage cracks are the main pathway of the phosphoric acid from the membrane though the GDL and out of the cell [40]. However, to conclude this long-term tests are needed.

Catalysts: Similar to LT-PEMFCs and PAFCs, carbon-supported platinum is the main catalyst material used in PBI-phosphoric acid fuel cells. A difference is the noble metal loading of the GDEs, which is approximately 1 mg/cm^2, much higher than the typical Pt loading reported for LT-PEMFCs (0.1–0.4 mg/cm^2). The high noble-metal loading is mainly accounted to the pure utilization of platinum because the electrolyte partially floods the catalyst layer. In addition, the anion adsorption impedes the ORR in concentrated phosphoric acid. To reduce the noble-metal loading of a fuel cell, platinum alloy catalysts such as PtNi and PtCo may be used. However, the stability of these Pt alloy catalysts is questionable partially because, under fuel cell operating conditions, transition metals such as nickel and cobalt are expected to form oxides or hydroxides that tend to dissolve from the electrode surface. Nevertheless, carbon-supported platinum/transition metal alloy catalysts are often used in conventional LT-PEMFCs as well as PAFCs. There is strong experimental evidence that platinum alloys outperform pure platinum catalysts [41-44]. There are many explanations in the literature why platinum alloys exhibit better oxygen reduction reaction kinetics. In brief, the enhanced catalytic activity of platinum alloys has been credited to various structural changes of platinum caused by alloying, which may result in shortening of the interatomic Pt–Pt distance [43]. Other researchers have suggested that the alloy layer beneath the platinum skin increases the d-band vacancy of the platinum itself improving, therefore, the oxygen reduction reaction [20]. A great deal of research on this subject was carried out from 1970's until the early 1990's within the framework of the phosphoric acid fuel cell (PAFC) development, but there are only a few publications in the context of PBI-based HT-PEMFCs [45,46].

Rao et al. [45] prepared carbon-supported Pt–Co alloy nanoparticles of various Pt/Co atomic ratios (1:1, 2:1, 3:1 and 4:1). Theses catalysts were evaluated in HT-PEMFCs. Improved performance was observed for Pt/Co atomic ratios of 1:1 and 2:1. These HT-PEMFCs, operating at 180 °C and 50 mA/cm^2, were stable over 50 h of fuel cell operation. Mamlouk and co-workers [46] tested commercial catalysts besides Pt/Co and also included Pt/Fe and Pt/Ni. All platinum alloys in this study had a composition of 1:1 in atomic ratio. They claimed only the Pt/Ni catalyst exhibited a better catalytic activity compared with the conventional platinum catalyst. However, both papers did not include long-term fuel cell tests so the stability of such alloy catalysts in HT-PEMs is yet to be evaluated.

Catalyst supports: Similar to LT-PEMFCs, high-surface-area carbon blacks (e.g., Vulcan-XC72 and Ketjen black) are often used as catalyst supports, despite the fact that operating the fuel cell under dynamic conditions (potential cycles) or at high potentials leads to severe corrosion of theses carbon materials, a drawback well-known from the PAFC research. Carbon nanotubes are a promising alternative for catalyst support because of their higher corrosion resistivity [47].

Matsumoto et al. [48] fabricated a catalyst material by wrapping individual carbon nanotubes in a PBI polymer layer covered with platinum nanoparticles. A schematic drawing and TEM images of this innovative catalyst concept are shown in Figure 7. The PBI wrapper serves as an ionomer and binder of the catalyst layer simultaneously. The polymer also glues the platinum nanoparticles onto carbon nanotubes, preventing agglomeration and detachment from the substrate. GDEs based on this type of material were prepared simply by vacuum filtration of a suspension of isopropanol and polymer-wrapped carbon nanotubes. The GDL, a carbon paper, was used as a filter. The GDEs were incorporated into MEAs for cell performances testing. The single cells achieved a peak power of over 100 mW/cm^2 at 120 °C with a relatively low platinum loading (0.45 mg/cm^2) for both the cathode and the anode.

Binder: The polymer-wrapped carbon nanotube catalyst concept elegantly incorporates the binder PBI into the GDE. Similar to the selection of materials for membranes, various types of PBI can be used as binders and ionomers in the catalyst layers of HT-PEMFCs. However, PBI materials are inconvenient to handle since they are only soluble in solvents with a high boiling point [49]. Some groups managed to overcome these difficulties and incorporated PBI within the catalyst layer [48,50,51]. However, there is no clear evidence that the PBI

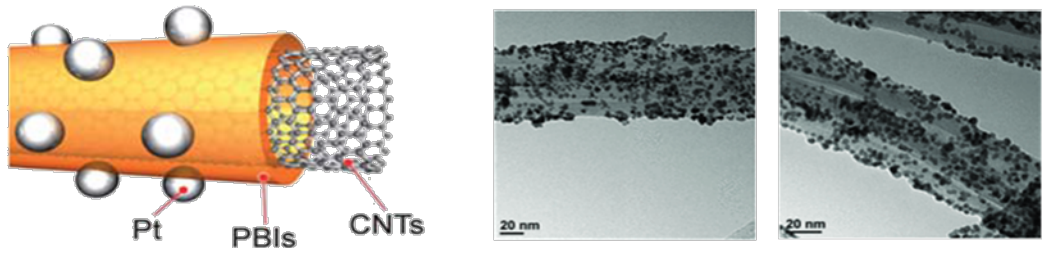

Figure 7: Left: Schematic drawing of an electrocatalyst composed of Pt nanoparticles loaded on the PBIs-wrapped carbon nanotubes (left). Reprinted with permission from [48], Copyright 2011 Royal Society of Chemistry. Right: TEM images of Pt nano-particles loaded on the PBIs-wrapped carbon nanotubes (right). Reprinted with permission from [49]. Copyright 2013 Wiley-VCH.

binder actually improves the cell performance. In HT-PEMFCs, since an ion conductor (molten phosphoric acid) is already present in the GDE, an insulator such as PTFE could serve as a suitable binder [12,24]. PTFE not only glues the catalyst particles together and, hence, keeps the catalyst layer mechanically intact with its hydrophobic nature; it also controls the wettability of the GDE, which affects the infiltration of phosphoric acid into the GDE. Both the molten acid and the reactant gas need access to the active sites of the catalyst. A complete network of three phase boundaries is created, consisting of proton conducting electrolyte, electron conducting catalysts, and reactant gases. This network can be fine-tuned simply by varying the PTFE content of the catalyst layer. As shown in Figure 8, the PTFE content controls the acid migration from the doped membrane to the catalyst layer and has therefore a significant effect on the cell performance. In case of MEAs employing fumapem® AM (AB-PBI·5H_3PO_4), the optimal PTFE content for HT-PEMFC electrodes was found to be 5% [52]. The optimum value may vary for different membrane types and doping degrees.

Nafion, the traditional binder in LT-PEMFC, is not practical for HT-PEMFCs operating at elevated temperatures. This is because under anhydrous conditions, Nafion is nonconductive and tends to encapsulate the platinum nanoparticles, resulting in blocking of the catalyst sites for hydrogen oxidation and oxygen reduction. It is even possible to prepare electrodes for high-temperature MEAs without any polymeric binder. The absence of binder material seems to affect the mechanical stability only little. MEAs built from binderless electrodes demonstrated a stable cell performance over 900 h of operation [53].

Characterisation techniques for HT-PEMFCs

Optical spectroscopy

Raman and infrared spectroscopy – Acid-doping process of PBI membranes: Raman and infrared (IR) spectroscopy are powerful tools to study the effects of acid-doping on PBI-type polymers because they are highly sensitive to molecular structural changes that occur during the acid–base proton exchange reaction between PBI and phosphoric acid as shown in Figure 5

$$H_3PO_4 + \left[-C{=}N-\right] \rightarrow H_2PO_4^- + \left[-C{=}N-\right]^+ .$$

They are also sensitive to molecular interactions between membrane components. Raman spectra of pristine and acid-doped PBI materials with various doping degrees have been recorded and relevant bands have been assigned [26,54-56]. Typical examples of such spectra are presented in Figure 9a [55]. The Raman band at 1000 cm^{-1} was assigned to the *meta*-benzene ring vibration, which remains roughly unchanged as the acid content in the membrane increases. In contrast, the band at 1539 cm^{-1}, which is associated with the symmetric stretch of the imidazole group, becomes stronger and shifts towards 1570 cm^{-1} with increasing acid content. During acid-

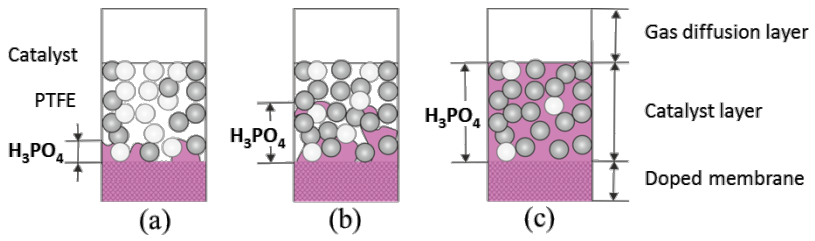

Figure 8: Schematic diagram illustrating the difference in the amount of phosphoric acid migration from the doped membrane to the catalyst layer with different PTFE content (a) high (b) medium and (c) low.

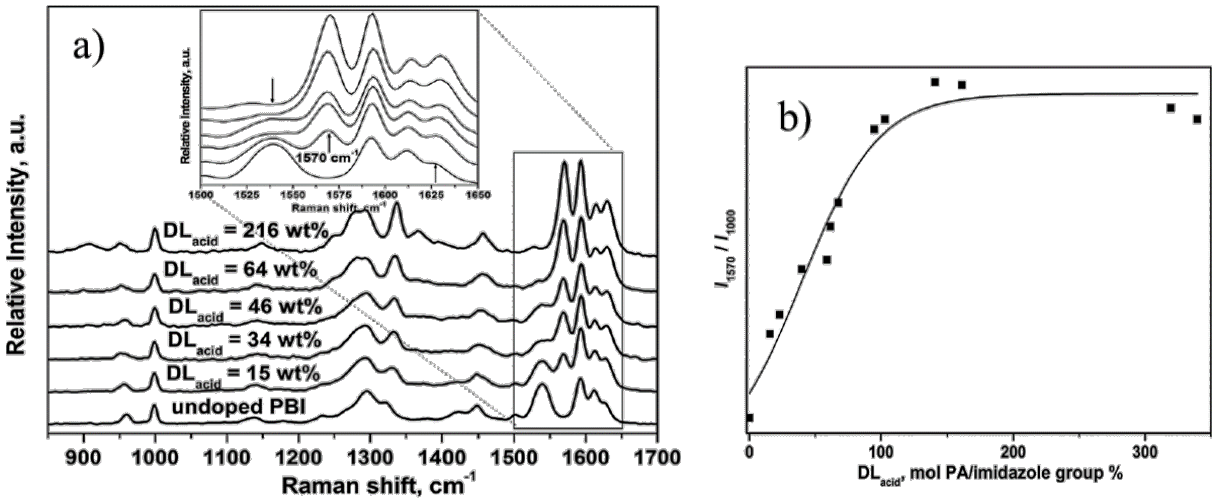

Figure 9: (a) Raman spectra of pristine and phosphoric acid-doped PBI. (b) Ratio of relative intensities versus acid doping level expressed in 1 M H_3PO_4 per polar group (%) for the peaks 1570 and 1000 cm^{-1} for PBI/ H_3PO_4. Reproduced with permission from [55]. Copyright 2014 Royal Society of Chemistry.

doping of the PBI polymer, the imidazole group becomes gradually protonated, which causes this Raman blue shift and increase of intensity. Once the protonation reaches saturation (two per repeating unit of PBI), the intensity of this band becomes constant. This is confirmed by plotting the ratio of the band intensity of 1570 cm^{-1} to that of 1000 cm^{-1} against the acid-doping level, as shown in Figure 9b [55]. The protonation of the basic N-sites does not occur homogenously within the polymer matrix. Specifically, for the commercial AB-PBI membrane material (fumapem® AM), the process could take several hours until the acid reaches all areas of the membrane sheet. This slow doping process can be monitored by confocal Raman microscopy. The integrated intensities of the bands at 1570 cm^{-1} and 1611 cm^{-1} were used as indicators for the interaction between the AB-PBI host and the phosphoric acid dopant. These two peaks overlap and cannot always be resolved individually in the spectra of the ABI-PBI samples. For convenience, both were selected for creating the integrated Raman intensity maps (the peak at 1611 cm^{-1} is less sensitive to increasing doping levels). Figure 10 shows the integrated Raman intensity maps for AB-PBI membrane sheets doped for 1 and 6 h in 120 °C hot phosphoric acid. With 6 h of doping time the color distribution of the map is more uniform compare to the one of 1 h indicating that after 6 h finally all basic N-sites have been protonated throughout the whole membrane matrix [34].

The gradual protonation of the N-sites by transferring protons from phosphoric acid to the imidazole groups of PBI with increasing acid content can also be observed with infrared spectroscopy [29,54,57,58]. IR spectra of the pristine and acid-doped PBI films are shown in Figure 11. The most relevant region of the spectra is from 2000 to 4000 cm^{-1} since the N–H stretching modes appear in this range. According to Muso et al. [58], there are three distinguishable bands at 3415, 3145, and

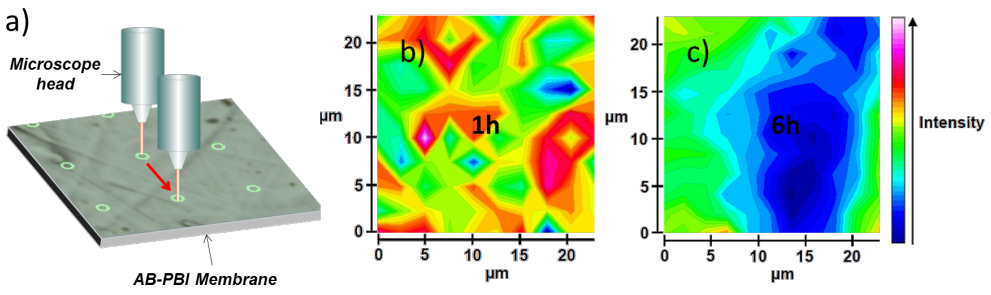

Figure 10: (a) Schematic drawing of confocal Raman microscopy mapping. Confocal Raman maps of phosphoric-acid-doped AB-PBI membranes. The membrane sheets were immersed in a 120 °C hot phosphoric acid bath for (b) 1 h and (c) 6 h. The Raman images show an increasing homogeneity of the phosphoric acid distribution in the membrane with prolonged doping time. Reproduced with permission from [34]. Copyright 2014 Elsevier.

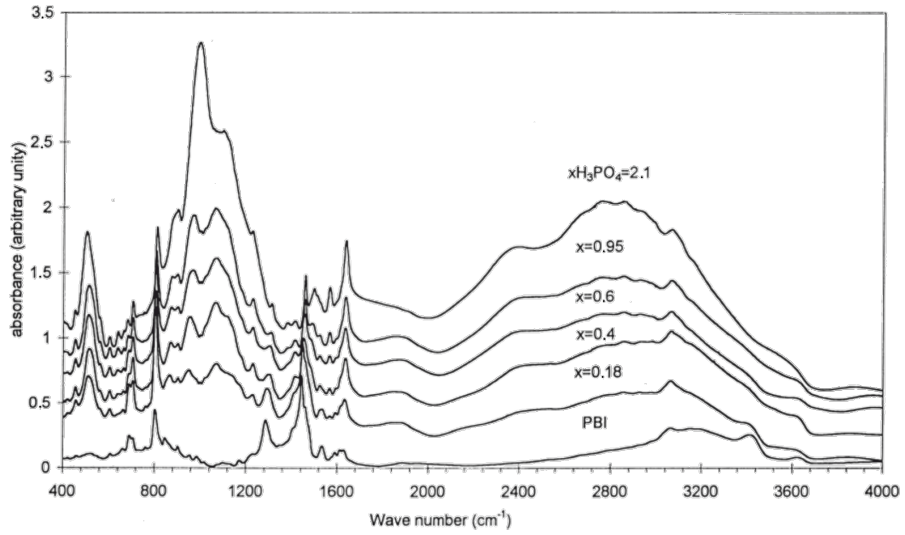

Figure 11: IR spectra of pristine and phosphoric-acid-doped PBI. Reprinted with permission from [29]. Copyright 1999 Elsevier.

3063 cm^{-1} visible in the pristine sample. The narrow peak at 3063 cm^{-1} corresponds to the stretching modes of the CH groups of the polymer backbone, whereas the other two are attributed to the various N–H stretching modes. The relatively sharp peak at 3415 cm^{-1} is assigned to the stretching vibration of isolated, non-bonded N−H groups, and the broad peak located at approximately 3145 cm^{-1} is linked to stretching vibration of self-associated, hydrogen-bonded N···H [56].

Once the PBI material is doped with phosphoric acid, a very broad absorption band appears in the wave number range between 2400 and 3000 cm^{-1}, which is consistent with protonation of the N-sites on the imidazole groups of PBI. The intensity of this new band increases with the doping level, while the absorption of both the N–H groups at 3415 and the N–H···N groups at 3145 cm^{-1} decreases [4]. The adsorption bands of the acid anion ($H_2PO_4^-$) between 400 and 1300 cm^{-1} in the IR-spectrum can also be used as markers for the degree of protonation of PBI. Specifically, the area of the peak at 1630 cm^{-1} [29] is sensitive to the acid content in the membrane. The value increases with the doping levels until it reaches a maximum corresponding to transfer of two protons from phosphoric acid to the two imidazole groups of the repeating unit of PBI.

Di Noto and co-workers [54] investigated IR-spectra of pristine and doped AB-PBI. They also examined the lower spectral range from 400 to 2000 cm^{-1}. The presence of the band at 942 cm^{-1} (attributed to $H_2PO_4^-$ ions) suggests that when the AB-PBI is exposed to H_3PO_4, an acid–base proton transfer reaction occurs. As the amount of acid in the membrane increases, the AB-PBI bands are gradually masked by those of phosphoric acid. The phosphoric acid band at 998 cm^{-1} continues to grow as the amount of acid in membrane exceeds the number of imidazole sites and free phosphoric acid accumulates in the membrane. While the presence of both H_3PO_4 and $H_2PO_4^-$ bands in the spectra of the acid-doped AB-PBI membranes suggests that an acid–base reaction has occurred, evidence of both these species is also present in the phosphoric acid spectrum due to the dissociation equilibrium that exists in aqueous phosphoric acid.

IR studies of the adsorption of phosphoric acid species on platinum: IR spectroscopy has been used as a tool to study electrochemical interfaces and to characterize adsorbed species on catalytic surfaces. Habib and Bockris [59] were the first who applied this technique to investigate the adsorption of phosphoric acid on platinum. Their goal was to determine the acid species, molecule or anion, which adsorbs onto the surface, depending on the electrode potential. The measurements were carried out in 1 M perchloric acid as the base electrolyte with various small concentrations of added phosphoric acid. They observed in their IR spectra a peak at 1074 cm^{-1} associated with a P–O stretch vibrational mode of H_3PO_4 molecules adsorbed on the platinum surface. The IR adsorption peak intensity varies parabolically with potential. Between 200–700 mV vs NHE the signal increases until it reaches its maximum and then decreases again. Based on this result, the authors speculated that the adsorbed species are most likely H_3PO_4 molecules because they are displaced by water or oxides at the platinum surface at higher potentials. This would not be the case if they were $H_2PO_4^-$ anions. Additionally, at pH 0 only about 1% of the H_3PO_4 molecules dissociate into $H_2PO_4^-$ ions, resulting in a rather small concentration of anions.

In 1992, Nart and Iwasita [60] conducted similar experiments and reached very different conclusions. Their FTIR instrument had much improved signal-to-noise ratio and spectral resolution. Furthermore, they measured the FTIR spectra with both s and p polarisations of light to exclude artifacts due to absorption of phosphoric acid in solution. The base electrolyte perchloric acid was replaced with hydrofluoric acid to prevent IR band interference. Nart and Iwasita found that both H_3PO_4 molecules and $H_2PO_4^-$ anions could adsorb onto the platinum surface depending on the potential. They also suggested possible orientations of the adsorbates. At low potentials, the undissociated H_3PO_4 molecules are likely to adsorb on platinum through the non-protonated oxygen atom under the C_{3v} symmetry. Only one IR peak at 1050 cm^{-1} associated with the P–O stretch vibration appears in the spectra. The adsorbed H_3PO_4 molecules are ionised to $H_2PO_4^-$ anions as the potential increases. The onset of ionisation depends on the pH of the solution. At 900 mV, the adsorbed $H_2PO_4^-$ anions undergo a symmetry change. Below 900 mV, the $H_2PO_4^-$ anions adsorb to the surface through the two oxygen atoms that are not bonded to hydrogen, presenting a C_{2v} symmetry. Above 900 mV, the dihydrogen phosphates change to a single coordination with a lower C_s symmetry. The probable orientations of the $H_2PO_4^-$ anions at different potentials are shown in Figure 12. This geometry change is most likely prompted by co-adoption of oxide spices on the platinum surface. In the IR spectra the absorption band at 1000 cm^{-1}, which corresponds to the $P–(OH)_2$ stretch vibration, decreases at higher potentials and indicates this symmetry change.

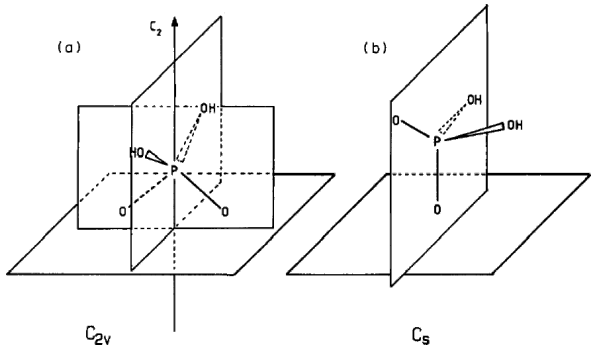

Figure 12: The $H_2PO_4^-$ ion under C_{2v} and C_s symmetries. These are the most probable orientations of $H_2PO_4^-$ at low and high positive potentials, respectively. Reprinted with permission from [60]. Copyright 1992 Elsevier.

So far all studies had been conducted on model systems that used single crystal electrodes [61] or polycrystalline films at low electrolyte concentrations. They help us understand fundamental aspects of the interactions between phosphoric acid and the catalyst, but these model systems are far away from realistic conditions in HT-PEMFCs. The exact nature of the adsorption of phosphate species on platinum, especially in a practical fuel cell environment at elevated temperatures and much higher acid concentrations, is still not well understood. Neophytides et al. [62] constructed an electrochemical cell for in situ FTIR measurements of HT-PEMFC MEA from room temperature up to 150 °C. The MEA consisted of a phosphoric-acid-doped pyridine-based aromatic polyether membrane and platinum film electrodes. The experimental setup and cell design were validated by using CO adsorption on nanoparticles of the platinum film and electrochemical stripping. Yet there has been no published data on the issue of phosphoric adsorption from this setup.

X-ray absorption spectroscopy to investigate the adsorption of phosphoric acid species on platinum

Very recently, Kaserer et al. [63] published a study on the catalyst poisoning effect of H_3PO_4 in HT-PEM by using in operando X-ray absorption spectroscopy (XAS) incorporating the Δμ technique. The goal of this study was also to investigate phosphoric acid adsorption on platinum in a real fuel cell. The technique is capable to determine adsorbates on the platinum catalyst particles by examining the X-ray near edge structure (XANES). For these analyses, the XANES measurements were taken from −20 to 50 eV relative to the Pt L_3 edge at 11.564 eV. The Pt L_3 absorption edge from a platinum foil was used as a reference. The Δμ signals were generated by using the subtractive method $\Delta\mu = \mu_{sample} - \mu_{foil}$.

With various cell potentials, different adsorbates were observed on the platinum nanoparticles as shown in Figure 13. Three potential regions were identified with distinctly different species covering the catalyst surface. At cell potentials lower than 300 mV, hydrogen is adsorbed. In the potential region between 300 and 400 mV, phosphoric acid species start to displace hydrogen and adsorb on platinum. Between 400 and 700 mV only little coverage of phosphoric acid is measured. The authors believed that the platinum surface is still fully coved with phosphoric acid in this potential range and speculated that phosphoric acid molecules or anions are very mobile on the surface and invisible to the Δμ technique. Only in the presence of other adsorbates (hydrogen and oxygen) does phosphoric acid adsorb in an ordered manner and become detectable. From 700 to 800 mV co-adsorption of oxygen and phosphoric acid species were observed. Above 900 mV only oxygen is present on the platinum surface.

These experiments provided new evidence that at higher temperatures phosphoric acid still blocks platinum atoms, thus hindering the oxygen reduction reaction. The technique, however, cannot distinguish between various adsorbing species,

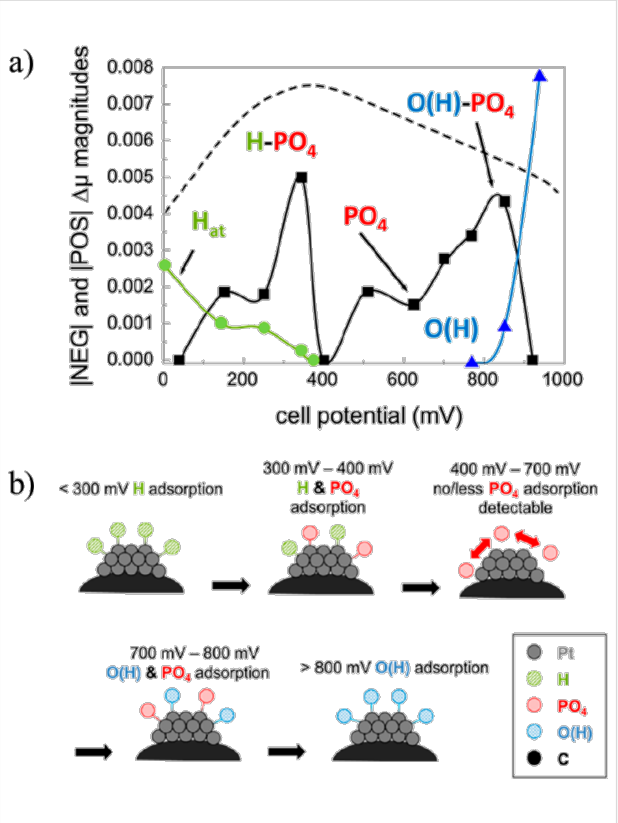

Figure 13: (a) Coverage of different adsorbates on platinum by analyzing |POS| and |NEG| Δμ amplitudes at various cell potentials. The dashed line indicates the expected PO_4^{3-} coverage according to He et al. [64]. (b) Illustration of adsorbates on platinum at different cell voltages. Reproduced with permission from [63]. Copyright 2013 American Chemical Society.

namely the phosphoric acid molecule or two different types of anions, on the platinum surface. Additionally, over a wide potential range (400–700 mV) the conclusion could only be drawn indirectly due to lack of measurement sensitivity.

To elucidate the origin of the reduced poisoning of Pt-alloy catalysts in the presence of phosphoric acid, Mukerjee and co-workers [64] conducted in situ X-ray absorption spectroscopy experiments. Similar to the previously described study [63], they investigated adsorbates on the catalyst surface by interpreting the X-ray near edge structure (XANES). They also applied the Δμ technique. The difference is that the measurements were carried out at room temperature while using perchloric acid as the base electrolyte with added small concentrations of phosphoric acid. Commercial carbon-supported Pt and Pt/Ni nanoparticle catalysts were used in this study. The authors concluded form their Δμ data analysis that phosphate species remain adsorbed up to a higher potential on Pt/Ni than on Pt, which prevents the adsorption of OH^- from the water activation. As a result more catalytic active sites are available for the oxygen reduction reaction.

The measured surface coverage of phosphoric acid on platinum as a function of the cell potential is very different from what was observed in [63]. Similar to the FTIR measurements from Iwasita et al. [60], they observed an increase of phosphoric acid adsorption starting from 0 mV. The maximum coverage in their experiments was found at a lower potential. Above 400 mV the phosphoric acid adsorption decreases. In their XANES data phosphoric acid is present on the platinum surface at all potentials, but this is not the case at elevated temperatures and higher acid concentrations as reported by Kaserer et al. [63].

Synchrotron X-ray radiography and tomography – acid distribution in HT-PEMFCs

Synchrotron X-ray radiography had been successfully applied to LT-PEMFCs for visualization of liquid water profiles under different operating conditions. It was also straightforward to extend the same technique to the studies of phosphoric acid concentrations and distribution changes in HT-PEMFCs [65-68]. In one of the first studies, Maier et al. [65] selected an in-plane experimental set-up to image the cross-section of an HT-PEMFC during load cycles. The cell hardware was modified to allow for a better transmission of X-rays. The attenuation coefficient of phosphoric acid is approximately 7 times higher than that of water. Hence, a beam energy of 30 keV was selected, higher than what is commonly used to visualize water in LT-PEMFCs, as a good compromise between signal intensity and selectivity to H_3PO_4.

Maier et al. [65] obtained radiographs of a HT-PEMFC during load cycle changes. The normalized radiographs of the cross-section of the MEA at different current densities are displayed in Figure 14. After changing from OCV to a current density $j = 140$ mA/cm^2 the membrane thickness increased by approximately 20%. A further increase in current density to 300 mA/cm^2 and 500 mA/cm^2 did not lead to a significant additional swelling of the membrane. After returning to zero current, the membrane thickness was restored to the original value before the load cycle. The swelling of the membrane can be explained by hydration of the membrane. This is also consistent with the observation that switching the fuel cell from OCV to a current density of $j = 140$ mA/cm^2 increases the transmission in the membrane. The changes of transmission ("grey value" in the X-ray radiograph) though the MEA are shown in Figure 15. The water production in the cell also increases the transmission of both anode and cathode catalyst layers. While the pores of the GDL get filled with hydrated phosphoric acid the transmission there decreases.

Recently, the same group reported [67] in situ X-ray radiography in the through-plane viewing direction, which allows to visualize structural changes of the electrodes during load cycles.

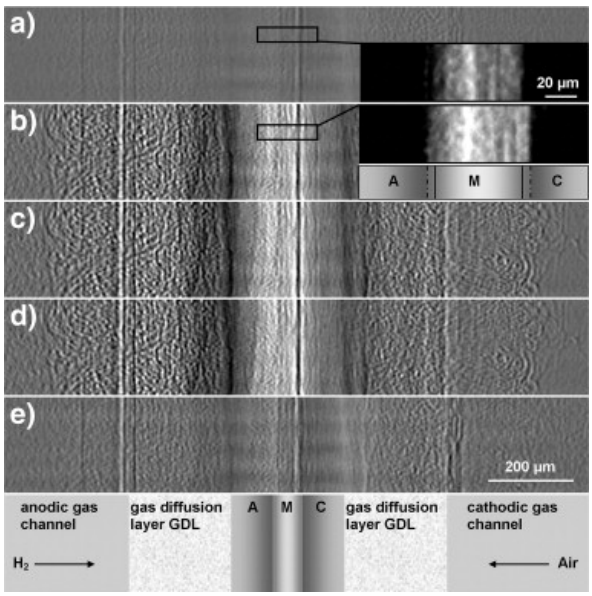

Figure 14: Normalized radiographs of the cross section of the MEA at different current densities *j*: a) 0 mA·cm^{-2} (OCV before), b) 140 mA·cm^{-2}, c) 300 mA·cm^{-2}, d) 550 mA·cm^{-2} and e) 0 mA·cm^{-2} (OCV after). Inset: Non-normalized enlarged radiographs of the membrane and parts of the catalyst layers at OCV and *j* = 140 mA·cm^{-2} (A, anode; M, membrane; C, cathode). Reprinted with permission from [65]. Copyright 2010 Elsevier.

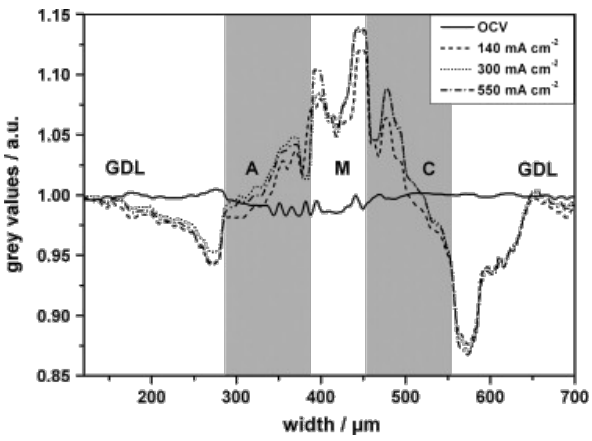

Figure 15: Changes of the transmission through the MEA (grey values) compared to steady-state conditions at OCV for different operating conditions: at OCV (solid line), 140 mA·cm^{-2} (dashed line), 300 mA·cm^{-2} (dotted line) and 550 mA·cm^{-2} (dot and dash line). Reprinted with permission from [65]. Copyright 2010 Elsevier.

For this study, the electrodes were prepared by coating and the catalyst layer exhibited a network of shrinkage cracks. The individual clots were clearly visible in the radiographs. During operation the membrane swelled, driving phosphoric acid and product water into the catalyst layer. This process was monitored by the change in the local transmittance of the cell during load cycles. The effect was more pronounced beneath the channel area because of the lower local compression rate of the MEA, which permitted stronger membrane deformation. The redistribution of phosphoric acid caused structural changes of the catalyst layer in the channel area. It was found that part of the electrode structure was displaced irreversibly after cell operation at load conditions that might lead to structural aging of the electrodes.

The simultaneous changes in the MEA structure and the phosphoric acid concentration make the quantitative analysis of X-ray radiographs challenging [40]. With additional 3D information, X-ray tomography is more effective in the localization and quantification of the acid electrolyte within the GDL and catalyst layer. It is necessary to establish a grayscale value reference for comparing the tomogram with known phosphoric acid concentrations. An important outcome of this research is a better understanding of acid loss during operation. Initial results indicate that the cracks in the catalyst layer and the micro porous layer (MPL) form the main pathway for phosphoric acid to escape from the interior of the MEA to the adjoining flow field.

X-ray tomography – morphologies of MEAs and GDEs: 3D X-ray tomography instruments are now commercially available. They are highly popular for studying internal structures of complex material assemblies. Fuel cell components such as MEAs and GDEs are certainly of such nature. Diedrichs et al. [69] used this analytical tool to investigate the impact of mechanical compression though the flow field of the bipolar plates on high-temperature MEAs. A sample holder was constructed with a serpentine flow field contact area for which the contact pressure could be adjusted between 0.5 and 2.5 MPa. From the X-ray tomography cross section images the changing thickness of the MEA was determined with increasing compression. The MEA bent itself into the flow field cannels, and bulges could be clearly seen in the X-ray tomography images. Beneath the channel area the MEA thickness increased with higher contact pressure, while the opposite occurred beneath the land area. Further compression led to irreversible structural damages of the MEA. The evaluated MEA manufactured by BASF utilized carbon paper as the GDL material. The rigid carbon fiber penetrated the soft membrane material, which resulted in small pinholes. Scanning electron microscopy (SEM) images showed broken GDL fibers piercing into the membrane and confirmed the observation made by X-ray tomography.

The same analytical tool has also been used to study the morphology of various GDEs [12] with the catalyst layers either sprayed or coated onto the GDLs. The impact of fabrication techniques on the macrostructure of the GDEs is presented in Figure 16.

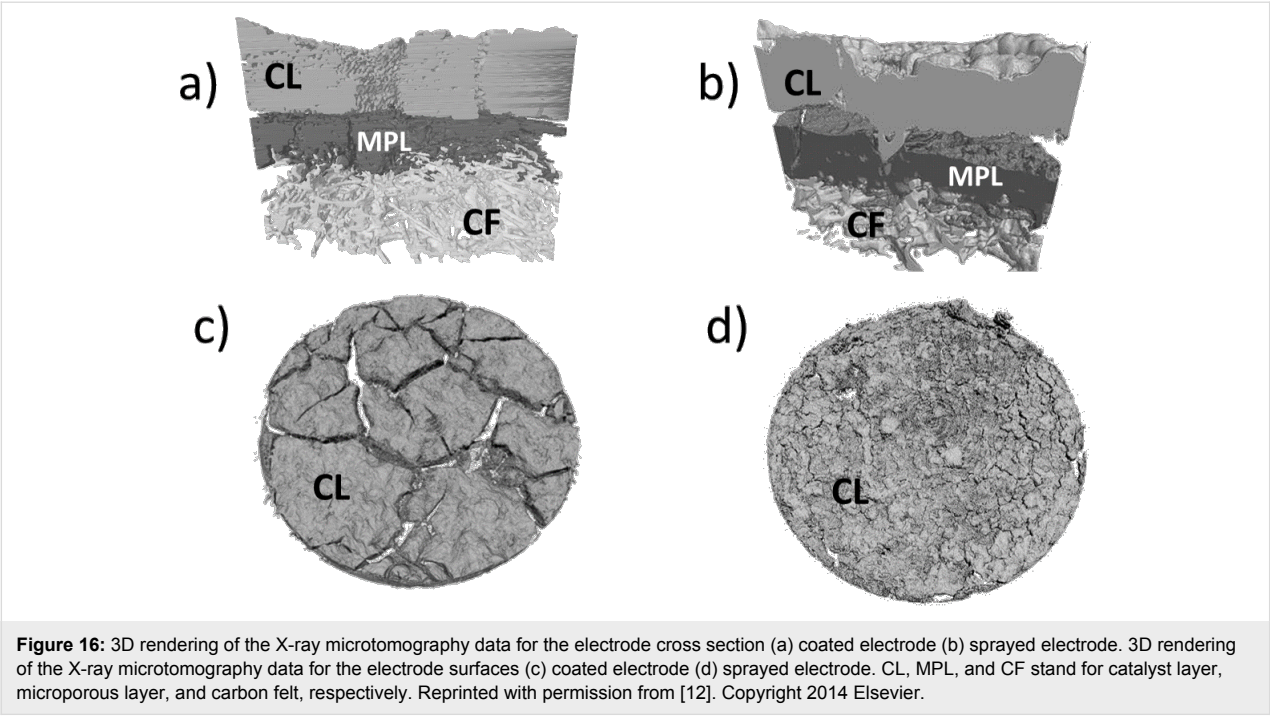

Figure 16: 3D rendering of the X-ray microtomography data for the electrode cross section (a) coated electrode (b) sprayed electrode. 3D rendering of the X-ray microtomography data for the electrode surfaces (c) coated electrode (d) sprayed electrode. CL, MPL, and CF stand for catalyst layer, microporous layer, and carbon felt, respectively. Reprinted with permission from [12]. Copyright 2014 Elsevier.

The coated catalyst layer showed a complete network of shrinkage cracks. The cracks went all the way though the catalyst layer. The clots were completely disconnected from each other. The scenario was quite different for the sprayed electrodes on a rough surface, where fine hairline cracks were present. Compared with the coated catalyst layer with its straight segments, the sprayed one appeared much more heterogeneous, e.g., it contained voids and void clusters of different shapes and sizes. The catalyst layer was partially delaminated from the MPL due to the fact that the solvent of the suspension drops on the surface had quickly evaporated after less than one minute for each layer. The 3D rendered image of the sprayed GDE in Figure 16 shows that the catalyst ink penetrated the MPL and filled up an exemplary large crack of MPL.

Neutron radiography – acid distribution in HT-PEMFCs

A substantial advantage of neutron imaging over X-rays is that there are no constraints to cell hardware due to the high transmission of neutrons though end- and bipolar plates, which are usually made of stainless steel and graphite. The attenuation of the neutrons originates mainly from hydrogen and hydrogenous compounds such as phosphoric acid. The first neutron radiography study of the acid distribution in HT-PEMFCs was published recently [70]. One of the challenges of this technique is a suitable reference for separating the attenuation due to phosphoric acid from contributions from other cell components. The authors [70] addressed this issue with isotope exchange between ^{1}H (protium) and ^{2}H (deuterium, D), a technique used earlier to study water transport in LT-PEMFCs. The deuteration and reprotonation of the phosphoric acid was achieved by supplying the cell with gases that were humidified with heavy water and light water, respectively. The process could be performed in less than 20 min.

The authors captured neutron radiographs of non-operating cells in both though-pane and in-plane imaging directions. The in-plane images showed that acid was present in both GDLs and, to some extent, in the flow channels and manifolds as well. The acid appeared to accumulate between the fiber bundles of the carbon cloth. To validate the technique, the authors also quantified the amount of acid of the cell using both viewing directions. Despite some minor discrepancy between though-pane and in-plane imaging directions, the quantitative analysis agreed quite well with the actual amount of acid in the cell.

Atomic force microscopy (conductive mode) – PTFE distribution and content of the catalyst layer

Conductive atomic force microscopy (AFM) can probe the local conductivity of a sample surface. Mack et al. [12] used this technique to measure the surface conductivity of HT-PEMFC electrodes by applying a constant potential between the AFM tip and the sample.

The spatially resolved current distribution maps of sprayed and coated GDE surfaces are presented in Figure 17. The bright regions of the map with high surface currents represent catalyst rich areas, whereas darker regions represent PTFE agglomer-

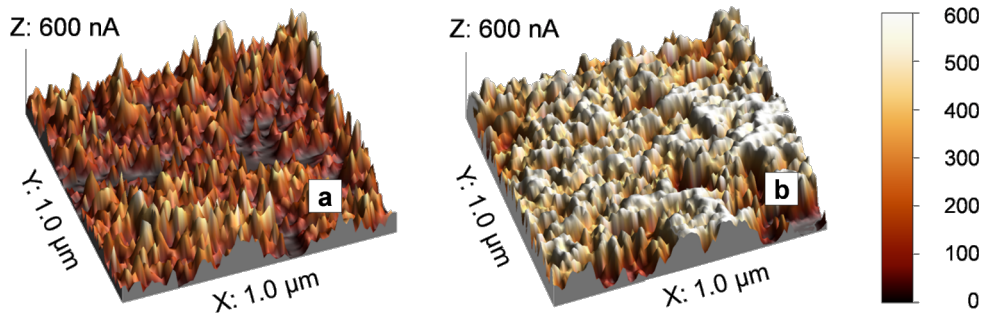

Figure 17: Locally resolved current maps of (a) coated and (b) sprayed gas diffusion electrode measured with the conductive AFM. The scan area is 1 µm × 1 µm. Reprinted with permission from [12]. Copyright 2014 Elsevier.

ates and gas pores with much lower conductivities. The average surface conductivity of the sprayed electrode is higher than that of the coated one. The PTFE distribution within the electrode is sensitive to its preparation technique. During spraying the small droplets of the catalyst ink dried instantly on the GDL, which resulted in a homogeneous PTFE distribution in the catalyst layer. In contrast, the drying process of the coated electrode took up to 12 h, during which the light PTFE particles could migrate to the top region of the catalyst layer and form a nonconductive "skin" on the electrode surface. This PTFE-rich layer affects not only the surface conductivity but also the wettability of the catalyst layer. The high PTFE content created a hydrophobic electrode surface, which slowed down the phosphoric acid uptake during the start-up period of the MEA.

Mack et al. [52] also evaluated the surface conductivity of catalyst layers with 10% and 40% PTFE contents. Less PTFE content in the electrode led to an improved surface conductivity due to fewer PTFE agglomerates in the surface layer. The hydrophobic nature of the PTFE binder controls the phosphoric acid wettability of the GDE and, in particular, the triple phase boundary between gas reactant, electrolyte and catalyst. Atomic force microscopy was proven suitable for investigating the PTFE distribution in the catalyst layer, which has a profound effect on the start-up and steady state performance of the cell.

Conclusion

Phosphoric acid-doped PBI-type fuel cells are so far the most promising candidates for practical high-temperature operation under ambient pressure. For commercial deployment, however, the performance and long-term stability of the high-temperature MEAs still need significant improvement. To achieve this goal, the MEA developers will rely on suitable analytical tools to evaluate single cells and their components. Great progress has been made in recent years. A broad range of characterization techniques are now available for the development of low-temperature PEM fuel cells. This has been the decisive factor behind the success of low-temperature MEA development thanks to a much better understanding of the underlying processes occurring in the MEA during fuel cell operation. We anticipate a similar trend in HT-PEMFC development. Advanced analytical tools suitable for HT-PEMFC will help optimize the MEA design and select the appropriate component materials that will withstand the harsh conditions of high-temperature operations.

Acknowledgements

The author acknowledges the financial support from the "Impuls- und Vernetzungsfonds der Helmholtz Gesellschaft" (Young Investigator Group project VH-NG-616).

References

1. Modestov, A. D.; Tarasevich, M. R.; Filimonov, V. Ya.; Davydova, E. S. *Electrochim. Acta* **2010,** *55,* 6073–6080. doi:10.1016/j.electacta.2010.05.068
2. Boaventura, M.; Sander, H.; Friedrich, K. A.; Mendes, A. *Electrochim. Acta* **2011,** *56,* 9467–9475. doi:10.1016/j.electacta.2011.08.039
3. Krishnan, P.; Park, J.-S.; Kim, C.-S. *J. Power Sources* **2006,** *159,* 817–823. doi:10.1016/j.jpowsour.2005.11.071
4. Li, Q.; Jensen, J. O.; Savinell, R. F.; Bjerrum, N. J. *Prog. Polym. Sci.* **2009,** *34,* 449–477. doi:10.1016/j.progpolymsci.2008.12.003
5. Bandlamudi, G. C.; Saborni, M.; Beckhaus, P.; Mahlendorf, F.; Heinzel, A. *J. Fuel Cell Sci. Technol.* **2010,** *7,* 014501. doi:10.1115/1.3119054
6. Holladay, J. D.; Wainright, J. S.; Jones, E. O.; Gano, S. R. *J. Power Sources* **2004,** *130,* 111–118. doi:10.1016/j.jpowsour.2003.11.055
7. Pan, C.; He, R.; Li, Q.; Jensen, J. O.; Bjerrum, N. J.; Hjulmand, H. A.; Jensen, A. B. *J. Power Sources* **2005,** *145,* 392–398. doi:10.1016/j.jpowsour.2005.02.056
8. Li, H.; Tang, Y.; Wang, Z.; Shi, Z.; Wu, S.; Song, D.; Zhang, J.; Fatih, K.; Zhang, J.; Wang, H.; Liu, Z.; Abouatallah, R.; Mazza, A. *J. Power Sources* **2008,** *178,* 103–117. doi:10.1016/j.jpowsour.2007.12.068
9. Bazylak, A. *Int. J. Hydrogen Energy* **2009,** *34,* 3845–3857. doi:10.1016/j.ijhydene.2009.02.084

10. Berg, P.; Promislow, K.; St Pierre, J.; Stumper, J.; Wetton, B. *J. Electrochem. Soc.* **2004,** *151,* A341–A353. doi:10.1149/1.1641033
11. Galbiati, S. Experimental Study of Polybenzimidazole Based High Temperature Polymer Electrolyte Fuel Cells. Ph.D. Thesis, Politechnico di Milano, Milan, Italy, 2012.
12. Mack, F.; Klages, M.; Scholta, J.; Jörissen, L.; Morawietz, T.; Hiesgen, R.; Kramer, D.; Zeis, R. *J. Power Sources* **2014,** *255,* 431–438. doi:10.1016/j.jpowsour.2014.01.032
13. Chandan, A.; Hattenberger, M.; El-Kharouf, A.; Du, S.; Dhir, A.; Self, V.; Pollet, B. G.; Ingram, A.; Bujalski, W. *J. Power Sources* **2013,** *231,* 264–278. doi:10.1016/j.jpowsour.2012.11.126
14. Gojković, S. Lj.; Zečević, S. K.; Savinell, R. F. *J. Electrochem. Soc.* **1998,** *145,* 3713–3720. doi:10.1149/1.1838864
15. Liu, Z.; Wainright, J. S.; Litt, M. H.; Savinell, R. F. *Electrochim. Acta* **2006,** *51,* 3914–3923. doi:10.1016/j.electacta.2005.11.019
16. Zhang, J.; Xie, Z.; Zhang, J.; Tanga, Y.; Song, C.; Navessin, T.; Shi, Z.; Song, D.; Wang, H.; Wilkinson, D. P.; Liu, Z.-S.; Holdcroft, S. *J. Power Sources* **2006,** *160,* 872–891. doi:10.1016/j.jpowsour.2006.05.034
17. Mader, J.; Xiao, L.; Schmidt, T. J.; Benicewicz, B. C. Polybenzimidazole/Acid Complexes as High-Temperature Membranes. In *Fuel Cells II;* Scherer, G. G., Ed.; Advances in Polymer Science, Vol. 216; Springer-Verlag: Berlin, Germany, 2008; pp 63–124. doi:10.1007/12_2007_129
18. Asensio, J. A.; Sánchez, E. M.; Gómez-Romero, P. *Chem. Soc. Rev.* **2010,** *39,* 3210–3239. doi:10.1039/b922650h
19. Li, Q.; He, R.; Jensen, J. O.; Bjerrum, N. J. *Chem. Mater.* **2003,** *15,* 4896–4915. doi:10.1021/cm0310519
20. Lehnert, W.; Wannek, C.; Zeis, R. Trends in High-Temperature Polymer Electrolyte Fuel Cells. In *Innovations in Fuel Cell Technologies;* Steinberger-Wilckens, R.; Lehnert, W., Eds.; Royal Society of Chemistry: Cambridge, UK, 2010; pp 41–75. doi:10.1039/9781849732109-00041
21. Wang, J.-T.; Savinell, R. F.; Wainright, J.; Litt, M.; Yu, H. *Electrochim. Acta* **1996,** *41,* 193–197. doi:10.1016/0013-4686(95)00313-4
22. Wainright, J. S.; Wang, J.-T.; Weng, D.; Savinell, R. F.; Litt, M. *J. Electrochem. Soc.* **1995,** *142,* L121–L123. doi:10.1149/1.2044337
23. Li, Q.; He, R.; Jensen, J. O.; Bjerrum, N. J. *Fuel Cells* **2004,** *4,* 147–159. doi:10.1002/fuce.200400020
24. Wannek, C.; Konradi, I.; Mergel, J.; Lehnert, W. *Int. J. Hydrogen Energy* **2009,** *34,* 9479–9485. doi:10.1016/j.ijhydene.2009.09.076
25. Oono, Y.; Sounai, A.; Hori, M. *J. Power Sources* **2009,** *189,* 943–949. doi:10.1016/j.jpowsour.2008.12.115
26. Conti, F.; Majerus, A.; Di Noto, V.; Korte, C.; Lehnert, W.; Stolten, D. *Phys. Chem. Chem. Phys.* **2012,** *14,* 10022–10026. doi:10.1039/c2cp40553a
27. Wannek, C.; Lehnert, W.; Mergel, J. *J. Power Sources* **2009,** *192,* 258–266. doi:10.1016/j.jpowsour.2009.03.051
28. Schmidt, T. J.; Baurmeister, J. *J. Power Sources* **2008,** *176,* 428–434. doi:10.1016/j.jpowsour.2007.08.055
29. Bouchet, R.; Siebert, E. *Solid State Ionics* **1999,** *118,* 287–299. doi:10.1016/S0167-2738(98)00466-4
30. Glipa, X.; Bonnet, B.; Mula, B.; Jones, D. J.; Roziere, J. *J. Mater. Chem.* **1999,** *9,* 3045–3049. doi:10.1039/a906060j
31. He, R.; Li, Q.; Jensen, J. O.; Bjerrum, N. J. *J. Polym. Sci., Part A: Polym. Chem.* **2007,** *45,* 2989–2997. doi:10.1002/pola.22053
32. He, R.; Li, Q.; Xiao, G.; Bjerrum, N. J. *J. Membr. Sci.* **2003,** *226,* 169–184. doi:10.1016/j.memsci.2003.09.002
33. Ma, Y.-L.; Wainright, J. S.; Litt, M. H.; Savinell, R. F. *J. Electrochem. Soc.* **2004,** *151,* A8–A16. doi:10.1149/1.1630037
34. Mack, F.; Heissler, S.; Laukenmann, R.; Zeis, R. *J. Power Sources* **2014,** *270,* 627–633. doi:10.1016/j.jpowsour.2014.06.171
35. Wippermann, K.; Wannek, C.; Oetjen, H.-F.; Mergel, J.; Lehnert, W. *J. Power Sources* **2010,** *195,* 2806–2809. doi:10.1016/j.jpowsour.2009.10.100
36. Zeis, R.; Mathur, A.; Fritz, G.; Lee, J.; Erlebacher, J. *J. Power Sources* **2007,** *165,* 65–72. doi:10.1016/j.jpowsour.2006.12.007
37. Mazúr, P.; Soukup, J.; Paidar, M.; Bouzek, K. *J. Appl. Electrochem.* **2011,** *41,* 1013–1019. doi:10.1007/s10800-011-0325-9
38. Gülzow, E.; Schulze, M.; Wagner, N.; Kaz, T.; Reissner, R.; Steinhilber, G.; Schneider, A. *J. Power Sources* **2000,** *86,* 352–362. doi:10.1016/S0378-7753(99)00451-6
39. Gasda, M. D.; Teki, R.; Lu, T.-M.; Koratkar, N.; Eisman, G. A.; Gall, D. *J. Electrochem. Soc.* **2009,** *156,* B614–B619. doi:10.1149/1.3097188
40. Eberhardt, S. H.; Büchi, F.; Schmidt, T. J. Determination of phosphoric acid concentrations in HT-PEFC components by X-ray tomographic microcscopy. *Paul Scherrer Institut, Electrochemistry Laboratory, Annual Report 2013;* Paul Scherrer Institut: Villingen, Switzerland, 2014; pp 13–14. doi:10.3929/ethz-a-007047464
41. Mukerjee, S.; Srinivasan, S. *J. Electroanal. Chem.* **1993,** *357,* 201–224. doi:10.1016/0022-0728(93)80380-Z
42. Paulus, U. A.; Wokaun, A.; Scherer, G. G.; Schmidt, T. J.; Stamenkovic, V.; Markovic, N. M.; Ross, P. N. *Electrochim. Acta* **2002,** *47,* 3787–3798. doi:10.1016/S0013-4686(02)00349-3
43. Antolini, E.; Salgado, J. R. C.; Gonzalez, E. R. *J. Power Sources* **2006,** *160,* 957–968. doi:10.1016/j.jpowsour.2006.03.006
44. Toda, T.; Igarashi, H.; Uchida, H.; Watanabe, M. *J. Electrochem. Soc.* **1999,** *146,* 3750–3756. doi:10.1149/1.1392544
45. Rao, C. V.; Parrondo, J.; Ghatty, S. L.; Rambabu, B. *J. Power Sources* **2010,** *195,* 3425–3430. doi:10.1016/j.jpowsour.2009.12.022
46. Mamlouk, M.; Jang, J. H.; Scott, K. *J. Fuel Cell Sci. Technol.* **2011,** *9,* 011002. doi:10.1115/1.4004461
47. Wang, X.; Li, W.; Chen, Z.; Waje, M.; Yan, Y. *J. Power Sources* **2006,** *158,* 154–159. doi:10.1016/j.jpowsour.2005.09.039
48. Matsumoto, K.; Fujigaya, T.; Sasaki, K.; Nakashima, N. *J. Mater. Chem.* **2011,** *21,* 1187–1190. doi:10.1039/c0jm02744h
49. Fujigaya, T.; Nakashima, N. *Adv. Mater.* **2013,** *25,* 1666–1681. doi:10.1002/adma.201204461
50. Lobato, J.; Cañizares, P.; Rodrigo, M. A.; Linares, J. J.; Pinar, F. J. *Int. J. Hydrogen Energy* **2010,** *35,* 1347–1355. doi:10.1016/j.ijhydene.2009.11.091
51. Seland, F.; Berning, T.; Børresen, B.; Tunold, R. *J. Power Sources* **2006,** *160,* 27–36. doi:10.1016/j.jpowsour.2006.01.047
52. Mack, F.; Morawietz, T.; Hiesgen, R.; Kramer, D.; Zeis, R. *ECS Trans.* **2013,** *58,* 881–888. doi:10.1149/05801.0881ecst
53. Martin, S.; Li, Q.; Steenberg, T.; Jensen, J. O. *J. Power Sources* **2014,** *272,* 559–566. doi:10.1016/j.jpowsour.2014.08.112
54. Giffin, G. A.; Conti, F.; Lavina, S.; Majerus, A.; Pace, G.; Korte, C.; Lehnert, W.; Di Noto, V. *Int. J. Hydrogen Energy* **2014,** *39,* 2776–2784. doi:10.1016/j.ijhydene.2013.04.152
55. Daletou, M. K.; Geormezi, M.; Vogli, E.; Voyiatzis, G. A.; Neophytides, S. G. *J. Mater. Chem. A* **2014,** *2,* 1117–1127. doi:10.1039/c3ta13335d
56. Li, Q.; He, R.; Berg, R. W.; Hjuler, H. A.; Bjerrum, N. J. *Solid State Ionics* **2004,** *168,* 177–185. doi:10.1016/j.ssi.2004.02.013

57. Musto, P.; Karasz, F. E.; MacKnight, W. J. *Polymer* **1993,** *34,* 2934–2945. doi:10.1016/0032-3861(93)90618-K
58. Musto, P.; Karasz, F. E.; MacKnight, W. J. *Polymer* **1989,** *30,* 1012–1021. doi:10.1016/0032-3861(89)90072-4
59. Habib, M. A.; Bockris, J. O'M. *J. Electrochem. Soc.* **1985,** *132,* 108–114. doi:10.1149/1.2113736
60. Nart, F. C.; Iwasita, T. *Electrochim. Acta* **1992,** *37,* 385–391. doi:10.1016/0013-4686(92)87026-V
61. Weber, M.; Nart, F. C.; de Moraes, I. R.; Iwasita, T. *J. Phys. Chem.* **1996,** *100,* 19933–19938. doi:10.1021/jp960952k
62. Neophytides, G.; Quaroni, L.; Büchi, F. N.; Orfanidi, A.; Neophytides, S. G.; Schmidt, T. *Electrochem. Commun.* **2013,** *34,* 200–203. doi:10.1016/j.elecom.2013.06.012
63. Kaserer, S.; Caldwell, K. M.; Ramaker, D. E.; Roth, C. *J. Phys. Chem. C* **2013,** *117,* 6210–6217. doi:10.1021/jp311924q
64. He, Q.; Shyam, B.; Nishijima, M.; Ramaker, D.; Mukerjee, S. *J. Phys. Chem. C* **2013,** *117,* 4877–4887. doi:10.1021/jp309282n
65. Maier, W.; Arlt, T.; Wannek, C.; Manke, I.; Riesemeier, H.; Kruger, P.; Scholta, J.; Lehnert, W.; Banhart, J.; Stolten, D. *Electrochem. Commun.* **2010,** *12,* 1436–1438. doi:10.1016/j.elecom.2010.08.002
66. Maier, W.; Arlt, T.; Wippermann, K.; Wannek, C.; Manke, I.; Lehnert, W.; Stolten, D. *J. Electrochem. Soc.* **2012,** *159,* F398–F404. doi:10.1149/2.024208jes
67. Tobias, A.; Wiebke, M.; Tötzke, C.; Wannek, C.; Markötter, H.; Wieder, F.; Banhart, J.; Lehnert, W.; Manke, I. *J. Power Sources* **2014,** *246,* 290–298. doi:10.1016/j.jpowsour.2013.07.094
68. Kuhn, R.; Scholta, J.; Krüger, P.; Hartnig, C.; Lehnert, W.; Arlt, T.; Manke, I. *J. Power Sources* **2011,** *196,* 5231–5239. doi:10.1016/j.jpowsour.2010.11.025
69. Diedrichs, A.; Rastedt, M.; Pinar, F. J.; Wagner, P. *J. Appl. Electrochem.* **2013,** *43,* 1079–1099. doi:10.1007/s10800-013-0597-3
70. Boillat, P.; Biesdorf, J.; Oberholzer, P.; Kaestner, A.; Schmidt, T. J. *J. Electrochem. Soc.* **2014,** *161,* F192–F198. doi:10.1149/2.023403jes

License and Terms

BEILSTEIN JOURNAL OF NANOTECHNOLOGY

Multiscale modeling of lithium ion batteries: thermal aspects

Arnulf Latz*[1,2,3] and Jochen Zausch[4]

Full Research Paper

Open Access

Address:
[1]German Aerospace Center (DLR), Stuttgart, Germany, [2]Helmholtz Institute for Electrochemical Energy Storage, Ulm, Germany, [3]University of Ulm, School of Chemistry, Ulm, Germany and [4]Fraunhofer Institute for Industrial Mathematics (ITWM), Kaiserslautern, Germany

Email:
Arnulf Latz* - Arnulf.Latz@dlr.de

* Corresponding author

Keywords:
lithium ion batteries; multiscale modeling; heat transport

Beilstein J. Nanotechnol. **2015,** *6,* 987–1007.
doi:10.3762/bjnano.6.102

Received: 16 September 2014
Accepted: 23 March 2015
Published: 20 April 2015

This article is part of the Thematic Series "Materials for sustainable energy production, storage, and conversion".

Guest Editor: M. Fichtner

Abstract

The thermal behavior of lithium ion batteries has a huge impact on their lifetime and the initiation of degradation processes. The development of hot spots or large local overpotentials leading, e.g., to lithium metal deposition depends on material properties as well as on the nano- und microstructure of the electrodes. In recent years a theoretical structure emerges, which opens the possibility to establish a systematic modeling strategy from atomistic to continuum scale to capture and couple the relevant phenomena on each scale. We outline the building blocks for such a systematic approach and discuss in detail a rigorous approach for the continuum scale based on rational thermodynamics and homogenization theories. Our focus is on the development of a systematic thermodynamically consistent theory for thermal phenomena in batteries at the microstructure scale and at the cell scale. We discuss the importance of carefully defining the continuum fields for being able to compare seemingly different phenomenological theories and for obtaining rules to determine unknown parameters of the theory by experiments or lower-scale theories. The resulting continuum models for the microscopic and the cell scale are numerically solved in full 3D resolution. The complex very localized distributions of heat sources in a microstructure of a battery and the problems of mapping these localized sources on an averaged porous electrode model are discussed by comparing the detailed 3D microstructure-resolved simulations of the heat distribution with the result of the upscaled porous electrode model. It is shown, that not all heat sources that exist on the microstructure scale are represented in the averaged theory due to subtle cancellation effects of interface and bulk heat sources. Nevertheless, we find that in special cases the averaged thermal behavior can be captured very well by porous electrode theory.

Introduction

The main challenge for establishing an ab initio multiscale simulation approach for batteries or electrochemical storage devices in general is the extremely complex chemical context in which those devices are operated [1]. There is no commercial battery which is produced from pure active materials for the electrodes and from a pure mixture of salt and solvent for the

electrolyte alone. Usually, it is necessary to add soot to the slurry for electrode production in order to counteract the poor electronic conductivity of the active materials of negative electrodes. The active material is not used as one block (except in thin film batteries) but is ground into a powder or artificially designed into complex nanostructures in order to increase the available surface for insertion or conversion reactions. To ensure the mechanical stability of the electrode, binder has to be added, which in turn is not without consequences for the electrochemical properties of the batteries. Therefore the nano- and micrometer-scale structure of the battery is as important as the material itself to obtain a "good" electrode, where "good" is defined with respect to the envisioned application and not with respect to the materials properties. Analogous modifications are necessary to obtain a good conducting electrolyte that is stable under high voltages and chemical compatible with the chosen electrode materials. Thus, additives are used in order to enhance the ionic conductivity and to improve the chemical compatibility. Also the properties of the solid electrolyte interphase (SEI) on the negative electrodes, which is essential for the long time stability of a battery [2], are strongly influenced by the composition of the electrolyte. Therefore it would not be possible to design with simulations an optimal electrolyte without considering, e.g., the impact of the electrolyte on the electrochemical reaction kinetics at the interface of electrolyte and active particles or the complex chemical reactions leading to the growth of the SEI, plating and electrochemical reactions initiated in the bulk of the electrolyte at high potentials.

A successful strategy for the development of predictive theories and simulation tools has therefore to guarantee that the theoretical concepts on the different spatial scales from atomistic to cell scale have sufficient overlap to ensure the possibility of a systematic upscaling procedure. This argument addresses the problem of identifying a representative volume element, which is small enough for being able to use the simulation techniques on the fine scale but big enough for the results to be usable on the large scale. This necessary condition requires the development of systematic rigorous theories on each scale from quantum chemistry for the atomistic scale, over particle-based models utilizing classical force fields to continuum theories. But even within continuum theories it is for practical reasons important to distinguish between microstructure-resolved and porous-electrode theories to develop consistent theories for both scales.

The knowledge of the material parameters and their dependency on composition or atomistic structure is the starting point for a rational design of energy storage materials [3]. Density functional theory with all its approximations [4,5] if combined with statistical mechanics methods is in this context the most successful method to simulate material properties of electrochemically active materials [3,6]. The combination with statistical methods is important to bridge the gap between zero-temperature DFT simulations in vacuum and the properties of the studied materials at finite temperatures in contact with different phases. Standard DFT simulations usually concentrate on individual electronic processes without considering the interplay with the environment or competing electronic processes, which might be statistically and thus macroscopically much more significant [7]. In ab initio thermodynamics, DFT is combined with ideas from statistical mechanics in order to obtain the Gibbs free energy of bulk and interfaces at finite temperatures. Especially for the calculation of differences of Gibbs free energies, which are relevant for the determination of stable equilibrium configurations, the accuracy is higher than might be expected from the absolute accuracy of the DFT simulation, which usually contain many simplification and assumptions on the structure of the solution [4,5]. By using cluster expansions [8] it is possible to combine DFT with kinetic Monte Carlo (KMC) simulations to obtain collective diffusion coefficients for lithium ions at concentrations beyond the dilute limit [9]. To obtain the collective diffusion coefficient is crucial since there is a difference between the self-diffusion coefficients and the collective diffusion coefficient [10]. As will be shown below, it is the collective diffusion coefficient that is relevant for the transport of lithium ions in the solid active particle as well as in the liquid electrolyte. The collective diffusion coefficient can be written as a product of a thermodynamic factor, which can be obtained from the chemical potential, and a kinetic coefficient, which is a measure of the energy barriers caused by the local environment of the Li ions. They may depend in solids on vacancy distributions as well as on the local lithium-ion concentration itself [9,11-13]. The diffusion coefficients for liquid electrolytes might more easily obtained from molecular dynamics (MD) simulations once the force fields for the interaction between the molecules are known [14,15].

Information on interface properties can be obtained from MD simulations and from DFT simulations [15]. MD simulations are especially relevant to study the solvation properties of the ions [15-17], which are important to understand contribution of solvation forces to the intercalation kinetics. The actual barriers for intercalation can be addressed by DFT simulations [18].

The change in mechanical properties upon intercalation is very important to understand degradation phenomena in batteries. Usually the change in the behavior of cells can be simulated by using macroscopic continuum models [19-21]. But knowledge of the change in the specific volume of the material as function of Li concentration and the change in the elastic constants is necessary to parameterize the continuum models. This informa-

tion can be extracted from DFT simulations [22,23]. Phase changes, initiated by the intercalation of lithium ions, require additional information on the stability of phases [24] and interface properties. The evolution of electrochemical active interfaces can be described by phasefield theories [25,26], which provide an approximate continuous description of the dynamics of interfaces [27]. They need as input the interface free energies between the phases. This interface free energy is accessible to DFT simulations [28,29]. On the basis of this information the intercalation properties of phase separating materials can be modeled [30]. Also, predictions for the stress [31] induced by the phase front and its influence on the intercalation dynamics [32] are possible. It should be mentioned that there are still many unsolved issues and not completely consistent predictions for the intercalation properties of phase-changing many-particle electrodes [33-37].

The production of heat in batteries is a very important information for the proper prediction of degradation phenomenon. Since heat is a thermodynamic concept it has to be dealt with on the macroscopic scale. From atomistic simulations the determination of Gibbs free energies, entropies and insertion properties (e.g., kinetic barriers, chemical potential of adsorbed species, solvation energies) are obtained. The relation of these quantities to the actual heat production has to be derived from systematic thermodynamic theories [38-41]. Most of the literature on heat transport in lithium ion batteries uses phenomenological porous electrode theories [42-49], which are not based on a systematically derived thermodynamic consistent theory. In [45], the porous electrode theory is derived with the help of volume averaging applied to the phenomenological pore scale model. Full 3D simulations of thermal effects in electrode microstructures do, to the best of our knowledge, not exist; except for [50] in which the heat sources in a microstructure of a $LiCoO_2$ cathode are obtained with the help of phenomenological expressions for the heat sources and the current distribution in the electrode [51].

A general overview about multiscale modeling and simulation strategy, including an overview about available software concepts in the context of electrochemical storage and conversion devices is given in [52].

We will concentrate in our article on the systematic derivation of fully coupled transport equations for ion, charge and heat transport in lithium ion batteries on the nano- and micrometer-scale as well as on the cell scale . The cell-level equations will be obtained from an analytical upscaling procedure to ensure the consistency with pore-resolved theory. Where possible, we will point out the necessary input from ab initio atomistic scale theories. The microscopic as well as the cell-level theory are simulated for a virtual microstructure and its homogenized effective porous electrode description . The comparison of the averaged results of the microscopic simulation exhibit remarkable agreement with the simulation of the porous electrode theory, but we find very strong fluctuations around the average. Especially for the prediction of degradation phenomena these fluctuations might be crucial.

Non-equilibrium thermodynamics

To make contact with theories on atomistic scales, it is necessary to formulate the continuum theories in terms of quantities that have a well defined physical meaning and can either be obtained by simulations on atomistic scales or from independent experiments. Even if information about energy barriers and reaction rates can be obtained from density functional theory for the system under investigation, additional modeling steps are necessary to obtain the relevant parameters for the kinetic models used in mesoscopic reaction–transport theories [53,54]. Especially the formalism of ab initio atomistic thermodynamics, which combines DFT simulations with strategies from statistical mechanics [3,6,7], allows one in principle to determine Gibbs free energies, reaction rates and relevant transport coefficients for materials used in electrochemical applications. The transport equations on the continuum scale have to be based on the same quantities. Only then, the information obtained from the quantum scale can be transferred to the continuum scale. Very often continuum scale equations are not derived, but formulated on phenomenological grounds. This approach leads to “effect driven” theories, which try to include the known phenomena (e.g., diffusion, electroosmosis, Peltier effect, double layer properties [53]) without considering the possible existence of an underlying coherent theoretical structure. Such a structure may require relations between transport coefficients in order to ensure positive entropy production and may reveal information about the nature of the considered continuum fields, which are essential to make contact to atomistic scale simulations and to experiment or influence the form of the charge distribution in the double layer [27]. Only a rigorous derivation within a systematic theoretical framework can reveal such a structure. In order to demonstrate the impact of the chosen continuum fields on the structure of a continuum theory we re-derive the equations for coupled transport of ions, charge and heat in a lithium ion battery by using the framework of rational thermodynamics [39,40]. This derivation recovers the equation in [41,55] and shows in the isothermal case the equivalence with the seemingly different theory of [27]. The theory is valid for transport on pore-scale-resolved battery structures. The cell-level equations, which are consistent with the derived microstructure theory are then derived by using systematic volume averaging. It is shown that some of the reversible heat sources of the bulk and the interfaces cancel each

other in the averaged macroporous theory. The cancelation is also demonstrated by explicitly simulating the coupled transport on the microscale and analyzing all heat sources in the bulk and the interfaces. Since heat sources lead to thermal stress, there are possible sources for degradation on the microscale that cannot be detected on the macroporous scale. The cancelation also demonstrates the importance of a consistent formulation of interface condition and transport equations. The usual "effect driven" procedure, in which bulk equations and interface conditions are formulated completely independent of each other, may easily miss such cancelation effects. A generic starting point for the derivation of the transport equations is a mixture of a positively charged and a negatively charged species, and a neutral component. This mixture is able to represent an electrolyte consisting of a salt, dissolved in a solvent as well as transport of Li ions and electrons in an active particles consisting of a neutral host lattice. Different derivations are necessary for ionic liquids (mixture of positive and negative charges only) and solid electrolytes (ionic conductors). In a liquid electrolyte these are positive cations, negative anions and a neutral solvent. In conventional Li ion batteries under normal operating conditions, mass convection can be excluded as transport mechanism, but will always be a possibility in a systematic theory. Especially, if there are side reactions leading to film growth or convective gas transport after electrolyte degradation, convective transport might be initiated as a consequence. In general, it is sufficient to consider transport driven by electric fields and gradients in concentration, temperature and stress. In our derivation, we follow closely the notations used in [40] and neglect stress gradients for simplicity.

Transport theory

First, the general transport theory for a bulk system consisting of three interacting species (negative, positive and neutral species) in a electric field will be derived, before we discuss the boundary conditions at the interfaces between different chemical environments (electrolyte and active particles). Starting point of the derivation are the conservation equations for the three mass densities ρ_α, the momentum **g** and the energy density ε of the system in an electric field. Although we will set the barycentric velocity **v** to zero at the end of the derivation, it is necessary to include at least a stationary velocity field, in order to obtain the coupling to electro-mechanical stresses. The mass conservation of the species can be written in the form

$$\dot{\rho}_\alpha = -\rho_\alpha \nabla\cdot\mathbf{v} - \nabla\cdot\left(M_\alpha \mathbf{N}_\alpha\right). \tag{1}$$

$\mathbf{N}_\alpha$ is the molecular flux and M_α the molar density (kg/mol) of the species α. The convective or total time derivative $\dot{\mathrm{A}}$ for some variable A is in the usual form given by

$$\dot{\mathrm{A}} = \mathrm{A}_t + \mathbf{v}\cdot\nabla\mathrm{A}\,, \tag{2}$$

where A_t is the partial derivative $\partial\mathrm{A}/\partial t$ Since the total density $\rho = \sum_\alpha \rho_\alpha$ is conserved, i.e., $\dot{\rho} + \rho\nabla\cdot\mathbf{v} = 0$, the requirement

$$\sum_\alpha M_\alpha \mathbf{N}_\alpha = 0 \tag{3}$$

has to be fulfilled. The equation for the momentum density has the very general form

$$\rho\dot{\mathbf{g}} = \nabla\cdot\sigma + \rho\mathbf{b}\,. \tag{4}$$

Here **b** is an external force density, σ is the stress tensor and $\left(\nabla\cdot\sigma\right)_i = \partial_j\sigma_{ij}$ (the Einstein summation convention for the repeating index is used). The equation for the energy density ε is given by

$$\rho\dot{\varepsilon} = \nabla\left(\sigma\cdot\mathbf{v}\right) + \rho\mathbf{b}\cdot\mathbf{v} + \rho\dot{Q}_\mathrm{H} - \nabla\left(\mathbf{q} + \mathcal{E}\times\mathcal{H}\right). \tag{5}$$

$\dot{Q}_\mathrm{H}$ is the local heat production, **q** is the heat flux, and $\mathcal{E}$ and $\mathcal{H}$ are the Galilei invariant electrical and magnetic fields,

$$\mathcal{E} = \mathbf{E} + \mathbf{v}\times\mathbf{B}\,, \tag{6}$$

$$\mathcal{H} = \mathbf{H} - \mathbf{v}\times\mathbf{D}\,, \tag{7}$$

which couple the electric field and magnetic field with the dielectric displacement **D** and the magnetic induction **B**. We may eliminate the force **b** from Equation 5 by using Equation 4 and obtain

$$\rho\dot{\varepsilon} = \sigma : \kappa + \rho\dot{\mathbf{g}}\cdot\mathbf{v} + \rho\dot{Q}_\mathrm{H} - \nabla\left(\mathbf{q} + \mathcal{E}\times\mathcal{H}\right), \tag{8}$$

where $\kappa_{ij} = \partial v_i/\partial x_j$ is the (non-symmetrized) strain rate tensor and $\sigma : \kappa := \sum_{ij}\sigma_{ij}\kappa_{ij}$. The Maxwell equations in the Galilei invariant approximation can be written as

$$\nabla\cdot\mathbf{D} = \rho_F \tag{9}$$

$$\nabla\times\mathcal{H} = \mathcal{J} + \overset{*}{\mathbf{D}} \tag{10}$$

$$\nabla\times\mathcal{E} = -\overset{*}{\mathbf{B}} \tag{11}$$

$$\nabla\cdot\mathbf{B} = 0 \tag{12}$$

$$\mathbf{D} = \varepsilon_0 \mathbf{E} + \mathbf{P} \tag{13}$$

$$\mathcal{H} = \mathbf{B}/\mu_0 - \mathbf{v} \times \varepsilon_0 \mathbf{E} - \mathcal{M} . \tag{14}$$

We introduced the Galilei invariant current $\mathcal{J} = \mathbf{j} - q\mathbf{v}$, the magnetization $\mathcal{M} = \mathbf{M} + \mathbf{v} \times \mathbf{P}$ and the flux derivative $\overset{*}{\mathbf{A}} = \dot{\mathbf{A}} + \mathbf{A}(\nabla \cdot \mathbf{v}) - (\mathbf{A} \cdot \nabla)\mathbf{v}$. The free charge density ρ_F is related to the molar density n_α by $\rho_e = \sum_\alpha F z_\alpha n_\alpha$, with z_α being the charge number (i.e., the multiples of positive or negative elementary charges) and F the Faraday number. $\mathbf{P}$ is the polarization due to bound charges.

In order to derive constitutive equations, we make use of the inequality for total change of the entropy density

$$\rho \dot{s} + \nabla \cdot \left(\frac{\mathbf{q} - \mu_\alpha \mathbf{N}_\alpha}{T} \right) - \frac{\rho \dot{Q}_\mathrm{H}}{T} = \frac{R}{T} \geq 0 . \tag{15}$$

Here R is the yet unknown entropy production and μ_α is the chemical potential of species α. An expression for μ_α will be derived shortly. By eliminating the heat production $\dot{Q}_\mathrm{H}$ from Equation 15 and some reformulations of $\nabla(\mathcal{E} \times \mathcal{H})$ we obtain

$$\begin{aligned} R = &-\rho \dot{\varphi}_\mathrm{H} - \rho s \dot{T} - \mathbf{P} \cdot \dot{\mathcal{E}} + \tau : \kappa + \\ &\mathcal{J} \cdot \mathcal{E} - \frac{\left(\mathbf{q} - \sum \mu_\alpha \mathbf{N}_\alpha \right)}{T} \cdot \nabla T - \nabla \cdot \left(\mu_\alpha \mathbf{N}_\alpha \right) . \end{aligned} \tag{16}$$

Here φ_H is the specific free energy density (with respect to the total mass) and the electromechanical stress tensor is given by (neglecting all contributions from magnetic fields)

$$\tau = \sigma + \left[\frac{1}{2} \varepsilon_0 E^2 \right] I - \varepsilon_0 \mathbf{E} \otimes \mathbf{E} - \mathcal{E} \otimes \mathbf{P} . \tag{17}$$

The electromagnetic specific (Helmholtz) free energy, φ_H, is given by

$$\varphi_\mathrm{H} = \varepsilon - Ts - \frac{1}{2} v^2 - \left[\frac{1}{2} \varepsilon_0 E^2 + \mathcal{E} \cdot \mathbf{P} \right] / \rho . \tag{18}$$

The constitutive equations follow from Equation 16 and the form of the material law for the free energy φ_H. The influence of magnetic fields on batteries is usually neglected. For the purpose of this article, we are also not interested in the calculation of mechanical strain of active particles. Therefore, the free energy density can be written as

$$\varphi_\mathrm{H} = \varphi_\mathrm{H} \left(\rho_\alpha, T, \mathcal{E} \right) . \tag{19}$$

If phase-changing materials are described, this free energy may also be interpreted as free energy functional. For instance, in the case that the free energy also depends on the spatial derivatives of the densities as in phase-field theories for batteries [30,56]. The total derivative of the free energy (Equation 19) is given by

$$\rho \dot{\varphi}_\mathrm{H} = \rho \frac{\partial \varphi_\mathrm{H}}{\partial \rho_\alpha} \dot{\rho}_\alpha + \rho \frac{\partial \varphi_\mathrm{H}}{\partial T} \dot{T} + \rho \frac{\partial \varphi_\mathrm{H}}{\partial \mathcal{E}} \dot{\mathcal{E}} . \tag{20}$$

With this and the equation for the free energy, Equation 16 can be transformed into

$$\begin{aligned} R = &-\rho \left(\frac{\partial \varphi_\mathrm{H}}{\partial T} + s \right) \dot{T} - \rho \left(\frac{\partial \varphi_\mathrm{H}}{\partial \mathcal{E}} + \mathbf{P} \right) \dot{\mathcal{E}} \\ &+ \left(\tau + \rho \rho_\alpha \frac{\partial \varphi_\mathrm{H}}{\partial \rho_\alpha} I \right) : \kappa n \\ &+ \nabla \left(\left(\rho \frac{\partial \varphi_\mathrm{H}}{\partial \rho_\alpha} M_\alpha - \mu_\alpha \right) \mathbf{N}_\alpha \right) n \\ &+ \mathcal{J} \mathcal{E} - \frac{\left(\mathbf{q} - \sum \mu_\alpha \mathbf{N}_\alpha \right)}{T} \nabla T n \\ &- \sum_\alpha \mathbf{N}_\alpha \nabla \mu_\alpha . \end{aligned} \tag{21}$$

The requirement, that the entropy production R of Equation 21 has to be strictly positive leads to the relations

$$s = -\frac{\partial \varphi_\mathrm{H}}{\partial T} \tag{22}$$

$$\mathbf{P} = -\rho \frac{\partial \varphi_\mathrm{H}}{\partial \mathcal{E}} \tag{23}$$

$$p = \rho \sum_\alpha \rho_\alpha \frac{\partial \varphi_\mathrm{H}}{\partial \rho_\alpha} \tag{24}$$

$$\sigma = -\left[p + \frac{1}{2} \varepsilon_0 E^2 \right] I + \varepsilon_0 \mathbf{E} \otimes \mathbf{E} + \mathcal{E} \otimes \mathbf{P} \tag{25}$$

$$\mu_\alpha = \rho \frac{\partial \varphi_\mathrm{H}}{\partial \rho_\alpha} M_\alpha \tag{26}$$

$$0 \leq \mathcal{J} \cdot \mathcal{E} - \frac{\mathbf{q}_\mathrm{D}}{T} \cdot \nabla T - \sum_\alpha \mathbf{N}_\alpha \cdot \nabla \mu_\alpha . \tag{27}$$

Here p is the pressure and σ is obtained from Equation 17 and the necessary condition $\tau + pI = 0$ imposed by the positivity of the entropy production R. We also introduced the purely diffusive heat flux $\mathbf{q}_D = \mathbf{q} - \sum_\alpha \mu_\alpha \mathbf{N}_\alpha$. If the velocity is allowed to change in time it can also be shown that the momentum density $\mathbf{g}$ is given by

$$\mathbf{g} = \mathbf{v} + \varepsilon_0 \mathbf{E} \times \mathbf{B} . \tag{28}$$

The momentum equation (Equation 4) can be written (by using Equation 4, Equation 25 and Equations 10–14) as

$$\rho \dot{\mathbf{g}} = -\nabla p + \rho_F \mathcal{E} + (\mathbf{P} \cdot \nabla)\mathcal{E} + \rho \mathbf{b} . \tag{29}$$

In most of the battery literature the momentum equation (Equation 29) is not used, although it implies, that large gradients in the pressure are to be expected for strong electric fields. This, for example, is the case in the double layer. Since the chemical potentials of the ionic species and the solvent are, in general, dependent on the pressure, they will in turn exhibit large gradients leading to a non-negligible contribution to the variation of the ion concentration [27]. For incompressible systems, i.e., $\rho = const$, the chemical potential depends linearly on the pressure and can be written as function of the pressure and mass or particle fractions $y_\alpha = n_\alpha/n$ [27] with $n = \sum_\alpha n_\alpha$ being the total molar density:

$$\mu_\alpha = M \frac{p}{\rho} + f(T, y_\alpha, \mathcal{E}) . \tag{30}$$

The energy equation (Equation 8) leads to

$$T\rho \dot{s} = \mathcal{J} \cdot \mathcal{E} + \rho \dot{Q} - \nabla \cdot \mathbf{q}_D - \sum_\alpha \mathbf{N}_\alpha \cdot \nabla \mu_\alpha . \tag{31}$$

Due to the constraint in Equation 3 there are only two independent fluxes and since the total density ρ can be safely considered to be constant, there are only two independent densities. The form of the constitutive equations depends on the choice of independent variables. This freedom seems to lead to different theories [27,55,57]. Our systematic derivation offers the possibility to formulate the transformation rules between the different set of independent fields, in order to analyze the similarities and differences of the theories.

If we choose as independent densities the molar densities c_+ and c_-, the corresponding fluxes are $\mathbf{N}_+$ and $\mathbf{N}_-$. The electric current $\mathbf{j}$ is written as $\mathbf{j} = z_+\mathbf{N}_+ + z_-\mathbf{N}_-$ and the electric field as $\mathbf{E} = -\nabla\Phi$. In addition, if we assume that there are no bulk heat sources $\dot{Q}_H = 0$ (i.e., no side reactions in the bulk), the resulting transport equations for $\mathbf{v} = 0$ and the entropy production are

$$\dot{c}_+ = -\nabla \cdot \mathbf{N}_+ \tag{32}$$

$$\dot{c}_- = -\nabla \cdot \mathbf{N}_- \tag{33}$$

$$T\rho \dot{s} = -\nabla \cdot \mathbf{q}_D - \sum_{\alpha=\pm} \mathbf{N}_\alpha \cdot \nabla \tilde{\mu}_\alpha^{el} \tag{34}$$

$$R = -\sum_{\alpha=\pm} \mathbf{N}_\alpha \cdot \nabla \tilde{\mu}_\alpha^{el} - \frac{\mathbf{q}_D}{T} \cdot \nabla T , \tag{35}$$

where $\tilde{\mu}_\pm = \mu_\pm - (M_\pm/M_0)\mu_0$ is the effective chemical potential for the ions and anions and $\tilde{\mu}_\pm^{el} = \tilde{\mu}_\pm + z_\pm F\Phi$ is the electrochemical potential. To guarantee the positivity of the entropy production, R, the fluxes and heat current are written in a form that gives R a strictly positive quadratic form. This can be achieved by choosing

$$\mathbf{N}_\pm = -\sum_{\beta=\pm} B_{\pm,\beta} \nabla \tilde{\mu}_\beta^{el} - \nu_\pm \nabla T \tag{36}$$

$$\frac{\mathbf{q}_D}{T} = -\sum_{\beta=\pm} \nu_\beta \nabla \tilde{\mu}_\beta^{el} - \frac{\gamma}{T} \nabla T . \tag{37}$$

This is the form of constitutive equations used in [27,58] for isothermal systems (i.e., $\nabla T = 0$). Specifically we obtain the well-known result that the fluxes are proportional to a combination of the electrochemical potentials and in addition to a term proportional to the gradient of the temperature. Choosing the mobility matrix to be a symmetric positive matrix guarantees the positivity of the entropy production for every solution of the transport equations. Specifically we get $B_{++} > 0$, $B_{--} > 0$ and $B_{++}B_{--} > B_{+-}^2$. In dilute solution theory, the mobility B_{+-} is set to zero, i.e., $B_{+-}^{dilute} = 0$. If temperature variations are included we obtain further conditions on the heat conductivity, λ (λ >0), and the off-diagonal terms $\nu_\pm$. Very often the constitutive equations are formulated in terms of chemical potentials $\tilde{\mu}_\alpha$, electrical or Galvani potentials Φ. This form can be easily obtained from Equation 36 and Equation 37:

$$\mathbf{N}_\pm = -\sum_{\beta=\pm} B_{\pm,\beta} \nabla \tilde{\mu}_\beta - \frac{t_\pm \kappa}{z_\pm F} \nabla\Phi - \nu_\pm \nabla T \tag{38}$$

$$\mathbf{j} = -\kappa \nabla\Phi - \frac{t_+ \kappa}{z_+ F} \nabla \tilde{\mu}_+ - \frac{t_- \kappa}{z_- F} \nabla \tilde{\mu}_- - \beta\kappa \nabla T \tag{39}$$

$$\frac{\mathbf{q}_D}{T} = -\sum_{\beta=\pm} \nu_\beta \nabla \tilde{\mu}_\beta - \beta\kappa \nabla\Phi - \frac{\gamma}{T} \nabla T . \tag{40}$$

The conductivity κ and the transference numbers are given by the components of the mobility matrix

$$\kappa = F^2\left(z_+^2 B_{++} + z_-^2 B_{--} + 2z_+ z_- B_{+-}\right) \tag{41}$$

$$t_\pm = \frac{F^2}{\kappa}\left(z_\pm^2 B_{\pm\pm} + z_+ z_- B_{+-}\right). \tag{42}$$

Note that $t_+ + t_- = 1$. The Seebeck coefficient β is defined by

$$\beta = \frac{F\left(z_+\nu_+ + z_-\nu_-\right)}{\kappa}. \tag{43}$$

It is related to the Peltier coefficient Π through $\Pi = T\cdot\beta$.

Since the ionic fluxes $\mathbf{N}_\pm$ and the (free) current $\mathbf{j}$ are not independent of each other, Equation 38 can also be brought into a more condensed form, obtained in [41,55] by using the definitions in Equation 41 and Equation 42 for $t_\pm$ and κ and introducing the chemo-electrical potential of the positive ions $\varphi = \tilde{\mu}_+^{el}/\left(z_+F\right)$.

$$\mathbf{N}_+ = -\frac{F^2 z_-^2}{\kappa}(\det B)\nabla\mu + \frac{t_+}{Fz_+}\mathbf{j} - \left(\nu_+ - \frac{t_+\kappa\beta}{Fz_+}\right)\nabla T \tag{44}$$

$$\mathbf{j} = -\kappa\nabla\varphi - \frac{\kappa\left(t_+ - 1\right)}{Fz_+}\nabla\mu - \kappa\beta\nabla T \tag{45}$$

$$\frac{\mathbf{q}_\mathrm{D}}{T} = -\left(\nu_+ - \frac{\beta\kappa}{F}\right)\nabla\mu - \kappa\beta\nabla\varphi - \frac{\gamma}{T}\nabla T \tag{46}$$

$$\mu = \tilde{\mu}_+ - \frac{z_+}{z_-}\tilde{\mu}_- \tag{47}$$

$$\varphi = \tilde{\Phi} + \mu/\left(Fz_+\right) = \Phi + \mu_+/\left(Fz_+\right). \tag{48}$$

To use φ is the choice in most of the electrochemical literature, naming it usually "electrical potential". This might be considered as an unfortunate semantic inaccuracy but it has in fact consequences for the relation to free electric charges. The latter are determined by Φ through Equation 10 and not by φ.

It is possible to obtain the formulation in Equation 44 and Equation 45 directly from the entropy law by choosing the flux $\mathbf{N}_+$ and the electric current $\mathbf{j}$ together with the molar density $c_+ = \rho_+/M_+ =: c$ and the free charge density $\rho_\mathrm{F} = F(z_+c_+ + z_-c_-)$ as primary variables.

In this formulation it can be easily seen as well that the diffusion coefficient D at vanishing current $\mathbf{j}$ is proportional to the determinant $\det B = B_{++}B_{--} - B_{+-}^2$ of the mobility matrix B. The requirement of positive entropy production mentioned above is therefore the equivalent of having a positive collective diffusion coefficient.

The transport of the anions is ruled by the same diffusion coefficient as the diffusion of cations, which can be easily seen from Equation 44 and Equation 45 and $\mathbf{N}_- = (\mathbf{j} - z_+\mathbf{N}_+)/z_+$. This shows that the relevant diffusion coefficient for the transport of ions in the electrolyte is not the self-diffusion coefficient, which would be different from the diffusion coefficient of the anions, but the unique collective inter-diffusion coefficient. It cannot be determined directly by using, for example, nuclear magnetic resonance (NMR) measurements. However, there are simple approximations to determine the inter-diffusion coefficients from the measured self-diffusion coefficients [10,59].

For the experimental determination of the diffusion coefficient is is important to distinguish between the diffusion coefficient at vanishing electrical current and at vanishing gradient of the electrical potential. Only the coefficient at vanishing electrical current, i.e., the one obtained from Equation 44 is experimentally accessible. In DFT calculations the diffusion coefficient is written as a product of a thermodynamic factor a_T and a kinetic coefficient [9,10]. The thermodynamic factor a_T is the thermodynamic derivative of the chemical potential with respect to concentration $a_T = \partial\mu/\partial c$ and from the relation for the flux (Equation 44), we see that the kinetic coefficient is related to the determinant of the mobility matrix B.

By using the obtained expressions for the fluxes and the electric current we finally obtain the equation for the electric charge ρ_F, the molar concentration of positive ions $c := c_+$ and the entropy density:

$$\dot{c} = \nabla\cdot\left(B_{++}\nabla\mu\right) + \nabla\cdot\left(\frac{\kappa t_+}{Fz_+}\nabla\tilde{\Phi}\right) + \nabla\cdot\left(\nu_+\nabla T\right) \tag{49}$$

$$\dot{\rho}_\mathrm{F} = \nabla\cdot\left(\kappa\nabla\tilde{\Phi}\right) + \nabla\cdot\left(\frac{\kappa t_+}{Fz_+}\nabla\mu\right) + \nabla\cdot\left(\kappa\beta\nabla T\right) \tag{50}$$

$$T\rho\dot{s} = -\nabla\cdot\mathbf{q}_\mathrm{D} - \mathbf{N}_+\nabla\mu - \mathbf{j}\nabla\tilde{\Phi}. \tag{51}$$

The electric charge density ρ_F is coupled to Coulomb's law (Equation 10) and to the pressure equation (Equation 29). The entropy production is given by

$$R = -\mathbf{N}_+ \nabla \mu - \mathbf{j} \nabla \tilde{\Phi} - \frac{\mathbf{q}_D}{T} \nabla T \,. \tag{52}$$

The different potentials Φ, $\tilde{\Phi}$ and φ have different physical meanings. Only the potential Φ is relevant for the calculation of electrical charges, e.g., in the double layer with the help of Coulomb's law (Equation 10). The chemical potentials μ, $\tilde{\mu}_\pm$ and μ_α are defined through Equation 26, once the materials law for the free energy density φ_H is defined.

Charge neutral systems

Most of the battery literature deals with locally charge-neutral systems, i.e., $\rho_F = 0$. This assumption is based on the observation that in a battery, under normal operating conditions, the potential differences required for charge separation exist only in a very thin layer around the active particles in the form of a double layer. To include the double layer, it is either necessary to solve the equations derived above without further assumptions on charge neutrality [27], or specific models for the double layer [60] or the form of the charge distributions around the active particles [61] are necessary. On a scale above a few nanometer one can safely assume, that the electrolyte is a charge neutral system, i.e., $\rho_F = 0$ and $c_- = (z_+/z_-)c_+$. This also applies to the active particles. The shielding is even more effective due to the high mobility of the electrons in the active particles. If we only deal with a binary salt, we have $z_+ = z_- = 1$, i.e., $c = c_+ = c_-$ at each point of the bulk of the electrolyte and the active particles. As a consequence it follows from Equation 26, that $\mu_+ = \mu_-$. The chemical potentials become a function of the temperature, the electric potential and the Li ion concentration, only. The pressure dependence can safely be neglected since it is only relevant in the double layer [27]. Also the possible dependence of the chemical potential on the electrical potential is usually not considered, since it is assumed that only short-ranged chemical forces are contributing to the chemical potential. No assumptions of this kind are necessary within the framework of rational thermodynamics. In the end, the form of the chosen materials law for the free energy φ_H (Equation 19) determines whether the chemical potential is dependent on the electrical potential or not. For example the chemical potential would depend on the electric field if the contribution of the polarizability of the electrolyte or the active particle to the free energy density depends not only on the electric field but also on ion concentrations. This would be the case in ion-conducting solid electrolytes. Neglecting these effects we may write

$$\nabla \mu = \left(\frac{\partial \mu}{\partial c}\right) \nabla c + \left(\frac{\partial \mu}{\partial T}\right) \nabla T \tag{53}$$

and introduce a new effective heat flux $\mathbf{Q}$

$$\mathbf{Q} = \mathbf{q} + \mathbf{N}_+ T \left(\frac{\partial \mu}{\partial T}\right) \tag{54}$$

to obtain the constitutive relations Equation 44 in the form

$$\mathbf{N}_+ = -D \nabla c + \frac{t_+}{z_+ F} \mathbf{j} - \frac{D c k_T}{T} \nabla T \tag{55}$$

$$\mathbf{j} = \kappa \mathbf{E} - \kappa \frac{t_+}{z_+ F} \left(\frac{\partial \mu}{\partial c}\right) \nabla c - \beta \kappa \nabla T \tag{56}$$

$$\mathbf{Q} = -\lambda \nabla T + \beta T \mathbf{j} + k_T c \left(\frac{\partial \mu}{\partial c}\right) \left(\mathbf{N}_+ - \frac{t_+}{z_+ F} \mathbf{j}\right). \tag{57}$$

The diffusion coefficient D, the heat conductivity λ and the Soret coefficient k_T are given by

$$D = \left(\frac{\partial \mu}{\partial c}\right) \frac{F^2 z_-^2}{\kappa} \det B \tag{58}$$

$$\lambda = \gamma + \left(\frac{\partial \mu}{\partial T}\right) \nu_+ - \left(\frac{\partial \mu}{\partial c}\right) \frac{D}{T} k_T^2 c^2 - \kappa T \beta^2 \tag{59}$$

$$\frac{D c k_T}{T} = \nu_+ \left(\frac{\partial \mu}{\partial T}\right) B_{++} - \frac{\kappa \beta t_+}{F z_+} \tag{60}$$

Using Equations 55–57, the expression for the entropy production (Equation 52) simplifies to

$$R = \lambda \frac{(\nabla T)^2}{T} + \frac{\mathbf{j}^2}{\kappa} + \left(\frac{\partial \mu}{\partial c}\right) \frac{\left(\mathbf{N}_+ - \frac{t_+}{F z_+} \mathbf{j}\right)^2}{D}. \tag{61}$$

From the requirement of a strictly positive entropy production we can easily conclude that each term in Equation 61 has to be positive and obtain the well-known fact that the transport coefficients heat conductivity λ, electric conductivity κ and interdiffusion coefficient D have to be positive. The equations of motion reduce to

$$\dot{c} = \nabla\cdot(D\nabla c) - \nabla\cdot\left(\frac{t_+}{Fz_+}\mathbf{j}\right) + \nabla\cdot\left(\frac{Dck_T}{T}\nabla T\right) \tag{62}$$

$$0 = \nabla\cdot\left(\kappa\nabla\tilde{\Phi}\right) + \nabla\cdot\left(\frac{\kappa t_+}{Fz_+}\left(\frac{\partial\mu}{\partial c}\right)\nabla c\right) + \nabla\cdot\left(\kappa\beta\nabla T\right) \tag{63}$$

$$T\rho\dot{s} = -\nabla\cdot\mathbf{q}_\mathrm{D} - \mathbf{N}_+\nabla\mu - \mathbf{j}\nabla\tilde{\Phi}\,. \tag{64}$$

The equation for the temperature follows from the entropy equation (Equation 64) by using

$$T\rho\dot{s} = \rho c_p\dot{T} + T\left.\frac{\partial s}{\partial c}\right|_T \partial_t c\,, \tag{65}$$

where c_p is specific heat per unit mass. With the thermodynamic relation

$$\left.\frac{\partial s}{\partial c}\right|_T = -\left.\frac{\partial\mu}{\partial T}\right|_c$$

and the continuity equation (Equation 62) it was shown in [41] that the equation for the temperature is given by

$$\begin{aligned} c_p\rho\partial_t T = {} & \nabla\cdot(\lambda\nabla T) + \frac{\mathbf{j}^2}{\kappa} + \left(\frac{\partial\mu}{\partial c}\right)\frac{\left(\mathbf{N}_+ - \frac{t_+}{Fz_+}\mathbf{j}\right)^2}{D} \\ & -\mu_T\cdot\mathbf{j}\nabla T + T\nabla\cdot\left(\left(\frac{\partial\mu}{\partial c}\right)\frac{k_T c}{T}D\nabla c\right). \end{aligned} \tag{66}$$

The Thomson coefficient μ_T is defined by the so called Thomson relation $\mu_\mathrm{T} = T\left(\partial\beta/\partial T\right)$. Terms of order $o\left(k_T^2\nabla\cdot\nabla T\right)$ are neglected. Temperature inhomogeneities are caused by four different types of heat sources and equilibrated by thermal conduction. The four heat sources are Joule's heat, heat of mixing, Thomson effect and the Soret effect (in the order of their appearance in Equation 66). Since usually k_T is very small we can safely neglect its contribution in most applications and obtain the approximated equation

$$c_p\rho\partial_t T = \nabla\cdot(\lambda\nabla T) + \frac{\mathbf{j}^2}{\kappa} + \left(\frac{\partial\mu}{\partial c}\right)D(\nabla c)^2 - \mu_T\mathbf{j}\cdot\nabla T\,. \tag{67}$$

Interface conditions

The equations derived above are valid in the electrolyte as well as in the active particles. The value and the physical mechanisms underlying the transport coefficients are different. Diffusion mechanisms in solids are different from those in electrolytes. Conduction in electrolytes is due to ion transport, but mostly of electronic nature in the active particles. These differences require different atomistic simulation techniques for the determination of the transport coefficients, but the form of the macroscopic equations is not affected by these differences. To couple the transport in the electrolyte and the active particles the formulations of interface conditions sometimes also called jump conditions are necessary. They are usually derived from the transport equations and models for processes on the interface, such as surface diffusion or electrochemical reactions on the interface, by using a pill box argument [39]. In this argument the transport equations are integrated over a small volume element, which includes the two sides of the interface. The thickness of the volume element is reduced to zero after the integration such that all volumetric contributions vanish compared to the surface contributions from the fluxes across the surfaces and the processes on the surface. To use the transport equations for the derivation of the interface conditions also guarantees that they are based on the same physical fields that are also used in the transport theory. In our case we need interface conditions that describe the intercalation and de-intercalation of ions, as well as the heat produced during this process.

Interface conditions for ionic flux and electric current

For cell-scale simulations, it is very difficult, if possible at all, to spatially resolve the processes involved in intercalation and de-intercalation numerically. Therefore it is common to use phenomenological global expressions for describing intercalation, although in reality this is a complex process that involves at least three steps: desolvation and adsorption on the external surface of the active particle, transfer of the Li ion from the external surface into the host material and shielding of the charges by lattice deformations and reorganization of the electronic charge density distribution. These elementary steps were identified experimentally [62,63] for the intercalation of Li in graphite. In this still very simple model no distinction is made between the various possible types of chemical bonds after intercalation. For instance, in [63] three different bonding states have been identified for the Li ions within various types of graphite. These different types of Li–graphite bonds are reflected by different chemical potentials and possibly different transition states for the respective intercalation step. For the actual intercalation step from the surface into the host material, it is possible to derive a Butler–Volmer-type expression from very general considerations by using only the mass action law and assuming the existence of a transition state [56,64-66]. A more realistic description of the intercalation will require the incorporation of at least the desolvation–adsorption step mentioned above. The extensions of the simple Butler–Volmer

theory obtained through this can be easily incorporated in a generalized interface condition. In [64] the current density across the interface i_{se} was derived from thermodynamic arguments, and a Butler–Volmer equation with modified expressions for the exchange current amplitude was obtained:

$$i_{se} = i_0\left(\exp\left[\frac{\alpha_a F}{RT}\eta_s\right] - \exp\left[\frac{-\alpha_c F}{RT}\eta_s\right]\right). \tag{68}$$

α_a and α_c with $\alpha_a + \alpha_c = 1$ are transfer coefficients, respectively. They quantify the fraction of the overpotential to the anodic and the cathodic charge transfer, respectively. It was shown in [64] that the sum of the transfer coefficients has to be 1 as a consequence of the law of mass action and requirement of positive entropy production during the transition from electrolyte to active particles. The overpotential is the difference between the electrochemical potentials of active particle and electrolyte, which vanishes in equilibrium:

$$\eta_s := \Phi_s - \Phi_e - \frac{\mu_e - \mu_s}{z_+ F}. \tag{69}$$

The same interpretation of the overpotential is also obtained in [56]. We can reformulate the overpotential (Equation 69) into the more conventional form

$$\eta_s := \Phi_s - \varphi_e - U_0\,, \tag{70}$$

where U_0 is the half-cell open circuit potential of the respective electrode relative to a Li metal electrode

$$U_0 = \frac{\mu_{\mathrm{Li}} - \mu_s}{z_+ F}. \tag{71}$$

Also the electrochemical potential of the electrolyte φ_e is defined relative to the chemical potential of Li metal:

$$\varphi_e := \Phi_e + \frac{\mu_e - \mu_{\mathrm{Li}}}{z_+ F}. \tag{72}$$

It is important to note, that as a consequence of introducing the open circuit voltage U_0, there appears the difference of the electrical potential of the active particle and the electrochemical potential of the electrolyte in the definition of the overpotential. Both are measurable quantities, whereas the electrical potential of the electrolyte is not directly measurable. The amplitude i_0 in Equation 68 deviates from the usual definition [67] due to thermodynamic reasons [64]

$$i_0 = k c^{\alpha_a} c_s^{\alpha_a}\,. \tag{73}$$

k is a reaction rate, which depends on the activation energy of the transition state for the ionic transfer from the electrolyte to the active particle. The full set of interface conditions for ionic flux and electric current follows from the assumption of continuity of ionic flux and electric current and the fact that only ions are transferred and, therefore, the whole electrical current across the interface is carried by the lithium ions. Side reactions leading to a degradation of the electrolyte [68] would lead to an additional electrical current due to electron transfer between active particles and electrolyte. With the normal $\mathbf{n}$ pointing from the solid into the electrolyte we obtain

$$\mathbf{j}_s \cdot \mathbf{n} = i_{se} \tag{74}$$

$$\mathbf{j}_e \cdot \mathbf{n} = i_{se} \tag{75}$$

$$\mathbf{N}_{+,s} \cdot \mathbf{n} = \frac{i_{se}}{z_+ F} \tag{76}$$

$$\mathbf{N}_{+,e} \cdot \mathbf{n} = \frac{i_{se}}{z_+ F}. \tag{77}$$

Thermal interface conditions

Under isothermal conditions, the values of the concentrations and potentials of the electrolyte and the solid particle at the interface can be determined from the interface conditions (Equations 74–76). If heat flux is considered the value of the temperature on the interface also has to be determined in order to be able to calculate the gradient of the temperature on the electrolyte side and solid side of the interface. The additional interface conditions can be derived by applying the pill box argument to the equations for the heat transport. We integrate the entropy balance equation (Equation 64) over an infinitesimal small volume element, which contains the whole thickness of double layer and use the jump discontinuity of the chemical potential and the electrical potential at the interface to obtain with Equation 74 and Equation 76

$$\begin{aligned}\iiint dV \rho\dot{s} = \iint dA \Bigg[& \mathbf{n}\cdot\left(\mathbf{Q}_s - \mathbf{Q}_e\right) \\ & + \frac{i_{se}}{z_+ F}\left(\mu_s - \mu_e + z_+ F(\Phi_s - \Phi_e)\right)\Bigg] \\ & - \frac{i_{se}}{z_+ F} T\left(\frac{\partial \mu_s}{\partial T} - \frac{\partial \mu_e}{\partial T}\right).\end{aligned} \tag{78}$$

In the limit of vanishing thickness of the pill box, the left hand side of Equation 78 vanishes. If the weak temperature dependence of the chemical potential of Li metal is neglected, we finally obtain from Equation 57, Equation 71, and Equation 72 the expression in Equation 79.

$$
\begin{aligned}
-\lambda_s \mathbf{n}\cdot\nabla T_s + \lambda_e \mathbf{n}\cdot\nabla T_e = & -i_{se}\eta_s \\
& -Ti_{se}\left\{\left(\beta_s-\beta_e\right)+\frac{\partial\left(U_0+\dfrac{\mu_e}{z_+F}\right)}{\partial T}\right\} \\
& +i_{se}\left(c_s\frac{\partial U_0}{\partial c}k_{T,s}+c_e\frac{\partial \mu_e}{\partial c}\frac{k_{T,e}\left(1-t_+\right)}{z_+F}\right)
\end{aligned}
\tag{79}
$$

The transference number of Li ions in the active particle was set to zero, since the whole electrical current in the active particles is assumed to be given by the flux of electrons. Formulated differently, the mobility of electrons is much larger than the mobility of ions. With this condition for the jump in the gradients of the temperature, in addition to Equations 74–76, the values of all concentrations and potentials, and the temperature on the surface can be determined. On the right hand side of Equation 79 are the interfacial irreversible and reversible heat sources. The first is the irreversible interfacial Joule heating, followed by the reversible Peltier effect and the reversible Soret effect. The Peltier coefficient is defined by

$$
\Pi = T\left(\beta_s-\beta_e\right)+T\frac{\partial\left(U_0+\dfrac{\mu_e}{z_+F}\right)}{\partial T}. \tag{80}
$$

In addition to the partial derivative of the open-circuit potential [69] also the differences in the Seebeck coefficients of the two phases and the thermal derivative of the chemical potential of the electrolyte are contributing to the Peltier coefficient. It can either be measured directly [70] or may be deduced from measurements of the open-circuit potential, the Seebeck coefficients of the two phases [71] and the thermodynamic derivatives of the chemical potential of the electrolyte.

Porous electrode theory: Volume averaging

The microscopic equations derived above allow one to study the spatial scale from about 10 nm up to a few hundred micrometer and are therefore suitable to analyze transport processes in the microstructure of a battery cell. The active particles and the electrolyte are treated as geometrically separate domains within this approach. Since the diameters of active particles range from a few micrometers down to tens of a nanometer, computationally resolving a cell of a few hundred micrometers thickness and lateral dimensions in the range of tens of a centimeter becomes very difficult, if possible at all. Therefore the preferred approach for simulating whole cells is the porous electrode theory, pioneered by Newman and coworkers [72-75]. A porous electrode theory for materials with phase transitions was formulated in [76]. To derive the porous electrode theory that corresponds to a given microscopic theory several methods of increasing complexity can be applied [77-79]. The most simple and straightforward approach is volume averaging. In this approach, the microscopic transport equations are integrated over a complex porous microstructure and the Gauss Theorem is used to derive the equations for the separate domains and the contribution of the interfaces to the transport [80]. This method does not constitute an analytical proof that the averaged solution of the microscopic equations does converge in a strict mathematical sense towards the solution of the averaged set of equations. Here, further analytical work or numerical convergence studies will be necessary.

If a quantity A is averaged over one phase, say the electrolyte phase V_e, in a representative volume element (RVE) of volume $V = V_s + V_e$, we obtain

$$
\langle A\rangle_{V_e} = \frac{1}{V_e}\int_{V_e} A dV . \tag{81}
$$

Central is the following theorem for the average of divergence terms, say $\langle\nabla\cdot\mathbf{A}\rangle$:

$$
\langle\nabla\cdot\mathbf{A}\rangle_{V_s} = \nabla\cdot\langle\mathbf{A}\rangle_{V_s} + \int_{\partial V_s}\mathbf{A}\cdot\hat{n}dA , \tag{82}
$$

where dA is an infinitesimal area element and $\hat{n}$ is the outward surface normal.

The volume-averaging method for isothermal systems is discussed in detail in [61,77,78]. For non-isothermal systems volume averaging was used to homogenize heuristic microscopic equations [45]. The terms proportional to ∇T in the ionic flux and electric current will give rise to a contribution of the volume-averaged temperature gradient and of the jump of the temperature gradients at the interfaces between electrolyte and active particles. As will be shown below the contribution of

these terms to the ionic fluxes and currents can be neglected compared to the volume-averaged gradients of the electrochemical potential and the jump of the electrochemical potentials at the interface. We therefore concentrate on the derivation of the volume-averaged temperature equation, consistent with the microscopic equation, derived above:

$$c_p\rho\frac{\partial T}{\partial t} = \underbrace{\nabla\cdot(\lambda\nabla T)}_{\text{(I)}} + \underbrace{\frac{\mathbf{j}^2}{\kappa}}_{\text{(II)}} \underbrace{-T\nabla\cdot(\beta\mathbf{j})}_{\text{(III)}} + \underbrace{\frac{\partial\mu}{\partial c}\frac{\left(\mathbf{N}_+ - \frac{t_+\mathbf{j}}{F}\right)^2}{D}}_{\text{(IV)}} + \underbrace{T\nabla\cdot\left(c\frac{\partial\mu}{\partial c}\frac{k_T}{T}\left(\mathbf{N}_+ - \frac{t_+\mathbf{j}}{F}\right)\right)}_{\text{(V)}}, \tag{83}$$

where the terms correspond to heat conduction (I), Joule heating (II), the Thomson effect (III), heat of mixing (IV) and Soret–Dufour effect (V). The technical details can be found in the Appendix. The final result for the volume averaged heat equation is

$$\begin{aligned} c_p\rho\frac{\partial T}{\partial t} &= \nabla\cdot\langle\lambda\nabla T\rangle_V + \varepsilon_s\frac{\langle\mathbf{j}_s^2\rangle_{V_s}}{\kappa_s} + \varepsilon_e\frac{\langle\mathbf{j}_e^2\rangle_{V_e}}{\kappa_e} \\ &\quad -T\varepsilon_s\nabla\cdot\langle\beta_s\mathbf{j}_s\rangle_{V_s} - T\varepsilon_e\nabla\cdot\langle\beta_e\mathbf{j}_e\rangle_{V_e} \\ &\quad +\varepsilon_e\left\langle\frac{\partial\mu_e}{\partial c_e}\frac{(\mathbf{N}_{+e} - t_+\mathbf{j}_e/F)^2}{D_e}\right\rangle_{V_e} \\ &\quad -T\varepsilon_e\nabla\cdot\left\langle c_e\frac{\partial\mu_e}{\partial c_e}\frac{k_{T,e}}{T}\left(\mathbf{N}_{+e} - \frac{t_+\mathbf{j}_e}{F}\right)\right\rangle_{V_e} \\ &\quad +ai_{se}\left(\eta + T\frac{\partial\left(U_0 + \mu_e/F\right)}{\partial T}\right). \end{aligned} \tag{84}$$

Interestingly, all surface terms due to the coupling of heat and ion transport (terms proportional to k_T) from the Soret–Dufour effect and due to heat–current coupling from the Thomson effect cancel exactly with the corresponding terms from the contribution of the heat conduction. What remains is the surface Joule heating and the Peltier effect (last line of Equation 84).

Comparison of microscopic and mesoscopic heat transport

There are many papers in literature, which present models and simulations of thermal effects on cell-level based on experimental investigations [44,49,81-84]. In this paper, we are not interested in fitting parameters to experimental results. Instead, we want to stress the intrinsic fundamental differences and similarities of models on two different spatial scales. Specifically, we will show that there are important phenomena on the microscopic scale which cannot be represented, in principle, through homogenized theories, but which may be very important for predictions of degradation phenomena.

In order to demonstrate these fundamental differences between microscopic and homogenized models, mostly based on porous electrode theory (we call it the mesoscopic approach), with respect to thermal aspects, we performed numerical computer simulations on a generic model system with two different micro structures and compared the results to meso-scale simulations of two corresponding setups.

Simulation details

In order to demonstrate the qualitative features of the microscopic electrochemical model, no measured electrode structure was used but rather a computer-generated random geometry with typical properties. To simplify the geometry further both electrodes have an identical structure. Two cases with different base particles were considered: one with spherical active particles of radius 5 μm and one with prolate spheroids of random orientation with half-axes of 5 μm and 16.8 μm. In both cases the porosity ε was set to 0.5 such that the capacity of each electrode is equal. The geometries are shown in Figure 1. The left and the right electrode are the anode and the cathode, respectively. They are connected to current collectors through which electrons enter. Note that although electrodes are equal, their interface area with electrolyte differs slightly since they are attached to the collector plates on opposite sides. The simulation was set up such that the virtual cell is almost empty and a constant current was applied to charge the cell. Details on the parametrization are summarized in Table 1. Note that no temperature-dependence of the parameters was considered here. In particular, there is no contribution of $\partial U_0/\partial T$ in the Peltier term (see Equation 80 and the last term of Equation 84), which might underestimate the contribution of this term.

To solve the PDE system of the thermal micro-model Equation 62, Equation 63 and Equation 66 for the unknown quantities concentration c, potential Φ and temperature T the finite-volume method [85] was employed. To this end the simulation domain of Figure 1 is discretized into a regular grid of cubic control volumes (CVs). In this discretization the unknown quantities are only defined in the center points of the CVs. Separate integration of the transport equations over the volume of each CV i and application of the Gauss theorem turn the PDE system into a large algebraic system that can be solved numeri-

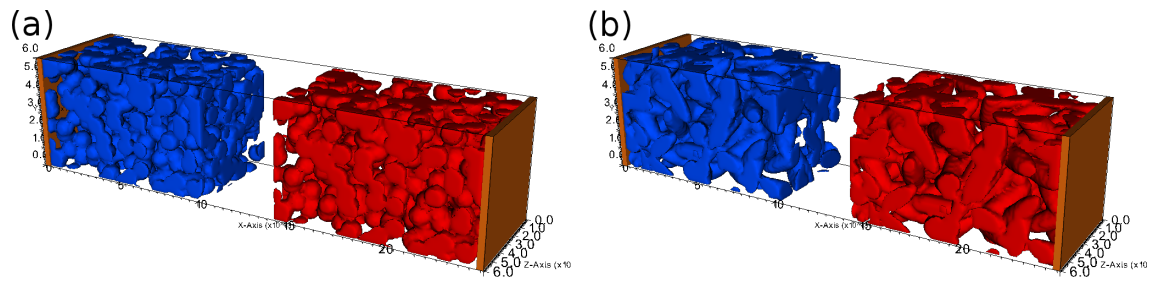

Figure 1: Geometry used for the microscopic simulation. It consists of an anode (blue), a cathode (red) and current collectors (brown). The space between particles and electrodes is filled with electrolyte. Geometry (a) consists of spherical particles of radius 5 µm, geometry (b) of a prolate spheroids of half-axes with 5 µm and 16.8 µm. The thickness of each electrode is 100 µm, the separator region 40 µm and the cross section area 60 × 60 µm^2.

Table 1: Summary of generic parameter set used for the microscopic simulations. Subscripts *s*, *e*, *cc*, *A*, and *C* denote solid, electrolyte, current collector, anode, and cathode, respectively. For the thermal equation this study chooses identical parameters for all materials species. Quantities marked with an asterisk differ in the meso-simulations. [a,b]

quantity / unit	value	quantity / unit	value
$D_{s,A}$ / cm^{2}s^{-1}	10^{-10}	$D_{s,C}$ / cm^{2}s^{-1}	10^{-10}
$\sigma_{s,A}$ / S/cm	^{*10}	$\sigma_{s,C}$ / S/cm	$^*0.38$
$\sigma_{cc,A}$ / S/cm	^{*10}	$\sigma_{cc,C}$ / S/cm	$^*0.38$
k / A cm$^{2.5}$ mol$^{-1.5}$	0.002	k / A cm$^{2.5}$ mol$^{-1.5}$	0.2
$c_{max,A}$ / mol/cm^3	$24681 \cdot 10^{-6}$	$c_{max,C}$ / mol/cm^3	$23671 \cdot 10^{-6}$
$c_{0,A}$ / mol/cm^3	$2639 \cdot 10^{-6}$	$c_{0,C}$ / mol/cm^3	$20574 \cdot 10^{-6}$
$c_{0,e}$ / mol/cm^3	$1200 \cdot 10^{-6}$	t_+ / 1	0.39989
D_e / cm^{2}s^{-1}	$^*1.622 \cdot 10^{-6}$	κ_e / S/cm	$^*0.02$
λ / W/(cm K)	0.006	c_p / J/(kg K)	4180
ρ / kg/cm^3	0.001	β / V/K	0.0002
k_T / 1	1	T_0 / K	298
i_{appl} / A/cm^2	0.00318		

[a] $U_{0,A}(soc)$/V = −0.132 + 1.41 × exp(−3.52 × *soc*)
[b] $U_{0,C}(soc)$/V=4.06279 + 0.0677504 × tanh(−21.8502 × soc + 12.8268) − 0.105734 × ((1.00167 − *soc*)$^{-0.379571}$ − 1.576) − 0.045 × exp(−71.69 × *soc*^{8}) + 0.01 × exp(−200 × (*soc* − 0.19))

cally by a computer. Time evolution is discretized by using the simple backward Euler scheme with a time step of 20 s. One time step consists of the following three steps:

1. Due to the strong coupling between concentration and potential the system Equation 62 and Equation 63 is solved monolithically.
2. Solution of the temperature system Equation 66.
3. In order to improve accuracy and maintain conservation properties step 1 is repeated with the new temperature.

Since the equations describe a nonlinear PDE-system a nonlinear solver must be used for each of the above steps. We employ a simple Newton algorithm in combination with the algebraic multigrid solver SAMG [86] to deal with the nonlinearities. This approach is implemented in the software BEST [87] (based on the CoRheoS framework [88]), which was applied to perform the simulations.

The geometry used for the mesoscopic simulations is shown in Figure 2. Except for the current collectors that have now a thickness of 40 µm the thicknesses of electrodes and separator are the same as in the case of the microscopic scale. The lateral dimensions were increased to 260 µm but the applied current was scaled proportionally. The parametrization was chosen such that meso- and micro-simulations can be compared (Table 2). To this end the effective transport properties required in the meso-case instead of bulk values are computed from the microstructure by using the software GeoDict [89].

As described in the previous section, the meso-model used here is a 3D + 1D model, i.e., three spatial dimensions for the

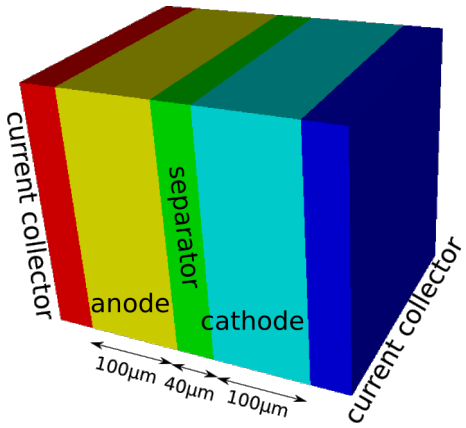

Figure 2: Geometry for mesoscopic simulations with the porous-electrode model.

Table 2: Parameters used for the mesoscopic simulations that differ from the case of microscopic simulations (cf. Table 1). Due to the different structures of spherical and ellipsoidal micro-geometries the effective transport parameters are different. Subscripts *e*, *s*, *AC* and *Sep* denote electrolyte, solid, anode/cathode and separator, respectively.

quantity / unit	value (sphere)	value (ellipsoid)
$D_{e,AC}$ / cm^2s^{-1}	$0.474 \cdot 10^{-6}$	$0.438 \cdot 10^{-6}$
$D_{e,Sep}$ / cm^2s^{-1}	$1.622 \cdot 10^{-6}$	$1.622 \cdot 10^{-6}$
$\sigma_{s,A}$ / S/cm	1.246	1.82
$\sigma_{s,C}$ / S/cm	0.047	0.069
$\kappa_{e,AC}$ / S/cm	0.00584	0.0054
$\kappa_{e,Sep}$ / S/cm	0.02	0.02
r_s / µm	4.89	5.93

unknown quantities electrolyte concentration, electrolyte potential, solid potential and temperature and, in each electrode CV, another virtual dimension for the concentration within a representative spherical particle (solid concentration) to mimic the diffusion into the active material. As in the micro-model a finite volume discretization is used for both the 3D cell geometry and the 1D domain representing a microscopic particle. Here, each 3D electrode voxel contains its extra dimension for the representative particle which is spatially discretized into 10 control volumes. The solution process of each time step with fixed step size of 15 s is as follows:

1. Solve the coupled system for the unknown quantities electrolyte concentration, electrolyte potential, solid potential in the 3D domain.
2. Solve the solid particle diffusion problems for the unknown solid concentration in the 1D domain for each electrode voxel individually.
3. Solve the temperature equation for T (in the 3D domain).
4. Repeat step 1 to improve accuracy and maintain conservation properties.

Steps 1 and 3 are solved implicitly with a simple Newton method and an algebraic multigrid solver [86] whereas step 2 uses an explicit forward Euler discretization based on the same time step and is thus fast to solve. However, due to the time-step limitations for explicit schemes the step size here can automatically decrease based on the given parameters to ensure stable convergence.

Despite the fact that on the microscale the basic particles are spherical and ellipsoidal, the porous electrode theory mimics the solid diffusion process always by a sphere of a certain radius. This radius r is related to the specific interface area a and the electrode porosity ε by $a = 3\varepsilon/r$. Here we chose the approach to determine a from the micro-geometry and compute the corresponding radius r but we note that there are also other reasonable approaches to fix r.

Results and Discussion

The simulation yields a three-dimensional field of lithium ion concentrations. Of interest is, for instance, the ion concentration in through-plane direction. A projection of the Li concentration of the electrolyte phase onto this axis is shown in Figure 3. The data from the microscopic simulations shows considerable scatter reflecting the inhomogeneous, random structure. There are even CVs that remain at their initial concentration of 1.2 mol/L since they are surrounded completely by active particles. Due to the electroneutrality condition they have to stay at their initial concentration. The porous electrode approach treats the complete electrode region as homogeneous effective medium. For this reason (and of course due to the application of symmetric boundary conditions) the concentration profile does not show any scatter and agrees reasonably well with the microscopic average. However, a quantitative agreement is only obtained in the separator region for the sphere-based micro-geometry. Especially in the electrodes far away from the separator there is a deviation of about 5%. Since the porous electrode model is in some sense a simplification of the microscopic approach its results must be scrutinized more carefully. The concentration within the electrolyte depends on the effective parameters for diffusion and ionic conductivity. In this study they were computed by performing a simplified transport simulation in the same microstructure that was used for the microscopic battery simulations. Due to the limited geometry size that was used it is likely that the effective parameters are not very exact. Furthermore, it is questionable whether the meso-approach is justified at all here since we use it on a similar scale. As pointed out in [79] the necessary condition of

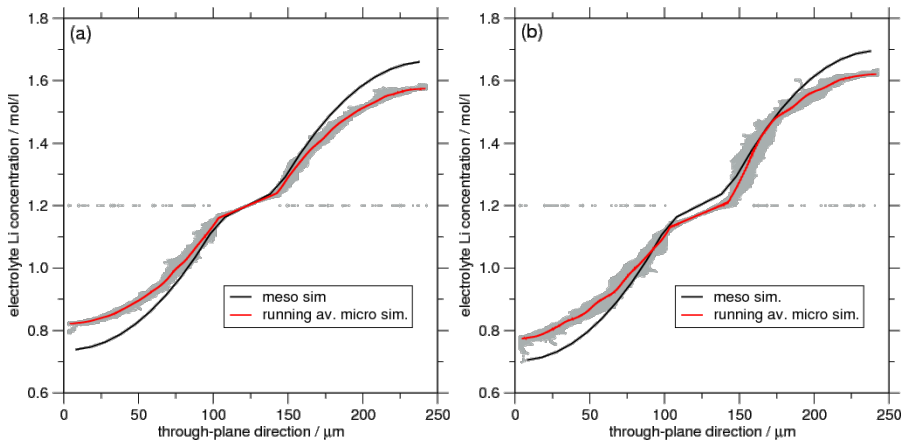

Figure 3: Distribution of electrolyte concentration in dependence of position in through-plane direction at a capacity ratio of 0.42 for (a) spherical particles and (b) prolate spheroids. Each panel compares results of the micro-simulation with a corresponding meso-scale simulation.

scale separation for using homogenization is not fulfilled in real lithium ion batteries. Very often electrodes have a thickness of the order of only ten particle diameters, which is not sufficient to justify the assumption of scale separation. Therefore it seems reasonable that for the ellipsoidal base particles the concentration in the separator region does not match well because in this case also the representative sphere of the meso-model is different from the actual micro-particle (ellipsoid). Thus, it is important to determine the effective properties as well as the representative particle size with great care. This is very relevant, for instance, for a prediction of the limiting current, at which the electrolyte is locally depleted of ions.

The concentration distribution within the active material is indirectly expressed through the cell potential (differences between current collector potential at cathode and anode). For the four simulation cases the cell-potential is shown in Figure 4a. Comparing the microscopic cell potentials it is interesting to note the higher voltage for the ellipsoidal geometry compared to the spherical geometry. This is explained by the different interface areas: While the ellipsoidal micro-geometry has an interface area of 0.18 mm^2, it is 0.22 mm^2 for the one based on spheres. Since in both cases the same current is applied a higher overpotential (and therefore cell potential) is required for smaller interface areas. Although the meso-simulation shows the same behavior the corresponding micro and meso simulations differ slightly. Since the lithium diffusion within active particles is modeled in the meso-case only by single, representative particles, the exact influence of the actual interface shape and connectivity between particles is neglected. Thus, it cannot be expected that both methods show a better agreement without more careful adjustment of parameters, in particular of the

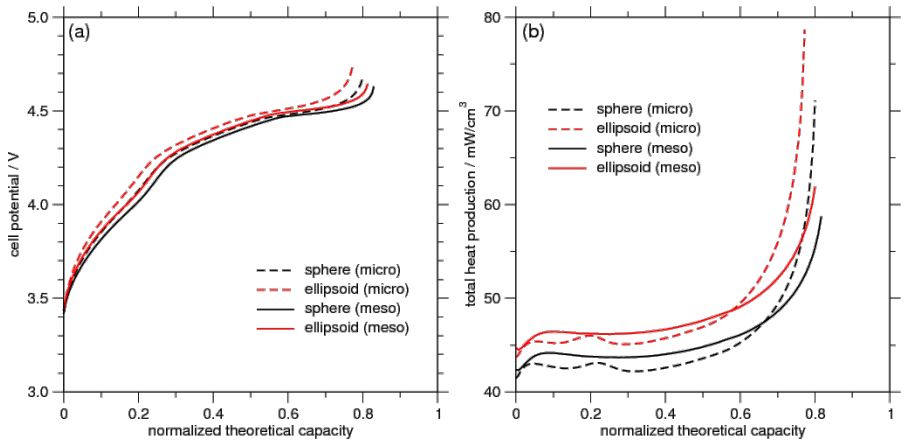

Figure 4: (a) Comparison of cell potential during charging simulations on micro- and meso-scale for the two base particles considered here, sphere and ellipsoid. (b) Comparison of heat production shown in a similar way as in (a).

radius r in the meso-model. However, even then it is not clear that this will lead to the same results also in other application scenarios, e.g., with a different applied current.

Thermal effects are of particular interest in this model comparison. Because the meso-model neglects structural details the current and the ion flow are very different compared to the microscopic model. In the latter, the current can be strongly localized due to the connective properties of the electrode structure. Thus, it is very surprising that a comparison of the total heat power per volume is very similar for both simulation approaches (see Figure 4b). Additionally, as before, we recognize a difference of heat production between spherical and ellipsoidal base particles. To understand this we need to analyze the different sources of heat.

The microscopic model allows one to study the heat sources with spatial resolution. As an example we show in Figure 5 the heat production caused by the Soret effect in bulk and at the interfaces. Since it is a reversible heat source, positive and negative contributions dependent on the local current directions are possible. It is clearly visible that heat sources can be strongly localized depending on the micro-structure. This is true also for other sources of heat. By computing the total power per volume for the different heat sources their relative magnitudes can be compared as function of state-of-charge during charging. Figure 6 shows the result for the microscopic simulation with ellipsoidal base particles. A very interesting feature is the time-dependence of the Soret heat: Although it oscillates strongly with a large magnitude and is very inhomogeneously distributed in space (cf. Figure 5) the total interface and bulk contributions cancel each other exactly such that the Soret effect is of no importance for the total heat production in this case. Responsible for the shape of the Soret curves is the derivative of the open-circuit potential (OCV) (cf. last terms in Equation 57 and Equation 79). After averaging those terms vanish for the mesoscopic model (cf. second last term of Equation 84). What remains is the divergence of the purely diffusive ion flux which is very small in the separator and has opposite signs in the electrodes. In a symmetric setup such as the one studied here with sufficiently small temperature gradients these (the last terms in Equation 57 and Equation 79) basically cancel. That is why the Soret contribution in the meso-simulations is of the order of 10^{-5} mW/cm^3.

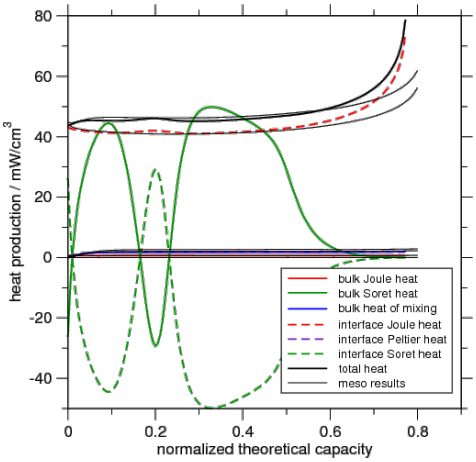

Figure 6: Heat production for ellipsoid-based micro-structure due to different heat sources. Thick lines show the results from the micro-simulation while the thin black lines are the results of the corresponding meso-simulation.

We realize from Figure 6 that the only significant contribution to the total heat production comes from the irreversible Joule heat created at the interface between active particle and electrolyte, i.e., basically the product of overpotential and Butler–Volmer current ηi_{se} (cf. last line of Equation 84). We further note the good agreement between micro- and meso-scale simulations. In particular the interface Joule heat as most relevant heat source can be captured in the meso-model quite well, although there is a deviation at the end of the charging process. Similar to the cell potential (cf Figure 4) also the interface Joule heat crucially depends on the overpotential. Therefore, the same reason as discussed before explains the difference.

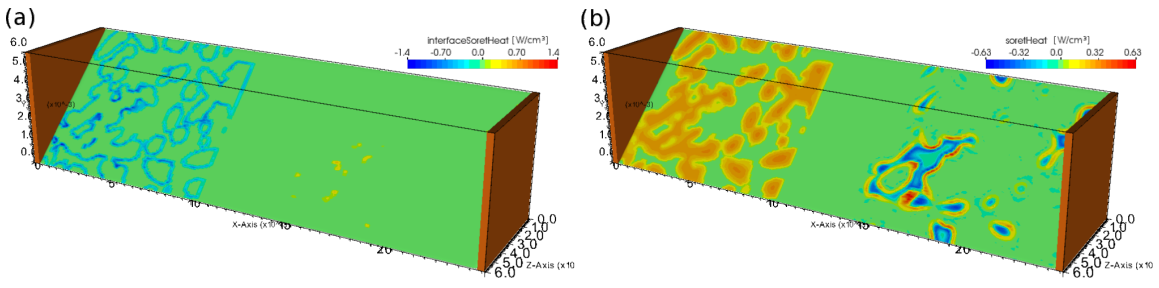

Figure 5: Cut through the ellipsoid-based micro-geometry showing heat production at a normalized capacity of 0.5 by (a) the interface Soret effect and (b) the bulk Soret effect.

From the above discussion one would expect that the overpotentials of micro- and meso-model are the same. In Figure 7a we study the overpotential at a fixed time as a function of the position in the through-plane direction. Comparing the overpotentials for each CV in the microscopic case (grey dots) a very large scatter is observed that is larger for the anode (left). The anode has a lower rate constant than the cathode and hence a larger overpotential. The large scatter is of course an expression of the complex microstructure and for better comparability we compute a running average of the data (red curve). In the homogeneous mesoscopic simulation the overpotential curve is, by construction, much smoother and it agrees well with the microscopic data. Due to the strong relationship between the interface Joule heating with the overpotential the same holds for this heat source shown in Figure 7b. From both figures it can thus be concluded that the meso-approach is capable of reproducing the average or global heat power. However, one should note that this is because it is the interface Joule heat that plays the dominant role. So as long as the geometry is such that overpotential and Butler–Volmer current density can be described well on the mesoscopic scale the respective simulation can compute the correct amount of heat. If other sources of heat that rely on the actual distribution of current or ion flux become more important, either due to different material parameter combinations or geometric properties, it is unlikely that a meso-simulation can reproduce the results of the full microscopic approach.

Many processes, e.g., the intercalation rate or degradation effects, depend on the local temperature. Having realized from Figure 5 and Figure 7 that heat sources are inhomogeneously distributed in the realistic microscopic geometry it is of interest whether the resulting temperature exhibits a similar behavior. Therefore Figure 8 shows the cell temperature as a function of the through-plane position for different times during the charging. There is no spatial temperature variation visible (even on changing the scale), only a global increase of T. This is not surprising since the thermal diffusivity $\lambda/c_p\rho = 0.0014\ \mathrm{cm}^2/\mathrm{s}$ and the cell thickness of 0.00246 cm lead to thermal diffusion time scale of less than 0.5 s. The energy produced in any point inside the cell is thus spread out very quickly such that no appreciable gradient can develop. This is particularly true for the strongly localized interface Joule heat sources.

One finding of the presented numerical experiments is that it is mainly the Joule heating at the interface between active material and electrolyte that determines the amount of heat production. However, we have to repeat in this context that a temperature dependence of the parameters was not considered here, which in particular affects the reversible Peltier term (Equation 80). Some studies claim this term to be also of relevant magnitude at least for low currents [50]. A reliable experi-

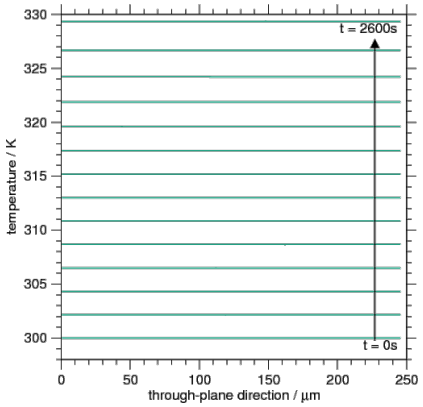

Figure 8: Spatial variation of temperature in through-plane direction for the microscopic ellipsoid case.

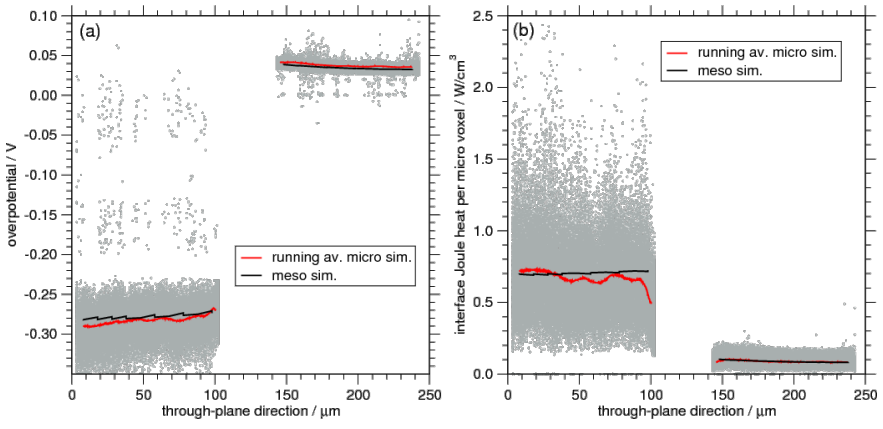

Figure 7: (a) Spatial distribution of the overpotential in through-plane direction for the ellipsoid-based microstructure at a capacity ratio of 0.42. Due to the strong variation of the data in the microscopic simulations (grey), a running average (red) is compared to the overpotentials of the mesoscopic simulations (black). (b) Similar as in (a) we compare the Joule heat at the interface between active particles and electrolyte.

mental determination of $\partial U_0/\partial T$ is, therefore, an important prerequisite for further computations including this effect, but they are not trivial since U_0 only very weakly depends on T.

In summary, we found that the mesoscopic simulation approach was able to quantitatively reproduce the amount of energy produced during charging with a constant current from the microscopic approach. Although this was at first surprising since the scatter of concentrations, potentials or currents in the meso-model is much weaker, this result could be explained by the fact that there is only one dominant source of heat, namely Joule heating at particle–electrolyte interface. This heat term does only depend on overpotentials and intercalation currents that are reproduced in this approach reasonably well. As long as the solid-diffusion behavior, which influences the overpotential, is captured correctly and as the interface Joule heating is the dominant effect one can expect that the thermal results of the meso-model are as trustworthy as a full microscopic simulation. While the former was easily obtained in this study because the basic particles were of very simple spherical or spheroidal shape of equal size the latter might be different for other cases (e.g., other materials with different parameters or geometries). When the active particles exhibit a broad size and shape distribution, as in reality, more care is necessary to adjust their size and the solid diffusion constant in the meso-model. That such an adjustment would be sufficiently universal to allow for predictive simulations for a wide range of application scenarios (e.g., different load cases) can be doubted. Other studies state at least that the mesoscopic simulation approach underestimates the total amount of generated heat [50] when compared to the micro-approach. The latter takes structural influences into account and is thus less dependent on parameter adjustments or data fitting. Therefore more realistic results can be expected from the micro-approach. On the other hand, micro-scale simulations are computationally much more expensive if a reasonable realistic and representative micro-structure (e.g., from measurements) is used.

Conclusion

Fully seamless multiscale simulations from atomistic to cell scale are not yet possible nowadays. There are unresolved issues on each scale, although tremendous progress for electrochemical storage applications have been achieved. In the main part of our paper, we addressed the problem on how the continuum scale, which stretches for battery cells from the nanometer to the centimeter scale can be systematically be brought in contact with the atomistic scale. We believe that systematic methods from non-equilibrium or rational thermodynamics may well be the tool to establish the connection with MD and DFT simulations, if all these methods are combined with methods from statistical mechanics to ensure the proper averaging strategies for obtaining the transport coefficients and thermodynamic derivatives [90]. In addition to giving a short overview over the available atomistic scale simulation tools, we concentrated on the problem of systematically deriving the coupled equations for ion, charge and heat transport in insertion batteries on the particle and pore resolved nano- and microscales of electrodes and upscaling these equations to the cell scale. In the derivation we presented a careful discussion on how the resulting form of the transport equations is influenced by the choice of the macroscopic fields and how the seemingly different models in the literature can be transformed into each other. The accuracy of the upscaling procedure was investigated numerically by comparing a fully 3D microstructure resolved model of a battery cell with the homogenized or upscaled representation of this cell. For the chosen microstructure the numerically thermal and voltage behavior of the cell under load was found to be astonishingly similar to the directly simulated results of the analytically averaged equations. This result cannot be considered to be true in general. We except that the differences can be much bigger for less homogeneously chosen microstructures. But even for the investigated homogenous microstructures huge fluctuations (larger then 100%) around the average for, e.g., overpotentials and Joule heating terms are found. As a consequence we may conclude that the probability for the occurence of degradation phenomena may be hugely underestimated. For example the occurence of plating depends on the local potential at the interface of the electrolyte and active particles. Since overpotentials are strongly underestimated, a porous electrode model cannot accurately detect the sites in the battery cell where, e.g., plating is likely to occur, that is where the total potential drops below the redox potential of Li/Li^+. The same is to be expected for the initiation for thermally induced degradation of the electrolyte due to the underestimation of the local heat production. Although the temperature is basically constant on the microstructural scale, it is, in addition to the temperature, the locally available energy on very short time scales, which is relevant for overcoming reaction barriers of degradation mechanisms. Therefore, the local fluctuations in the heat sources may be relevant for the identification of critical structural properties of electrodes. For the design of optimal cells a combination of cell-scale simulations with pore-resolved simulations will be necessary to identify the best global behavior as well as the optimal structure on the nano-and micrometerscale, once the optimal material parameters have been identified with DFT- and MD- simulations.

Appendix

To obtain the volume-averaged transport equation for heat (Equation 84), the volume averaging technique is applied to each term of Equation 83, where the convention is adopted that the normals always point from solid to electrolyte phase.

Heat conduction

$$\begin{aligned}\left\langle \nabla\cdot(\lambda\nabla T)\right\rangle_V &= \varepsilon_s\nabla\cdot\langle\lambda_s\nabla T\rangle_{V_s} + \varepsilon_e\nabla\cdot\langle\lambda_e\nabla T\rangle_{V_e}\\ &+\frac{1}{V}\int_{\partial V}\left(\lambda_s\nabla T-\lambda_e\nabla T\right)\cdot\hat{n}dA\\ &=\varepsilon_s\nabla\cdot\langle\lambda\nabla T\rangle_{V_s}+\varepsilon_e\nabla\cdot\langle\lambda\nabla T\rangle_{V_e}\\ &+ai_{se}\eta\\ &+aTi_{se}\left[\left(\beta_s-\beta_e\right)+\frac{\partial\left(U_0+\mu_e/F\right)}{\partial T}\right]\\ &-ai_{se}\left[c_s\frac{\partial U_0}{\partial c_s}k_{T,s}+c_e\frac{\partial\mu_e}{\partial c_e}\frac{k_{T,e}\left(1-t_+\right)}{F}\right].\end{aligned} \tag{85}$$

In the last step the microscopic expression for the thermal interface conditions was applied. Here and in the following $a = A/V$ denotes the specific surface area.

Joule heating

$$\left\langle\frac{\mathbf{j}^2}{\kappa}\right\rangle=\varepsilon_s\frac{\langle\mathbf{j}_s^2\rangle_{V_s}}{\kappa_s}+\varepsilon_e\frac{\langle\mathbf{j}_e^2\rangle_{V_e}}{\kappa_e}. \tag{86}$$

Thomson effect

$$\begin{aligned}\left\langle-T\nabla\cdot(\beta\mathbf{j})\right\rangle_V &= -T\varepsilon_s\nabla\cdot\langle\beta_s\mathbf{j}_s\rangle_{V_s}\\ &-T\varepsilon_e\nabla\cdot\langle\beta_e\mathbf{j}_e\rangle_{V_e}-T\cdot ai_{se}\left(\beta_s-\beta_e\right).\end{aligned} \tag{87}$$

Heat of mixing

$$\begin{aligned}\left\langle\frac{\partial\mu}{\partial c}\frac{\left(\mathbf{N}_+-t_+\mathbf{j}/F\right)^2}{D}\right\rangle_V &= \varepsilon_s\left\langle\frac{\partial\mu_s}{\partial c_s}\frac{\mathbf{N}_{+s}^2}{D_s}\right\rangle_{V_s}\\ &+\varepsilon_e\left\langle\frac{\partial\mu_e}{\partial c_e}\frac{\left(\mathbf{N}_{+e}-t_+\mathbf{j}_e/F\right)^2}{D_e}\right\rangle_{V_e}.\end{aligned} \tag{88}$$

In the first term on the right hand side the transference number in the solid is zero.

Soret–Dufour effect

The mathemiatical expression for the Soret–Dufour effect is given in Equation 89. Adding up all the contribution and assuming that there is no direct inter-particle transport of ions, i.e., $\langle\mathbf{N}_{+s}\rangle_{V_s}=0$, we obtain the volume-averaged heat equation (Equation 84).

$$\begin{aligned}\left\langle-T\nabla\cdot\left(c\frac{\partial\mu}{\partial c}\frac{k_T}{T}\left(\mathbf{N}_+-t_+\mathbf{j}/F\right)\right)\right\rangle_V &= -T\varepsilon_s\nabla\cdot\left\langle c_s\frac{\partial\mu_s}{\partial c_s}\frac{k_{T,s}}{T}\mathbf{N}_{+s}\right\rangle_{V_s}\\ &-T\varepsilon_e\nabla\cdot\left\langle c_e\frac{\partial\mu_e}{\partial c_e}\frac{k_{T,e}}{T}\left(\mathbf{N}_{+e}-t_+\mathbf{j}_e/F\right)\right\rangle_{V_e}\\ &-a\frac{i_{se}}{F}c_s\frac{\partial\mu_s}{\partial c_s}k_{T,s}+a\frac{i_{se}}{F}(1-t_+)c_e\frac{\partial\mu_e}{\partial c_e}k_{T,e}.\end{aligned} \tag{89}$$

Acknowledgements

The thermal extension of BEST was financially supported by the German Federal Ministry of Education and Research (BMBF) through the project ”TopBat”, grant 16N12529.

References

1. Scrosati, B.; Abraham, K. M.; van Schalkwijk, W. A.; Hassoun, J. *Lithium Batteries: Advanced Technologies and Applications;* Wiley, 2013.
2. Balbuena, P. B.; Wang, Y. *Lithium-Ion Batteries: Solid-Electrolyte Interphase;* World Scientific, 2004.
3. Meng, Y. S.; Arroyo-de Dompablo, M. E. *Energy Environ. Sci.* **2009,** *2,* 589–609. doi:10.1039/b901825e
4. Capelle, K. *Braz. J. Phys.* **2006,** *36,* 1318–1343.
5. Keith, J. A.; Jerkiewicz, G.; Jacob, T. *ChemPhysChem* **2010,** *11,* 2779–2794. doi:10.1002/cphc.201000286
6. Calle-Vallejo, F.; Koper, M. T. M. *Electrochim. Acta* **2012,** *84,* 3–11. doi:10.1016/j.electacta.2012.04.062
7. Reuter, K.; Stampfl, C.; Scheffler, M. Ab initio atomistic thermodynamics and statistical mechanics of surface properties and functions. In *Handbook of Materials Modeling;* Yip, S., Ed.; Springer, 2005; Vol. 1, pp 149–194. doi:10.1007/978-1-4020-3286-8_10
8. Sanchez, J. M.; Ducastelle, F.; Gratias, D. *Physica A* **1984,** *128,* 334–350. doi:10.1016/0378-4371(84)90096-7
9. Van der Ven, A.; Ceder, G.; Asta, M.; Tepesch, P. D. *Phys. Rev. B* **2001,** *64,* 184307. doi:10.1103/PhysRevB.64.184307
10. Gomer, R. *Rep. Prog. Phys.* **1990,** *53,* 917–1002. doi:10.1088/0034-4885/53/7/002
11. Van der Ven, A.; Thomas, J. C.; Xu, Q.; Swoboda, B.; Morgan, D. *Phys. Rev. B* **2008,** *78,* 104306. doi:10.1103/PhysRevB.78.104306
12. Persson, K.; Sethuraman, V. A.; Hardwick, L. J.; Hinuma, Y.; Meng, Y. S.; van der Ven, A.; Srinivasan, V.; Kostecki, R.; Ceder, G. *J. Phys. Chem. Lett.* **2010,** *1,* 1176–1180. doi:10.1021/jz100188d
13. Van der Ven, A.; Bhattacharya, J.; Belak, A. A. *Acc. Chem. Res.* **2013,** *46,* 1216–1225. doi:10.1021/ar200329r
14. Calero, C.; Faraudo, J.; Aguilella-Arzo, M. *Mol. Simul.* **2011,** *37,* 123–134. doi:10.1080/08927022.2010.525513
15. Borodin, O. Molecular Modeling of Electrolytes. In *Modern Aspects of Electrochemistry;* Jow, T.; Xu, K.; Borodin, O.; Ue, M., Eds.; Springer, 2014; Vol. 58, pp 371–401. doi:10.1007/978-1-4939-0302-3_8

16. Kalcher, I.; Schulz, J. C. F.; Dzubiella, J. *J. Chem. Phys.* **2010,** *133,* 164511. doi:10.1063/1.3490666
17. Merlet, C.; Salanne, M.; Rotenberg, B.; Madden, P. A. *Electrochim. Acta* **2013,** *101,* 262–271. doi:10.1016/j.electacta.2012.12.107
18. Lee, E.; Persson, K. A. *Nano Lett.* **2012,** *12,* 4624–4628. doi:10.1021/nl3019164
19. Zhang, X.; Shyy, W.; Sastry, A. M. *J. Electrochem. Soc.* **2007,** *154,* A910–A916. doi:10.1149/1.2759840
20. Zhang, X.; Sastry, A. M.; Shyy, W. *J. Electrochem. Soc.* **2008,** *155,* A542–A552. doi:10.1149/1.2926617
21. Soni, S. K.; Sheldon, B. W.; Xiao, X.; Bower, A. F.; Verbrugge, M. W. *J. Electrochem. Soc.* **2012,** *159,* A1520–A1527. doi:10.1149/2.009209jes
22. Qi, Y.; Guo, H.; Hector, L. G., Jr.; Timmons, A. *J. Electrochem. Soc.* **2010,** *157,* A558–A566. doi:10.1149/1.3327913
23. Rohrer, J.; Albe, K. *J. Phys. Chem. C* **2013,** *117,* 18796–18803. doi:10.1021/jp401379d
24. Lee, E.; Persson, K. A. *Chem. Mater.* **2013,** *25,* 2885–2889. doi:10.1021/cm4014738
25. Guyer, J. E.; Boettinger, W. J.; Warren, J. A.; McFadden, G. B. *Phys. Rev. E* **2004,** *69,* 021603. doi:10.1103/PhysRevE.69.021603
26. Guyer, J. E.; Boettinger, W. J.; Warren, J. A.; McFadden, G. B. *Phys. Rev. E* **2004,** *69,* 021604. doi:10.1103/PhysRevE.69.021604
27. Dreyer, W.; Guhlke, C.; Müller, R. *Phys. Chem. Chem. Phys.* **2013,** *15,* 7075–7086. doi:10.1039/c3cp44390f
28. Van der Ven, A.; Garikipati, K.; Kim, S.; Wagemaker, M. *J. Electrochem. Soc.* **2009,** *156,* A949–A957. doi:10.1149/1.3222746
29. Wagemaker, M.; Mulder, F. M.; Van der Ven, A. *Adv. Mater.* **2009,** *21,* 2703–2709. doi:10.1002/adma.200803038
30. Singh, G. K.; Ceder, G.; Bazant, M. Z. *Electrochim. Acta* **2008,** *53,* 7599–7613. doi:10.1016/j.electacta.2008.03.083
31. Huttin, M.; Kamlah, M. *Appl. Phys. Lett.* **2012,** *101,* 133902. doi:10.1063/1.4754705
32. Cogswell, D. A.; Bazant, M. Z. *ACS Nano* **2012,** *6,* 2215–2225. doi:10.1021/nn204177u
33. Dreyer, W.; Jamnik, J.; Guhlke, C.; Huth, R.; Moskon, J.; Gaberscek, M. *Nat. Mater.* **2010,** *9,* 448–453. doi:10.1038/nmat2730
34. Dreyer, W.; Gaberšček, M.; Guhlke, C.; Huth, R.; Jamnik, J. *Eur. J. Appl. Math.* **2011,** *22,* 267–290. doi:10.1017/S0956792511000052
35. Dreyer, W.; Guhlke, C.; Huth, R. *Phys. D (Amsterdam, Neth.)* **2011,** *240,* 1008–1019. doi:10.1016/j.physd.2011.02.011
36. Bai, P.; Cogswell, D. A.; Bazant, M. Z. *Nano Lett.* **2011,** *11,* 4890–4896. doi:10.1021/nl202764f
37. Malik, R.; Abdellahi, A.; Ceder, G. *J. Electrochem. Soc.* **2013,** *160,* A3179–A3197. doi:10.1149/2.029305jes
38. DeGroot, S.; Mazur, P. *Non-Equilibrium Thermodynamics;* Dover Publications, 1984.
39. Müller, I. *Thermodynamics;* Interaction of Mechanics and Mathematics Series; Pitman, 1985.
40. Kovetz, A. *Electromagnetic Theory;* Oxford University Press, 2006.
41. Latz, A.; Zausch, J. *J. Power Sources* **2011,** *196,* 3296–3302. doi:10.1016/j.jpowsour.2010.11.088
42. Bernardi, D.; Pawlikowski, E.; Newman, J. *J. Electrochem. Soc.* **1985,** *132,* 5–12. doi:10.1149/1.2113792
43. Pals, C. R.; Newman, J. *J. Electrochem. Soc.* **1995,** *142,* 3274–3281. doi:10.1149/1.2049974
44. Botte, G. G.; Johnson, B. A.; White, R. E. *J. Electrochem. Soc.* **1999,** *146,* 914–923. doi:10.1149/1.1391700
45. Gu, W. B.; Wang, C. Y. *J. Electrochem. Soc.* **2000,** *147,* 2910–2922. doi:10.1149/1.1393625
46. Thomas, K. E.; Newman, J. *J. Electrochem. Soc.* **2003,** *150,* A176–A192. doi:10.1149/1.1531194
47. Kumaresan, K.; Sikha, G.; White, R. E. *J. Electrochem. Soc.* **2008,** *155,* A164–A171. doi:10.1149/1.2817888
48. Kim, U. S.; Shin, C. B.; Kim, C.-S. *J. Power Sources* **2008,** *180,* 909–916. doi:10.1016/j.jpowsour.2007.09.054
49. Cai, L.; White, R. E. *J. Power Sources* **2011,** *196,* 5985–5989. doi:10.1016/j.jpowsour.2011.03.017
50. Yan, B.; Lim, C.; Yin, L.; Zhu, L. *Electrochim. Acta* **2013,** *100,* 171–179. doi:10.1016/j.electacta.2013.03.132
51. Yan, B.; Lim, C.; Yin, L.; Zhu, L. *J. Electrochem. Soc.* **2012,** *159,* A1604–A1614. doi:10.1149/2.024210jes
52. Franco, A. A. *RSC Adv.* **2013,** *3,* 13027–13058. doi:10.1039/c3ra23502e
53. de Morais, R. F.; Sautet, P.; Loffreda, D.; Franco, A. A. *Electrochim. Acta* **2011,** *56,* 10842–10856. doi:10.1016/j.electacta.2011.05.109
54. Eberle, D.; Horstmann, B. *Electrochim. Acta* **2014,** *137,* 714–720. doi:10.1016/j.electacta.2014.05.144
55. Latz, A.; Zausch, J.; Iliev, O. Modeling of Species and Charge Transport in Li-Ion Batteries Based on Non-equilibrium. In *Numerical Methods and Applications;* Dimov, I.; Dimova, S.; Kolkovska, N., Eds.; Lecture Notes in Computer Science, Vol. 6064; Springer, 2011; pp 329–337. doi:10.1007/978-3-642-18466-6_39
56. Bazant, M. Z. *Acc. Chem. Res.* **2013,** *46,* 1144–1160. doi:10.1021/ar300145c
57. Lai, W.; Ciucci, F. *Electrochim. Acta* **2011,** *56,* 4369–4377. doi:10.1016/j.electacta.2011.01.012
58. Lai, W. *J. Power Sources* **2011,** *196,* 6534–6553. doi:10.1016/j.jpowsour.2011.03.055
59. Less, G. B.; Seo, J. H.; Han, S.; Sastry, A. M.; Zausch, J.; Latz, A.; Schmidt, S.; Wieser, C.; Kehrwald, D.; Fell, S. *J. Electrochem. Soc.* **2012,** *159,* A697–A704. doi:10.1149/2.096205jes
60. Quiroga, M. A.; Xue, K.-h.; Nguyen, T.-k.; Tułodziecki, M.; Huang, H.; Franco, A. A. *J. Electrochem. Soc.* **2014,** *161,* E3302–E3310. doi:10.1149/2.029408jes
61. Landstorfer, M.; Jacob, T. *Chem. Soc. Rev.* **2013,** *42,* 3234–3252. doi:10.1039/c2cs35050e
62. Xu, K. *J. Electrochem. Soc.* **2007,** *154,* A162–A167. doi:10.1149/1.2409866
63. Dahn, J. R.; Zheng, T.; Liu, Y.; Xue, J. S. *Science* **1995,** *270,* 590–593. doi:10.1126/science.270.5236.590
64. Latz, A.; Zausch, J. *Electrochim. Acta* **2013,** *110,* 358–362. doi:10.1016/j.electacta.2013.06.043
65. Colclasure, A. M.; Kee, R. J. *Electrochim. Acta* **2010,** *55,* 8960–8973. doi:10.1016/j.electacta.2010.08.018
66. Rubi, J. M.; Kjelstrup, S. *J. Phys. Chem. B* **2003,** *107,* 13471–13477. doi:10.1021/jp030572g
67. Thomas, K. E.; Newman, J.; Darling, R. M. Mathematical Modeling of Lithium Batteries. In *Advances in Lithium-Ion Batteries;* Schalkwijk, W. A.; Scrosati, B., Eds.; Kluver, 2002; pp 345–392.
68. Vetter, J.; Novak, P.; Wagner, M. R.; Veit, C.; Möller, K.-C.; Besenhard, J. O.; Winter, M.; Wohlfahrt-Mehrens, M.; Vogler, C.; Hammouche, A. *J. Power Sources* **2005,** *147,* 269–281. doi:10.1016/j.jpowsour.2005.01.006
69. Newman, J. *Ind. Eng. Chem. Res.* **1995,** *34,* 3208–3216.
70. Kuzminskii, Y. V.; Gorodyskii, A. V. *J. Electroanal. Chem.* **1988,** *252,* 21–38. doi:10.1016/0022-0728(88)85068-X

71. Wood, C.; Chmielewski, A.; Zoltan, D. *Rev. Sci. Instrum.* **1988,** *59,* 951–954. doi:10.1063/1.1139756
72. Newman, J.; Tiedemann, W. *AIChE J.* **1975,** *21,* 25–41. doi:10.1002/aic.690210103
73. Doyle, M.; Fuller, T. F.; Newman, J. *J. Electrochem. Soc.* **1993,** *140,* 1526–1533. doi:10.1149/1.2221597
74. Fuller, T. F.; Doyle, M.; Newman, J. *J. Electrochem. Soc.* **1994,** *141,* 1–10. doi:10.1149/1.2054684
75. Doyle, M.; Newman, J.; Gozdz, A. S.; Schmutz, C. N.; Tarascon, J. M. *J. Electrochem. Soc.* **1996,** *143,* 1890–1903. doi:10.1149/1.1836921
76. Ferguson, T. R.; Bazant, M. Z. *J. Electrochem. Soc.* **2012,** *159,* A1967–A1985. doi:10.1149/2.048212jes
77. De Vidts, P.; White, R. E. *J. Electrochem. Soc.* **1997,** *144,* 1343–1353. doi:10.1149/1.1837595
78. Wang, C. Y.; Gu, W. B.; Liaw, B. Y. *J. Electrochem. Soc.* **1998,** *145,* 3407–3417. doi:10.1149/1.1838820
79. Ciucci, F.; Lai, W. *Transp. Porous Media* **2011,** *88,* 249–270. doi:10.1007/s11242-011-9738-5
80. Slattery, J. *Momentum, Energy, and Mass Transfer in Continua;* R. E. Krieger Publishing Company, 1978.
81. Kim, U. S.; Shin, C. B.; Kim, C.-S. *J. Power Sources* **2009,** *189,* 841–846. doi:10.1016/j.jpowsour.2008.10.019
82. Forgez, C.; Vinh Do, D.; Friedrich, G.; Morcrette, M.; Delacourt, C. *J. Power Sources* **2010,** *195,* 2961–2968. doi:10.1016/j.jpowsour.2009.10.105
83. Kim, G.-H.; Smith, K.; Lee, K.-J.; Santhanagopalan, S.; Pesaran, A. *J. Electrochem. Soc.* **2011,** *158,* A955. doi:10.1149/1.3597614
84. Zhang, X. *Electrochim. Acta* **2011,** *56,* 1246–1255. doi:10.1016/j.electacta.2010.10.054
85. Patankar, S. V. *Numerical Heat Transfer and Fluid Flow;* Hemisphere Publishing Corporation: New York, 1980.
86. *SAMG - Algebraic Multigrid Methods for Systems;* SCAI, Fraunhofer: http://www.scai.fraunhofer.de/samg, 2014.
87. *BEST - Battery and Electrochemistry Simulation Tool;* ITWM, Fraunhofer: http://www.itwm.fraunhofer.de/best, 2014.
88. *CoRheoS - Complex Rheology Solvers;* ITWM, Fraunhofer: http://www.itwm.fraunhofer.de/corheos, 2014.
89. *GeoDict;* Math2Market: http://www.geodict.de, 2014.
90. Götze, W.; Latz, A. *J. Phys.: Condens. Matter* **1989,** *1,* 4169. doi:10.1088/0953-8984/1/26/013

License and Terms

BEILSTEIN JOURNAL OF NANOTECHNOLOGY

From lithium to sodium: cell chemistry of room temperature sodium–air and sodium–sulfur batteries

Philipp Adelhelm[*1,2], Pascal Hartmann[2,3], Conrad L. Bender[2], Martin Busche[2], Christine Eufinger[2] and Juergen Janek[*2,4]

Review

Open Access

Address:
[1]Institute for Technical Chemistry and Environmental Chemistry, Center for Energy and Environmental Chemistry, Friedrich-Schiller-University Jena, Lessingstraße 12, 07743 Jena, Germany, [2]Institute of Physical Chemistry, Justus-Liebig-University Giessen, Heinrich-Buff-Ring 58, 35392 Giessen, Germany, [3]BASF SE, 67056 Ludwigshafen, Germany and [4]Battery and Electrochemistry Laboratory, Institute of Nanotechnology, Karlsruhe Institute of Technology, Hermann-von-Helmholtz-Platz 1, 76344 Eggenstein-Leopoldshafen, Germany

Email:
Philipp Adelhelm* - philipp.adelhelm@uni-jena.de; Juergen Janek* - juergen.janek@phys.chemie.uni-giessen.de

* Corresponding author

Keywords:
energy storage; lithium–oxygen battery; lithium–sulfur battery; sodium–oxygen battery; sodium–sulfur battery

Beilstein J. Nanotechnol. **2015,** *6,* 1016–1055.
doi:10.3762/bjnano.6.105

Received: 19 November 2014
Accepted: 05 March 2015
Published: 23 April 2015

This article is part of the Thematic Series "Materials for sustainable energy production, storage, and conversion".

Guest Editor: M. Fichtner

Abstract

Research devoted to room temperature lithium–sulfur (Li/S_8) and lithium–oxygen (Li/O_2) batteries has significantly increased over the past ten years. The race to develop such cell systems is mainly motivated by the very high theoretical energy density and the abundance of sulfur and oxygen. The cell chemistry, however, is complex, and progress toward practical device development remains hampered by some fundamental key issues, which are currently being tackled by numerous approaches. Quite surprisingly, not much is known about the analogous sodium-based battery systems, although the already commercialized, high-temperature Na/S_8 and $Na/NiCl_2$ batteries suggest that a rechargeable battery based on sodium is feasible on a large scale. Moreover, the natural abundance of sodium is an attractive benefit for the development of batteries based on low cost components. This review provides a summary of the state-of-the-art knowledge on lithium–sulfur and lithium–oxygen batteries and a direct comparison with the analogous sodium systems. The general properties, major benefits and challenges, recent strategies for performance improvements and general guidelines for further development are summarized and critically discussed. In general, the substitution of lithium for sodium has a strong impact on the overall properties of the cell reaction and differences in ion transport, phase stability, electrode potential, energy density, etc. can be thus expected. Whether these differences will benefit a more reversible cell chemistry is still an open question, but some of the first reports on room temperature Na/S_8 and Na/O_2 cells already show some exciting differences as compared to the established Li/S_8 and Li/O_2 systems.

Review

1 Introduction

Rechargeable lithium-ion batteries (LIBs) have rapidly become the most important form of energy storage for all mobile applications since their commercialization in the early 1990s. This is mainly due to their unrivaled energy density that easily surpasses other rechargeable battery systems such as metal–hydride or lead–acid. However, the ongoing need to store electricity even more safely, more compactly and more affordably necessitates continuous research and development. The need for inexpensive stationary energy storage has become an additional challenge, which also triggers research on alternative batteries. Major efforts are directed towards continuous improvements of the different Li-ion technologies by more efficient packaging, processing, better electrolytes and optimized electrode materials, for example. Although significant progress has been achieved with respect to the power density over the last years, the increase in energy density (volumetrically and gravimetrically) was relatively small [1]. A comparison of different battery technologies with respect to their energy densities is shown in Figure 1.

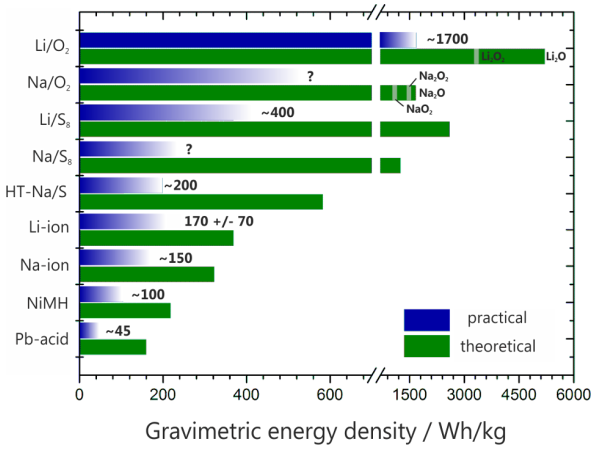

Figure 1: Theoretical and (estimated) practical energy densities of different rechargeable batteries: Pb–acid – lead acid, NiMH – nickel metal hydride, Na-ion – estimate derived from data for Li-ion assuming a slightly lower cell voltage, Li-ion – average over different types, HT-Na/S_8 – high temperature sodium–sulfur battery, Li/S_8 and Na/S_8 – lithium–sulfur and sodium–sulfur battery assuming Li_2S and Na_2S as discharge products, Li/O_2 and Na/O_2 – lithium–oxygen battery (theoretical values include the weight of oxygen and depend on the stoichiometry of the assumed discharge product, i.e., oxide, peroxide or superoxide). Note that the values for practical energy densities can largely vary depending on the battery design (size, high power, high energy, single cell or battery) and the state of development. All values for practical energy densities refer to the cell level (except Pb–acid, 12 V). The values for the Li/S_8 and Li/O_2 batteries were taken from the literature (cited within the main text) and are used to estimate the energy densities for the Na/S_8 and Na/O_2 cells. Of the above technologies, only the lead acid, NiMH, Li-ion and high temperature Na/S_8 technologies have been commercialized to date.

Ultimately, the energy density of a practical battery is determined by the cell reaction itself, that is, the electrode materials being used. The need for a proper cell design and packaging considerably reduces the practical energy density of a battery compared to the theoretical energy density. The cell reaction of Li-ion batteries is not fixed and different electrode materials and mixtures are used depending on the type of application. Graphite/carbon and to a lesser degree $Li_{4/3}Ti_{5/3}O_4$ (LTO) serve as the negative electrodes. Recently, silicon has been added in small amounts to graphite to increase the capacity. Layered oxides (the classic $LiCoO_2$, LCO) and related materials ($LiNi_{1-x-y}Mn_xCo_yO_2$, NMC; $LiNi_{0.8}Co_{0.15}Al_{0.05}O_2$, NCA; olivines, $LiFePO_4$, LFP; spinels, $LiMn_2O_4$, LMO) are applied as positive electrodes. The underlying storage principle of all these electrode materials is a one-electron transfer per formula unit. In this process, the de-/intercalation of one Li-ion is linked to a change in the transition metal oxidation state by one ($Co^{3+/4+}$, $Fe^{2+/3+}$, $Mn^{3+/4+}$, etc.), as illustrated in Figure 2a. However, since the positive electrode materials often suffer from stability issues at too low lithium contents, only a fraction of the theoretical capacity can be achieved in practice (with LFP being an exception). For example, only 0.5 electrons per formula unit can be reversibly exchanged for LCO. The electrode reaction for LCO can therefore be written as

$$Li_{0.5}CoO_2 + 0.5Li^+ + 0.5e^- \underset{\text{charge}}{\overset{\text{discharge}}{\rightleftharpoons}} LiCoO_2. \quad (1)$$

The amount of charge that can be stored during this process is therefore limited and the capacities of positive insertion-type and intercalation-type electrode materials are around 120–180 mAh/g. Employing graphite as a negative electrode (372 mAh/g), the theoretical energy densities of single cells for current Li-ion technology are limited to around 350–400 Wh/kg and 1200–1400 Wh/L. Roughly about one fourth to one half is achieved in practice due to the additional weight and volume of the current collectors, separator, electrolyte, cell housing, and so forth.

Significantly higher energy densities can only be achieved by using electrode reactions such as multielectron transfer and/or lighter elements. A broad range of so-called conversion reactions has been studied which are based on the full reduction of the transition metal [2]. The general electrode reaction can be written as:

$$M_aX_b + (b\cdot c)\,Li^+ + (b\cdot c)\,e^- \rightleftharpoons aM + bLi_cX, \quad (2)$$

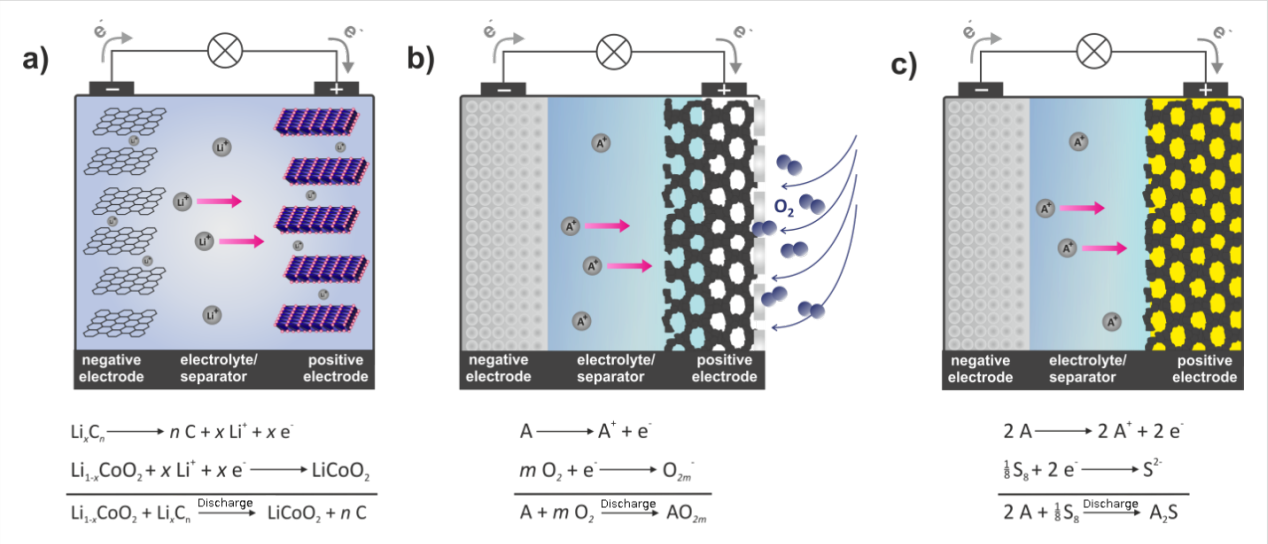

Figure 2: Operating principles of (a) a lithium-ion battery, (b) a metal–oxygen battery (non-aqueous electrolyte) and (c) a metal–sulfur battery during discharge. (A = Li, Na). A lithium-ion battery is based on intercalation compounds as electrodes. The exact cell reaction depends on the materials used. In this example, the reaction equation is formulated for the classical LIB with graphite as the negative and $LiCoO_2$ as the positive electrode. The same concept can be applied for a sodium-ion battery. Metal–oxygen and metal–sulfur batteries perform best with a lithium or sodium metal as the anode. The positive electrode consists of a porous support, usually carbon. In a metal–oxygen battery, this support enables the reduction of atmospheric oxygen and accommodates the insulating discharge products of Li_2O_2, Na_2O_2, NaO_2, or ideally, Li_2O and Na_2O. In metal–sulfur batteries, the support hosts the insulating end members of the cell reaction, which are sulfur (before discharge) and ideally Li_2S and Na_2S (after discharge). The sketch in Figure 2 illustrates the most frequently studied cell concepts for metal–oxygen and metal–sulfur cells. Other concepts, for example, solid electrolytes or liquid electrodes, are also currently being studied.

where M is either a transition metal (Cu, Co, Fe, etc.) or Mg, and X is an anion (F, O, S, etc.). The overall success has been limited as conversion reactions typically show large irreversible capacities during the first cycle and a large hysteresis during cycling. This irreversible capacity is mostly caused by the need for complete lattice reconstruction and the corresponding formation of new interfaces.

The most appealing multielectron transfer systems are the lithium–sulfur battery and the lithium–air (or more precisely, the lithium–oxygen battery) in which a non-metal is the redox-active element. Both batteries combine very high theoretical energy densities with the advantage of using abundant and thus resource-uncritical elements. Both systems have been intensively studied over the last years. For example, more than 250 publications appeared in the field of lithium–sulfur batteries in 2014 alone and about 200 publications in 2014 are concerned with lithium–oxygen batteries. The cell concepts are entirely different from conventional Li-ion technology, as depicted in Figure 2. Here, elemental sulfur and atmospheric oxygen are reduced at the positive electrode to form Li_2S and Li_2O_2 during discharge, which is expressed by:

$$1/8S_8 + 2Li^+ + 2e^- \rightleftarrows Li_2S \quad (3)$$

$$O_2 + 2Li^+ + 2e^- \rightleftarrows Li_2O_2. \quad (4)$$

Moreover, the cells ideally operate with metallic lithium as the negative electrode. No heavy transition metals participate in the cell reaction and theoretical energy densities of 2613 Wh/kg for the Li/S_8 and 3458 Wh/kg for the Li/O_2 cell can be calculated.

Perhaps the most important conceptual differences between these cell systems and Li-ion batteries are (1) that the redox centers (oxygen and sulfur) are lighter and spatially more concentrated, allowing for higher energy densities and (2) that the redox-active (molecular) species are mobile in liquid electrolytes and new phases form and decompose during cycling. In intercalation compounds, the redox centers (transition metal cations) are immobile as they are pinned to the fixed positions of the crystal lattice and are, therefore, spatially diluted. However, due to the poor conductivity of sulfur, Li_2S and Li_2O_2, the non-metal redox materials also require a suitable conductive support structure. For the Li/S_8 and Li/O_2 batteries, this means that significant complexity is added, as a series of transport steps and nucleation/decomposition processes take place that will depend on the morphology, microstructure and surface chemistry of the conductive support. Side reactions with the metallic anode and dendrite formation further complicate the cell chemistry, and therefore, the cycle life of both cell systems remains insufficient to date. The Li/O_2 cell particularly

suffers from additional side reactions related to electrolyte decomposition at the positive electrode. Many challenges therefore must be tackled in order to develop practical systems.

Research on sodium-ion batteries (NIBs) has recently been revived and is largely motivated by the natural abundance of sodium [3-10]. The sodium content in the earth's crust and water amount to 28,400 mg/kg and 11,000 mg/L compared to 20 mg/kg and 0.18 mg/L for lithium [11]. Additionally, the number of known sodium compounds is much larger as compared to lithium, and thus combinations of electrode materials that enable the development of batteries based solely on low cost elements (or that provide specific advantages that complement Li-ion technology in special applications) are expected. It is interesting to note that sodium-ion and lithium-ion batteries were studied in the 1970s and 1980s. However, due to the success of the lithium-ion battery (and probably the insufficient overall quality of materials, electrolytes and glove boxes [3]), research on sodium-based batteries was largely abandoned. The only exceptions were the high temperature systems Na/S_8 and $Na/NiCl_2$ [12-15].

Although one would initially assume very similar cell chemistries for otherwise identical LIBs and NIBs, the behavior is in most cases quite different. The reason is related to the larger size of the sodium ion that affects the phase stability, the transport properties and the interphase formation. The basic characteristics of multielectron transfer reactions involving sodium-based conversion reactions have been recently summarized and appear quite attractive. However, similar challenges compared to lithium-based conversion reactions are also found [10].

The intriguing question is whether the chemical differences between sodium and lithium could help to solve some of the challenges known for the Li/S_8 and Li/O_2 cells. Although an unavoidable penalty with respect to the energy density is paid when replacing lithium by sodium, the theoretical value for a room-temperature Na/S_8 battery with Na_2S as a discharge product (1273 Wh/kg) and a Na/O_2 cell with Na_2O_2 as a discharge product (1600 Wh/kg) are still very high compared to LIBs. However, to date, only very little is known about the room temperature chemistry of Na/S_8 and Na/O_2 cells. Only around thirty studies have been published as of 2014 in total. Although there is some dispute about the stoichiometry of the discharge products in these cells, it has been demonstrated that Na/O_2 cells can be cycled with much better performance as compared to the analogue Li/O_2 cell. Replacing lithium by sodium might therefore be an effective strategy to improve the reversibility of high energy battery systems, notwithstanding the reduced theoretical energy capacity.

Some general differences between lithium and sodium cells are immediately apparent:

1. The lower melting point of sodium ($T_{m,Na}$ = 98 °C) as compared to lithium ($T_{m,Li}$ = 181 °C) and its generally higher chemical reactivity pose additional safety issues for cells using metal anodes. On the other hand, cell concepts with a molten anode might be easier to realize given the advantages of better kinetics and prevention of dendrite formation.
2. Sodium is softer than lithium, making handling and processing more difficult. On the other hand, avoiding dendrite formation by means of mechanical pressure can be easier.
3. Sodium is less reducing than lithium, meaning that more substances are thermodynamically stable in direct contact with the metal. This can be an important advantage when designing cell concepts including solid ion-conducting membranes. Many Li-ion conducting solid electrolytes degrade exposed to direct contact with metallic lithium [16]. Moreover, by employing beta-alumina, an excellent Na-ion conducting solid electrolyte is commercially available.
4. The total number of known sodium compounds is larger compared to lithium, so cell reactions might require more intermediate steps or stop at a different stoichiometry. Two notable exceptions exist that might be of advantage for sodium cells. Aluminium forms binary alloys with lithium but not with sodium. Therefore, aluminium instead of the more expensive copper can be used as a current collector for the negative electrode in sodium batteries. Another exception that might have practical relevance is that sodium, in contrast to lithium, does not form a stable nitride when exposed to N_2 atmosphere. This has an immediate impact on Li/O_2 and Na/O_2 cells when operated under air.
5. The larger sizes of the sodium atom and ion compared to lithium (+82% for the atom and +25% to +55% for the ion, depending on the coordination) lead to larger volume changes during cycling. Sodium-based electrodes might therefore degrade faster and the formation of stable interfaces might become more difficult. But the smaller size of the lithium ion corresponds to a larger charge density, and the lithium ion polarizes it environment stronger than the sodium ion. This causes severe differences in chemical bonding and ion mobility.
6. The solubility of sodium and lithium compounds in solvents are different. The discharge products and/or interphases (SEI formation) can therefore dissolve to different degrees and electrolyte solutions might have different properties.

2 Lithium–oxygen (Li/O_2) and sodium–oxygen (Na/O_2) batteries

This section is organized as follows. Firstly, the basic operating principles and energy densities of Li/O_2 and Na/O_2 cells are discussed. Secondly, the state-of-the-art knowledge on Li/O_2 cells is summarized. As several reviews have been published in this field, we will only briefly highlight important achievements and discuss recent developments. Thirdly, the available literature on the Na/O_2 cell is summarized and similarities and differences to the analogue Li/O_2 cell are discussed. Li/S_8 and Na/S_8 batteries are discussed the same way in chapter 3. The section will end with a brief summary and outlook.

2.1 Operating principles and general remarks

The operating principle of a lithium–oxygen battery is depicted in Figure 2b. The major difference compared to Li-ion batteries is that the battery is designed as an open system that enables uptake and release of atmospheric oxygen at the cathode during cycling (hence the name "lithium–air battery", which is misleading as mostly pure oxygen gas is used). During discharge, lithium is oxidized at the negative electrode and oxygen is reduced on the positive electrode. Similar to a fuel cell cathode, the positive electrode is a porous, electron-conducting support (gas diffusion layer, GDL) that enables oxygen transport, oxygen reduction (ORR) and oxygen evolution (OER) during cell cycling. Carbon-based materials are mostly used for this purpose. Considering the basic principle of this cell concept, some challenges are immediately obvious: (1) The implementation of special membranes is necessary to prevent contamination of the cell by unwanted gases from the atmosphere (N_2, CO_2, and also H_2O for the case of non-aqueous systems) and to protect the metal electrode from oxygen exposure. At the same time, drying out of the cell due to solvent evaporation must be avoided. (2) The gas transport must be fast enough to enable sufficiently fast discharging and charging. (3) The cell needs to provide enough free volume to accommodate the discharge product.

The reaction product depends on the type of electrolyte used. In aqueous electrolytes, water becomes part of the cell reaction and dissolved LiOH is formed during discharge, which precipitates as $LiOH{\cdot}H_2O$ once the solubility limit is reached. The need to protect the lithium anode from direct contact with water is experimentally challenging, so most research has been devoted to lithium–oxygen batteries with an aprotic electrolyte. Some possible discharge products can be directly predicted from the Li–O phase diagram shown in Figure 3a. Under ambient conditions, the thermodynamically stable phases are lithium oxide (Li_2O) and lithium peroxide (Li_2O_2). As these compounds are insulators, GDLs with a high surface area are used to improve the kinetics. Two other cell concepts that have been studied to a lesser extent are cells with a mixed aprotic/aqueous electrolyte and cells based on solid electrolytes. A sodium–oxygen battery can be designed exactly the same way but the phase diagram (Figure 3b) shows that in addition to Na_2O_2 and Na_2O, sodium superoxide (NaO_2) can also be formed (although possibly only kinetically stable under ambient conditions). The relative stability of NaO_2 was recently calculated by two groups with somewhat controversial results (see the section The sodium–oxygen (Na/O_2) battery for more details). Sodium ozonide (NaO_3) has been frequently reported as being unstable under ambient conditions and hence is not considered. Different discharge products may form in alkali-metal–oxygen cells. As will be discussed later in more detail, the discharge products in aprotic electrolytes are Li_2O_2 in Li/O_2 cells, and Na_2O_2 and NaO_2 (and $Na_2O_2{\cdot}2H_2O$) in Na/O_2 cells. It is an open and interesting question whether the relative stability of the different alkali oxides is correctly represented in

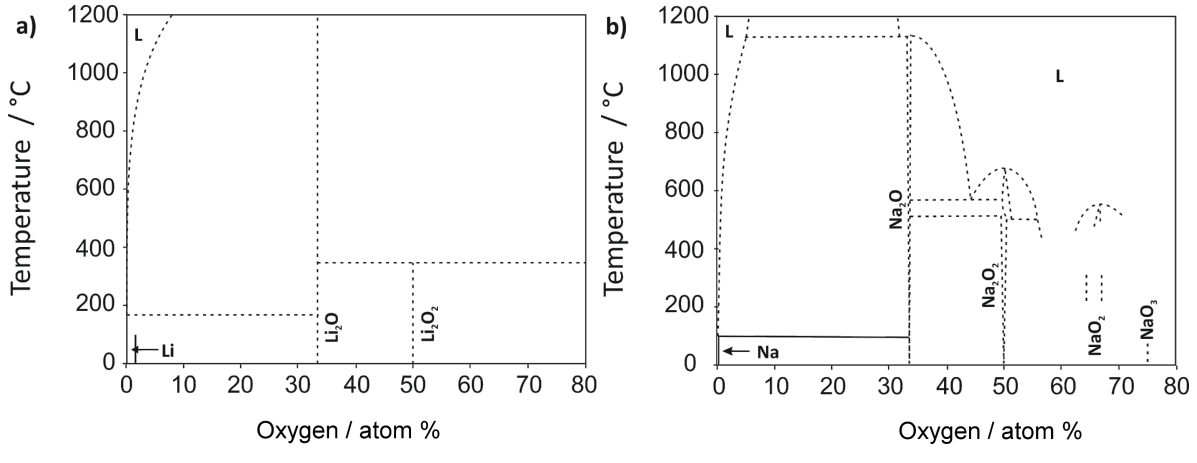

Figure 3: (a) The Li–O phase diagram. (b) The Na–O phase diagram. Figure redrawn based on [18] and [19].

the phase diagrams, as the influence of water may have been overlooked. It is well known that even small amounts of water can stabilize oxide phases, which are otherwise absent in the phase diagram [17].

The theoretical cell voltages and energy densities of the cell reactions are summarized in Table 1. We note that also potassium-oxygen batteries are being studied [20,21]. The energy densities however, are lower. The values for energy densities vary depending on whether the weight of oxygen is included or not, but all metal–oxygen batteries are superior compared to Li-ion batteries in terms of theoretical energy capacity. This is also the case for cells with NaO_2 as a discharge product, although they are based on one-electron transfer. It is important to note that all values in Table 1 are theoretical values. As the concept of metal–oxygen batteries requires many additional design-related components (e.g., gas diffusion layer, membranes to minimize oxygen diffusion towards the metal anode and to minimize access of other detrimental gases from the atmosphere) the weight penalty for reaching a commercial product will be much higher as compared to LIBs. The estimated values of the practical energy density vary greatly. Values of 1700 Wh/kg at the cell level and 850 Wh/kg at the battery level have been suggested by Girishkumar et al. [22], while Christensen et al. estimated around 1300 Wh/kg for the cell level [23]. PolyPlus, one of the leading companies working on lithium–air batteries, project 600 Wh/kg and 1000 Wh/L, respectively [24]. Recently, Gallagher et al. comprehensively studied the use of Li–air batteries for electric vehicles (EVs) and predicted values of around 250–500 Wh/kg and 300–450 Wh/L on the system level. The authors concluded that Li–air batteries will not be a viable option for commercial automotive applications [25], which then also would exclude Na–air systems. An additional challenge for electric vehicle application is that the current densities of lithium–oxygen cells (usually below 1 mA/cm^2) are still too small and an improvement by one to two orders of magnitude is necessary, as the target current density should be in the range of 8–80 mA/cm^2 [23,26]. Although these estimates depend on the assumptions made, it is clear that the competition between lithium–oxygen batteries and LIB technology will depend on the application. In any case, the limits of such a technology will only be fully apparent once a meaningful prototype has been built. The only report of a fully engineered cell reported in the literature is given by PolyPlus for a primary, aqueous, lithium–air battery. Their cells with a total capacity of about 10 Ah achieved 800 Wh/kg at a current density of 0.3 mA/cm^2 [24]. Given the fact that research on rechargeable lithium–oxygen cells is still at a more fundamental level, possible applications should therefore not be restricted to EVs.

For sodium cells, the theoretical energy densities are smaller compared to the analogue lithium systems. Therefore, the development of a high energy device might be more challenging unless the sodium cell chemistry provides specific advantages which might include: (1) faster kinetics of the oxygen electrode

Table 1: Theoretical cell voltage, $E°$, gravimetric and volumetric energy density, W_{th}, and charge density Q_{th} for lithium–oxygen and sodium–oxygen batteries with a metal anode. Values for the gravimetric energy densities are given without and including the weight of oxygen. All other values given refer to the discharged state. Thermodynamic data derived from HSC chemistry for all compounds in their standard state at 25 °C. Calculations for the aqueous systems are simplified and assume formation of hydrated hydroxide with all water resulting from the electrolyte.

Cell reaction	$E°$ / V	W_{th} / Wh/kg	Q_{th} / mAh/g	W_{th} / Wh/L	Q_{th} / mAh/cm^3
$4Li + O_2 + 2H_2O \underset{Charge}{\overset{Discharge}{\rightleftharpoons}} 4LiOH \cdot H_2O$	3.40	2684 / 2172	639	3280	1634
$2Li + \frac{1}{2}O_2 \underset{Charge}{\overset{Discharge}{\rightleftharpoons}} Li_2O$	2.91	11229 / 5216	1794	10501	3606
$2Li + O_2 \underset{Charge}{\overset{Discharge}{\rightleftharpoons}} Li_2O_2$	2.96	11421 / 3456	1168	7983	2698
$4Na + O_2(g) + 2H_2O \underset{Charge}{\overset{Discharge}{\rightleftharpoons}} 4NaOH \cdot H_2O$	2.77	1486 / 1281	462	–	–
$2Na + \frac{1}{2}O_2 \underset{Charge}{\overset{Discharge}{\rightleftharpoons}} Na_2O$	1.95	2273 / 1687	867	3828	1968
$2Na + O_2 \underset{Charge}{\overset{Discharge}{\rightleftharpoons}} Na_2O_2$	2.33	2717 / 1602	689	4493	1936
$Na + O_2 \underset{Charge}{\overset{Discharge}{\rightleftharpoons}} NaO_2$	2.27	2643 / 1105	488	2431	1074
Li-ion (average cathode vs Li/Li$^+$)	3.8	530	140	2300	600

in the case of NaO_2 as a discharge product, (2) a higher tolerance against atmospheric nitrogen as no stable nitride exists, (3) cell concepts with a molten sodium electrode [26], or (4) the availability of beta-alumina as a solid electrolyte that might enable cell concepts including solid membranes.

Considering all of these aspects, lithium–oxygen and sodium–oxygen batteries are very attractive means for energy storage in theory, but the development of practical cells is an ambitious goal. Even in the best scenario, such materials are unlikely to be developed for EV applications. However, the major showstopper for the development of rechargeable alkali–air devices is that the cell systems usually suffer from severe side reactions that hinder stable cell cycling for a large number of cycles. As will be discussed below, the sodium–oxygen cell indeed shows some promising advantages over the lithium system but several fundamental challenges must be understood and solved before the development of a practical battery might become feasible.

2.2 Classification of voltage profiles

The basic properties of a cell reaction can be easily discerned from diagrams showing the voltage profiles (discharge/charge curves) as their shape provides direct information on the complexity, reversibility and efficiency of the cell reactions. At moderate currents, most of the Li/O_2 and Na/O_2 batteries show quite similar discharge curves: the discharge voltage is more or less constant and comparably close to the theoretical cell potential. The discharging stage ends with a sudden potential drop ("sudden death"). The charging curves, however, vary significantly and heavily depend on the cell configuration (sodium or lithium cell, type of electrolyte, use of catalysts, type of GDL, etc.). So in order to more easily discuss the experimental results, the classification of the voltage profiles according to the shape of the charging curves is useful (Figure 4).

The starting point of the matrix is the ideal cell reaction, classified as Type 1A. The voltage profile is characterized by negligible overpotentials for discharge and charge and a Coulombic

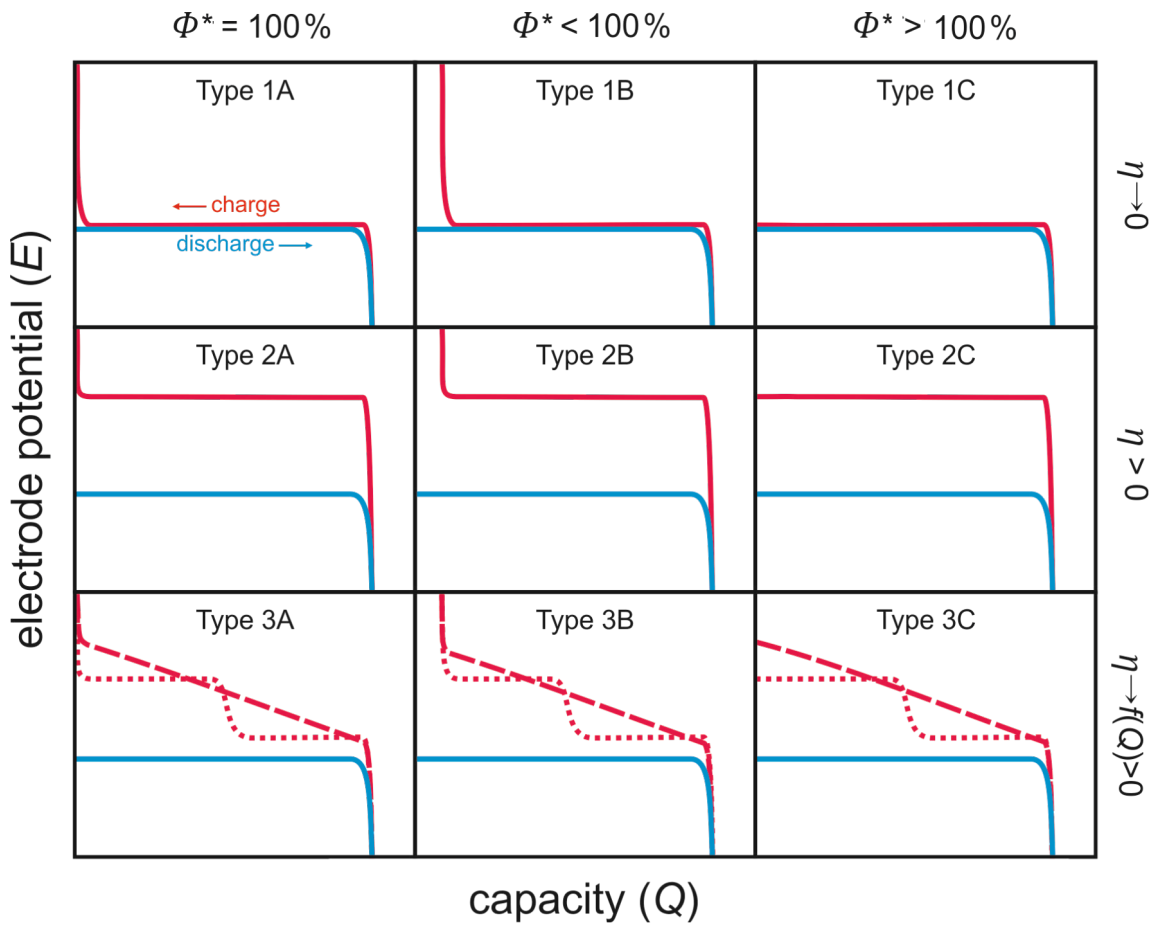

Figure 4: Matrix for classifying voltage profiles of metal–oxygen batteries. Type 1A is the ideal case. Frequently observed are Type 1B, 2C, 3B and 3C. The coulombic efficiency is calculated as $\Phi = Q_{charge}/Q_{discharge} \times 100\%$.

efficiency of Φ = 100%, that is, the charging voltage is close to its theoretical value and charging ends with a sudden increase in cell potential as soon as all discharge products are decomposed. Based on this ideal cell reaction, the following matrix can be derived.

Type 1: The combined overpotentials (sum of the overpotentials during discharge and charge) approach zero, meaning that kinetic limitations are negligible.

A: Coulombic efficiency = 100%. The cell reaction is completely reversible. B: Coulombic efficiency < 100 %. The reaction is only partially reversible. Possible reasons are that some of the discharge product became electrochemically inactive, lost contact to the electrode, or underwent irreversible side reactions with other cell components. C: Coulombic efficiency > 100 %. Either electrochemical side reactions or a so-called shuttle process (chemical shortcut) between both electrodes takes place. A shuttle process can be intentional (e.g., overcharge protection in LIBs) or unintentional (e.g., polysulfide shuttle in lithium–sulfur batteries). Unless it is intentional, Coulombic efficiencies exceeding 100% are always a sign of undesired side reactions. Note that in this case the Coulombic efficiency of the desired cell reaction is also below 100%. Values exceeding 100% simply arise from the fact the shuttling/side reactions give rise to additional external currents leading to charging capacities exceeding the discharge capacities.

Type 2: Considerably high combined overpotential occurs and the cell kinetics are sluggish. Various processes can contribute to overpotential, but using catalysts or optimizing the transport properties might be effective strategies for improvement.

Type 3: The voltage continuously increases during charging and might exhibit additional plateaus. Such a behavior indicates a more complex electrode reaction. In most cases, this is a strong indication of undesired side reactions. Additional plateaus during charging can originate from the electrochemical decomposition of side products stemming from undesired side reactions between cell components and the discharge product. For example, Li_2O_2 can react with the electrolyte to form Li_2CO_3, which decomposes during charging at high voltages. Another possibility is that the cell discharge was incomplete (e.g., the discharged state is a mixture of Na_2O_2 and NaO_2) and the different discharge products decompose at different potentials during charging.

The matrix certainly includes some simplifications: side reactions might be time dependent, the voltage profile can change during cycling, overpotential increases with current density, etc. However, the matrix allows for a straightforward classification of the large number of different experimental results published. Briefly, the more different the voltage profile is from the ideal case (Type 1A), the more challenges that have to be tackled to achieve a reversible cell reaction. So far most metal–oxygen batteries show the following behavior when cycled at moderate rates: Type 1B is found for Na/O_2 cells with NaO_2 as discharge product. Type 2C, 3B, and 3C are found for Li/O_2 and Na/O_2 cells with either Li_2O_2, Na_2O_2, or $Na_2O_2{\cdot}2H_2O$ as a discharge product.

It is important to note that values for the capacity, *Q*, of metal–oxygen cells are presented differently as it is usually done. The common way in battery research is to state the capacity in mAh per gram of active material, that is, per gram of LCO or sulfur, for example. This is possible because the electrode contains all active material and the battery is a closed system. In open metal–oxygen batteries, the active material (oxygen) is not part of the electrode and the discharge product forms as a new phase during discharge. Therefore, capacity values are usually given in mAh per gram of carbon support. As the absolute amount of carbon used is usually very small, the reported capacity values can reach very high numbers, easily exceeding 1000 mAh/g. Stating this value only, however, is clearly not sufficient to judge the performance of the cell and may easily mislead the uninformed reader [22,27]. At a minimum, carbon loading (mg/cm^2), electrode size and thickness of the carbon layer (if known) and the total amount of charge should be stated. Given this, the charge density (mAh/cm^3) and areal capacity (mAh/cm^2) can be calculated and benchmarked against commercialized LIB materials (approximately 1–4 mAh/cm^2 and 350–600 mAh/cm^3). A comparable problem is that the common definition of the C rate cannot be applied to metal–oxygen cells without further assumptions, and therefore, discharge and charge rates are usually given as current density (calculated by using the cell cross section).

2.3 State-of-the art and recent developments

2.3.1 The lithium–oxygen (Li/O_2) battery: In 1969, A. E. Lyall filed a patent application on "A room-temperature-operated fuel cell comprising an oxygen electrode, a lithium metal-containing electrode, and an electrolyte comprising an inert, aprotic organic solvent […], which contains an inorganic or organic ionizable salt […]" [28]. Interestingly, the components of this Li/O_2 battery are remarkably close to those utilized today. The pioneering work on rechargeable, room temperature, Li/O_2 batteries with a non-aqueous electrolyte can be summarized as follows. In 1996, Abraham et al. reported on "A polymer electrolyte-based rechargeable lithium/oxygen battery" [29]. This cell could be re-charged at room temperature at least three times at potentials as low as 3.8 V. In 2002, Read characterized a Li/O_2 cell comprising different carbon materials and

different electrolyte formulations [30]. This was the first work to analyze and correlate the amount of consumed gaseous oxygen with respect to the transferred electric charge, and found that this value varies strongly depending on electrolyte composition. As will be discussed in the following sections, this kind of characterization is crucial for both evaluating and understanding aprotic Li/O_2 cells. He interpreted this variation using mixtures of Li_2O_2 and Li_2O which are formed during discharge.

Today's strong interest in Li/O_2 batteries was most likely initiated by the work of Bruce et al. who reported on a Li/O_2 cell in 2008 that could be efficiently cycled, resulting in capacities as high as 3000 mAh/g_{carbon} by introducing α-MnO_2 nanowires as catalyst in the oxygen cathode [31]. From 2008 onwards, the number of publications on Li/O_2 batteries rapidly increased. The progress in Li/O_2 research and development is the subject of numerous review articles [22,32-34]; therefore, we focus here on a brief summary of, in our opinion, the major trends in current research efforts.

2.3.1.1 Catalysts: As shown by Bruce et al., Li/O_2 cells with liquid aprotic electrolyte can apparently be recharged, but rather high potentials (>4 V vs Li/Li^+) for the decomposition of Li_2O_2 (OER) are required. Hence, research focused on the preparation and characterization of catalytically active materials for Li/O_2 cells is aimed at higher discharge capacities and lower overpotentials during cycling. Various metal oxide materials, mostly manganese oxides (MnO_2, Mn_3O_4), but also others have been

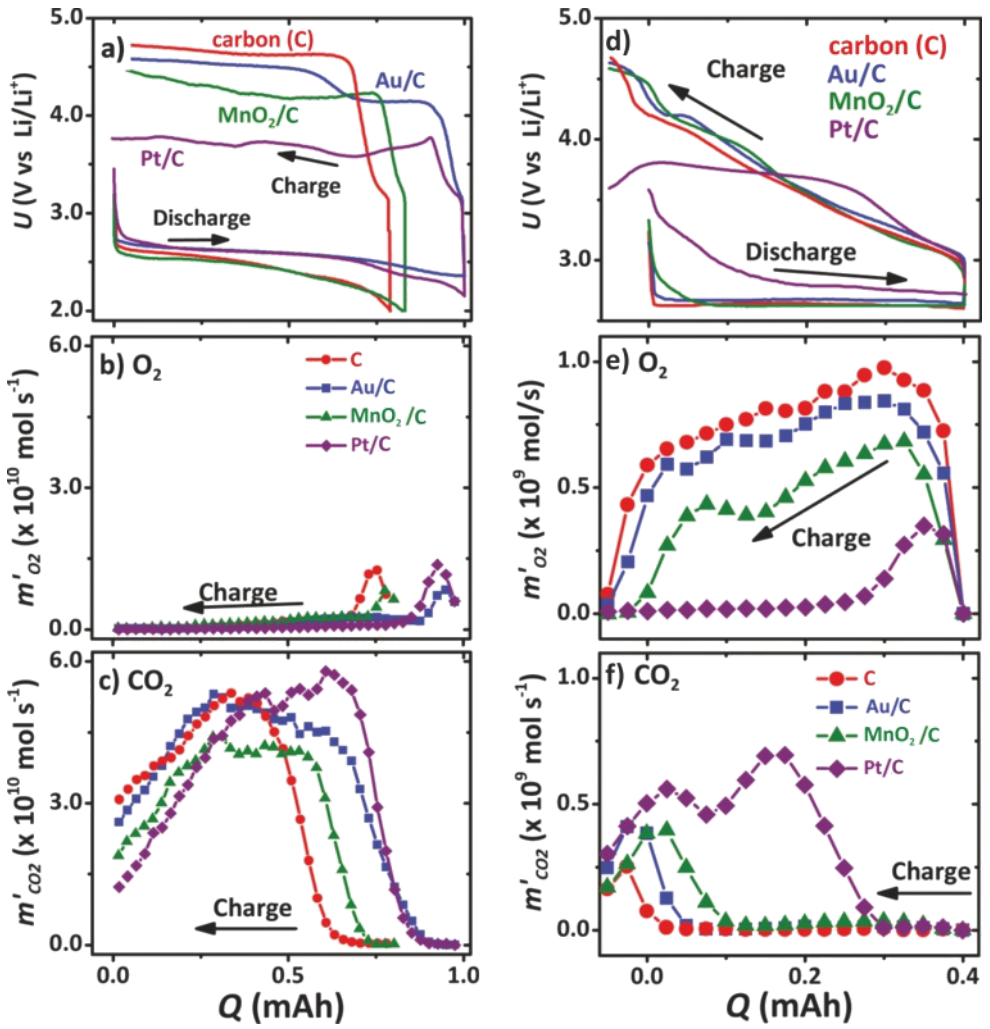

Figure 5: DEMS analysis of Li/O_2 cells with different electrolyte compositions, namely a mixture of propylene carbonate and dimethoxyethane, PC:DME, (a–c) and pure dimethoxyethane, DME, (d–f). Furthermore, gold, platinum and manganese dioxide were tested as heterogeneous catalysts. (a) and (d) show the galvanostatic cycling characteristics. (b) and (d) show the desired oxygen (O_2) evolution during charging, and (c) and (f) show the corresponding carbon dioxide (CO_2) evolution measured. Figure adapted with permission from [42], copyright 2011 American Chemical Society.

proposed [9,31,35-38] as well as noble metals [39-41]. In 2011, McCloskey et al. attentively figured out that catalysts such as Pt, MnO_2 or Au also promote the decomposition of the aprotic electrolyte rather than the oxygen evolution reaction (see also Figure 5) [42]. Although both the functionality and the necessity of heterogeneous catalysts in Li/O_2 cells remain unsolved, the search for improved heterogeneous catalysts for improved cyclability is still the subject of many new articles on Li/O_2 batteries. The most promising catalyst material, ruthenium nanocrystals, was reported by Sun et al., and the cells show a type 3A hysteresis (see Figure 4) with a charge potential as low as 3.5 V [41].

2.3.1.2 Electrolyte instability: Liquid aprotic electrolytes containing carbonate-based solvents such as propylene carbonate (PC), ethylene carbonate (EC), diethyl carbonate (DEC), or dimethyl carbonate (DMC) have been applied in almost all of the experimental studies on catalyst materials between 2006 and 2010, because these compounds are well used in LIBs. A comprehensive overview of the properties of liquid lithium electrolytes is given in [43]. In the beginning, only minor attention had been paid to clarify the chemistry taking place in the cells, for example by analyzing all chemical species being formed during cycling. In 2010 Mizuno et al. reported an FTIR and TEM study of the reaction products in Li/O_2 cells employing a PC based electrolyte [44]. They concluded that, although the cell was cycled up to 100 times, lithium carbonate (Li_2CO_3) and lithium alkyl carbonate species (RO–(C=O)–OLi) instead of Li_2O_2 were found as discharge products. In the following, similar observations for various carbonate-based solvents were reported by other groups as well [45-48]. The experimental findings are supported by computational studies looking into molecule stability and possible decomposition pathways for the solvents [49,50] and it is now clear that carbonate-based electrolytes are not suitable for aprotic Li/O_2 cells. In addition it was found that many electrolyte salts are at least partially decomposed during cell cycling as well [47,51-53]. From this perspective, it is of note that even as early as 1991, Aurbach et al. reported the irreversible decomposition of propylene carbonate (PC) in the presence of oxygen during cyclic voltammetry experiments [54].

2.3.1.3 Stable electrolytes: The finding that the decomposition of the carbonate solvents was responsible for much of the capacity in Li/O_2 cells was a setback that quickly changed the research focus to the stability and potential decomposition reactions of the electrolyte components. Three different reactive oxygen species may be involved in solvent decomposition reactions: (a) molecular oxygen (O_2), (b) superoxide ($O_2^{\bullet -}$, "LiO_2") and (c) peroxide species (O_2^{2-}, Li_2O_2). The individual role of these different species in the decomposition reactions is still unclear. In a number of studies on different solvents have been made including ionic liquids [55-57], sulfoxides (DMSO) [58-60], amides [61,62], and others [62-64]. The ether-based glyme solvents with the general structure CH_3–O–(CH_2–CH_2–O)$_n$–CH_3 with n = 1–4 are the current state-of-the-art solvents [65-69], although they are not entirely stable. A solvent with better performance still must be found. Adams et al. recently reported on a chemically modified monoglyme (DME), 2,3-dimethyl-2,3-dimethyoxybutane, as a promising solvent as it leads to a significantly lower CO_2 evolution (see DEMS) and lower overpotentials for both discharge and charge [70]. Analogous to the lithium–sulfur batteries, the use of lithium nitrate ($LiNO_3$) seems to improve the cyclability of Li/O_2 cells as well. In publications by Liox Power Inc., it was shown that $LiNO_3$ leads to an improved stability of the lithium electrode solid electrolyte interphase (SEI) formation [61]. Kang et al. showed that it also leads to an improved stability of carbon at the cathode [71].

2.3.1.4 Differential electrochemical mass spectrometry (DEMS) studies: The electrolyte decomposition is a major drawback that made DEMS studies inevitable in Li/O_2 cell research. Today, this real-time analysis of the gaseous species being consumed or released during cell cycling is a necessary standard technique. In an ideally operating cell, only oxygen (O_2) evolves during recharge, but in reality, other products such as CO_2, H_2O or H_2 are detected and give evidence for unwanted side reactions. Therefore, DEMS or online electrochemical mass spectrometry (OEMS) was introduced into the Li/O_2 battery field and is now one of the most important, but seldom employed, diagnostic tools of current research [46,72-77]. Figure 5 shows the potential of DEMS analysis when comparing different electrolyte and oxygen electrode materials in an Li/O_2 cell [42]. Figure 5a,d shows the galvanostatic cycling characteristics for a PC:DME electrolyte and a pure DME electrolyte, respectively. For both electrolytes, in addition to a pure carbon electrode, heterogeneous catalysts, such as Pt, Au and MnO_2 were also tested. It was shown that the catalysts (especially in combination with the PC:DME electrolyte) lead to a significant reduction of the charge overpotential, and in the case of Pt, by almost 1 V in comparison to pure carbon. However, the corresponding DEMS data in Figure 5b,c clearly prove that only minor amounts of oxygen (O_2) but mainly CO_2 is evolved during the charging of the cell. Thus, by means of DEMS, McCloskey et al. could clearly prove that the improved rechargeability due to the heterogeneous catalysts is not related to an improvement of the Li_2O_2 decomposition, but rather to the promotion of the electrolyte decomposition. In contrast, in pure DME electrolyte, oxygen evolution is indeed observed. However, in this case, the catalyst materials had almost no impact on the charge overpotential, but again only led to an increased evolution of CO_2.

2.3.1.5 Number of electrons per oxygen molecule, e^-/O_2: As already mentioned above, Read observed that in certain electrolytes the oxygen consumption during discharge was too low for the sole formation of Li_2O_2 and proposed that Li_2O is formed in concomitance [30]. Looking back to these results, one can now definitively assume that Read observed the partial decomposition of the electrolyte during discharge rather than the formation of Li_2O species. Hence, it is of crucial importance to understand that for metal–oxygen cells the reversibility cannot be proven by solely stating Coulombic efficiencies. It is, as introduced by Read, the ratio between consumed or released oxygen and the amount of transferred charge that gives the true reversibility. For an ideal Li/O_2 cell, where Li_2O_2 is reversibly formed, two electrons are transferred for each reacting oxygen molecule, or 2.16 mAh for 1 mL of gaseous oxygen at 298 K and 10^5 Pa. Any deviation from this ratio is a strong indication for (partial) malfunction and hence, this value is essential, especially when new electrolyte or electrode components are tested. A simple but effective way to measure this ratio is the usage of a pressure sensor and a hermetic gas reservoir as introduced by McCloskey et al. [46,78] or via quantitative DEMS/OEMS, which in addition allows for the identification and separation of the gaseous reactants [42,60,66,68,74]. In addition to the analysis of gaseous reactants, first attempts are also made to quantify the amount of discharge product formed [67,78-80]. This will also be an important step towards true reversibility evaluation.

2.3.1.6 Electrode materials: Obviously a Li/O_2 cell is a very reactive environment and it seems likely that the different oxygen species would also react with other components of the oxygen electrode. Black et al. exposed battery components to potassium superoxide dissolved in aprotic liquids and found that polyvinylidene fluoride (PVDF), a common binder material, decomposes while lithium fluoride (LiF) is formed [81]. They suggest that LiO_2, a strong base that is formed as an intermediate in a Li/O_2 cell, extracts protons from the PVDF polymer. From the thermodynamic point of view, carbon is also reactive towards, for example, Li_2O_2 or oxygen at high oxidative potentials, too. For this purpose McCloskey et al. employed a ^{13}C carbon electrode and monitored CO_2 species via DEMS evolved during the charge process [82]. The appearance of $^{13}CO_2$ at the end of the charge process was taken as evidence for carbon oxidation. Similar findings were made by Thotiyl et al. (Figure 6) who proposed that carbon oxidation can be avoided as long as potentials remain below 3.5 V vs Li/Li^+ [83]. The same group also investigated non-carbon electrodes, such as nanoporous gold or titanium carbide (TiC) [60,84]. Both materials are claimed to significantly improve the cycle performance compared to carbon electrodes due to a higher chemical stability towards lithium oxide species. On the other hand, the solvent employed in their study (DMSO) is known to be unstable in Li/O_2 cells [85,86]. Notwithstanding the above, the understanding of electrode corrosion and the search for stable electrode materials, either modified carbons or non-carbon materials, is of crucial importance for a reliable Li/O_2 battery.

2.3.1.7 Particle growth and dissolution: At first glance, the chemistry of a Li/O_2 cell may appear quite simple, however, due to worldwide research efforts within the last four years, it was recognized that it is in fact, a very complex cell chemistry. As a consequence it was necessary to refocus on fundamental aspects such as the growth and dissolution process of Li_2O_2 particles during cycling on a microscopic scale. Various morphologies of Li_2O_2 deposits are reported in literature. On the one hand, so-called Li_2O_2 "donuts" or toroids are reported

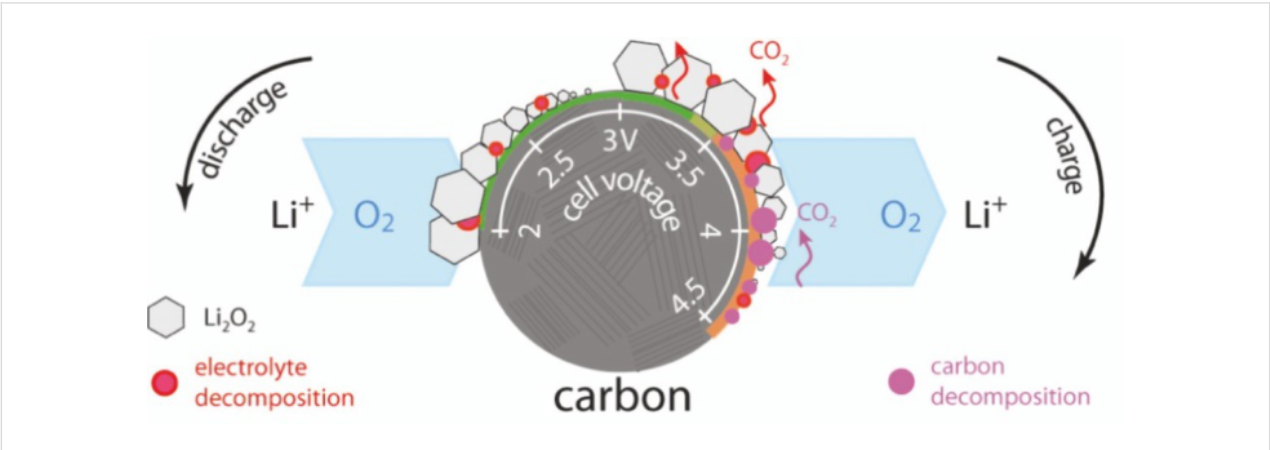

Figure 6: Sketch by Thotiyl et al. illustrating their findings on the oxidation of the carbon electrode. At discharge at potentials below 3 V, mostly Li_2O_2 is electrochemically formed and accompanied by electrolyte decomposition. During recharge at potentials between 3.0 and 3.5 V, CO_2 evolution is mainly related to electrolyte decomposition. Lastly, at potentials higher than 3.5 V, oxidation of the carbon electrode takes place. Figure adapted with permission from [83], copyright 2012 American Chemical Society.

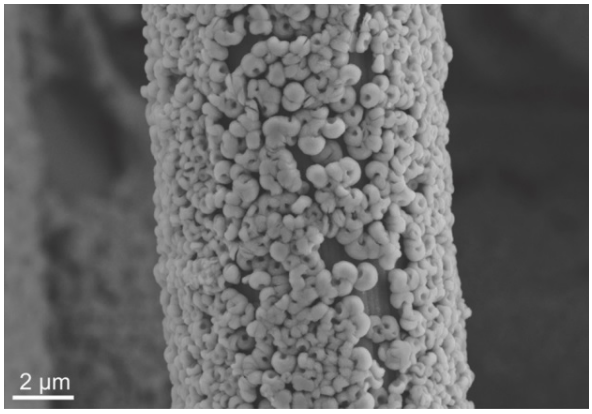

Figure 7: SEM image of toroidal Li_2O_2 nanoparticles on a carbon fiber (10 µm in diameter) that form as a discharge product in lithium–oxygen cells (C. L. Bender, JLU Giessen).

that form to a diameter of up to 1 µm, depending on solvent and cycling conditions (see Figure 7). On the other hand, thin film coverage of the carbon electrode is found. It is reported that at low current densities large toroid-like particles form and that at high current densities Li_2O_2 film formation takes place [32,87]. Interestingly, Read basically made the same observation in 2002 and concluded that large particles could only grow if the oxide (Li_2O_2) is (a) soluble in the electrolyte (b) able to migrate on electrode surface or (c) capable of catalyzing the oxygen reduction [30]. Theoretical studies are particularly focused on possibility (c) and look for electric transport in Li_2O_2. Since Li_2O_2 is an intrinsic wide band gap insulator, additional transport mechanisms such as transport along metal-type surfaces or hole polaron transport are proposed [88-91]. The assumption of a soluble redox-active species (e.g., soluble O_2^-), as polysulfides in the case of lithium–sulfur or sodium–sulfur batteries, has only very recently been seriously taken into account. Viswanathan et al. suggest that Li_2O_2 grows only to film deposits of 5–10 nm in thickness because charge transport through the Li_2O_2 layer can only proceed by hole tunneling [92,93]. In a very recent study they propose that the comparably large donut structures can only be observed in the presence of water in the electrolyte, which leads to soluble superoxide species [94]. Their findings, however, are in contrast to those of Zheng et al. who were able to operate a model all-solid-state Li/O_2 cell, without any liquid electrolyte, in an environmental SEM and observed the formation of large toroid particles larger than 500 nm [95]. To conclude, even the dissolution process of Li_2O_2 during battery operation is not fully understood and continues to be a part of research efforts.

2.3.1.8 Electrolyte additives: The electrochemical activity of Li_2O_2 itself is quite poor without doubt, especially for the charge process (OER). Hence catalysis is necessary especially when aiming for experimental current densities. The results of heterogeneous catalysts until now did not fulfill the expectations. A new and promising concept is to add soluble and redox-active molecules to the liquid electrolyte. In 2011 Liox Power Inc. filed a patent application on such "soluble oxygen evolving catalysts for rechargeable metal–air batteries" [96]. Those often called redox mediators (RM) molecules possess a redox potential higher than that of Li_2O_2 ($E°_{RM} > E°_{Li2O2}$ = 2.96 V vs Li/Li^+). During recharge of the battery the RM molecules are oxidized at the oxygen electrode. Subsequently, the oxidized RM molecules oxidize Li_2O_2 chemically and hence catalyze the OER. In 2013 Chen et al. reported on tetrathiafulvalene (TTF) as RM with redox potentials, TTF/TTF^+ and TTF^+/TTF^{2+}, of 3.4 to 3.7 V. With TTF in a DMSO:$LiClO_4$ electrolyte the Li/O_2 cells showed a Type 1C hysteresis and significantly improved kinetics for the charge process. In addition e^-/O_2 ratios very close to two, as expected for Li_2O_2 oxidation, were claimed [97]. Also lithium iodide [98] and TEMPO [99] have been recently studied as RMs with promising results (see Figure 8). It is worth noting that redox mediators (also called "relays") are used also in other applications for the improvement of poor electrode kinetics.

An interesting and complementary approach is to increase the solubility of oxides species (e.g., Li_2O_2) in the liquid electrolyte which would allow fast transport of oxide species to active electrode sites. Lim et al. synthesized TFSI based cations that are able to considerably increase the solubility of Li_2O_2 in DMSO [98], and Lopez et al. reported on hexacarboxamide cryptands that are capable of incorporation of peroxide dianions in solution [100]. As these approaches are quite new, several questions such as long term functionality and stability of the molecular additives in an Li/O_2 battery need to be investigated. Nevertheless, we believe that major improvements are possible due to chemical tailoring of the molecules with respect to desired functionality.

In conclusion, several challenges for the development of aprotic Li/O_2 cells with competitive performance remain. Within the last few years more and more researchers focus on the chemical processes taking place during operation of metal–oxygen batteries, which surely will lead to deeper understanding of Li/O_2 batteries and its potential in application. This is remarkable, especially in the fast moving field of battery research, as experimental mechanistic studies are usually time demanding and require both a careful execution of experiments and the use of complex and often expensive analytical methods.

2.3.2 The sodium–oxygen (Na/O_2) battery: The sodium–oxygen battery is based on the same cell concept as the lithium–oxygen battery, however, only very little literature is

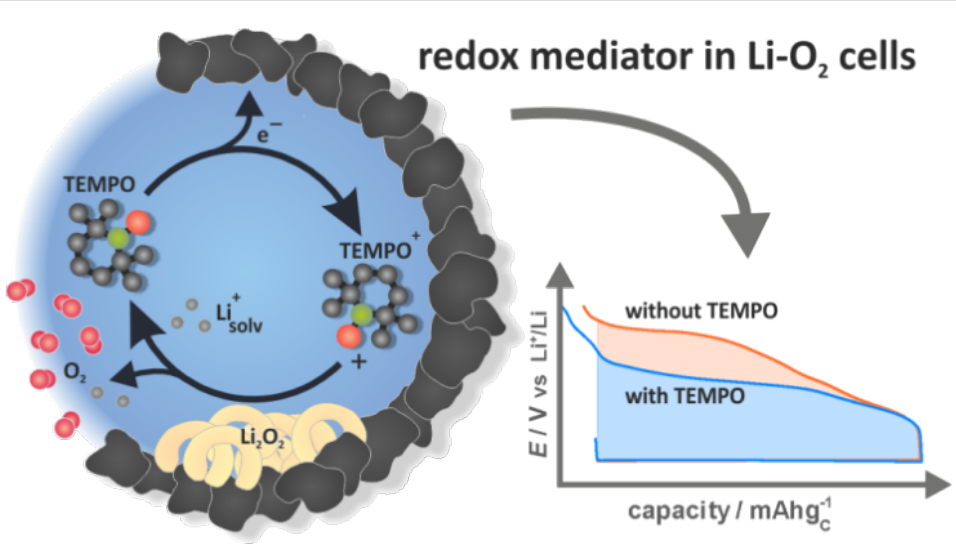

Figure 8: Illustration of TEMPO as a redox mediator (RM) in an Li/O_2 cell reversibly catalyzing the Li_2O_2 oxidation. Figure adapted with permission from [99], copyright 2014 American Chemical Society.

available. Mostly aprotic electrolytes have been used and only one study on a mixed aprotic/aqueous electrolyte has been published. This may be due to the strong reactivity of sodium with water. Although research on Na/O_2 cells started only in 2010 the number of publications now rapidly increases. To date, more than 20 studies have been published altogether. The currently most striking characteristic of aprotic Na/O_2 cells is that, in contrast to Li/O_2 cells, a number of different discharge products have been reported: sodium superoxide (NaO_2), sodium peroxide (Na_2O_2), sodium carbonate (Na_2CO_3), hydrated sodium peroxide ($Na_2O_2{\cdot}2H_2O$) and sodium hydroxide (NaOH). The underlying reason for this is not clear yet but it might be also related to the different experimental conditions used in the different studies. A summary of selected experimental parameters and reported discharge products is shown in Table 2.

Table 2: Literature overview on Na/O_2 cells summarizing experimental conditions and reported discharge products.

Reference	Cathode composition	Electrolyte	Discharge product	Verified by	Max. dis. capacity / mAh/g	Type[a]
Peled et al. [26]	E-TEK air electrode, 10% Pt support, XC72 coated with Na_2CO_3	0.1 M calixpyrrole, 1 M $NaClO_4$ in PEGDME/PC (90:10) + 1 wt % Al_2O_3	Na_2O_2 (assumed)	–	–	2C
Sun et al. [101]	Diamond-like carbon thin film	1 M $NaPF_6$ in EC:DMC 1:1	Na_2O_2 (Na_2CO_3)	FTIR , SAED	3600	2C
Das et al. [102]	Super P	1 M $NaClO_4$ in tetraglyme 0.75 M NaOTf in EMIM OTf	Na_2O_2 (O_2) / Na_2CO_3, $Na_2C_2O_4$ (O_2 + CO_2)	FTIR , XRD	1390 (O_2) / 183 (CO_2) / 3500 (40% CO_2)	–
Liu et al. [103]	Graphene nanosheets	0.25 M $NaPF_6$ in DME 0.25 M $NaClO_4$ in DME	Na_2O_2	SAED	9268	2C
Li et al. [104]	Graphene nanosheets and nitrogen-doped graphene nanosheets	0.5 M NaOTf in diglyme	Na_2O_2	XRD	8600	3B
Liu et al. [105]	$NiCo_2O_4$ nanosheets on Ni foam	1 M $NaClO_4$ in DME	Na_2O_2	FTIR, SAED	1762	3B
Kim et al. [106]	Ketjenblack	1 M $NaClO_4$ in PC, 1 M $NaClO_4$ in tetraglyme	Na_2CO_3 $Na_2O_2 \cdot 2H_2O$ / NaOH	FTIR, Raman, XRD	2800 (PC) / 6000 (4G)	2C
Jian et al. [107]	CNT paper	0.5 M NaOTf in diglyme, 0.5 M NaTFSI in tetraglyme	$Na_2O_2 \cdot 2H_2O$	Raman, XRD	7530	3B

Table 2: Literature overview on Na/O_2 cells summarizing experimental conditions and reported discharge products. (continued)

Yadegari et al. [108]	Carbon black N330 / NH_3 or CO_2 treated	0.5 M NaOTf in diglyme	$Na_2O_2 \cdot 2H_2O$ / little NaO_2	FTIR, XRD	2873	3C
Hartmann et al. [109]	Gas diffusion layer H2315	0.5 M NaOTf in diglyme	NaO_2	Raman, XRD	300	1B
Hartmann et al. [78]	GDL H2315	0.5 M NaOTf in diglyme	NaO_2	Raman, XRD	490	1B
Hartmann et al. [110]	GDL H2315	0.5 M NaOTf in diglyme	NaO_2	Pressure monitoring	280	1B
McCloskey et al. [67]	P50 Avcarb carbon paper	0.2 M NaOTf in DME	NaO_2	–	–	1B
Bender et al. [27]	GDL H2315, Ketjenblack, etc.	0.5 M NaOTf in diglyme	NaO_2	XRD	4000	1B
Zhao et al. [111]	Vertically aligned carbon nanotubes (VACNTs)	0.5 M NaOTf in tetraglyme	NaO_2	SAED, XRD	4200	1B/3B

[a]See Figure 4 for graphical representations of the different types.

Figure 9 shows a literature timeline of all studies on sodium–oxygen cells. Most of them report on the general cell chemistry and performance improvements in terms of capacity and cycle life. Some related studies including carbon dioxide assisted cells or high temperature cells are also included. These reports are shown in grey and will be discussed at the end of this literature survey. Also two review papers by Das et al. [112] and Ha et al. [113] have been very recently published.

Peled et al. were the first to publish an electrochemical cell based on the reaction of sodium with oxygen in 2010 [26]. The cell was adopted from a fuel cell design and consisted of a molten sodium electrode, a polyglyme/PC (90:10) based electrolyte with different additives and a Pt containing carbon electrode. The cell operated at 105–110 °C. The high temperature concept with molten anode was chosen for several reasons: Counteracting the sluggish cathode reactions, lowering the cell impedance, eliminating dendrites and minimizing interference with water and carbon dioxide. On the other hand, the high reactivity towards the electrolyte was an issue. The cell discharged at 1.75 V (100 µA) and was charged at 3.0 V (50 µA). The discharge product of a full discharge was assumed to be sodium peroxide without further proof by analytical techniques. Later on, the same group published a follow-up study with the main focus on investigating SEI formation and sodium plating/stripping in an ionic liquid based electrolyte [114]. Na_2SO_4 was added to the electrolyte as SEI former. Although sodium plating/stripping was obtained for 300 cycles without internal shortcuts, the efficiency with around 70–80% was still unsatisfying. In general, these results underline that studying the reversibility of the ORR/OER reactions in metal–air batteries is not sufficient as also plating/stripping of the alkali metal needs to be reversible in order to achieve a long cycle life. Cell discharge using this IL based electrolyte at 25 µA/cm^2 was characterized by a sloping decrease, charging (250 µA/cm^2) mainly occurred at about 3 V. As we will see in the following, the overall cycling behavior of this cell is very different from cells operating with a solid sodium anode at room temperature.

In 2011, Sun et al. showed first results on an aprotic, room temperature sodium oxygen cell (Figure 10a) [101]. In contrast

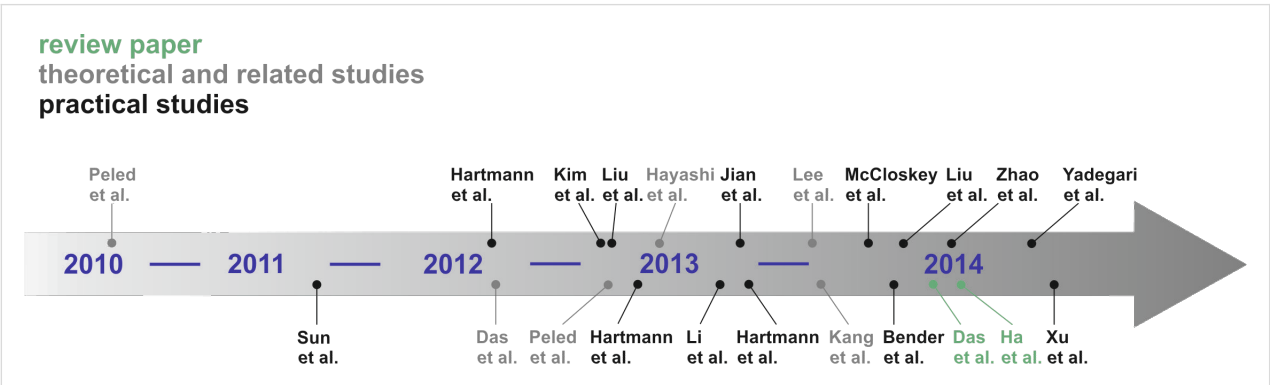

Figure 9: Literature timeline of research papers on aprotic sodium–oxygen batteries (ranked after date of acceptance).

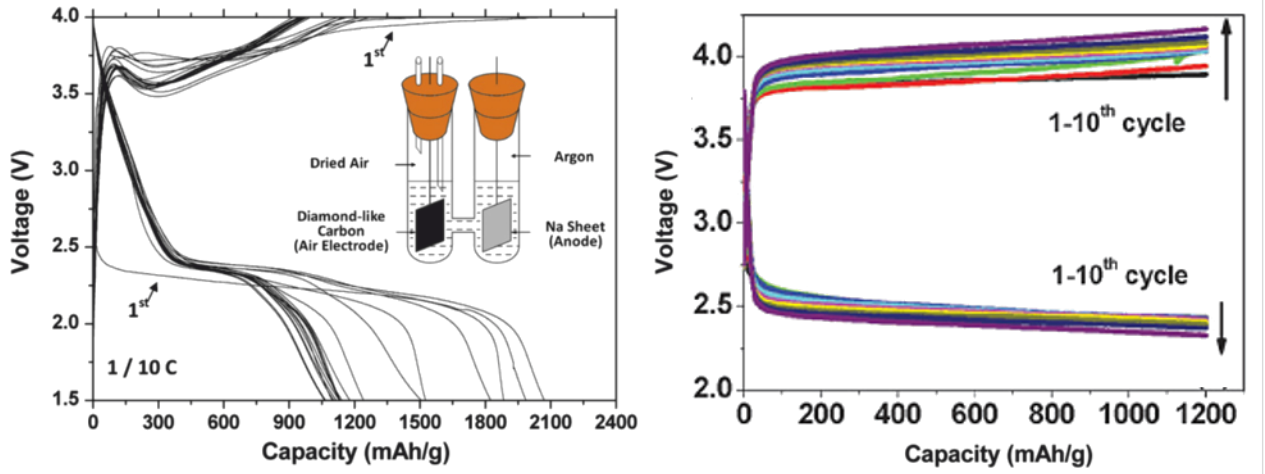

Figure 10: Sketch of the first room temperature sodium–oxygen cell and its discharge and charge potentials during the first ten cycles (left), Figure adapted with permission from [101], copyright 2012 Elsevier B.V. The voltage profile can be classified as Type 2C. Voltage profile of a sodium–oxygen cell with graphene nanosheets as cathode and $NaPF_6$ in DME as electrolyte (Type 2C) (right). The discharge product was identified as sodium peroxide. Figure adapted with permission from [103], copyright 2013 The Royal Society of Chemistry.

to Peled et al. they made use of a solid sodium foil as anode and a diamond-like carbon thin film electrode as cathode. In accordance with typical lithium–oxygen cells they used 1 M $NaPF_6$ in EC:DMC 1:1 as the liquid, aprotic electrolyte. The cell setup was an H-shaped glass cell. Using transmission electron microscopy, single area electron diffraction and Fourier transform infrared spectroscopy sodium peroxide (Na_2O_2) and sodium carbonate (Na_2CO_3) were proven as discharge products. These products vanished during charge with overpotentials exceeding 1 V similar to lithium–oxygen cells. Overall, the cell performed just like a typical lithium–oxygen battery, however, the discharge potentials were slightly lower (around 2.4 V), as expected. In 2013, the same group (Liu et al., [103]) used graphene nanosheets as cathode and $NaPF_6$ dissolved in monoglyme as electrolyte. This way, discharge capacities as high as 9268 mAh/g_{carbon} were achieved. Again, sodium peroxide was described as the discharge product and large overpotentials were observed (Figure 10b). In both cases, the voltage profile can be classified as Type 2C.

In 2012 Hartmann et al. [109] reported a sodium–oxygen battery with sodium superoxide (NaO_2) as discharge product. Unequivocal proofs for superoxide formation were provided by X-ray diffraction, Raman spectroscopy and pressure monitoring. SEM studies revealed that, in contrast to Li/O_2 cells for which nanoscopic Li_2O_2 toroids are found, NaO_2 forms large micrometer-sized cubic crystallites (compare Figure 7 with Figure 11). The cells showed only very small combined overpotentials of about 200 mV during cycling which was attributed to the kinetically favored one-electron transfer. Shortly after, similar findings were reported for potassium–oxygen cells. Here, KO_2 forms during discharge and a very similar voltage profile has been found [20]. The Coulombic efficiency of the sodium superoxide cell in the first cycle was around 90%, discharging and charging ended with a sudden voltage drop and increase, respectively. The voltage profile can therefore be classified as Type 1B, meaning that the cell cycles more ideal than Li/O_2 cells or Na/O_2 cells with peroxides as discharge products. The achieved discharge capacity with 300 mAh/g_{carbon} was relatively low due to the high mass of the free standing electrode. On the other hand, the absolute capacities were comparably high. Cycle life, however, was poor and the capacity faded to virtually zero within ten cycles. The study also included a direct comparison in cycling behavior between otherwise identical Na/O_2 and Li/O_2 cells. The latter showed a much smaller discharge capacity and the expected large overpotentials. Although the Na/O_2 cell with NaO_2 as discharge product shows a much more reversible cell reaction compared to the Li/O_2 cell, it should be noted that also the Na/O_2 cell is not entirely free from side reactions either. Overall, this study provided clear evidence that lithium–oxygen and sodium–oxygen batteries can behave completely different.

Later on, the same group published a more comprehensive study on their findings using a range of different methods including DEMS, pressure monitoring, XPS, SEM, UV–vis spectroscopy, XRD and Raman spectroscopy [78]. The reason why NaO_2 grows to such large crystals is still not clear yet, but precipitation of NaO_2 from a supersaturated solution was suggested as a possible growth mechanism. XPS studies

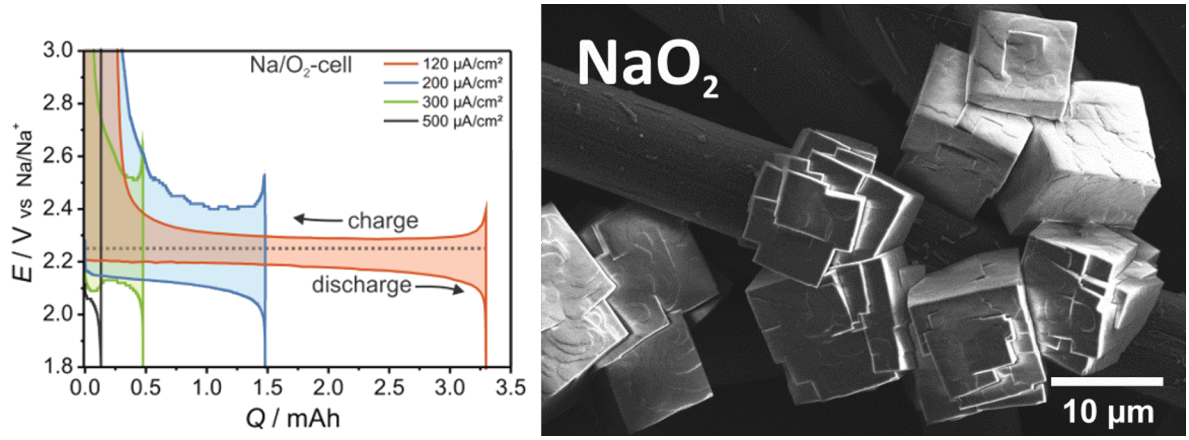

Figure 11: Discharge/charge curves (Type 1B) of a sodium–oxygen battery with NaO_2 as discharge product. The main differences compared to Li/O_2 cells are that only small overpotentials are observed and that the crystallite size of the discharge product is much larger (see SEM image on the right) [109].

showed that the reason for the poor overall reversibility might be due to decomposition of the conductive salt. Further, the issue of dendrite formation in Na/O_2 cells was discussed.

Kim et al. studied the influence of the electrolyte solvent on the discharge product in sodium–oxygen cells [106]. The electrode was made of Ketjenblack, a typical high surface area carbon. Capacities of 2800 mAh/g and even 6000 mAh/g were reported for PC and tetraglyme, respectively. The voltage profiles were of Type 2C. The discharge product was not the same as reported in literature before. Using FTIR spectroscopy and X-ray diffraction they found that sodium carbonate was the major discharge product for carbonate based electrolytes and hydrated sodium peroxide ($Na_2O_2{\cdot}2H_2O$) was the discharge product for tetraglyme. The authors suggested that the water molecules stem from the irreversible decomposition of the electrolyte. But comparing this result to the study by Hartmann et al. who found NaO_2 using diglyme as solvent, it becomes clear that a direct link between ether solvents and formation of $Na_2O_2{\cdot}2H_2O$ cannot be drawn. Indeed, the reason why different groups find different discharge products is not clear yet.

Liu et al. studied the influence of nitrogen doping of the carbon electrode on the performance of sodium–oxygen batteries [103]. Compared to a pure graphene cathode the doped one showed considerably higher discharge capacities reaching up to 8600 mAh/g_{carbon}. In both cases, Na_2O_2 formed during discharge as evidenced by XRD. Galvanostatic cycling and cyclic voltammetry revealed that nitrogen doping is effective in reducing the overpotentials during discharge and charge. The hysteresis, however, can be still classified as a Type 3B. SEM was used to study the morphology of the discharge product as a function of the discharge current. In line with what is known from Li/O_2 cells, particles form at low currents whereas film formation is observed at higher currents.

Only a short time later another high capacity cathode was presented by Jian et al. [107]. They used a carbon nanotube electrode in combination with two different electrolytes, namely NaTFSI in tetraglyme and NaTfO in diglyme. Although the latter showed a higher discharge capacity (7530 mAh/g compared to 6000 mAh/g), the overall performance was similar. During discharge hydrated sodium peroxide was formed as evidenced by XRD. Charging started at small overpotentials but was quickly followed by a rapid increase in voltage. Only 50% of the capacity could be recovered during charging. The performance could be improved by shallow cycling at around 13% of the full capacity, however, all voltage profiles can by classified as Type 3B.

Additional physicochemical aspects of the Na/O_2 cell with NaO_2 as discharge product were discussed by Hartmann et al. in 2014 [110]. Here, pressure monitoring was successfully combined with the standard electrochemical methods galvanostatic cycling and cyclic voltammetry. Furthermore, electrochemical pressure impedance spectroscopy (EPIS) was introduced as a tool to study the transport properties within the cell. With this, the experimental data were fitted by a quantitative microkinetic model that is based relevant parameters and transport process describing the cell. Further, solubility and diffusion coefficients of oxygen in several solvents were determined and operation of the Na/O_2 cell under mixed O_2/N_2 gas atmosphere was demonstrated. Importantly, NaO_2 was found as discharge product despite the addition of nitrogen gas. On the other hand, the discharge capacity under synthetic air was much lower compared to pure oxygen. This result underlines that

metal–air batteries need to be studied also at lower oxygen partial pressures when aiming at practical applications.

Around the same time two theoretical studies were published. Lee et al. studied the phase stabilities of different possible discharge products as a function of the oxygen partial pressure and calculated that NaO_2 and respectively Li_2O_2 are most stable under standard conditions [115]. Surface energies were calculated and used to predict the Wulff equilibrium shape of the different phases. The cubic crystallites predicted for NaO_2 are well in line with what has been experimentally reported (see Figure 11). Finally, it was calculated that the OER from superoxides is kinetically favored compared to peroxides. Kang et al. studied the phase stabilities of sodium–oxygen compounds as a function of temperature, partial pressure and, importantly, also crystal size [116]. In contrast to the results of Lee et al., they found that Na_2O_2 is the most stable phase at standard conditions in the bulk phase. In the nanometer regime, however, NaO_2 becomes more stable due to its lower surface energy. The threshold under standard conditions is approximately reached for crystal sizes of ≈6 nm in diameter. For the same reason, also nucleation of NaO_2 is preferred over Na_2O_2 at any oxygen pressure and temperature. The authors state that NaO_2, once nucleated during discharge, may never transform to Na_2O_2.

The fundamental difference in cell behavior between otherwise identical Li/O_2 and Na/O_2 cells was further pointed out by McCloskey et al. [67]. They compared lithium–oxygen to sodium–oxygen cells with ether based electrolytes by means of DEMS measurements. Ratios for $n(e^-)/n(O_2)$ of around 2 and 1 were found for the different cells, respectively, indicating formation of Li_2O_2 in Li/O_2 cells and formation of NaO_2 in Na/O_2 cells. In line with other studies finding NaO_2, the voltage hysteresis showed a Type 1B behavior, that is, small overpotentials during charging (≈200 mV) and a sudden voltage increase at the very end of charging. The Li/O_2 cell showed Type 3C behavior, that is, an increase in voltage during charging resulting in very high overpotentials of more than 1.5 V. Interestingly, this significant difference in overpotentials is not seen by cyclic voltammetry using a glassy carbon working electrode. The authors suggest that the difference in overpotentials between lithium and sodium based cells is due to the different reactivity of the discharge products: During charging, Li_2O_2 reacts with the electrolyte and carbon cathode to form Li_2CO_3 leading to a continuous increase in overpotential. In contrast, NaO_2 is less reactive and hence no Na_2CO_3 forms. As a consequence, overpotentials during charging remain small.

Bender et al. discussed possible origins for the different discharge products observed in Li/O_2 and Na/O_2 cells by comparing tabulated thermodynamic data of the different phases [27]. A graphical representation is shown in Figure 12 and is based on thermodynamic data of the bulk phases (T = 298 K, p = 1 bar). The kinetic barriers shown are only a guide to the eye as absolute values are not known. Three relevant aspects can be seen: (1) In both systems, the peroxide is thermodynamically most stable at standard pressure and should therefore form as discharge product, (2) In the Na/O_2 system, NaO_2 and Na_2O_2 are thermodynamically quite close, whereas in the Li/O_2 system, Li_2O_2 and Li_2O are very close. For Na/O_2 cells this means that the cell voltages for NaO_2 (2.27 V) and Na_2O_2 (2.33 V) formation are very close. Given the uncertainty

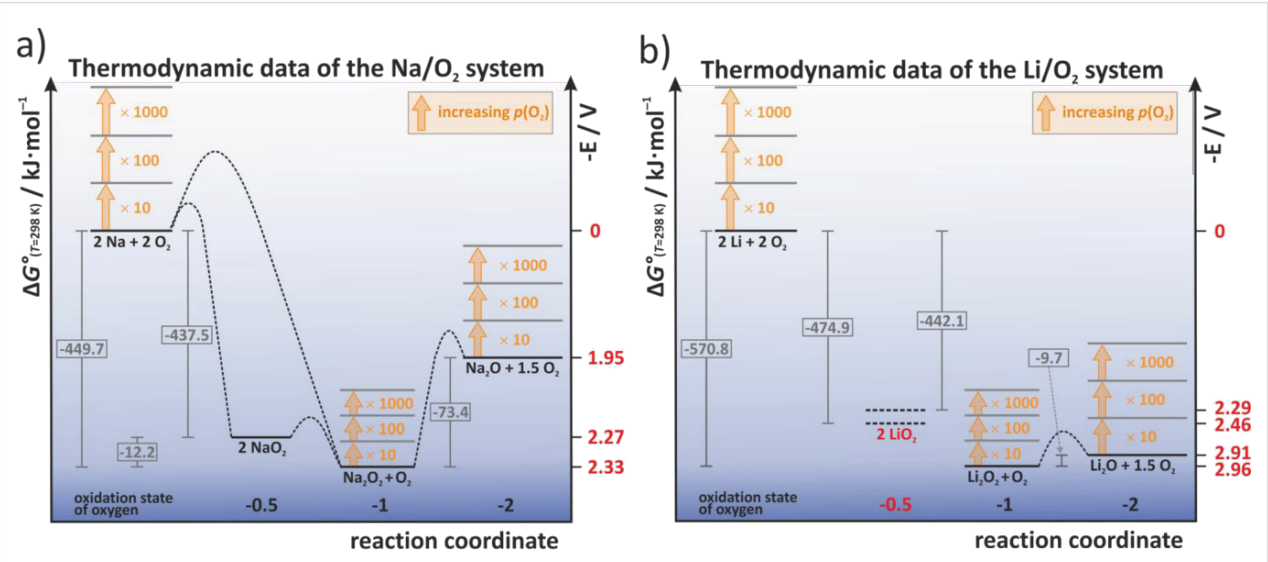

Figure 12: The thermodynamic landscape of (a) sodium– and (b) lithium–oxygen cells. All values are calculated for the reaction $2A + 2O_2 \rightarrow A_2O_y + (2–y/2)O_2$, where y = 1,2,4. Figure adapted with permission from [27], copyright 2014 Wiley-VCH.

of the thermodynamic data it becomes clear that the discharge mechanism cannot be simply derived from the discharge potential. (3) The phase stability naturally depends on the oxygen partial pressure, meaning that NaO_2 or LiO_2 might become more stable than the peroxides at elevated pressures. For NaO_2, the threshold can be estimated to 133 bar, which well explains why the chemical synthesis of phase pure NaO_2 from Na_2O_2 in autoclaves occurs at partial pressures and temperatures of around 280 bar and 475 °C [117].

The authors suggested that as the energetic difference between NaO_2 and Na_2O_2 is so small (about 12 kJ/mol), slight differences in the kinetic properties might lead to either of them as discharge products. A reasonable assumption for what controls the kinetics of the cell reaction is the type of carbon electrode. Indeed, the different groups reporting on Na/O_2 cells all used different carbon materials which might explain the different findings. The authors therefore tested a range of different carbon materials but concluded that the type of carbon has no influence on the nature of the discharge product as in all cases NaO_2 was found as major discharge product. Overall, Type 1B behavior was found in all cases. The achievable capacities, however, were significantly affected by the type of carbon (Figure 13, left). Furthermore, shallow cycling at around 33% of full capacity enabled cycling of the cell for more than 50 cycles with a capacity of 1666 mAh/g using a Ketjenblack electrode with 0.5 M NaOTf in diglyme as electrolyte.

Liu et al. substituted the commonly used carbon electrode by a nickel based composite electrode consisting of nickel foam covered with $NiCo_2O_4$ nanosheets [105]. $NaClO_4$ in monoglyme was used as electrolyte. The pure nickel foam was shown to be inactive. For the composite, however, a discharge capacity of 1762 mAh/g (at 20 mA/g based on the mass of the nanosheets was found). A strong capacity fade was observed during cycling. The voltage profiles can be classified as Type 3B/3C. IR spectroscopy and TEM/SAED were used to determine the discharge products. Sodium peroxide and, as a result of side reactions, Na_2CO_3 were found. The electrodes after discharge were further studied by SEM. Flat sheets with a diameter of around 20 µm were found (Figure 13, right). Obviously, this morphology is very different from the cubic particles reported for cells with NaO_2 formation.

Another study discussing reasons for the different types of discharge products reported in literature was published Zhao et al. [111]. Vertically aligned carbon nanotubes grown on a steel substrate were used as oxygen electrode, sodium triflate in tetraglyme was used as electrolyte. Voltage profiles were of Type 1B and consequently also NaO_2 in form of cubic particles was observed as discharge product. The cell delivered a capacity of more than 4000 mAh/g_{carbon}. Improved cycle life was achieved with shallow cycling at 750 mAh/g (19% DOD). More than 100 cycles have been achieved this way. Rate performance was improved by electrochemically predepositing a thin layer of NaO_2 at low currents (67 mA/g). This procedure was applied to increase the overall number of nucleation sites for product formation during subsequent cycles at higher currents. By doing so, a capacity of around 1500 mAh/g was achieved at 667 mA/g, for example. An important feature of the study was that the cells were not only cycled under static atmosphere in a sealed container but additionally also under continuous gas flow. Pure oxygen or an Ar/O_2 (80/20) mixture were used. Interestingly, the authors found NaO_2 under static conditions and $Na_2O_2{\cdot}2H_2O$ under continuous gas flow. The authors suggest that humidity is likely to be introduced when applying a

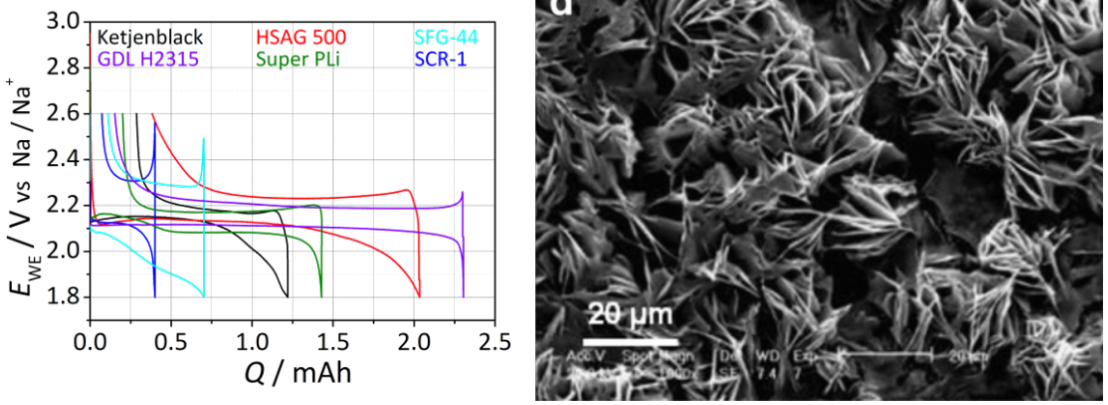

Figure 13: Voltage hysteresis of different carbon materials for the cathode of a sodium oxygen cell (left), figure adapted with permission from [27], copyright 2014 Wiley-VCH. SEM image of the oxygen electrode of a Na/O_2 cell after discharge with Na_2O_2 and Na_2CO_3 as discharge product (right), figure adapted with permission from [105], copyright 2014 Elsevier.

constant flow (presumably due to leakage or gas impurity). Charging was followed by XRD and it was found that $Na_2O_2{\cdot}2H_2O$ decomposes to form water, O_2 and NaOH leading to higher overall potentials and a Type 3B behavior, see Figure 14. It is important to note that a continuous gas flow is closer to the operation mode of a practical cell operating with atmospheric oxygen. Further studies are therefore needed to clarify the source and impact of H_2O on the cell reaction.

Yadegari et al. studied the relation between specific surface area and discharge capacity using chemical activation of commercial carbon black by NH_3 or a CO_2 gas [108]. Sodium triflate in diglyme was used as electrolyte. The results can be summarized as follows: The longer the chemical treatment, the higher the specific surface area, the higher the discharge capacity. The major discharge product was $Na_2O_2{\cdot}2H_2O$ although small amounts of Na_2O_2 and NaO_2 were also detected by combining different methods. As the PVDF binder used in this study is known to be unstable against the superoxide radical, the authors suggested that the formation of the hydrated peroxide is related to the binder decomposition. As a result of the complex mixture of discharge products, the charging curves were characterized by several steps. Overall, all voltage profiles were of Type 3C. The morphology of the electrode after discharge showed quite some similarities compared to the study by Liu et al. It was further shown that the discharge rate influences the voltage behavior during charging.

Overall comparison

For a better comparison of the published literature, we digitalized the voltage profiles and grouped them according the different discharge products. The result is shown in Figure 15. Groups finding sodium superoxide as discharge product find a Type 1B behavior with low overpotentials and a sudden voltage

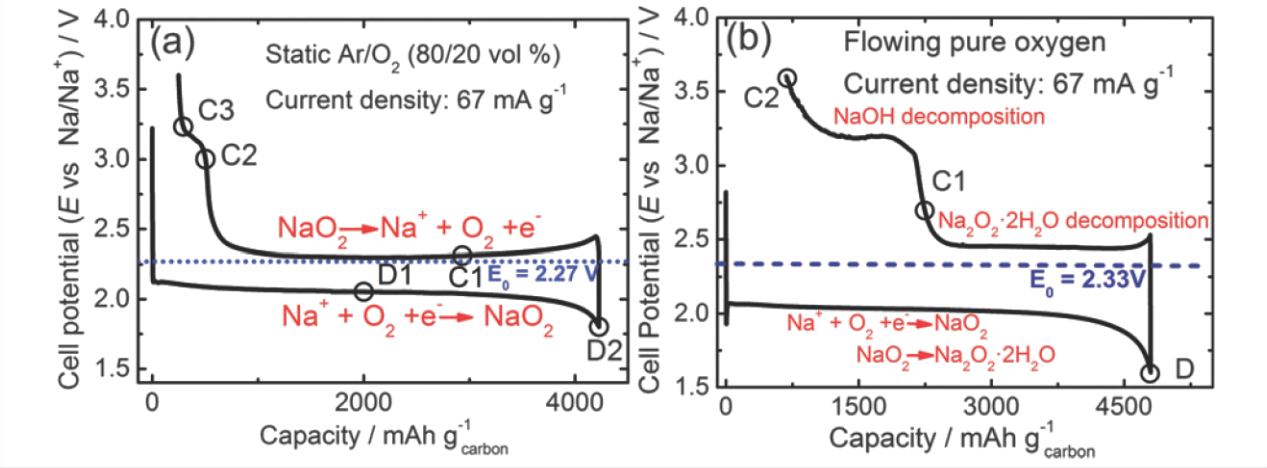

Figure 14: Voltage profiles of Na/O_2 cells under static gas atmosphere and flowing gas atmosphere (Type 1B/3B). Figure adapted with permission from [111], copyright 2014 The Royal Society of Chemistry.

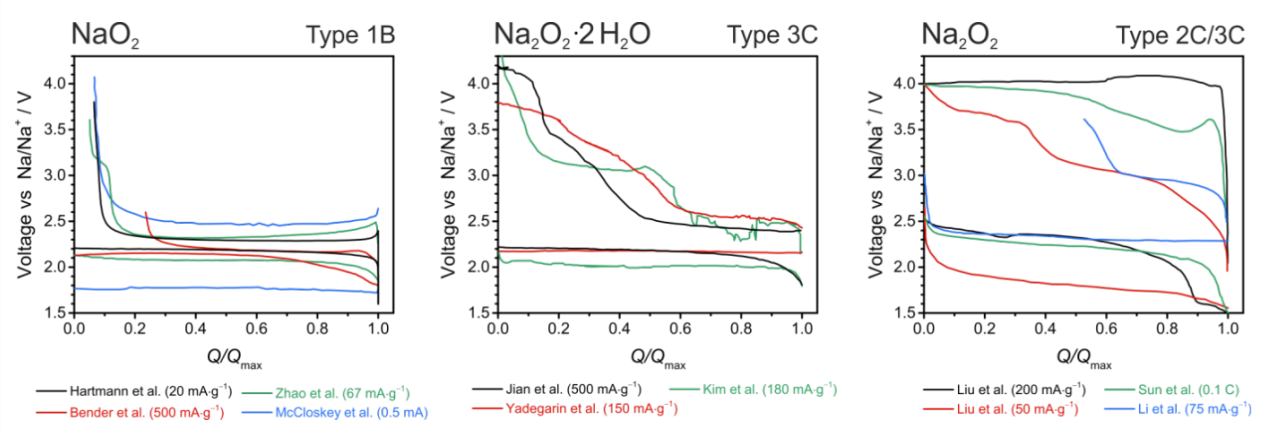

Figure 15: Literature overview on different studies of Na/O_2 cells. The comparison shows the voltage profile of the first cycle. Data has been digitalized from the different publications. Only cells with NaO_2 as discharge product show a defined voltage hysteresis, combined with low overpotentials and a defined end point during recharge. Please note that some groups measure in 3-electrode, others in 2-electrode configuration.

increase once the end or recharge is reached. Efficiencies are typically above 80%. Groups finding $Na_2O_2·2H_2O$ as discharge product find a Type 3C behavior. Characteristic for this behavior are increasing potentials and no defined end point of charge, indicating a complex charging mechanism and side reactions. Different sources for H_2O have been suggested, but its origin is still a matter of debate. Groups finding Na_2O_2 as discharge product usually observe voltage profiles with Type 2C or 3C behavior. A sudden or sloping increase in potential during charging and no defined end point of charge are observed in these cases.

Related concepts

In addition to the studies discussed so far some other related concepts have been suggested. Das et al. proposed a cell concept that mainly aims at CO_2 capture while at the same time generating electrical energy [102]. Their cells can be therefore described as $Na/(O_2 + CO_2)$. The authors investigated the cell discharge behavior under different gas ratios and found that a 50:50 mixture of O_2 and CO_2 yielded higher discharge capacities than the single gases. Na_2CO_3 and $Na_2C_2O_4$ were suggested as discharge products. No charging curves were shown as the cell was designed as primary cell. In a later study, the same group used an organic/inorganic hybrid liquid electrolyte in order to enable partial recharge [118]. The voltage profiles are of Type 3C and show combined overpotentials of up to around 2.5 V. The discharge product was found to be $NaHCO_3$.

Hayashi et al. published results on a Na/O_2 battery with a mixed aqueous/aprotic electrolyte. Both electrolytes were separated by a Nasicon solid electrolyte [119]. Discharge capacities of about 600 mAh/g (based on the weight of Na and H_2O) with NaOH as the discharge product were achieved, which is only 30% lower than the theoretical capacity of the cell reaction; however, no data on rechargeability was shown. The concept of combining different types of electrolytes has been already applied for Li/O_2 cells. But the authors point out that the much higher solubility of NaOH in aqueous electrolytes compared to LiOH might be of an important advantage. Clogging of the cathode by precipitated hydroxide might be delayed and an even higher energy density could be obtained.

3 Lithium–sulfur (Li/S_8) and sodium–sulfur (Na/S_8) batteries

3.1 Operating principles and general remarks

The lithium–sulfur battery system has been studied for several decades. The first patents and reports on lithium–sulfur batteries date back to the 1960s and 70s [120-122]. However, a rapid increase in research efforts and progress in development was only achieved within the last 10 to 15 years. The number of research publications is growing exponentially. The most studied cell concept is based on lithium as a negative electrode and solid sulfur as a positive electrode. Lithium sulfide (Li_2S) is the final discharge product and the only thermodynamically stable binary Li–S phase, as shown in Figure 16a. The theoretical cell voltage of 2.24 V is comparably low but due to the high capacity of sulfur (1672 mAh/g) the theoretical energy density by weight (2615 Wh/kg) exceeds that of LIB by a factor of five. The basic cell concept of a lithium–sulfur battery is depicted in Figure 2c. The main challenges of the lithium–sulfur battery are related to two intrinsic properties:

1. Sulfur and Li_2S are insulators, and intimate contact to a conductive support and sufficiently small particle sizes are necessary to render a complete cell reaction. At the same time, the support must accommodate the volume change of 80% that arises from the difference in molar volumes of sulfur (15.5 mL/mol) and Li_2S (28.0 mL/mol).

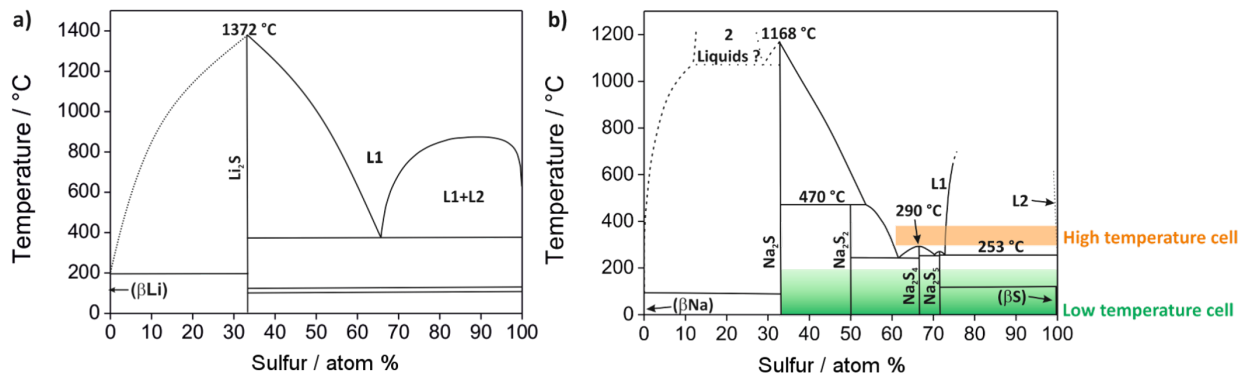

Figure 16: (a) The Li–S phase diagram. (b) The Na–S phase diagram. Redrawn from references [129,130]. The Na–S phase diagram also depicts the operating window of the commercialized high temperature cell and alternative cell concepts operating at low temperature – including room temperature – that are on the research level.

2. Formation of Li_2S from sulfur does not occur directly but via a series of polysulfide intermediates (Li_2S_2 and Li_2S_x, $x > 2$). Polysulfides of the stoichiometry Li_2S_x are highly soluble in commonly used electrolytes, meaning that the active material diffuses out of the positive electrode and eventually reacts with the negative electrode or deposits somewhere else in the cell where it remains inactive. So cycling sulfur in a Li/S_8 battery is essentially based on dissolution and precipitation processes as schematically illustrated in Figure 17. Despite several efforts, however, it is still not well understood in which amounts and stoichiometries polysulfides form. The polysulfide solubility leads to a parasitic phenomenon called the ‘‘shuttle mechanism’’ [123] (Figure 18) that corresponds to a chemical shortcut of the cell. This effect essentially leads to continuous self-discharging during discharge, charge and rest. The degree of the shuttle effect heavily depends on the experimental conditions. Shuttling becomes stronger at small current and/or higher temperatures [123,124]. Moreover, also sulfur S_8 itself is mobile and was found to diffuse rapidly [125].

The complex cell reaction gives rise to a characteristic discharge/charge profile as shown in Figure 19. Both the discharge and the charge voltage profiles consist of two voltage plateaus occurring at about 2.3 V and 2.1 V (discharge) or 2.3 V and 2.4 V (charge), respectively. Within the higher discharge plateau the soluble intermediate polysulfides are formed, corresponding to reduction of S^0 to $S^{-0.5}$ (S_4^{2-}), accounting for a quarter of the overall capacity. Further reduction leads to formation and precipitation of insoluble species leading to an overall two electron reduction of S with Li_2S as end product. During the following charge, Li_2S is reconverted to S_8 via intermediate polysulfides, ideally. The characteristic minimum between the upper and the lower discharge plateau is attributed to the nucleation of solid products [126,127]. The exact position of the potentials also depends on the electrolyte solvent [128].

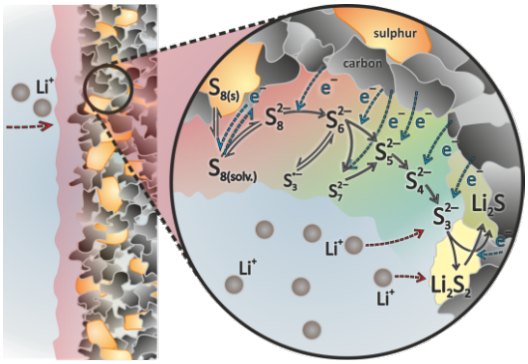

Figure 17: Schematic illustration of the reduction processes at the negative electrode during discharge of a Li/S_8 battery. Reduction of sulfur S_8 proceeds over several soluble polysulfide intermediates (Li_2S_x) before the final precipitation of solid phases, Li_2S and eventually Li_2S_2 occurs. The cell discharge can be also followed by UV–vis spectroscopy, as different polysulfides give rise to different coloration. Illustration adapted from [124].

As a result of these effects, the Coulombic efficiency is low, utilization of sulfur in Li/S_8 cells is poor and the capacity diminishes within a few cycles. Therefore special measures have to be taken in order to improve the performance of Li/S_8 cells.

The most frequently applied strategy to improve the cell performance is to use (nano)porous carbon materials as support that provide high surface area and electronic conductivity and at the same time prevent or delay the loss of active material towards

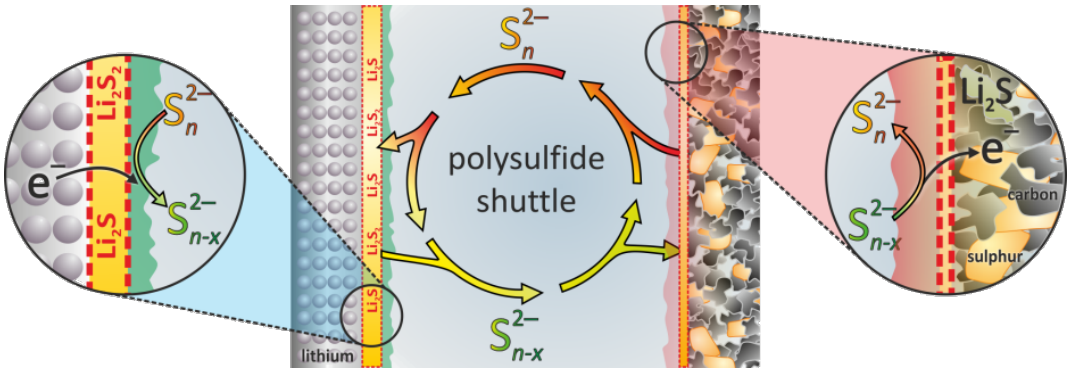

Figure 18: Schematic illustration of the polysulfide shuttle mechanism after Mikhaylik and Akridge [123]. Long polysulfides diffuse towards the lithium electrode where they are reduced to shorter polysulfides. Subsequently, these shorter polysulfides diffuse back to the positive electrode where they are oxidized. As a result, a cyclic process (“shuttle mechanism”) develops that corresponds to a chemical shortcut of the cell. Illustration adapted from [124].

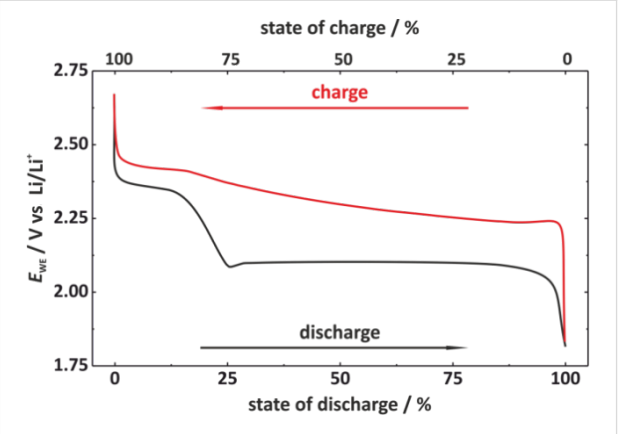

Figure 19: Typical voltage profile of a lithium/sulfur cell. A similar behavior can be expected for an analogous sodium/sulfur cell.

the electrolyte. Electrode mixtures are prepared by simply mixing the carbon materials with sulfur or by infiltrating the carbon matrix with molten sulfur above its melting point (T_m = 119 °C). A typical electrode for Li/S_8 batteries then contains typically around 50–70 wt % sulfur, 30–50 wt % carbon and a small amount of binder. For comparison, the amount of carbon as conductive additive for electrodes in conventional LIBs is well below 5 wt %.

During the last 5–10 years, a large number of different sulfur/carbon nanocomposite materials has been studied and often considerable improvements in terms of sulfur utilization and cycle life were achieved compared to cells with conventional carbon materials. Overall, nowadays several tenths to several hundreds of cycles with capacity values around 700–1000 mAh/g are realized and the combined overpotentials in the first cycles are roughly around 200 mV. But whether the improvements are really due to specific structural properties of the nanocomposite is, however, not easy to answer considering the complexity of the possible reactions in a lithium–sulfur cell. It also turned out that the characterization of sulfur/carbon nanocomposite materials may pose problems and results can be misleading due to the high sulfur mobility [125]. The main issue, however, is that the performance of Li/S_8 cells is particularly sensitive to the properties of the electrode (thickness, sulfur content, sulfur loading, preparation method, etc.) and the amount of electrolyte and lithium. In fact, quite reasonable results can be obtained with commercially available carbon materials once the electrode preparation is optimized [131,132]. Assessing the achievements of the last years, in general, long cycle life and high sulfur utilization has so far obtained only for low sulfur loadings (often <1 mg/cm^2) and large excess of both electrolyte and lithium. Excess of lithium and electrolyte are necessary as both continuously react with each other during cycling. However, low loadings and large excess of lithium and electrolyte are no option for practical devices, and it will be the key to competitive Li/S_8 cells to bring cathodes with high sulfur loading (about 5 mg/cm^2) and a low electrolyte/sulfur ratio to function [131,133-137]. Overall, to enable a high energy battery, the electrolyte:sulfur ratio should be smaller than 5:1 (for comparison, the ratio of electrolyte and active material in conventional LIBs is around 1:3) and the sulfur content of the electrode should be at least 70% providing at least 2–4 mAh/cm^2 (i.e., the typical areal capacity for LIBs).

Besides the attempts to improve the cathode design, also a number of other strategies are followed in order to improve the performance of lithium/sulfur batteries (see section, The lithium–sulfur (Li/S_8) battery). The cell concept shown in Figure 2c is by far the most studied one but also other concepts have been proposed. The high solubility of polysulfides can be used to design cells with a liquid electrode (catholyte), for example. Although this concept has been studied already many years ago [121], it only recently regained attention [138]. On the other hand, solid-state concepts are being considered [139-141].

The theoretical energy densities of the lithium–sulfur battery are summarized in Table 3. But from the above arguments it becomes clear that experimental energy densities will be much lower. No lithium–sulfur cell has been commercialized yet but several companies announced (gravimetric) energy densities for rechargeable cells significantly exceeding lithium-ion technology. Sion Power currently reports 350 Wh/kg on the cell level but aims for over 600 Wh/kg and 600 Wh/L in the near future [142]. Oxis Energy reports 300 Wh/kg (2014) and predicts 400 Wh/kg (forecast in 2016) [143]. The rate capability of lithium–sulfur cells is thought to be competitive with high-rate LIBs [144]. At moderate rates of C/10, the combined overpotentials of Li/S_8 amount to roughly 150–250 mV. By and large, the lithium–sulfur cell as rechargeable energy store appears to have a realistic chance for commercialization, but will compete with continuously optimized LIB.

In contrast to the lithium–sulfur battery, the analogue room temperature sodium–sulfur battery has been hardly studied to date but the challenges for the construction of well functioning cells will be quite similar. However, the theoretical energy density of a Na/S_8 cell is roughly 50% smaller compared to the analogous Li/S_8 cell, due to higher atomic mass of sodium. So if only energy density is considered, the Na/S_8 cell will not be competitive with LIB technology both in terms of volumetric and probably also gravimetric energy density. Besides, the even larger volume change of the sulfur electrode during cycling (170% for Na_2S formation compared to 80% for Li_2S formation) will pose additional problems.

Table 3: Theoretical cell voltages, gravimetric and volumetric energy (Wh/kg, Wh/L) and charge (mAh/g, mAh/cm^3) densities for lithium– and sodium–sulfur batteries with a metal anode. Due to the large differences in their densities, the volumetric energy densities of metal–sulfur cells strongly depend on whether they are in the charged or discharged state. Charge densities refer to the discharged state, that is, to the sulfides. Thermodynamic data were derived from HSC Chemistry for all compounds in their standard state at 25 °C or 300 °C. Densities at 300 °C are estimates. In contrast to LIBs, metal–sulfur cells are usually assembled in the charged state. The theoretical capacity of the positive electrode is therefore usually given based on the mass of sulfur only, so the theoretical capacity is Q_{th} = 1672 mAh/g for full reduction of sulfur to form Li_2S or Na_2S.

Cell reaction	$E°$ / V	W_{th} / Wh/kg	Q_{th} / mAh/g	W_{th} / Wh/L	Q_{th} / mAh/cm^3
$2Li + \frac{1}{8}S_8 \underset{Charge}{\overset{Discharge}{\rightleftharpoons}} Li_2S$	2.24	2615	1167	4289 / 2896	1914
$2Na + \frac{1}{8}S_8 \underset{Charge}{\overset{Discharge}{\rightleftharpoons}} Na_2S$	1.85	1273	687	2364 / 1580	1245
$2Na + \frac{1}{2}S_8 \underset{Charge}{\overset{Discharge}{\rightleftharpoons}} Na_2S_4$ (25 °C)	2.03	626	308	1326 / 997	653
$2Na + \frac{1}{2}S_8 \underset{Charge}{\overset{Discharge}{\rightleftharpoons}} Na_2S_4$ (300 °C)	1.90	583	308	1124 / 845	653
Li-ion (average cathode vs Li/Li^+)	3.8	530	140	2300	600

A look at the phase diagrams shows that different cell reactions might occur in Li/S_8 and Na/S_8 cells, as several Na_2S_x compounds are thermodynamically stable at room temperature. This means that during cell discharge, polysulfides might not only dissolve in the electrolyte, but may also precipitate as solids. Whether the stability of solid Na_2S_x polysulfides is of advantage or disadvantage for a reversible cell reaction remains an open question, but – generally speaking – solid phases are likely to have detrimental effects on the cell kinetics compared to dissolved Na_2S_x species. It is worth noting that also Na_2S_3 has been reported as stable phase, however, it turned out to be a eutectic mixture of the stable polysulfides Na_2S_2 and Na_2S_4 [130]. The Na–S phase diagram (see Figure 16b) also depicts the high-temperature Na/S_8 cell that operates with molten electrodes and a solid electrolyte. As the polysulfides Na_2S_x have high melting points, the cell reaction at around 300 °C is limited to a narrower stoichiometric window, meaning that full reduction of sulfur cannot be achieved. The theoretical energy density for high temperature Na/S_8 cells is therefore limited. In practice, 200 Wh/kg has been achieved on the battery level.

Overall, one can look at the room-temperature Na/S_8 cell from two perspectives: (1) Compared to a Li/S_8 cell, substituting lithium by the more abundant sodium appears attractive, and the same strategies for improving Li/S_8 batteries (sulfur utilization, cycle life) might apply for Na/S_8 batteries. An advantage for sodium could be that sodium solid electrolytes are commercially available, that would enable efficient protection of the metal anode from polysulfides. On the other hand, the theoretical energy densities are lower and the larger volume expansion might lead to severe problems. (2) Compared to a high-temperature Na/S_8 cell, decreasing the operating temperature would be attractive because safety and corrosion issues are reduced. In addition, if full reduction of sulfur to Na_2S can be accomplished, an increase in system's energy density might be possible.

A compromise could be to operate the cell at intermediate temperatures below 200 °C [145-147]. Here, the sodium anode (T_m = 98 °C) can be either solid or liquid, a NASICON-membrane (Na Super Ionic Conductor) or beta-alumina membrane is used as solid electrolyte and the cathode is based on a mixture of sulfur or Na_2S_x in an organic solvent. Such an approach has been already discussed in 1980 by G. Weddigen [148].

3.2 State-of-the-art and recent developments

3.2.1 The lithium–sulfur (Li/S_8) battery: As mentioned earlier, a considerable number of papers are currently being published in the field of lithium–sulfur batteries. This summary is intended to highlight the key strategies currently followed for improving the performance of Li/S_8 batteries. The same strategies might be adopted to improve the performance of the analogue room temperature Na/S_8 battery, although research in this field is still on an exploratory level. For a more comprehensive and complete overview on lithium–sulfur batteries, the authors refer to more specialized reviews [149-155].

The challenges of the Li/S_8 system address all of its main components. Hence, main approaches striving to find a solution for these challenges, address (1) cathode composition and architecture, (2) electrolyte composition and additives and (3) improve-

ments or alternatives to the Li anode. Beyond the improvement of the single components – both from fundamental and engineering point of view – a comprehensive understanding of the complicated redox chemistry of the Li/S_8 system has to be obtained. Therefore, the demand in analytics and simulation studies of the electrochemistry is constantly growing. This section will close with an outlook to new cell design approaches to address the special chemistry of Li/S_8 batteries.

3.2.1.1 Cathode: The ideal cathode of a lithium–sulfur battery should provide the following features: (a) A high electronic conductivity and fine dispersion of the active material to achieve a complete active mass utilization and high rate capability. (b) A structure confining the active mass to prevent the loss of polysulfides and hence the shuttle effect. (c) A flexible structure to accommodate the volume changes during cycling. (d) A sufficient active mass loading to compete at least with current lithium ion batteries (LIBs). Points a–c can be addressed by developing and engineering conductive supports. Mostly porous carbon or carbon composite materials are used for this purpose. Again, we emphasize that the sulfur loading on the electrodes needs to be sufficiently high in order to achieve high energy densities in practice. For example, a sulfur loading of more than 2 mg/cm^2 and 100% sulfur utilization is necessary in order to reach technically relevant areal capacities of about 3.5 mAh/cm^2. This aspect has been often overlooked in the last years but needs to be considered when claims on the practical rather than the academic relevance of new electrode architectures are made.

A few of the recent approaches are highlighted in the following. General remarks on the electrode preparation methods will be given at first.

Electrode preparation and binders: Intimate contact between carbon and sulfur is usually obtained by heating sulfur/carbon mixtures above the melting point of sulfur, leading to melt infiltration of the porous support. Some more specific approaches combine a first melting step followed by evaporation of excess surface–sulfur [156] or deposition of sulfur over the gas phase [157]. Apart from some binder-free cathode approaches (see below), binders play a particularly important role when preparing the final electrodes from the sulfur/carbon mixtures. Beyond the ability to bond the cathode components and link them to the current collector, binders have to be flexible enough to accommodate the volume change. Furthermore, they should favor a maximum dispersion of the active material and the conductive agent and limit polysulfide dissolution. Established binders for LIBs such as polytetrafluorethylene (PTFE) or polyvinylidene fluoride (PVDF) have been used long time for Li/S_8 cells but may not provide sufficiently good properties. Polyethylene glycol (PEO, PEG) as one of the earliest alternative binders may improve cycle life [158,159] by electrolyte modification through partial dissolution. As first published by Sun et al. [160], gelatin as an environmentally benign and abundant binder shows improved bonding and helps to improve the dispersion of the active mass. It also may cause an improvement of the redox reversibility [160] and the rate capability [161]. Other binders, such as polyvinylpyrrolidone (PVP)/polyethyleneimine (PEI) show similar abilities [162]. Furthermore, the water-soluble binder SBR/CMC (styrene-butadiene rubber/carboxyl methyl cellulose) favors a uniform distribution and a network-like cathode structure [163].

Porous carbon structures: A straightforward approach to achieve favorable conductivities is to mix the insulating active material with porous carbons. Depending on the major pore size, d, they are distinguished as microporous carbon (d < 2 nm), mesoporous carbon (2 nm < d < 50 nm) or macroporous carbon (d > 50 nm). Especially microporous carbons combine electronic conductivity with an ability to trap polysulfides as first published by Wang et al. in 2002 [164]. Zhang et al. claimed that micropores can work as micro-reactors confining the active mass in the cathode [165]. In more recent studies by Guo and coworkers, an effective steering of the chain length of the active material was obtained by pore sizes smaller than S_8 molecules of orthorhombic sulfur needing a space of about 0.7 nm [166-168]. The shorter chain length polysulfides show strong adsorption to the carbon matrix and the unfavorable transition between S_8 and S_4^{2-} with intermediate polysulfides is hindered, resulting in high cycle life at a lower discharge plateau of 1.9 V [153,169].

Especially for microporous supports, a sulfur loading exceeding 50% is difficult due to the limited overall porosity that is provided by microporous carbons [165,169-171]. Also mesoporous carbons are able to trap polysulfides and provide space for a higher sulfur loading [127,170]. As published by Li et al. [172], there is always a tradeoff between complete filling with sulfur resulting in topmost energy density and partial filling leading to better battery performance but lowering energy output. Macroporous supports have been less investigated despite of their high pore volume, as the open structure does not seem to favor polysulfide confinement. However, when immobilizing the polysulfides by providing strong interaction to the matrix [170,173,174] or the use of a highly viscous electrolyte [175], macroporous carbon frameworks may be useful. For both meso- and macro-porous supports, nitrogen doping is promising to improve polysulfide confinement [176]. Bimodal or hierarchical porous carbons were used as compromise to combine confinement of sulfur in small pores while enabling also a higher sulfur loading due to larger pores. Bimodal pore struc-

tures were first published by Liang et al. [177]. Although possessing a 3D structure (see below), it should be noted that the CMK-3 ordered mesoporous carbon published by Ji, Lee and Nazar [178,179] was a major starting point for studying tailored, hierarchical carbon materials (see Figure 20).

A range of other special carbon nanostructures have been tested for Li/S_8 batteries. They are applied in pure form or in combination with conventional carbon materials such as carbon black or activated carbon. Interwoven networks can be obtained by using carbon fibers or nanotubes, for example [179,181]. Cao et al., Zhou et al. and others have reported on sandwich-like electrodes with two graphene layers incorporating the active material, one used as a lightweight current collector, the second used as a barrier for polysulfides [33,182,183]. On the other hand, graphene oxide sheets have been used for wrapping poly(ethylene glycol) covered sulfur particles to obtain confining structures [184].

To completely avoid polysulfide leakage, core–shell- or yolk–shell-structures have been developed to confine the active material inside their electronic and ionic conductive hull. Hollow carbon spheres (void up to 500 nm) with porous shell (up to 50 nm thickness) can be obtained via a hard template nanocasting [157], for example. However, when dealing with an active material that undergoes volumetric expansion and constriction during cycling, closed structures can break. Therefore "yolk–shell"-structures have been suggested that leave enough room for expansion. The latter approach was published by Cui and coworkers [180] comprising sulfur nanoparticles as yolk inside a TiO_2 shell. The material showed excellent stability for more than 1000 cycles and high Coulombic efficiencies, but only low cathode loadings were reported.

Binder-free electrodes: As the additional weight of the binder reduces the overall energy density of Li/S_8 cells, binder-free electrodes are studied as alternative. The preparation of binder-free electrodes also avoids the use of often toxic solvents that are necessary for conventional electrode preparation. Elazari et al. reported on a carbon fiber cloth that was able to maintain mechanical strength and conductivity during cycling [170], for example. Vertically aligned carbon nanotubes (VACNTs), directly grown via CVD-process on a metal current collector were published by Dörfler et al. [185]. The high void volume inside the ≈200 µm thick (94 vol %) films was especially favorable for high sulfur uptake, which was later on shown by Hagen and Dörfler et al. [185,186]. Vertically aligned CNTs without a substrate were produced by Zhou [187] using an aluminum anodic oxidized template. Another attempt was published by Manthiram et al., using self-interweaving MWCNTs as free-standing electrodes [188]. Overall, binder-free electrodes might be a viable alternative to standard electrodes. Areal loadings of 7.1 mg/cm^2 yielding areal capacities of about 5.5 mAh/cm^2 (50% S utilization) were achieved, although at a low rate of 5/C, for example [185]. Lower loadings allow higher rates of up to 3.5C with specific capacities around 700 mAh/g after 25 cycles [187]. However, reports of more than 100 cycles have not been published yet.

Lithium–sulfide cathode*:* Li/S_8 cells are usually assembled in the charged state which is less ideal considering safety. Cell assembly in the discharged state, that is, with Li_2S as positive electrode is intrinsically more safe and has another advantage: The use of anode materials such as Si [189] and Sn [190] and other alloys becomes feasible [189,191,192]. Beginning in the 1970s [193], numerous approaches for Li_2S cathode formation and investigation on the basic principles have been published. As claimed by Yang et al. [194], when cycling Li_2S as a cathode material, the first charge is hindered by a potential barrier originating from the slow charge transfer during the oxidation of Li_2S to $Li_{2-x}S$, requiring a higher cut-off voltage up to 4 V. Beyond, the hygroscopic property of Li_2S prohibits handling in air. As stated above, Li_2S is also an ionic and electronic insulator and requires conductive agents to function as an electrode, hence, comparable approaches to the S composite cathodes have been used [189,190,192,195]. More interesting is

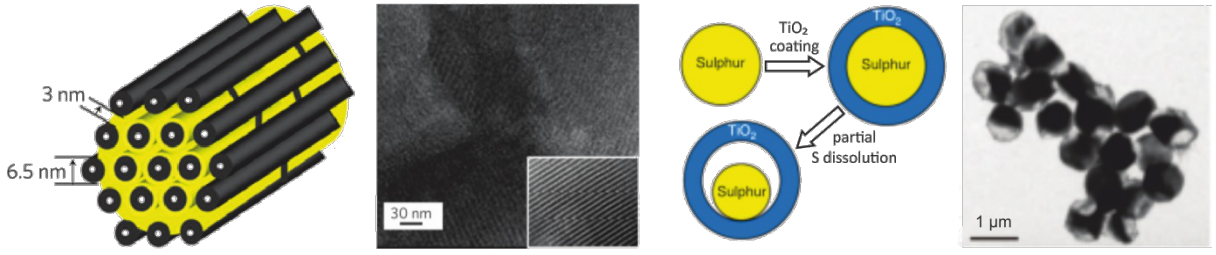

Figure 20: Schematic diagram of the interconnected pore structure of mesoporous CMK-3 impregnated with sulfur (left). TEM image of the impregnated and the pristine (small inset) CMK-3. Figure adapted with permission from [178], copyright 2009 Macmillan Publishers Ltd. Process of formation of S–TiO_2 yolk–shell structures via core–shell formation and partial dissolution of sulfur (right) [180]. TEM image of the yolk–shell structure with nanoparticles of 800 nm size and shell thickness of 15 nm. Figure adapted with permission from [180], copyright 2013 Macmillan Publishers Ltd.

the direct chemical synthesis of Li_2S electrodes without Li_2S as the starting material: It can be obtained by lithiating a sulfur–carbon composite with stabilized lithium metal powder in situ by compression [196] or with *n*-butyllithium [189]. Archer and coworkers have investigated two different novel approaches towards Li_2S–C composites: (1) The well-known Leblanc process can be used to reduce sulfates with carbon [197] and (2) Li_2S builds strong crosslinks with the nitrile groups of polyacrylonitrile (PAN) [198]. Both result in Li_2S–C composites after carbonization and show promising results. Recently, Lin and coworkers used the reaction of Li_2S and P_2S_5 in THF to form a Li_2S–Li_3PS_4 core–shell structure [199].

3.2.1.2 Electrolytes: The electrolyte will probably play the most fundamental role in the Li/S_8 battery – potentially even more important than the cathode microstructure, as the solubility of polysulfides and hence the shuttle-effect are dramatically affected by the solvent [121,200-202]. Furthermore, the electrolyte has to be suitable for both the highly reactive Li anode and the sulfur-composite cathode with its special requirements. One important property is good polysulfide solubility to ensure fast and complete reactions between Li and the sulfur [155,200]. On the other hand, a high solubility will accelerate shuttling and loss of active material. Most ether-based solvents can dissolve polysulfides very well, most prominent examples are 1,3-dioxolane (DOL) and 1,2-dimethoxyethane (DME), tetraethylene glycol dimethyl ether (TEGDME, tetraglyme) and sometimes ethers with longer chain length [200,203-205]. Carbonate-based solvents used for conventional LIBs will most likely not be used in future Li/S_8 batteries. This is due to their reactivity with polysulfides and because they are less compatible with lithium [205-208]. Nowadays, the most common solvent is a binary mixture of a cyclic ether (DOL) and a linear ether (DME), which was found to provide a good overall compromise between sulfur utilization, rate capability, temperature window and anode compatibility [209]. Lithium bis(trifluoromethanesulfonyl)imide ($LiN(SO_2CF_3)_2$, LiTFSI) is commonly used as a conductive salt. Aurbach et al. pointed out the significance of $LiNO_3$ (lithium nitrate) as an electrolyte additive [205,210-215] to build up a both relatively stable and flexible SEI on the lithium anode that suppresses the polysulfide shuttle. However, $LiNO_3$ is progressively consumed during cycling and decomposes at the cathode at potentials below 1.6 V [215]. Increasing the conductive salt concentration might alleviate the polysulfide shuttle due to increased viscosity and salting-out effects as stated by Suo et al. [216]. In their work on "solvent-in-salt" electrolytes, an electrolyte with 7 M LiTFSI was found to suppress both polysulfide dissolution and dendrite growth. On the other hand, an increased viscosity generally opposes fast kinetics. Recently, Cuisinier et al. reported on a new "binary" electrolyte comprising a solvent–salt complex (acetonitrile$(CAN)_2$–LiTFSI) and hydrofluoroether (HFE) that provide minimum solubility of polysulfides [217]. Hence, a different electrochemical behavior occurs, still forming polysulfide intermediates but suppressing parasitic disproportionation, enabling an earlier Li_2S formation. Based on the weak Lewis acidity or basicity of ionic liquids (ILs) the solubility of PS is limited as well [218]. Drawbacks of ILs are their high viscosity and therefore lower conductivity resulting in low active mass utilization. The combination with lower viscosity solvents such as DME should be favorable [219] but at the cost of increased polysulfide dissolution. Beyond liquid electrolytes, polymer electrolytes are also used in Li/S_8 cells that show favorable properties with respect to polysulfide blocking but yet suffer from low ionic conductivity [140,191,213,220]. Despite intense research efforts, the ideal electrolyte has not been identified yet. The possible cure could be to combine a fast conducting liquid electrolyte with a solid lithium-ion-selective separator or solid electrolyte membrane separating both electrodes, thus relying on reliably protected lithium anodes (PLAs) [221,222].

3.2.1.3 Anodes: As the reduction of sulfur occurs at potentials below 2.5 V vs Li/Li^+, lithium metal is the preferred choice as negative electrode in order to achieve reasonable cell voltages. Moreover, the high theoretical capacity of lithium (3860 mAh/g) is a good match with the high capacity of sulfur (1672 $mAhg^{-1}$). The well-known drawbacks of lithium electrodes (chemical reactivity and dendrite formation) are tried to be minimized by an ex situ applied protection layer or the in situ formed solid electrolyte interphase (SEI) as noted in the previous section. Both in situ and ex situ have to accommodate the changes in volume and morphology during cycling without fracture [223]. To obtain artificial protection layers (artificial SEI), polymer films [224] and inorganic solid electrolytes [221,222] have been applied on the Lithium metal surface. More common is the use of electrolyte additives to favor the formation of a stable SEI, as first published by Aurbach et al. [210,225] referring to $LiNO_3$. More recently P_2S_5 was suggested as promising additive: A passivating layer mainly consisting of Li_3PS_4 with rather high ionic conductivity is formed throughout the reaction of P_2S_5 with Li_2S_x [226]. The SEI formation in situ results from the reaction of lithium with the electrolyte components. Therefore, a fraction of the anode material is irreversibly lost and has to be provided as excess. An alternative route to suppress dendrite growth was suggested by Ding et al. [227]. Here, selected cations (Cs^+ and Rb^+) are added that shield emerging lithium dendrites from further Li^+ access, thus enabling a smoother lithium deposition.

The interest in non-lithium anodes such as Si [189] and Sn [190] has been growing, but these – apart of being pre-lithiated [228] – can only be combined with Li_2S composite cathodes.

Due to the severe volumetric expansion exceeding 300% from Si to $Li_{15}Si_4$, Si in anodes can only provide stable cycling behavior when being nanosized [229]. Beyond, the theoretical energy density of Li–Si/S_8 cells is reduced to 1862.45 Wh/kg (3299.25 Wh/L) and to 922.84 Wh/kg (2628.19 Wh/L) for Li–Sn/S_8 cells, respectively, due to the additional weight and the reduced cell voltage. Also high capacity carbon materials have been studied [230]. The supposed advantages of these anode materials over lithium are improved safety and possibly increased cycle life. But whether this can outweigh the lower energy densities and the disadvantages arising from the decreased cell voltage remains to be clarified.

3.2.1.4 Analytics: Despite the fact that the Li/S_8 cell has been investigated for a long time, a complete understanding of the redox chemistry and all the electrochemical and chemical processes has still not been achieved. This is foremost due to two reasons: (a) In contrast to the rocking chair LIB, the cell chemistry of Li/S_8 cells is very complicated, and the reduction of the S_8 molecule to Li_2S requires the transfer of 16 electrons. (b) As the processes are particularly sensitive to – for example – the electrolyte composition, often different studies are hardly comparable [124,231,232]. Only recently, in situ methods have been applied to achieve a more realistic overview on the real cell reactions.

X-ray diffraction is generally a powerful tool to analyze cell reactions in situ [127,233,234] and has been applied to follow the crystalline solid phases appearing during cell cycling. Unfortunately, some discrepancies still remain: The final discharge product Li_2S is not detected (to be crystalline) in some works ex situ [235] and in situ [233] while others show evidence ex situ [236] and in situ [127,234]. Furthermore, the re-oxidation to orthorhombic sulfur is detected by some groups [233] via XRD, while others see evidence for a different allotrope [127,234] or contradict the formation of elemental sulfur from polysulfides [236-239] at all. One of the most recent studies of in situ XRD is shown in Figure 21 (right), detecting formation of crystalline Li_2S at the beginning of the 2nd discharge step and precipitation of monoclinic β-sulfur at the end of the charge step. Other methods are necessary to study the soluble polysulfide intermediates. Barchasz et al. proposed a possible mechanism for sulfur reduction in Li/S_8 batteries by combining high performance liquid chromatography (HPLC), UV–vis absorption and electron spin resonance (ESR) [232]. Further UV–vis analysis was carried out by Patel et al. [240]. Cuisinier et al. published a study on sulfur speciation during cycling using K-edge XANES (X-ray absorption near-edge spectroscopy) [241]. They analyzed intermediate species and followed dissolution and precipitation of redox end members during cycling, finally proposing a cell reaction as denoted in Figure 21 (left). Combination of in situ and in operando techniques is a powerful tool to obtain a clearer qualitative understanding of the cell chemistry. However, challenges remain because – as stated before – the redox chemistry highly depends on the electrolyte, making different approaches hardly comparable. To understand the cell chemistry from a theoretical point of view, microkinetic models of the processes with special focus on the polysulfide shuttling were published by Mikhaylik et al. [123] and Kumaresan et al. [126]. Fronczek et al. used a

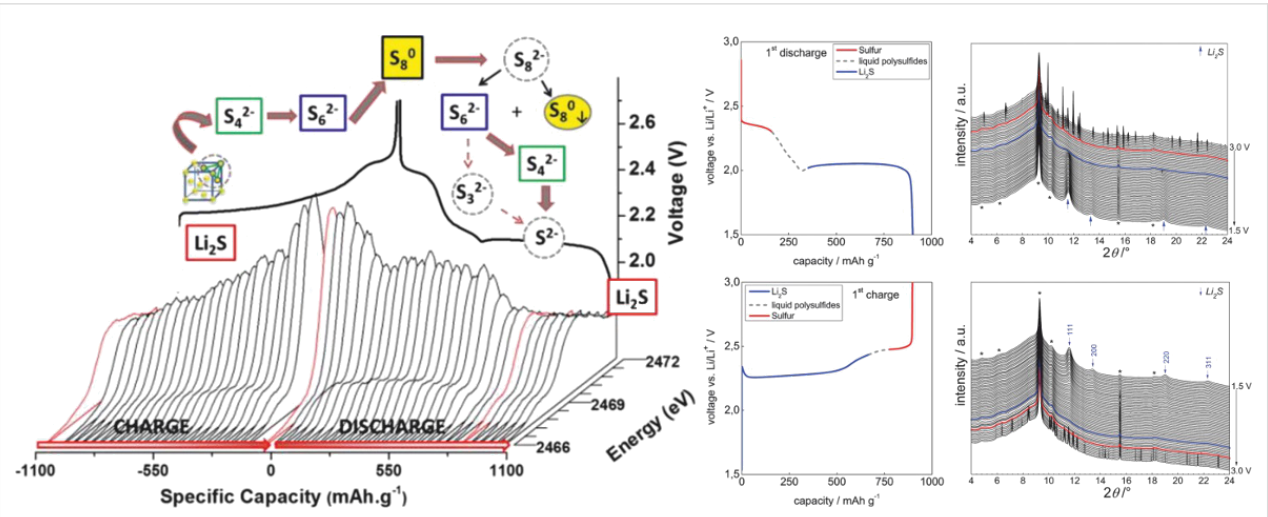

Figure 21: Operando X-ray absorption near-edge spectroscopy (XANES) measurements (left) during first charge and second discharge at 10C rate. The sulfur species denoted on top represent the proposed charge and discharge mechanism based on the measurements. Figure adapted with permission from [241], copyright 2013 American Chemical Society. In situ XRD patterns (right) during discharge and charge at 20C rate with corresponding voltage profiles (left). The * indicates packaging contribution to the patterns, red and blue lines indicate crystalline phases of sulfur and Li_2S, respectively. Figure adapted with permission from [127], copyright 2013 The Royal Society of Chemistry.

modeling framework based on computational fluid dynamics (CFD) to develop a one-dimensional continuum model of a Li/S_8 cell with parameters based on this reference [126] to simulate concentration profiles, voltage and current curves as well as impedance behavior during cycling [231]. Kinetics play a particular role in the Li/S_8 battery especially because of the divided appearance of fast reactions in solution and sluggish solid state reactions as shown by transient galvanostatic intermittent titration technique (GITT) studies [124]. Hence, both cycling characteristics and performance are affected by the cycling rate and temperature.

3.2.1.5 Alternative cell concepts: As the cell chemistry of Li/S_8 cells is very different from conventional LIBs, it is also worth considering alternative cell concepts. Negative effects arising from the shuttle effect can be obviated by separating both electrodes with an additional membrane that conducts lithium ions only. This way, polysulfides cannot reach the lithium electrode as suggested by Visco et al, for example [242]. A range of different membranes has recently been tested: lithium ion-exchanged Nafion [243], Nafion-coated polymeric separator [244], Al_2O_3-coated [244] and V_2O_5-coated [245] separators, and a commercial glass ceramic from Ohara Inc. [185,246]. Manthiram et al. introduced different electronically conductive interlayers between cathode and separator to absorb and reactivate dissolved polysulfides [152]. Obviously, the extra weight and extra resistance of a membrane or layer decreases energy density and rate capability, respectively. However, with the current state-of-the-art, it might be the only reliable cure to the shuttle effect apart from designing an all solid state sulfur battery. This latter attempt may imply new challenges, including (1) low ionic conductivity of solid electrolytes compared to liquid electrolytes for most solid Li-ion conductors, (2) stability of the interface SE/Li-anode and (3) sluggish interfacial kinetics at both electrodes. Additionally, as the ionic contact of the active mass is no longer provided by the liquid electrolyte, a reasonable fraction of finely dispersed ion conductor has to be introduced into the cathode architecture. This leads to a further decrease in energy density. However, with solid electrolytes approaching conductivities that are on par with liquid electrolytes, that is, members of the thio-LISICON (Li Super Ionic Conductor) and Li_2S–P_2S_5 families [247-252], all-solid-state lithium–sulfur batteries might be an attractive option. Moreover, avoiding flammable liquid electrolytes would be an important advantage with respect to battery safety.

3.2.2 The sodium–sulfur (Na/S_8) battery: The large amount of research publications on lithium–sulfur batteries is in stark contrast to what has been reported on the cell chemistry of the analogue sodium system. Altogether only a few publications on the room temperature cell chemistry of sodium–sulfur batteries are currently available but – similarly to the Na/O_2 battery – the majority appeared within the last two years. An overview of the available literature is shown in form of a timeline (Figure 22).

Assuming an ideal discharge process, that is, considering thermodynamically stable solids only, sulfur is subsequently reduced to form different polysulfides (Na_2S_x, x = 2, 4, 5) and finally the end product Na_2S. The theoretical cell potentials of the different steps can be calculated from the corresponding thermodynamic data (no data was found for Na_2S_5):

$$2\mathrm{Na} + \frac{1}{2}\mathrm{S_8} \rightleftarrows \mathrm{Na_2S_4} \qquad E°(25\ °\mathrm{C}) = 2.03(32)\ \mathrm{V} \quad (5)$$

$$2\mathrm{Na} + \mathrm{Na_2S_4} \rightleftarrows 2\mathrm{Na_2S_2} \qquad E°(25\ °\mathrm{C}) = 2.03(26)\ \mathrm{V} \quad (6)$$

$$2\mathrm{Na} + \mathrm{Na_2S_2} \rightleftarrows 2\mathrm{Na_2S} \qquad E°(25\ °\mathrm{C}) = 1.68\ \mathrm{V} \quad (7)$$

$$2\mathrm{Na} + \frac{1}{8}\mathrm{S_8} \rightleftarrows \mathrm{Na_2S} \qquad E°(25\ °\mathrm{C}) = 1.85\ \mathrm{V} \quad (8)$$

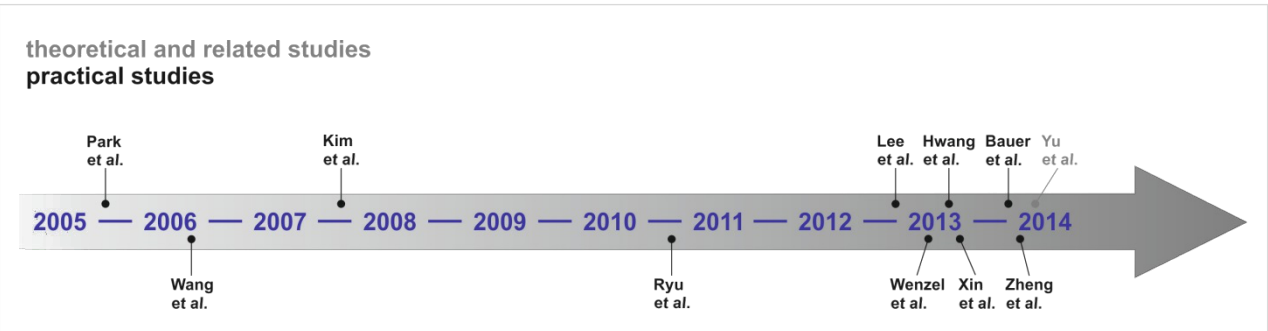

Figure 22: Literature timeline of research papers on room temperature Na/S_8 batteries (ranked after date of acceptance). Experimental studies: all journal publications in which full discharge–charge capacity profiles were shown for at least one complete cycle. The paper by Yu et al. [253] describes a related concept based on a catholyte.

The weighted average voltage of the different steps equals the standard cell potential of the overall reaction. In cells with liquid electrolytes, the reaction path is of course more complex, as, similarly to the Li/S_8 cell, the phase behavior becomes much more complex as many polysulfides are highly soluble and metastable phases exist. Na_2S_2 and Na_2S, however, are the least soluble compounds in organic solvents so a solid state reaction as stated in Equation 7 is expected at the calculated potential.

Before providing an overview of the current literature it is worth noting beforehand that the overall understanding of the cell chemistry is poor and quite different results have been reported with respect to sulfur utilization and cycle life. This is probably also due to the fact that the experimental conditions were very different (Table 4).

The first recent report on room temperature sodium–sulfur batteries was published by Park et al. [254] who prepared a cell using a PVDF/tetraglyme-based gel polymer electrolyte with sodium triflate ($NaCF_3SO_3$) as conductive salt ($\sigma = 5.1 \cdot 10^{-4}$ S/cm at 25 °C). The discharge profile was characterized by two plateaus separated by a sloping potential

Table 4: Cathode- and electrolyte-compositions as well as discharge capacities of all sodium–sulfur cells with an elemental sodium anode that are found in the literature.

Reference	Cathode composition[a]	Electrolyte	1st dis. capacity / mAh/g	10th dis. capacity / mAh/g
Park et al. [254]	70 wt % S 20 wt % C 10 wt % PEO	gel polymer: $NaCF_3SO_3$ in PVDF–TEGDME (1:3:6)	490	105
Wang et al. [255]	70 wt % S/PAN-based comp. (viz. 45 wt % S) 20 wt % CB 10 wt % PTFE	1 M $NaClO_4$ in EC:DMC (2:1)	1455	1110
Kim et al. [256]	70 wt % S 20 wt % CB 10 wt % PEO	gel polymer: $NaCF_3SO_3$ in PVDF/HFP–TEGDME (1:3:6)	390	120
Ryu et al. [257]	60 wt % S 20 wt % C 20 wt % PEO	1 M $NaCF_3SO_3$ in TEGDME	540	225
Lee et al. [258]	60 wt % S/HollowC comp. (viz. 27 wt % S) 20 wt % CB 20 wt % PEO	$NaCF_3SO_3$ in TEGDME (4:1 mol %)	1200	600
Wenzel et al. [259]	50 wt % S 40 wt % C 10. wt % PVDF	(a) 1 M $NaCF_3SO_3$ in DME:DOL (1:1); (b) (a) + beta alumina membrane	450 (a) 475 (b)	190 (a) 325 (b)
Hwang et al. [260]	70 wt % S/C–PAN comp. (viz. 32 wt % S) 15 wt % CB 15 wt % PVDF	0.8 M $NaClO_4$ in EC:DMC (1:1)	1115	1000
Xin et al. [261]	80 wt % S/(CNT@MPC) comp. (viz. 32 wt % S) 10 wt % CB 10 wt % PVDF	1 M $NaClO_4$ in PC:EC (1:1 v/v)	1610	1100
Bauer et al. [262]	42.5 wt % S 42.5 wt % C 12 wt % PVDF 3 wt % PTFE (dry)	(a) 1 M $NaClO_4$ in TEGDME, (b) (a) + Nafion coating on PP separator	340 (a) 400 (b)	210 (a) 370 (b)
Zheng et al. [263]	80 wt % HSMC–Cu–S comp. (viz. 50 wt % S) 10 wt % CB 10 wt % CMC (in H_2O)	1 M $NaClO_4$ in EC/DMC (1:1)	1000	690
Yu et al. [253]	60 wt % S 30 wt % CB 10 wt % PVDF	1.5 M $NaClO_4$ 0.3 M $NaNO_3$ in TEGDME	900	600

[a]PEO: polyethylene oxide, $NaCF_3SO_3$: sodium triflate, PVDF: polyvinylidene fluoride, TEGDME: tri- or tetraglyme, PAN: polyacrylonitrile, $NaClO_4$: sodium perchlorate, CB: carbon black, PTFE: polytetrafluoroethylene, HFP: hexafluoropropylene, HollowC: hollow carbon spheres, CNT@MPC: carbon nanotube core@microporous carbon shell particle, PP: polypropylene, HSMC: high surface area mesoporous carbon, CMC: sodium carboxymethyl cellulose.

region, indicative for a stepwise reduction of sulfur over polysulfides. The first discharge capacity was 489 mAh/g and a rapid capacity fading was observed for the subsequent cycles. The authors concluded that a mixture of Na_2S_2 and Na_2S_3 has been formed during discharge and some sulfur remained inactive. Similar results were obtained for a PEO-based polymer electrolyte but at 90 °C [264]. Later on, the same group (Kim et al. [256]) studied the cell with gel polymer electrolyte in more detail. Again, a similar behavior was found with a capacity of 392 mAh/g for the first discharge followed by a rapid capacity decay. Moreover, the impedance of the cell increased during cell storage which was attributed to the growth of a passivation layer between sodium anode and the gel polymer electrolyte.

Wang et al. [255] reported on a Na/S_8 cell with liquid electrolyte ($NaClO_4$ in EC:DMC) with a high capacity of 1455 mAh/g (or 655 mAh/$g_{cathode}$) and stable cycling over 20 cycles. The cathode material was prepared by heat treating a mixture of PAN and sulfur under inert atmosphere [176]. The sulfur induced the cyclization of the PAN polymer forming H_2S. The resulting composite consisted of heterocyclic structures and it was suggested that excess sulfur was finely dispersed and eventually covalently bonded to the carbon. The enhanced interaction between sulfur and carbon might explain the high sulfur utilization and stability, at the same time it might be the reason for the unexpected shape of the voltage profile and the lower average cell voltage. No further characterization of the discharge or charge products was provided.

In 2011, Ryu et al. [257] studied the performance of Na/S_8 cells in a liquid ether based electrolyte ($NaCF_3SO_3$ in tetraglyme). Again, the discharge profile and capacity (538 mAh/g) were comparable to what the same group reported for the cell with gel polymer electrolyte. The voltage profile is shown in Figure 23. In order to provide further insight into the cell reaction, electrodes at different states of discharge and charge (points (a) to (e)) were characterized by differential scanning calorimetry (DSC) (Figure 3b). As several Na_2S_x polysulfides are thermodynamically stable, their presence in the electrode might be confirmed over their melting points, as shown in the phase diagram in Figure 16b. Notably, this is not possible for the Li/S_8 cell as Li_2S is the only stable compound with a defined melting point. The DSC curves indicate that the elemental sulfur disappears during discharge (signal at 114 °C disappears) and sodium polysulfides Na_2S_4 and Na_2S_5 form (signals 303 °C and 321 °C appear). After full discharge, these polysulfides are absent. After charging, the melting points of sulfur and Na_2S_5 reappear. Combined with results from XRD the authors concluded that Na_2S_n ($4 > n \geq 2$) forms during discharge and sulfur and Na_2S_n ($5 > n \geq 3$) during charge. The ideal discharge product, Na_2S, was not detected.

Lee et al. [258] studied the performance of a sodium–sulfur battery with the same ether-based electrolyte ($NaCF_3SO_3$ in tetraglyme), but using a cathode based on a composite of hollow carbon spheres and sulfur. The cell showed a high initial discharge capacity (1200 mAh/g with a low voltage cut-off at 0.5 V) with the following 20 cycles achieving around 600 mAh/g. At the same time, the discharge potential was only around 1 V (see Figure 24a). No further characterization on the discharge products was provided. In another configuration, the sodium anode was replaced by a Na–Sn–C composite electrode and so presented the first room temperature sodium-ion sulfur battery.

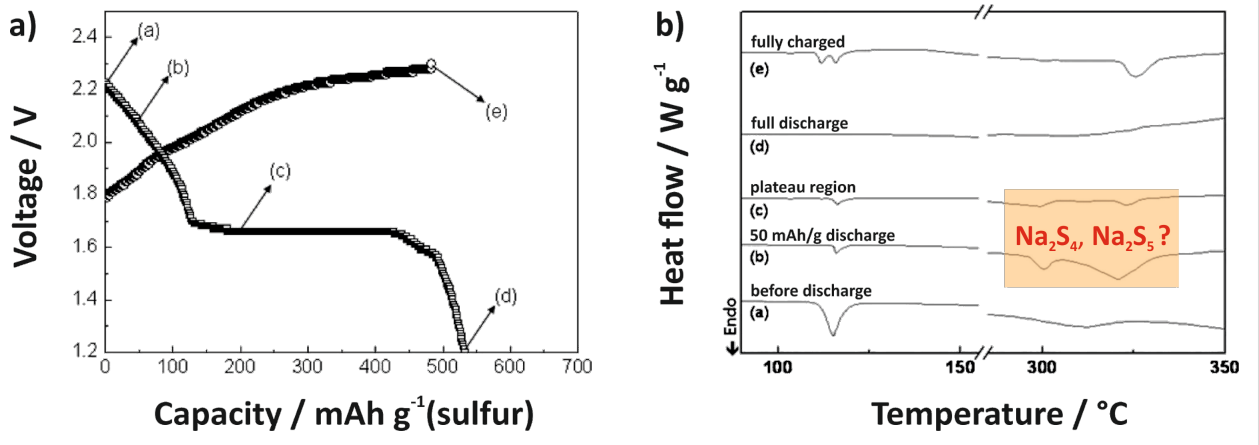

Figure 23: (a) First discharge–charge curve of a Na/S_8 battery with liquid electrolyte at room temperature and analysis points of sulfur electrode such as (a) pristine, (b) discharged to 50 mAh/g sulfur in sloping region, (c) discharged to 200 mAh/g sulfur in plateau region, (d) fully discharged to 1.2 V and (e) fully charged to 2.3 V. (b) DSC curves of the sulfur electrode with various cut-off voltage conditions as shown in (a). Figure adapted with permission from [257], copyright 2011 Elsevier.

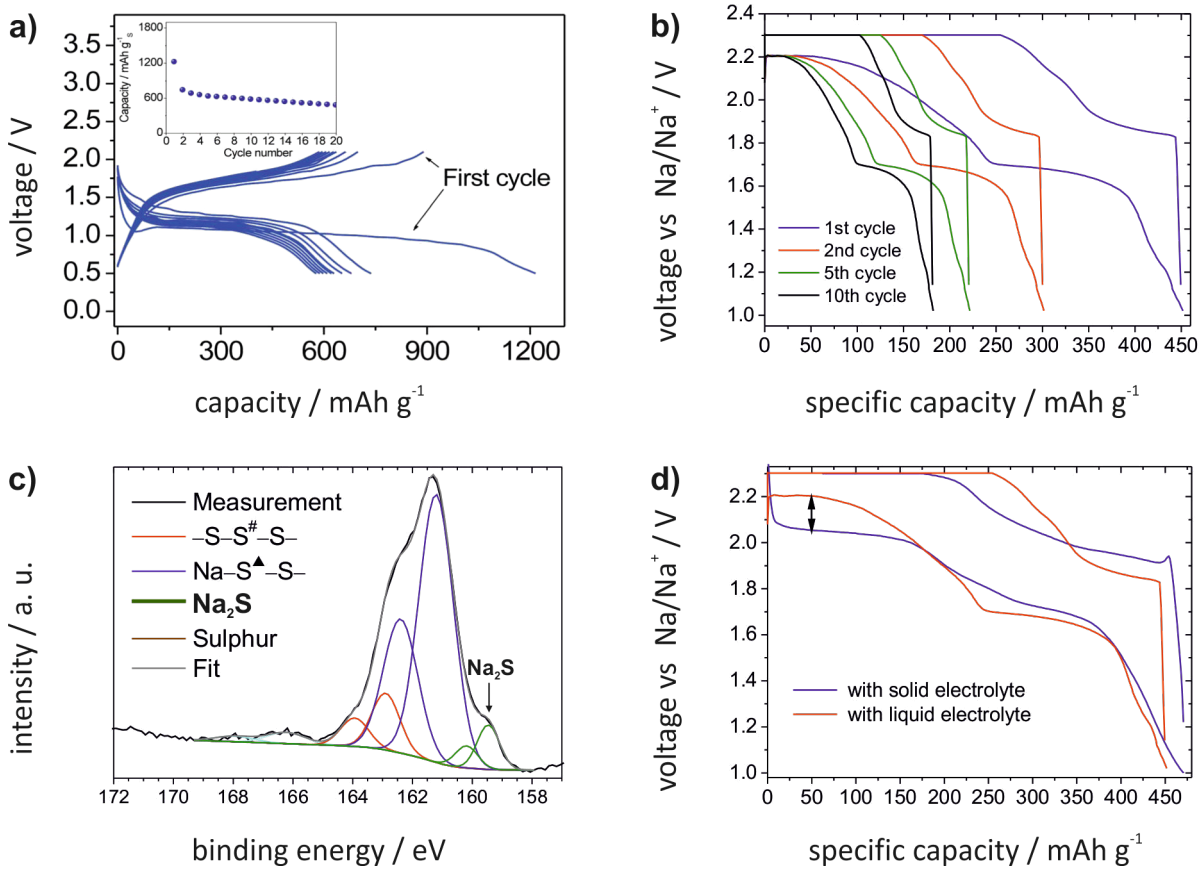

Figure 24: (a) Voltage profiles a of Na/S_8 cells with a TEGDME-based electrolyte and a nanostructured carbon/sulfur composite as cathode. Figure adapted with permission from [258], copyright 2013 The Royal Society of Chemistry. (b) Voltage profiles of a Na/S_8 cell with DOL:DME-based electrolyte and a cathode based on commercial materials. (c) XPS spectra of the sulfur electrode after discharge. (d) Comparison ov voltage profiles recorded at a rate of 10C for Na/S_8 cells with or without solid electrolyte. Figure adapted with permission from [259], copyright 2013 Elsevier.

Wenzel et al. [259] studied cells with an ether based electrolyte. Similarly to the results from Ryu et al., an initital discharge capacity of around 450 mAh/g and poor cycle life was found (see Figure 24b). Both the sodium anode and the sulfur cathode were studied by XPS. It was shown for the first time that – although sulfur reduction was incomplete – the ideal discharge product Na_2S formed during discharge and disappeared during charging (see Figure 24c). At the same time, a large amount of polysulfides and Na_2S was found on the sodium anode, indicating a very strong shuttle mechanism – in line what can be expected from Li/S_8 cells. To prevent this shuttle mechanism, an additional inorganic solid electrolyte membrane (beta-alumina) was implemented. With this hybrid electrolyte system, Coulombic efficencies close to 100% were found and somewhat higher capacities could be achieved during cycling. More importantly, cycling at a reasonable rate of 0.1C was still possible meaning that the solid electrolyte did not significantly increase the cell resistance (Figure 24d). This is different from Li/S_8 cells, where so far only poor kinetics were found for cells with free standing solid electrolyte membranes. We note that the availability of commercially available sodium-ion conducting solid electrolytes with good transport properties in the bulk and through the interfaces with liquid electrolytes offers additional opportunities in designing catholyte based cells. Nevertheless the cells still suffered from strong fading which was finally attributed to the decomposition of the PVDF binder in the presence of polysulfides.

Hwang et al. [260] followed the approach by Wang et al. and produced a composite based on heat treating a mixture of PAN and sulfur; however, PAN nanofibers instead of powder were used. Also here, a carbonate based electrolyte was used ($NaClO_4$ in EC:DMC). The cell showed a first discharge capacity of 800 mAh/g and an excellent an cycle life. On the other hand, the sulfur loading was quite small (0.31–0.38 mg/cm^2). In line with the results by Wang et al., the voltage profile shows an overall sloping behavior and partially low voltages. The authors further showed that the sodium anode

was free of sulfur after 500 cycles. This means that polysulfide diffusion from the cathode to the anode can be effectively suppressed by chemically binding sulfur to carbon.

Xin et al. [261] studied the performance of a nanostructured composite consisting of CNTs covered with a microporous layer. The material was designed to alter the reaction mechanism in a beneficial way and had been tested for Li/S_8 cells by the same group in an earlier study [169]. The idea is that the confinement of nanopores only allows the formation of small compounds, thus, the formation of large S_8 molecules and large, highly soluble polysulfides is prevented. As a result, the cell reaction is restricted to small S_{2-4} molecules and Li_2S only, thus improving cycle life and rate capabitlity. The concept also leads to improvements in case of Na/S_8 cells. An initial discharge capacity of about 1610 mAh/g was found, followed by stable cycling at 1000 mAh/g. Also here, a carbonate-based electrolyte was employed (1 M $NaClO_4$ in PC:EC) and the voltage shifts to low values (more than half of the capacity is achieved at voltages below 1.5 V).

Bauer et al. [262] used a polymer membrane to reduce the shuttle mechanism in Na/S_8 cells with ether-based electrolyte ($NaClO_4$ in TEGDME). The membrane was prepared by coating a standard polypropylene separator with Nafion. The initial discharge capacity was around 400 mAh/g, which is similar to what other groups obtained when using ether based electrolytes.

Zheng et al. [263] studied the performance of composite materials containing a high surface area mesoporous carbon, sulfur and copper nanoparticles. The copper nanoparticles were added in order to trap soluble polysulfides by CuS_x formation [263] and a carbonate-based electrolyte was applied ($NaClO_4$ in EC:DMC). The first discharge mainly occurs at very low voltage platetau of around 1.0 V and reaches almost 1000 mAh/g. After this activation cycle, stable capacities of around 600 mAh/g are achieved for more than 100 cycles, with Coulombic efficiencies close to 100% and sloping potential curves. Also here, the average voltage values during discharge remain relatively small to what would be ideally expected for the formation of Na_2S. On the downside, the sulfur loading of the electrode is very small. Although the copper content of the electrodes is small (10%), the cycling behavior shows quite some similarity to a conventional conversion between sodium and CuS_x for which an activation cycle and sloping potentials are well known. Ideally, the conversion reaction of sodium with CuS and Cu_2S would occur at 1.58 V and 1.39 V, respectively [10].

Yu et al. [253] suggested that the often observed capacity fade in Na/S_8 cells is due to the poor reversibility of the insoluble discharge products Na_2S_n ($1 \leq n < 4$). Therefore the group used a cell design optimized for shallow cycling between sulfur and soluble long chain polysulfides with the overall reaction $nS + 2\ Na^+ + 2\ e^- = Na_2S_n$ ($4 \leq n \leq 8$) (see Figure 25). Essentially, this approach is close to a catholyte concept. Evidence for the cell reaction was provided by XPS and UV–vis measurements. A comparable approach was successfully applied in Li/S_8 cells before by the same group [265,266]. Shuttling of the highly soluble, long polysulfides towards the sodium anode was delayed by implementing an additional nanostructured carbon

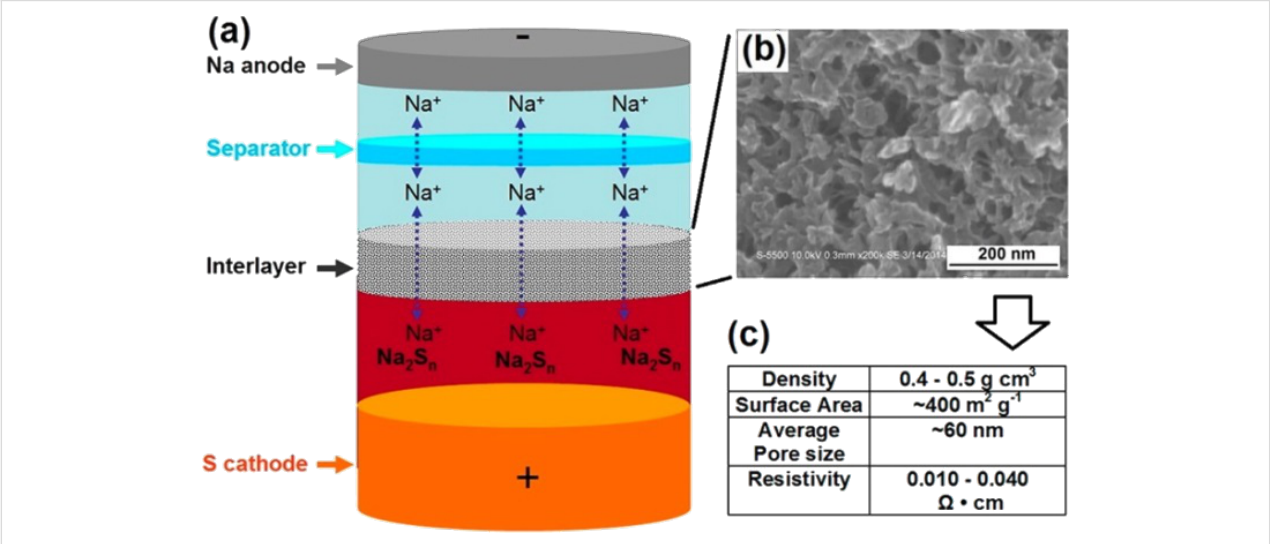

Figure 25: Room temperature sodium–sulfur battery based on shallow cycling between sulfur and soluble long chain polysulfides. An additional interlayer is used to reduce diffusion of polysulfides towards the sodium anode. Figure adapted with permission from [253], copyright 2014 American Chemical Society.

interlayer (thickness not reported) and using a concentrated electrolyte including $NaNO_3$ (1.5 M $NaClO_4$ and 0.3 M $NaNO_3$ in TEGDME). $LiNO_3$ is a well-known anti-shuttling agent in Li/S_8 cells that protects the lithium anode. Overall, very stable cycling of the cell at 250 mAh/g was achieved for 50 cycles. The average discharge voltage during galvanostatic cycling was around 2.25 V, however, charging curves were not shown so it remains unclear whether the shuttle effect could be prevented.

Overall comparison: In order to compare the different experimental results on Na/S_8 cells, we digitalized literature data of the first galvanostatic cycle (if available) and plotted them into one diagram (see Figure 26). More data is summarized in Table 4. Obviously some noticeable differences exist.

Results for cells can be grouped according to their voltage profiles as follows:

1. Studies using solvents that are frequently used in Li/S_8 cells (DOL:DME, tetraglyme) found a discharge behavior that is qualitatively quite similar to what is known from Li/S_8 cells, that is, one or two plateaus occur at voltages not too far away from the overall expected cell potential (1.85 V). Charging occurs at slightly larger overpotentials compared the Li/S_8 cell. The main difference, however, is that the achieved capacities are very low. Although it was shown that the theoretical end product Na_2S forms during discharge, the reaction is incomplete and only about 350–550 mAh/g are found corresponding to an overall composition of Na_2S_x ($3 \leq x \leq 5$). So solvents that work well for Li/S_8 cells seem to perform bad in Na/S_8 cells. A notable exception is the work from Lee et al. [258] who used tetraglyme and found a capacity of 1200 mAh/g. But here, discharge mainly occurs at voltages close to 1 V only (cut-off potential of 0.5 V).
2. Studies with carbonate based solvents showed much higher capacities and often also superior cycle life. In one study, the capacity was even close to the theoretical value. At the same time, the voltage profiles of these cells are very different from Li/S_8 cells and usually exhibit sloping potentials during subsequent cycling and much of the capacity is obtained at voltages below 1.5 V. Such low voltages are also undesired with respect to energy density. One could argue that also the conductive salt might have an influence, however, one can conclude from results obtained for Li/S_8 cells that this is less likely [205].

Assuming bulk thermodynamics, it is interesting to note that the lowest cell voltage possible is due to the reaction Equation 7:

$$2Na + Na_2S_2 \rightleftharpoons 2Na_2S$$

for which $E° = 1.68$ V can be calculated (see above). This reaction contributes to half of the theoretical capacity of sulfur (836 mAh/g). During discharge, the cell voltage should therefore fall below this value at some point which is fulfilled for all results shown in Figure 26. During charge, one should immediately exceed this voltage; however, this is not always the case. It seems that cells with high discharge capacity partially charge below this thermodynamically derived threshold. Assuming that the thermodynamic data is correct, one has to conclude that other reactions take place. In some cases, this unexpected

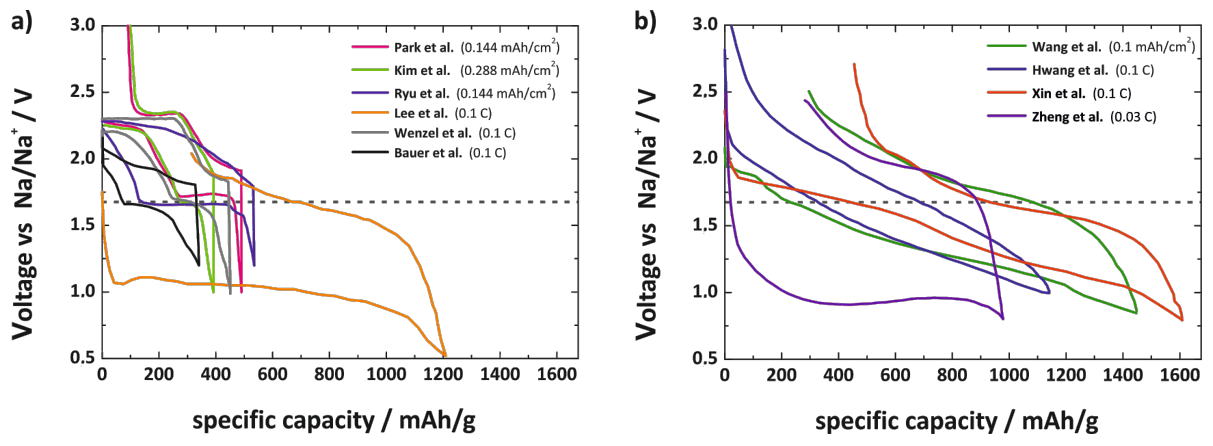

Figure 26: Literature overview on different studies of Na/S_8 cells with liquid electrolyte operating at room temperature. The comparison shows the first cycle. The data was digitalized from the different publications. (a) Cells with ether-based electrolytes. (b) Cells with carbonate-based electrolytes. The dotted line indicates the lowest cell voltage possible assuming bulk thermodynamics for the solid state reaction from Na_2S_2 to Na_2S. This reaction theoretically accounts for 836 mAh/g.

voltage profile might be due to sulfur bound covalently to carbon [255,260] or due to CuS_x [255] formation, however, a clear understanding is missing. Taking these results together, many questions remain and further studies are needed to clarify the link between voltage profile, cycle life, sulfur utilization, and electrolyte composition. As it is well known from Li/S_8 cells that carbonate based electrolytes are unstable against polysulfides [205,267], future studies should clarify whether side reactions contribute to the high capacities reported for some Na/S_8 cells.

Moreover, all studies reporting capacities exceeding 1000 mAh/g were only achieved with small sulfur loadings meaning that the sulfur content of the electrode was considerably smaller than 50 wt %. In line with research on Li/S_8 batteries one has to emphasize the need to increase this value in case an application should become feasible. Given the very early state of research, however, the overall perspective for Na/S_8 cells is yet unclear, and further work is required to better judge the practical potential.

Conclusion

Lithium–sulfur and lithium–oxygen cells have attracted enormous interest in the last ten years, and the frequency of publications is still increasing. In the case of Li–sulfur batteries the major challenges have been obvious already at the very beginning (e.g., lithium dendrites, polysulfide shuttle) but still await a proper and effective solution. While incremental improvements can be recognized, it is unclear whether the Li–sulfur battery can finally beat LIB technology with respect to energy capacity. It is interesting to note that the majority of papers deals with the design of carbon/sulfur papers rather than targeting the critical issue of the anode.

In the case of lithium–oxygen batteries the current status is different. After an initial phase of enthusiasm major drawbacks (electrolyte decomposition, carbon instability, the need for pure oxygen) have damped too optimistic expectations, and Li/O_2 batteries are now again primarily the target of academic research.

As both systems rely on multielectron transfer reactions at the cathode, and as solid phases are being formed and dissolved during cycling, the kinetics are slow compared to LIB and the energy efficiency as also the power density are not competitive yet. This may easily lead to a pessimistic outlook, but this would not be an appropriate conclusion. Rather one should consider lithium–sulfur and lithium–oxygen batteries as attractive targets which have already triggered numerous valuable technical and chemical innovations – but which still require major innovations in electrolyte and electrode design.

In contrast, (room temperature) sodium–sulfur and sodium–oxygen cells have only very recently attracted interest. Obviously, the lower theoretical energy capacity makes sodium-based systems second choice at first glance. On the other hand, sodium systems can provide some specific advantages that might help to overcome the obstacles known from the analogue lithium based cells. Several aspects have been discussed in this review. The availability of Na beta-alumina as highly conductive room temperature solid electrolyte that is also chemically stable in contact with sodium might be an important advantage for designing future cell concepts, for example. Moreover, sodium has the advantage to be much more abundant than lithium.

An intriguing example was also shown for the Na/O_2 cell, where formation of NaO_2 as discharge product offers significant advantages compared to the Li/O_2 cell with respect to energy efficiency and reversibility. Comparing results on metal–oxygen batteries is generally difficult as research groups usually use different cell designs, materials and measurement conditions. However, the shape of voltage profile (voltage hysteresis) gives a first impression on the cell performance with respect to reversibility and efficiency. We therefore suggest using a simple 3 × 3 matrix that allows quick assessment of the overall performance of metal–oxygen cells. The ideal voltage profile corresponds to Type 1A which is not found for any of the metal–oxygen cell yet. Most close to this behavior are Na/O_2 cells with NaO_2 as discharge product and are classified as Type 1B. Most other metal–oxygen cells show a Type 2C/3B or Type 3C behavior. Still, very little is known about the cell chemistry of sodium–oxygen cells and it is surprising that different groups find different discharge products. Giving a reasonable explanation for this is an important research task.

Even less is known about the cell chemistry of room-temperature Na/S_8 cells. The research overview showed that (with one exception), the voltage profile seems to depend on the electrolyte composition. In ether based electrolytes, the voltage profile shows similarity to what is known from Li/S_8 cells. But although Na_2S forms as discharge product, only low capacities and poor cycle life is achieved. The situation is different when carbonate based electrolytes are used. Much higher capacities and improved cycle life have been reported. On the other hand, the voltage profiles are much less defined and carbonates might be simply instable against polysulfides as it is known from Li/S_8 cells. Clearly, there is a need to further understand the cell reaction. At the current state, Na/S_8 cells are not competitive with Li/S_8 cells.

In conclusion, given the relatively early state of research, (room temperature) sodium–sulfur and sodium–oxygen cells already

show some attractive properties and the recent increase in research activity is a clear sign for the development of two new independent research fields. At the same time, we emphasize that just as for the analogue lithium-based systems, the road towards practical systems is long and might not necessarily lead to application – in particular in view of the energy densities which may finally not beat the LIB. Aiming for low cost stationary energy stores seems most attractive, especially considering the Na/S_8 system. Progress towards practical devices will be only achieved when challenges of all cell components, that is, anode, cathode and electrolyte, are addressed and side reactions are minimized. Moreover, understanding the of role impurities on the cell reactions need further attention. Innovative approaches in both fundamental research and technical development are therefore needed.

Acknowledgements

The authors are grateful to the Federal state of Hessen (ElCh infrastructure support, LOEWE program STORE-E) and the Funds of the Chemical Industry (FCI) for financial support. Long term support and invaluable discussions within the International Network for Electrochemistry and Batteries of BASF SE (Ludwigshafen) are also gratefully acknowledged.

References

1. Zaghib, K.; Mauger, A.; Groult, H.; Goodenough, J. B.; Julien, C. M. *Materials* **2013,** *6,* 1028–1049. doi:10.3390/ma6031028
2. Cabana, J.; Monconduit, L.; Larcher, D.; Rosa Palacin, M. *Adv. Mater.* **2010,** *22,* E170–E192. doi:10.1002/adma.201000717
3. Kubota, K.; Yabuuchi, N.; Yoshida, H.; Dahbi, M.; Komaba, S. *MRS Bull.* **2014,** *39,* 416–422. doi:10.1557/mrs.2014.85
4. Dahbi, M.; Yabuuchi, N.; Kubota, K.; Tokiwa, K.; Komaba, S. *Phys. Chem. Chem. Phys.* **2014,** *16,* 15007–15028. doi:10.1039/C4CP00826J
5. Ellis, B. L.; Nazar, L. F. *Curr. Opin. Solid State Mater. Sci.* **2012,** *16,* 168–177. doi:10.1016/j.cossms.2012.04.002
6. Kim, S.-W.; Seo, D.-H.; Ma, X.; Ceder, G.; Kang, K. *Adv. Energy Mater.* **2012,** *2,* 710–721. doi:10.1002/aenm.201200026
7. Palomares, V.; Serras, P.; Villaluenga, I.; Hueso, K. B.; Carretero-González, J.; Rojo, T. *Energy Environ. Sci.* **2012,** *5,* 5884–5901. doi:10.1039/c2ee02781j
8. Pan, H. L.; Hu, Y. S.; Chen, L. Q. *Energy Environ. Sci.* **2013,** *6,* 2338–2360. doi:10.1039/c3ee40847g
9. Slater, M. D.; Kim, D.; Lee, E.; Johnson, C. S. *Adv. Funct. Mater.* **2013,** *23,* 947–958. doi:10.1002/adfm.201200691
10. Klein, F.; Jache, B.; Bhide, A.; Adelhelm, P. *Phys. Chem. Chem. Phys.* **2013,** *15,* 15876–15887. doi:10.1039/c3cp52125g
11. Holleman, A.; Wiberg, N. *Lehrbuch der Anorganischen Chemie,* 102nd ed.; De Gruyter: Berlin, 2007.
12. Wen, Z.; Cao, J.; Gu, Z.; Xu, X.; Zhang, F.; Lin, Z. *Solid State Ionics* **2008,** *179,* 1697–1701. doi:10.1016/j.ssi.2008.01.070
13. Akhil, A. A.; Boyes, J. D.; Bulter, P. C.; Doughty, D. H. Batteries for electrical energy storage applications. In *Linden's Handbook of Batteries,* 4th ed.; Reddy, T. B., Ed.; McGraw-Hill: New York, 2011.
14. Hueso, K. B.; Armand, M.; Rojo, T. *Energy Environ. Sci.* **2013,** *6,* 734–749. doi:10.1039/c3ee24086j
15. Oshima, T.; Kajita, M.; Okuno, A. *Int. J. Appl. Ceram. Technol.* **2004,** *1,* 269–276. doi:10.1111/j.1744-7402.2004.tb00179.x
16. Hartmann, P.; Leichtweiss, T.; Busche, M. R.; Schneider, M.; Reich, M.; Sann, J.; Adelhelm, P.; Janek, J. *J. Phys. Chem. C* **2013,** *117,* 21064–21074. doi:10.1021/jp4051275
17. Eufinger, J.-P.; Schmidt, A.; Lerch, M.; Janek, J. *Phys. Chem. Chem. Phys.* **2015,** *17,* 6844–6857. doi:10.1039/C4CP05442C
18. Sangster, J.; Pelton, A. D. *J. Phase Equilib.* **1992,** *13,* 296–299. doi:10.1007/BF02667558
19. Wriedt, H. A. *Bull. Alloy Phase Diagrams* **1987,** *8,* 234–246. doi:10.1007/BF02874915
20. Ren, X.; Wu, Y. *J. Am. Chem. Soc.* **2013,** *135,* 2923–2926. doi:10.1021/ja312059q
21. Ren, X.; Lau, K. C.; Yu, M.; Bi, X.; Kreidler, E.; Curtiss, L. A.; Wu, Y. *ACS Appl. Mater. Interfaces* **2014,** *6,* 19299–19307. doi:10.1021/am505351s
22. Girishkumar, G.; McCloskey, B.; Luntz, A. C.; Swanson, S.; Wilcke, W. *J. Phys. Chem. Lett.* **2010,** *1,* 2193–2203. doi:10.1021/jz1005384
23. Christensen, J.; Albertus, P.; Sanchez-Carrera, R. S.; Lohmann, T.; Kozinsky, B.; Liedtke, R.; Ahmed, J.; Kojic, A. *J. Electrochem. Soc.* **2012,** *159,* R1–R30. doi:10.1149/2.086202jes
24. Visco, S. J.; Nimon, V. Y.; Petrov, A.; Pridatko, K.; Goncharenko, N.; Nimon, E.; De Jonghe, L.; Volfkovich, Y. M.; Bograchev, D. A. *J. Solid State Electrochem.* **2014,** *18,* 1443–1456. doi:10.1007/s10008-014-2427-x
25. Gallagher, K. G.; Goebel, S.; Greszler, T.; Mathias, M.; Oelerich, W.; Eroglu, D.; Srinivasan, V. *Energy Environ. Sci.* **2014,** *7,* 1555–1563. doi:10.1039/c3ee43870h
26. Peled, E.; Golodnitsky, D.; Mazor, H.; Goor, M.; Avshalomov, S. *J. Power Sources* **2011,** *196,* 6835–6840. doi:10.1016/j.jpowsour.2010.09.104
27. Bender, C. L.; Hartmann, P.; Vračar, M.; Adelhelm, P.; Janek, J. *Adv. Energy Mater.* **2014,** *4,* 1301863. doi:10.1002/aenm.201301863
28. Lyall, A. E. U.S. Patent US3625769, Dec 7, 1971.
29. Abraham, K. M.; Jiang, Z. *J. Electrochem. Soc.* **1996,** *143,* 1–5. doi:10.1149/1.1836378
30. Read, J. *J. Electrochem. Soc.* **2002,** *149,* A1190–A1195. doi:10.1149/1.1498256
31. Débart, A.; Paterson, A. J.; Bao, J.; Bruce, P. G. *Angew. Chem., Int. Ed. Engl.* **2008,** *47,* 4521–4524. doi:10.1002/anie.200705648
32. Lu, Y.-C.; Gallant, B. M.; Kwabi, D. G.; Harding, J. R.; Mitchell, R. R.; Whittingham, M. S.; Shao-Horn, Y. *Energy Environ. Sci.* **2013,** *6,* 750–768. doi:10.1039/c3ee23966g
33. Zhou, G.; Pei, S.; Li, L.; Wang, D.-W.; Wang, S.; Huang, K.; Yin, L.-C.; Li, F.; Cheng, H.-M. *Adv. Mater.* **2014,** *26,* 664. doi:10.1002/adma.201470027
34. Garcia-Araez, N.; Novák, P. *J. Solid State Electrochem.* **2013,** *17,* 1793–1807. doi:10.1007/s10008-013-1999-1
35. Débart, A.; Bao, J.; Armstrong, G.; Bruce, P. G. *J. Power Sources* **2007,** *174,* 1177–1182. doi:10.1016/j.jpowsour.2007.06.180
36. Jin, L.; Xu, L.; Morein, C.; Chen, C.-H.; Lai, M.; Dharmarathna, S.; Dobley, A.; Suib, S. L. *Adv. Funct. Mater.* **2010,** *20,* 3373–3382. doi:10.1002/adfm.201001080
37. Ominde, N.; Bartlett, N.; Yang, X.-Q.; Qu, D. *J. Power Sources* **2008,** *185,* 747–753. doi:10.1016/j.jpowsour.2008.07.065

38. Zhang, G. Q.; Zheng, J. P.; Liang, R.; Zhang, C.; Wang, B.; Au, M.; Hendrickson, M.; Plichta, E. J. *J. Electrochem. Soc.* **2011,** *158,* A822. doi:10.1149/1.3590736
39. Lu, Y.-C.; Xu, Z.; Gasteiger, H. A.; Chen, S.; Hamad-Schifferli, K.; Shao-Horn, Y. *J. Am. Chem. Soc.* **2010,** *132,* 12170–12171. doi:10.1021/ja1036572
40. Cheng, H.; Scott, K. *Appl. Catal., B: Environ.* **2011,** *108–109,* 140–151. doi:10.1016/j.apcatb.2011.08.021
41. Lu, J.; Lei, Y.; Lau, K. C.; Luo, X.; Du, P.; Wen, J.; Assary, R. S.; Das, U.; Miller, D. J.; Elam, J. W.; Albishri, H. M.; El-Hady, D. A.; Sun, Y.-K.; Curtiss, L. A.; Amine, K. *Nat. Commun.* **2013,** *4,* 2383. doi:10.1038/ncomms3383
42. McCloskey, B. D.; Scheffler, R.; Speidel, A.; Bethune, D. S.; Shelby, R. M.; Luntz, A. C. *J. Am. Chem. Soc.* **2011,** *133,* 18038–18041. doi:10.1021/ja207229n
43. Xu, K. *Chem. Rev.* **2004,** *104,* 4303–4417. doi:10.1021/cr030203g
44. Mizuno, F.; Nakanishi, S.; Kotani, Y.; Yokoishi, S.; Iba, H. *Electrochemistry* **2010,** *78,* 403–405. doi:10.5796/electrochemistry.78.403
45. Freunberger, S. A.; Chen, Y.; Peng, Z.; Griffin, J. M.; Hardwick, L. J.; Bardé, F.; Novák, P.; Bruce, P. G. *J. Am. Chem. Soc.* **2011,** *133,* 8040–8047. doi:10.1021/ja2021747
46. McCloskey, B. D.; Bethune, D. S.; Shelby, R. M.; Girishkumar, G.; Luntz, A. C. *J. Phys. Chem. Lett.* **2011,** *2,* 1161–1166. doi:10.1021/jz200352v
47. Veith, G. M.; Dudney, N. J.; Howe, J.; Nanda, J. *J. Phys. Chem. C* **2011,** *115,* 14325–14333. doi:10.1021/jp2043015
48. Xu, W.; Viswanathan, V. V.; Wang, D.; Towne, S. A.; Xiao, J.; Nie, Z.; Hu, D.; Zhang, J.-G. *J. Power Sources* **2011,** *196,* 3894–3899. doi:10.1016/j.jpowsour.2010.12.065
49. Bryantsev, V. S.; Giordani, V.; Walker, W.; Blanco, M.; Zecevic, S.; Sasaki, K.; Uddin, J.; Addison, D.; Chase, G. V. *J. Phys. Chem. A* **2011,** *115,* 12399–12409. doi:10.1021/jp2073914
50. Laino, T.; Curioni, A. *Chemistry* **2012,** *18,* 3510–3520. doi:10.1002/chem.201103057
51. Hyoung Oh, S.; Yim, T.; Pomerantseva, E.; Nazar, L. F. *Electrochem. Solid-State Lett.* **2011,** *14,* A185–A188. doi:10.1149/2.003112esl
52. Chalasani, D.; Lucht, B. L. *ECS Electrochem. Lett.* **2012,** *1,* A38–A42. doi:10.1149/2.010202eel
53. Veith, G. M.; Nanda, J.; Delmau, L. H.; Dudney, N. J. *J. Phys. Chem. Lett.* **2012,** *3,* 1242–1247. doi:10.1021/jz300430s
54. Aurbach, D.; Daroux, M.; Faguy, P.; Yeager, E. *J. Electroanal. Chem.* **1991,** *297,* 225–244. doi:10.1016/0022-0728(91)85370-5
55. Mizuno, F.; Takechi, K.; Higashi, S.; Shiga, T.; Shiotsuki, T.; Takazawa, N.; Sakurabayashi, Y.; Okazaki, S.; Nitta, I.; Kodama, T.; Nakamoto, H.; Nishikoori, H.; Nakanishi, S.; Kotani, Y.; Iba, H. *J. Power Sources* **2013,** *228,* 47–56. doi:10.1016/j.jpowsour.2012.11.077
56. Cecchetto, L.; Salomon, M.; Scrosati, B.; Croce, F. *J. Power Sources* **2012,** *213,* 233–238. doi:10.1016/j.jpowsour.2012.04.038
57. Allen, C. J.; Mukerjee, S.; Plichta, E. J.; Hendrickson, M. A.; Abraham, K. M. *J. Phys. Chem. Lett.* **2011,** *2,* 2420–2424. doi:10.1021/jz201070t
58. Xu, D.; Wang, Z.-L.; Xu, J.-J.; Zhang, L.-L.; Zhang, X.-B. *Chem. Commun.* **2012,** *48,* 6948–6950. doi:10.1039/c2cc32844e
59. Trahan, M. J.; Mukerjee, S.; Plichta, E. J.; Hendrickson, M. A.; Abraham, K. M. *J. Electrochem. Soc.* **2012,** *160,* A259–A267. doi:10.1149/2.048302jes
60. Chen, Y.; Freunberger, S. A.; Peng, Z.; Bardé, F.; Bruce, P. G. *J. Am. Chem. Soc.* **2012,** *134,* 7952–7957. doi:10.1021/ja302178w
61. Giordani, V.; Walker, W.; Bryantsev, V. S.; Uddin, J.; Chase, G. V.; Addison, D. *J. Electrochem. Soc.* **2013,** *160,* A1544–A1550. doi:10.1149/2.097309jes
62. Wang, H.; Liao, X.-Z.; Li, L.; Chen, H.; Jiang, Q.-Z.; He, Y.-S.; Ma, Z.-F. *J. Electrochem. Soc.* **2012,** *159,* A1874–A1879. doi:10.1149/2.012212jes
63. Zhang, Z.; Lu, J.; Assary, R. S.; Du, P.; Wang, H.-H.; Sun, Y.-K.; Qin, Y.; Lau, K. C.; Greeley, J.; Redfern, P. C.; Iddir, H.; Curtiss, L. A.; Amine, K. *J. Phys. Chem. C* **2011,** *115,* 25535–25542. doi:10.1021/Jp2087412
64. Xu, D.; Wang, Z.-L.; Xu, J.-J.; Zhang, L.-L.; Wang, L.-M.; Zhang, X.-B. *Chem. Commun.* **2012,** *48,* 11674–11676. doi:10.1039/c2cc36815c
65. Sharon, D.; Etacheri, V.; Garsuch, A.; Afri, M.; Frimer, A. A.; Aurbach, D. *J. Phys. Chem. Lett.* **2013,** *4,* 127–131. doi:10.1021/jz3017842
66. Meini, S.; Tsiouvaras, N.; Schwenke, K. U.; Piana, M.; Beyer, H.; Lange, L.; Gasteiger, H. A. *Phys. Chem. Chem. Phys.* **2013,** *15,* 11478–11493. doi:10.1039/c3cp51112j
67. McCloskey, B. D.; Garcia, J. M.; Luntz, A. C. *J. Phys. Chem. Lett.* **2014,** *5,* 1230–1235. doi:10.1021/jz500494s
68. McCloskey, B. D.; Bethune, D. S.; Shelby, R. M.; Mori, T.; Scheffler, R.; Speidel, A.; Sherwood, M.; Luntz, A. C. *J. Phys. Chem. Lett.* **2012,** *3,* 3043–3047. doi:10.1021/jz301359t
69. Freunberger, S. A.; Chen, Y.; Drewett, N. E.; Hardwick, L. J.; Bardé, F.; Bruce, P. G. *Angew. Chem., Int. Ed. Engl.* **2011,** *50,* 8609–8613. doi:10.1002/anie.201102357
70. Adams, B. D.; Black, R.; Williams, Z.; Fernandes, R.; Cuisinier, M.; Berg, E. J.; Novak, P.; Murphy, G. K.; Nazar, L. F. *Adv. Energy Mater.* **2015,** *5,* 1400867. doi:10.1002/aenm.201400867
71. Kang, S. J.; Mori, T.; Narizuka, S.; Wilcke, W.; Kim, H. C. *Nat. Commun.* **2014,** *5,* 3937. doi:10.1038/ncomms4937
72. Xu, W.; Xu, K.; Viswanathan, V. V.; Towne, S. A.; Hardy, J. S.; Xiao, J.; Nie, Z.; Hu, D.; Wang, D.; Zhang, J.-G. *J. Power Sources* **2011,** *196,* 9631–9639. doi:10.1016/j.jpowsour.2011.06.099
73. Walker, W.; Giordani, V.; Uddin, J.; Bryantsev, V. S.; Chase, G. V.; Addison, D. *J. Am. Chem. Soc.* **2013,** *135,* 2076–2079. doi:10.1021/ja311518s
74. Tsiouvaras, N.; Meini, S.; Buchberger, I.; Gasteiger, H. A. *J. Electrochem. Soc.* **2013,** *160,* A471–A477. doi:10.1149/2.042303jes
75. Novák, P.; Panitz, J.-C.; Joho, F.; Lanz, M.; Imhof, R.; Coluccia, M. *J. Power Sources* **2000,** *90,* 52–58. doi:10.1016/S0378-7753(00)00447-X
76. Barile, C. J.; Gewirth, A. A. *J. Electrochem. Soc.* **2013,** *160,* A549–A552. doi:10.1149/2.033304jes
77. Armstrong, A. R.; Holzapfel, M.; Novák, P.; Johnson, C. S.; Kang, S.-H.; Thackeray, M. M.; Bruce, P. G. *J. Am. Chem. Soc.* **2006,** *128,* 8694–8698. doi:10.1021/ja062027+
78. Hartmann, P.; Bender, C. L.; Sann, J.; Dürr, A. K.; Jansen, M.; Janek, J.; Adelhelm, P. *Phys. Chem. Chem. Phys.* **2013,** *15,* 11661–11672. doi:10.1039/c3cp50930c
79. McCloskey, B. D.; Valery, A.; Luntz, A. C.; Gowda, S. R.; Wallraff, G. M.; Garcia, J. M.; Mori, T.; Krupp, L. E. *J. Phys. Chem. Lett.* **2013,** *4,* 2989–2993. doi:10.1021/jz401659f
80. Hase, Y.; Ito, E.; Shiga, T.; Mizuno, F.; Nishikoori, H.; Iba, H.; Takechi, K. *Chem. Commun.* **2013,** *49,* 8389–8391. doi:10.1039/c3cc44723e

81. Black, R.; Oh, S. H.; Lee, J.-H.; Yim, T.; Adams, B.; Nazar, L. F. *J. Am. Chem. Soc.* **2012,** *134,* 2902–2905. doi:10.1021/ja2111543
82. McCloskey, B. D.; Speidel, A.; Scheffler, R.; Miller, D. C.; Viswanathan, V.; Hummelshøj, J. S.; Nørskov, J. K.; Luntz, A. C. *J. Phys. Chem. Lett.* **2012,** *3,* 997–1001. doi:10.1021/jz300243r
83. Ottakam Thotiyl, M. M.; Freunberger, S. A.; Peng, Z.; Bruce, P. G. *J. Am. Chem. Soc.* **2013,** *135,* 494–500. doi:10.1021/ja310258x
84. Ottakam Thotiyl, M. M.; Freunberger, S. A.; Peng, Z.; Chen, Y.; Liu, Z.; Bruce, P. G. *Nat. Mater.* **2013,** *12,* 1050–1056. doi:10.1038/nmat3737
85. Younesi, R.; Norby, P.; Vegge, T. *ECS Electrochem. Lett.* **2014,** *3,* A15–A18. doi:10.1149/2.001403eel
86. Sharon, D.; Afri, M.; Noked, M.; Garsuch, A.; Frimer, A. A.; Aurbach, D. *J. Phys. Chem. Lett.* **2013,** *4,* 3115–3119. doi:10.1021/Jz4017188
87. Adams, B. D.; Radtke, C.; Black, R.; Trudeau, M. L.; Zaghib, K.; Nazar, L. F. *Energy Environ. Sci.* **2013,** *6,* 1772–1778. doi:10.1039/c3ee40697k
88. Radin, M. D.; Siegel, D. J. *Energy Environ. Sci.* **2013,** *6,* 2370–2379. doi:10.1039/c3ee41632a
89. Radin, M. D.; Rodriguez, J. F.; Tian, F.; Siegel, D. J. *J. Am. Chem. Soc.* **2012,** *134,* 1093–1103. doi:10.1021/ja208944x
90. Garcia-Lastra, J. M.; Myrdal, J. S. G.; Christensen, R.; Thygesen, K. S.; Vegge, T. *J. Phys. Chem. C* **2013,** *117,* 5568–5577. doi:10.1021/jp3107809
91. Gerbig, O.; Merkle, R.; Maier, J. *Adv. Mater.* **2013,** *25,* 3129–3133. doi:10.1002/adma.201300264
92. Viswanathan, V.; Thygesen, K. S.; Hummelshøj, J. S.; Nørskov, J. K.; Girishkumar, G.; McCloskey, B. D.; Luntz, A. C. *J. Chem. Phys.* **2011,** *135,* 214704. doi:10.1063/1.3663385
93. Luntz, A. C.; Viswanathan, V.; Voss, J.; Varley, J. B.; Nørskov, J. K.; Scheffler, R.; Speidel, A. *J. Phys. Chem. Lett.* **2013,** *4,* 3494–3499. doi:10.1021/jz401926f
94. Aetukuri, N. B.; McCloskey, B. D.; Garcia, J. M.; Krupp, L. E.; Viswanathan, V.; Luntz, A. C. *arXiv [cond-mat.mtrl-sci]* **2014,** No. 1406.3335.
95. Zheng, H.; Xiao, D.; Li, X.; Liu, Y.; Wu, Y.; Wang, J.; Jiang, K.; Chen, C.; Gu, L.; Wei, X.; Hu, Y.-S.; Chen, Q.; Li, H. *Nano Lett.* **2014,** *14,* 4245–4249. doi:10.1021/nl500862u
96. Chase, G. V.; Zecevic, S.; Walker, W.; Uddin, J.; Sasaki, K. A.; Giordani, V.; Bryantsev, V. S.; Blanco, M.; Addison, D. U.S. Patent US2011/033821, Oct 27, 2011.
97. Chen, Y.; Freunberger, S. A.; Peng, Z.; Fontaine, O.; Bruce, P. G. *Nat. Chem.* **2013,** *5,* 489–494. doi:10.1038/nchem.1646
98. Lim, H.-D.; Song, H.; Kim, J.; Gwon, H.; Bae, Y.; Park, K.-Y.; Hong, J.; Kim, H.; Kim, T.; Kim, Y. H.; Lepró, X.; Ovalle-Robles, R.; Baughman, R. H.; Kang, K. *Angew. Chem.* **2014,** *126,* 4007–4012. doi:10.1002/ange.201400711
99. Bergner, B. J.; Schürmann, A.; Peppler, K.; Garsuch, A.; Janek, J. *J. Am. Chem. Soc.* **2014,** *136,* 15054–15064. doi:10.1021/ja508400m
100. Lopez, N.; Graham, D. J.; McGuire, R., Jr.; Alliger, G. E.; Shao-Horn, Y.; Cummins, C. C.; Nocera, D. G. *Science* **2012,** *335,* 450–453. doi:10.1126/science.1212678
101. Sun, Q.; Yang, Y.; Fu, Z.-W. *Electrochem. Commun.* **2012,** *16,* 22–25. doi:10.1016/j.elecom.2011.12.019
102. Das, S. K.; Xu, S.; Archer, L. A. *Electrochem. Commun.* **2013,** *27,* 59–62. doi:10.1016/j.elecom.2012.10.036
103. Liu, W.; Sun, Q.; Yang, Y.; Xie, J.-Y.; Fu, Z.-W. *Chem. Commun.* **2013,** *49,* 1951–1953. doi:10.1039/c3cc00085k
104. Li, Y.; Yadegari, H.; Li, X.; Banis, M. N.; Li, R.; Sun, X. *Chem. Commun.* **2013,** *49,* 11731–11733. doi:10.1039/C3CC46606J
105. Liu, W.-M.; Yin, W.-W.; Ding, F.; Sang, L.; Fu, Z.-W. *Electrochem. Commun.* **2014,** *45,* 87–90. doi:10.1016/j.elecom.2014.05.021
106. Kim, J.; Lim, H.-D.; Gwon, H.; Kang, K. *Phys. Chem. Chem. Phys.* **2013,** *15,* 3623–3629. doi:10.1039/c3cp43225d
107. Jian, Z.; Chen, Y.; Li, F.; Zhang, T.; Liu, C.; Zhou, H. *J. Power Sources* **2014,** *251,* 466–469. doi:10.1016/j.jpowsour.2013.11.091
108. Yadegari, H.; Li, Y.; Norouzi Banis, M.; Li, X.; Wang, B.; Sun, Q.; Li, R.; Sham, T.-K.; Cui, X.; Sun, X. *Energy Environ. Sci.* **2014,** *7,* 3747–3757. doi:10.1039/c4ee01654h
109. Hartmann, P.; Bender, C. L.; Vračar, M.; Dürr, A. K.; Garsuch, A.; Janek, J.; Adelhelm, P. *Nat. Mater.* **2013,** *12,* 228–232. doi:10.1038/nmat3486
110. Hartmann, P.; Grübl, D.; Sommer, H.; Janek, J.; Bessler, W. G.; Adelhelm, P. *J. Phys. Chem. C* **2014,** *118,* 1461–1471. doi:10.1021/jp4099478
111. Zhao, N.; Li, C.; Guo, X. *Phys. Chem. Chem. Phys.* **2014,** *16,* 15646–15652. doi:10.1039/c4cp01961j
112. Das, S. K.; Lau, S.; Archer, L. A. *J. Mater. Chem. A* **2014,** *2,* 12623–12629. doi:10.1039/c4ta02176b
113. Ha, S.; Kim, J.-K.; Choi, A.; Kim, Y.; Lee, K. T. *ChemPhysChem* **2014,** *15,* 1971–1982. doi:10.1002/cphc.201402215
114. Peled, E.; Golodnitsky, D.; Hadar, R.; Mazor, H.; Goor, M.; Burstein, L. *J. Power Sources* **2013,** *244,* 771–776. doi:10.1016/j.jpowsour.2013.01.177
115. Lee, B.; Seo, D.-H.; Lim, H.-D.; Park, I.; Park, K.-Y.; Kim, J.; Kang, K. *Chem. Mater.* **2014,** *26,* 1048–1055. doi:10.1021/cm403163c
116. Kang, S.; Mo, Y.; Ong, S. P.; Ceder, G. *Nano Lett.* **2014,** *14,* 1016–1020. doi:10.1021/nl404557w
117. Stephanou, S. E.; Schechter, W. H.; Argersinger, W. J.; Kleinberg, J. *J. Am. Chem. Soc.* **1949,** *71,* 1819–1821. doi:10.1021/ja01173a083
118. Xu, S.; Lu, Y.; Wang, H.; Abruña, H. D.; Archer, L. A. *J. Mater. Chem. A* **2014,** *2,* 17723–17729. doi:10.1039/c4ta04130e
119. Hayashi, K.; Shima, K.; Sugiyama, F. *J. Electrochem. Soc.* **2013,** *160,* A1467–A1472. doi:10.1149/2.067309jes
120. Rao, M. L. B. U.S. Patent US3413154 A, Nov 26, 1968.
121. Rauh, R. D.; Abraham, K. M.; Pearson, G. F.; Surprenant, J. K.; Brummer, S. B. *J. Electrochem. Soc.* **1979,** *126,* 523–527. doi:10.1149/1.2129079
122. Abraham, K. M. *J. Power Sources* **1981,** *7,* 1–43. doi:10.1016/0378-7753(81)80058-4
123. Mikhaylik, Y. V.; Akridge, J. R. *J. Electrochem. Soc.* **2004,** *151,* A1969–A1976. doi:10.1149/1.1806394
124. Busche, M. R.; Adelhelm, P.; Sommer, H.; Schneider, H.; Leitner, K.; Janek, J. *J. Power Sources* **2014,** *259,* 289–299. doi:10.1016/j.jpowsour.2014.02.075
125. Raiß, C.; Peppler, K.; Janek, J.; Adelhelm, P. *Carbon* **2014,** *79,* 245–255. doi:10.1016/j.carbon.2014.07.065
126. Kumaresan, K.; Mikhaylik, Y.; White, R. E. *J. Electrochem. Soc.* **2008,** *155,* A576–A582. doi:10.1149/1.2937304
127. Waluś, S.; Barchasz, C.; Colin, J.-F.; Martin, J.-F.; Elkaïm, E.; Leprêtre, J.-C.; Alloin, F. *Chem. Commun.* **2013,** *49,* 7899–7901. doi:10.1039/c3cc43766c
128. Schneider, H.; Gollub, C.; Weiss, T.; Kulisch, J.; Leitner, K.; Schmidt, R.; Safont-Sempere, M. M.; Mikhaylik, Y.; Kelley, T.; Scordilis-Kelley, C.; Laramie, M.; Du, H. *J. Electrochem. Soc.* **2014,** *161,* A1399–A1406. doi:10.1149/2.0991409jes

129. Okamoto, H. *J. Phase Equilib.* **1995,** *16,* 94–97. doi:10.1007/bf02646258
130. Sangster, J.; Pelton, A. D. *J. Phase Equilib.* **1997,** *18,* 89–96. doi:10.1007/bf02646762
131. Kulisch, J.; Sommer, H.; Brezesinski, T.; Janek, J. *Phys. Chem. Chem. Phys.* **2014,** *16,* 18765–18771. doi:10.1039/C4CP02220C
132. Urbonaite, S.; Novák, P. *J. Power Sources* **2014,** *249,* 497–502. doi:10.1016/j.jpowsour.2013.10.095
133. Huang, J. P.; Yuan, D. D.; Zhang, H. Z.; Cao, Y. L.; Li, G. R.; Yang, H. X.; Gao, X. P. *RSC Adv.* **2013,** *3,* 12593–12597. doi:10.1039/c3ra42413h
134. Brückner, J.; Thieme, S.; Grossmann, H. T.; Dörfler, S.; Althues, H.; Kaskel, S. *J. Power Sources* **2014,** *268,* 82–87. doi:10.1016/j.jpowsour.2014.05.143
135. Hagen, M.; Fanz, P.; Tübke, J. *J. Power Sources* **2014,** *264,* 30–34. doi:10.1016/j.jpowsour.2014.04.018
136. Kang, S.-H.; Zhao, X.; Manuel, J.; Ahn, H.-J.; Kim, K.-W.; Cho, K.-K.; Ahn, J.-H. *Phys. Status Solidi A* **2014,** *211,* 1895–1899. doi:10.1002/pssa.201330569
137. Song, J.; Xu, T.; Gordin, M. L.; Zhu, P.; Lv, D.; Jiang, Y.-B.; Chen, Y.; Duan, Y.; Wang, D. *Adv. Funct. Mater.* **2014,** *24,* 1243–1250. doi:10.1002/adfm.201302631
138. Yang, Y.; Zheng, G.; Cui, Y. *Energy Environ. Sci.* **2013,** *6,* 1552–1558. doi:10.1039/c3ee00072a
139. Lin, Z.; Liu, Z.; Fu, W.; Dudney, N. J.; Liang, C. *Angew. Chem., Int. Ed.* **2013,** *52,* 7460–7463. doi:10.1002/anie.201300680
140. Hassoun, J.; Scrosati, B. *Adv. Mater.* **2010,** *22,* 5198–5201. doi:10.1002/adma.201002584
141. Nagata, H.; Chikusa, H. *J. Power Sources* **2014,** *264,* 206–210. doi:10.1016/j.jpowsour.2014.04.106
142. S. P. Corporation. http://www.sionpower.com/ (accessed March 5, 2015).
143. O. E. Ltd.. http://www.oxisenergy.com/ (accessed March 5, 2015).
144. Doughty, D. H. Rechargeable Lithium Metal Batteries (Ambient Temperature). In *Linden's Handbook of Batteries,* 4th ed.; Reddy, T. B., Ed.; McGraw-Hill: New York, 2011.
145. Gordon, J.; Watkins, J. U.S. Patent US 20100239893 A1, Sept 23, 2010.
146. Lu, X.; Kirby, B. W.; Xu, W.; Li, G.; Kim, J. Y.; Lemmon, J. P.; Sprenkle, V. L.; Yang, Z. *Energy Environ. Sci.* **2013,** *6,* 299–306. doi:10.1039/C2EE23606K
147. Lu, X.; Li, G.; Kim, J. Y.; Mei, D.; Lemmon, J. P.; Sprenkle, V. L.; Liu, J. *Nat. Commun.* **2014,** *5,* 4578. doi:10.1038/ncomms5578
148. Weddigen, G. *J. Electrochem. Soc.* **1980,** *127,* 1225–1227. doi:10.1149/1.2129860
149. Ji, X.; Nazar, L. F. *J. Mater. Chem.* **2010,** *20,* 9821–9826. doi:10.1039/b925751a
150. Etacheri, V.; Marom, R.; Elazari, R.; Salitra, G.; Aurbach, D. *Energy Environ. Sci.* **2011,** *4,* 3243–3262. doi:10.1039/c1ee01598b
151. Barghamadi, M.; Kapoor, A.; Wen, C. *J. Electrochem. Soc.* **2013,** *160,* A1256–A1263. doi:10.1149/2.096308jes
152. Manthiram, A.; Fu, Y.; Chung, S.-H.; Zu, C.; Su, Y.-S. *Chem. Rev.* **2014,** *114,* 11751–11787. doi:10.1021/cr500062v
153. Yin, Y.-X.; Xin, S.; Guo, Y.-G.; Wan, L.-J. *Angew. Chem., Int. Ed. Engl.* **2013,** *52,* 13186–13200. doi:10.1002/anie.201304762
154. Chen, L.; Shaw, L. L. *J. Power Sources* **2014,** *267,* 770–783. doi:10.1016/j.jpowsour.2014.05.111
155. Zhang, S. S. *J. Power Sources* **2013,** *231,* 153–162. doi:10.1016/j.jpowsour.2012.12.102
156. Wang, J.; Liu, L.; Ling, Z.; Yang, J.; Wan, C.; Jiang, C. *Electrochim. Acta* **2003,** *48,* 1861–1867. doi:10.1016/S0013-4686(03)00258-5
157. Jayaprakash, N.; Shen, J.; Moganty, S. S.; Corona, A.; Archer, L. A. *Angew. Chem.* **2011,** *123,* 6026–6030. doi:10.1002/ange.201100637
158. Cheon, S.-E.; Cho, J.-H.; Ko, K.-S.; Kwon, C.-W.; Chang, D.-R.; Kim, H.-T.; Kim, S.-W. *J. Electrochem. Soc.* **2002,** *149,* A1437–A1441. doi:10.1149/1.1511187
159. Lacey, M. J.; Jeschull, F.; Edström, K.; Brandell, D. *Chem. Commun.* **2013,** *49,* 8531–8533. doi:10.1039/c3cc44772c
160. Sun, J.; Huang, Y.; Wang, W.; Yu, Z.; Wang, A.; Yuan, K. *Electrochim. Acta* **2008,** *53,* 7084–7088. doi:10.1016/j.electacta.2008.05.022
161. Wang, Q.; Wang, W.; Huang, Y.; Wang, F.; Zhang, H.; Yu, Z.; Wang, A.; Yuan, K. *J. Electrochem. Soc.* **2011,** *158,* A775–A779. doi:10.1149/1.3583375
162. Jung, Y.; Kim, S. *Electrochem. Commun.* **2007,** *9,* 249–254. doi:10.1016/j.elecom.2006.09.013
163. He, M.; Yuan, L.-X.; Zhang, W.-X.; Hu, X.-L.; Huang, Y.-H. *J. Phys. Chem. C* **2011,** *115,* 15703–15709. doi:10.1021/jp2043416
164. Wang, J. L.; Yang, J.; Xie, J. Y.; Xu, N. X.; Li, Y. *Electrochem. Commun.* **2002,** *4,* 499–502. doi:10.1016/S1388-2481(02)00358-2
165. Zhang, B.; Qin, X.; Li, G. R.; Gao, X. P. *Energy Environ. Sci.* **2010,** *3,* 1531–1537. doi:10.1039/c002639e
166. Meyer, B. *Chem. Rev.* **1976,** *76,* 367–388. doi:10.1021/cr60301a003
167. Ye, H.; Yin, Y.-X.; Xin, S.; Guo, Y.-G. *J. Mater. Chem. A* **2013,** *1,* 6602–6608. doi:10.1039/c3ta10735c
168. Greenwood, N. N.; Earnshaw, A. *Chemistry of the Elements;* Elsevier Science: Oxford, 1997.
169. Xin, S.; Gu, L.; Zhao, N.-H.; Yin, Y.-X.; Zhou, L.-J.; Guo, Y.-G.; Wan, L.-J. *J. Am. Chem. Soc.* **2012,** *134,* 18510–18513. doi:10.1021/ja308170k
170. Elazari, R.; Salitra, G.; Garsuch, A.; Panchenko, A.; Aurbach, D. *Adv. Mater.* **2011,** *23,* 5641–5644. doi:10.1002/adma.201103274
171. Li, X.; Cao, Y.; Qi, W.; Saraf, L. V.; Xiao, J.; Nie, Z.; Mietek, J.; Zhang, J.-G.; Schwenzer, B.; Liu, J. *J. Mater. Chem.* **2011,** *21,* 16603–16610. doi:10.1039/C1JM12979A
172. Ryu, H. S.; Park, J. W.; Park, J.; Ahn, J.-P.; Kim, K.-W.; Ahn, J.-H.; Nam, T.-H.; Wang, G.; Ahn, H.-J. *J. Mater. Chem. A* **2013,** *1,* 1573–1578. doi:10.1039/C2TA00056C
173. Guo, J.; Xu, Y.; Wang, C. *Nano Lett.* **2011,** *11,* 4288–4294. doi:10.1021/nl202297p
174. Zheng, G.; Yang, Y.; Cha, J. J.; Hong, S. S.; Cui, Y. *Nano Lett.* **2011,** *11,* 4462–4467. doi:10.1021/nl2027684
175. Tachikawa, N.; Yamauchi, K.; Takashima, E.; Park, J.-W.; Dokko, K.; Watanabe, M. *Chem. Commun.* **2011,** *47,* 8157–8159. doi:10.1039/c1cc12415c
176. Wang, J.; Yang, J.; Xie, J.; Xu, N. *Adv. Mater.* **2002,** *14,* 963–965. doi:10.1002/1521-4095(20020705)14:13/14<963::AID-ADMA963>3.0.CO;2-P
177. Liang, C.; Dudney, N. J.; Howe, J. Y. *Chem. Mater.* **2009,** *21,* 4724–4730. doi:10.1021/cm902050j
178. Ji, X.; Lee, K. T.; Nazar, L. F. *Nat. Mater.* **2009,** *8,* 500–506. doi:10.1038/nmat2460
179. He, G.; Ji, X.; Nazar, L. *Energy Environ. Sci.* **2011,** *4,* 2878–2883. doi:10.1039/c1ee01219c

180. Wei Seh, Z.; Li, W.; Cha, J. J.; Zheng, G.; Yang, Y.; McDowell, M. T.; Hsu, P.-C.; Cui, Y. *Nat. Commun.* **2013,** *4,* 1331. doi:10.1038/ncomms2327
181. Rao, M.; Song, X.; Cairns, E. J. *J. Power Sources* **2012,** *205,* 474–478. doi:10.1016/j.jpowsour.2012.01.047
182. Cao, Y.; Li, X.; Aksay, I. A.; Lemmon, J.; Nie, Z.; Yang, Z.; Liu, J. *Phys. Chem. Chem. Phys.* **2011,** *13,* 7660–7665. doi:10.1039/c0cp02477e
183. Wang, X.; Wang, Z.; Chen, L. *J. Power Sources* **2013,** *242,* 65–69. doi:10.1016/j.jpowsour.2013.05.063
184. Wang, H.; Yang, Y.; Liang, Y.; Robinson, J. T.; Li, Y.; Jackson, A.; Cui, Y.; Dai, H. *Nano Lett.* **2011,** *11,* 2644–2647. doi:10.1021/nl200658a
185. Dörfler, S.; Hagen, M.; Althues, H.; Tübke, J.; Kaskel, S.; Hoffmann, M. J. *Chem. Commun.* **2012,** *48,* 4097–4099. doi:10.1039/c2cc17925c
186. Hagen, M.; Dörfler, S.; Althues, H.; Tübke, J.; Hoffmann, M. J.; Kaskel, S.; Pinkwart, K. *J. Power Sources* **2012,** *213,* 239–248. doi:10.1016/j.jpowsour.2012.04.004
187. Zhou, G.; Wang, D.-W.; Li, F.; Hou, P.-X.; Yin, L.; Liu, C.; Lu, G. Q. M.; Gentle, I. R.; Cheng, H.-M. *Energy Environ. Sci.* **2012,** *5,* 8901–8906. doi:10.1039/c2ee22294a
188. Su, Y.-S.; Fu, Y.; Manthiram, A. *Phys. Chem. Chem. Phys.* **2012,** *14,* 14495–14499. doi:10.1039/c2cp42796f
189. Yang, Y.; McDowell, M. T.; Jackson, A.; Cha, J. J.; Hong, S. S.; Cui, Y. *Nano Lett.* **2010,** *10,* 1486–1491. doi:10.1021/nl100504q
190. Hassoun, J.; Sun, Y.-K.; Scrosati, B. *J. Power Sources* **2011,** *196,* 343–348. doi:10.1016/j.jpowsour.2010.06.093
191. Hassoun, J.; Scrosati, B. *Angew. Chem., Int. Ed.* **2010,** *49,* 2371–2374. doi:10.1002/anie.200907324
192. Hassoun, J.; Kim, J.; Lee, D.-J.; Jung, H.-G.; Lee, S.-M.; Sun, Y.-K.; Scrosati, B. *J. Power Sources* **2012,** *202,* 308–313. doi:10.1016/j.jpowsour.2011.11.060
193. Whittingham, S. U.S. Patent US4009052 A, Feb 22, 1977.
194. Yang, Y.; Zheng, G.; Misra, S.; Nelson, J.; Toney, M.; Cui, Y. *J. Am. Chem. Soc.* **2012,** *134,* 15387–15394. doi:10.1021/ja3052206
195. Cai, K.; Song, M.-K.; Cairns, E. J.; Zhang, Y. *Nano Lett.* **2012,** *12,* 6474–6479. doi:10.1021/nl303965a
196. Zheng, S.; Chen, Y.; Xu, Y.; Yi, F.; Zhu, Y.; Liu, Y.; Yang, J.; Wang, C. *ACS Nano* **2013,** *7,* 10995–11003. doi:10.1021/nn404601h
197. Yang, Z.; Guo, J.; Das, S. K.; Yu, Y.; Zhou, Z.; Abruña, H. D.; Archer, L. A. *J. Mater. Chem. A* **2013,** *1,* 1433–1440. doi:10.1039/C2TA00779G
198. Guo, J.; Yang, Z.; Yu, Y.; Abruña, H. D.; Archer, L. A. *J. Am. Chem. Soc.* **2012,** *135,* 763–767. doi:10.1021/ja309435f
199. Lin, Z.; Liu, Z.; Dudney, N. J.; Liang, C. *ACS Nano* **2013,** *7,* 2829–2833. doi:10.1021/nn400391h
200. Chang, D.-R.; Lee, S.-H.; Kim, S.-W.; Kim, H.-T. *J. Power Sources* **2002,** *112,* 452–460. doi:10.1016/S0378-7753(02)00418-4
201. Wang, W.; Wang, Y.; Huang, Y.; Huang, C.; Yu, Z.; Zhang, H.; Wang, A.; Yuan, K. *J. Appl. Electrochem.* **2010,** *40,* 321–325. doi:10.1007/s10800-009-9978-z
202. Kim, S.; Jung, Y.; Lim, H. *Electrochim. Acta* **2004,** *50,* 889–892. doi:10.1016/j.electacta.2004.01.093
203. Peled, E.; Sternberg, Y.; Gorenshtein, A.; Lavi, Y. *J. Electrochem. Soc.* **1989,** *136,* 1621–1625. doi:10.1149/1.2096981
204. Shim, J.; Striebel, K. A.; Cairns, E. J. *J. Electrochem. Soc.* **2002,** *149,* A1321–A1325. doi:10.1149/1.1503076
205. Gao, J.; Lowe, M. A.; Kiya, Y.; Abruña, H. D. *J. Phys. Chem. C* **2011,** *115,* 25132–25137. doi:10.1021/jp207714c
206. Aurbach, D. *J. Power Sources* **2000,** *89,* 206–218. doi:10.1016/S0378-7753(00)00431-6
207. Kim, S.; Jung, Y.; Park, S.-J. *Electrochim. Acta* **2007,** *52,* 2116–2122. doi:10.1016/j.electacta.2006.08.028
208. Barchasz, C.; Leprêtre, J.-C.; Patoux, S.; Alloin, F. *Electrochim. Acta* **2013,** *89,* 737–743. doi:10.1016/j.electacta.2012.11.001
209. Mikhaylik, Y. V.; Kovalev, I.; Schock, R.; Kumaresan, K.; Xu, J.; Affinito, J. *ECS Trans.* **2010,** *25,* 23–34. doi:10.1149/1.3414001
210. Aurbach, D.; Pollak, E.; Elazari, R.; Salitra, G.; Kelley, C. S.; Affinito, J. *J. Electrochem. Soc.* **2009,** *156,* A694–A702. doi:10.1149/1.3148721
211. Xiong, S.; Xie, K.; Diao, Y.; Hong, X. *J. Power Sources* **2014,** *246,* 840–845. doi:10.1016/j.jpowsour.2013.08.041
212. Mikhaylik, Y. V. U.S. Patent US 7354680 B2, April 8, 2008; pp 1–18.
213. Liang, X.; Wen, Z.; Liu, Y.; Zhang, H.; Huang, L.; Jin, J. *J. Power Sources* **2011,** *196,* 3655–3658. doi:10.1016/j.jpowsour.2010.12.052
214. Gorkovenko, A. U.S. Patent US 7316868 B2, Jan 8, 2008.
215. Zhang, S. S. *Electrochim. Acta* **2012,** *70,* 344–348. doi:10.1016/j.electacta.2012.03.081
216. Suo, L.; Hu, Y.-S.; Li, H.; Armand, M.; Chen, L. *Nat. Commun.* **2013,** *4,* 1481. doi:10.1038/ncomms2513
217. Cuisinier, M.; Cabelguen, P.-E.; Adams, B. D.; Garsuch, A.; Balasubramanian, M.; Nazar, L. F. *Energy Environ. Sci.* **2014,** *7,* 2697–2705. doi:10.1039/C4ee00372a
218. Park, J.-W.; Yamauchi, K.; Takashima, E.; Tachikawa, N.; Ueno, K.; Dokko, K.; Watanabe, M. *J. Phys. Chem. C* **2013,** *117,* 4431–4440. doi:10.1021/jp400153m
219. Wang, L.; Byon, H. R. *J. Power Sources* **2013,** *236,* 207–214. doi:10.1016/j.jpowsour.2013.02.068
220. Marmorstein, D.; Yu, T. H.; Striebel, K. A.; McLarnon, F. R.; Hou, J.; Cairns, E. J. *J. Power Sources* **2000,** *89,* 219–226. doi:10.1016/S0378-7753(00)00432-8
221. Visco, S.; Nimon, Y. Aqueous electrolyte lithium sulfur batteries. US Pat. 8,828,575 B2, Sept 9, 2014.
222. Visco, S. J.; Nimon, V. Y.; Petrov, A.; Pridatko, K.; Goncharenko, N.; Nimon, E.; De Jonghe, L.; Volfkovich, Y. M.; Bograchev, D. A. *J. Solid State Electrochem.* **2014,** *18,* 1443–1456. doi:10.1007/s10008-014-2427-x
223. Kim, H.; Jeong, G.; Kim, Y.-U.; Kim, J.-H.; Park, C.-M.; Sohn, H.-J. *Chem. Soc. Rev.* **2013,** *42,* 9011–9034. doi:10.1039/C3CS60177C
224. Lee, Y. M.; Choi, N.-S.; Park, J. H.; Park, J.-K. *J. Power Sources* **2003,** *119–121,* 964–972. doi:10.1016/S0378-7753(03)00300-8
225. Mikhaylik, Y. V. Electrolytes for lithium sulfur cells. U.S. Patent US 8828610 B2, Jan 6, 2004.
226. Lin, Z.; Liu, Z.; Fu, W.; Dudney, N. J.; Liang, C. *Adv. Funct. Mater.* **2013,** *23,* 1064–1069. doi:10.1002/adfm.201200696
227. Ding, F.; Xu, W.; Graff, G. L.; Zhang, J.; Sushko, M. L.; Chen, X.; Shao, Y.; Engelhard, M. H.; Nie, Z.; Xiao, J.; Liu, X.; Sushko, P. V.; Liu, J.; Zhang, J.-G. *J. Am. Chem. Soc.* **2013,** *135,* 4450–4456. doi:10.1021/ja312241y
228. Liu, N.; Hu, L.; McDowell, M. T.; Jackson, A.; Cui, Y. *ACS Nano* **2011,** *5,* 6487–6493. doi:10.1021/nn2017167
229. Magasinski, A.; Dixon, P.; Hertzberg, B.; Kvit, A.; Ayala, J.; Yushin, G. *Nat. Mater.* **2010,** *9,* 353–358. doi:10.1038/nmat2725
230. Brückner, J.; Thieme, S.; Böttger-Hiller, F.; Bauer, I.; Grossmann, H. T.; Strubel, P.; Althues, H.; Spange, S.; Kaskel, S. *Adv. Funct. Mater.* **2014,** *24,* 1284–1289. doi:10.1002/adfm.201302169

231. Fronczek, D. N.; Bessler, W. G. *J. Power Sources* **2013,** *244,* 183–188. doi:10.1016/j.jpowsour.2013.02.018
232. Barchasz, C.; Molton, F.; Duboc, C.; Leprêtre, J.-C.; Patoux, S.; Alloin, F. *Anal. Chem.* **2012,** *84,* 3973–3980. doi:10.1021/ac2032244
233. Nelson, J.; Misra, S.; Yang, Y.; Jackson, A.; Liu, Y.; Wang, H.; Dai, H.; Andrews, J. C.; Cui, Y.; Toney, M. F. *J. Am. Chem. Soc.* **2012,** *134,* 6337–6343. doi:10.1021/ja2121926
234. Cañas, N. A.; Wolf, S.; Wagner, N.; Friedrich, K. A. *J. Power Sources* **2013,** *226,* 313–319. doi:10.1016/j.jpowsour.2012.10.092
235. Ryu, H. S.; Guo, Z.; Ahn, H. J.; Cho, G. B.; Liu, H. *J. Power Sources* **2009,** *189,* 1179–1183. doi:10.1016/j.jpowsour.2008.12.073
236. Yuan, L.; Qiu, X.; Chen, L.; Zhu, W. *J. Power Sources* **2009,** *189,* 127–132. doi:10.1016/j.jpowsour.2008.10.033
237. Akridge, J. R.; Mikhaylik, Y. V.; White, N. *Solid State Ionics* **2004,** *175,* 243–245. doi:10.1016/j.ssi.2004.07.070
238. Cheon, S.-E.; Ko, K.-S.; Cho, J.-H.; Kim, S.-W.; Chin, E.-Y.; Kim, H.-T. *J. Electrochem. Soc.* **2003,** *150,* A796–A799. doi:10.1149/1.1571532
239. Ryu, H.-S.; Ahn, H.-J.; Kim, K.-W.; Ahn, J.-H.; Lee, J.-Y. *J. Power Sources* **2006,** *153,* 360–364. doi:10.1016/j.jpowsour.2005.05.037
240. Patel, M. U. M.; Demir-Cakan, R.; Morcrette, M.; Tarascon, J.-M.; Gaberscek, M.; Dominko, R. *ChemSusChem* **2013,** *6,* 1177–1181. doi:10.1002/cssc.201300142
241. Cuisinier, M.; Cabelguen, P.-E.; Evers, S.; He, G.; Kolbeck, M.; Garsuch, A.; Bolin, T.; Balasubramanian, M.; Nazar, L. F. *J. Phys. Chem. Lett.* **2013,** *4,* 3227–3232. doi:10.1021/jz401763d
242. Visco, S. J.; Katz, B. D.; Nimon, Y. S.; De Jonghe, L. C. U.S. Patent US 8293398 B2, Oct 23, 2012.
243. Jin, Z.; Xie, K.; Hong, X.; Hu, Z.; Liu, X. *J. Power Sources* **2012,** *218,* 163–167. doi:10.1016/j.jpowsour.2012.06.100
244. Huang, J.-Q.; Zhang, Q.; Peng, H.-J.; Liu, X.-Y.; Qian, W.-Z.; Wei, F. *Energy Environ. Sci.* **2014,** *7,* 347–353. doi:10.1039/C3EE42223B
245. Li, W.; Hicks-Garner, J.; Wang, J.; Liu, J.; Gross, A. F.; Sherman, E.; Graetz, J.; Vajo, J. J.; Liu, P. *Chem. Mater.* **2014,** *26,* 3403–3410. doi:10.1021/cm500575q
246. Vizintin, A.; Patel, M. U. M.; Genorio, B.; Dominko, R. *ChemElectroChem* **2014,** *1,* 1040–1045. doi:10.1002/celc.201402039
247. Kobayashi, T.; Imade, Y.; Shishihara, D.; Homma, K.; Nagao, M.; Watanabe, R.; Yokoi, T.; Yamada, A.; Kanno, R.; Tatsumi, T. *J. Power Sources* **2008,** *182,* 621–625. doi:10.1016/j.jpowsour.2008.03.030
248. Hayashi, A.; Ohtomo, T.; Mizuno, F.; Tadanaga, K.; Tatsumisago, M. *Electrochem. Commun.* **2003,** *5,* 701–705. doi:10.1016/S1388-2481(03)00167-X
249. Kanno, R.; Hata, T.; Kawamoto, Y.; Irie, M. *Solid State Ionics* **2000,** *130,* 97–104. doi:10.1016/S0167-2738(00)00277-0
250. Kanno, R.; Murayama, M. *J. Electrochem. Soc.* **2001,** *148,* A742–A746. doi:10.1149/1.1379028
251. Seino, Y.; Ota, T.; Takada, K.; Hayashi, A.; Tatsumisago, M. *Energy Environ. Sci.* **2014,** *7,* 627–631. doi:10.1039/c3ee41655k
252. Kamaya, N.; Homma, K.; Yamakawa, Y.; Hirayama, M.; Kanno, R.; Yonemura, M.; Kamiyama, T.; Kato, Y.; Hama, S.; Kawamoto, K.; Mitsui, A. *Nat. Mater.* **2011,** *10,* 682–686. doi:10.1038/nmat3066
253. Yu, X.; Manthiram, A. *J. Phys. Chem. Lett.* **2014,** *5,* 1943–1947. doi:10.1021/jz500848x
254. Park, C.-W.; Ahn, J.-H.; Ryu, H.-S.; Kim, K.-W.; Ahn, H.-J. *Electrochem. Solid-State Lett.* **2006,** *9,* A123–A125. doi:10.1149/1.2164607
255. Wang, J.; Yang, J.; Nuli, Y.; Holze, R. *Electrochem. Commun.* **2007,** *9,* 31–34. doi:10.1016/j.elecom.2006.08.029
256. Kim, J.-S.; Ahn, H.-J.; Kim, I.-P.; Kim, K.-W.; Ahn, J.-H.; Park, C.-W.; Ryu, H.-S. *J. Solid State Electrochem.* **2008,** *12,* 861–865. doi:10.1007/s10008-008-0504-8
257. Ryu, H.; Kim, T.; Kim, K.; Ahn, J.-H.; Nam, T.; Wang, G.; Ahn, H.-J. *J. Power Sources* **2011,** *196,* 5186–5190. doi:10.1016/j.jpowsour.2011.01.109
258. Lee, D.-J.; Park, J.-W.; Hasa, I.; Sun, Y.-K.; Scrosati, B.; Hassoun, J. *J. Mater. Chem. A* **2013,** *1,* 5256–5261. doi:10.1039/c3ta10241f
259. Wenzel, S.; Metelmann, H.; Raiß, C.; Dürr, A. K.; Janek, J.; Adelhelm, P. *J. Power Sources* **2013,** *243,* 758–765. doi:10.1016/j.jpowsour.2013.05.194
260. Hwang, T. H.; Jung, D. S.; Kim, J.-S.; Kim, B. G.; Choi, J. W. *Nano Lett.* **2013,** *13,* 4532–4538. doi:10.1021/nl402513x
261. Xin, S.; Yin, Y.-X.; Guo, Y.-G.; Wan, L.-J. *Adv. Mater.* **2014,** *26,* 1261–1265. doi:10.1002/adma.201304126
262. Bauer, I.; Kohl, M.; Althues, H.; Kaskel, S. *Chem. Commun.* **2014,** *50,* 3208–3210. doi:10.1039/c4cc00161c
263. Zheng, S.; Han, P.; Han, Z.; Li, P.; Zhang, H.; Yang, J. *Adv. Energy Mater.* **2014,** *4,* 1400226. doi:10.1002/aenm.201400226
264. Park, C.-W.; Ryu, H.-S.; Kim, K.-W.; Ahn, J.-H.; Lee, J.-Y.; Ahn, H.-J. *J. Power Sources* **2007,** *165,* 450–454. doi:10.1016/j.jpowsour.2006.11.083
265. Su, Y.-S.; Manthiram, A. *Nat. Commun.* **2012,** *3,* 1166. doi:10.1038/ncomms2163
266. Zu, C.; Su, Y. S.; Fu, Y.; Manthiram, A. *Phys. Chem. Chem. Phys.* **2013,** *15,* 2291–2297. doi:10.1039/c2cp43394j
267. Yim, T.; Park, M.-S.; Yu, J.-S.; Kim, K. J.; Im, K. Y.; Kim, J.-H.; Jeong, G.; Jo, Y. N.; Woo, S.-G.; Kang, K. S.; Lee, I.; Kim, Y.-J. *Electrochim. Acta* **2013,** *107,* 454–460. doi:10.1016/j.electacta.2013.06.039

License and Terms

BEILSTEIN JOURNAL OF NANOTECHNOLOGY

Current–voltage characteristics of manganite–titanite perovskite junctions

Benedikt Ifland[1], Patrick Peretzki[2], Birte Kressdorf[1], Philipp Saring[2], Andreas Kelling[1], Michael Seibt[2] and Christian Jooss[*1]

Full Research Paper

Open Access

Address:
[1]Institute of Materials Physics, University of Goettingen, Friedrich-Hund-Platz 1, 37077 Goettingen, Germany and
[2]4th Physical Institute, University of Goettingen, Friedrich-Hund-Platz 1, 37077 Goettingen, Germany

Email:
Christian Jooss[*] - jooss@material.physik.uni-goettingen.de

* Corresponding author

Keywords:
current–voltage characteristics; perovskites; photovoltaics; polarons

Beilstein J. Nanotechnol. **2015,** *6,* 1467–1484.
doi:10.3762/bjnano.6.152

Received: 06 March 2015
Accepted: 16 June 2015
Published: 07 July 2015

This article is part of the Thematic Series "Materials for sustainable energy production, storage, and conversion".

Guest Editor: M. Fichtner

Abstract

After a general introduction into the Shockley theory of current voltage (J–V) characteristics of inorganic and organic semiconductor junctions of different bandwidth, we apply the Shockley theory-based, one diode model to a new type of perovskite junctions with polaronic charge carriers. In particular, we studied manganite–titanate p–n heterojunctions made of n-doped $SrTi_{1-y}Nb_yO_3$, $y = 0.002$ and p-doped $Pr_{1-x}Ca_xMnO_3$, $x = 0.34$ having a strongly correlated electron system. The diffusion length of the polaron carriers was analyzed by electron beam-induced current (EBIC) in a thin cross plane lamella of the junction. In the J–V characteristics, the polaronic nature of the charge carriers is exhibited mainly by the temperature dependence of the microscopic parameters, such as the hopping mobility of the series resistance and a colossal electro-resistance (CER) effect in the parallel resistance. We conclude that a modification of the Shockley equation incorporating voltage-dependent microscopic polaron parameters is required. Specifically, the voltage dependence of the reverse saturation current density is analyzed and interpreted as a voltage-dependent electron–polaron hole–polaron pair generation and separation at the interface.

Introduction

At present, photovoltaic devices are mainly based on high purity elemental or compound inorganic semiconducting materials with large electronic bandwidths. The doping of such semiconductors allows for the variation in the electrical conductivity and character of the charge carriers. In this way, junctions based on p- or n-doped materials can be tailored. In these materials, the charge carriers are quasi-free, that is, the effective mass is relatively small, the mobility is large and the diffusion length of excited electron–hole pairs can be in the 100 µm range for indirect semiconductors [1].

The examination of photovoltaic materials with properties deviating from conventional solar cells can lead to new strategies for a wide variety of solar cells. In recent years, organic and

other narrow bandwidth semiconductors came into the focus of research efforts [2-7]. They often result in new types of quasi-particles such as polarons (i.e., bound states of charge and lattice distortions). Polarons are present in organic semiconductors such as conjugated polymers [8] as well as some perovskite oxides [9-11]. Perovskites have the general formula ABX_3, where the A cation in a cuboctahedral site coordinates with 12 anions, and the B cation in an octahedral site coordinates with 6 anions. New perovskite materials under evaluation for photovoltaic systems reveal vastly different properties ranging from narrow band gap manganite oxides perovskites with hopping transport to broad band gap lead halide perovskites [9,12-14]. For the lead halide perovskites the constituents are: $A = CH_3NH_3^+$, B = Pb, and X = I, Br, Cl, mixed halides. The constituents for manganite oxide are: A = rare earth, alkali metal, mixed composition, B = Mn, and X = O.

The organic/inorganic halide perovskites exhibit good optical absorption and favorable electrical properties, thus offering the possibility for use in high efficiency solar cells [12-14]. Even though the junctions made of halide perovskites exhibit high open-circuit voltages, V_{OC} = 0.9–1.15 V [15,16], and a large carrier diffusion length, L > 1 μm, for the mixed halide, $CH_3NH_3Pb_{3-x}Cl_x$ [17,18], these junctions seem not to be stable in the long term [19,20].

On the other hand, the manganite oxide perovskites are strongly correlated electron systems that exhibit a strong electron–phonon interaction. This leads to the formation of small polarons [21]. The polaron-like character of the quasi-particles in perovskite oxides provides at least two exciting issues related to photovoltaic energy conversion [22]: the possibility of light absorption by intraband excitations of charge carriers and the harvesting hot carriers due to the rather long-lived excited states [21,23]. Hence, such materials are suitable to study the pathways of photovoltaic energy conversion beyond the Shockley–Queiser limit [24] by reducing fundamental losses due to long wavelength transparency and thermalization of excess carriers generated by the short wavelength part of the solar spectrum.

For this study, junctions of p-doped $Pr_{1-x}Ca_xMnO_3$ (PCMO) with x = 0.34 and n-doped $SrTi_{1-y}Nb_yO_3$ (STNO) with y = 0.002 were prepared. In PCMO, the charge carriers are small polarons and doping with Ca leads to a variety of different electronic and magnetic ground states. For a certain doping range, Ca doping leads to field-induced electronic phase transitions such as the colossal magneto-resistance (CMR) and the colossal electro-resistance (CER). For the perovskite heterojunction $La_{0.32}Pr_{0.33}Ca_{0.33}MnO_3$ with 0.5 wt % Nb-doped $SrTiO_3$, the influence of a magnetic field on the temperature-dependent photovoltaic effect was reported [5]. In contrast, STNO has a band gap of around E_g = 3.2 eV [25] and the reported type of charge carriers in STO varies from large to small polarons [26,27] or a mixture of both [28].

To gain more insight into the underlying mechanism of the photovoltaic effect in perovskite-based materials, it is important to analyze the properties at the interface. The electronic interface structure of conventional semiconductor p–n junctions is well-described in terms of electrochemical equilibrium of quasi-free electrons [29]. Charge carriers are transferred across the interface until a specific Fermi level of the carriers on both sides of the interface is established. Consequently, an electrostatic potential is generated, which modifies the band structure at the interface. The modified interfacial band structure is successfully described by band bending of more or less rigid electron bands. In heterojunctions, materials with different bandgaps meet at the interface. In addition to band bending, this leads to sharp discontinuities of the band structure at the interface and is modelled in the framework of a sharp junction [30].

In many perovskite oxides, the band structure is determined to a large degree by the correlation interactions [31]. Since these correlations strongly depend on the charge density and the material structure, the concept of bending rigid electronic bands at an interface can break down because of the emergence of new types of quasiparticles and order [32]. The nature of polaron quasiparticles may change during their interfacial transfer because of the variation of the electron–phonon interaction across the interface. Under a large electric field, the polaron may even dissociate as indicated by polaron simulations of polymer junctions [33]. On the other hand, the concept of the electrochemical equilibrium at the interface naturally takes into account the spatial variation of the correlation interactions and is quite successfully applied to the near-equilibrium interfacial band structure of oxide junctions [22] (see Figure 4 later in this article).

An additional important difference compared to conventional semiconductors is the small electronic bandwidth of the conduction bands in transition metal perovskite oxides. Because of the small electronic overlap between transition metal 3d and oxygen 2p states, the width of the unnormalized conduction band in the manganite $Pr_{1-x}Ca_xMnO_3$ is of the order 1 eV [34], in contrast to Si with a bandwidth of ≈20 eV. The renormalization of the bandwidth by the electron–phonon interaction further reduces the bandwidth to a few meV [35]. This small bandwidth has strong impact on the matching of electronic states at the interface. Even after establishment of electrochemical equilibrium (which may be hindered by small charge transfer rates), the electronic overlap of narrow bands can be very small. In

other words, the orbital mismatch of the electronic states on both sides of the interface may strongly affect the charge transfer process.

The width of the space charge region (SCR) at the junctions of conventional semiconductors can be well estimated in the framework of rigid band concepts, taking Debye or Thomas–Fermi screening into account. For the studied PCMO/STNO junction, the extensions of the SCR at room temperature calculated from the sharp junction model are d_{PCMO} = 0.2 nm and d_{STNO} = 10 nm, respectively [22]. Since the width of the SCR is on the order of one unit cell or even less, the rigid band model is not applied. Nevertheless, the calculated values roughly agree with the band bending region deduced from electron energy loss spectroscopy [22].

The strength of the electron lattice coupling also strongly affects the mobility of the electrons or holes. Compared to Si, where the mobility strongly depends on the doping level ($\mu_e \approx 675$ cm^2/V·s and $\mu_h \approx 331$ cm^2/V·s for a doping level of 10^{17} cm^{-3} [36]), the mobility in polaronic materials is several orders of magnitude smaller (≈1 cm^2/V·s in STNO, 10^{-2} cm^2/Vs in PCMO down to 5×10^{-7} cm^2/V·s in hole-doped polymers) depending on the polaron effective mass. In addition to recombination rates, the mobility influences the diffusion length of electron–hole-type excitations. In polymer–fullerene solar cells, the diffusion length is significantly reduced down to the 10 nm range, which consequently reduces a typical device thickness [2]. For perovskite oxides, no direct measurement of the diffusion length has been reported so far.

From the experimental viewpoint, one of the main tools to study photovoltaic devices is the temperature-dependent analysis of current–voltage (*J*–*V*) curves measured across the charge separating junction. Typical diode-like characteristics are observed in the dark and under illumination. This provides a wealth of information related to the underlying microscopic processes such as excess carrier generation and recombination as well as transport properties in the bulk and across junction interfaces.

However, the insight that the *J*–*V* curves provide into microscopic processes is intimately linked to the applied analysis. It is quite remarkable that for the limiting cases of quasi-free electrons and small polarons, the analysis of *J*–*V* curves is performed in the framework of the classical Shockley theory [37]. This theory was originally developed for generation and recombination currents of quasi-free electrons. In more recent works, a Shockley-like equation describing a diode-like rectifying behavior has been derived from rate equations for generation, dissociation and recombination of polaron pairs at the interface [38,39]. Such a scenario is typical for photovoltaic energy conversion in polymer systems with small polaron charges. Hence, a more general description using Shockley's equations for different p–n junctions having a different charge carrier nature is needed. A simple equivalent circuit can be set up, where in addition to the diode, a parallel resistance, R_P, and a series resistance, R_S, is added. The temperature dependence of the diode parameters and the resistance contributions in the dark reflect the different underlying microscopic mechanisms and the nature of the charge carriers. R_P and R_S may reveal the typical small polaron fingerprints, the thermally activated hopping mobility [40], the nonlinear current–voltage dependence and the appearance of colossal resistance effects.

This article is organized as follows: First the key features of a Shockley-type model for homo- and hetero-junctions with large bandwidths and quasi-free electrons are introduced. Then we summarize the Shockley-type model for small bandwidth organic junctions with strongly localized charge carriers. The one diode-based equivalent circuit is then applied to the analysis of data sets collected from PCMO/STNO p–n heterojunctions. Despite the absence of a band gap above the charge ordering temperature of $T_{CO} \approx 240$ K, photocarrier lifetimes in PCMO are of the order of ns [41]. The diffusion length of electron–hole-type excitations at room temperature is determined by EBIC. Finally, the Discussion section represents our analysis of the microscopic parameters obtained by fitting the *J*–*V* curves with and without illumination by using the Shockley-based one diode model. The previously reported presence of a band discontinuity at the interface [22] is confirmed in the dark and under illumination, exemplifying the self-consistency of the Shockley-based analysis. Furthermore, the temperature dependence of the characteristic parameters of the equivalent circuit provides insight into the transport mechanism in the junction and across the interface. The observed differences between simulated and measured *J*–*V* curves and the presence of a CER effect in the shunt resistance show the need to modify the Shockley equation with the introduction of bias-dependent microscopic parameters.

Shockley equation for quasi-free electrons

Let us first consider a p–n homojunction made of a semiconducting material with quasi-free charge carriers (e.g., doped silicon). Bringing n- and p-type Si in contact leads to currents that compensate for the different concentration of electrons and holes in both materials (see Figure 1a). Thus, the electrons diffuse from the n-type material to the p-type material (and holes from the p-type to the n-type material), leaving a SCR formed by immobile, ionized acceptors and donors on the p- and n-side of the junction, respectively. This current is called the recombination current density, J_{Rec}. Thermally generated electron–hole pairs can diffuse into the space charge region

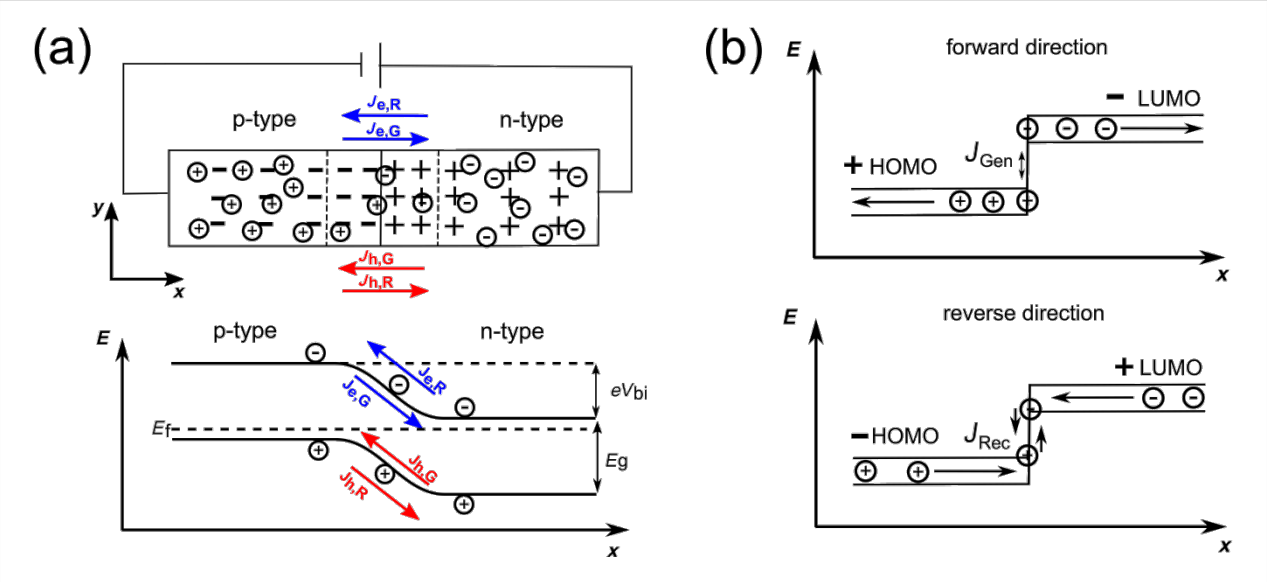

Figure 1: Schematic overview of electrochemical equilibrium (a) in large bandwidth inorganic semiconductors and (b) in low bandwidth organic solar cells. In both cases a recombination and generation current can be defined. In the forward direction, the recombination current is always the dominant contribution to the total current, whereas for the reverse direction, the generation current is the dominant contribution.

where they are attracted by the electric field, resulting in electrons moving from the p- towards the n-region and holes moving in the opposite direction. This current is called the generation current density, J_{Gen}. Thus the origin of J_{Gen} and J_{Rec} are related to the differences in the chemical and electrical potentials, respectively. In electrochemical equilibrium, there is a balance of these two currents and no net charge current, J_C, flows:

$$J_C = \frac{\sigma_e}{e}\text{grad}\eta_e - \frac{\sigma_h}{e}\text{grad}\eta_h = 0. \quad (1)$$

Here $\sigma_{e/h}$ is the contribution of electrons and holes to the electrical conductivity, $\eta_{e/h}$ is the electrochemical potential and e the elementary charge. As a result, a voltage drop between the n- and p-type materials, V_{bi}, occurs. This is known as the built-in voltage or diffusion voltage.

Under bias, the electrochemical equilibrium is modified and a net charge current flows. The assumptions underlying the Shockley model of the J–V curve of a junction are [37]: (a) the voltage completely drops across the SCR; (b) a weak injection condition; and (c) no recombination occurs in the SCR.

In the ideal case, the generation current is nearly independent of the applied voltage, V, since the voltage has no effect on the rate of thermally generated electron–hole pairs. On the other hand, the recombination current is strongly affected by the applied voltage and is proportional to the built-in potential. For example, for the electrons from the n-region:

$$J_{n,Rec} \propto \exp\left[\frac{-e(V_{bi}-V)}{k_BT}\right]. \quad (2)$$

Here, k_BT is the thermal energy. If the diode is biased in the forward direction, the barrier for the recombination current decreases and the current rises exponentially. For the reverse direction, the recombination current decreases, whereas the generation current is not influenced by the external electric field. The obtained J–V characteristic for an ideal p–n homojunction can then be described within the Shockley theory [37]:

$$J(V) = J_S\left(\exp\left[\frac{eV}{k_BT}\right]-1\right), \quad (3)$$

where the saturation current density, J_S, can be written as

$$J_S = J_{n,Gen} + J_{p,Gen} = e\cdot n_i^2\cdot\left(\frac{D_p}{n_D L_p}+\frac{D_n}{n_A L_n}\right). \quad (4)$$

Here $D_{n,p}$ is the diffusion coefficient and $L_{n,p}$ is the diffusion length for electrons and holes. Far from the junction, the density of charge carriers for completely ionized donors and acceptors in the conduction or valence band is given by n_D and n_A, respectively. Since the temperature dependence of the intrinsic charge carrier density, n_i, is given by

$$n_i^2 = N_C N_V \cdot \exp\left[-\frac{E_g}{k_B T}\right], \quad (5)$$

the saturation current is also temperature dependent

$$J_S = eN_C N_V \cdot \left(\frac{D_p}{n_D L_p} + \frac{D_n}{n_A L_n}\right) \cdot \exp\left[-\frac{E_g}{k_B T}\right] = J_0 \cdot \exp\left[-\frac{E_g}{k_B T}\right], \quad (6)$$

where N_C and N_V are the effective densities of states of the conduction and valence band, respectively, and J_0 is nearly independent of the temperature.

Heterojunction

If two different semiconducting materials are used, for example, a junction made of Ge and GaAs, the device is called a p–n heterostructure. One of the main differences is the presence of discontinuities in the conduction and valence bands, so-called band offsets, which can be calculated by the difference in the electron affinities, $\chi_{n,p}$ as

$$\begin{aligned} \Delta E_C &= \chi_p - \chi_n \\ \Delta E_V &= \Delta E_g - \Delta E_C. \end{aligned} \quad (7)$$

Because the materials have different band gaps and Fermi energies, the total built-in potential, V_{bi}, is the sum of the partial built-in potentials of the semiconductor 1 and 2, named $V_{bi,1}$ and $V_{bi,2}$

$$V_{bi} = V_{bi,1} + V_{bi,2}. \quad (8)$$

A model for the electronic structure of the interface has been developed by Anderson et al., assuming a sharp junction with band discontinuities [30]. For the derivation of the *J*–*V* curve, it is assumed that the transport mechanism is governed by injection over the barriers in the conduction and valence band. Furthermore, there are no influences of interface states taken into account that might give rise to additional space charges and barriers. If we consider a narrow band gap, p-type semiconductor 1, and a wide gap, n-type semiconductor 2, the *J*–*V* characteristics can be written as

$$J(V) = A \cdot \exp\left[-\frac{eV_{bi,2}}{k_B T}\right]\left[\exp\left[\frac{eV_2}{k_B T}\right] - \exp\left[-\frac{eV_1}{k_B T}\right]\right]. \quad (9)$$

Here the partial voltage decrease over semiconductor 1 and 2 is given by V_1 and V_2. If we consider a p–n heterojunction, where $V_{bi,1} > \Delta E_C$, there is no barrier for the charge carriers in semiconductor 1 to reach the semiconductor 2 and the equation can be reformulated as

$$J(V) = A_0 \cdot \exp\left[-\frac{e\cdot(V_{bi} - \Delta E_C)}{k_B T}\right]\cdot\left[\exp\left[\frac{eV}{k_B T}\right] - 1\right], \quad (10)$$

with

$$A_0 = XaeN_{V,2}\left(\frac{D_p}{\tau_p}\right)^{1/2}. \quad (11)$$

Here the assumption is made that the current is limited by the rate at which holes can diffuse in the narrow band gap material. X is the fraction of those carriers having sufficient energy to cross the barrier, a is the junction area and $N_{V,2}$ is the effective density of states of the valence band for the semiconductor 2. This leads to a *J*–*V* curve of similar form to the ideal Shockley equation curve.

Up to this point, no other transport mechanisms such as tunneling through the interface barrier, recombination at the interface, or a voltage-dependent barrier height have been taken into account. If these processes are relevant for the *J*–*V* characteristics, the temperature-dependent J_S (the exponential prefactor in Equation 10) can be written as:

$$J_S = J_0 \cdot \exp\left[-\frac{E_B}{n\cdot k_B \cdot T}\right], \quad (12)$$

where E_B is the effective energy barrier for the transport across the interface and n is the ideality factor described below.

Photovoltaic effect

Under illumination, additional charge carriers are generated and are separated in the electric field of the SCR, resulting in a photocurrent. The typical parameters characterizing the photovoltaic effect in solar cells are the short-circuit current density, J_{SC}, and the open circuit voltage, V_{OC}. The analysis of the temperature dependence of these parameters gives additional information about the electronic structure of the p–n interface and the transport mechanism across the interface. In inorganic junctions, the temperature dependence of the open circuit voltage is given by

$$eV_{OC} = E_g - k_B T \cdot \ln\left(\frac{1}{I_{SC}} \cdot eN_V N_C \cdot \left(\frac{D_p}{n_D L_p} + \frac{D_n}{n_A L_n}\right)\right), \quad (13)$$

for $J_S << J_{SC}$. For a heterojunction, the low temperature limit of V_{OC} is given by the smaller bandgap, that is, E_g is replaced by $\min(E_{g1}, E_{g2})$. In the presence of a band discontinuity, the energy barrier/spike E_B which is generated at the heterointerface determines the upper limit of V_{OC} for $T = 0$ K [42].

Equivalent circuit

A real photovoltaic device is often described by an equivalent circuit. The simplest one is shown in Figure 2 and consists of one diode, which represents the ideal J–V characteristics in terms of the Shockley equation, an external power supply, a current source for the photocurrent and two ohmic resistors. These parasitic resistances describe losses, which reduce the efficiency of a solar cell. The series resistor, R_S, consists of all bulk, interface and cable resistances and the parallel resistor, R_P, represents losses, for example, leakage currents across the junction due to imperfections. Another important variable is the ideality factor, n. For an ideal diode this is $n = 1$. Evaluating the equivalent circuit yields the J–V characteristics in an implicit form,

$$J(V) = J_S\left(\exp\left[\frac{e(V - JR_S)}{nk_BT}\right] - 1\right) + \frac{V - JR_S}{R_P} - J_{SC}. \quad (14)$$

The analysis of data presented in this paper was performed using the one diode model.

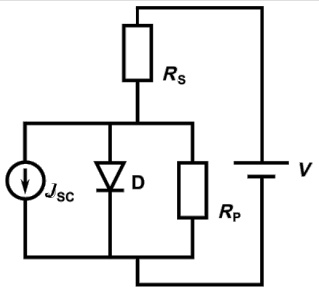

Figure 2: Equivalent circuit for the one diode model. The diode, D, describes the part of the circuit that represents the ideal diode equation with an ideality factor $n = 1$. R_S and R_P represent the parasitic resistances taking ohmic losses into account. J_{SC} represents the short circuit current density.

Organic solar cells: ideal diode equation for localized charge carriers, polarons

The J–V characteristics of organic solar cells formed by junctions of conjugated polymers and fullerenes are commonly described in the framework of the Shockley model [43] in combination with either one or two diode electrical circuits [44].

Since the nature of the charge carriers is fundamentally different, the applicability of a Shockley-like equation is far from obvious. In contrast to inorganic p–n junctions, where the current across the junction is due to drift diffusion and/or recombination within the SCR, the current in organic heterojunctions is carried by hole and electron-type polarons. These are formed after injection at the electrodes and can form polaron pairs at the interface.

In contrast to Si, having a large mobility, the mobility in the organic compounds is several orders of magnitude smaller. Typical values at $T = 300$ K are $\mu_e = 2.0 \times 10^{-3}$ cm^2/V·s in the electron-doped fullerene C61-butyric acid methyl ester (PCBM) and $\mu_h = 5.0 \times 10^{-7}$ cm^2/V·s in the hole-doped polymer poly(2-methoxy-5-(3′,7′-dimethyloctyloxy)-*p*-phenylenevinylene) (MDMO–PPV) [2].

Absorption of photons leads to formation of tightly bound excitons that have a very low probability of dissociation. The exciton binding energy can be high due to the low dielectric constant of the organic semiconductors and can exceed 1 eV. Charge separation is typically hindered by a high exciton binding energy, however, it can be facilitated at a heterojunction due to formation of a more loosely bound exciton–polaron pair, which can dissociate or recombine at the interface [45].

The theoretical foundation of the Shockley equation in such systems was given by Giebink et al. [38,39], who showed that for a trap-free heterojunction under stationary state conditions, the Shockley equation is

$$J(V) = J_S\left(\exp\left[\frac{eV}{k_BT}\right] - r\right), \quad (15)$$

where $r = k_{ppd}/k_{ppd,eq}$ and k_{ppd} and $k_{ppd,eq}$ denote the polaron pair dissociation rate under transport and equilibrium conditions, respectively. The polaron dissociation mainly affects the reverse direction of the junction $V < 0$, where the increased electric field at the interface facilitates the polaron dissociation and k_{ppd} exceeds $k_{ppd,eq}$. This can typically be observed in organic junctions as an increasing reverse saturation current with increasing reverse bias. More generally, $r > 1$ can evolve due to any bias dependence of the generation current. Such an effect is disregarded in the Shockley model. However, in the forward direction, k_{ppd} approaches $k_{ppd,eq}$ and Equation 15 reduces to the conventional Shockley equation with ideality factor $n = 1$.

Disorder and polycrystalline structure have a strong impact on the electrical transport in organic junctions, since the polarons can be trapped at defects. Consequently, the absolute value and the temperature dependence of R_S strongly depend on disorder.

Since either the electron- or the hole-type polaron can be trapped, the resulting two different bimolecular recombination processes can be modelled as two different currents, which thus gives rise to an effective two diode Shockley equation with two reverse saturation currents and two ideality factors [38,39]. The contributions of both currents depend on the balance of the voltage drop across the junction as well as their characteristic trap temperatures.

The origin of the open circuit voltage, V_{OC}, has been controversially discussed for many years. Indeed, it shows a linear increase with decreasing temperature [43,46]. Currently, there seems to be an agreement that the energy difference between the HOMO of the donor and the LUMO of the acceptor modified by the polaron binding energy controls the low temperature limit [47]. The resulting open circuit voltage is described by [38,39]

$$eV_{OC} = E_{DA} - k_B T \cdot \ln\left[\left(\frac{k_{ppr}}{k_{ppd}}\right)\frac{k_{Rec} e N_{HOMO} N_{LUMO}}{I_{SC}}\right], \quad (16)$$

where E_{DA} is the energy difference between the HOMO of the donor and the LUMO of the acceptor modified by the polaron binding energy. The short circuit current density, J_{SC}, increases with increasing temperature, reflecting the thermally activated hopping conductivity of small polarons. It should be noted, however, that this trend can be overlaid by temperature dependent changes the in morphology of the active layer [44].

The dominating loss mechanisms of organic solar cells are still under debate [48]. There seems to be some evidence that genuine (intramolecular) recombination can be disregarded compared to bimolecular recombination. The latter is due to recombination of mobile electrons and holes at the interface. The question of whether bimolecular recombination is typically affected by localized states in the band gap (similar to Shockley–Read–Hall recombination at deep traps in inorganic semiconductors) or if it involves the recombination of free carriers is highly debated (see, e.g., [45]).

Kirchartz et al. [49] introduced a voltage-dependent ideality factor (for both with and without illumination), in order to study recombination mechanisms in polymer–fullerene solar cells. They concluded that in their devices, the recombination is a trap-assisted recombination at lower voltages and surface recombination at higher voltages. However, intramolecular recombination of excitons at traps within single-blend compounds depends strongly on the exciton binding energy. Theoretical estimates show that increasing the binding energy, E_B, from values of $\approx k_B T$ to 0.2 eV will increase the recombination rate by two orders of magnitude [2]. Typically, an experimental value for E_B in polymer solar cells is in the range of 0.2–0.4 eV.

Modeling diffusion length determination by EBIC

The charge carrier diffusion length, L, is an important parameter to determine the recombination-limited charge transport processes in electronic devices [50]. It is connected to the charge carrier lifetime, τ, and mobility, μ, by the Einstein relation:

$$L = \sqrt{D\tau} = \sqrt{\frac{k_B T}{e}\mu\tau}. \quad (17)$$

While the lifetime is determined by recombination and relaxation processes, the mobility is inherent to the material system. From the simple Einstein relation, the diffusion coefficient is proportional to the mobility. This leads to typical diffusion lengths in the µm and nm range for inorganic and organic semiconductors, respectively. This large difference is due to the fact that the typical mobility in organic and inorganic semiconductors differs by several orders of magnitude. Given that the mobility in the PCMO–STNO system is larger than that of organic semiconductors, a diffusion length on the order of that of organic semiconductors is expected. However, the situation may be different for excited charge carriers in a correlated material system as the applicability of the simple Einstein relation is questionable: Here, the assumption of a non-degenerate system in thermal equilibrium may not hold (see, e.g., [51]). As a consequence, it is necessary to directly determine the diffusion length in a PCMO–STNO p–n junction.

An established technique to measure the charge carrier diffusion length in devices with p–n junctions is by mapping the electron beam-induced current (EBIC) across the sample without any applied voltage (see, e.g., the review by Leamy [52]). Injected high-energy electrons excite electron–hole pairs, which are subject to diffusion in the sample. In the limit of weak injection, diffusion is limited by minority charge carriers. A typical experimental method for measuring the minority charge carrier diffusion length, L, is to vary the beam acceleration voltage, moving the excitation maximum perpendicular to the p–n interface, or by preparing a wedge-shaped layer to vary the depth of the interface in the sample. For a point-like source generating electron–hole pairs with a rate, G, at a distance, W, from the p–n interface, the resulting EBIC current is [50]

$$I_{EBIC} = eG\exp\left[-\frac{W}{L}\right]. \quad (18)$$

If W and L are of similar size, varying W allows the L of the minority charge carriers to be determined.

A more realistic diffusion model for charge carriers in solids incorporates the extension of the generation volume produced by a penetrating electron beam. This is especially important if the extension of the generation volume is of the order of the diffusion length. As the penetrating electrons suffer multiple scattering events with ions and electrons constituting the solid, they gradually lose their initial energy, frequently resulting in a pear-shaped generation volume [53]. This shape mainly depends on the initial electron energy, which is determined by the beam acceleration voltage and the density of the solid. It can be described by an analytical function [53] or simulated by a Monte Carlo method [54].

In this work, we measure an EBIC linescan from a p-doped to an n-doped region as a cross-section in order to extract the diffusion length. This eliminates the influence of the sample surface structure and layer thickness in addition to reducing the generation volume. In order to take the generation volume into account, the measured linescan must be compared to a simulation. For this, we convolute a simulated generation volume with a function describing the fraction of generated charge carriers contributing to the EBIC signal. For the case without diffusion processes, this function is given as

$$f_{\mathrm{SCR}} = \begin{cases} 1, & -d_{\mathrm{p}} < x < d_{\mathrm{n}} \\ x, & \text{otherwise} \end{cases} \tag{19}$$

where d_{p} and d_{n} are the width of the space charge region on the p- (negative x) and n-side (positive x), respectively. This is equivalent to the assumption that all charge carriers generated in the range of the strong electric field within the space charge region are charge separated and contribute to the EBIC signal. For the case of the diffusion lengths L_{p} and L_{n}, excited charge carriers in a certain area around the space charge region will also contribute to the EBIC signal. Thus, the distance from the space charge region can be exponentially weighted:

$$f_{\mathrm{SCR+D}} = \begin{cases} \exp\left[\left(d_{\mathrm{p}} + x\right) \Big/ L_{\mathrm{p}}\right], & x < -d_{\mathrm{p}} \\ 1, & x \geq 0 \\ \exp\left[\left(d_{\mathrm{n}} - x\right) \Big/ L_{\mathrm{n}}\right], & x > d_{\mathrm{n}} \end{cases} \tag{20}$$

Assuming a uniform generation function in both regions, and using the convolution functions f_{SCR} and $f_{\mathrm{SCR+D}}$, an integrated EBIC linescan, ΣI_{EBIC}, can be described for both cases. By dividing these two factors, the integrated generation volume is canceled out and leaves only:

$$\frac{\sum I_{\mathrm{EBIC,SCR+D}}}{\sum I_{\mathrm{EBIC,SCR}}} = 1 + \frac{L_{\mathrm{p}} + L_{\mathrm{n}}}{d_{\mathrm{p}} + d_{\mathrm{n}}}, \tag{21}$$

which can be used as a robust estimate for $L_{\mathrm{p}} + L_{\mathrm{n}}$ if the width of the SCR is known.

Results

EBIC measurements

The measurements were performed at an electron beam acceleration voltage of 2 kV, as the generation volume is smallest there (see Figure 3a). Thus. it represents the situation closest to the ideal case of a point-like electron–hole pair generation source. Using even smaller acceleration voltages did not result in measureable EBIC in our setup. A cross-section lamella of the sample was prepared by means of a focused ion beam microscope. An EBIC scan across the p–n interface is shown in Figure 3b, together with a simulated EBIC linescan, taking into account only the generation volume and the space charge region.

The electron beam generation volume was calculated using the CASINO implementation of a Monte Carlo simulation developed by Drouin et al. [55]. In the simulation, we use the SCR width d_{PCMO} = 0.2–2.5 nm (Figure 3b for d_{PCMO} = 2.5 nm) and d_{STNO} = 27 nm, as suggested by Saucke et al. for junctions of the same materials [22]. As illustrated in Figure 3a, the differences in the generation volume on both sides of the junction are negligible. Therefore, we assume the same generation volume for PCMO and STNO.

Comparing the two linescans clearly shows the experimental curve to be broader than the simulated one, which manifests the contributions of excess carriers generated outside the space charge region (i.e., the finite diffusion lengths in STNO and PCMO). We then integrated both linescans and applied Equation 21 using the simulated, $I_{\mathrm{EBIC-S}}$, and the experimental, $I_{\mathrm{EBIC,S+L}}$. This leads to a combined diffusion length, $L_{\mathrm{PCMO}} + L_{\mathrm{STNO}}$ = 21.4(2) nm. The noticeable asymmetry in the experimental EBIC linescan indicates that a larger part of the combined diffusion length can be attributed to L_{STNO}.

Current–voltage characteristics without illumination

The measured current–voltage characteristics of the analyzed manganite–titanate junction are summarized in Figure 4, where J is the current density. For all measurements at different

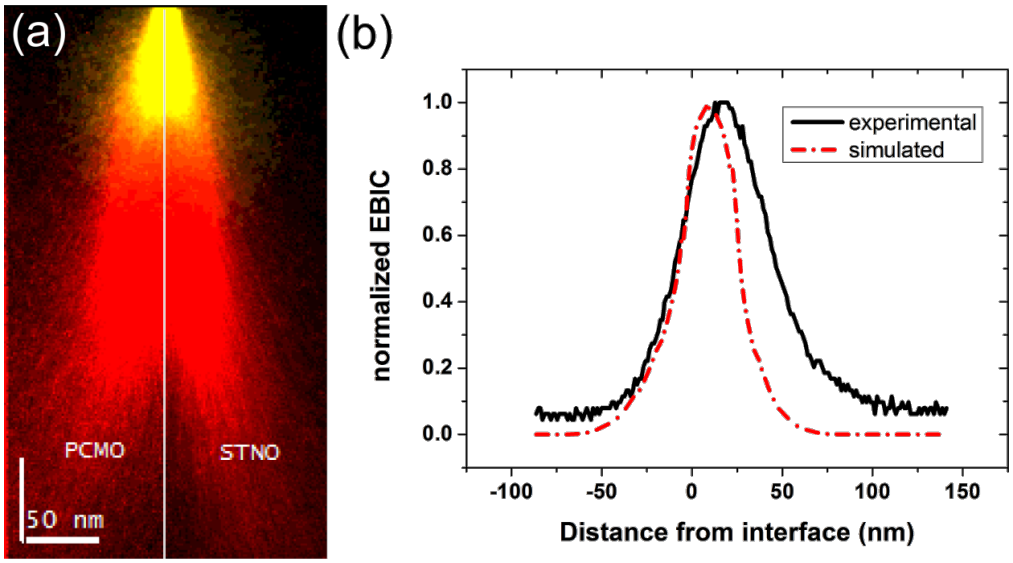

Figure 3: (a) Cross section of a simulated electron beam generation volume directly at the PCMO–STNO interface for electron beam acceleration voltages of 2 kV (yellow, bright) and 10 kV (red, dark). (b) Measured EBIC signal for a 2 kV line scan across the PCMO–STNO interface and corresponding simulation (see text), normalized to their maximum.

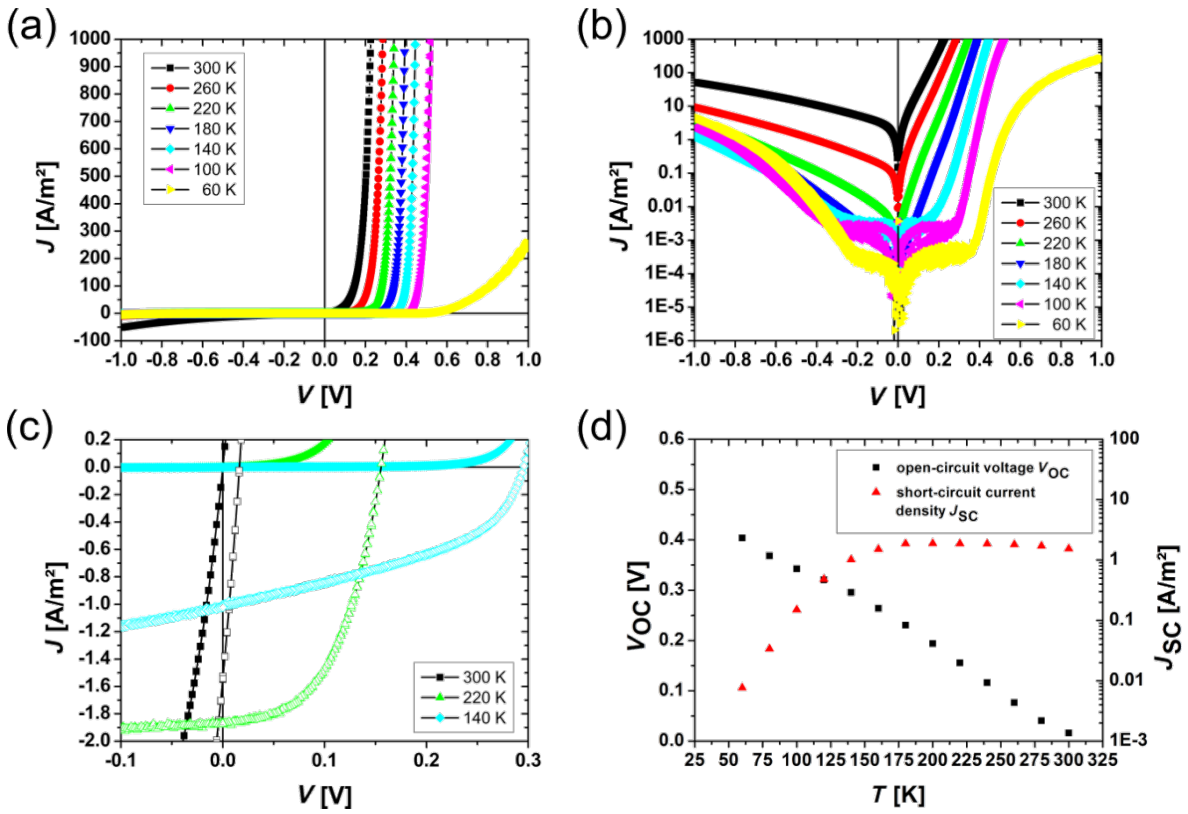

Figure 4: Temperature dependence of the *J*–*V* characteristics for the PCMO–STNO junction: (a) in a linear and (b) in a semi-logarithmic illustration. Over the whole measured temperature range the *J*–*V* curves show rectifying behavior. (c) Comparison of *J*–*V* curves with and without illumination. (d) The open circuit voltage increases for decreasing temperature and the short circuit current breaks down at a temperature around 180 K.

temperatures, the rectifying characteristic of the junction can be recognized. By decreasing the temperature, a plateau evolves for the reverse direction as well as for the forward direction for $|V| \leq 0.2$ V. Furthermore, the exponential increase of the current is shifted to higher voltages in the forward direction.

In Figure 4c the J–V curves with and without illumination are compared. A clear photovoltaic effect is visible for all measured temperatures. Even at 300 K, without a band gap in the PCMO, the photovoltaic effect is visible. The open circuit voltage, V_{OC}, increases with decreasing temperature, while the short circuit current density, J_{SC}, is constant until the temperature reaches values below T = 140 K. Below this temperature, J_{SC} breaks down and decreases exponentially (see Figure 4d). In this work, the collected data sets are analyzed within the one diode model by two methods. Only the forward branch of the J–V curve is used to determine the four parameters, J_S, n, R_S and R_P and the resistance is treated as ohmic.

(i) Manual parameter identification: Here the equivalent circuit is used, which is described in Figure 2, and the analysis is illustrated in Figure 5a. The assumption is made that the influence of the four parameters becomes dominant in different regimes in the forward direction. For small values of the voltage, the voltage mainly drops over the parallel resistance, R_P. The parallel resistance can be determined by fitting the J–V curve linearly in a small region around V = 0. Since the influence of R_S is neglected, this value describes the lower limit of R_P. In the intermediate voltage range, the current is governed by the influence of the diode and thus the ideality factor as well as the saturation current density can be extracted in this region. Therefore, the J–V curves are plotted semi-logarithmically and fitted linearly at the point with highest local slope in the forward branch. The ideality factor can be calculated from the slope and the saturation current is given by the ordinate intercept. For high values of the applied voltage, the current is limited by the series resistance, R_S. To determine the series resistance, the difference between the linear extrapolated curve from the linear fit and the measured curve is calculated by $R_S = \Delta V / I_{max}$.

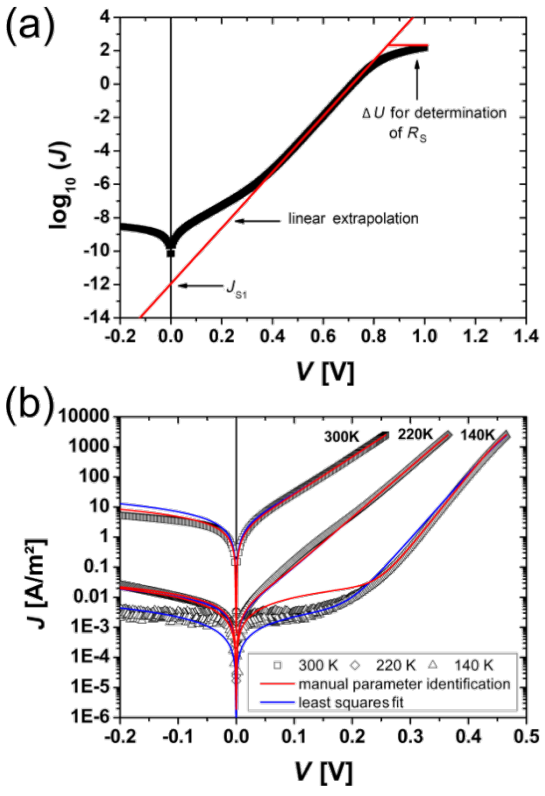

Figure 5: (a) Illustration of the manual parameter identification method, (b) Comparison of the measured data and the two different analysis methods for 300 K, 220 K and 140 K (open black symbols). The red line shows the result of the manual parameter identification, while the blue line is the result of the least squares fit.

(ii) Parameter identification with least squares fit: The second way to analyze the J–V curves is by performing a least squares fit of the implicit Equation 14 for J_{SC} = 0 using a fitting routine. Here the trust region, reflective algorithm implemented in the program MATLAB was used. The four unknown parameters were limited to physically conceivable lower and upper limits. To find the best result within these bounds, the fit was performed by using uniformly distributed starting points within the bounds and the best parameter set was evaluated. Since the slope of the J–V curve is very different for low and high voltages, the sensitivity of the fit routine was adjusted accordingly.

Figure 5b shows typical results for both analysis methods for measurement temperatures of 300 K, 220 K and 140 K. Both methods correctly reconstruct the measured J–V curve in the forward direction for 300 K and 220 K. At a measurement temperature of 140 K, the manual parameter identification only fits to the linear part of the J–V curve, where the influence of the diode is dominant and overestimates the current in the low voltage regime. In contrast to this, results from the least squares fit are in good agreement with the whole forward branch. Both methods do not include any breakdown mechanism in the reverse direction. Thus, the reverse direction cannot be described well in the framework of the one diode model without any modification.

The results for J_S, n, R_S and R_P are plotted in Figure 6 for both methods. With decreasing temperature, the saturation current, J_S, decreases exponentially over several orders of magnitude. This is in good agreement with the theoretically predicted temperature dependence (see Equation 12). For a wide temperature range, the ideality factor, n, increases slowly for values

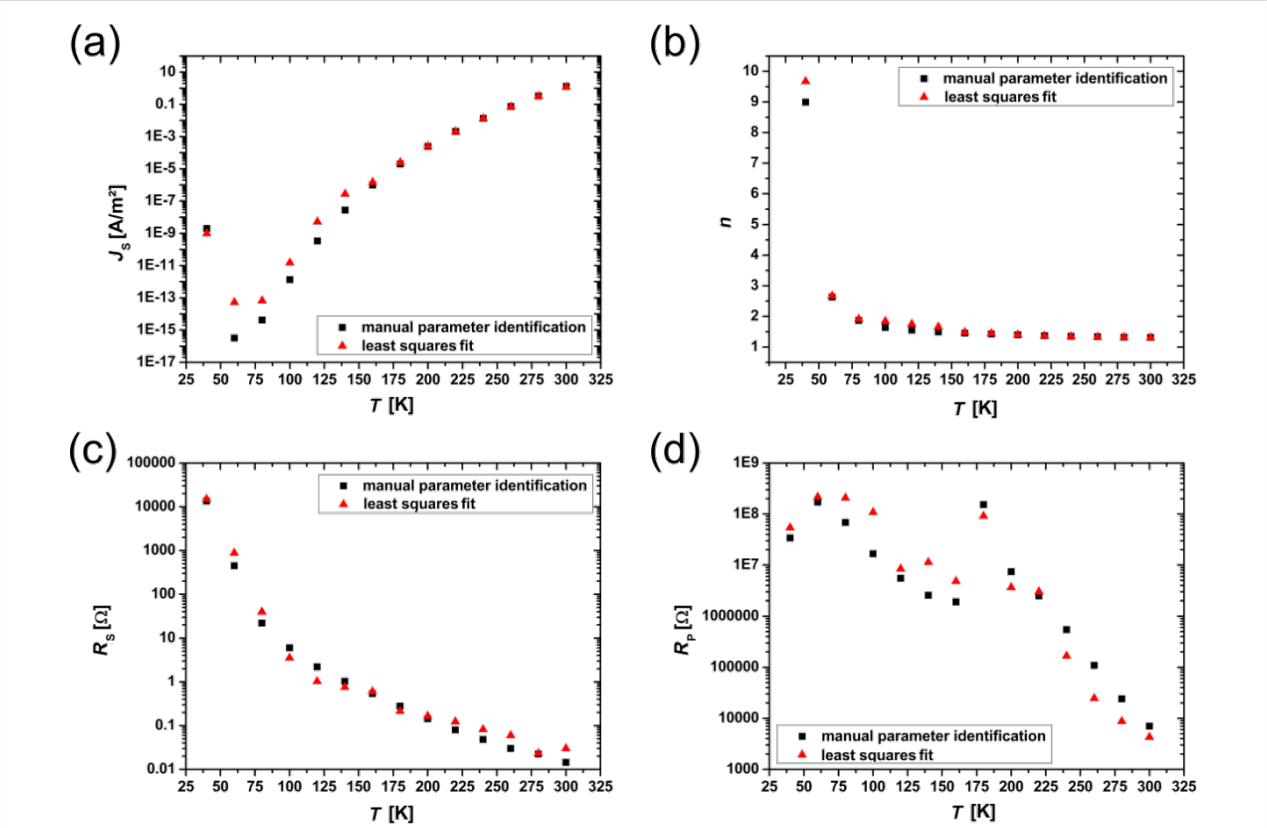

Figure 6: Overview of the temperature dependence of the extracted diode parameters for the two analysis methods. The black squares show the manual parameter identification results and the red triangles show the least squares fit results. (a) Saturation current, J_S, (b) ideality factor, n, (c) series resistance, R_S, (d) parallel resistance, R_P. While J_S decreases with decreasing temperature, n as well as R_S increases. R_S shows the characteristic behavior of thermally activated transport and seems to be dominated by the PCMO resistance. R_P increases with decreasing temperature and shows two different regimes of exponential increase with a different slope.

below 2 and strongly rises above $n = 2$ below $T \approx 80$ K. This may indicate tunneling enhanced recombination at the interface or in the SCR [56]. The resistance, R_S, shows the typical temperature dependence of a thermally activated transport process, where the resistance increases for lower temperatures and therefore is mainly dominated by the PCMO bulk resistance. In contrast to this, the parallel resistance shows two different regimes of exponential increase with a different slope in the semi-logarithmic plot. This is similar to the resistance drop caused by the CER effect in PCMO [9].

Discussion

In the following, we discuss the temperature dependence of the determined parameters of the one diode model, in order to gain insight into the interfacial charge transfer and separation processes of polarons. The polaronic nature of the charge carriers is visible in the thermally activated hopping transport in the series and the CER-like resistance drop in the parallel resistance. Furthermore, the voltage dependence of the saturation current is discussed. We compare our results to those obtained from thin film electric transport measurements in lateral geometry from the literature. For the analysis, we use the parameters determined by the method of manual parameter identification. While the fit was found to describe the whole J–V curve in the framework of the one diode model, the manual method is more sensitive to the evaluation of the different parameters in a certain region of the J–V curve, and is thus expected to lead to more accurate parameters.

Applicability of the Shockley-based one diode model

The temperature dependence of the reverse saturation current is given by Equation 12 and its energy barrier can be determined by

$$n \cdot \ln\left(J_S\right) = -\frac{E_B}{k_B} T^{-1} + n \cdot \ln\left(J_0\right) \qquad (22)$$

In Figure 7a the product of $n \cdot \ln(J_S)$ is plotted versus the inverse temperature. From this, an energy barrier of $E_B = 597.4(1)$ meV was calculated. According to Saucke et al. [22] this energy barrier is interpreted in the model for a heterojunction as evi-

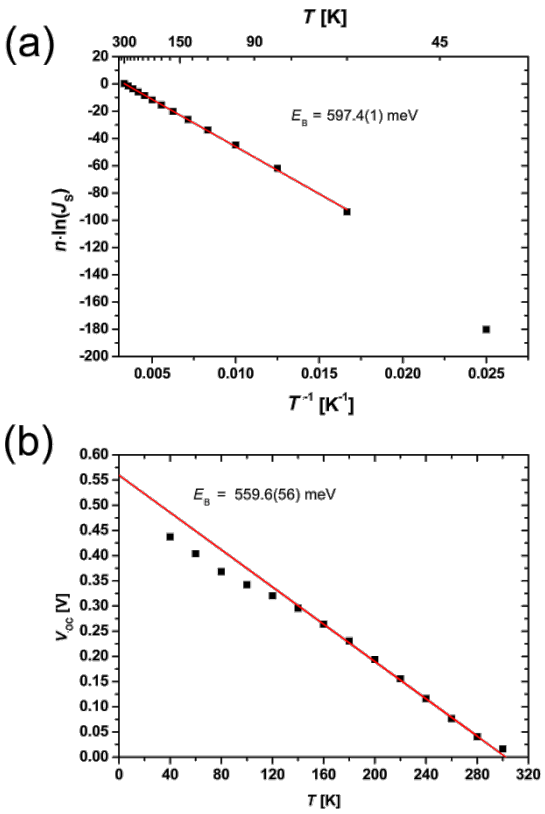

Figure 7: Determination of the energy barrier E_B: (a) from the diode parameter analysis of the *J*–*V* characteristics without illumination E_B = 597.4(1) meV, (b) from the linear extrapolation (towards T = 0 K) of the open circuit voltage E_B = 559.6(56) meV. The calculated energy barrier determined by the *J*–*V* curves with and without illumination has nearly the same value.

dence for the presence of an energy spike (band offset) in the conduction band. The theoretical value of the band offset can be approximately calculated by the difference of the work functions of the p- and n-doped material. For the materials used, these are W = 4.9 eV for PCMO [57] and W = 4.13 eV for STNO [58]. Therefore, the expected barrier height is ΔW = 770 meV. The slightly smaller value of the experimentally determined E_B compared to ΔW can be explained by a slight interdiffusion of *B*-cations at the p–n hetero-interface on the order of less than 1 nm [22], which may induce new states.

The energy barrier can also be determined from *J*–*V* curves under illumination if the temperature dependence of the open circuit voltage is taken into account, as shown in Equation 13 and Equation 16. Both equations are linear in temperature and the slope is mainly influenced by the properties of the materials. For example, one parameter in Equation 16 is the dissociation rate of exciton polaron pairs. In this work, we focus only on the intercepts of Equation 13 or Equation 16, which represent an energy barrier in both cases. By fitting in the linear region of V_{OC} and extrapolating towards T = 0 K (see Figure 7b), we obtain an energy barrier of E_B = 559.6(56) meV, which can be interpreted as the same barrier calculated from *J*–*V* curves in the dark. The result that the same value for the energy barrier is obtained from analysis of transport properties in the dark and under illumination (Equation 22 and Equation 16, respectively) confirms the consistency of the analysis and applicability of the Shockley-based model as a first step.

Conventionally, in large bandwidth inorganic semiconductors, an ideality factor with a value between $1 < n < 2$ is seen as evidence for a contribution of Shockley–Read–Hall recombination. Therefore, in many cases, an improved fit of the *J*–*V* curves of p–n junctions can be obtained by using a second additional diode with an ideality factor of n = 2. If the ideality factor reaches values of $n > 2$, this could be an indication of tunneling enhanced recombination at the interface or in the SCR occurs [56]. Since these models and parameters are derived for quasi-free electrons, they cannot be easily transferred to solar cells made of oxides with strongly correlated electrons.

Another reason to introduce a second diode is given by Giebink et al. [38,39]. They introduce a second diode in organic systems in order to take the voltage dependence of different charge carrier recombination mechanisms into account. Here, hole or electron-type polarons can change their character from trapped to mobile, respectively. In our model system, the last effect is not taken into account, since the mobile carriers in the STNO are always electrons for all voltage ranges.

Even if values for the ideality factor are between $1 < n < 2$ for higher temperatures, for our results, it is reasonable to consider only one diode because the dominating part of the current originates from the SCR. At low temperatures, the ideality factor is $n > 2$, which suggests the transition from thermionic emission to tunneling across the interface [56]. Indeed, due to the lower thermal population of phonon states, small polaron mobility at low temperatures generally exhibits an increasing tunneling fingerprint [59]. In order to improve the fit of the *J*–*V* curves for polaronic systems, it seems to be more reasonable to take the voltage dependence of the microscopic parameters into account, such as a parallel resistance, $R_P(V)$, rather than introducing a second diode.

Thermally activated transport of small polarons and correlation effects

In Figure 8 the Arrhenius plot of R_S/T is shown. At temperatures below half of the Debye temperature, $\Theta_D/2 \approx 160$ K, the probability of polaron tunneling between neighboring sites increases. Therefore, the measured resistance is below the expected value in the model of thermally activated hopping in

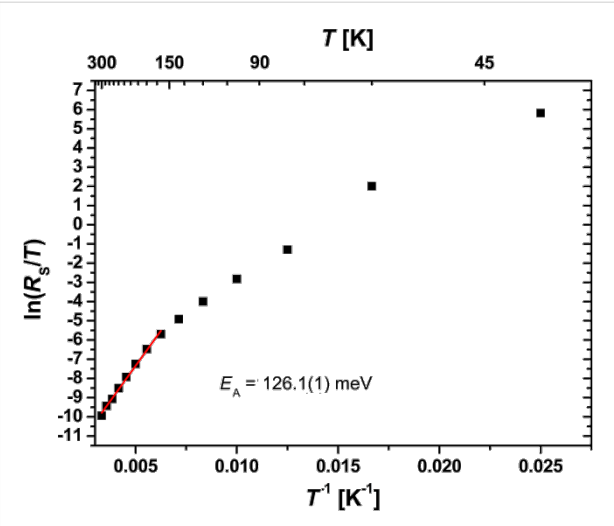

Figure 8: Determination of the activation energy, $E_{A,RS}$, for thermally activated hopping transport from the series resistance, R_S. At lower temperatures the resistance is below the values expected in the thermally activated hopping theory. Here the probability of polarons tunneling to neighboring sites is enhanced.

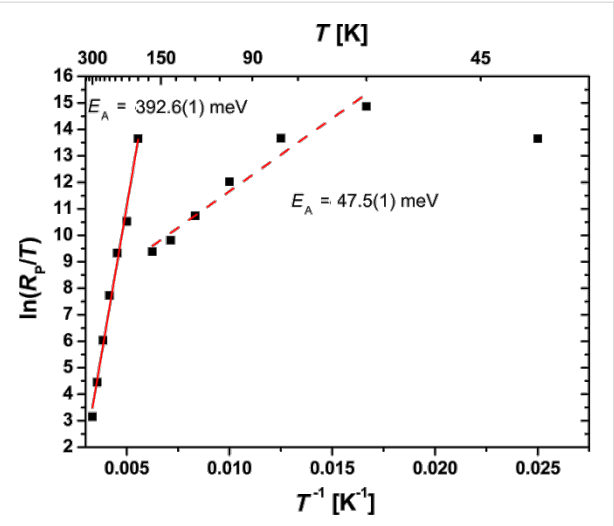

Figure 9: Determination of the activation energy, $E_{A,RP}$, of the thermally activated hopping transport for the parallel resistance, R_P. At high temperatures, the activation energy is on the order of the polaron formation energy. The second regime can be modified by the influence of a strong electric field and can be seen as an effective $E_{A,RP}$.

that case [40]. Consequently, we only use the slope from the temperature range $T > \Theta_D/2$ to determine the activation energy of the thermally activated hopping of small polarons. According to Bogomolov et al. [40], in the adiabatic limit, the resistivity can be written as

$$R(T) = R_0 \cdot T \cdot \exp\left(\frac{E_A}{k_B T}\right), \tag{23}$$

with a prefactor, R_0. For the measured J–V curves, the activation energy is calculated to be $E_{A,RS}$ = 126.1(1) meV. This value is in agreement with results found for PCMO in the literature, $E_{A,Lit}$ = 132 meV [9]. Thus, the bulk resistance of the PCMO seems to be the dominating contribution to the series resistance, R_S. The experimental value is slightly smaller because of the large electric field on the order of $E = 10^7$ V/m in a cross-plane measurement geometry. This value considerably exceeds that in lateral measurement geometries. A strong electric field leads to a reduction of the activation energy, E_A [9].

In Figure 9 the Arrhenius plot of R_P/T is shown. For high temperatures, the obtained activation energy of $E_{A,RP}$ = 392.6(1) meV for R_P is on the order of the polaron formation energy in PCMO. The presence of two branches in the Arrhenius plot in Figure 9, hints at the influence of the colossal electro-resistance (CER) [9,60], which is caused by correlation effects of polarons in manganite oxides. The reduced $E_{A,RP}$ at lower temperatures is due to an electric field-induced transition to driven polaron states and a related reduction of the activation energy for polaron transport [9]. A similar effect has been observed in PCMO–STNO junctions for the series resistance, R_S [22]. In addition, current-induced melting of charge-ordered domains is observed [61]. Since the CER in bulk PCMO samples is visible in the temperature range, where the charge ordered and disordered phase coexist and the formation of percolation paths depends on the structure as well as on the electrical pre-history, the determination of a critical electrical field is hardly possible. We assume that in our devices, the observed CER in $R_P(T)$ stems from such polaronic processes at the interface. This is additionally evidenced by the observation of an interfacial colossal magneto-resistance (CMR) effect at metal–PCMO interfaces [62]. In contrast to the observation of a CER in $R_S(T)$ by Saucke et al. [22], in the junctions studied here, the dominating contribution of R_P could originate from a higher interface resistance.

Bias dependence of the reverse saturation current

A strong voltage dependence effect is visible in the reverse saturation current. This can be discussed according to Figure 10, where the expected simplified band diagram of the manganite–titanate junction is shown for electro-chemical equilibrium and with applied voltage in both forward and reverse directions. We disregard here all changes of the electronic structure of the PCMO near the interface due to local variations of the correlation interactions and the small screening length and assume that the main voltage drop happens in the STNO. If the diode is biased in the forward direction, the barrier for the recombination current is decreased, whereas it is increased for

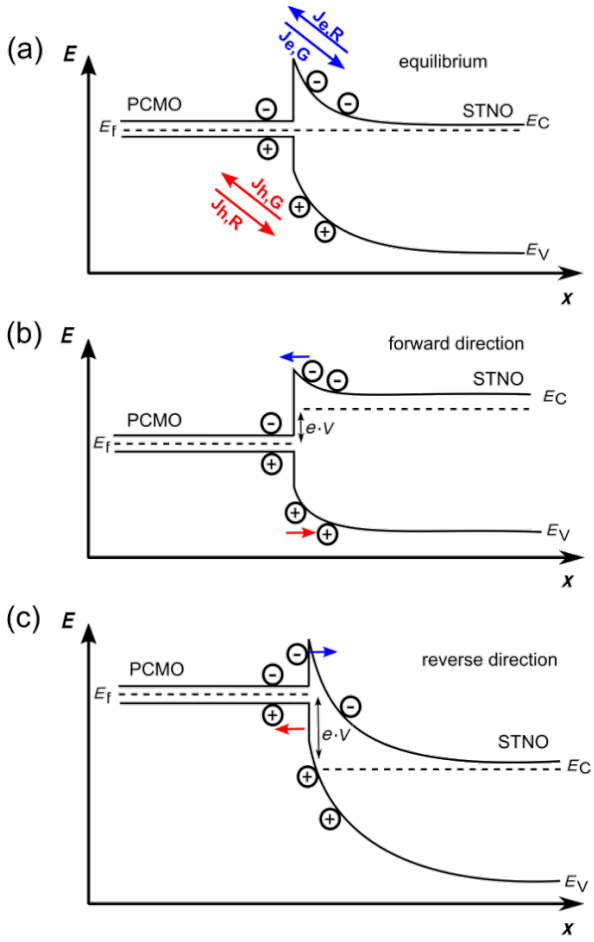

Figure 10: Schematic band structure of a PCMO–STNO heterojunction (a) at zero bias, (b) in the forward direction and (c) in the reverse direction.

the reverse direction. Therefore, the generation current should be the dominating contribution to the total current measured in the reverse direction. The energy barrier calculated from the Arrhenius plot of $n \cdot \ln(J_S)$ has been interpreted as the presence of a band offset in the conduction band. For this reason, the transport in the reverse direction of the solar cells is governed by thermally generated charge carriers in the PCMO, which must overcome the barrier to diffuse into the STNO. If the applied voltage in the reverse direction is high enough, the barrier could be reduced or become narrower. In this way, thermally activated as well as tunneling induced charge transfer is facilitated, leading to an increasing saturation current.

Since the results from the least squares fit method describe the influence of the saturation current on the whole *J*–*V* characteristic more accurately, it is used to compare the reverse saturation current calculated on the basis of the one diode model with the measured *J*–*V* curves.

In Figure 11a this comparison is shown for a temperature of 220 K. For the reverse direction, a significant difference between the expected *J* (based on the determined R_P) and the measured *J* is observed. Therefore, an additional voltage dependence of the reverse saturation current exists that cannot be described in the framework of the Shockley model. The differences between the measured curve and the least squares fit data can be expressed as the rate, *r*, in Equation 15 given by

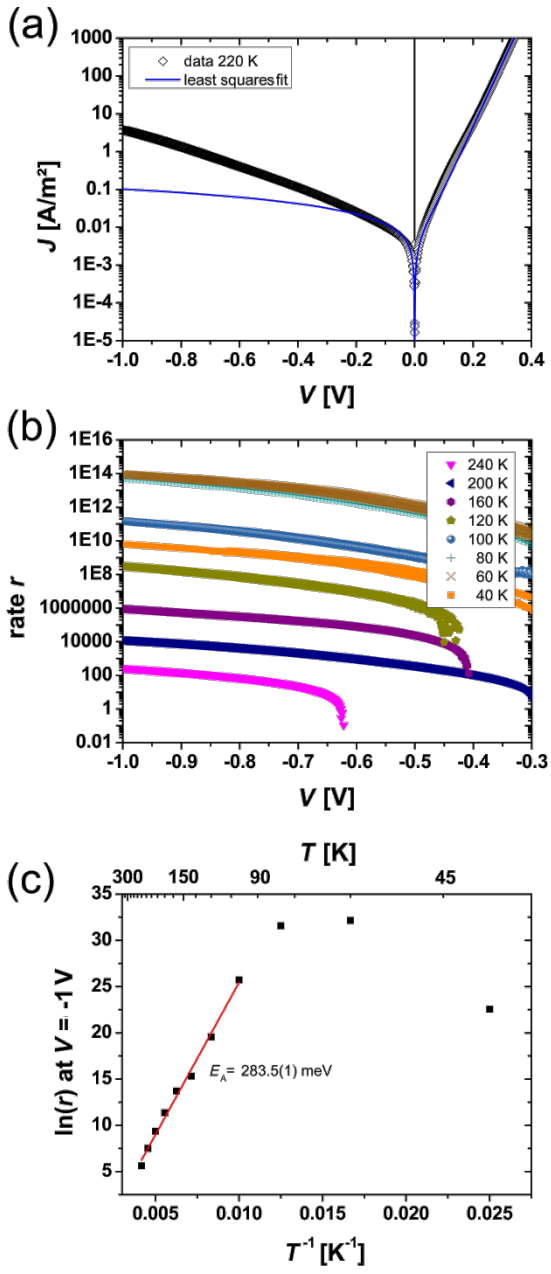

Figure 11: (a) Comparison of *J*–*V* curves from the least squares fit and exemplarily data at a temperature of 220 K, (b) extracted generation rate *r* as a function of the applied voltage for temperatures 40 K < *T* < 240 K, (c) determination of the energy barrier, E_B, for an applied voltage of *V* = −1 V.

$$r = \frac{\left(J_{\text{measure}} - J_{\text{fit}}\right)}{J_{\text{S}}} = \frac{\Delta J}{J_{\text{S}}}. \quad (24)$$

In Figure 11b the rate, r, is plotted against the voltage, V. At a temperature below 240 K and a voltage $|V| > 0.7$ V in the reverse direction, the rate is clearly higher than one. For higher temperatures or smaller voltages, this effect is too small. The presence of a finite R_{P} clearly cannot describe the full bias dependence of J in the reverse direction, since it determines only the small voltage regime of the solid curve given by the one diode model. In the forward branch of the curve for high voltages, the series resistance R_{S} limits the current density and a voltage-dependent R_{P} cannot be extracted. Thus, the influence of a voltage-dependent parallel resistance should be only visible in the large voltage regime of the reverse saturation current. Since the forward direction of the J–V curve is not strongly affected by the voltage dependence of R_{P}, we assume that the dominant contribution to the current in the reverse direction stems from a voltage dependence of J_{S}, where breakdown mechanisms can be excluded. The measurements are performed during the cooling down and heating of the solar cell and deliver reproducible data (the data from heating process is not shown here). In contrast to this observation, an electrical breakdown would irreversibly change the junction. In comparison to the process introduced by Giebink et al. [38,39], here, the rate r may not represent a pure polaron pair dissociation rate. This is because the strong electric field at the interface may increase the polaron mobility, and thus also may influence the barrier height of the band discontinuity at the interface. Since a finite current density in the reverse direction can only be due to electron–hole polaron pair generation at the interface, we interpret the rate r as being limited by the generation rate of polaron pairs, which are separated in the SCR. The voltage dependence of the polaron pair generation as well as the bias dependent drop of E_{B} can both give rise to a rate $r > 1$. For PCMO, exciton binding energies can be neglected because of the high dielectric constant of $\varepsilon = 30$ [63].

By lowering the temperature the rates increase until a temperature of 80 K is reached. For 80 K and 60 K, a constant rate is visible. At a temperature of 40 K, the rate drops by several orders of magnitudes. The constant value of r at a low temperature and the reduction below 60 K can indicate the transition from thermally induced separation at the interface to tunneling through the barrier. This is supported by the large n values. We assume that the determined barrier height, $E_{\text{B}} = 283.5$ meV (see Figure 11c), in the reverse direction is strongly decreased due to the buildup of a large electric field at the junction interface.

Previous studies of a PCMO–STNO junction show the rectifying character of the J–V curve can predict a p–n diode-type band diagram for this type of junction [64]. In contrast to our study, a lower doping level of Nb ($y = 0.0002$) was used, which leads to a more extended space charge region in the STNO. The rectifying J–V characteristic shows no noticeable breakdown in the reverse direction up to very high voltages and an ideality factor of $n = 1.05$–1.10 indicates thermally induced separation processes across the junction.

In our study, a clear contribution of the series resistance in the forward direction at higher voltages is attributed to the bulk resistance of the PCMO thin film. Furthermore, the higher Nb doping reduces the resistance contribution of the STNO bulk. In addition, the space charge region in the STNO is much smaller and therefore the probability for tunneling processes across the interface at lower temperatures is increased. Both effects are an important prerequisite for the analysis of the polaronic carriers on the energy conversion in a correlated oxide solar cell.

Evaluation of the measured diffusion length

The sum of the diffusion lengths in PCMO and STNO $L_{\text{PCMO}} + L_{\text{STNO}} = 21$ nm measured by EBIC is closer to the values found in polymer–fullerene solar cells than the ones typical for inorganic semiconductors. In our simulation, we neglect any surface recombination processes, which could reduce the exponential decay width in the measured EBIC linescan, leading to apparently smaller diffusion lengths. Consequently, we interpret the result found here as a lower limit to the real diffusion lengths.

The asymmetry in the measured EBIC signal suggests L_{PCMO} is smaller than L_{STNO}, coinciding with much smaller charge carrier mobility in PCMO than in STNO. The small diffusion length substantiates the importance of the polaron carrier model for this material class. Furthermore, it suggests that a substantial part of the current stems from excitations in the SCR. This emphasizes the importance of conduction processes in or near the SCR in manganite–titanate junctions.

Conclusion

In this contribution we have analyzed the current–voltage characteristics of a PCMO–STNO junction in the framework of the one diode model based on Shockley theory. The model seems to be applicable for these types of junctions given the consistency of the determined parameters and their reasonable temperature behavior. However, modifications must be taken into account. The microscopic interpretation of each of these parameters must include the strong correlation effects of the involved materials and their local change at the interface. Our EBIC measurements show a relatively small diffusion length comparable to

that of organic semiconductors with low mobilities. The series resistance, R_S, reflects the thermally activated hopping mobility of small polarons in PCMO. In addition, the CER-like behavior of the parallel resistance, R_P, also points to strong correlation effects. In addition, the absence of the CER-like behavior in R_S is an indication that the main contribution of R_P originates from the interface. The very strong voltage dependence of the reverse saturation current can be explained by the generation and separation of electron and hole polaron pairs at the interface with a voltage-dependent generation rate, r. The dominate contribution to the current in the reverse direction is the generation current in the SCR of PCMO and this current is both limited by the electron–hole polaron pair generation and their separation due to the interfacial energy spike of the conduction band. More work must be performed in the future in order to develop a microscopic understanding of the origin of the interfacial energy spike, which may involve the effects of band offset, orbital mismatch between states of different symmetry as well as local correlation effects.

Experimental

An epitaxial thin film of p-doped $Pr_{1-x}Ca_xMnO_3$ (PCMO, $x = 0.34$) was deposited on single crystalline n-doped $SrTi_{1-y}Nb_yO_3$ (STNO, $y = 0.002$) to fabricate p–n heterojunctions. The thin film was deposited via reactive ion beam sputtering from a stoichiometric target with a film thickness of $t \approx 100$ nm. During the deposition, the process temperatures was $T_{dep} = 750$ °C, the pressure of the Xe sputtering gas was $p_{Xe} = 1 \times 10^{-4}$ mbar and the pressure of the oxygen background gas was $p_{O2} = 1.4 \times 10^{-4}$ mbar. Ohmic contacts were provided by sputtered Ti contacts with a Au protection coating on the STNO substrate and Au contacts on the PCMO. Here the area of the contacts was 1×4 mm^2 and they were structured by the use of a shadow mask at a process temperature of $T_{dep} = 200$ °C. After deposition, the quality of the films was checked by XRD techniques.

For electrical characterization, the sample was connected in a two point geometry, where the resistances of the supply cables were excluded in a cryostat with a Suprasil entry window. The geometry is shown in Figure 12a. During the measurement, the maximum current density flow through the junction was set to $J = 2500$ A/m² and the voltage range was between $V = \pm 1$ V. For every measurement, the positive pole was connected to the contact on the PCMO. To illuminate the sample, a Xe arc lamp with a power density of $p_{ph} \approx 155$ mW/cm² was used.

The EBIC measurements were carried out in a FEI Nova Nanolab 600 dual beam focused ion beam microscope. Standard EBIC equipment from Gatan was used, including a Stanford SR570 current amplifier. The cross section (see Figure 12b for a sketch of the geometry) was prepared using a standard focused ion beam TEM lamella preparation at 30 kV ion acceleration voltage, with the final cleaning of the surfaces at 5 kV.

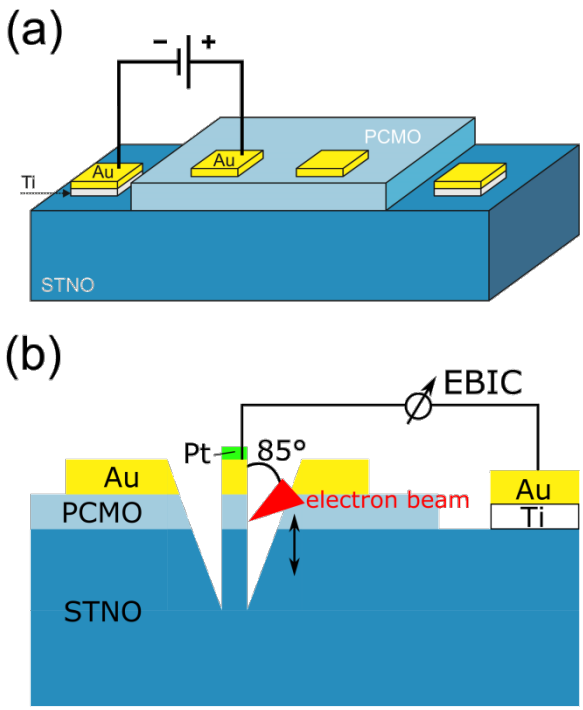

Figure 12: (a) Sketch of the sample geometry for the electrical measurements in the cryostat, and (b) sketch of the sample geometry for the cross-section EBIC measurement. The lamella thickness along the beam direction was estimated from SEM measurements to be about 330 nm at the PCMO–STNO interface.

Acknowledgements

We thank Pablo Marín Perera for valuable help with the EBIC measurements. Funding from the Deutsche Forschungsgemeinschaft (DFG) under Grant No. SFB1073, project B02 is acknowledged.

References

1. Zhu, J. M.; Shen, W. Z.; Zhang, Y. H.; Dekkers, H. F. W. *Phys. B (Amsterdam, Neth.)* **2005,** *355,* 408–416. doi:10.1016/j.physb.2004.11.069
2. Blom, P. W. M.; Mihailetchi, V. D.; Koster, L. J. A.; Markov, D. E. *Adv. Mater.* **2007,** *19,* 1551–1566. doi:10.1002/adma.200601093
3. Ameri, T.; Khoram, P.; Min, J.; Brabec, C. J. *Adv. Mater.* **2013,** *25,* 4245–4266. doi:10.1002/adma.201300623
4. Nelson, J. *Mater. Today* **2011,** *14,* 462–470. doi:10.1016/S1369-7021(11)70210-3
5. Sun, J. R.; Shen, B. G.; Sheng, Z. G.; Sun, Y. P. *Appl. Phys. Lett.* **2004,** *85,* 3375–3377. doi:10.1063/1.1806560
6. Sheng, Z. G.; Zhao, B. C.; Song, W. H.; Sun, Y. P.; Sun, J. R.; Shen, B. G. *Appl. Phys. Lett.* **2005,** *87,* 242501. doi:10.1063/1.2140878
7. Chen, Y. Z.; Sun, J. R.; Wei, A. D.; Lu, W. M.; Liang, S.; Shen, B. G. *Appl. Phys. Lett.* **2008,** *93,* 152515. doi:10.1063/1.3003868

8. Brabec, C. J.; Sariciftci, N. S.; Hummelen, J. C. *Adv. Funct. Mater.* **2001,** *11,* 15–26. doi:10.1002/1616-3028(200102)11:1<15::AID-ADFM15>3.0.CO;2-A
9. Schramm, S.; Hoffmann, J.; Jooss, C. *J. Phys.: Condens. Matter* **2008,** *20,* 395231. doi:10.1088/0953-8984/20/39/395231
10. Zhao, G.-m.; Wang, Y. S.; Kang, D. J.; Prellier, W.; Rajeswari, M.; Keller, H.; Venkatesan, T.; Chu, C. W.; Greene, R. L. *Phys. Rev. B* **2000,** *62,* R11949. doi:10.1103/PhysRevB.62.R11949
11. Hartinger, C.; Mayr, F.; Loidl, A.; Kopp, T. *Phys. Rev. B* **2006,** *73,* 024408. doi:10.1103/PhysRevB.73.024408
12. Burschka, J.; Pellet, N.; Moon, S.-J.; Humphry-Baker, R.; Gao, P.; Nazeeruddin, M. K.; Grätzel, M. *Nature* **2013,** *499,* 316–319. doi:10.1038/nature12340
13. Ball, J. M.; Lee, M. M.; Hey, A.; Snaith, H. J. *Energy Environ. Sci.* **2013,** *6,* 1739–1743. doi:10.1039/c3ee40810h
14. Noh, J. H.; Im, S. H.; Heo, J. H.; Mandal, T. N.; Seok, S. I. *Nano Lett.* **2013,** *13,* 1764–1769. doi:10.1021/nl400349b
15. Tanaka, K.; Takahashi, T.; Ban, T.; Kondo, T.; Uchida, K.; Miura, N. *Solid State Commun.* **2003,** *127,* 619–623. doi:10.1016/S0038-1098(03)00566-0
16. Grätzel, M. *Nat. Mater.* **2014,** *13,* 838–842. doi:10.1038/nmat4065
17. Stranks, S. D.; Eperon, G. E.; Grancini, G.; Menelaou, C.; Alcocer, M. J. P.; Leijtens, T.; Herz, L. M.; Petrozza, A.; Snaith, H. J. *Science* **2013,** *342,* 341–344. doi:10.1126/science.1243982
18. Xing, G.; Mathews, N.; Sun, S.; Lim, S. S.; Lam, Y. M.; Grätzel, M.; Mhaisalkar, S.; Sum, T. C. *Science* **2013,** *342,* 344–347. doi:10.1126/science.1243167
19. Kim, H.-S.; Im, S. H.; Park, N.-G. *J. Phys. Chem. C* **2014,** *118,* 5615–5625. doi:10.1021/jp409025w
20. Park, N.-G. *Mater. Today* **2015,** *18,* 65–72. doi:10.1016/j.mattod.2014.07.007
21. Schirmer, O. F.; Imlau, M.; Merschjann, C.; Schoke, B. *J. Phys.: Condens. Matter* **2009,** *21,* 123201. doi:10.1088/0953-8984/21/12/123201
22. Saucke, G.; Norpoth, J.; Jooss, C.; Su, D.; Zhu, Y. *Phys. Rev. B* **2012,** *85,* 165315. doi:10.1103/PhysRevB.85.165315
23. Woike, T.; Berben, D.; Imlau, M.; Buse, K.; Pankrath, R.; Krätzig, E. *J. Appl. Phys.* **2001,** *89,* 5663–5666. doi:10.1063/1.1328779
24. Shockley, W.; Queisser, H. J. *J. Appl. Phys.* **1961,** *32,* 510–519. doi:10.1063/1.1736034
25. Noland, J. A. *Phys. Rev.* **1954,** *94,* 724. doi:10.1103/PhysRev.94.724
26. Bi, C. Z.; Ma, J. Y.; Yan, J.; Fang, X.; Zhao, B. R.; Yao, D. Z.; Qiu, X. G. *J. Phys.: Condens. Matter* **2006,** *18,* 2553–2561. doi:10.1088/0953-8984/18/8/017
27. Hao, X.; Wang, Z.; Schmid, M.; Diebold, U.; Franchini, C. *Phys. Rev. B* **2015,** *91,* 085204. doi:10.1103/PhysRevB.91.085204
28. Eagles, D. M.; Georgiev, M.; Petrova, P. C. *Phys. Rev. B* **1996,** *54,* 22–25. doi:10.1103/PhysRevB.54.22
29. Sze, S. M. *Physics of Semiconductor Devices;* Wiley-Interscience: New York, NY, U.S.A., 1969.
30. Anderson, R. L. *Solid-State Electron.* **1962,** *5,* 341–351. doi:10.1016/0038-1101(62)90115-6
31. Dagotto, E. *Nanoscale Phase Separation and Colossal Magnetoresistance;* Springer Series in Solid-State Sciences, Vol. 136; Springer: Berlin, Germany, 2003. doi:10.1007/978-3-662-05244-0
32. Hwang, H. Y.; Iwasa, Y.; Kawasaki, M.; Keimer, B.; Nagaosa, N.; Tokura, Y. *Nat. Mater.* **2012,** *11,* 103–113. doi:10.1038/nmat3223
33. Rakhmanova, S. V.; Conwell, E. M. *Appl. Phys. Lett.* **1999,** *75,* 1518–1520. doi:10.1063/1.124741
34. Mildner, S.; Hoffmann, J.; Jooss, C.; Blöchl, P. E.; Techert, S. *Phys. Rev. B* **2015,** in press.
35. Hoffmann, J.; Moschkau, P.; Mildner, S.; Norpoth, J.; Jooss, C.; Wu, L.; Zhu, Y. *Mater. Res. Express* **2014,** *1,* 046403. doi:10.1088/2053-1591/1/4/046403
36. Strachan, A. Modeling equations and parameters for numerical simulation. *Properties of Crystalline Silicon;* The Institute of Electrical Engineers: London, U.K., 1999; pp 457–475.
37. Shockley, W. *Bell Syst. Tech. J.* **1949,** *28,* 435–489. doi:10.1002/j.1538-7305.1949.tb03645.x
38. Giebink, N. C.; Wiederrecht, G. P.; Wasielewski, M. R.; Forrest, S. R. *Phys. Rev. B* **2010,** *82,* 155305. doi:10.1103/PhysRevB.82.155305
39. Giebink, N. C.; Lassiter, B. E.; Wiederrecht, G. P.; Wasielewski, M. R.; Forrest, S. R. *Phys. Rev. B: Condens. Matter Mater. Phys.* **2010,** *82,* 155306. doi:10.1103/PhysRevB.82.155306
40. Bogomolov, V. N.; Kudinov, E. K.; Firsov, Y. A. *Phys. Solid State* **1968,** *9,* 2502–2513.
41. Grossmann, P.; Rajkovic, I.; Moré, R.; Norpoth, J.; Techert, S.; Jooss, C.; Mann, K. *Rev. Sci. Instrum.* **2012,** *83,* 053110. doi:10.1063/1.4718936
42. Perlman, S. S.; Feucht, D. L. *Solid-State Electron.* **1964,** *7,* 911–923. doi:10.1016/0038-1101(64)90070-X
43. Katz, E. A.; Faiman, D.; Tuladhar, S. M.; Kroon, J. M.; Wienk, M. M.; Fromherz, T.; Padinger, F.; Brabec, C. J.; Sariciftci, N. S. *J. Appl. Phys.* **2001,** *90,* 5343–5350. doi:10.1063/1.1412270
44. Kumar, P.; Gaur, A. *J. Appl. Phys.* **2013,** *113,* 094505. doi:10.1063/1.4794356
45. Lakhwani, G.; Rao, A.; Friend, R. H. *Annu. Rev. Phys. Chem.* **2014,** *65,* 557–581. doi:10.1146/annurev-physchem-040513-103615
46. Chirvase, D.; Chiguvare, Z.; Knipper, M.; Parisi, J.; Dyakonov, V.; Hummelen, J. C. *J. Appl. Phys.* **2003,** *93,* 3376–3383. doi:10.1063/1.1545162
47. Vandewal, K.; Tvingstedt, K.; Gadisa, A.; Inganäs, O.; Manca, J. V. *Nat. Mater.* **2009,** *8,* 904–909. doi:10.1038/nmat2548
48. Arnab, S. M.; Kabir, M. Z. *J. Appl. Phys.* **2014,** *115,* 034504. doi:10.1063/1.4861725
49. Kirchartz, T.; Deledalle, F.; Tuladhar, P. S.; Durrant, J. R.; Nelson, J. *J. Phys. Chem. Lett.* **2013,** *4,* 2371–2376. doi:10.1021/jz4012146
50. Orton, J. W.; Blood, P. *Tech. Phys.* **1990,** *13,* 308–315.
51. Luque, A.; Hegedus, S., Eds. *Handbook of Photovoltaic Science and Engineering;* John Wiley & Sons: Chichester, U.K., 2003. doi:10.1002/0470014008
52. Leamy, H. J. *J. Appl. Phys.* **1982,** *53,* R51. doi:10.1063/1.331667
53. Donolato, C. *Phys. Status Solidi A* **1981,** *65,* 649–658. doi:10.1002/pssa.2210650231
54. Drouin, D.; Hovington, P.; Gauvin, R. *Scanning* **1997,** *19,* 20–28. doi:10.1002/sca.4950190103
55. Drouin, D.; Couture, A. R.; Joly, D.; Tastet, X.; Aimez, V.; Gauvin, R. *Scanning* **2007,** *29,* 92–101. doi:10.1002/sca.20000
56. Nadenau, V.; Rau, U.; Jasenek, A.; Schock, H. W. *J. Appl. Phys.* **2000,** *87,* 584–593. doi:10.1063/1.371903
57. Reagor, D. W.; Lee, S. Y.; Li, Y.; Jia, Q. X. *J. Appl. Phys.* **2004,** *95,* 7971–7975. doi:10.1063/1.1737802
58. Zagonel, L. F.; Bäurer, M.; Bailly, A.; Renault, O.; Hoffmann, M.; Shih, S.-J.; Cockayne, D.; Barrett, N. *J. Phys.: Condens. Matter* **2009,** *21,* 314013. doi:10.1088/0953-8984/21/31/314013
59. Fratini, S.; Ciuchi, S. *Phys. Rev. Lett.* **2003,** *91,* 256403. doi:10.1103/PhysRevLett.91.256403
60. Asamitsu, A.; Tomioka, Y.; Kuwahara, H.; Tokura, Y. *Nature* **1997,** *388,* 50–52. doi:10.1038/40363

61. Jooss, C.; Wu, L.; Beetz, T.; Klie, R. F.; Beleggia, M.; Schofield, M.; Schramm, S.; Hoffmann, J.; Zhu, Y. *Proc. Natl. Acad. Sci. U. S. A.* **2007,** *104,* 13597–13602. doi:10.1073/pnas.0702748104
62. Scherff, M.; Hoffmann, J.; Meyer, B.; Danz, T.; Jooss, C. *New J. Phys.* **2013,** *15,* 103008. doi:10.1088/1367-2630/15/10/103008
63. Biškup, N.; De Andrés, A.; Martinez, J. L.; Perca, C. *Phys. Rev. B* **2005,** *72,* 024115. doi:10.1103/PhysRevB.72.024115
64. Sawa, A.; Fujii, T.; Kawasaki, M.; Tokura, Y. *Appl. Phys. Lett.* **2005,** *86,* 112508. doi:10.1063/1.1883336

License and Terms

BEILSTEIN JOURNAL OF NANOTECHNOLOGY

Thermal energy storage – overview and specific insight into nitrate salts for sensible and latent heat storage

Nicole Pfleger*[1], Thomas Bauer[2], Claudia Martin[1], Markus Eck[1] and Antje Wörner[1]

Review

Open Access

Address:
[1]German Aerospace Center (DLR), Pfaffenwaldring 38–40, 70569 Stuttgart, Germany and [2]German Aerospace Center (DLR), Linder Höhe, 51147 Köln, Germany

Email:
Nicole Pfleger* - Nicole.Pfleger@dlr.de

* Corresponding author

Keywords:
eutectic mixture; molten salt; nitrate; phase change material; thermal decomposition

Beilstein J. Nanotechnol. **2015,** *6,* 1487–1497.
doi:10.3762/bjnano.6.154

Received: 13 February 2015
Accepted: 17 June 2015
Published: 09 July 2015

This article is part of the Thematic Series "Materials for sustainable energy production, storage, and conversion".

Guest Editor: M. Fichtner

Abstract

Thermal energy storage (TES) is capable to reduce the demand of conventional energy sources for two reasons: First, they prevent the mismatch between the energy supply and the power demand when generating electricity from renewable energy sources. Second, utilization of waste heat in industrial processes by thermal energy storage reduces the final energy consumption. This review focuses mainly on material aspects of alkali nitrate salts. They include thermal properties, thermal decomposition processes as well as a new method to develop optimized salt systems.

Review

Introduction

Thermal energy storage (TES) is achieved by different techniques (Figure 1): sensible heat storage, latent heat storage and chemical heat storage.

The term “sensible heat” indicates that the storage process can be sensed by a change of the temperature. The relation of the change in temperature and the stored heat is given by the heat capacity c_p.

In contrast to the storage of sensible heat latent heat cannot be sensed: The energy which is absorbed or released is stored by a phase transition which takes place at a constant temperature and therefore appears to be latent. Materials used for latent heat storage are called PCMs (phase change materials) because the heat storage is achieved by a phase change.

Another technique to store heat is thermochemical heat storage (TCS). TCS makes use of the enthalpy of reaction ΔH. In reactions featuring a positive change of ΔH (endothermic reaction) heat can be stored. The energy can be released by a backward reaction ($\Delta H < 0$) afterwards.

Because of the possibility to store the compounds separately without the loss of energy thermochemical storage is appro-

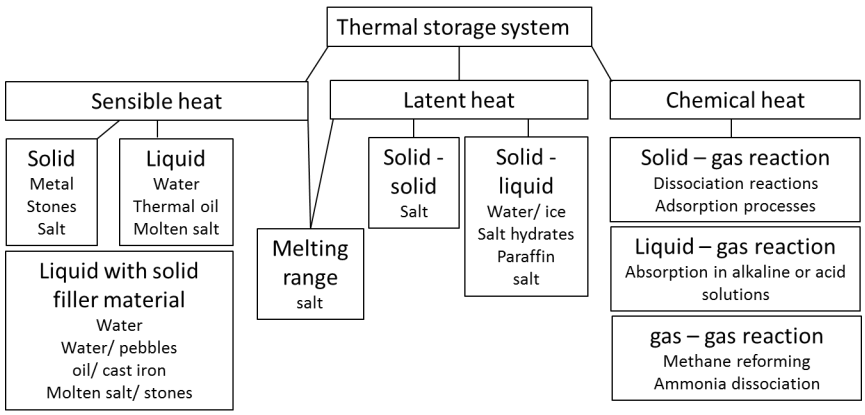

Figure 1: Classification of heat storage media.

priate for thermal energy storage over large period of times. TES is applied in the field of power generation, industrial process heat, space heating/ cooling as well as the management of thermal energy processes in vehicles. These classifications of storage characteristics and applications result in specific operation parameters and designs of TES systems.

Several TES media exist such as water, metals, ceramics, stones and salts. Table 1 gives an overview of sensible, latent and thermochemical TES processes using salts.

Table 1: Overview of salt application.

Temp. level	Salt type	TES type
<0 °C	Water–salt mixtures	PCM slurry
0–100 °C	Melting of salt hydrates in crystallization water	PCM
40–300 °C	Dehydration of salt hydrates	TCS
40–150 °C	Absorption in concentrated salt solutions	TCS
120–500 °C	Solid–liquid conversion in anhydrous salts	PCM
100–800 °C	Anhydrous molten salts	Sensible
100–800 °C	Anhydrous solid salts	Sensible
100–800 °C	Solid–solid conversion in anhydrous salts	PCM

The focus of this chapter is on salts in sensible and latent heat storage systems. Salt systems differ by important properties such as melting temperature and thermal stability which define the lower and upper limits of usable temperature in sensible heat storage systems. In latent storage systems the melting temperature defines the temperature at which the heat is stored. In thermal power plants the stored heat can be used to generate steam which drives turbines to produce electricity. Because the heat is generated at a specific and constant temperature and because of the temperature dependent water to steam transition the pressure of the steam can be adjusted to a level which is required by the turbine. Besides the melting temperature another important parameter for PCM applications is the melting enthalpy H (e.g., $kJ \cdot kg^{-1}$) which in addition to the material costs (e.g., $€ \cdot kg^{-1}$) determine the specific material investment costs (e.g., $€ \cdot kW^{-1} \cdot h^{-1}$). In case of sensible heat storage the specific material investment costs (e.g., $€ \cdot kW^{-1} \cdot h^{-1}$) are defined by the material costs, the heat capacity c_p and the usable temperature range. The size of the sensible heat storage system is given by the product of the heat capacity and the density. The thermochemical properties depend on the ion system used. What concerns the anions the most important ions are nitrates, nitrate/nitrite mixtures, carbonates, chlorides, fluorides and carbonates. The cationic part of state of the art fluids usually consists of alkali/alkaline earth elements. The remainder of this chapter considers the respective materials more into detail.

Sensible energy storage in anhydrous molten salts/nitrates

For sensible heat storage at elevated temperatures ($T > 100$ °C) molten salts are most suitable. Advantages of molten salts are the high thermal stability, relatively low material costs, high heat capacity, high density, non-flammability and low vapor pressure. Due to the low vapor pressure pressurized vessels are not required.

Compared to organic heat transfer fluids the melting point of molten salts is higher. Thus one major challenge with molten salts is to avoid freezing during operation. Hence, typically auxiliary heating systems or the development of salt formulations with low melting temperatures are required. A novel method to identify the composition of salt mixtures featuring a decreased melting temperature is presented at the end of this section.

Additionally limitations of molten salt storage may arise due to storage media costs, the risk of corrosion and the difficulty in hygroscopic salt handling.

For sensible heat storage in solar power plants, a non-eutectic molten salt mixture consisting of 60 wt % sodium nitrate ($NaNO_3$) and 40 wt % potassium nitrate (KNO_3) is used. This mixture is usually known as "Solar Salt". Due to the increased amount of $NaNO_3$ as compared to the eutectic mixture the material costs can be reduced. The non-eutectic mixture has a liquidus temperature of about 240 °C and the temperature limit of thermal stability is about 550 °C. For applications at higher temperatures salts with other anions, such as carbonates, chlorides and fluorides might be potential candidates. However experience with oxyanion salts and halogen salts is currently limited to theoretical studies [1,2].

Physico-chemical properties: thermal properties

Characterization of thermal energy storage in molten salts requires data of salt properties in the liquid phase. For sensible storage media the storage capacity is directly proportional to the heat capacity which therefore is an essential parameter. Several data exist which are summarized in the following. The data show that the heat capacity is slightly increasing with temperature (see Figure 2).

Concerning the thermal conductivity several data exist which are not consistent and therefore rather give a rough idea, as shown in Figure 3. Even though the data differ in the different publications the measurements show that the thermal conductivity increases with temperature. More precise data require additional experiments.

As to the density there are consistent data from the literature in the liquid range. Also the density of multicomponent nitrate mixtures consisting of $Ca(NO_3)_2$, KNO_3, $LiNO_3$ and $NaNO_3$ has been investigated [15]. It was shown that the temperature dependent molar volume can be estimated by a linear volumetric additivity rule based on the values of the individual constituents. However, only one literature source could be identified for the density in the solid range (Figure 4). Because accurate information of the salt property behavior in the solid-

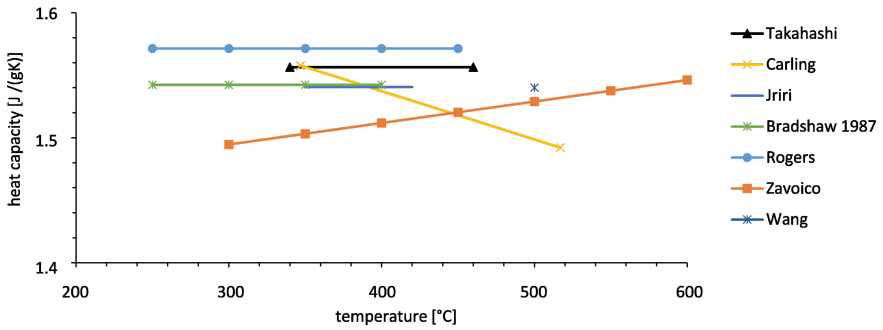

Figure 2: Heat capacity of Solar Salt in the liquid phase [3-9].

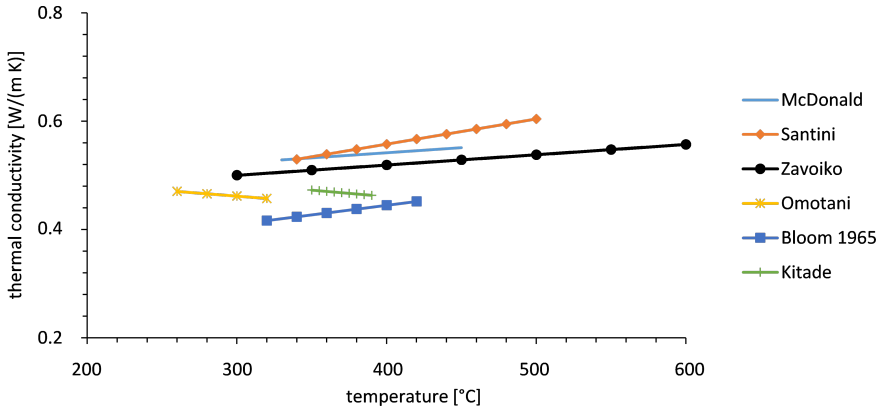

Figure 3: Thermal conductivity of Solar Salt reported by several groups [8,10-14].

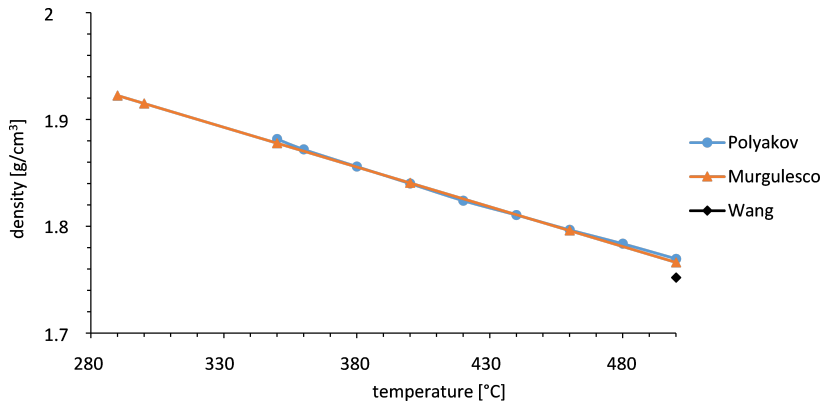

Figure 4: Density of Solar Salt in the liquid state [9,16,17].

phase is necessary for recovery processes from a freeze event, the density of solid salt needs to be investigated further.

The viscosity is an important property for sensible storage media used in heat transfer applications with molten salt pumping. Figure 5 shows that the viscosity in the liquid range at 500 °C is in the same order of magnitude as the viscosity of water at ambient temperature.

Physico-chemical properties: thermal decomposition

The thermal decomposition of nitrate salts is a complex process which is dependent on the conditions, such as the cation composition, atmosphere, temperature and pressure. The cations have a significant effect on the thermal stability as their polarization power differs strongly. With increasing polarization power the distortion in the electron distribution in the anion is increased and thereby the stability of the salt is decreased [20]. Because the polarization power increases with the charge of the cation, the thermal stability decreases with the groups (columns) in the periodic table. Within one group the charge stays constant. Still the polarization power changes within one group because the second parameter affecting the polarization power is the radius. The higher the radius the lower is the polarization power. Because the radius is increasing with the period (rows) of the periodic table the stability increases within the group of the periodic table.

Thermal stabilities can be described by the temperature dependent equilibrium constant of decomposition reactions. Temperature dependent values are given for nitrates by Stern [21]:

$$2MNO_3 = M_2O + 2NO_{2(g)} + \frac{1}{2}O_{2(g)}$$

M: alkali metal cation

$$M(NO_3)_2 = MO + 2NO_{2(g)} + \frac{1}{2}O_{2(g)}$$

M: alkaline earth metal cation

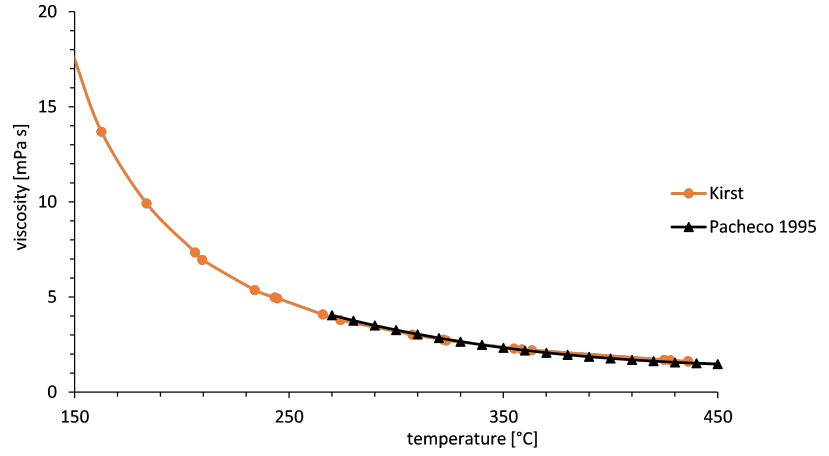

Figure 5: Viscosity of Solar Salt [18,19].

Figure 6 shows the temperature dependent equilibrium constant K. For a value of $K \leq 10^{-25}$ the concentrations of the decomposition products are very low. Hence the salt can be considered stable.

Figure 7 shows the decomposition with an equilibrium constant of $K = 1 \times 10^{-25}$ [21] versus the position of the elements in the periodic table (periods and the two groups alkali earth and alkaline earth metals). It can be shown that with increasing period in the periodic table the stability is increasing. The figure also shows that with increasing groups/charge of the cation the stability is decreasing. This is the reason why salts from groups > 2 are less suitable for heat storage application.

Development of new salt formulations with low melting point

The application of the state of the art sensible storage material "Solar Salt" is limited to processes with a lower operating temperature of 270 °C approximately. In particular parabolic through plants with molten salt as a heat transfer fluid in the solar field require mixtures with lower melting temperatures to avoid salt freezing and to simplify the solar field operation. Therefore salt formulations need to be developed with a reduced melting temperature. A new method has been presented by the authors in another article to develop new salt formulations [22] which is summarized in this section. Whereas compositions with low melting temperature have been identified by time consuming high-throughput experiments previously, the alternative method significantly reduces the number of experiments to identify the compositions of minimum melting mixtures.

The principle of the method is that the liquidus temperature of salts can be reduced by an increased number of ions. In other words, multicomponent salt mixtures can have lower liquidus temperatures as compared to simple binary or ternary salt systems. The liquid to solid phase transition of multicomponent salt mixtures is most conveniently obtained by inspection of the liquidus temperature in phase diagrams. The determination of phase diagrams however gets more challenging the more ionic species the salt mixture contains. Therefore the innovative method was developed to find salts with lower melting temperature without the need to fully determine phase diagrams. The method is based on liquid phase formation which is known from several processes: Eutectic bonding is a method to combine surfaces by eutectic alloy formation which occurs upon heating above the eutectic temperature. Similarly liquid phase sintering (LPS) is used in the field of high-temperature ceramics and

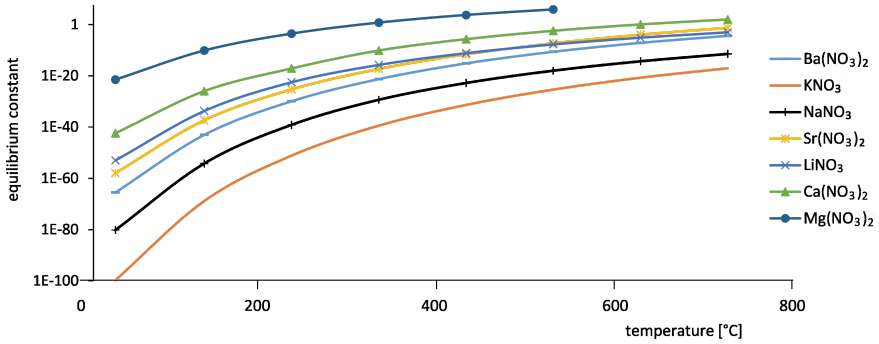

Figure 6: Temperature dependent equilibrium constant for alkali metal nitrates and alkaline metal nitrates.

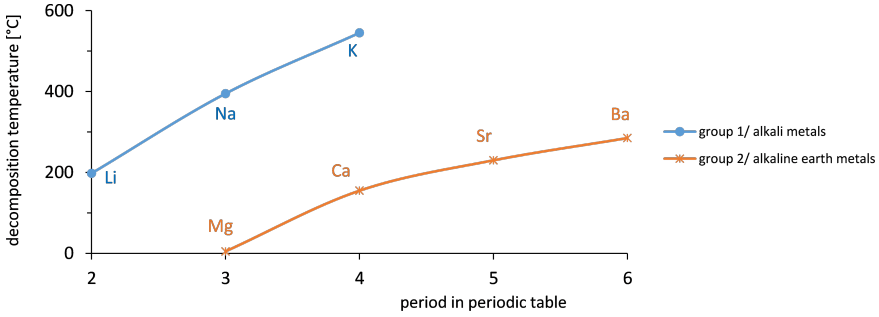

Figure 7: Relative decomposition temperature of nitrate vs position in the periodic table.

metals. The innovative salt synthesis approach described in this section utilizes the liquid phase formation at the contact surface of different solid salts upon heating. The contact layer contains the eutectic composition. Figure 8 and Figure 9 illustrate the innovative salt synthesis approach.

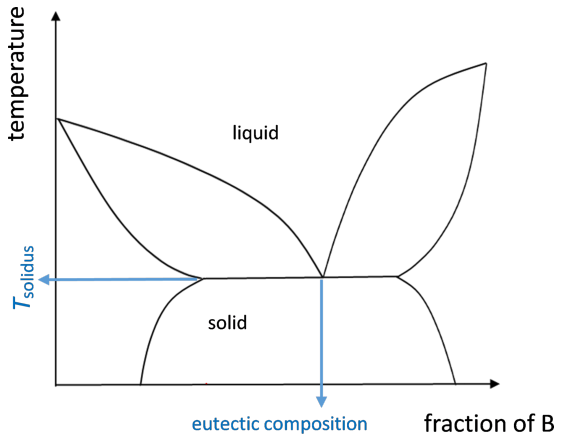

Figure 8: Scheme of phase diagram with eutectic mixture.

A salt mixture of arbitrary non eutectic composition (for example $X_{non\text{-}eu}$) is slowly heated above the solidus temperature $T_{solidus}$. A measurement system detects the liquid phase above $T_{solidus}$. The scheme of the phase diagram in Figure 8 shows that the molten salt composition is mainly the eutectic composition X_{eu} at the temperature T_{max}. Following the detection of the liquid phase it is extracted via a filter and a valve. To find the composition of the salt system with reduced melting temperature, the extracted phase can be analyzed in terms of composition by analytical standard methods.

Sensible energy storage in the liquid state with solid filler materials

The nitrate salts discussed in the previous sections are state of the art materials for the two tank concept. In the two tank concept two containers exist, referred to as “hot tank” and as “cold tank”. The heat is stored when pumping cold salt from the “cold tank” via a heat exchanger - providing heat by a heat transfer fluid - into the “hot tank”. The heat is recovered by the heat transfer fluid when hot salt is pumped from the “hot tank” to the “cold tank” via the heat exchanger. A drawback of this concept is the costs for the two tanks. In order to reduce the costs a lot of research was performed to find alternative storage concepts using other storage materials like concrete [23] or using a single-tank molten salt concept [24]. The single-tank molten salt concept provides a single storage tank by using the different densities of the cold and hot molten salt caused by the thermal gradient. Additionally cost reductions can result from partially replacing the molten salt storage material by low-cost filler material. This thermocline concept is described by [24]. Filler materials need to meet the following criteria:

- Inexpensive and widely available
- High heat capacity
- Low void fraction
- Compatibility with the heat storage materials such as nitrate salts
- Non-hazardous

A thermocline system with low-cost materials has the potential to reduce costs as compared to a two-tank molten salt storage system. The material selection of the filler material was supported by a geologist and a nitrate salt expert. Various natural stones were tested in Hitec XL® (43 wt % KNO_3 + 42 wt % $Ca(NO_3)_2$ + 15 wt % $NaNO_3$) and in Solar Salt (60 wt % $NaNO_3$ + 40 wt % KNO_3) with a maximum temperature of 400 °C and maximum exposure duration of 1000 h in Hitec XL® or 400 h in Solar Salt. The filler materials quartzite rocks and silica filter sand did not show any decomposition after 500 thermal cycles. Another advantage is the high availability.

The investigations were continued by Brosseau [25]. They focused on quartzite rock. Isothermal tests with a test-duration of one year were realized at temperatures of 450 and 500 °C.

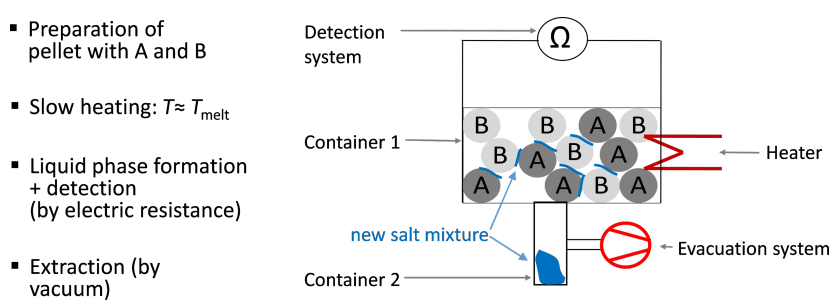

Figure 9: Schematic of the novel experimental method and apparatus to synthesize new salt mixtures.

Additionally, 10 000 thermal cycles in the temperature range between 285 to 450 °C were performed. The heat transfer medium Hitec XL® was used. The material tests of the quartzite rocks as well as sand were successful, apart from the observed calcium carbonate crust formation in the high temperature tests. Implementations in commercial-scale solar power plants do not exist so far because of concerns due to the calcium carbonate crust formation and its treatment in a large scale thermal storage unit.

The stability of the filler material is influenced by the molten salt (Solar Salt, HITEC XL®, etc.) and by the maximum operation temperature. In the recent years, material investigations were performed to reduce costs of the one-tank thermocline concept further by using filler materials with very low costs or improved material properties such as a higher heat capacity. One optional filler material is a very inexpensive material called Cofalit®. Cofalit® is manufactured by the INERTAM Company in France and is produced by high-temperature plasma treatment (1500 °C) of asbestos-containing waste called ACW. Cofalit® is a calcium magnesium iron alumina-silicate [26]. The thermophysical properties meet the required criteria of potential filler materials. It has a density of 3120 $kg \cdot m^{-3}$ and a specific heat capacity of 0.86 $kJ \cdot kg^{-1} \cdot K^{-1}$. The heat conductivity is relatively low with a value of 2.7 $W \cdot m^{-1} \cdot K^{-1}$. The compatibility of Cofalit® with Solar Salt and Hitec XL has been investigated by Calvet [26]. The maximum operation temperature of the isothermal test was 500 °C during a test duration of 500 h. In Solar Salt the Cofalit® ceramic is stable at the chosen steady state conditions. However its compatibility still requires investigations at dynamic thermo-chemical conditions. In the heat transfer medium HITEC XL, a thin layer consisting of calcium silicate was formed on the surface of the Cofalit® ceramic.

Ortega [27] investigated another industrial waste product as potential filler material in hot air, synthetic oil and molten salt: Two electric arc furnace slags from two different steel manufactures in Spain. The slags are in direct contact with the Solar Salt for 500 h and a maximum operation temperature of 500 °C. No contamination of the molten salt or interaction layers between slag and salt were observed after the thermal treatment [27]. Disadvantages of the industrial waste as filler material are the uncertain availability in future as well as the toxicity and environmental compatibility.

Grirate [28] did investigate granite, basalt, quartzite, marble and hornfels from Morocco. The natural stones were analysed in terms of form, colour, grain size, hardness as well as the presence of carbonate elements. Additionally, physical properties (porosity, density, compressive strength, heat capacity) and the thermal stability up to 400 °C in an air atmosphere have been determined. Quartzite was chosen as the most suitable filler material because of its high thermal conductivity (caused by the high percentage of the mineral quartz) and the high compressive strength and hardness.

Similar investigations of natural stones have been performed by Martin [29]. Basalt, diabas and quartzite were chosen as potential filler materials due to their high density and compressive strength. Initially, the thermal stability up to 900 °C in air and the presence of carbonate elements, using hydrochloric acid, have been determined. Additionally basalt and quartzite were investigated in Solar Salt at isothermal and cyclic conditions up to 560 °C with a maximum operation duration of 1000 h. Furthermore the specific heat capacity of basalt and quartzite was determined. Visual inspection of both basalt and quartzite showed that they are compatible with Solar Salt at high temperatures. The stability was confirmed by thermogravimetry analysis. Further analyses of the mineral content before and after the thermo-chemical oven test and thermal test in Solar Salt with higher test duration are necessary [29].

Latent heat storage in nitrates

In case of latent energy storage another thermal property needs to be considered, the thermal conductivity k. This property gets important because no common heat exchanger can be utilized to assist with the heat transfer. Additionally the density and the enthalpy at the phase transition are important because they determine the volumetric storage capacity. At the phase transition – which occurs within a temperature range of approximately 10 K or less – the change of enthalpy per temperature $(\partial H/\partial T)_p$ increases considerably.

Therefore the energy stored within a limited temperature range of 10 K is increased by approximately more than one order of a magnitude in phase change materials compared to sensible storage materials. For example a phase transition taking place within 10 K with a melting enthalpy of 150 $kJ \cdot kg^{-1}$ requires a heat capacity of 15 $kJ \cdot kg^{-1} \cdot K^{-1}$ to result in an equal storage capacity per 10 K. For KNO_3 the melting enthalpy was measured to be ≈100 $kJ \cdot kg^{-1}$ [3].

For the calculation of the volumetric storage capacity the density has to be known as well. In Figure 10 the density of $NaNO_3$ is plotted versus the temperature.

As was discussed above the thermal conductivity is an important parameter. Therefore consistent data are required. However there is a lack of consistent data for the thermal conductivity as is shown in Figure 11. Further investigations need to be performed to clarify the discrepancy of the values.

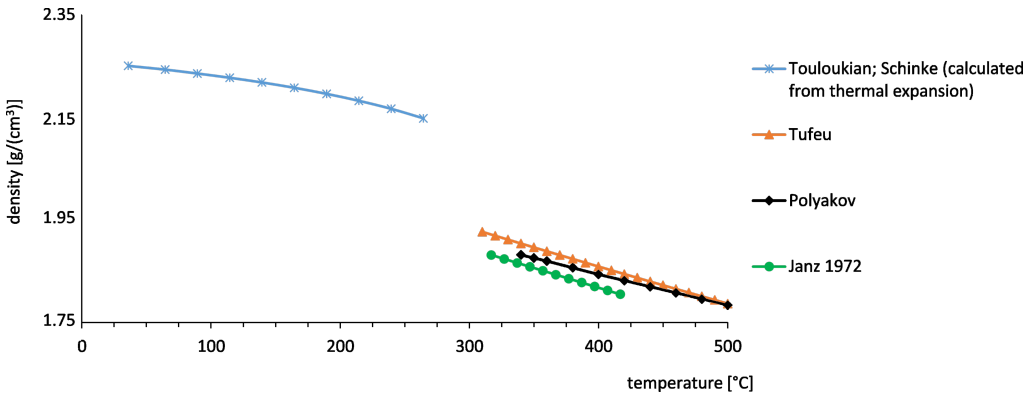

Figure 10: Density of $NaNO_3$ [16,30-32].

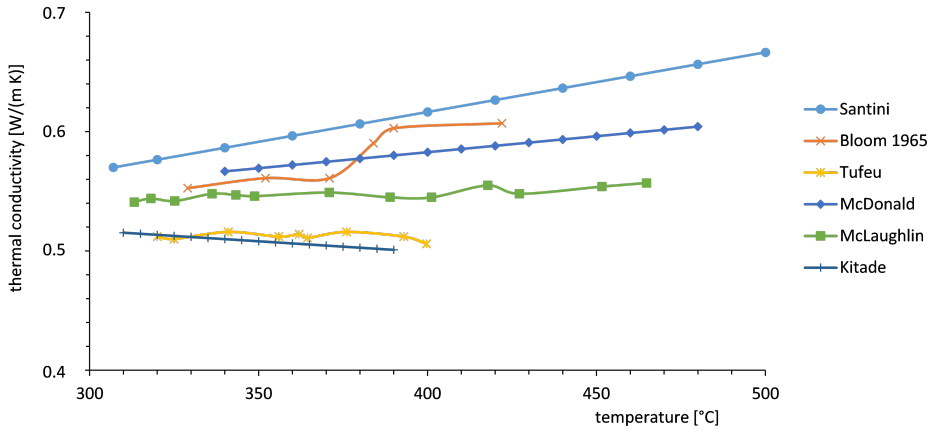

Figure 11: Thermal conductivity of $NaNO_3$ in the liquid range [10,11,13,14,31,33].

Combination of PCMs with sensible heat storage for effective heat capacity enhancement

Common storage systems are sensible materials or phase change materials. Some research has been performed on the combination of several phase change materials which can result in a sensible storage type system with enhanced effective heat capacity as will be discussed more into detail in the following section.

Sensible storage materials are characterized by the specific heat capacity. The amount of stored sensible heat in storage materials is correlated with the temperature range used and with the specific heat capacity of the storage material. An improved heat storage material could additionally use the enthalpy of fusion of the storage material in order to realize higher effective specific heat capacities. The advantage of combined specific heat capacity of the material and enthalpy of fusion of the phase change process is a higher energy density. A possibility to realise that purpose is the application of serially connected phase change materials with various melting temperatures. Alternatively phase change materials with a melting range as opposed to a melting point can be used.

Storage materials with melting range can be salt mixtures or alloys. At temperatures below the phase transition solid components are in equilibrium. During the storage process the ratio of molten to solid state increases as well as the temperature. This technique therefore combines sensible and latent heat storage. Figure 12 illustrates the phase diagram of a common salt mixture (KNO_3 + $NaNO_3$) and the temperature characteristic during the charging process for the salt mixture with 30 wt % potassium nitrate and 70 wt % sodium nitrate.

The temperature of the storage material increases during the charging process, which is characteristic for sensible storage

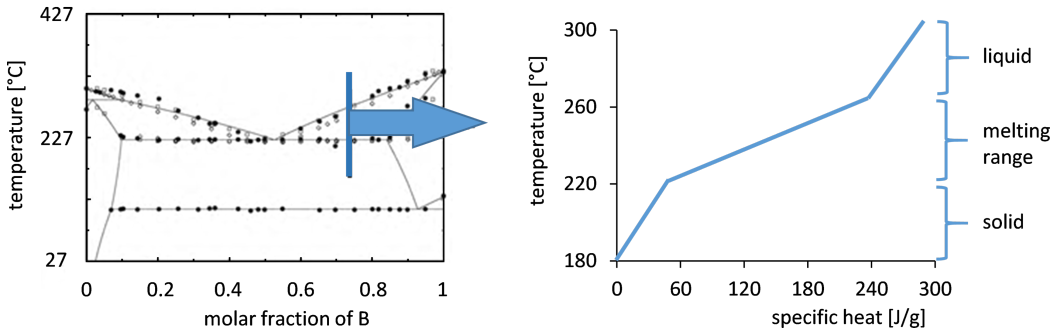

Figure 12: Phase diagram of KNO_3–$NaNO_3$ [34] and the phase dependent enthalpy increase during thermal charging of the selected salt mixture (30 wt % KNO_3 + 70 wt % $NaNO_3$).

materials. The stored heat is used for both melting and heating of the salt. Hence the temperature rise is lower than by a sensible storage material with the same specific heat capacity. The reason is that the effective specific heat capacity of the salt mixture with a melting range is considerably higher as compared to the common molten salt mixtures. The effective average specific heat capacity in the melting range $c_{p,eff}$ consists of two terms: the specific heat capacity c_p in the melting range and the ratio of the melting enthalpy h and temperature range T of the melting range:

$$c_{p,eff} = \frac{h_{melting}}{T_{melting\ range}} + c_{p,melting\ range}.$$

The implementation of salt mixtures with melting range in effective processes requires the uniform distribution of the enthalpy of fusion in the melting range which is influenced by the miscibility of the salt mixture in the solid state [35]. Binary salt mixtures can be also classified on the basis of its miscibility in the solid state. In the liquid state most salt mixtures are completely miscible [36]. Various types of binary phase diagrams do exist [36,37]:

- Complete miscibility in the liquid and solid state with or without minimum melting point (continuous solid solution)
- Complete miscibility in the liquid state and insolubility in the solid state (simple eutectic system)
- Complete miscibility in the liquid state and partial miscibility in the solid state
  a) Segregation by eutectic reaction (eutectic system with limited solid solubility)
  b) Segregation by peritectic reaction
- System with intermetallic phases
  a) Congruently melting compounds
  b) Incongruently melting compounds

Based on the data of Martin [35,38], binary mixtures with complete and partial miscibility in the solid state are suitable as heat storage material with a melting range. Peritectic reactions are diffusion-controlled, so that the reaction can be inhibited by fast heating or cooling rates. As a result of the inhibited peritectic reaction, the composition of the solid salt and the melting characteristic can change.

In the studies of the mixture of 30 wt % potassium nitrate (KNO_3) and 70 wt % sodium nitrate ($NaNO_3$) the investigations focused on the distribution of the enthalpy of fusion as shown in Figure 13. The salt mixture has an enthalpy of fusion of 120 $kJ \cdot kg^{-1}$ that is distributed uniformly in a melting range from about 222 to 260 °C.

In the lab-scale storage unit an effective specific heat capacity of about 3 $kJ \cdot kg^{-1} \cdot K^{-1}$ can be achieved. Thus the specific heat capacity of the salt mixture is doubled at least by using a salt mixture with melting range. Thus the use of salt mixtures with a melting range is an interesting option to increase the thermal energy density of sensible storage materials.

Conclusion

This chapter presented various types of thermal energy storage materials and concepts. At the time of writing, in the field of concentrated power applications (CSP), molten nitrate salts (predominantly a mixture of 60 wt % $NaNO_3$ and 40% KNO_3, so called “Solar Salt”) are used exclusively. Concerning the thermal properties of these salts, reliable data of single salts are available. However, salt mixtures consisting of ions different from sodium and potassium have to be investigated further in the future. Those multicomponent salt mixtures feature much lower melting points compared to Solar Salt and could be attractive materials for direct thermal energy storage for CSP applications.

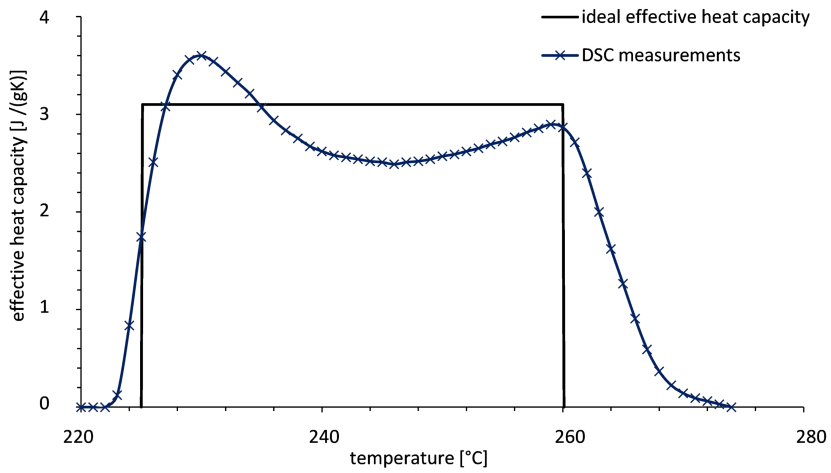

Figure 13: Specific enthalpy of fusion for the salt mixture KNO_3–$NaNO_3$ [35,38].

With regard to the thermal decomposition, the investigation is complex. Many factors influence decomposition reactions, such as the type of the salt, the temperature and the gas phase composition. There is still a need to examine thermal decomposition processes of nitrate salts.

Research also has been performed on storage materials with a melting range with the aim to increase the effective average specific heat capacity. The concept was demonstrated with a mixture of 30 wt % KNO_3 and 70 wt % $NaNO_3$. However there is still a need to examine the handling of the salt and the cyclic stability.

In order to reduce costs of sensible energy storage materials, molten salts are partially replaced by filler materials. It was shown that concrete and mortars experienced softening when thermally cycled in molten salts and therefore are less suitable. In contrast, basalt and quartzite look promising from the first experiments, but long-term stability measurements are still required.

Acknowledgements

We express our thanks especially to Ulrike Kröner and Markus Braun for the experimental molten salt work.

References

1. Forsberg, C. W.; Peterson, P. F.; Zhao, H. *J. Sol. Energy Eng.* **2006,** *129,* 141–146. doi:10.1115/1.2710245
2. Singer, C.; Buck, R.; Pitz-Paal, R.; Müller-Steinhagen, H. *J. Sol. Energy Eng.* **2010,** *132,* 041010. doi:10.1115/1.4002137
3. Takahashi, Y.; Sakamoto, R.; Kamimoto, M. *Int. J. Thermophys.* **1988,** *9,* 1081–1090. doi:10.1007/BF01133275
4. Carling, R. W. *Thermochim. Acta* **1983,** *60,* 265–275. doi:10.1016/0040-6031(83)80248-2
5. Jriri, T.; Rogez, J.; Bergman, C.; Mathieu, J. C. *Thermochim. Acta* **1995,** *266,* 147–161. doi:10.1016/0040-6031(95)02337-2
6. Bradshaw, R. W.; Carling, R. W. A review of the chemical and physical properties of molten alkali nitrate salts and their effect on materials used for solar central receivers. *Report SAND87-8005;* Sandia National Laboratories: Albuquerque, New Mexico, U.S.A., 1987.
7. Rogers, D. J.; Janz, G. J. *J. Chem. Eng. Data* **1982,** *27,* 424–428. doi:10.1021/je00030a017
8. Zavoiko, A. B. Solar Power Tower. *Report SAND2001-2100;* Sandia National Laboratories: Albuquerque, New Mexico, U.S.A., 2001.
9. Wang, T.; Mantha, D.; Reddy, R. G. *Appl. Energy* **2013,** *102,* 1422–1429. doi:10.1016/j.apenergy.2012.09.001
10. McDonald, J.; Davis, H. T. *J. Phys. Chem.* **1970,** *74,* 725–730. doi:10.1021/j100699a007
11. Santini, R.; Tadrist, L.; Pantaloni, J.; Cerisier, P. *Int. J. Heat Mass Transfer* **1984,** *27,* 623–626. doi:10.1016/0017-9310(84)90034-6
12. Omotani, T.; Nagasaka, Y.; Nagashima, A. *Int. J. Thermophys.* **1982,** *3,* 17–26. doi:10.1007/BF00503955
13. Bloom, H.; Doroszkowski, A.; Tricklebank, S. B. *Aust. J. Chem.* **1965,** *18,* 1171–1176. doi:10.1071/CH9651171
14. Kitade, S.; Kobayashi, Y.; Nagasaka, Y.; Nagashima, A. *High Temp. - High Pressures* **1989,** *21,* 219–224.
15. Bradshaw, R. W. Effect of Composition on the Density of Multi-Component Molten Nitrate Salts. *Report SAND2009-8221;* Sandia National Laboratories: Albuquerque, New Mexico, U.S.A., 2009; Vol. 2009.
16. Polyakov, V. D.; Beruli, V. D. *Izv. Sekt. Fiz.-Khim. Anal., Inst. Obshch. Neorg. Khim., Akad. Nauk SS SR* **1955,** *26,* 164–172.
17. Murgulescu, I. G.; Zuca, S. *Electrochim. Acta* **1969,** *14,* 519–526. doi:10.1016/0013-4686(69)87037-4
18. Kirst, W. E.; Nagle, W. M.; Castner, J. B. *Trans. Am. Inst. Chem. Eng.* **1940,** *36,* 371–390.
19. Pacheco, J. E.; Ralph, M. E.; Chavez, J. M.; Dunkin, S. R.; Rush, E. E.; Ghanbari, C. M.; Matthews, M. W. Results of molten salt panel and component experiments for solar central receivers: cold fill, freeze/thaw, thermal cycling and shock, and instrumentation tests. *Report SAND-94-2525;* Sandia National Laboratories: Albuquerque, New Mexico, U.S.A., 1995.

20. Addison, C. C.; Logan, N. *Adv. Inorg. Chem. Radiochem.* **1964,** *6,* 71–142. doi:10.1016/s0065-2792(08)60225-3
21. Stern, H. K. *High Temperature Properties and Thermal Decomposition of Inorganic Salts with Oxyanions;* CRC Press: Boca Raton, FL, U.S.A., 2001.
22. Bauer, T.; Braun, M.; Eck, M.; Pfleger, N.; Laing, D. Development of salt formulations with low melting temperatures. 18th SolarPaces Conference, Marrakech, Morocco, Sept 11–14, 2012; .
23. Laing, D.; Bahl, C.; Bauer, T.; Fiß, M.; Breidenbach, N.; Hempel, M. *Proc. IEEE* **2012,** *100,* 516–524. doi:10.1109/jproc.2011.2154290
24. Pacheco, J. E.; Showalter, S. K.; Kolb, W. J. *J. Sol. Energy Eng.* **2002,** *124,* 153–159. doi:10.1115/1.1464123
25. Brosseau, D. A.; Hlava, P. F.; Kelly, M. J. Testing Thermocline Filler materials and Molten-Salt Heat transfer Fluid for Thermal Energy Storage Systems Used in Parabolic Trough Solar Power Plants. Sandia National Laboratories: Albuquerque, New Mexico, U.S.A., 2004.
26. Calvet, N.; Gomez, J. C.; Faik, A.; Roddatis, V. V.; Meffre, A.; Glatzmaier, G. C.; Doppiu, S.; Py, X. *Appl. Energy* **2013,** *109,* 387–393. doi:10.1016/j.apenergy.2012.12.078
27. Ortega, I.; Rodriguez-Aseguinolaza, J.; Gil, A.; Faik, A.; D'Aguanno, B. New Thermal Energy Storage Materials from Industrial Wastes: Compatibility of Steel Slags with the most common Heat transfer Fluids. In *Proceddings of the ASME 2014 8th International Conference on Energy Sustainability,* Boston, MA, U.S.A.; .
28. Grirate, H.; Zari, N.; Elamrani, I.; Couturier, R.; Elmchaouri, A.; Belcadi, S.; Tochon, P. *Energy Procedia* **2014,** *49,* 810–819. doi:10.1016/j.egypro.2014.03.088
29. Martin, C.; Breidenbach, N.; Eck, M. Screening and Analysis of Potential Filler Material for Molten Salt Thermocline Storages. In *Proceedings of the ASME 2014 8th International Conference on Energy Sustainability,* Boston, MA, U.S.A., June 30–July 2, 2014; The American Society of Mechanical Engineers: New York, NY, U.S.A., 2014; V001T02A025. doi:10.1115/es2014-6493
30. Touloukian, Y. S.; Kirby, R. K.; Taylor, E. R.; Lee, T. Y. R. Thermal Expansion - Nonmetallic Solids. In *Thermophysical Properties of Matter;* Touloukian, Y. S., Ed.; The TRPC Data Series, Vol. 13; New York, NY, U.S.A.; pp 1–1689.
31. Tufeu, R.; Petitet, J. P.; Denielou, L.; Le Neindre, B. *Int. J. Thermophys.* **1985,** *6,* 315–330. doi:10.1007/BF00500266
32. Janz, G. J.; Krebs, U.; Siegenthaler, H. F.; Tomkins, R. P. T. *J. Phys. Chem. Ref. Data* **1972,** *1,* 581–746. doi:10.1063/1.3253103
33. McLaughlin, E. *Chem. Rev.* **1964,** *64,* 389–428. doi:10.1021/cr60230a003
34. Beneš, O.; Konings, R. J. M.; Wurzer, S.; Sierig, M.; Dockendorf, A. *Thermochim. Acta* **2010,** *509,* 62–66. doi:10.1016/j.tca.2010.06.003
35. Martin, C. Schmelzbereichsspeicher für die Speicherung sensibler Wärme hoher Temperaturen. Ph.D. Thesis, Universität Stuttgart, Stuttgart, Germany, 2014.
36. Bloom, H. *The Chemistry of molten salts;* W. A. Benjamin Inc.: New York, NY, U.S.A., 1967.
37. Worch, H.; Pompe, W.; Schatt, W. *Werkstoffwissenschaften;* Wiley-VCH: Berlin, Germany, 2011.
38. Martin, C.; Bauer, T.; Müller-Steinhagen, H. *Appl. Therm. Eng.* **2013,** *56,* 159–166. doi:10.1016/j.applthermaleng.2013.03.008

License and Terms

The definitive version of this article is the electronic one which can be found at:
doi:10.3762/bjnano.6.154

BEILSTEIN JOURNAL OF NANOTECHNOLOGY

Metal hydrides: an innovative and challenging conversion reaction anode for lithium-ion batteries

Luc Aymard*[1,§], Yassine Oumellal[2] and Jean-Pierre Bonnet[1]

Review

Open Access

Address:
[1]Laboratoire de Réactivité et Chimie des Solides - LRCS, UMR CNRS-UPJV 7314, 33 rue Saint-Leu, 80039 Amiens, France and [2]Institut de Chimie et des Matériaux Paris-Est - ICMPE, UMR CNRS-UPEC 7182, 2-8 Rue Henri Dunant, 94320 Thiais, France

Email:
Luc Aymard* - luc.aymard@u-picardie.fr

* Corresponding author
§ Tel.: +33 3 22 82 75 74

Keywords:
conversion reaction; lithium-ion batteries; metal hydrides

Beilstein J. Nanotechnol. **2015,** *6,* 1821–1839.
doi:10.3762/bjnano.6.186

Received: 10 October 2014
Accepted: 07 August 2015
Published: 31 August 2015

This article is part of the Thematic Series "Materials for sustainable energy production, storage, and conversion".

Guest Editor: M. Fichtner

Abstract

The state of the art of conversion reactions of metal hydrides (MH) with lithium is presented and discussed in this review with regard to the use of these hydrides as anode materials for lithium-ion batteries. A focus on the gravimetric and volumetric storage capacities for different examples from binary, ternary and complex hydrides is presented, with a comparison between thermodynamic prediction and experimental results. MgH_2 constitutes one of the most attractive metal hydrides with a reversible capacity of 1480 $mA{\cdot}h{\cdot}g^{-1}$ at a suitable potential (0.5 V vs Li^+/Li^0) and the lowest electrode polarization (<0.2 V) for conversion materials. Conversion process reaction mechanisms with lithium are subsequently detailed for MgH_2, TiH_2, complex hydrides Mg_2MH_x and other Mg-based hydrides. The reversible conversion reaction mechanism of MgH_2, which is lithium-controlled, can be extended to others hydrides as: $MH_x + xLi^+ + xe^-$ in equilibrium with $M + xLiH$. Other reaction paths—involving solid solutions, metastable distorted phases, and phases with low hydrogen content—were recently reported for TiH_2 and Mg_2FeH_6, Mg_2CoH_5 and Mg_2NiH_4. The importance of fundamental aspects to overcome technological difficulties is discussed with a focus on conversion reaction limitations in the case of MgH_2. The influence of MgH_2 particle size, mechanical grinding, hydrogen sorption cycles, grinding with carbon, reactive milling under hydrogen, and metal and catalyst addition to the MgH_2/carbon composite on kinetics improvement and reversibility is presented. Drastic technological improvement in order to the enhance conversion process efficiencies is needed for practical applications. The main goals are minimizing the impact of electrode volume variation during lithium extraction and overcoming the poor electronic conductivity of LiH. To use polymer binders to improve the cycle life of the hydride-based electrode and to synthesize nanoscale composite hydride can be helpful to address these drawbacks. The development of high-capacity hydride anodes should be inspired by the emergent nano-research prospects which share the knowledge of both hydrogen-storage and lithium-anode communities.

Review

Introduction

To satisfy the continuously raising need for energy is now a key priority worldwide. The challenge is to obtain environmentally friendly renewable power sources with enhanced electrical energy conversion efficiency at moderate costs. However, these energy sources, such as windmill or solar cells, are intrinsically intermittent and, consequently, need to be associated with efficient energy storage devices in order to provide electricity on demand. With regard to this, lithium-ion (Li-ion) batteries can present an attractive solution, provided that they exhibit sufficient potential and gravimetric/volumetric capacities. Graphite, which is usually used as negative electrode with an intercalation reaction of lithium, is not suitable here due to its intrinsic insufficient specific capacities (370 A·h·kg^{-1}, 840 A·h·L^{-1}). To overcome these restrictions, new concepts for the negative electrode must be developed, i.e., the Li/graphite intercalation reaction needs to be replaced by either alloying or conversion reactions with lithium. Previously, metal oxides, nitrides, sulfides, phosphides and fluorides were successively investigated as conversion-reaction materials for the negative electrodes of Li-ion batteries [1-4]. In 2008, metal hydrides were proposed for this purpose [5]. Compared to other conversion compounds MgH_2 exhibits remarkable properties such as the lowest polarization value for conversion electrodes (less than 0.2 V) at an average potential of 0.5 V vs Li^+/Li^0 and a high reversible capacity (1480 mA·h·g^{-1} which is four times that of Li/C electrodes). All these properties make MgH_2 suitable as a material for negative electrodes. MgH_2 reacts with lithium ions in a reversible lithium-driven conversion reaction generating lithium hydride and magnesium metal: $MgH_2 + 2Li^+ + 2e^- \rightleftharpoons Mg + 2LiH$. Moreover, this conversion reaction is not restricted to MgH_2. It can also be carried out with several different binary and ternary hydrides. The general chemical reaction is then: $MH_x + xLi^+ + xe^- \rightleftharpoons M + xLiH$.

The purpose of this review is to describe the properties of these metal hydrides properties in the reaction vs Li^+/Li^0 (conversion reaction) with a focus on thermodynamics, involved reaction mechanisms, and some key issues to improve the performance of hydride-based electrodes.

I Conversion reaction of hydrides with lithium ions

I.1 Gravimetric and volumetric storage capacity of hydrides

Figure 1 shows both theoretical gravimetric and volumetric capacities of some binary and ternary hydrides. It can be noticed that the capacities of all hydrides are larger than that of graphite (370 A·h·kg^{-1}, 840 A·h·L^{-1}). Regarding ternary hydrides, the gravimetric capacities are between 340 A·h·kg^{-1} ($LaNi_4MnH_5$) and 750 A·h·kg^{-1} ($ZrV_2H_{4.9}$). The highest values are obtained with binary hydrides of light metals, namely 1074 A·h·kg^{-1} and 2038 A·h·kg^{-1} for TiH_2 and MgH_2, respectively. Volumetric capacities are above 2000 A·h·L^{-1} for all hydrides, for instance, 2298 A·h·L^{-1}, 2878 A·h·L^{-1}, 3815 A·h·L^{-1} for $LaNi_4MnH_5$, MgH_2 and TiH_2, respectively. Complex hydrides based on Mg follow this general trend of hydrides (i.e., capacities larger than graphite with Mg_2NiH_4: 963 A·h·kg^{-1}, 2822 A·h·L^{-1}; Mg_2CoH_5: 1191 A·h·kg^{-1}, 3200 A·h·L^{-1}; Mg_2FeH_6: 1456 A·h·kg^{-1}, 3995 A·h·L^{-1}). These large capacities render hydrides as good candidate material for negative electrodes in lithium-ion batteries for stationary as well as mobile applications for which the volumetric capacity plays a key role.

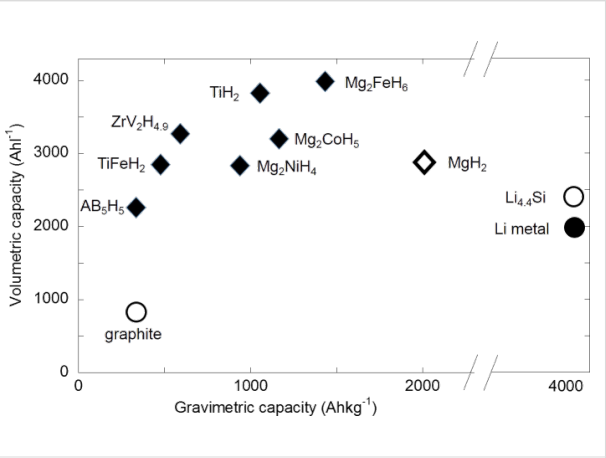

Figure 1: Gravimetric and theoretical volumetric capacities of metals and complex hydrides compared with those of graphite and other materials for negative electrodes. Reproduced with permission from [13]. Copyright 2013 Elsevier.

I.2 Thermodynamics of hydrides

After experimental results on the conversion reaction with MgH_2/Li [5,6] were reported, other systems that could be involved in the electrochemical conversion process were addressed from thermodynamic rules. The general reaction between hydride and lithium is given in Equation 3, where MH_x is the hydride, M the metal or the intermetallic phase, and x the number of hydrogen atoms. Under standard conditions (p = 1 atm and T = 298 K), the Gibbs free energy of the reaction in Equation 3, $\Delta_r G$ in kJ·mol^{-1}, can be calculated from the values of Gibbs free energy of formation of MH_x and LiH ($\Delta_f G°_{298}$(LiH) and $\Delta_f G°_{298}$(MH_x). It corresponds to the sum of reactions (Equation 1 + Equation 2) given as:

$$x\left(\mathrm{Li} + 1/2\,\mathrm{H_2} \rightarrow \mathrm{LiH}\right);\quad x\Delta_f G°_{298}\left(\mathrm{LiH}\right), \qquad (1)$$

$$MH_x \rightarrow M + x/2\,H_2;\quad -\Delta_f G°_{298}\left(MH_x\right), \tag{2}$$

$$MH_x + xLi \rightarrow M + xLiH;\quad \Delta_r G°_{298}. \tag{3}$$

The Gibbs free energy of the reaction in Equation 3 is:

$$\begin{aligned}\Delta_r G°_{298} &= \left[\Delta_f G°_{298}(M) + x\Delta_f G°_{298}(LiH)\right] \\ &\quad -\left[\Delta_f G°_{298}\left(MH_x\right) + x\Delta_f G°_{298}(Li)\right] \\ \Delta_r G_{298} &= \Delta_r G°_{298} \\ &= x\Delta_f G°_{298}(LiH) - \Delta_f G°_{298}\left(MH_x\right).\end{aligned}$$

According to the thermodynamics rules, the reaction is feasible for $\Delta_r G°_{298} \le 0$ and spontaneous for $\Delta_r G°_{298} < 0$.

Given the fact that the formation of LiH independent from the type of hydride MH_x (common reaction product), another simple criterion to predict the possibility of the conversion process is the Gibbs free energy of formation of the hydride MH_x divided by x. This value must be above that of LiH ($\Delta_f G°_{298}(MH_x)/x > \Delta_f G°_{298}(LiH)$). The knowledge of reaction Gibbs free energy allows for the evaluation of the electromotive force (emf) and of the equilibrium potential of the cell, E, by using the Nernst law: $\Delta_r G° = -x{\cdot}E{\cdot}F$ (F: Faraday constant, x: number of electrons involved in the reaction). The equilibrium potential of the cell is deduced from the half reaction (Equation 4 and Equation 5) and the sum reaction (Equation 6).

$$MH_x + xLi^+ + xe^- \rightarrow M^0 + xLiH;\quad \Delta G°_{I,298}\,, \tag{4}$$

$$xLi^0 \rightarrow xe^- + xLi^+;\quad \Delta G°_{II,298}\,, \tag{5}$$

$$MH_x + xLi^+ \rightarrow M^0 + xLiH;\quad \Delta G°_{III,298}\,. \tag{6}$$

Hess's law gives:

$$\Delta G°_{III,298} = \Delta G°_{I,298} + \Delta G°_{II,298},$$

$$\Delta G°_{I,298} = -xE°_0\left(MH_x/M^0, LiH\right)F,$$

$$\Delta G°_{II,298} = -xE°_0\left(Li^+/Li^0\right)F = 0,$$

the couple $\left(Li^+/Li^0\right)$ being used as reference,

$$\Delta G°_{III,298} = \Delta G°_{I,298} = \Delta_r G°_{298},$$

$$\Delta_r G°_{298} = -xEF = -xE°_0\left(MH_x/M^0, LiH\right)F,$$

$$E°_0\left(MH_x/M^0, LiH\right)F = -\Delta_r G°_{298}/xF.$$

With a lithium activity $a(Li) = 0$, and a lithium ion concentration $[Li^+] = 1$ M ($[Li^+]$ inside the electrolyte), the equilibrium potential of the cell (E_{eq}) is:

$$E_{eq}\left(MH_x/M^0, LiH\right) = E°_0\left(MH_x/M^0, LiH\right)$$

$$E_{eq}\left(MH_x/M^0, LiH\right) = -\Delta_r G°_{298}/xF.$$

This calculation was applied for different binary and ternary hydrides used to represent the different intermetallic families. The HSC database [7] and literature data [8] were used to obtain the $\Delta_f H$, $\Delta_f G$ and $\Delta_f S$ values.

I.2.1 Binary hydrides: Figure 2a shows the equilibrium potential of the MH_x/Li cell for different binary hydrides M = Y, La, Ba, Ca, Zr, Ti, Na, Cs, Mg. The potential versus Li^+/Li^0 is positive for Zr, Ti, Na, Cs and Mg and negative for Y, La, Ba and Ca hydrides. It can be clearly concluded from this figure that the conversion reaction is favorable, from a thermodynamics point of view, for Zr, Ti, Na, Cs and Mg hydrides and not possible for Y, La, Ba, Ca. The Gibbs free enthalpy of forma-

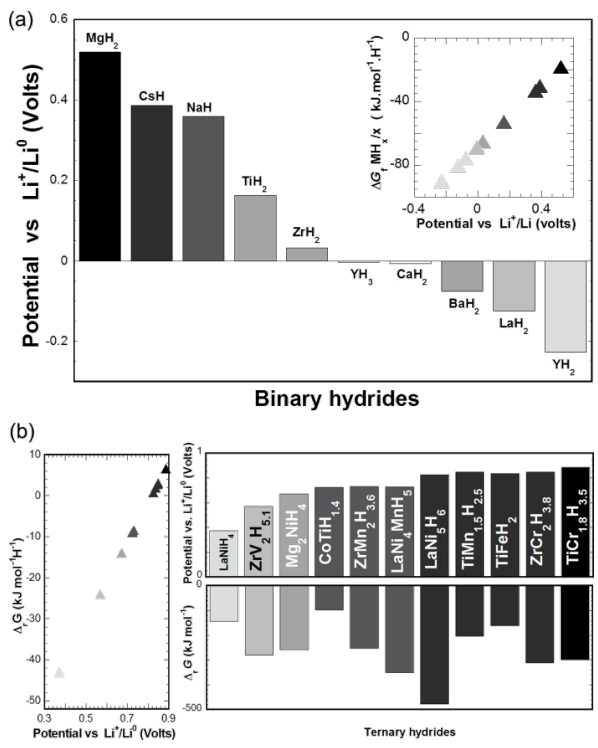

Figure 2: Theoretical equilibrium potential for the MH_x/Li cell vs Li^+/Li^0. a) For binary hydrides M = Y, La, Ba, Ca, Zr, Ti, Na, Cs, Mg. Inset: Gibbs free formation enthalpy of these hydrides as a function of the equilibrium potential. b) For ternary hydrides Mg_2NiH_4, $LaNiH_4$, $CoTiH_{1.4}$, $TiFeH_2$, $ZrV_2H_{5.1}$, $ZrCr_2H_{3.8}$, $ZrMn_2H_{3.6}$, $TiMn_{1.5}H_{2.5}$, $TiCr_{1.8}H_{3.5}$, $LaNi_5H_6$, $LaNi_4MnH_5$ [11].

tion (divided by the amount of substance of hydrogen) of these hydrides is smaller than that of LiH (inset Figure 2a).

I.2.2 Ternary hydrides: In the case of ternary hydrides, equilibrium potentials of the MH_x/Li cells were evaluated for different representative compounds AB_x of intermetallic families (with x = 0.5, 1, 2 and 5) and their corresponding hydrides (Mg_2NiH_4, $LaNiH_4$, $CoTiH_{1.4}$, $TiFeH_2$, $ZrV_2H_{5.1}$, $ZrCr_2H_{3.8}$, $ZrMn_2H_{3.6}$, $TiMn_{1.5}H_{2.5}$, $TiCr_{1.8}H_{3.5}$, $LaNi_5H_6$, $LaNi_4MnH_5$). Figure 2b (lower part) shows that the Gibbs free enthalpy of formation value for all these ternary hydrides (per mole hydrogen) is above that of LiH. For these hydrides the equilibrium potential of the cell is positive (Figure 2b) and the conversion reaction can be achieved. Equilibrium potentials are in the range of 0.3–1.0 V vs Li^+/Li^0, which is suitable for a negative electrode in Li-ion batteries. The equilibrium potential of the cell can be adjusted for different AB_x intermetallic families by varying the site substitutions of A and B [8]. In fact, the plateau pressure of hydride correlates with the lattice cell volume, allows one to change the thermodynamic stability of the hydrides, especially for the families AB_5 and AB_2. Depending of the nature of the hydrides a wide range of hydrogen sorption temperatures from −40 to 300 °C gives another argument to a tailor a negative electrode for the desired applications [9].

I.3 Comparison between thermodynamic prediction and experience

Figure 3 shows the experimentally measured potential vs Li^+/Li^0 for electrochemical MH_x/Li cells using binary and ternary hydrides. The potential–capacity curves recorded are in agreement with the assumption based on thermodynamics that the conversion reaction is possible for MgH_2, TiH_2, NaH and ternary hydrides. These discharge curves correspond to the theoretical reaction $MH_x + xLi^+ + xe^- \rightarrow M^0 + xLiH$ and their lengths are in agreement with the number of hydrogen atoms that react with lithium (Figure 3a). For instance the discharge curves of MgH_2, TiH_2 [10], NaH involve two and one lithium respectively for two and one hydrogen [11]. Values superior to the number of hydrogen atoms x can, however, be reached in relation with either a plateau corresponding to the electrolyte decomposition on carbon at 0.8 V or with a metal alloying reaction at low potentials, especially for Mg (0.17 V vs Li^+/Li^0). The potential–capacities curves are lower than the theoretical equilibrium potential due to internal resistance of the cell and are also not totally flat due to kinetic limitations of the system. The equilibrium potential of the MH_x/Li cells can be obtained by galvanostatic intermittent titration (GITT) in open circuit voltage with, for instance, an experimental value of 0.537 V for the MgH_2/Li cell [11], which is in good agreement with the theoretical value of 0.560 V versus Li^+/Li^0 obtained from Nernst law.

Regarding AB_x intermetallic compounds, typical discharge curves obtained from ternary hydrides $LaNi_4MnH_5$, TiNiH [12], bcc $Ti_{0.20}V_{0.78}Fe_{0.02}H_{1.55}$ and $Mg_{0.65}Sc_{0.35}H_{2.25}$ are presented in Figure 3b. Lengths of discharge curves of x = 4.8, 1.2, 1.3, and 2.2 are recorded for $LaNi_4MnH_5$, TiNiH, bcc $Ti_{0.20}V_{0.78}Fe_{0.02}H_{1.55}$ and $Mg_{0.65}Sc_{0.35}H_{2.25}$ hydrides, respectively. It must be noted that a nice flat plateau is obtained for the AB_5 compound.

Conversion reactions with lithium ions were also carried out with different complex hydrides based on Mg or Al, especially Mg_2FeH_6, Mg_2CoH_5 and Mg_2NiH_4. These complex hydrides were prepared by reactive grinding [13,14]. They react with lithium ions at average potentials of 0.25, 0.24 and 0.27 V and give discharge capacities of 6.6, 5.5 and 3.6 Li, respectively. Using AlH_3 [15], Li_3AlH_6 [16] or more recently $LiAlH_4$, $NaAlH_4$ and Na_3AlH_6 [17,18] as negative electrode of Li-ion batteries was also reported. It demonstrates the possibility to extend the conversion process to numerous versatile complex hydrides. For these last cases, the discharge curves involve conversion process and alloying reaction, in relation to the close potential of both reaction types.

II Conversion process reaction mechanisms for hydrides

Reactivity of hydrides with lithium ions predicted from thermodynamic rules and experimentally confirmed for different hydrides is assumed to be a conversion reaction as $MH_x + xLi \rightarrow M + xLiH$. While this general mechanism is obvious, more complex reactions path involving the formation of alloys, solid solutions, metastable or amorphous phases can also be noticed. In the following paragraph reaction mechanisms occurring with MgH_2 [5,11], TiH_2 [10], $Mg_{0.85}Sc_{0.65}H_2$ and Mg_2TMH_x (TM = Fe, Co, Ni, x = 6, 5 , 4) [14] hydrides will be described.

II.1 Reaction of MgH_2 with lithium

The reaction of Mg hydride with lithium ions is the first example reported in the literature of a Li-driven conversion reaction with hydrides [5,11]. The electrochemical curve recorded at a low cycling rate (one equivalent of lithium in 100 h) during the reaction of MgH_2 with Li (inset of Figure 4a) shows that the full discharge (length x = 2.5 Li) involves two plateaus at 0.44 V and 0.095 V. The XRD patterns, collected at different discharge steps, are presented in Figure 4a. The XRD patterns corresponding to the first plateau (until x = 1.8 Li) show a decrease of the intensity of MgH_2 (tetragonal and orthorhombic phases) Bragg peaks and the appearance of hcp Mg and bcc Li peaks ((100, 002, 101) and (111, 200), respectively). Above x = 1.8 (Figure 4b) the first slope observed in the discharge curve corresponds to a shift of the Mg XRD lines in

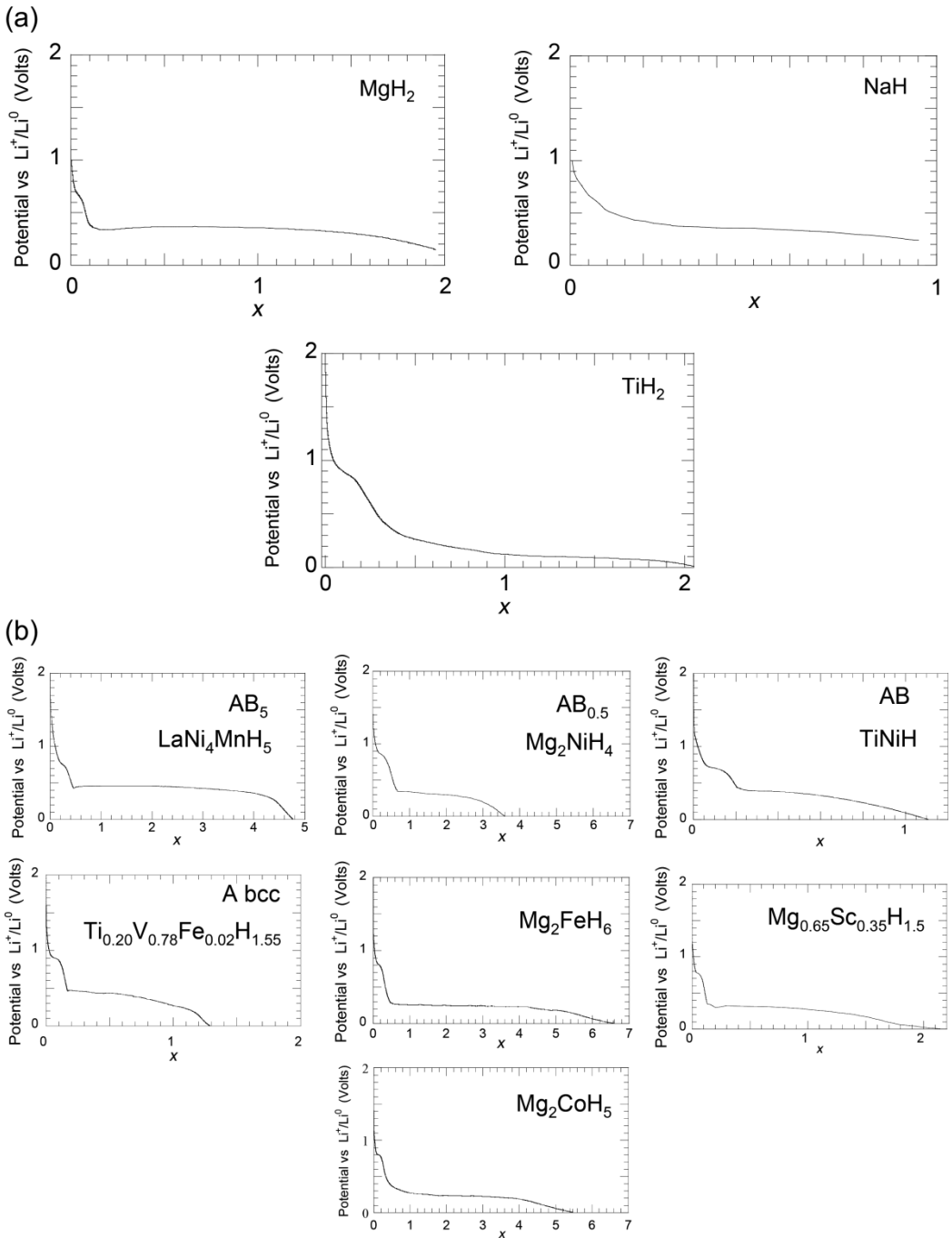

Figure 3: Potentials vs Li^+/Li^0 of MH_x/Li cells (V) as a function of the mole fraction of Li (x) recorded between 3 and 0.005 V; (a) MgH_2, NaH and TiH_2, (b) $LaNi_4MnH_5$, $Ti_{0.20}V_{0.78}Fe_{0.02}H_{1.55}$, Mg_2NiH_4, Mg_2FeH_6, Mg_2CoH_5, TiNiH, and $Mg_{0.65}Sc_{0.35}H_{2.25}$ [11,79].

agreement with the formation of a Mg-type solid solution (Figure 4b, no. 6 and Table 1). The last slope corresponds to the formation of a bcc Li-type solid solution (Figure 4b, no. 8), and the plateau to the coexistence of both solid solution types (Li and Mg) (Figure 4b, no. 7). In short, MgH_2 reacts with Li ions to form Mg and LiH within the conversion process $MgH_2 + 2Li^+ + 2e^- \rightarrow Mg + 2LiH$ at around 0.44 V vs Li^+/Li^0. Then the freshly formed Mg can react with Li ions at a low potential to form alloys (hcp Mg-type and bcc Li-type solid solutions).

Li–Mg alloying reactions can be avoided by limiting the discharge curve to $x = 2$ (Figure 5). In this case a reversible capacity of 1500 $mA{\cdot}h{\cdot}g^{-1}$ (irreversible loss of 25%) can be

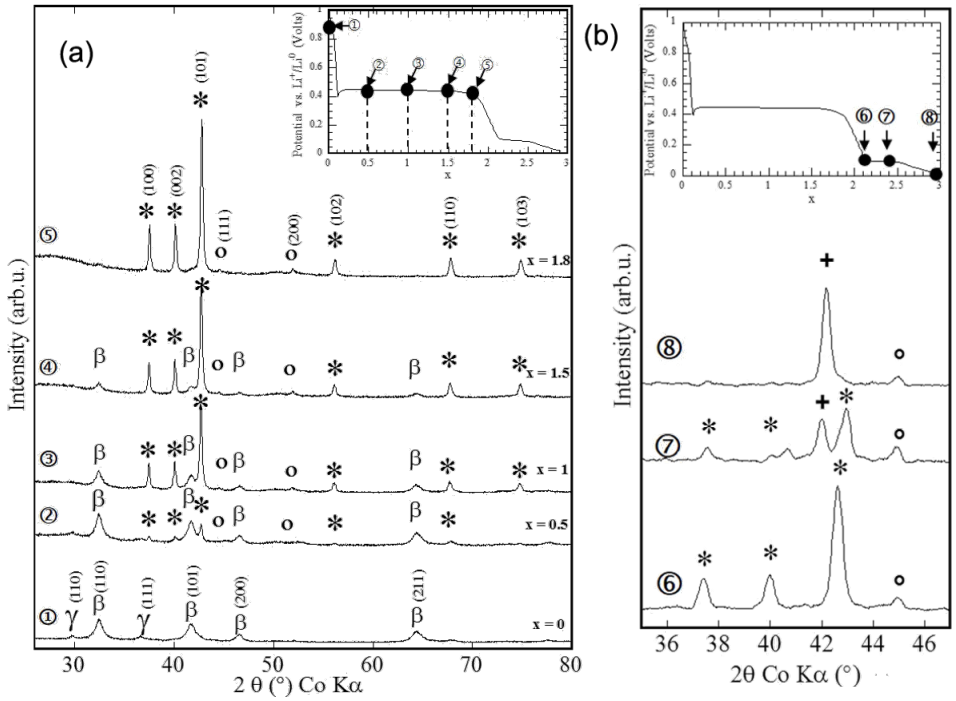

Figure 4: Potential profile and XRD patterns of MgH_2 electrode at different stages of the conversion reaction. (a) Inset: Evolution of the potential (V) as a function of *x* (mole fraction of Li) for a MgH_2 electrode cycled between 3 and 0.005 V at a rate of one equivalent of lithium in 100 h. The recorded XRD patterns are associated with the various stages of the discharge, denoted by the numbers (1), (2), (3), (4) and (5) in panel and correspond to *x* = 0 (starting electrode material), *x* = 0.5, 1, 1.5 and 1.8, respectively. The X-ray peaks marked by an asterisk, β, γ and circle correspond to Mg, β-MgH_2, γ-MgH_2 and LiH, respectively. b) Inset: Inset: Evolution of the potential (V) as a function of *x* (mole fraction of Li) for a MgH_2 electrode cycled between 3 and 0.005 V at a rate of one equivalent of lithium in 100 h. The XRD patterns (6), (7), and (8) corresponding to *x* = 2.1, 2.35 and 2.9. The Bragg peaks marked by an asterisk and plus sign correspond to Mg (hcp) and Li (bcc) solid solutions, respectively. Adapted from [5] (copyright 2008 Nature Publishing Group) and [11].

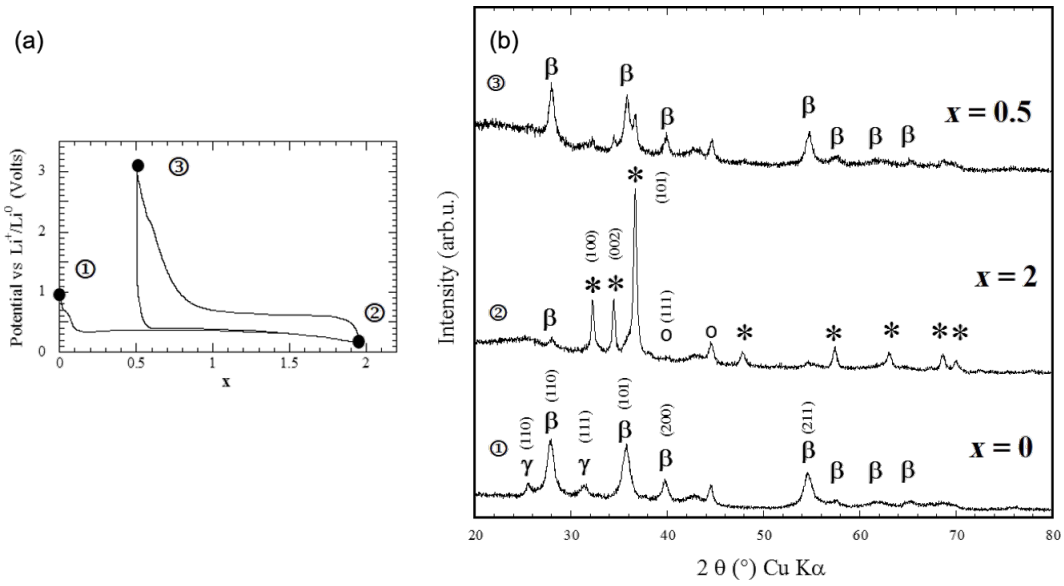

Figure 5: Potential profile and XRD patterns of MgH_2 electrode at various stages of the conversion reaction. a) Evolution of the potential (V) as a function of *x* for a Li/MgH_2 cell that was cycled down to *x* = 2 at a rate of one equivalent of lithium in 10 h. b) XRD patterns taken at various stages of the discharge, (1) *x* = 0 (starting electrode material), (2) *x* = 2 (end of the first discharge) and (3) *x* = 0.5 (end of the first charge). The Bragg peaks marked by an asterisk, β, γ, and circle correspond to Mg, β-MgH_2, γ-MgH_2 and LiH, respectively. Adapted from [5] (copyright 2008 Nature Publishing Group) and [11].

Table 1: Lattice parameters for Mg and Mg-type solid solution formed during the reaction of MgH_2 with Li.

	Mg	Mg hcp solid solution
lattice parameters	a = 3.2090(3) Å c = 5.2100(4) Å	a = 3.1970(2) Å c = 5.1410(6) Å

obtained while a reversible capacity of 2700 mA·h·g^{-1} (irreversible loss 33%) is measured for both processes (Figure 6).

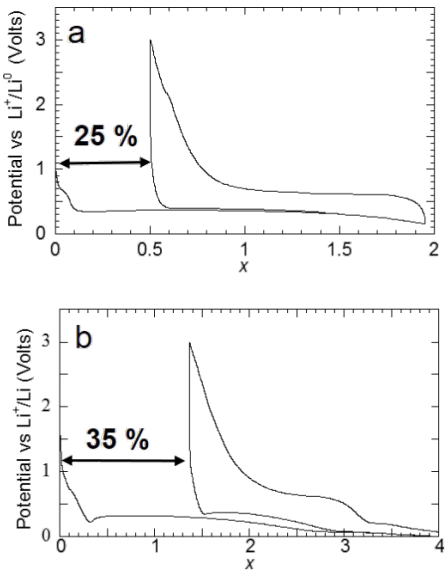

Figure 6: Potential profile of a MgH_2 electrode at various stages of the conversion reaction. a) Evolution of the potential (V) as a function of x for a Li/MgH_2 cell that was cycled down to x = 2 at a rate of one equivalent of lithium in 10 h. b) Evolution of the potential (V) as a function of x for a Li/MgH_2 cell that was cycled down to x = 4 at a rate of one equivalent of lithium in 10 h. Adapted from [5] (copyright 2008 Nature Publishing Group) and [11].

II.2 Reaction of TiH_2 with lithium

The study of the reactions of titanium hydride with lithium is motivated by the chemical and structural properties of TiH_2 [10]. As shown on Figure 1, TiH_2 is attractive regarding its high theoretical capacities (like all binary hydrides). In addition, an improvement of the conversion process kinetics is expected because of the good electrode conductivity due to the metallic properties of titanium hydride. This reaction can be studied without any parasite reaction as Ti does not form alloys with lithium.

The TiH_2 discharge capacity, presented in Figure 7, drastically differs from that of MgH_2 through the presence of two slopes prior to a pseudo plateau. XRD analyses of the electrode during electrochemical discharge show that the reaction of TiH_2 with Li involves three steps. The two first slopes correspond to the formation of an fcc δ-TiH_{2-x} solid solution until x = 0.34 (first slope) that transforms partially from x = 0.34 to 1 in a distorted face-centered orthorhombic phase δ-TiH (fco) (second slope). Note that from x = 0.34 to 1, the peritectic transformation: hcp α-Ti(H) → fcc δ-TiH_{2-x} + δ-TiH explains hexagonal close-packed (hcp) α-formation absence. Finally, conversion process occurs in the pseudo plateau with the formation of hcp α-Ti and LiH.

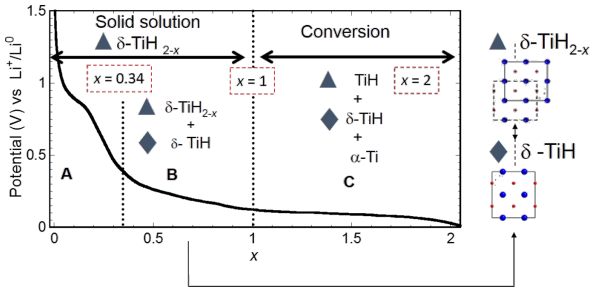

Figure 7: Summary of the dehydrogenation process of TiH_2 electrode δ-TiH_{2-x} (fcc): black triangles, TiH (fco): black diamonds, projection along the b-axis of δ-TiH_{2-x} (fcc): black triangles and TiH (fco): black diamonds showing the relationship between fcc (black triangles) and fco (black triangles) structures. Adapted from [10] (copyright 2012 Elsevier) and [11].

II.3 Reaction of Mg_2MH_x with lithium

After studying the reaction of titanium hydride with lithium, during which a reaction path involving the formation of the metastable fco δ-TiH phase occurs, the complex hydrides Mg_2FeH_6, Mg_2CoH_5, Mg_2NiH_4 were chosen as models system for a conversion process with high energy storage capacities and unusual thermodynamics properties [13,19]. In fact, the decomposition of Mg_2FeH_6 and Mg_2CoH_5, which is expected during their electrochemical reaction with lithium, can be used for the formation of a conductive Fe or Co matrix, which is helpful to reverse the reaction between Mg and LiH. In addition, the far-from-equilibrium electrochemical process is an interesting tool to search for new intermetallic compounds consisting of Mg and Fe or Co [20,21]. As shown in Section I.3, Mg_2MH_x (M = Fe, Co, Ni , x = 6,5,4) react with lithium at roughly the same potential (around 0.25 V vs Li^+/Li^0) and the capacities measured during the discharge are close to the theoretically obtained values (Figure 8). From a structural point of view, a common behavior can be noticed for the reaction of lithium with all complex hydrides from the XRD characterizations of the electrodes. A complete (for the case of Mg_2FeH_6) or partial disappearance of the parent phases is observed, which occurs without any formation of metals (Figure 9). This loss of

crystallinity suggests the formation of an electrode with nanocrystalline or amorphous structure. The formation of nanoscale Fe during the decomposition of Mg_2FeH_6 is confirmed by XAS and Mössbauer spectroscopy [22]. Ex situ XAS spectroscopy of the Mg_2CoH_5 and Mg_2NiH_4 electrodes revealed the formation of disordered MgCo and Mg_2Ni intermetallic compounds.

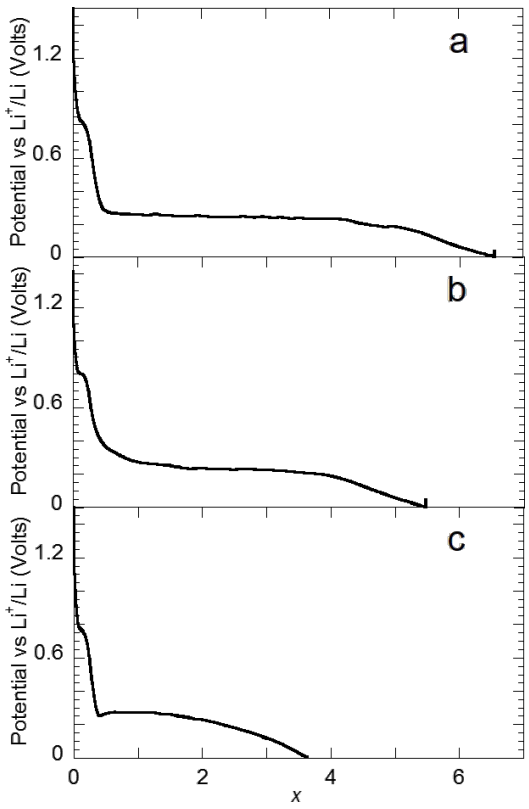

Figure 8: Discharge curves for a) Mg_2FeH_6, b) Mg_2CoH_5 and c) Mg_2NiH_4 electrodes prepared by reactive grinding as a function of Li (*x*) mole fraction, recorded at a current rate of one equivalent of Li in 10 h. Adapted from [13] (copyright 2013 Elsevier) and [19].

The intensity reduction of the XRD lines, which occurs without broadening, involves shifts of the lattice parameters. For instance, theMg_2CoH_5 lattice parameters *a* and *c* rise until $x = 1$ (from 4.4940(3) to 4.517(2) Å and from 6.582(1) to 6.608(1) Å, respectively; a cell volume expansion of 1.44%), evoking a phase transformation. For Mg_2NiH_4 the lattice parameter *c* decreases from 6.538(1) to 6.477(2) Å, which is concomitant with a phase transformation involving a low-hydrogen-content hydride for $x \leq 3$: $Mg_2NiH_4 \rightarrow Mg_2NiH$ [23,24].

The reaction mechanism can therefore be summarized as follows:

$$Mg_2FeH_6 + 6Li \rightarrow 2Mg + \text{amorphous Fe} + 6LiH\,,$$

$$Mg_2CoH_5 + 5Li \rightarrow Mg + \text{disordered MgCo} + 5LiH\,,$$

$$Mg_2NiH_4 + 3Li \rightarrow Mg_2NiH + 3LiH + Li \rightarrow \text{disordered } Mg_2Ni + 4LiH\,.$$

The reaction with Mg_2FeH_6 during the conversion process with lithium ions is the first example for the production of an amorphous phase "2Mg + Fe".

II.4 Reaction of other Mg-based hydrides with lithium

The reactions of $2MgH_2$ + M (M = Cu, Si) and 0.65Mg + 0.35M (M = ScH_2, Ti) mixtures prepared by reactive grinding under 90 bar of hydrogen pressure with lithium ions were also studied [19,25-27]. The electrochemical behavior of MgH_2 is not affected by the presence of a second element, Cu or Si, and significant reversible capacities for the conversion process (>1000 mA·h·g^{-1}) are obtained. In the case of the mixture $2MgH_2$ + Si, an additional capacity below 0.2 V vs Li^+/Li^0 due to the alloying reaction of Si with Li is observed. This combined conversion (MgH_2)/alloying (Si) system presents the highest theoretical capacity anode with the possibility to reach approximately 6000 mA·h·g^{-1}.

The production of pure $Mg_{0.65}Sc_{0.35}H_{2.25}$ (1900 mA·h·g^{-1}) by reactive grinding from magnesium and scandium hydride (MgH_2 + ScH_2) is not possible. Instead, a mixture of 68% of $Mg_{0.65}Sc_{0.35}H_{2.25}$, 20% of MgH_2 and 12% Mg_2FeH_6 is obtained. The formation of Mg_2FeH_6 is due to the strong abrasion of the grinding tools through scandium hydride. The discharge curves of this hydride mixture involves 2.25Li at 0.32 V vs Li^+/Li^0 and the corresponding X-ray diffraction pattern obtained at the end of the discharge shows the presence of both $Mg_{0.65}Sc_{0.35}H_{0.8}$ and $Mg_{0.65}S_{0.35}H_{1.5}$ cubic phases in agreement with the results obtained in KOH electrolyte and reported by Notten et al. [28].

Such desirable electrochemical behavior is also obtained with the $Mg_{0.65}Ti_{0.35}H_{2.25}$ mixture prepared by reactive grinding with a reversible conversion process involving both MgH_2 and TiH_2 without the addition of carbon. As expected, TiH_2 increases the conductivity of the electrode and a full discharge process is obtained without carbon. The development of such Mg-based system appears to be a promising opportunity.

III Kinetics limitations of hydrides for conversion reactions: example of MgH_2

The huge numbers of hydrides reported in the literature exhibit different structures, electronic properties and thermodynamics stabilities. Using the hydrides classification proposed by

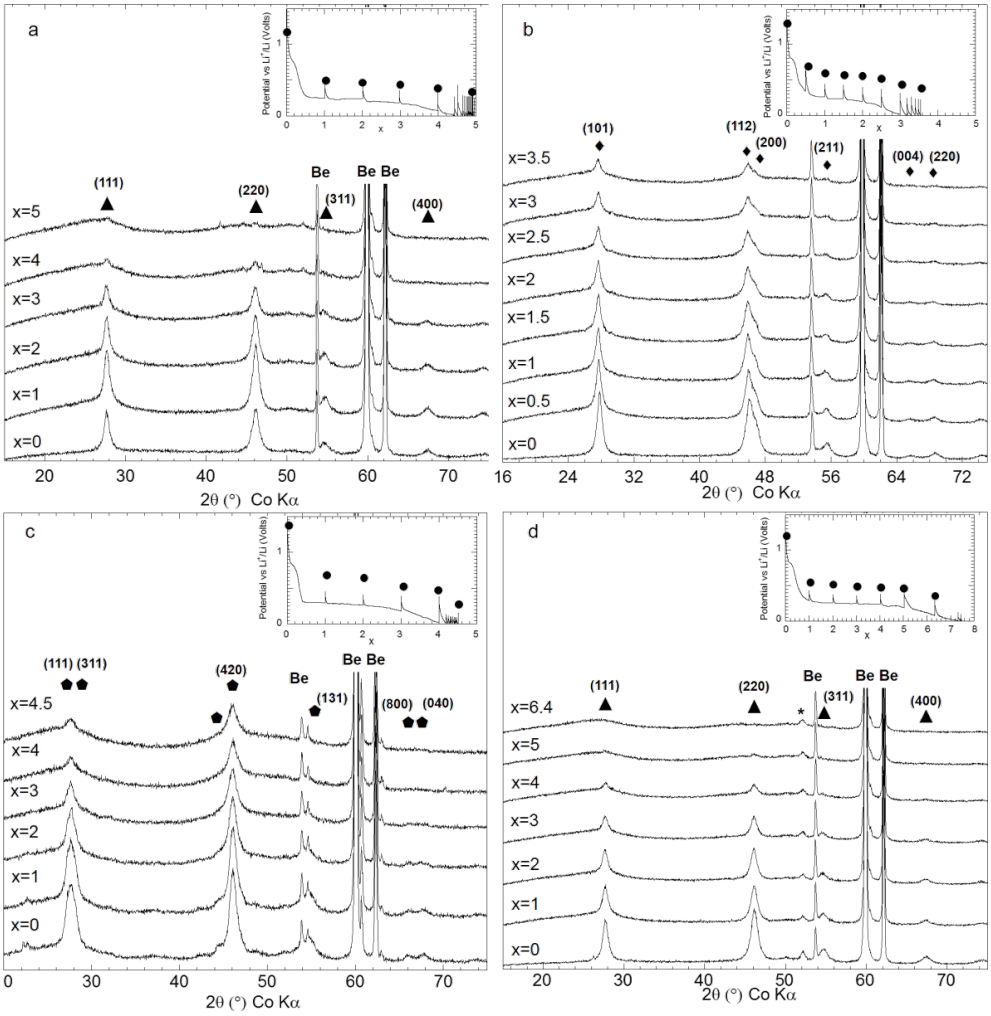

Figure 9: In situ XRD patterns of a) Mg_2FeH_6, b) Mg_2CoH_5 and c) Mg_2NiH_4 and d) Mg_2FeH_6-10% Ct,*z* electrodes prepared by reactive grinding as a function of the mole fraction of Li (*x*) Inset: Potential profile of a) b) c) and d) obtained during GITT (rate: one equivalent of Li in 10 h, relaxation time: 10 h). Adapted from [13] (copyright 2013 Elsevier) and [19].

Libowitz et al. [29,30] metallic, covalent and ionic hydrides can be identified.

Given the fact that the electric behavior is an important parameter for the electrochemical reaction, the issue of the poor electric conductivity of ionic and iono-covalent hydrides must be solved. For instance, the ionic hydride MgH_2 exist as α, β and γ, with the space groups $P4_2/mnm$ (tetragonal, $a = b = 4.516$ Å, $c = 3.020$ Å) $Pa{-}3$ (cubic) and $Pbcn$ (orthorhombic, $a = 4.526$ Å, $b = 5.448$ Å, $c = 4.936$ Å), respectively. The tetragonal phase is the more stable phase. These hydrides exhibit band gap energies of 5.3, 5.6 and 4.2 eV, respectively, and are not electronic conductors but insulators [31].

Figure 10 shows the poor electrochemical reactivity of commercially available tetragonal MgH_2 vs Li^+/Li^0, with no electrochemical capacity during the first discharge. The addition of an electronic conductive material, such as the graphite Super P (electronic conductivity: 10^3 S·cm^{-1}) increases the electronic conductivity of the electrode. As presented in Figure 10a, the discharge capacity of the hydride increases with the amount of graphite. The addition of 25% of graphite gives a discharge capacity of 1.4Li for 2 h for a current of one mole of electron in 100 h. The contribution of Super P carbon to the total capacity remains very small and the maximum of the contribution that can be reached is less or equal to $x = 0.25$.

Note that the conductivity of the electrode is not only influenced by MgH_2 but also by conducting metallic Mg and insulating LiH, which are generated during the reaction. The improvement of the poor electronic conductivity of the active material in powder form has been widely addressed in the litera-

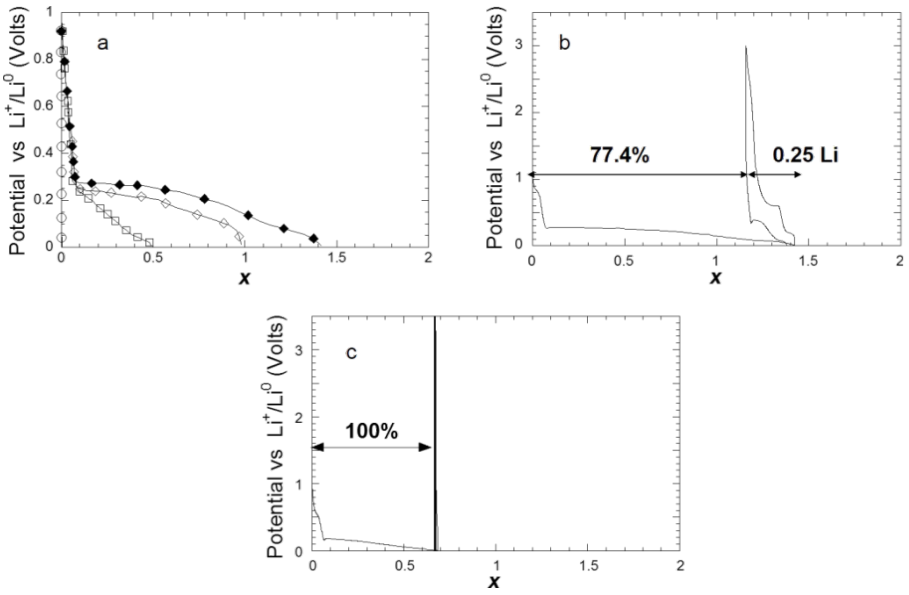

Figure 10: The evolution of the potential (V) as a function of *x* (mole fraction of Li) for a MgH_2 electrode prepared with commercial hydride cycled between 3 and 0.005 V. a) Discharge curves at a rate of one equivalent of lithium in 100 h as function of the content of Super p carbon of the electrode: open circles: 0%, open squares: 15%, open diamonds: 20%, black diamonds: 25%. b) Discharge–charge curve at a rate of one equivalent of lithium in 100 h for a content of 25% of Super P carbon. c) Discharge–charge curve at a rate of one lithium in 10 h for a content of 25% of Super P carbon at a rate of one lithium in 10 h [11].

ture for different electrode materials (in aqueous and non-aqueous electrolytes). A solution is carbon-coating through chemical or physical methods. For electrochemical reactions carried out in thin films in KOH electrolyte with non-conductive hydrides such as MgH_2, or Mg_2NiH_4, the presence of a small amount of non-hydrogenated compound (few percent), as Mg or Mg_2Ni, in the starting material is sufficient to produce a satisfactory electronic conductivity inside the electrode and the addition of carbon is not necessary. Another issue consists in the production of ternary hydrides films with Mg, Ti and H [32,33]. The metallic behavior TiH_2 counters the insulating influence of MgH_2.

III.1 Influence of the particle size on the reversibility of the conversion process

Regarding the reversibility of the conversion reaction, the poor capacities obtained during the first charge for electrodes composed of commercial MgH_2 (0Li and 0.25Li for a current rate of one equivalent of Li in 10 and 100 h, respectively) clearly show than the benefit of the addition of Super P carbon to the electronic conductivity of the active material seems completely lost when the reaction is inversed (Figure 10b,c).

Other parameters than the conductivity of the active material also govern the efficiency of the conversion process. In fact, the volume variation of the electrode during the conversion process $MH_x + xLi^+ + xe^- \rightarrow M^0 + xLiH$ drastically affects the conductivity between the particles. For MgH_2 the volume variation is 83% between MgH_2 (61.59 $Å^3$) and Mg (46.46 $Å^3$) + 2LiH (2 × 33.3 $Å^3$). Thus, during the discharge the electrode volume increases with the lithium transfer and decreases during the lithium extraction. As a consequence, voids are created inside the electrode and disconnect the particles from each other and from the current collector at the same time. Decreasing the particle size is one way to accommodate for the volume variation of the electrode and to maintain cohesion of the interfaces and the connection between particles and the current collector. Reducing the length of diffusion for Li and H can be helpful for volume accommodation and preserving interfaces. Different approaches to reduce the particles sizes and to accommodate the volume variation of the electrode can be considered and will be presented in the following paragraph: Effect of grinding on commercial hydride, effect of three hydrogen sorption, effect of grinding commercial hydride with carbon, effect of activation by sorption cycles follow by the grinding with carbon, reactive milling.

III.2 Effect of mechanical grinding on commercial MgH_2

Grinding of commercial MgH_2 enables a faster hydrogen desorption with a desorption maximum at 372 °C compared to 445 °C for the untreated commercial material (Figure 11a). As expected, discharge efficiency increases with the amount of Super P carbon added to the electrode (Figure 11b). In this case,

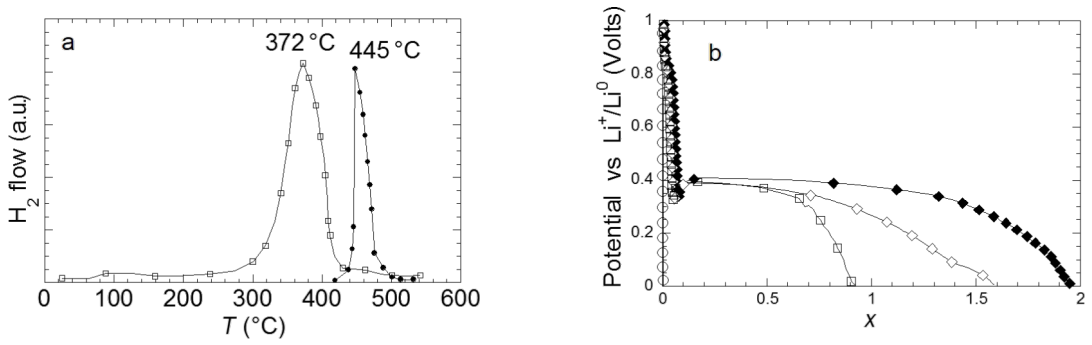

Figure 11: a) DSC traces of commercial MgH_2 unground and ground for 20 h. b) Evolution of the potential (V) as a function of *x* (mole fraction of Li) for a MgH_2 electrode prepared with commercial hydride ground for 20 h in the Spex mixer mill and cycled between 3 and 0.005 V at a rate of one equivalent of lithium in 100 h. Super P carbon content (%) of the electrode: open circles: 0%, open squares: 15%, open diamonds: 20%, black diamonds: 25% [11].

a full discharge capacity of $x = 1.95$Li can be achieved when 25% of graphite is added. The improved performance of the ground sample is due to a reduction of the crystallite size down to few nanometers, which facilitates the diffusion of hydrogen and lithium by increasing the number of diffusion paths. However, despite an improvement of the discharge kinetic, the reversibility of the hydride is hardly changed (Figure 12a). The reversible capacity of ground commercial MgH_2 after 30 h of grinding is actually $x = 0.26$Li.

The particle size cannot be reduced below 0.1 µm through grinding, because immediate agglomeration of smaller particles occurs (Figure 12b,c). So, even if crystallite size of few nanometers can be reached during grinding, the formation of agglomerates of 5 to 30 µm (consisting of primary particles of 0.1–5 µm, Figure 12b) limits the reversibility of the conversion process.

III.3 Effect of hydrogen sorption cycles on MgH_2

The particle size of the hydride is also reduced through decrepitation during hydrogen desorption–absorption cycles. This solid–gas reaction not only reduces the particle size of the hydride but also enhances its reactivity vs Li-ions. In the case of the system Mg/MgH_2, 5% of Super P carbon was mixed with the Mg powder in order to increase the thermal conductivity of the powder and to prevent the necking of particles during sorption cycles.

Figure 13a and Figure 13b show the hydrogen sorption kinetics at 350 °C for Mg/MgH_2 for the first and the third cycles (uptake and loss in wt % hydrogen). Hydrogen sorption kinetics and capacities increase from the first to the third cycle and then are constant for the subsequent cycles (not shown here). This activation process observed during the first three cycles can be correlated with a particle size reduction (Figure 13c and

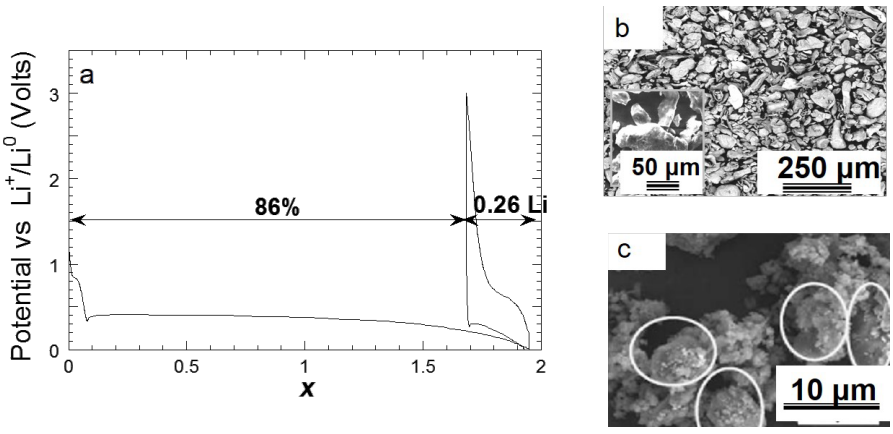

Figure 12: a) Evolution of the potential (V) as a function of *x* (mole fraction of Li) for a MgH_2 electrode prepared with commercial hydride, ground 30 h in a Spex mixer mill and cycled between 3 and 0.005 V at a rate of one equivalent of lithium in 100 h. b) SEM image of a MgH_2 commercial powder ground 30 h in the Spex mixer mill. c) SEM image of MgH_2 commercial powder ground 30 h in the Spex mixer mill showing the agglomeration of particles [11].

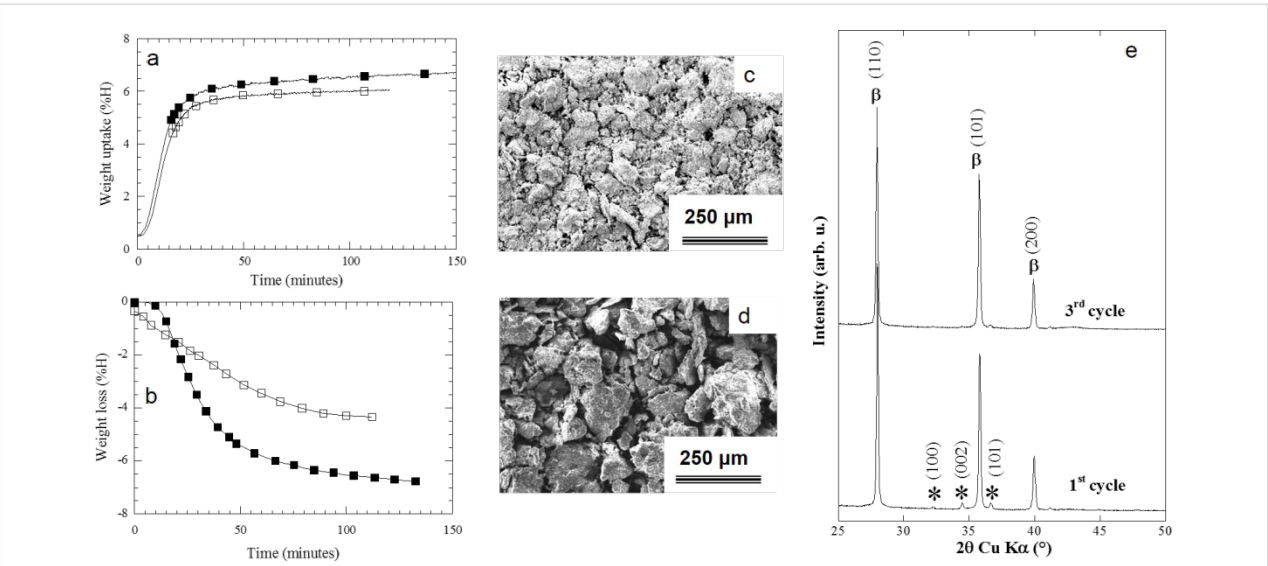

Figure 13: a) Absorption and b) desorption kinetics at 350 °C for Mg–10%$C_{10,320}$ composite (open squares): first cycle, black squares: third cycle; c) SEM image of the MgH_2 powder after one absorption; d) SEM image of the MgH_2 powder after three absorptions; e) XRD patterns of the MgH_2 powder after one and after three absorptions [11].

Figure 13d) and an increase of the BET surface area from 7 to 14 $m^2 \cdot g^{-1}$ while no change of the hydride crystallinity is observed (Figure 13e).

The effect of three sorption cycles on the reaction of MgH_2 with lithium (Figure 14) shows that reversible capacity drastically increases compared to that of ground commercial hydride and reaches 0.88Li after three sorption cycles (Figure 14c). Despite an attractive increase of reversible capacity, an irreversible loss (48%) can be noticed on potential–capacity curves.

III.4 Effect of grinding of MgH_2 with carbon

Grinding of commercial MgH_2 with a pre-ground $C_{t,z}$ carbon, where t refers to the pre-grinding time and z to the carbon BET surface area, was used to enhance the efficiency of the conversion reaction. Grinding of commercial MgH_2 with $C_{t,z}$ carbon is supposed to create of a porosity volume inside the electrode, corresponding to a volume increase due to matter transfer. This porous volume is then recovered during the lithium extraction and the total volume change of the electrode is then minimized. In addition, the carbon also acts as conductive additive and a coating agent, which prevents the agglomeration of the hydride particles during grinding. A detailed study of the effect of mechanical milling on the physical/chemical and electrochemical properties compared to AB_5 alloys is available in [34].

Figure 15 shows the evolution of the BET surface z (in $m^2 \cdot g^{-1}$) and of the $d(002)$ interplanar spacing of carbon $C_{t,z}$, as a function of the milling time t (in h). Two main grinding steps can be noticed in Figure 15. First the BET surface area increase while

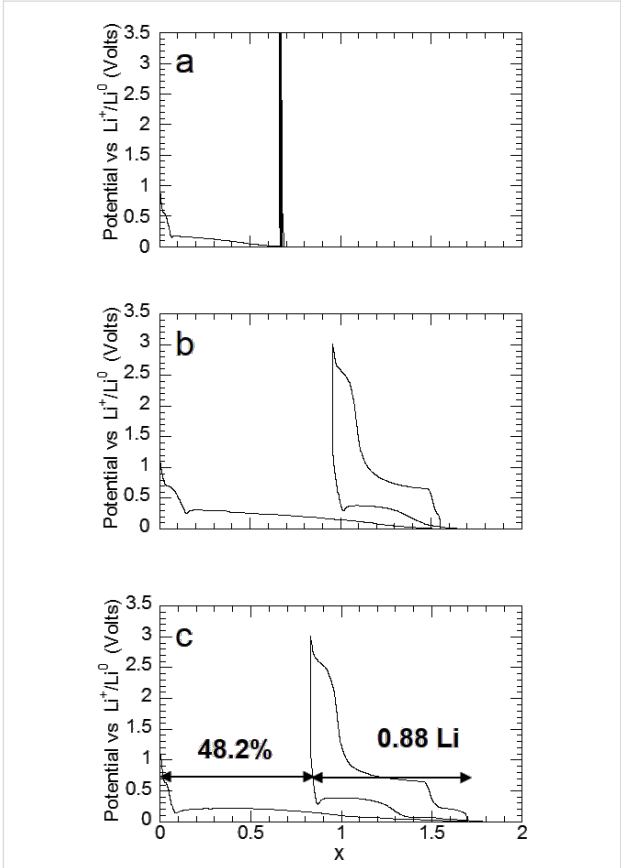

Figure 14: Evolution of the potential (V) as a function of x (mole fraction of Li) for MgH_2 electrodes cycled between 3 and 0.005 V at a rate of one equivalent of lithium in 10 h. a) MgH_2 commercial hydride; b) MgH_2 obtained after one absorption of hydrogen; c) MgH_2 obtained after three absorptions of hydrogen [11].

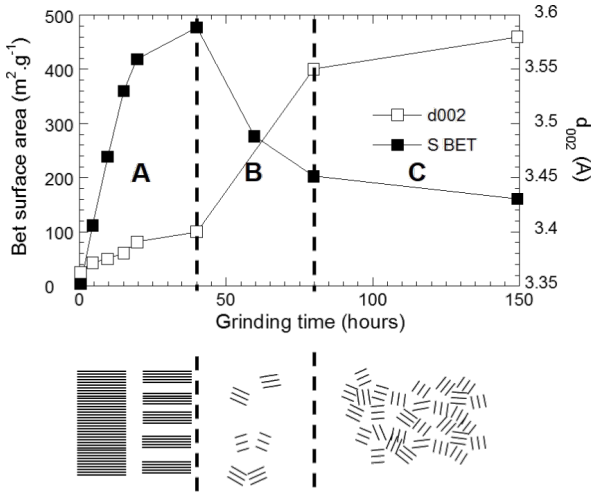

Figure 15: Graphite BET surface area ($m^2 \cdot g^{-1}$) and *d*(002) interlayer distance (Å) as a function of grinding time (h) [11].

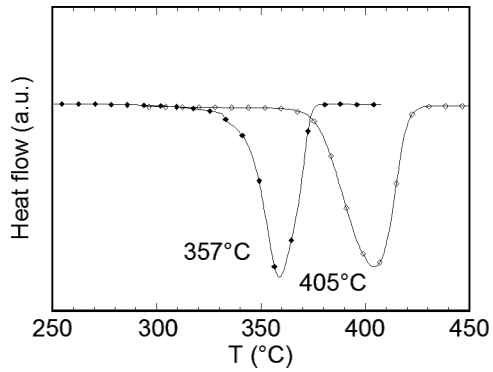

Figure 16: Thermodesorption of commercial MgH_2 (black diamonds) and commercial MgH_2 ground 4 h with 10% of $C_{t,z}$ carbon (open diamonds) [11].

d(002) remains almost constant (step A) and then the BET surface area decrease and *d*(002) drastically increases (step B). Firstly, The mechanical energy transferred to the carbon produces an exfoliation of the graphene layer. Then, the cumulated mechanical energy coming from the grinding is sufficient to promote fissure propagation within the graphene layer, resulting in the fracture of the C–C covalent bonds, leading to the formation of very reactive edge carbon atoms and unstable particles which agglomerate together. The degree of disorder for carbonaceous materials increases with increased milling time and is proportional to the *d*(002) distance, as previously established [35,36]. Note that the C-free bonds created during the fracture of the graphene layer serve as oxygen scavengers, and their agglomeration and coating of the alloy particles enable a better chemical/physical protection against oxidation [34].

Based on the milling behavior of carbonaceous material [34,35], MgH_2 is ground using a carbon having the maximum BET surface area in order to agglomerate carbon particles on MgH_2 particles. DSC traces of MgH_2–10% $C_{t,z}$ composite obtained after 4 h of grinding shows a decrease of 48 °C of the desorption peak maximum of hydride carbon composite compared to the commercial hydride, as expected (Figure 16).

The dispersion of the hydride particles into carbon increases the thermal conductivity of the powder and helps the hydrogen release. With regard to the electrochemical properties, the potential–capacity curves of an electrode composite of MgH_2–10% $C_{t,z}$ obtained after 4 h of grinding shows a spectacular enhancement of the reversible capacity with 0.96Li (= 1000 $mA \cdot h \cdot g^{-1}$) for an irreversible loss of 48% (Figure 17b).

The grinding of MgH_2 with carbon was also carried out with MgH_2 that was activated through three sorption cycles. A synergic effect, involving both the hydride activation by solid–gas reaction and grinding with a $C_{t,z}$ carbon to enhance the reversibility was noticed (Figure 17c,d). For instance, a capacity of 1500 $mA \cdot h \cdot g^{-1}$ for an irreversible loss of 35% after three sorption cycles and 4 h of grinding with 10% of $C_{t,z}$ carbon was obtained (Figure 17d). This reactivity enhancement enables to obtain interesting reversibilities, free of alloying reaction (with a cut of voltage of 0.15 V vs Li^+/Li^0). When the grinding time of the activated $MgH_2 + C_{t,z}$ mixture varied from 4 to 6 h, a reversible capacity of 1480 $mA \cdot h \cdot g^{-1}$ for an irreversible loss of 25% is thus obtained at 0.15 V vs Li^+/Li^0 (Figure 18).

III.5 Effect of reactive milling under hydrogen

Reactive milling under hydrogen constitutes a powerful method for the synthesis of hydrides with the advantage to grind and to hydrogenate the sample in one single step. Applied to MgH_2, a subsequent grinding step with carbon $C_{t,z}$ is needed to obtain similar electrochemical performances than for the sample prepared by three hydrogen sorption steps followed by grinding with the carbon $C_{t,z}$ (1600–1700 $mA \cdot h \cdot g^{-1}$ at 0.005 V vs Li^+/Li^0 for 6 h of grinding with carbon).

III.6 Effect of metal catalyst addition to the MgH_2 carbon composite

The improvement of the sorption kinetics of MgH_2 through catalyst addition (i.e., transition metals [37,38] transition metal oxides [39-41] and halides [42]) has been widely studied in the literature. Nb_2O_5 is one of the most efficient catalysts [43] enabling fast hydrogen desorption kinetics with 7.6 wt % of hydrogen desorbed in 100 s at 300 °C. To improve the conversion reaction of MgH_2 with lithium, the addition of a metal catalyst, which is more suitable than oxides in relation with the

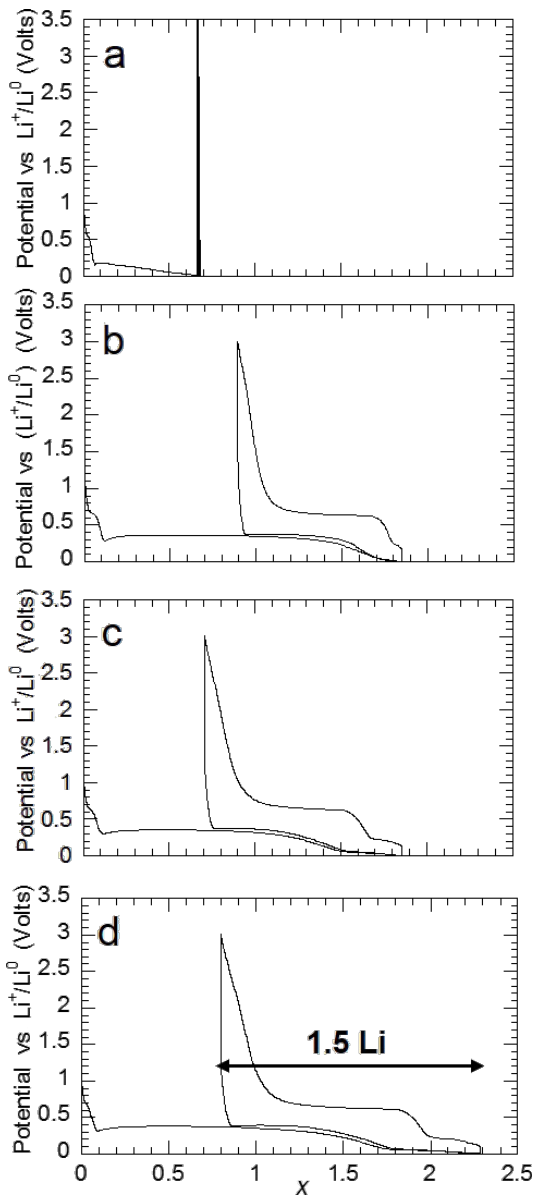

Figure 17: Evolution of the potential (V) as a function of *x* (mole fraction of Li) for MgH_2 electrodes cycled between 3 and 0.005 V at a rate of one equivalent of lithium in 10 h. a) MgH_2 commercial hydride; b) MgH_2 commercial hydride ground for 4 h with 10% of $C_{t,z}$ carbon; c) MgH_2 after one absorption of hydrogen and then ground for 4 h with 10% of $C_{t,z}$ carbon; d) MgH_2 after three absorptions of hydrogen and then ground for 4 h with 10% of $C_{t,z}$ carbon [11].

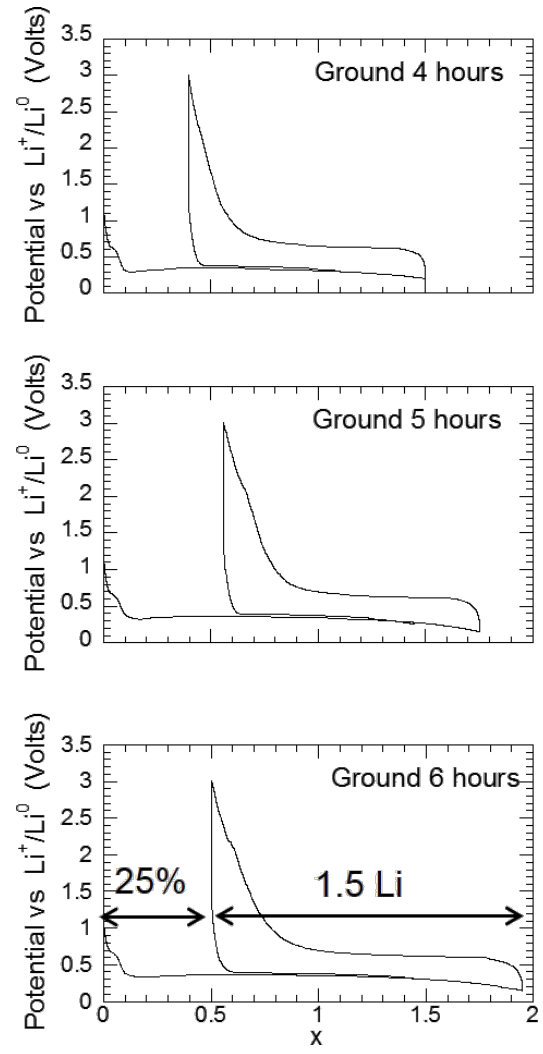

Figure 18: Evolution of the potential (V) as a function of *x* for a Li/MgH_2 cell that was cycled down to 0.15 V vs Li^+/Li^0 at a rate of one equivalent of lithium in 10 h. (MgH_2 is obtained after three absorptions of hydrogen and then ground 4, 5 or 6 h with 10% of $C_{t,z}$ carbon) [11].

electrode conductivity, has been reported by Nakayama et al. in a patent [44,45]. A charge–discharge efficiency of 93.9% for the conversion reaction with MgH_2 is reported by the grinding addition of 3 atom % of a nickel catalyst (particle size 20 nm) in the hydride MCMB carbon mixture. In this last case the irreversible loss can be drastically reduced to 7% for a reversibility capacity of 2608 $mA{\cdot}h{\cdot}g^{-1}$ at 0.01 V vs Li^+/Li^0 and a current rate of C/50.

IV Performance improvements of hydride-based electrodes

Different samples preparation methods for MgH_2–18% $C_{t,z}$ (activation by three hydrogen sorption steps or reactive milling followed by grinding with $C_{t,z}$ carbon) are able to produce an hydride carbon composite electrode with full discharge capacity and 75% reversibility (1500 $mA{\cdot}h{\cdot}g^{-1}$ at 0.15 V vs Li^+/Li^0) during the first charge for a current of one equivalent of electrons in 10 h. Despite this improvement of the electrode reversibility of the MgH_2 carbon composite, the cycle life is however limited due to the 83% volume variation, leading to an electronic interparticular conduction loss. Moreover, at a high current rate, the slow hydrogen motion leads to a limitation of the reversible capacity. The influence of the current rate and of the number of electrochemical cycles on the reactivity of the

MgH_2 carbon composite will be described in the two following paragraphs.

IV.1 Influence of the current rate on the electrode reactivity: example of MgH_2

The experimental capacity decreases when the current rate increases and, for an exchange rate of one equivalent of electrons in one hour, the capacity is close to zero. This result shows that the reactivity improvement with different sample preparation methods is still insufficient for real application requiring electrode power and fast charge (Figure 19). However, for a thin film of MgH_2 (200 nm) (prepared by R. Griessen group at the Vrije Universiteit Amsterdam) a full discharge capacity of 2Li can be obtained for a current of one equivalent of electrons in one hour. This fact definitively confirms than the reduction of the diffusion distances is the key to achieve high power electrodes with hydrides for conversion reaction.

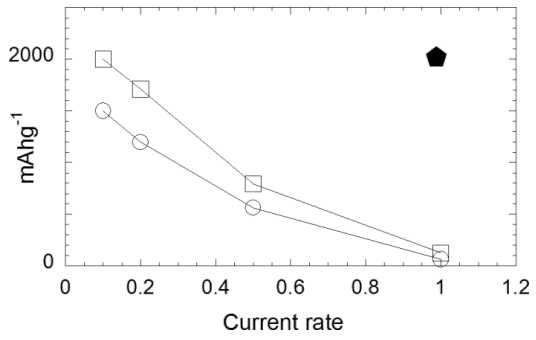

Figure 19: Capacities of a MgH_2 electrode obtained after three absorptions of hydrogen and then ground for 4 h with 10% of $C_{t,z}$ carbon as a function of the current rate (number of Li exchange per hours) open squares: discharge capacity, open circles: charge capacity; black pentagon: discharge capacity of a MgH_2 thin film of 200 nm [11].

IV.2 Effect of polymer binders on MgH_2-based electrode cycle life

The electrochemical cycling behavior of MgH_2–18% $C_{t,z}$/Li was studied and compared with that of MgH_2–33.3% CMC–33.3% $C_{t,z}$/Li and MgH_2–33.3% CMC-f–33.3% $C_{t,z}$/Li cells where CMC and CMC-f are polymer binders (sodium carboxymethylcellulose and sodium carboxymethylcellulose-formate, respectively [46]). CMC [47,48], which was already widely investigated for silicon-based electrodes [49-60], surprisingly sustains the 270% volume change taking place during cycling of the Si-based electrode. Beattie et al. [54] estimated the CMC binder and carbon quantity needed to fill the holes created during lithium extraction from the Si alloy electrode to be around 66%. It was experimentally confirmed that large capacities and long cycle lives of the electrodes are obtained for a 33% Si/33% CMC/33% C mixture. This ratio of active material/binder/carbon was chosen to improve the electrode cycle life of MgH_2. In addition to CMC, a derivative binder with a formyl ester group was tested (CMC-f) [61].

MgH_2–18% $C_{t,z}$/Li, MgH_2–33.3% CMC–33.3% $C_{t,z}$/Li and MgH_2–33.3% CMC-f–33.3% $C_{t,z}$/Li discharge–charge curves are shown in Figure 20. It appears there that high reversible capacities are preserved independently of the amount of active material additives in the electrode. Indeed, reversible capacities of 1700 $mA{\cdot}h{\cdot}g^{-1}$, 1800 $mA{\cdot}h{\cdot}g^{-1}$ and 1900 $mA{\cdot}h{\cdot}g^{-1}$ are obtained for the MgH_2–18% $C_{t,z}$/Li (Figure 20a), MgH_2–33.3% CMC–33.3% $C_{t,z}$/Li (Figure 20b) and MgH_2–33.3% CMC-f–33.3% $C_{t,z}$/Li (Figure 20c) cells, respectively. An increase of the carbon content from 18 to 33% leads to an increase of the irreversible loss (from 25 to 39%) due to electrolyte decomposition at the carbon surface. The reversible capacities of the MgH_2 electrodes as a function of the cycle number are presented in Figure 21 (MgH_2–18% $C_{t,z}$/Li, MgH_2–33.3% CMC–33.3% $C_{t,z}$/Li and MgH_2–33.3% CMC-f–33.3% $C_{t,z}$/Li). From theses curves it is clear that the presence of the CMC-type binder enhances the cycle life of the electrode. While a capacity value of 174 $mA{\cdot}h{\cdot}g^{-1}$ is obtained for the electrode without binder, 240 $mA{\cdot}h{\cdot}g^{-1}$ and 542 $mA{\cdot}h{\cdot}g^{-1}$ are obtained for CMC and CMC-f binders after 40 cycles, respectively. The weak capacity, which originates from carbon (20 $mAh{\cdot}g^{-1}$ after 40 cycles) is not at the origin of the better capacity retention of the MgH_2–33.3% CMC–33.3% $C_{t,z}$/Li and MgH_2–33.3% CMC-f–33.3% $C_{t,z}$/Li electrodes. Thus, porosity created by the polymers might explain the better volume accommodation of the electrode during lithium extraction. Further studies are needed for a better understanding of the nature of the polymeric interactions with carbon and metal hydride and their role during the solid mixing of CMC-type binders with MgH_2 and $C_{t,z}$.

IV.3 Role of interface and particle size on reversibility of the conversion reaction: example of TiH_2

The reaction of titanium hydride (TiH_2) with lithium ions previously described involves a reaction path that can be summarized as follows:

$x \leq 0.34$: $\delta\text{-}TiH_2(fcc) + 0.34Li \rightarrow \delta\text{-}TiH_{1.66} + 0.34LiH$,

$0.34 < x \leq 1$: $\delta\text{-}TiH_{2-x} + xLi \rightarrow \delta\text{-}TiH(fco) + xLiH$,

$1 < x \leq 2$: $\delta\text{-}TiH_{2-x}(fcc) + \delta\text{-}TiH(fco) + Li \rightarrow \alpha\text{-}Ti(hcp) + LiH$.

Within this conversion process, a full discharge capacity of 1072 $mA{\cdot}h{\cdot}g^{-1}$ is obtained for the TiH_2 ground with 10% of

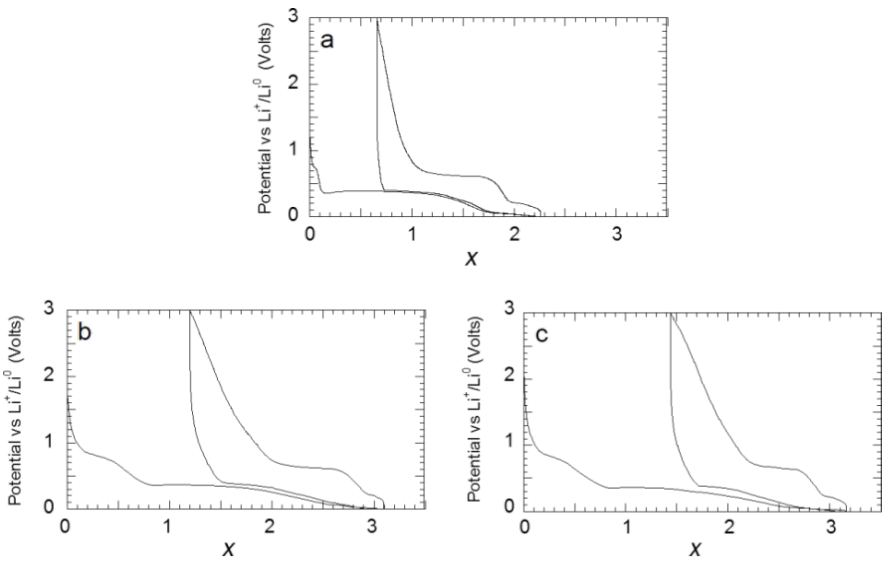

Figure 20: Evolution of the potential (V) as a function of *x* (mole fraction of Li) for MgH_2 electrodes cycled between 3 and 0.005 V at a rate of one equivalent of lithium in 10 h. (a) MgH_2–18% $C_{t,z}$; (b) 33.3% MgH_2–33.3% CMC–33.3% $C_{t,z}$; (c) 33.3% MgH_2–33.3% CMC-f–33.3% $C_{t,z}$. Adapted from [46]. Copyright 2011 Elsevier.

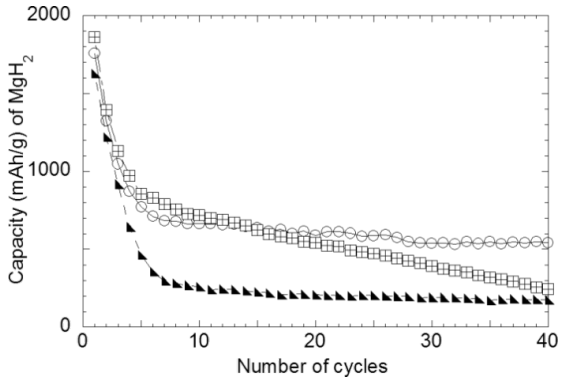

Figure 21: Electrochemical cycling performance for MgH_2 composite electrodes: MgH_2–18% $C_{t,z}$ (black triangles), 33.3% MgH_2–33.3% CMC–33.3% $C_{t,z}$ (open squares) and 33.3% MgH_2–33.3% CMC-f–33.3% $C_{t,z}$ (open circles). Cycling between 3 and 0.005 V, rate of one equivalent of lithium in 10 h. Adapted from [46]. Copyright 2011 Elsevier.

$C_{t,z}$ carbon for 5 h. However, while this reaction is free of any alloying reaction with lithium, no electrochemical reversibility was noticed during electrode charge (Figure 22a). To support the idea that interfaces and particles sizes play a key role on conversion reaction reversibility with titanium hydride, the electrochemical behavior of a (2LiH + Ti) composite was studied [6]. This composite was prepared through a mechanochemical reaction between TiH_2 and metallic Li. The capacity of the first charge reached 455 $mA{\cdot}h{\cdot}g^{-1}$ whereas after one cycle the reversible capacity was still 428 $mA{\cdot}h{\cdot}g^{-1}$, corresponding to a capacity retention of 94% (Figure 22b). The XRD pattern collected at the end of the first charge indicated the formation of titanium hydride in agreement with the theoretical conversion reaction: $2LiH + Ti \rightarrow TiH_2 + 2Li^+ + 2e^-$. This is a clear example showing that when thermodynamics allow a conversion reaction to occur, interfaces and particles size constitute the pertinent parameters that governs the process reversibility.

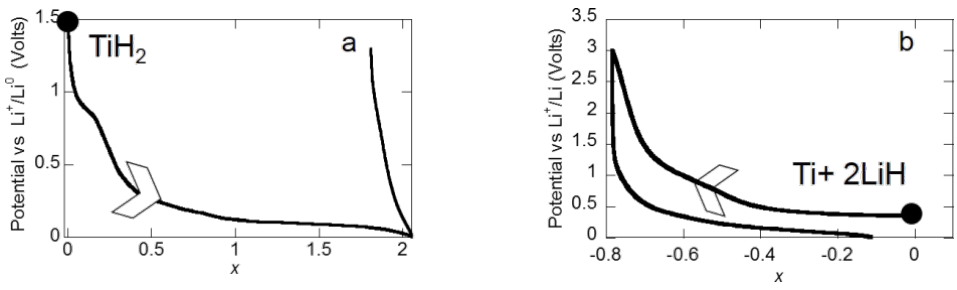

Figure 22: Potential profile of a) TiH_2 electrode ground for 5 h with 10% of $C_{t,z}$ carbon b) Ti + 2LiH electrode as a function of *x*, the mole fraction of Li (rate one equivalent of Li in 100 h). Adapted from [6]. Copyright 2009 Elsevier.

IV.4 Synthesis of nanoscale composite hydrides: a perspective to achieve all solid state batteries

It must be emphasized first that production of hydride nanoparticles by reactive milling seems to be an unsuccessful route as long as the agglomeration of the freshly fractured particles is not controlled. Cryomilling could be a potential solution to avoid metal welding and to produce material on the laboratory scale, but this will require significant technological improvements to become economically viable for large scale material production.

Chemical methods, such as encapsulation or confinement strategies used in the design of energy storage and conversion materials, also constitute new synthetic routes that have shown promising results [62,63]. Thus, for solid-state hydrogen storage applications, very fast hydrogen absorption/desorption kinetics have been indeed confirmed for nanoscale Mg hydride (MgH_2) confined into the porosity of different carbon hosts [64,65] or chemical matrices [66,67]. Very recently, composites containing MgH_2 nanoparticles (with a narrow size distribution of 1–10 nm) which were well-dispersed into a porous carbon host have been prepared by Zlotea et al. [68]. These were produced with varying metal content up to 50 wt % and were designed to be used as a negative electrode for Li-ion batteries. These composites show interesting electrochemical behavior, especially regarding their cycle life stability (500 $mA{\cdot}h{\cdot}g^{-1}$ after 40 cycles) and have a stable nanoparticle size distribution during electrochemical cycling.

Other promising materials, produced through a physical vapor transport deposition method such as Mg/MgH_2 nanowires or nanofibers are under development for a few years now [69-71]. For instance Mg nanowire shows interesting modifications of both thermodynamics and kinetics compared to the bulk material: a decrease of the dissociation energy of about 12%, (30–50 nm nanowires: 65.3 $kJ{\cdot}(mol\ H_2)^{-1}$ bulk material: 74 $kJ{\cdot}(mol\ H_2)^{-1}$).

Hydriding chemical vapor deposition (HCVD) is also a powerful method to produce in situ high purity nano/microscale MgH_2 under hydrogen. This method, which enables to play with temperature and pressure, is a nice tool for the preparation of a variety of particles having controlled size and shapes (nanofibers, nanoparticles, microdendrites, irregular bulk, hexagonal microplates and microspheres). A good picture of this synthesis method, leading to the production of tailored materials, is given by a pressure–temperature diagram, similar to the diagram of Nakaya et al. [72]. Mass production and applications of such materials in the field of hydrogen storage and batteries technologies will be an interesting challenge for the next decade.

IV.5 Use of computational methods to look for better materials

Computational methods can also offer interesting alternatives to help the search and development of materials for hydrogen storage and batteries. The idea is, for instance, to look for materials having high volume capacity, minimal expansion volume and high lithium mobility. A recent study by molecular dynamics simulations has revealed that the Li diffusion in MgH_2 nanocluster doped with Fe, Ni, Ti or V is independent of the presence of the transitions metal [73]. The metals improve the hydrogen desorption kinetics. Again, this example shows the mutual interest of this kind of device for hydrogen storage and batteries technologies.

The search for the existence of new stable hydrides in the Mg–Li–H system was also addressed by several groups through density functional theory approach (DFT) [74,75]. Ternary hydrides in the system Li–Mg–H, such as Li_2MgH_4 and $LiMgH_3$, are insulators dominated by ionic bonds. Their preparation from Li, Mg and H_2 is energetically favorable, but may be kinetically inhibited by separation into pure phases. The effects of various light-metal (Mg, Al, Li) and transition-metals (V, Cr, Mn, Fe, Co, Cu, Zn) dopant on the electrochemical properties of NiTiH hydrides as anodes for Li-ion batteries where theoretically studied by Qian et al. [76,77] with Al, Cr, Mn and Fe being the most promising according to the authors.

Conclusion

Studies of the reaction of hydrides with lithium ions started with the pioneer work with MgH_2, where lithium-driven conversion reactions were firstly demonstrated for the metal hydride family. The study was subsequently extended to other metal and complex hydrides, especially TiH_2 and AlH_3, and is in now in progress, particularly because of the important number of different potential interesting compounds [78]. Metal hydrides present the advantage of having high capacities in a safe potential window of 0.1–1 V vs Li^+/Li^0. Moreover, these hydrides show the lowest polarization reported to date for conversion reaction electrodes, as compared to oxides, sulfides, nitrides, phosphides and fluorides compounds, and therefore, constitute promising candidates for negative electrodes in Li-ion batteries.

This research field focuses now mainly on nanocomposite synthesis in order to enhance the limited electrochemical cycling performances, the main drawback of hydrides. Electrode technology is, thus, the next challenge, considering the design of the current collector, the preparation of polymeric binders and the mixing of hydride and electrolyte together with careful studies to achieve better capacity retention performance or to scale up the nanocomposite elaboration process. On the other hand, the results obtained at the present time emphasize the importance of

the knowledge of fundamentals aspects to control the conversion complex process where reaction paths, interfaces and particle size are the keys parameters. Use of hydrides as anode for Li-ion batteries needs also strong interactions between batteries and fuel-cell communities to be wholly fruitful [79]. In the final analysis, hydrides as a new concept for negative electrodes bridges Li-ion battery and hydrogen storage technologies together and can constitute a promising opportunity for the discovery and the achievement of new energy storage technology for the next 20 years.

References

1. Cabana, J.; Monconduit, L.; Larcher, D.; Palacín, M. R. *Adv. Mater.* **2010,** *22,* E170–E192. doi:10.1002/adma.201000717
2. Bruce, P. G.; Scrosati, B.; Tarascon, J.-M. *Angew. Chem., Int. Ed.* **2008,** *47,* 2930–2946. doi:10.1002/anie.200702505
3. Breitung, B.; Reddy, M. A.; Chakravadhanula, V. S. K.; Engel, M.; Kübel, C.; Powell, A. K.; Hahn, H.; Fichtner, M. *Beilstein J. Nanotechnol.* **2013,** *4,* 705–713. doi:10.3762/bjnano.4.80
4. Nitta, N.; Yushin, G. *Part. Part. Syst. Charact.* **2014,** *31,* 317–336. doi:10.1002/ppsc.201300231
5. Oumellal, Y.; Rougier, A.; Nazri, G. A.; Tarascon, J.-M.; Aymard, L. *Nat. Mater.* **2008,** *7,* 916–921. doi:10.1038/nmat2288
6. Oumellal, Y.; Rougier, A.; Tarascon, J.-M.; Aymard, L. *J. Power Sources* **2009,** *192,* 698–702. doi:10.1016/j.jpowsour.2009.03.003
7. *HSC Chemistry,* v5.11; Chemistry Software Ltd.: South Nutfield, Surrey, UK.
8. Griessen, R.; Riesterer, T. Hydrogen in intermetallic compounds I. In *Hydrogen in intermetallic compounds I;* Schlapbach, L., Ed.; Topics in Applied Physics, Vol. 63; Springer, 1988; pp 219–284. doi:10.1007/3540183337_13
9. Sandrock, G. D.; Huston, E. L. *CHEMTECH* **1981,** *11,* 754–762.
10. Oumellal, Y.; Zaïdi, W.; Bonnet, J.-P.; Cuevas, F.; Latroche, M.; Zhang, J.; Bobet, J.-L.; Rougier, A.; Aymard, L. *Int. J. Hydrogen Energy* **2012,** *37,* 7831–7835. doi:10.1016/j.ijhydene.2012.01.107
11. Oumellal, Y. Réactivité électrochimique des hydrures métalliques vis-à-vis du lithium. Ph.D. Thesis, Université de Picardie, Jules Verne, France, 2009.
12. Bououdina, M.; Oumellal, Y.; Dupont, L.; Aymard, L.; Al-Gharni, H.; Al-Hajry, A.; Maark, T. A.; De Sarkar, A.; Ahuja, R.; Deshpande, M. D.; Qian, Z.; Rahane, A. B. *Mater. Chem. Phys.* **2013,** *141,* 348–354. doi:10.1016/j.matchemphys.2013.05.021
13. Zaïdi, W.; Bonnet, J.-P.; Zhang, J.; Cuevas, F.; Latroche, M.; Couillaud, S.; Bobet, J.-L.; Sougrati, M. T.; Jumas, J.-C.; Aymard, L. *Int. J. Hydrogen Energy* **2013,** *38,* 4798–4808. doi:10.1016/j.ijhydene.2013.01.157
14. Zhang, J.; Cuevas, F.; Zaïdi, W.; Bonnet, J.-P.; Aymard, L.; Bobet, J.-L.; Latroche, M. *J. Phys. Chem. C* **2011,** *115,* 4971–4979. doi:10.1021/jp2005293
15. Hanada, N.; Kamura, A.; Suzuki, H.; Takai, K.; Ichikawa, T.; Kojima, Y. *J. Alloys Compd.* **2011,** *509,* S584–S587. doi:10.1016/j.jallcom.2010.10.069
16. Fleischmann, S.; Bekaert, E.; Emmel, U.; Wohlfahrt-Mehrens, M., Eds. *Trilithium hexahydroaluminate (Li_3AlH_6) as negative electrode material for lithium-ion batteries,* 2nd International Conference on Materials for Energy, Karlsruhe, Germany, May 12–16, 2013; EnMat II: Karlsruhe, Germany, 2013.
17. Latroche, M.; Cuevas, F.; Zhang, J., Eds. *Nanostuctured Metal Hydrides as Efficient Anode Materials for Advanced Batteries,* TMS 2014, 143rd annual meeting, San Diego, California, USA, Feb 16–20, 2014; San Diego, California, USA, 2014.
18. Teprovich, J. A., Jr.; Zhang, J.; Colón-Mercado, H.; Cuevas, F.; Peters, B.; Greenway, S.; Zidan, R.; Latroche, M. *J. Phys. Chem. C* **2015,** *119,* 4666–4674. doi:10.1021/jp5129595
19. Zaidi, W. Hydrures: matériaux de conversion pour accumulateurs lithium-ion. Ph.D. Thesis, Université de Picardie, Jules Verne, France, 2013.
20. Bobet, J.-L.; Pechev, S.; Chevalier, B.; Darriet, B. *J. Mater. Chem.* **1999,** *9,* 315–318. doi:10.1039/a804971h
21. Nayeb-Hashemi, A.; Clark, J. *J. Phase Equilib.* **1985,** *6,* 238–244.
22. Zhang, J.; Zaïdi, W.; Paul-Boncour, V.; Provost, K.; Michalowicz, A.; Cuevas, F.; Latroche, M.; Belin, S.; Bonnet, J.-P.; Aymard, L. *J. Mater. Chem. A* **2013,** *1,* 4706–4717. doi:10.1039/c3ta01482g
23. Selvam, P.; Viswanathan, B.; Swamy, C. S.; Srinivasan, V. *Int. J. Hydrogen Energy* **1988,** *13,* 749–759. doi:10.1016/0360-3199(88)90036-5
24. Selvam, P.; Viswanathan, B.; Swamy, C. S.; Srinivasan, V. *Thermochim. Acta* **1988,** *125,* 1–8. doi:10.1016/0040-6031(88)87205-8
25. Mg hydride based system conversion reaction with lithium ion - Unpublished work.
26. Couillaud, S.; Kirikova, M.; Zaïdi, W.; Bonnet, J.-P.; Marre, S.; Aymonier, C.; Zhang, J.; Cuevas, F.; Latroche, M.; Aymard, L.; Bobet, J.-L. *J. Alloys Compd.* **2013,** *574,* 6–12. doi:10.1016/j.jallcom.2013.03.229
27. Braga, M. H.; El-Azab, A. *Phys. Chem. Chem. Phys.* **2014,** *16,* 23012–23025. doi:10.1039/C4CP01815J
28. Latroche, M.; Kalisvaart, P.; Notten, P. H. L. *J. Solid State Chem.* **2006,** *179,* 3024–3032. doi:10.1016/j.jssc.2006.05.032
29. Libowitz, G. G. *The Solid State Chemistry of Binary Metal Hydrides;* W.A. Benjamin: New York, 1965.
30. Sandia National Laboratories, Hydride Information Center. http://www.sandia.gov/ (accessed Oct 8, 2014).
31. Moysés Araùjo, C.; Ahuja, R. *J. Alloys Compd.* **2005,** *404–406,* 220–223. doi:10.1016/j.jallcom.2004.10.085
32. Gremaud, R.; Broedersz, C. P.; Borsa, D. M.; Borgschulte, A.; Mauron, P.; Schreuders, H.; Rector, J. H.; Dam, B.; Griessen, R. *Adv. Mater.* **2007,** *19,* 2813–2817. doi:10.1002/adma.200602560
33. Vermeulen, P.; Niessen, R. A. H.; Notten, P. H. L. *Electrochem. Commun.* **2006,** *8,* 27–32. doi:10.1016/j.elecom.2005.10.013
34. Aymard, L.; Lenain, C.; Courvoisier, L.; Salver-Disma, F.; Tarascon, J.-M. *J. Electrochem. Soc.* **1999,** *146,* 2015–2023. doi:10.1149/1.1391884
35. Disma, F.; Aymard, L.; Dupont, L.; Tarascon, J.-M. *J. Electrochem. Soc.* **1996,** *143,* 3959–3972. doi:10.1149/1.1837322
36. Dahn, J. R.; Sleigh, A. K.; Shi, H.; Reimers, J. N.; Zhong, Q.; Way, B. M. *Electrochim. Acta* **1993,** *38,* 1179–1191. doi:10.1016/0013-4686(93)80048-5
37. Liang, G.; Huot, J.; Boily, S.; Schulz, R. *J. Alloys Compd.* **2000,** *305,* 239–245. doi:10.1016/S0925-8388(00)00708-8
38. Liang, G.; Huot, J.; Boily, S.; Van Neste, A.; Schulz, R. *J. Alloys Compd.* **1999,** *292,* 247–252. doi:10.1016/S0925-8388(99)00442-9
39. Barkhordarian, G.; Klassen, T.; Bormann, R. *J. Alloys Compd.* **2004,** *364,* 242–246. doi:10.1016/S0925-8388(03)00530-9
40. Barkhordarian, G.; Klassen, T.; Bormann, R. *Scr. Mater.* **2003,** *49,* 213–217. doi:10.1016/S1359-6462(03)00259-8

41. Ikeda, S.; Ichikawa, T.; Yamaguchi, S.; Miyaoka, H.; Kojima, Y. *J. Jpn. Inst. Energy* **2014,** *93,* 926–930. doi:10.3775/jie.93.926
42. Bhat, V. V.; Rougier, A.; Aymard, L.; Darok, X.; Nazri, G.; Tarascon, J. M. *J. Power Sources* **2006,** *159,* 107–110. doi:10.1016/j.jpowsour.2006.04.059
43. Borgschulte, A.; Lohstroh, W.; Westerwaal, R. J.; Schreuders, H.; Rector, J. H.; Dam, B.; Griessen, R. *J. Alloys Compd.* **2005,** *404–406,* 699–705. doi:10.1016/j.jallcom.2005.01.137
44. Nakayama, H.; Matsunaga, T.; Nobuhara, K.; Kon, M. Anode material, metal secondary battery, and method for production of anode material. U.S. Patent Appl. WO 2012/007830 A1, Jan 19, 2012.
45. Nakayama, H.; Nobuhara, K.; Kon, M.; Matsunaga, T. *218th ECS Meeting Abstract* **2010,** *1002,* 1052.
46. Zaïdi, W.; Oumellal, Y.; Bonnet, J.-P.; Zhang, J.; Cuevas, F.; Latroche, M.; Bobet, J.-L.; Aymard, L. *J. Power Sources* **2011,** *196,* 2854–2857. doi:10.1016/j.jpowsour.2010.11.048
47. Heinze, T.; Koschella, A. *Macromol. Symp.* **2005,** *223,* 13–40. doi:10.1002/masy.200550502
48. Heinze, T. *Macromol. Chem. Phys.* **1998,** *199,* 2341–2364. doi:10.1002/(SICI)1521-3935(19981101)199:11<2341::AID-MACP2341>3.0.CO;2-J
49. Urbonaite, S.; Baglien, I.; Ensling, D.; Edström, K. *J. Power Sources* **2010,** *195,* 5370–5373. doi:10.1016/j.jpowsour.2010.03.042
50. Guo, J.; Wang, C. *Chem. Commun.* **2010,** *46,* 1428–1430. doi:10.1039/b918727h
51. Mazouzi, D.; Lestriez, B.; Roué, L.; Guyomard, D. *Electrochem. Solid-State Lett.* **2009,** *12,* A215–A218. doi:10.1149/1.3212894
52. Bridel, J.-S.; Azaïs, T.; Morcrette, M.; Tarascon, J.-M.; Larcher, D. *Chem. Mater.* **2010,** *22,* 1229–1241. doi:10.1021/cm902688w
53. Hochgatterer, N. S.; Schweiger, M. R.; Koller, S.; Raimann, P. R.; Wöhrle, T.; Wurm, C.; Winter, M. *Electrochem. Solid-State Lett.* **2008,** *11,* A76–A80. doi:10.1149/1.2888173
54. Beattie, S. D.; Larcher, D.; Morcrette, M.; Simon, B.; Tarascon, J.-M. *J. Electrochem. Soc.* **2008,** *155,* A158–A163. doi:10.1149/1.2817828
55. Li, J.; Lewis, R. B.; Dahn, J. R. *Electrochem. Solid-State Lett.* **2007,** *10,* A17–A20. doi:10.1149/1.2398725
56. Lestriez, B.; Bahri, S.; Sandu, I.; Roué, L.; Guyomard, D. *Electrochem. Commun.* **2007,** *9,* 2801–2806. doi:10.1016/j.elecom.2007.10.001
57. Dimov, N.; Xia, Y.; Yoshio, M. *J. Power Sources* **2007,** *171,* 886–893. doi:10.1016/j.jpowsour.2007.06.026
58. Yoshio, M.; Tsumura, T.; Dimov, N. *J. Power Sources* **2006,** *163,* 215–218. doi:10.1016/j.jpowsour.2005.12.078
59. Buqa, H.; Holzapfel, M.; Krumeich, F.; Veit, C.; Novák, P. *J. Power Sources* **2006,** *161,* 617–622. doi:10.1016/j.jpowsour.2006.03.073
60. Liu, W.-R.; Yang, M.-H.; Wu, H.-C.; Chiao, S. M.; Wu, N.-L. *Electrochem. Solid-State Lett.* **2005,** *8,* A100–A103. doi:10.1149/1.1847685
61. Heinze, T.; Heinze, U. *Macromol. Rapid Commun.* **1997,** *18,* 1033–1040. doi:10.1002/marc.1997.030181206
62. Schüth, F. *Chem. Mater.* **2014,** *26,* 423–434. doi:10.1021/cm402791v
63. Zlotea, C.; Latroche, M. *Colloids Surf., A* **2013,** *439,* 117–130. doi:10.1016/j.colsurfa.2012.11.043
64. Zlotea, C.; Chevalier-César, C.; Léonel, E.; Leroy, E.; Cuevas, F.; Dibandjo, P.; Vix-Guterl, C.; Martens, T.; Latroche, M. *Faraday Discuss.* **2011,** *151,* 117–131. doi:10.1039/c0fd00016g
65. Nielsen, T. K.; Manickam, K.; Hirscher, M.; Besenbacher, F.; Jensen, T. R. *ACS Nano* **2009,** *3,* 3521–3528. doi:10.1021/nn901072w
66. Zhao-Karger, Z.; Hu, J.; Roth, A.; Wang, D.; Kübel, C.; Lohstroh, W.; Fichtner, M. *Chem. Commun.* **2010,** *46,* 8353–8355. doi:10.1039/c0cc03072d
67. Paskevicius, M.; Sheppard, D. A.; Buckley, C. E. *J. Am. Chem. Soc.* **2010,** *132,* 5077–5083. doi:10.1021/ja908398u
68. Oumellal, Y.; Zlotea, C.; Bastide, S.; Cachet-Vivier, C.; Léonel, E.; Sengmany, S.; Leroy, E.; Aymard, L.; Bonnet, J.-P.; Latroche, M. *Nanoscale* **2014,** *6,* 14459–14466. doi:10.1039/C4NR03444A
69. Zhu, C.; Hosokai, S.; Matsumoto, I.; Akiyama, T. *Cryst. Growth Des.* **2010,** *10,* 5123–5128. doi:10.1021/cg100856n
70. Matsumoto, I.; Akiyama, T.; Nakamura, Y.; Akiba, E. *J. Alloys Compd.* **2010,** *507,* 502–507. doi:10.1016/j.jallcom.2010.07.218
71. Zhu, C.; Hayashi, H.; Saita, I.; Akiyama, T. *Int. J. Hydrogen Energy* **2009,** *34,* 7283–7290. doi:10.1016/j.ijhydene.2009.06.080
72. Nakaya, U. *Snow Crystals, Natural and Artificial;* Harvard University Press: Cambridge, MA, USA, 1954. doi:10.4159/harvard.9780674182769
73. Ramzan, M.; Lebègue, S.; Ahuja, R. *Int. J. Hydrogen Energy* **2010,** *35,* 10373–10376. doi:10.1016/j.ijhydene.2010.07.024
74. Mason, T. H.; Liu, X.; Hong, J.; Graetz, J.; Majzoub, E. H. *J. Phys. Chem. C* **2011,** *115,* 16681–16687. doi:10.1021/jp203056n
75. Li, D.; Zhang, T.; Yang, S.; Tao, Z.; Chen, J. *J. Alloys Compd.* **2011,** *509,* 8228–8234. doi:10.1016/j.jallcom.2011.05.084
76. Qian, Z.; Jiang, X.; De Sarkar, A.; Adit Maark, T.; Deshpande, M. D.; Bououdina, M.; Johansson, B.; Ahuja, R. *Solid State Ionics* **2014,** *258,* 88–91. doi:10.1016/j.ssi.2014.02.007
77. Qian, Z.; De Sarkar, A.; Adit Maark, T.; Jiang, X.; Deshpande, M. D.; Bououdina, M.; Ahuja, R. *Appl. Phys. Lett.* **2013,** *103,* 033902. doi:10.1063/1.4813596
78. Wietelmann, U. *Chem. Ing. Tech.* **2014,** *86,* 2190–2194. doi:10.1002/cite.201400097
79. Fichtner, M. *J. Alloys Compd.* **2011,** *509* (Suppl. 2), S529–S534. doi:10.1016/j.jallcom.2010.12.179

License and Terms